VOYAGER SUPPORT STUDY

LM DESCENT STAGE APPLICATIONS

FINAL REPORT

VOLUME IV

GUIDANCE AND CONTROL

STUDIES

N68-10066 (ACCESSION NUMBER) (THRU)
337 (PAGES) 1 (CODE)
CR-89996 (NASA CR OR TMX OR AD NUMBER) 31 (CATEGORY)
FF No. 602(C)

TRW
SYSTEMS GROUP

04480-6007-R000

VOYAGER SUPPORT STUDY

LM DESCENT STAGE APPLICATIONS

FINAL REPORT

VOLUME IV

GUIDANCE AND CONTROL STUDIES

JULY 1967

Prepared for
California Institute of Technology
Jet Propulsion Laboratory
Pasadena, California

Under Contract Number 951113

TRW SYSTEMS
ONE SPACE PARK
REDONDO BEACH, CALIFORNIA

PRECEDING PAGE BLANK NOT FILMED.

PREFACE

The LM Descent Stage Application Task of the TRW Voyager Support Study involves extending and updating selected areas of the TRW Voyager Spacecraft Phase IA Task B preliminary design. The work emphasizes propulsion considerations, and the areas of interest relate to the use of liquid propulsion (specifically utilizing the LM Descent Engine) for the Voyager spacecraft application. Potential problems directly within the propulsion subsystem as well as those relating to integration of propulsion with other subsystems are covered by this task.

The work is made up of five major subtasks which have been carried out and reported individually. The LM Descent Stage Applications Final Report therefore consists of five volumes as follows:

Volume I	Propulsion Studies, February 1967
Volume II	Thermal Control Studies, February 1967
Volume III	Propellant Hydrodynamic Studies, February 1967
Volume IV	Guidance and Control Studies, July 1967
Volume V	Configuration Study, July 1967

PRECEDING PAGE BLANK NOT FILMED.

CONTENTS

		Page
1.	INTRODUCTION	1
2.	PROPELLANT SLOSH INTERACTION DURING COAST	3
2.1	Introduction	3
2.2	Cruise Mode With Capsule	7
2.2.1	Models and General Assumptions	7
2.2.2	Search for Reinforcement Without Disturbance	10
2.2.3	Search for Reinforcement With Solar Pressure Disturbance Torque	12
2.2.4	Recovery From Initial Conditions	25
2.2.5	Slosh Mass Variations	26
2.2.6	Attitude Control Parameter Variations	26
2.3	Cruise Mode Without Capsule	41
2.3.1	Search for Reinforcement Without Disturbance	41
2.3.2	Search for Reinforcement With Solar Pressure Disturbance Torque	43
2.3.3	Recovery From Initial Conditions	43
2.3.4	Slosh Mass Variations	44
2.3.5	Attitude Control Parameter Variation	44
2.4	Transition From Powered Flight To Cruise	44
2.4.1	Configuration With Capsule	65
2.4.2	Configuration Without Capsule	90
2.5	Conclusions	117
3.	POWERED FLIGHT STABILITY	125
3.1	Introduction	125
3.2	Stability With Capsule On	128
3.3	Stability With Capsule Off	145
3.4	Bus Propellant Slosh Damping	146
3.4.1	Mars Orbit Insertion	155
3.4.2	Mars Orbit Trim	155
3.5	Capsule Propellant Slosh Damping	155
3.6	Solar Array Struts	168
3.7	Autopilot Filtering	183
3.7.1	Noise Filtering	183
3.7.2	Lead-Lag Filter Change	184
3.8	Electronic Integrators	184

CONTENTS (Continued)

			Page
	3.8.1	Attitude and Engine Angle Interpretation	203
	3.8.2	Attitude Integration Only	204
4.	THRUST VECTOR POINTING ERROR		233
	4.1	Introduction	233
	4.2	TVC Errors Without Electronic Integrators	238
	4.3	TVC Errors With Attitude Feedback Integration	241
	4.4	TVC Errors With Attitude and Engine Angle Feedback Integration	243
5.	ACTUATOR DESIGN		250
	5.1	Introduction	250
	5.2	Design Description	251
	5.2.1	Mathematical Model	251
	5.2.2	Reliability	253
	5.2.3	Power	254
	5.2.4	Size and Weight	254
	5.3	Control System Performance	254
	5.3.1	Control System Nonlinear Model	255
	5.3.2	Nominal Actuator Design	256
	5.3.3	Without Initial Attitude Rates	281
	5.3.4	Stability Boundary With Initial Attitude Rates	281
6.	REFERENCES		313
APPENDIX A		VOYAGER NATURAL MODES AND FREQUENCIES	315

ILLUSTRATIONS

		Page
1.	Cruise Mode Block Diagram	7
2.	Low g Slosh Model	8
3.	Phase Plane Plot, ω_{11} = 0.1048 Rad/Sec	13
4.	Phase Plane Plot, ω_{11} = 0.0151 Rad/Sec	15
5.	Phase Plane Plot, ω_{11} = 0.0225 Rad/Sec	17
6.	Phase Plane Plot, ω_{11} = 0.02 Rad/Sec	19
7.	Phase Plane Plot, ω_{11} = 0.0150 Rad/Sec	23
8.	Phase Plane Plot, ω_{11} = 0.01953 Rad/Sec	27
9.	Phase Plane Plot, ω_{11} = 0.02 Rad/Sec	29
10.	Phase Plane Plot	31
11.	Phase Plane Plot, ω_{11} = 0.02 Rad/Sec	33
12.	Phase Plane Plot, ω_{11} = 0.020 Rad/Sec	35
13.	Phase Plane Plot, ω_{11} = 0.02 Rad/Sec	37
14.	Phase Plane Plot, ω_{11} = 0.02 Rad/Sec	39
15.	Phase Plane Plot, ω_{11} = 0.01489 Rad/Sec	45
16.	Phase Plane Plot, ω_{11} = 0.01489 Rad/Sec	47
17.	Phase Plane Plot, ω_{11} = 0.02 Rad/Sec	49
18.	Phase Plane Plot, ω_{11} = 0.02 Rad/Sec	51
19.	Phase Plane Plot, ω_{11} = 0.020 Rad/Sec	53
20.	Phase Plane Plot, ω_{11} = 0.020 Rad/Sec	55
21.	Phase Plane Plot, ω_{11} = 0.02 Rad/Sec	57
22.	Phase Plane Plot, ω_{11} = 0.02 Rad/Sec	59
23.	Phase Plane Plot, ω_{11} = 0.02 Rad/Sec	61
24.	Phase Plane Plot, ω_{11} = 0.02 Rad/Sec	63

ILLUSTRATIONS (Continued)

		Page
25.	Rate Gyro Mode Block Diagram	65
26.	Nominal Rate Gyro Mode Performance, Configuration with Capsule	67
27.	Rate Gyro Mode, Configuration with Capsule, DRI Time Constant = 10 Sec, Rigid Body Representation of Vehicle	69
28.	Rate Gyro Mode, Configuration with Capsule, DRI Time Constant = 1 Sec, Rigid Body Representation of Vehicle	71
29.	Rate Gyro Mode, Configuration with Capsule, DRI Time Constant = 1 Sec	73
30.	Rate Gyro Mode, Configuration with Capsule, DRI Filter Removed	77
31.	Rate Gyro Mode, Configuration with Capsule, DRI Filter Limit L = 3 Deg	79
32.	Rate Gyro Mode, Configuration with Capsule, DRI Filter Limit L = 0.2 Deg	81
33.	Rate Gyro Mode, Configuration with Capsule, 0.2 Deg Limit DRI, $x_{11}(o) = x_{21}(o) = +6$ In.	83
34.	Rate Gyro Mode, Configuration with Capsule, 0.2 Deg Limit DRI, $x_{11}(o) = x_{21}(o) = -6$ In.	85
35.	Rate Gyro Mode, Configuration with Capsule, 0.2 Deg Limit DRI, Slosh Mass Increased by 10	87
36.	Position Gyro Mode Block Diagram without Lead-Lag Filter	89
37.	Position Gyro Mode without Lead-Lag Filter	91
38.	Position Gyro Mode Block Diagram with Lead-Lag Filter	93
39.	Position Gyro Mode, Configuration with Capsule, Response with Lead-Lag Filter, $\dot{\theta}(o) = 1.5$ Deg/Sec	95
40.	Position Gyro Mode, Configuration with Capsule, Response with Lead-Lag Filter, $\dot{\theta}(o) = 1.0$ Deg/Sec	97

ILLUSTRATIONS (Continued)

		Page
41.	Position Gyro Mode, Configuration with Capsule, Response with Lead-Lag Filter, $\dot{\theta}(o)$ = 0.5 Deg/Sec	99
42.	Position Gyro Mode, Configuration with Capsule, Response with Lead-Lag Filter, $x_{11}(o) = x_{21}(o)$ = -6 In.	101
43.	Position Gyro Mode, Configuration with Capsule, Response with Lead-Lag Filter, Slosh Mass Increased by Factor of 10	103
44.	Rate Gyro Mode to Position Gyro Mode Sequence, Configuration with Capsule	105
45.	Rate Gyro Mode, Configuration without Capsule, DRI Filter L = 0.2 Deg, $\dot{\theta}(o)$ = 1.5 Deg/Sec	107
46.	Rate Gyro Mode, Configuration without Capsule, DRI Filter L = 0.2 Deg, $x_{11}(o) = x_{21}(o)$ = +6 In.	109
47.	Rate Gyro Mode, Configuration without Capsule, DRI Filter L = 0.2 Deg, $x_{11}(o) = x_{21}(o)$ = -6 In.	111
48.	Rate Gyro Mode, Configuration without Capsule, DRI Filter L = 0.2 Deg, Slosh Mass Increased by Factor of 10	113
49.	Position Gyro Mode, Configuration without Capsule, Response with Lead-Lag Filter, $\dot{\theta}(o)$ = 1.5 Deg/Sec	115
50.	Position Gyro Mode, Configuration without Capsule, Response with Lead-Lag Filter, $x_{11}(o) = x_{21}(o)$ = +6 In.	119
51.	Position Gyro Mode, Configuration without Capsule, Response with Lead-Lag Filter, $x_{11}(o) = x_{21}(o)$ = -6 In.	121
52.	Position Gyro Mode, Configuration without Capsule, Response with Lead-Lag Filter, Slosh Mass Increased by Factor of 10	123
53.	Block Diagram of the Powered Flight Control System Model	126
54.	Matrix of Homogeneous Equations	129

ILLUSTRATIONS (Continued)

		Page
55.	Gain-Phase Plot, Start MCC, with Capsule	137
56.	Gain-Phase Plot, Start MOI, with Capsule	139
57.	Gain-Phase Plot, End MOI, with Capsule	141
58.	Gain-Phase Plot, MOT, with Capsule	143
59.	Gain-Phase Plot, MCC, without Capsule	147
60.	Gain-Phase Plot, Start MOI, without Capsule	149
61.	Gain-Phase Plot, End MOI, without Capsule	151
62.	Gain-Phase Plot, MOT, without Capsule	153
63.	Gain-Phase Plot, End MOI, without Capsule, Nominal Bus Slosh Damping	157
64.	Gain-Phase Plot, End MOI, without Capsule, 4X Nominal Bus Slosh Damping	159
65.	Gain-Phase Plot, End MOI, without Capsule, 8X Nominal Bus Slosh Damping	161
66.	Gain-Phase Plot, MOT, without Capsule, 4X Nominal Bus Slosh Damping	163
67.	Gain-Phase Plot, MOT, without Capsule, 8X Nominal Bus Slosh Damping	165
68.	Slosh Dome Damping Versus Slosh Mass Displacement	167
69.	Gain-Phase Plot, Start MOI, with Capsule, 0.5X Nominal Capsule Slosh Damping	169
70.	Gain-Phase Plot, Start MOI, with Capsule, 0.25X Nominal Capsule Slosh Damping	171
71.	Gain-Phase Plot, Start MOI, with Capsule, 0.125X Nominal Capsule Slosh Damping	173
72.	Gain-Phase Plot, MCC, with Capsule, Solar Array Struts Added	175
73.	Gain-Phase Plot, Start MOI, with Capsule, Solar Array Struts Added	177

ILLUSTRATIONS (Continued)

		Page
74.	Gain-Phase Plot, End MOI, with Capsule, Solar Array Struts Added	179
75.	Gain-Phase Plot, MOT, with Capsule, Solar Array Struts Added	181
76.	Gain-Phase Plot, End MOI, with Capsule, Solar Array Struts Added, Noise Filter Added	185
77.	Gain-Phase Plot, End MOI, with Capsule, Solar Array Struts Added, Noise Filter Added	187
78.	Gain-Phase Plot, End MOI, with Capsule, Solar Array Struts Added, Noise Filter Added	189
79.	Gain-Phase Plot, Start MOI, with Capsule, Solar Array Struts Added, Noise Filter Added	191
80.	Gain-Phase Plot, MOT, with Capsule, Solar Array Struts Added, Noise Filter Added	193
81.	Gain-Phase Plot, MCC, with Capsule, Solar Array Struts Added, Lead-Lag Filter Change	195
82.	Gain-Phase Plot, Start MOI, with Capsule, Solar Array Struts Added, Lead-Lag Filter Change	197
83.	Gain-Phase Plot, End MOI, with Capsule, Solar Array Struts Added, Lead-Lag Filter Change	199
84.	Gain-Phase Plot, MOT, with Capsule, Solar Array Struts Added, Lead-Lag Filter Change	201
85.	Gain-Phase Plot, Start MOI, with Capsule, Solar Array Struts Added, Integral Attitude and Engine Angle Feedback	205
86.	Gain-Phase Plot, Start MOI, with Capsule, Solar Array Struts Added, Integral Attitude and Engine Angle Feedback	207
87.	Gain-Phase Plot, Start MOI, with Capsule, Solar Array Struts Added, Integral Attitude and Engine Angle Feedback	209
88.	Gain-Phase Plot, Start MOI, with Capsule, Solar Array Struts Added, Integral Attitude and Engine Angle Feedback	211

		Page
89.	Gain-Phase Plot, End MOI, with Capsule, Solar Array Struts Added, Integral Attitude and Engine Angle Feedback	213
90.	Gain-Phase Plot, MCC, with Capsule, Solar Array Struts Added, Integral Attitude and Engine Angle Feedback	215
91.	Gain-Phase Plot, MCC, with Capsule, Solar Array Struts Added, Integral Attitude and Engine Angle Feedback	217
92.	Gain-Phase Plot, MOT, with Capsule, Solar Array Struts Added, Integral Attitude and Engine Angle Feedback	219
93.	Gain-Phase Plot, MOT, with Capsule, Solar Array Struts Added, Integral Attitude and Engine Angle Feedback	221
94.	Gain-Phase Plot, Start MOI, with Capsule, Solar Array Struts Added, Integral Attitude and Engine Angle Feedback	223
95.	Gain-Phase Plot, Start MOI, with Capsule, Solar Array Struts Added, Integral Attitude and Engine Angle Feedback	225
96.	Gain-Phase Plot, End MOI, with Capsule, Solar Array Struts Added	227
97.	Gain-Phase Plot, MCC, with Capsule, Solar Array Struts Added	229
98.	Gain-Phase Plot, MOT, with Capsule, Solar Array Struts Added	231
99.	Coordinates and Angles Used in Analysis	235
100.	Thrust Vector Pointing Error Model	236
101.	Gain and Phase Margins without Electronic Integrators	238
102.	ϵ_T without Electronic Integrators	239
103.	V_T without Electronic Integrators	239
104.	Steady-State Orientation without Electronic Integrators	240

ILLUSTRATIONS (Continued)

		Page
105.	Gain and Phase Margins with Attitude Feedback Integration	241
106.	ϵ_T with Attitude Feedback Integration	242
107.	V_T with Attitude Feedback Integration	242
108.	Steady-State Orientation with Attitude Feedback Integration	243
109.	Gain and Phase Margins with Attitude and Engine Angle Feedback Integration, $K_{I\delta}$, 0.125	244
110.	Gain and Phase Margins with Attitude and Engine Angle Feedback Integration, $K_{I\delta}$ = 0.02	244
111.	$_T$ with Attitude and Engine Angle Feedback Integration	245
112.	V_T with Attitude and Engine Angle Feedback Integration	245
113.	Steady-State Orientation with Attitude and Engine Angle Feedback Integration	246
114.	Block Diagram of Thrust Vector Control Actuator	252
115.	Nominal Actuation System, Vehicle Attitude Versus Time	257
116.	Nominal Actuation System, Vehicle Rate Versus Time	259
117.	Nominal Actuation System, Attitude Rate Versus Vehicle Attitude	261
118.	Nominal Actuation System, Engine Angle Versus Time	263
119.	Nominal Actuation System, Actuator Rate Versus Time	265
120.	Nominal Actuation System, Slosh Amplitude Versus Time	267
121.	Nominal Actuation System, Vehicle Attitude Versus Time	269
122.	Nominal Actuation System, Attitude Rate Versus Time	271

ILLUSTRATIONS (Continued)

		Page
123.	Nominal Actuation System, Attitude Rate Versus Vehicle Attitude	273
124.	Nominal Actuation System, Engine Angle Versus Time	275
125.	Nominal Actuation System, Actuator Rate Versus Time	277
126.	Nominal Actuation System, Slosh Amplitude Versus Time	279
127.	Attitude Rate Versus Vehicle Attitude	283
128.	Attitude Rate Versus Vehicle Attitude	285
129.	Attitude Rate Versus Vehicle Attitude	287
130.	Attitude Rate Versus Vehicle Attitude	289
131.	Attitude Rate Versus Vehicle Attitude	291
132.	Attitude Rate Versus Vehicle Attitude	293
133.	Attitude Rate Versus Vehicle Attitude	295
134.	Attitude Rate Versus Vehicle Attitude	297
135.	Attitude Rate Versus Vehicle Attitude	299
136.	Initial Attitude Rate Stability Boundary Versus Actuator Rate Limit	301
137.	Vehicle Attitude Versus Time	303
138.	Vehicle Attitude Versus Time	305
139.	Engine Angle Versus Time	307
140.	Actuator Rate Versus Time	309
141.	Slosh Amplitude Versus Time	311

1. INTRODUCTION

The work reviewed in this volume pertains to the performance of the attitude control system during coast phases of the Voyager flight and of the thrust vector control system during powered flight. The control system design and spacecraft properties given in the TRW Systems Task B study report were employed in these studies.

In Section 2 the effects of low-g propellant slosh on the performance of the attitude control system are discussed. By means of analog simulations a search was made for slosh reinforcement modes. In addition, the transition from powered flight to the cruise mode was investigated. These simulations led to the following conclusions:

1) Low-g propellant slosh effects on the coast phase attitude control system performance are not deleterious.

2) For the initial Saturn IVB separation phase, either a position gyro mode with a lead-lag filter or a rate gyro with 0.2-degree modulation limit filter is desirable. Further studies into mode sequences and design variations are recommended.

Section 3 analyzes the stability of the powered flight thrust vector control system. Powered flight propellant slosh and body bending resonance problems are considered. The control system stability margins with various autopilot filter designs, propellant damping variations, and electronic integrator designs are determined. Gain-phase stability plots are given. The major conclusions reached in Section 3 are:

1) Bus propellant slosh modes for nominal mission phases are stable. (This assumes that considerable propellant damping exists at the tank bottom for Mars orbit trim firings without the capsule on.)

2) Bus propellant slosh modes for the abort or contingency configurations (without capsule) are unstable and require damping if these configurations are to be employed.

3) Capsule propellant slosh modes are not significant; however, propellant fill levels of 90 percent or greater in both tanks are desirable to reduce these effects further.

4) The resonance mode of the solar array or aft equipment module poses control system stability problems. The addition of struts to stiffen attachment to the bus is recommended.

5) The use of electronic integrators to reduce trajectory errors is acceptable from stability considerations provided that reasonably low integrator gains are employed.

Section 4 reviews the performance of integral feedback loops in the reduction of powered flight thrust vector pointing errors. These errors were combined with gyro drift errors, ACS errors, etc., to give a total expected thrust vector pointing error. It is concluded that integrator feedback loops in the powered flight control system are desirable to reduce either thrust misalignment trajectory errors or thrust offset and cg offset trajectory errors.

The last section investigates the suitability of the Task B powered flight actuator design for the Voyager spacecraft, employing engine parameters associated with the modified LM descent engine. Actuator design specifications, descriptions, and performance characteristics are given. The performance of the powered flight control system with the nominal actuator design and design variations is investigated. Digital simulation results are included. It is shown that:

1) The Task B electromechanical actuator design is suitable for the Voyager spacecraft. This design provides for more than ample control of the engine and could be reduced in size or reduced in performance requirements to achieve greater reliability.

2) The powered flight control system performance with the Task B actuator design is satisfactory. Reductions in the actuator torque and rate limits would be acceptable.

2. PROPELLANT SLOSH INTERACTION DURING COAST

2.1 INTRODUCTION

The effects of propellant slosh during unpowered flight were investigated. The sustained vehicle accelerations to be expected from vehicle maneuvers and solar radiation forces were computed and found to be less than the critical levels defining the low-g state. Below this critical g level, the capillary and surface tension restoring forces are dominant, producing the spring-mass system described in Reference 1.

This spring-mass system was employed in cruise mode propellant slosh simulation studies for the vehicle with and without the capsule. The model spring constant and mass were varied in an attempt to obtain an undesirable slosh reinforcement mode. The effects of solar pressure disturbances were included to alter the cruise mode control system limit cycle characteristics, thereby possibly aiding the slosh reinforcement. Recovery from initial conditions was investigated and the attitude control design parameters varied. The attitude control system consisted of attitude error signals from the sun and star sensors which activated a derived rate increment (DRI) modulator which in turn activated low level (0.2 pound) gas jets.

Transition between the powered flight and cruise mode was also simulated. The control system modes investigated included a rate gyro mode with DRI variations, including its removal; a rate gyro mode with a low DRI limit, and its response to slosh variations; a position gyro mode with DRI modulators; a position gyro mode with a lead-lag filter, and responses to slosh variations. In addition, a gyro rate to position mode switching sequence was simulated.

The conclusions reached from this study are as follows:

1) Low-g propellant slosh effects upon the cruise mode employing a DRI circuit are initially noticeable but soon become damped to negligible levels after a few limit cycles. After the initial transient from switching into the cruise mode, a single minimum pulse limit cycle ensues; hence, attitude control gas requirements are not increased by low-g slosh effects.

2) Low-g propellant slosh effects on the attitude control system during the transition between the powered flight and cruise mode phases are not significant.

3) The reduction of the DRI filter limit or removal of the filter during the initial S-IVB separation phase is recommended in order to obtain better control system convergence properties. The use of a position gyro mode with an added lead-lag filter or a rate gyro mode with a 0.2-degree DRI filter limit appears to give the desirable convergence characteristics. The use of a lead-limited, lead-lag filter design for the position gyro mode should be further considered.

Although high-g slosh analysis has become well established, very little application to control systems has been made by low-g slosh analysis. As in Reference 1, low g is defined as being less than 7×10^{-5} g for aerozine-50 and less than 2.8×10^{-5} g for N_2O_4. Under an Apollo task, work was initiated by TRW Systems to develop the low-g slosh models based upon the effects of surface tension between the liquid-vapor interface and the contact angle between the liquid and propellant tank, and this work served as a foundation for the low-g slosh models obtained for the Voyager spacecraft. The work performed under the Apollo task is given in References 5, 6, and 7. Reference 4 presents low-g slosh models obtained by the Southwest Research Institute. The same basic approach to the low-g slosh problem as in Reference 1 was taken in the SRI report.

Table 1 lists the phase-dependent acceleration levels sensed by the spacecraft both in the axial direction, due to thrusting and solar radiation forces, and radially due to vehicle maneuver rates. The thrust acceleration due to the gas jet pulsing is not listed since its duration is considerably shorter than the propellant slosh period. The pitch maneuvers require less than 1.5 seconds of thruster on-time, which is negligible compared to the 400-second slosh mode period. The g level over this duration would be 5.7×10^{-4}. Although this level is higher than the specified low-g levels, since its relative duration is extremely short its effect can be represented by an impulsive change in the vehicle angular rate rather than a sustained acceleration level. This is also true for the minimum pulse limit cycles in which the pulse durations are 0.025 second.

Table 1. Vehicle Acceleration Levels (g's)

Phase		
Powered, S-IVB with main engine	205,000-lb thrust	4 axial
Powered, S-IVB with hydrogen venting ullage engines	114-lb thrust	3×10^{-3} axial
Coast, attitude hold in earth eclipse	None	0
Coast, sun acquisition (0.2 deg/sec)	$L\dot{\theta}^2$ centrifugal force	3.5×10^{-6} radial
Coast, magnetometer calibration roll spin (0.22 deg/sec)	$R\dot{\theta}^2$ centrifugal force	3.1×10^{-6} radial
Coast, star search roll spin (0.1 deg/sec)	$R\dot{\theta}^2$ centrifugal force	0.6×10^{-6} radial
Coast, cruise to midcourse corrections	3.2×10^{-5} lb solar radiation force	2×10^{-9} axial
Coast, reorientations during cruise phases (0.2 deg/sec)	$L\dot{\theta}^2$ centrifugal force	3.5×10^{-6} radial
Powered, midcourse correction	1040-lb thrust	5.2×10^{-2} axial with capsule
Coast, cruise to Mars orbit insertion	2.4×10^{-5} lb solar radiation force	1.5×10^{-9} axial
Powered, Mars orbit insertion	7750-lb thrust	0.41 to 0.85 with capsule, 0.48 to 1.17 without capsule
Powered, Mars orbit trim	1040-lb thrust	0.12 with capsule 0.17 without capsule
Coast, Mars orbit cruise	1.6×10^{-5} lb solar radiation force	1×10^{-9} axial

Note: L = distance from slosh mass attach point to vehicle cg;
R = tank radius; θ = vehicle angular rate

The solar radiation force was based on a solar pressure area of 300 ft^2 and a reflectivity coefficient of 0.3. A reflectivity coefficient of unity would increase the solar radiation force by 57 percent.

The acceleration levels during the coast phases are shown to be less than the critical g levels; therefore, the low-g slosh model given in Reference 1 can be employed. Moreover, since the maneuver rates produce centrifugal accelerations less than this level, capillary and surface tension forces are still dominant, and the liquid-vapor interface will follow the rotation of the tank, thereby maintaining its relationship with the tank wall. The surface tension forces are those which shape bubbles in the form of spheres, the minimum surface configuration. Capillary forces tend to produce a nonorthogonal contact of the fluid with the tank walls. Therefore, these forces produce a spherical or hemispherical liquid-vapor boundary at low g levels. If the bubble diameter is larger than the tank diameter, a hemispherical boundary results. Distortion of this boundary surface by propellant mass movement produces a restoring force analogous to the restoring force produced by a balloon when distorted; a slosh spring-mass system therefore results. This spring-mass system is damped by the damping inherent in fluid motion; transition from distorted bubble shapes to spherical bubbles is not possible without this damping since an oscillatory bubble configuration would persist.

The first objectives of this study were to determine if attitude control system propellant requirements increase due to propellant slosh effects and if a corresponding increase in attitude control system angular rates and excursion would result which could affect tracking requirements. For an undisturbed spacecraft, convergence to a single minimum pulse limit cycle is expected. If a double minimum pulse limit cycle is obtained, the propellant requirement for this phase will increase by a factor of 4. Similarly, if a N pulse limit cycle is obtained, the propellant requirement will be increased by a factor of N^2. Therefore, one of the objectives of the study was to determine if a single minimum pulse limit cycle could be maintained.

A second objective was to determine the effects of these slosh modes during transition from a high energy powered flight to the cruise mode energy levels. Various possible control system operating modes and sequences for the transition operation were investigated.

2.2 CRUISE MODE WITH CAPSULE

During cruise, the attitude control system mode is described by Figure 1; the vehicle is locked on the star Canopus and the sun, and the low level (0.2 lb) thrusters are used for control. The major objective of the study was to determine whether excessive fuel consumption or system instabilities could be induced by the interaction between propellant sloshing and the attitude control operation.

2.2.1 Models and General Assumptions

For the control system represented in Figure 1, the nominal values used were

Modulator deadzone, D	=	0.5 deg (Reference 2)
Modulator hysteresis, h	=	0.1 deg (Reference 2)
Modulator time constant, τ	=	50 sec nominally; τ was varied from 25 to 100 sec during the simulation

Two 0.2-pound thrusters are separated by 19.3 feet and provide a pure couple. The minimum impulse bit per jet is 0.005 lb-sec or an equivalent minimum on-time of 0.025 second.

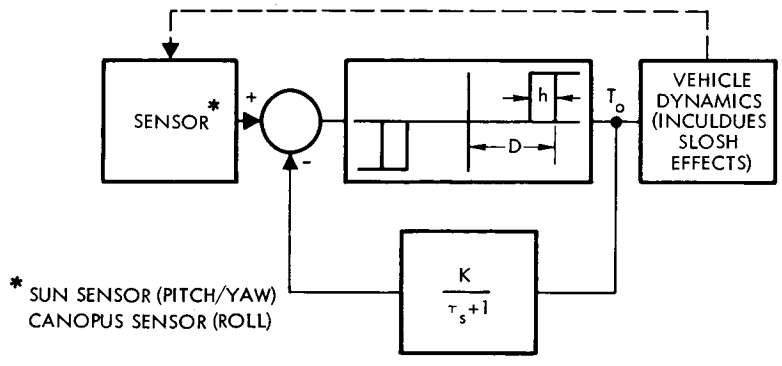

Figure 1. Cruise Mode Block Diagram

The low-g spring-mass slosh model of Reference 1 was used. Solar pressure on the vehicle through cruise imparts much less acceleration to the vehicle than the 10^{-4} g boundary, thus permitting use of the low-g model of Reference 1.

Incorporation of the model into the study is illustrated in Figure 2. The equations of motion for this figure are

$$N_T = \ddot{\phi} I_T + m_{11}(y_{1b} + d_{11})\ddot{x}_{11} + m_{12}(y_{1b} + d_{12})\ddot{x}_{12}$$

$$+ m_{21}(y_{2b} + d_{21})\ddot{x}_{21} + m_{22}(y_{2b} + d_{22})\ddot{x}_{22}$$

$$0 = m_{11}\ddot{x}_{11} + C_{11}\dot{x}_{11} + K_{11}x_{11} + m_{11}(y_{1b} + d_{11})\ddot{\phi}$$

$$0 = m_{12}\ddot{x}_{12} + C_{12}\dot{x}_{12} + K_{12}x_{12} + m_{12}(y_{1b} + d_{12})\ddot{\phi}$$

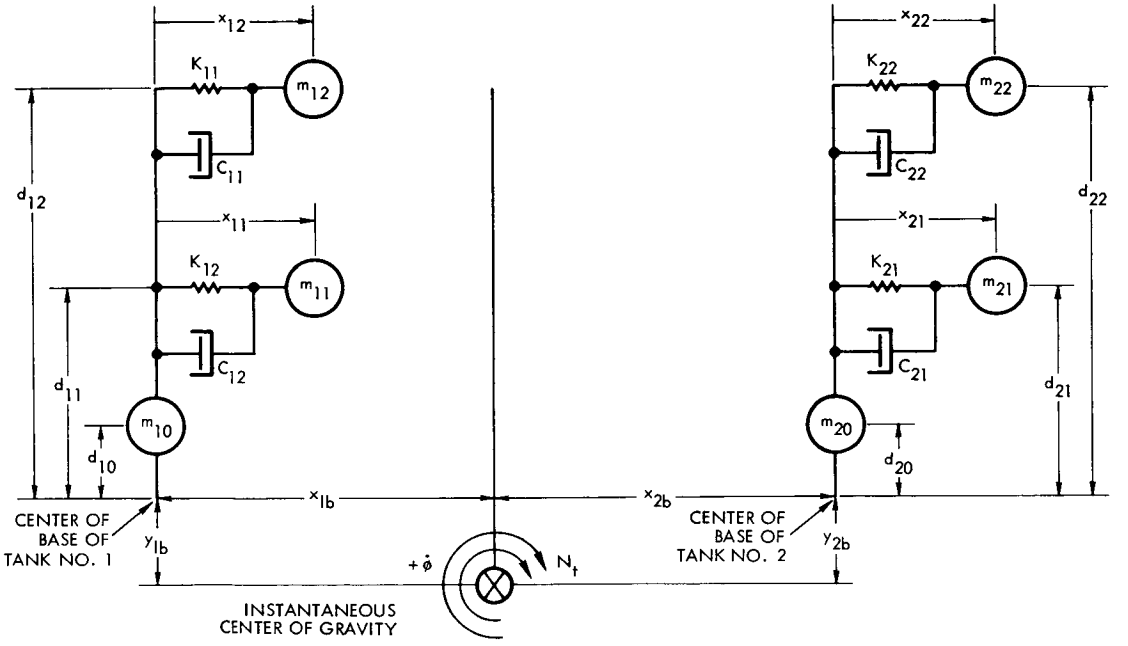

m_{11}	MASS OF FIRST SLOSH MODE IN FUEL TANK	ζ_{12}	DAMPING OF SECOND SLOSH MODE IN FUEL TANK
m_{12}	MASS OF SECOND SLOSH MODE IN FUEL TANK	ζ_{21}	DAMPING OF FIRST SLOSH MODE IN OXIDIZER TANK
m_{21}	MASS OF FIRST SLOSH MODE IN OXIDIZER TANK	ζ_{22}	DAMPING OF SECOND SLOSH MODE IN OXIDIZER TANK
m_{22}	MASS OF SECOND SLOSH MODE IN OXIDIZER TANK	D	MODULATOR DEADZONE
N_T	APPLIED TORQUE (PROVIDED BY CONTROL SYSTEM)	h	MODULATOR HYSTERESIS
I_T	"RIGID BODY" INERTIA OF VEHICLE	τ	MODULATOR TIME CONSTANT
ζ_{11}	DAMPING OF FIRST SLOSH MODE IN FUEL TANK		

Figure 2. Low g Slosh Model

$$0 = m_{21}\ddot{x}_{21} + C_{21}\dot{x}_{21} + K_{21}x_{21} + m_{21}(y_{2b} + d_{21})\ddot{\phi}$$

$$0 = m_{22}\ddot{x}_{22} + C_{22}\dot{x}_{22} + K_{22}x_{22} + m_{22}(y_{2b} + d_{22})\ddot{\phi}$$

Centrifugal acceleration and Coriolis terms are not reflected in these equations since the terms are small, and the linear slosh model does not consider these nonlinear effects.

The fluid levels in both fuel tanks were assumed to be equal; therefore, the fuel slosh masses, spring constants, and slosh mass attach points were identical for both fuel tanks. Hence the two-fuel spring-mass systems could be conveniently lumped into a single spring-mass system. Similarly, since the fluid levels in the oxidizer tanks are equal, the same equivalence can be made for the oxidizer slosh modes.

Only the first slosh modes are simulated since the frequency of the second slosh mode is four to five times the frequency of the first slosh mode and the second mode slosh mass is only about 20 percent of the first mode slosh mass.

The configurations with the largest amount of propellant were assumed to provide the greatest slosh problems. Two configurations were studied: Vehicle with capsule and "full" propellant tanks,* and vehicle without capsule and "full" propellant tanks (abort or contingency configuration). The characteristics of the configurations are as follows:

a) Vehicle with Capsule and "Full" Propellant Tanks

Rigid body inertia = 25.6×10^3 slug-ft^2

Station of center of gravity = 170 in.

Station of oxidizer first slosh mode = 142.2 in.

Station of fuel first slosh mode = 142.7 in.

Mass of oxidizer first slosh mode = 59.6 slugs

Mass of fuel first slosh mode = 35.4 slugs

Natural frequency of oxidizer mode = 0.015 rad/sec (Ref. 3)

Natural frequency of fuel mode = 0.020 rad/sec (Ref. 3)

*The term "full" is defined as the propellant loading at the start of the interplanetary coast phase.

b) Vehicle without Capsule and "Full" Propellant Tanks

The characteristics of the vehicle without capsule are the same as above except the rigid body inertia is 14.6×10^3 slug-ft^2 and the center of gravity is at Station 150.1 inches.

2.2.2 Search for Reinforcement without Disturbance

The following investigation was conducted to determine if the firing of the control jets for attitude correction, coupled with the oxidizer and fuel slosh dynamics, could produce system instability or excessive fuel usage. The basic assumptions for this portion of the study were:

1) No external disturbance torques were applied to the vehicle for the initial investigation.

2) Only the first slosh modes were considered.

3) The frequency of the fuel and oxidizer first slosh modes are made identical. This was done to enable coincidence of maximum fuel and oxidizer slosh mass displacement rates; thereby amplifying the effects of sloshing.

4) The slosh mode was not damped ($C_{11} = C_{21} = 0.0$).

The approach used was:

1) For a nominal attitude control system limit cycle, the number of slosh oscillation periods between sequential firings of the control jets was determined.

2) The frequency of the first slosh mode was varied over a range representing greater than ±90-degree phase shift relative to the nominal ACS limit cycle. The objective was to produce coincidence between the peak amplitudes of the slosh mass displacement rates and firing of the control jets, thereby causing reinforcement.

The nominal limit cycle rate was determined by the following equation:

$$\dot{\theta} \approx \frac{H\ell}{2I_T} = 0.11 \times 10^{-3} \text{ deg/sec}$$

where H = minimum impulse bit per thruster = 0.005 lb-sec

I_T = inertia of vehicle = 25.6×10^3 slug-ft^2

ℓ = moment arm between thrusters = 19.3 ft

For both oxidizer and fuel at the same frequency, the frequency of the slosh coupled with the rigid body was determined from the equations of motion to be the following:

$$\omega' = \omega_{11}\sqrt{1 + \frac{m_{11}(y_{1b} + d_{11})^2 + m_{21}(y_{2b} + d_{21})^2}{I_{T'}}}$$

where $I_{T'} = I_T - m_{11}(y_{1b} + d_{11})^2 - m_{21}(y_{2b} + d_{21})^2$

ω_{11} = uncoupled slosh frequency

All other terms in the equation are defined in the slosh model of Figure 2.

Typically in this vehicle, the coupled frequency is only about 1 percent greater than the uncoupled frequency. Therefore, the uncoupled slosh frequency was used to determine the approximate number of slosh cycles between thruster firing during limit cycling. The number of cycles between firings was determined from the following equation.

$$N \approx \frac{D\omega_{11}}{\dot{\theta}\pi} \approx 22 \text{ cycles for } \omega_{11} = 0.015 \text{ rad/sec (Reference 1)}$$

where N = number of cycles between thruster firings

D = deadzone of modulator

ω' = frequency of coupled slosh mode

$\dot{\theta}$ = limit cycle rate

Therefore, to produce coincidence of a thruster firing during the limit cycle with a slosh mode peak, the slosh frequency should be varied by approximately $\pm(0.25/22)(100) = \pm 1.14$ percent. Another way of looking at this is that varying the slosh frequency by ±1.14 percent shifts the slosh peak by about ±90 degrees relative to the thruster firing time.

The slosh frequency was changed in 0.7 percent increments (ω = 0.0150 ±0.0001, ±0.0002, etc.) until the slosh peak relative to the thruster firing time had been shifted ±110 degrees. Reinforcement of the slosh rates, however, could not be obtained. Figures 3 and 4 are typical of the runs conducted.

Generally (as illustrated in Figures 3 and 4) the nominal magnitude of the positive and negative rates during a limit cycle are not equal. Therefore, the time intervals between control engine firings for the positive and negative positions of the limit cycle are not equal.

The frequency of the slosh mode can be adjusted such that firing of the control engines could produce slosh reinforcement over one portion of the limit cycle. Since the durations of the negative and positive portions of the limit cycle are not equal, such a procedure does not necessarily provide for reinforcement of the slosh oscillations over the second portion of the limit cycle. In fact, because of the relative phasing of the slosh displacement rate and engine firings, the engine firings can oppose and reduce the slosh rates.

With the oxidizer slosh frequency maintained constant at 0.0150 rad/sec, numerous computer runs were made in which the fuel slosh frequency was varied to determine the beating effects of the two frequencies. No deleterious effects were found. Figure 5 is representative of these runs.

Some damping inherent in liquid motion is expected in the fuel and oxidizer slosh modes. This damping increases as the g levels are reduced, as indicated in Reference 1. If baffles or screens are used, the damping will be further increased. As Figure 6 illustrates, even 1 percent damping decays the slosh amplitude to a negligible value by the time another thruster fires.

2.2.3 Search for Reinforcement with Solar Pressure Disturbance Torque

The analysis described in this section was performed to determine whether a constant solar disturbance torque could aid the control system slosh reinforcement. The following assumptions were made:

1) Solar pressure torque, T_S, is constant and unidirectional

2) The solar pressure torque is less than 2×10^{-4} ft-lb. A solar torque of 2×10^{-4} ft-lb is typical of the 20-foot diameter antenna configuration with antenna extended per Reference 3. The Task B configuration with the 9.5-foot diameter antenna has less surface area normal to the sun line, and shorter torque moment arms; therefore, the solar pressure torque on the vehicle is more than a factor of 4 smaller.

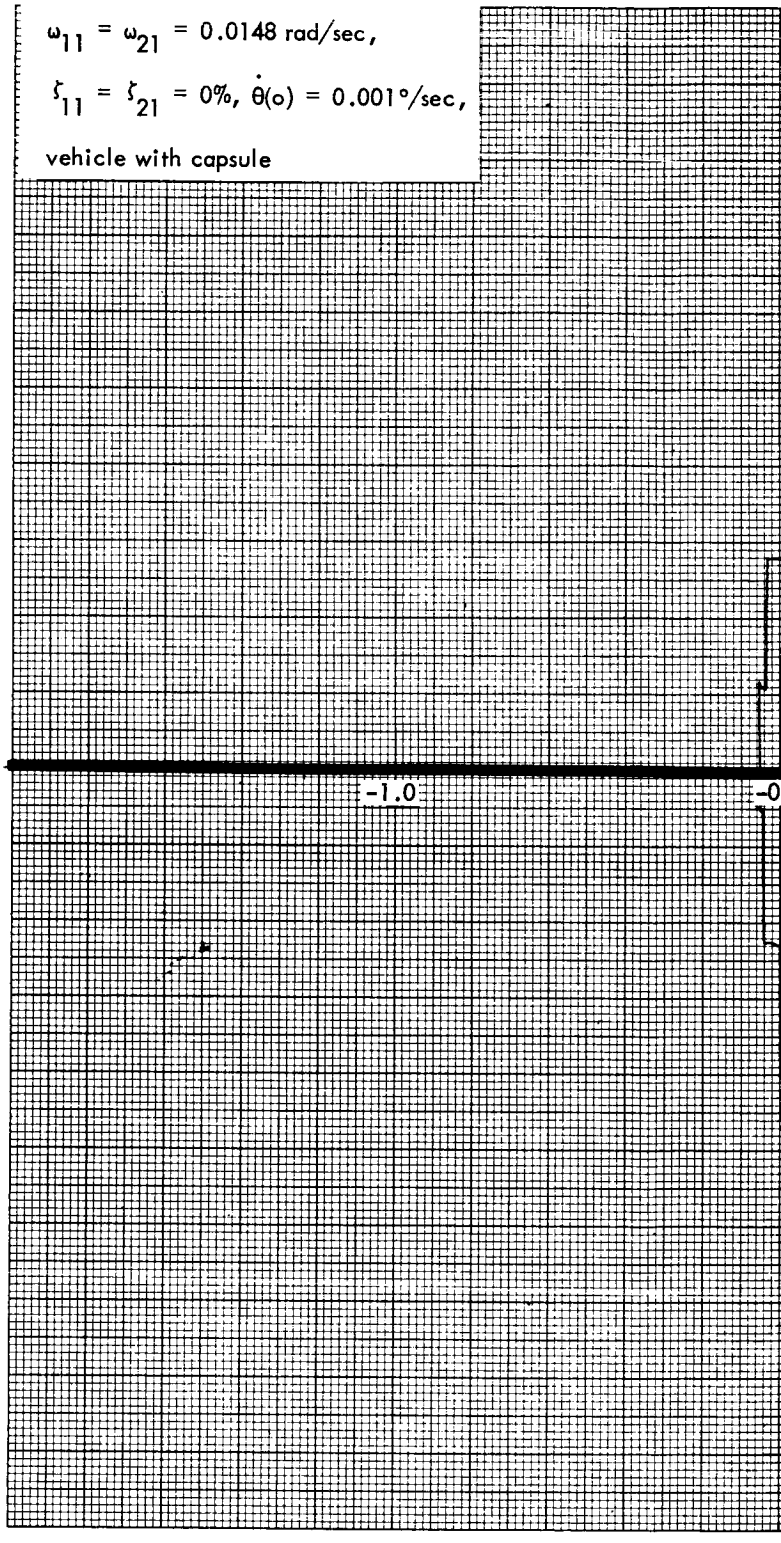
$\omega_{11} = \omega_{21} = 0.0148$ rad/sec,
$\zeta_{11} = \zeta_{21} = 0\%$, $\dot{\theta}(o) = 0.001°$/sec,
vehicle with capsule
-1.0
-0

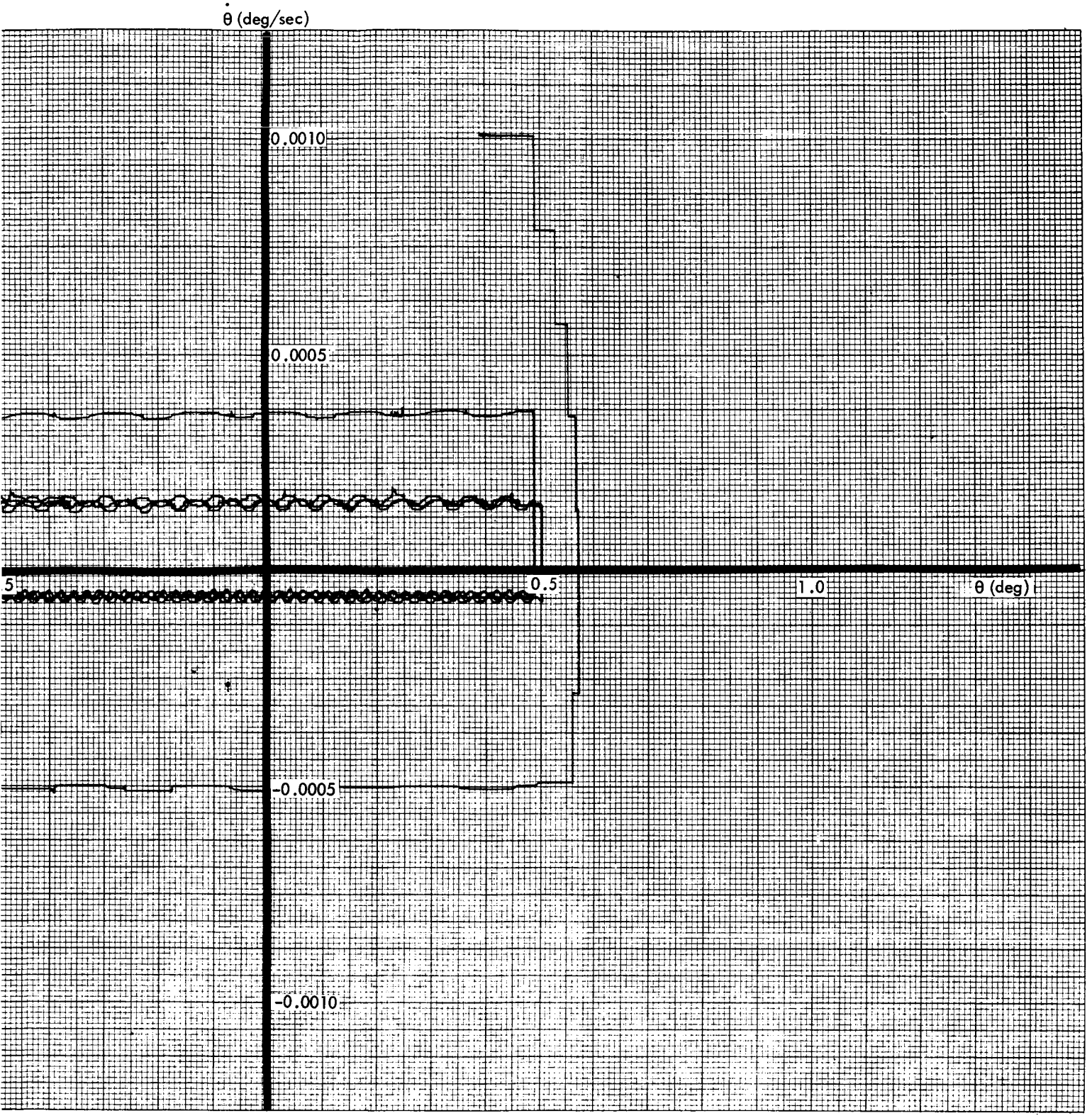

Figure 3. Phase Plane Plot, ω_{11} = 0.0148 Rad/Sec

$\omega_{11} = \omega_{21} = 0.0151$ rad/sec,

$\zeta_{11} = \zeta_{21} = 0\%$, $\dot{\theta}(o) = 0.001°$/sec,

vehicle with capsule

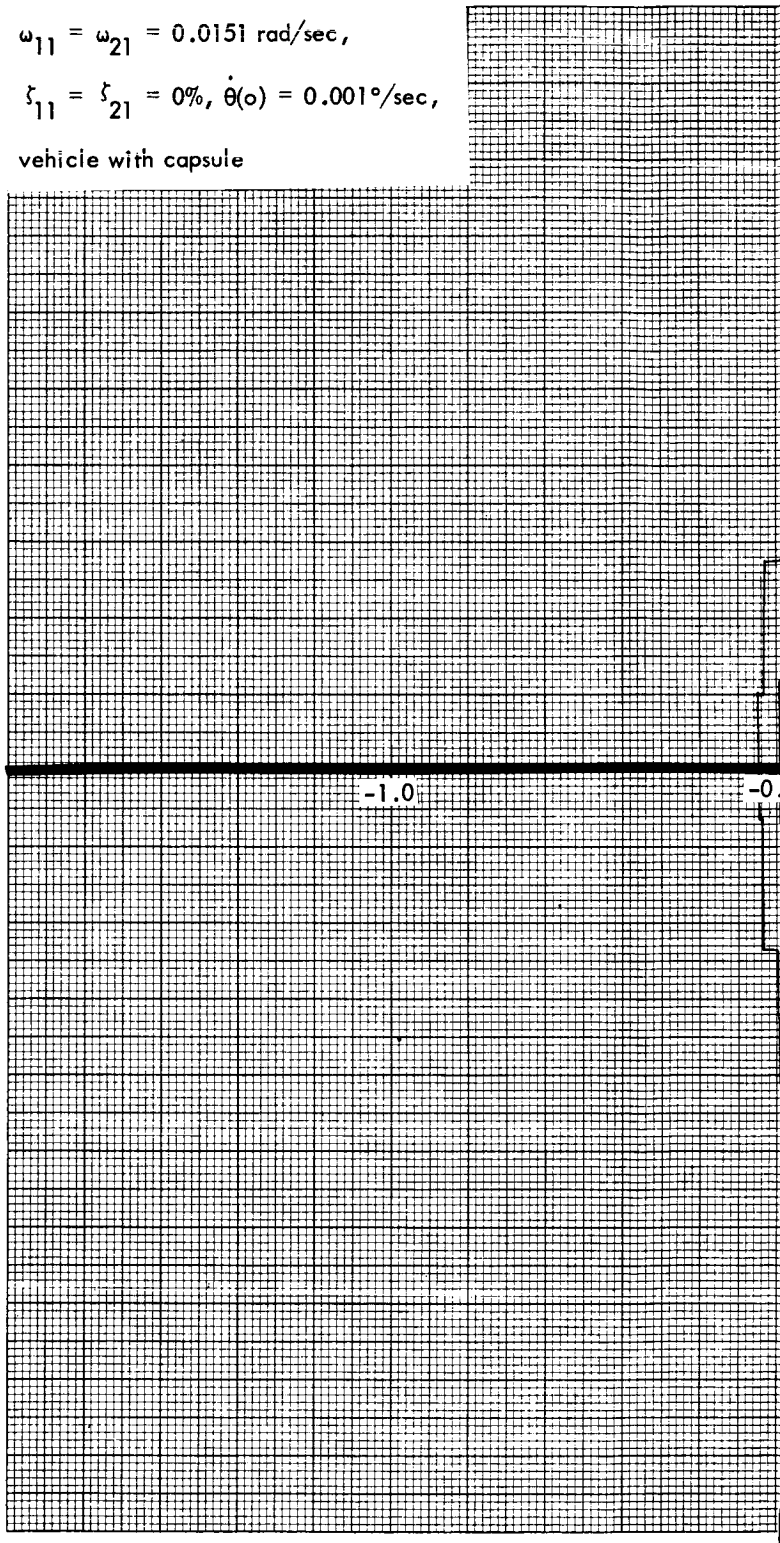

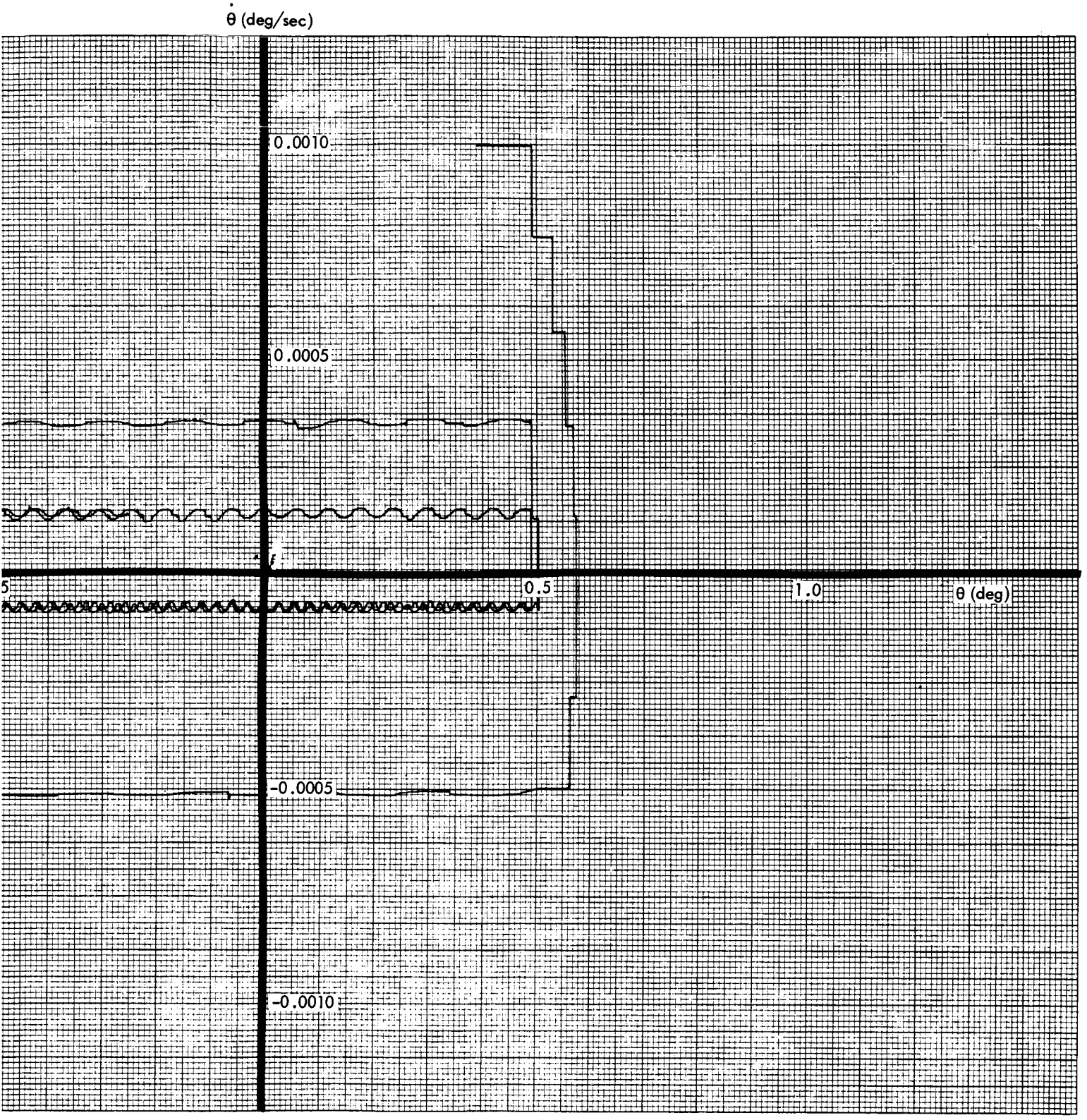

Figure 4. Phase Plane Plot, ω_{11} = 0.0151 Rad/Sec

ω_{11} = 0.0225 rad/sec, ω_{21} = 0.0150 rad/sec,

ζ_{11} = ζ_{21} = 0%, $\dot{\theta}(o)$ = 0.001°/sec,

configuration with capsule

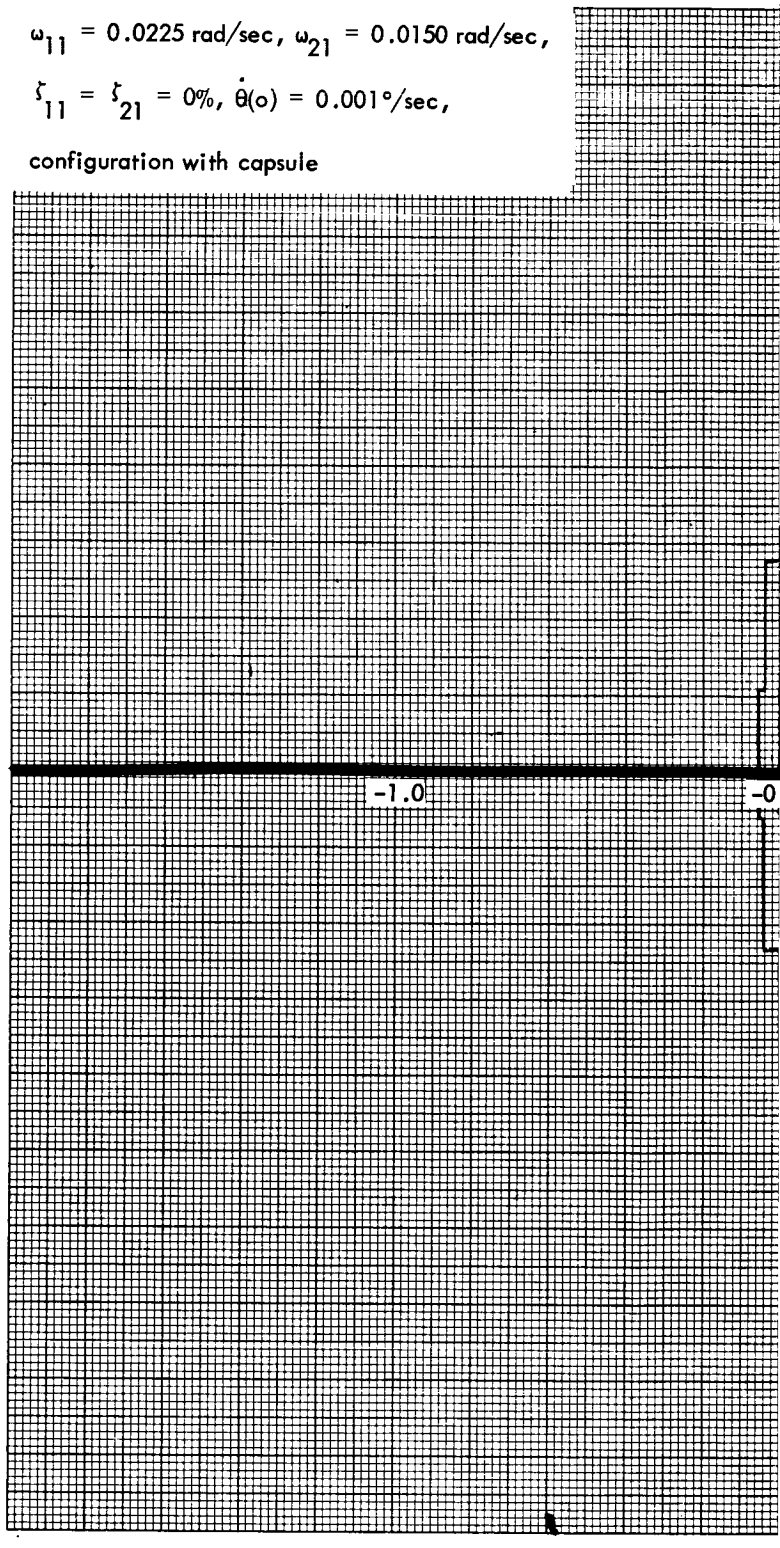

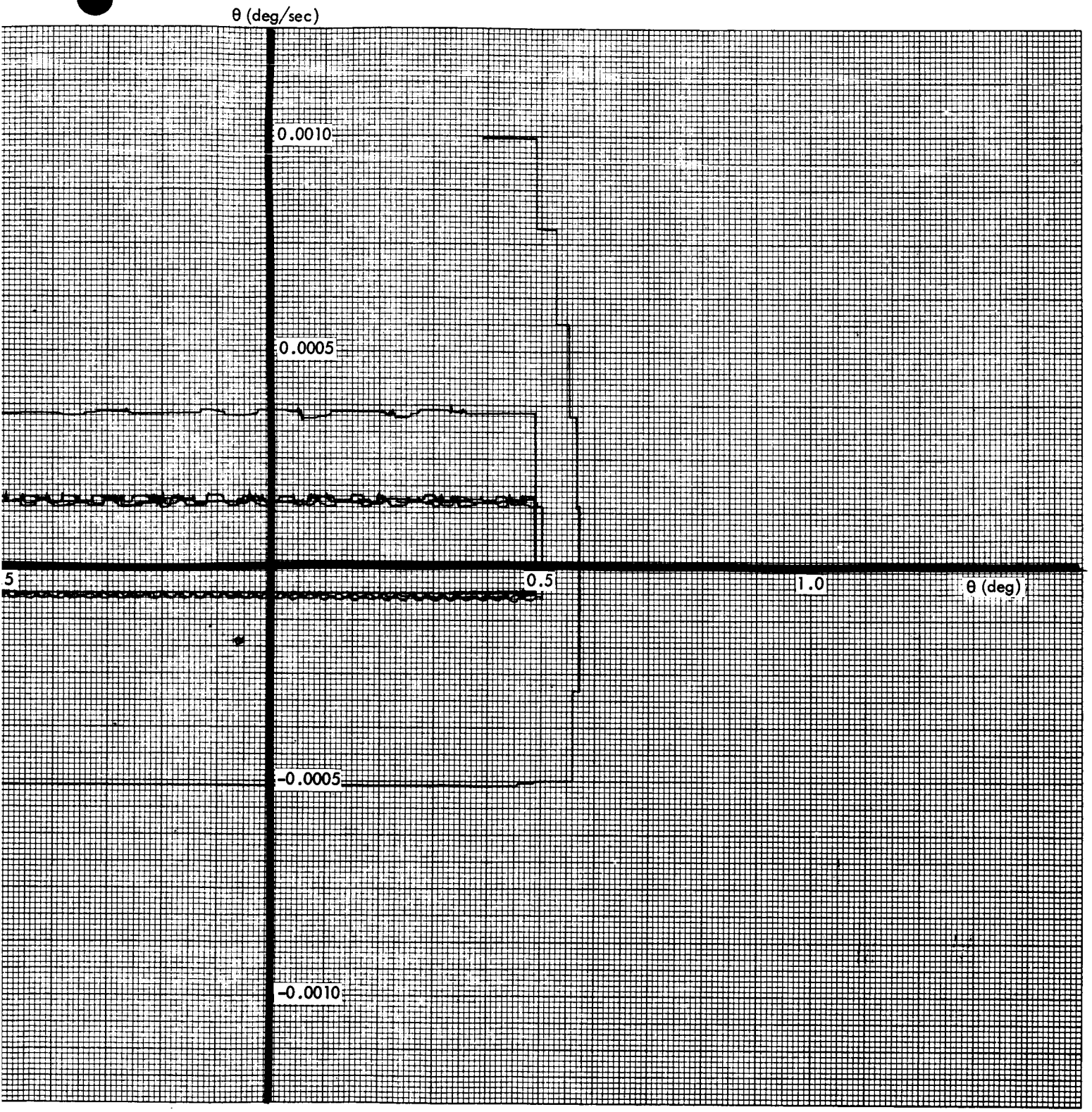

Figure 5. Phase Plane Plot, ω_{11} = 0.0225 Rad/Sec

ω_{11} = 0.02 rad/sec, ω_{21} = 0.0150 rad/sec,

$\zeta_{11} = \zeta_{21}$ = 1%, $\dot{\theta}(o)$ = 0.001°/sec,

vehicle with capsule

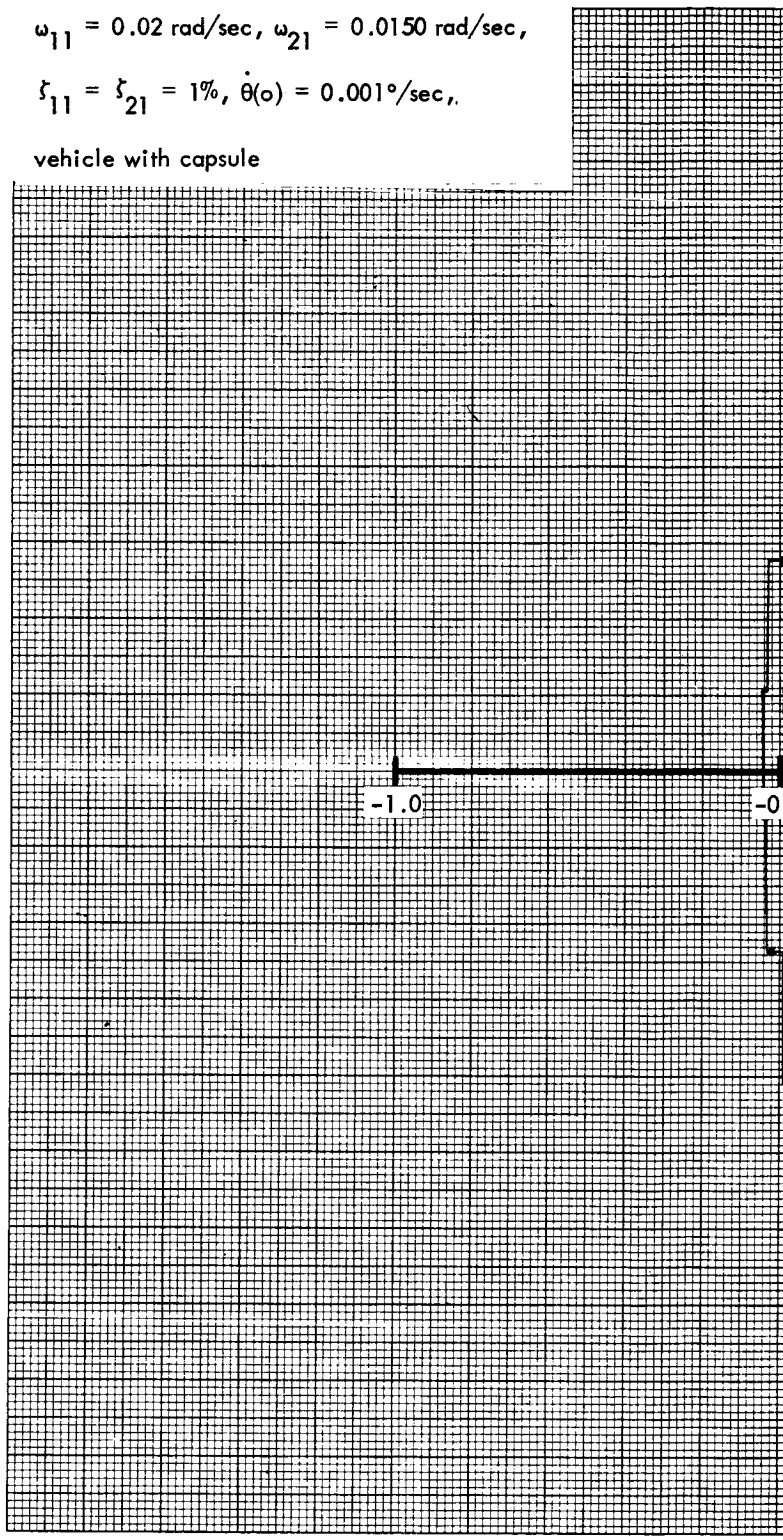

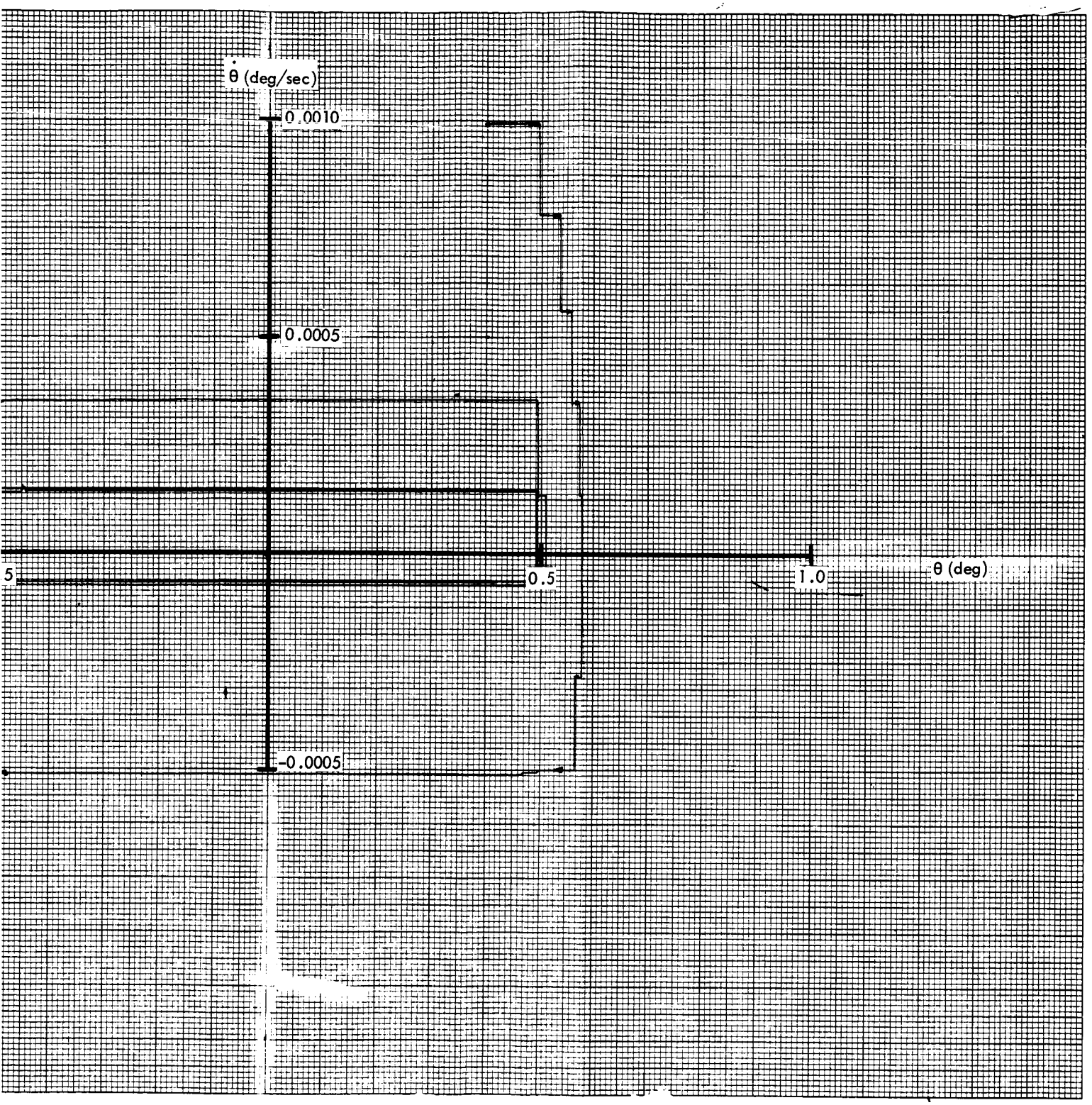

Figure 6. Phase Plane Plot, ω_{11} = 0.02 Rad/Sec

PRECEDING PAGE BLANK NOT FILMED.

3) The probability of slosh reinforcement increases with solar torque magnitude. The interval between control engine firings is reduced as the solar torque is increased; therefore, fewer slosh periods occur between control engine firings. This then would increase the probability of slosh reinforcement.

4) Only first slosh modes are considered.

5) Fuel and oxidizer slosh frequencies are identical.

6) The slosh mode is not damped.

For a rigid body subjected to a constant disturbance torque the time, t_1, between successive firings of the control engines is given by the following equation:

$$t_1 = \frac{2\dot{\theta}_o I}{T_s}$$

where $\dot{\theta}_o$ = maximum limit cycle rate

I = inertia

T_s = solar pressure disturbance torque

In the above equation, the initial rate is assumed small enough that the maximum attitude excursion during t_1 is less than twice the modulator deadzone. The maximum attitude excursion θ during the interval t_1 is determined from the following equation:

$$\theta = \frac{\dot{\theta}_o^2 I}{2T_s}$$

Three rigid body simulation runs are shown in Figure 7 for different initial vehicle rates and a solar radiation torque of 2×10^{-4} ft-lb. The steady-state limit cycle characteristics are shown to be similar but not identical.

The following reasoning was followed in an attempt to select a set of initial conditions and a slosh frequency which would cause reinforcement of the slosh by the control jet firings. Consider the two pulse "limit cycle" illustrated in the phase plane below.

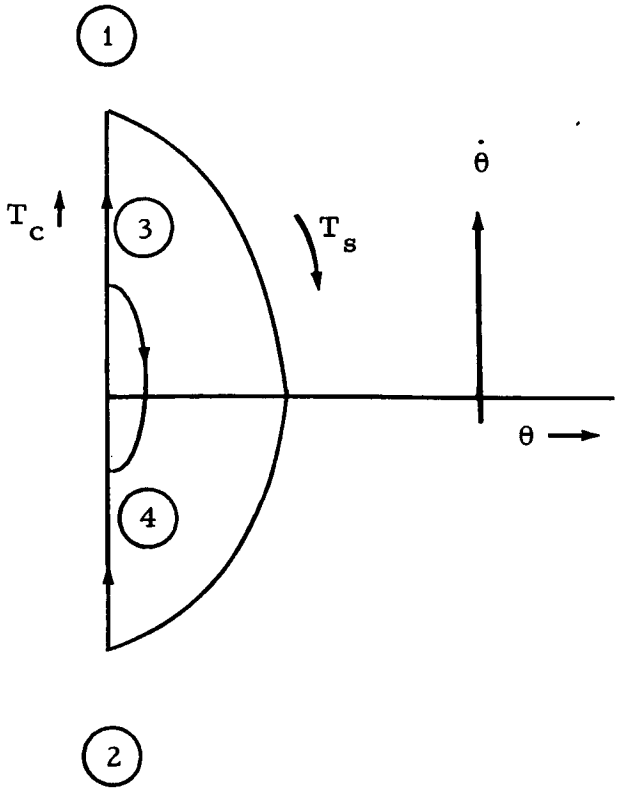

To sustain the limit cycle, the momentum imparted to the vehicle by the solar pressure disturbance torque, T_s, must equal the momentum imparted to the vehicle by the control thrusters. Therefore,

$$(t_{12} + t_{34})\, T_s = 2T_c\, t_{on}$$

where t_{12} = time to traverse from (1) to (2)

$t_{23} = t_{on}$ = minimum "on" time of control jets = 0.025 sec

t_{34} = time to traverse from (3) to (4)

$t_{41} = t_{on}$ = minimum "on" time = 0.025 sec

T_c = control torque

As seen from the above equation, $(t_{12} + t_{34})$ is a constant during limit cycling. A multiple of the slosh period was set equal to $(t_{12} + t_{34})$ to produce reinforcement of the slosh oscillations through the following equation:

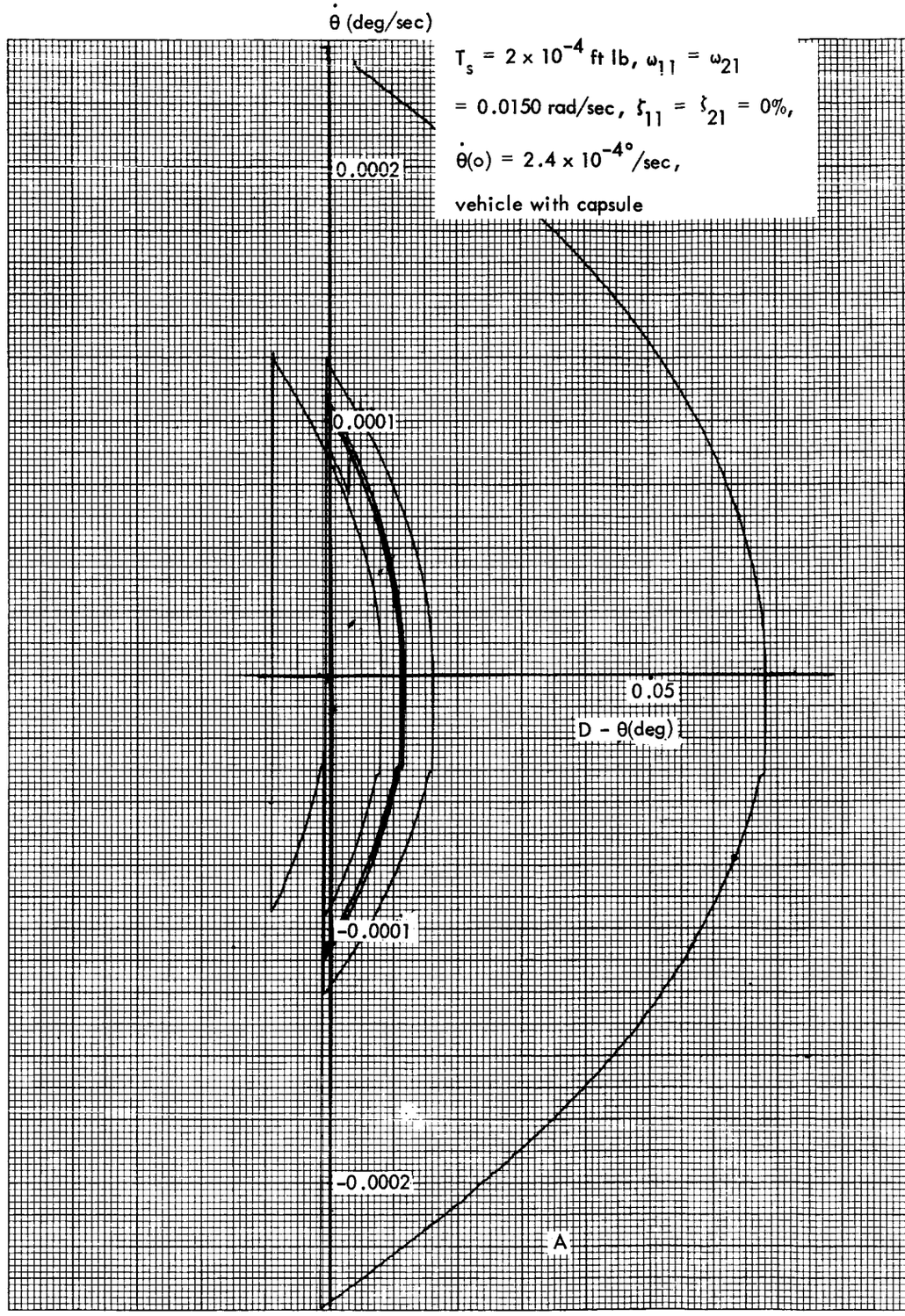
θ̇ (deg/sec)
$T_s = 2 \times 10^{-4}$ ft lb, $\omega_{11} = \omega_{21}$
= 0.0150 rad/sec, $\zeta_{11} = \zeta_{21} = 0\%$,
$\dot{\theta}(o) = 2.4 \times 10^{-4}$°/sec,
vehicle with capsule
0.0002
0.0001
0.05
D - θ(deg)
-0.0001
-0.0002
A

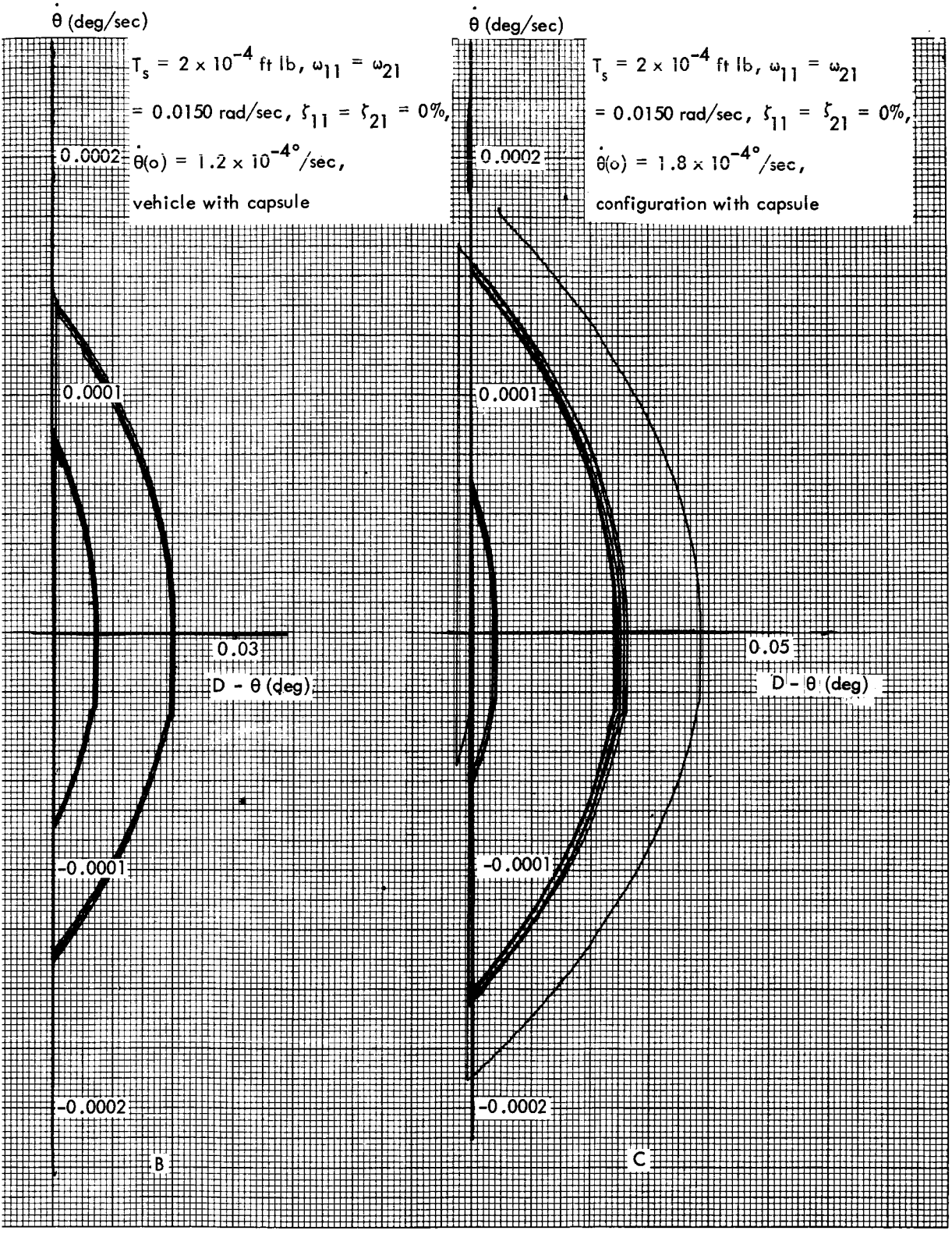

Figure 7. Phase Plane Plot, $\omega_{11} = 0.0150$ Rad/Sec

$$\frac{2\pi N}{\omega_{11}} = \frac{2T_c t_{on}}{T_s}$$

Since ω_{11} in Reference 1 is approximately 0.015 rad/sec, N was selected to be 3 (the nearest integer from the above equation for $T_s = 2 \times 10^{-4}$ ft-lb). A re-adjusted frequency $\omega_{11} = 0.01953$ rad/sec was determined for $N = 3$ using the above equation.

The initial rate $\dot{\theta}(o)$ was selected to coincide with the limit cycle conditions of Figure 7a. The oscillations grew and the phasing of the sloshing relative to the control jet firing changed, and finally the system returned to approximately its initial state. This sequence is shown in Figures 8a through 8e.

Setting the slosh frequency ω_{11} to the value above obviously is not all that is required to produce continuous reinforcing. The conditions required to induce continuous reinforcement (if any such conditions do exist) are not known. Since the conditions to induce continuous reinforcement are difficult to obtain, the probability of occurrence appears to be low. Damping inherent in the fluids (larger if baffles or other damping methods are employed) which were not included will further reduce the slosh amplitudes exhibited between control pulses.

To determine if the attitude control gas consumption (previously predicted by rigid body considerations) was affected by propellant sloshing, the vehicle response with sloshing was compared to the rigid body response. The solar torque was varied from 1.6×10^{-5} to 2×10^{-4} ft-lb. The propellant expended with sloshing was identical to the fuel used with the rigid body representation. Figure 9 is a typical run.

2 2.4 Recovery from Initial Conditions

To examine the recovery of the system from the two following types of initial conditions,

- Maximum expected rate at initiation of the cruise mode
- Initial displacement of the slosh mass

the cruise mode is assumed to be initiated at the termination of acquisition. The maximum rate at the end of acquisition is 0.01 deg/sec if a rate gyro gain of 50 seconds and a modulator deadzone of 0.5 degree is assumed

(Reference 2). The rigid body vehicle recovery from 0.01 deg/sec is presented in Figure 10; the vehicle response with sloshing is presented in Figure 11. Comparison of Figures 10 and 11 indicates that sloshing does not greatly affect the response of the vehicle. The maximum excursions of the fuel and oxidizer slosh masses during these runs were 0.1 and 0.2 inch, respectively.

Initial displacements of the slosh masses of 1.0 inch were imposed upon the vehicle as shown in Figure 12. The sloshing damped quickly and the system provided the desired single pulse limit cycle.

2.2.5 Slosh Mass Variations

To estimate the safety margin afforded by the present design, the slosh effects of the fuel and oxidizer were increased by a factor of 10. This corresponds to the movement of all the propellants as a single slosh mass and an increase in the slosh mass moment arm by a factor of 3. A typical run is presented in Figure 13. Even with this extreme condition, a single pulse limit cycle occurred, thus giving strong indications that additional fuel is not required during the cruise mode for propellant slosh effects.

2.2.6 Attitude Control Parameter Variations

With the modulator time constant, τ, reduced to 25 seconds, and no damping in the slosh model, a two-pulse limit cycle occurred (Figure 14). Without slosh effects, for $\tau = 25$ sec, a rigid body simulation of the system produced a one-pulse limit cycle.

The response obtained in Figure 14 was noteworthy. The first pulse of the two-pulse limit cycle coincided exactly with the occurrence of a zero slosh displacement rate for the oxidizer mass (the predominant slosh mass) and reduced the vehicle rate to zero. The magnitude of the vehicle rate was then increased by the slosh force in a direction opposing the rate change provided by the first engine firing. After the filter in the modulator discharged adequately, the second control pulse was produced. This phenomenon was repeated for every set of sequential engine firings during the limit cycle. Although definite conclusions cannot be made at this time, the simulation results indicate that the probability of multiple

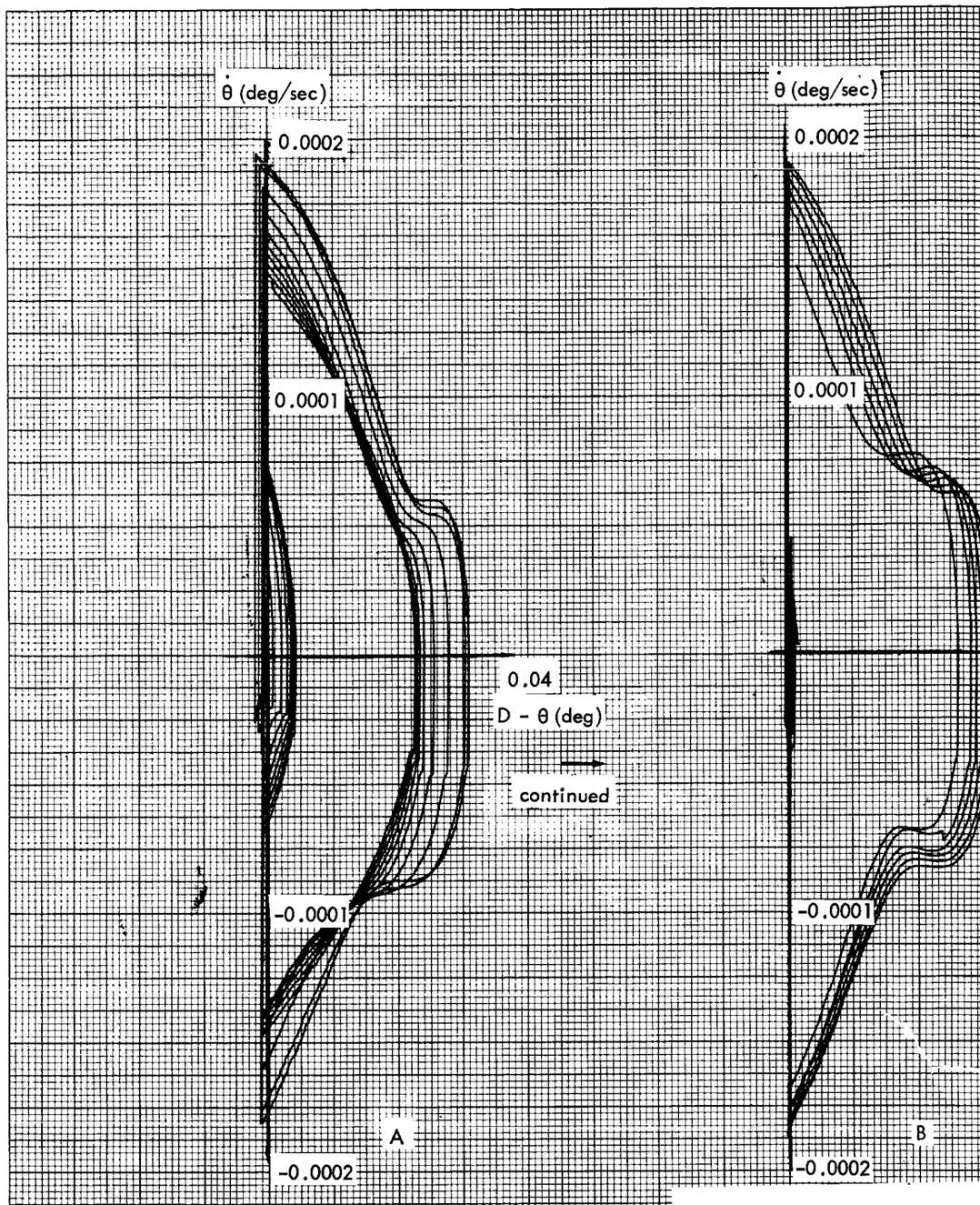
θ̇ (deg/sec)
0.0002
0.0001
-0.0001
-0.0002
0.04
D - θ (deg)
continued
A
θ̇ (deg/sec)
0.0002
0.0001
-0.0001
-0.0002
B
$T_s = 2 \times 10^{-4}$ ft lb, $\omega_{11} = \omega_{21} = 0.019$

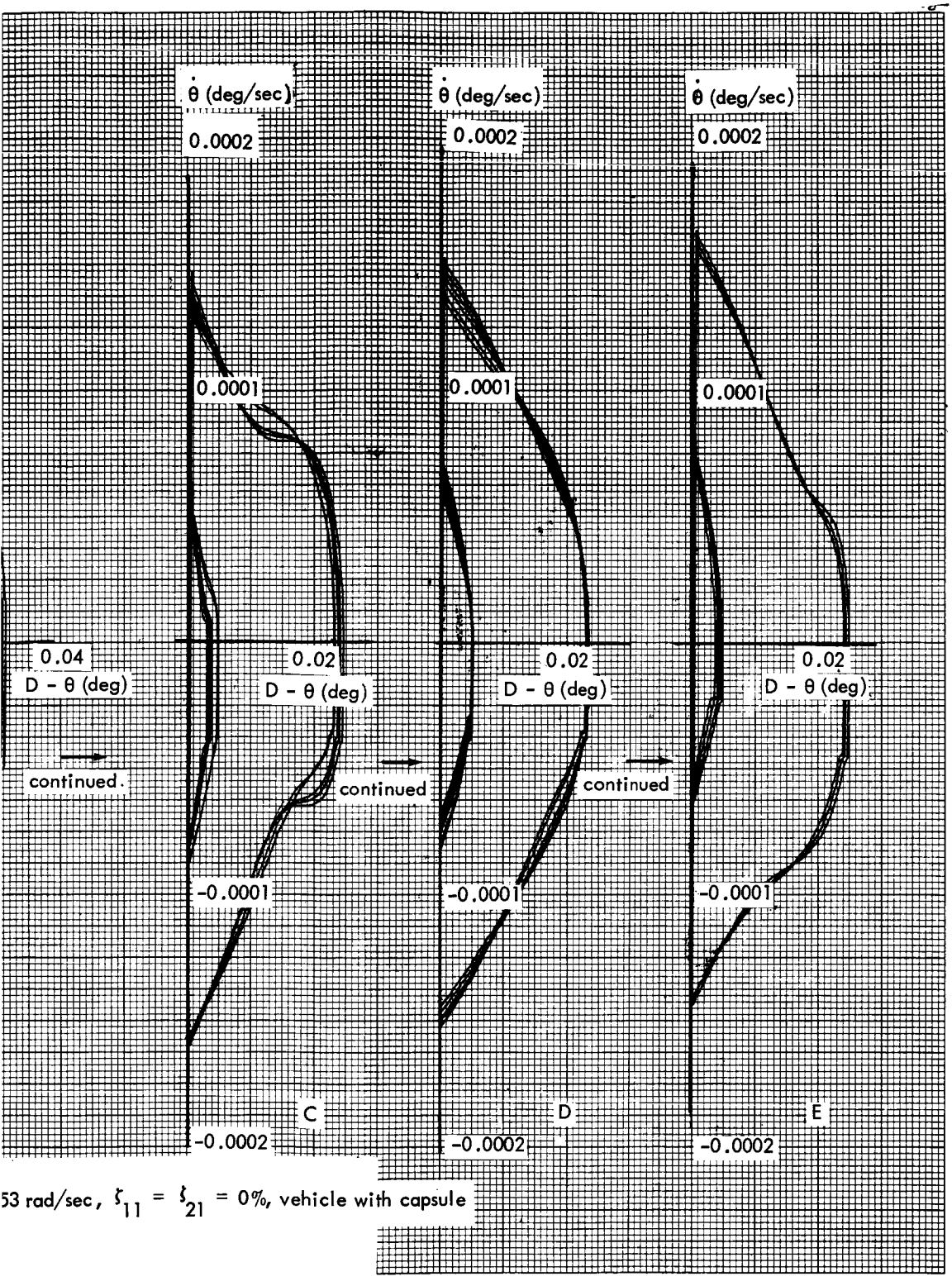

Figure 8. Phase Plane Plot, ω_{11} = 0.01953 Rad/Sec

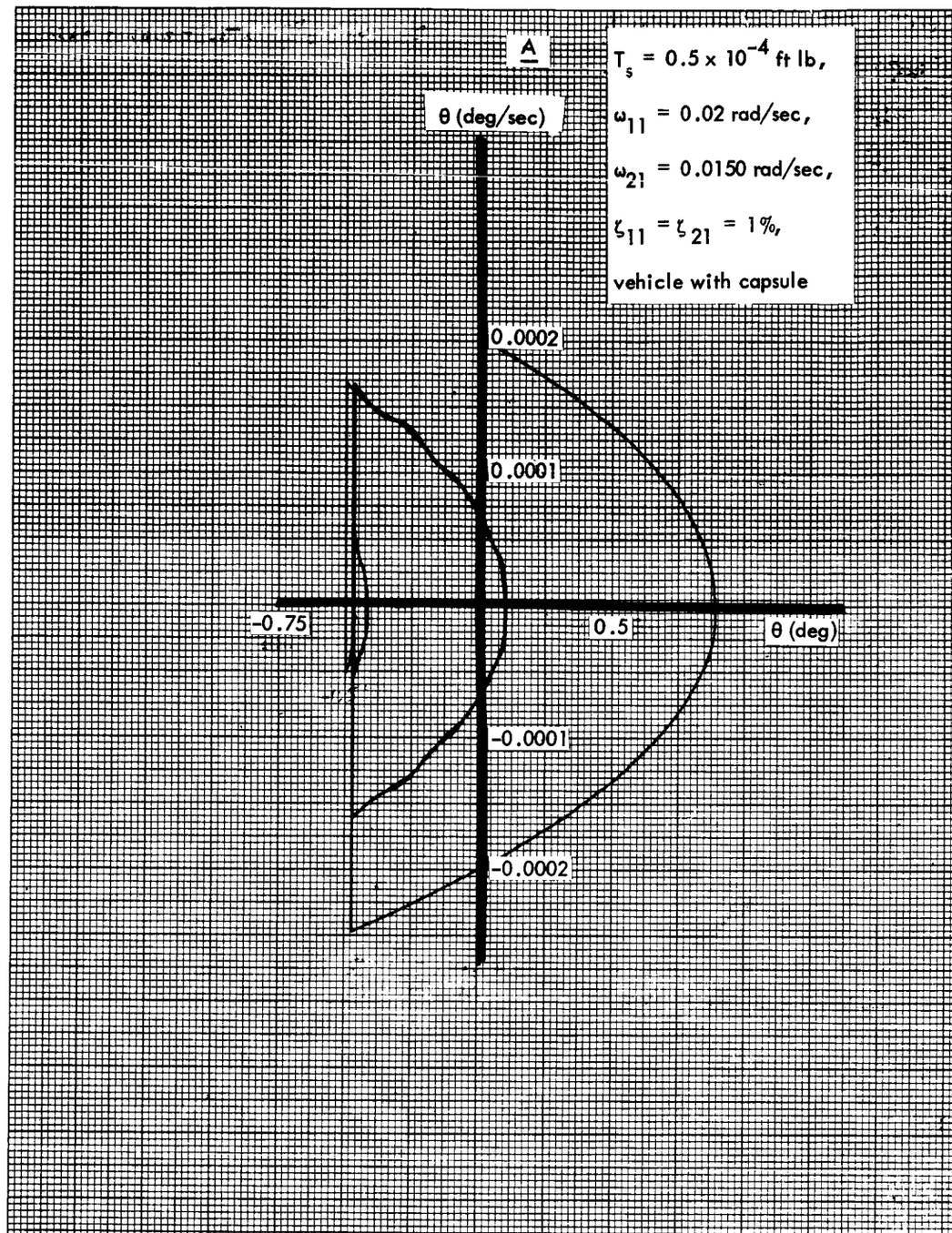
A
θ (deg/sec)
$T_s = 0.5 \times 10^{-4}$ ft lb,
$\omega_{11} = 0.02$ rad/sec,
$\omega_{21} = 0.0150$ rad/sec,
$\zeta_{11} = \zeta_{21} = 1\%$,
vehicle with capsule
0.0002
0.0001
-0.75
0.5
θ (deg)
-0.0001
-0.0002

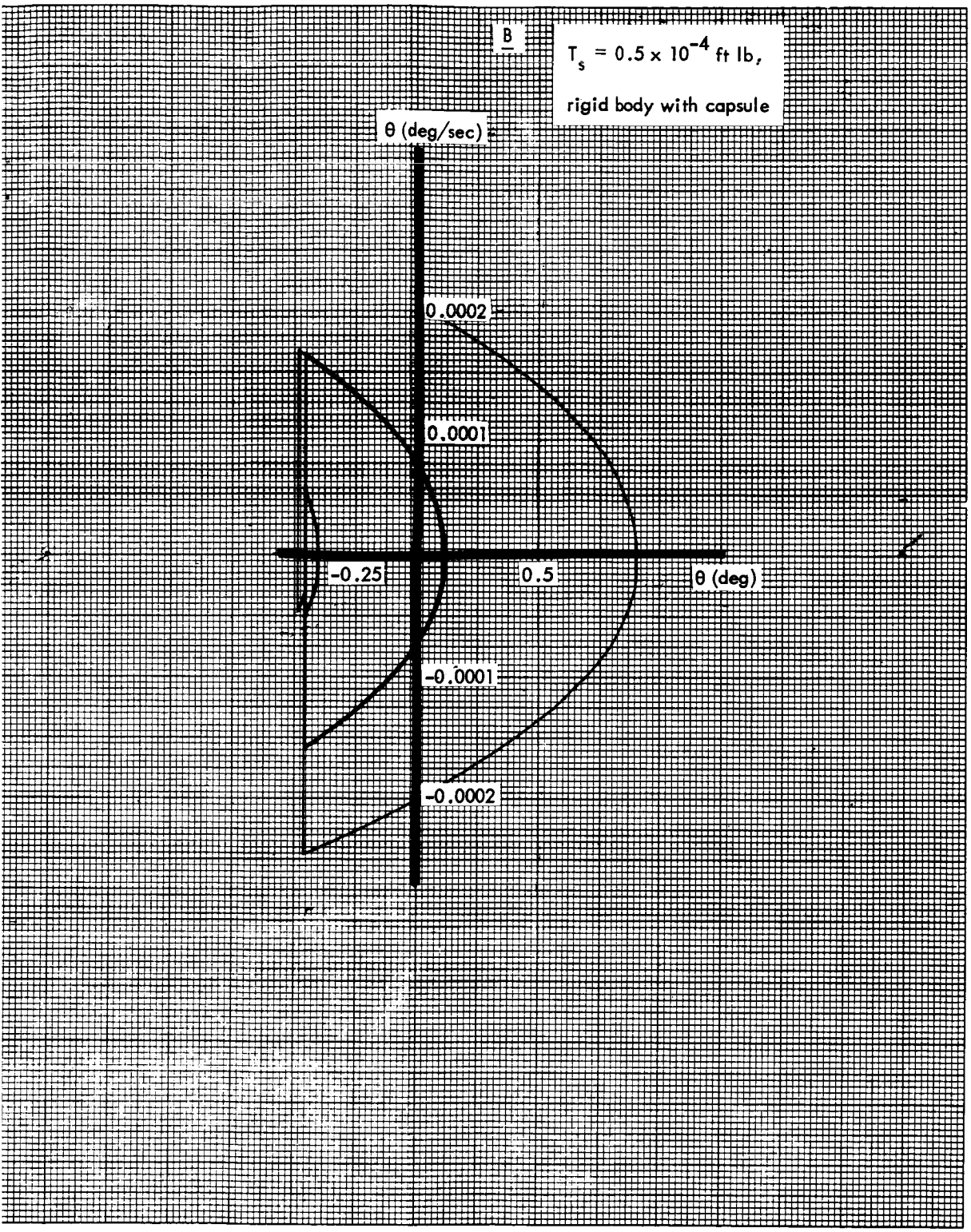

Figure 9. Phase Plane Plot, ω_{11} = 0.02 Rad/Sec

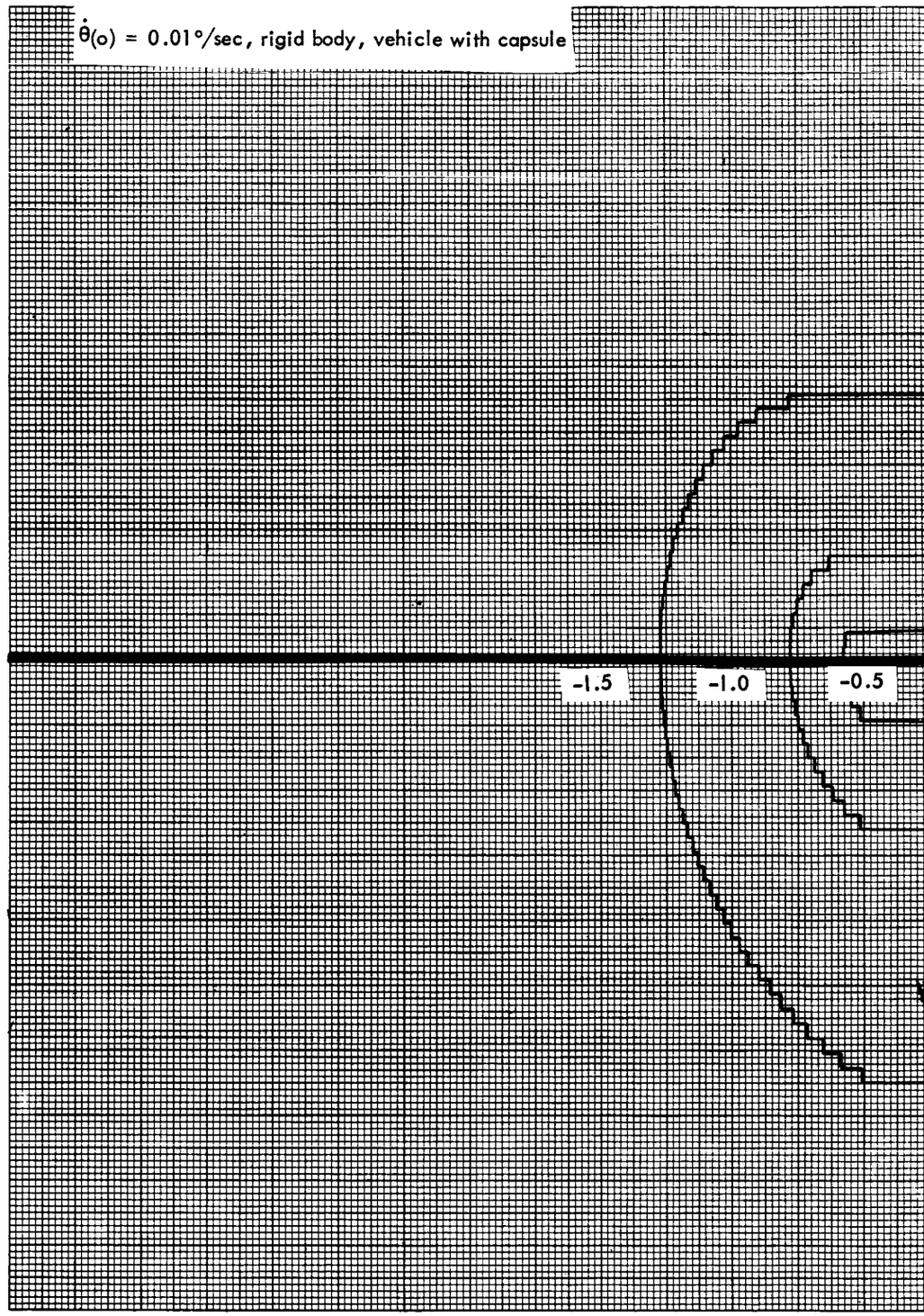
$\dot{\theta}(o)$ = 0.01°/sec, rigid body, vehicle with capsule
-1.5
-1.0
-0.5

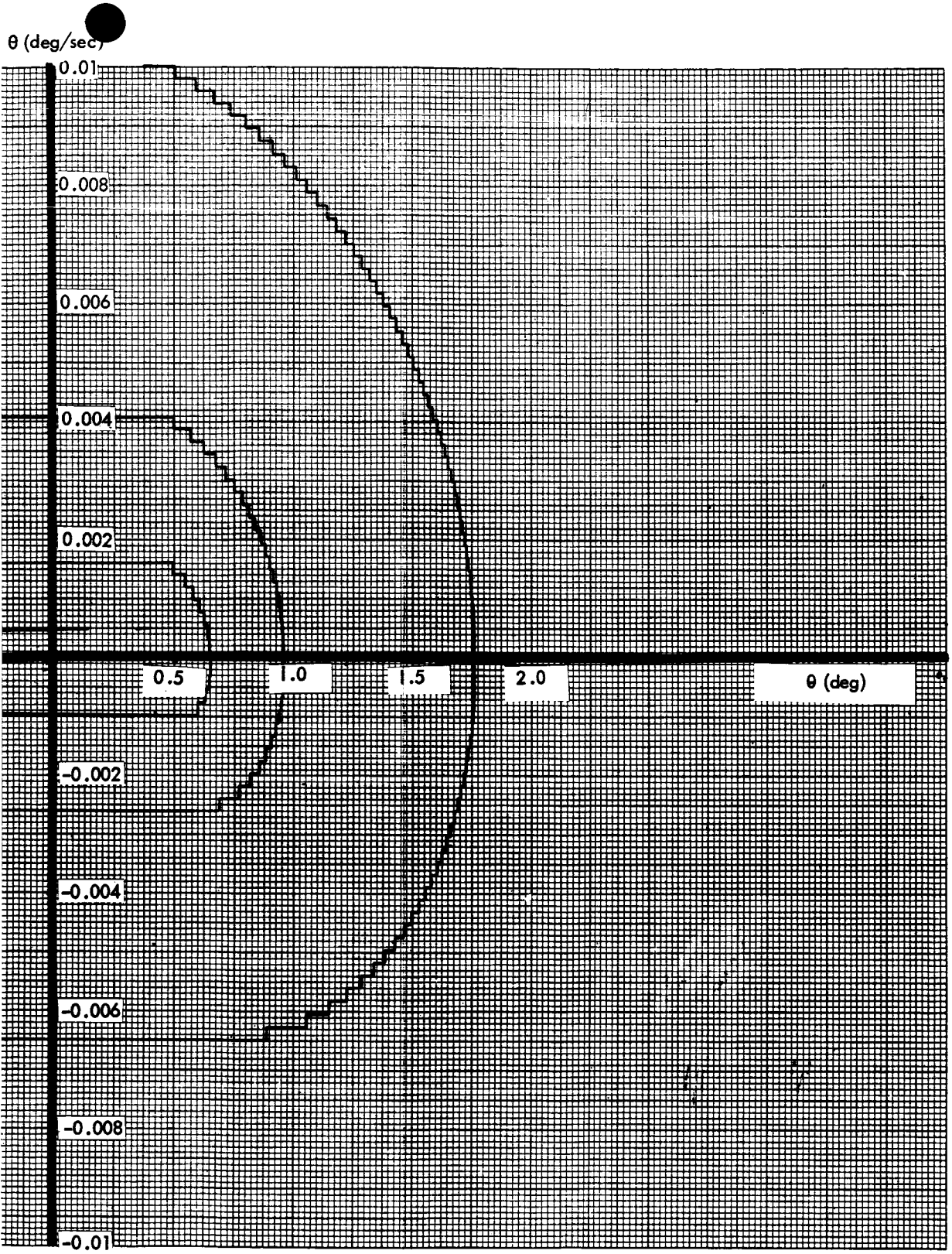

Figure 10. Phase Plane Plot

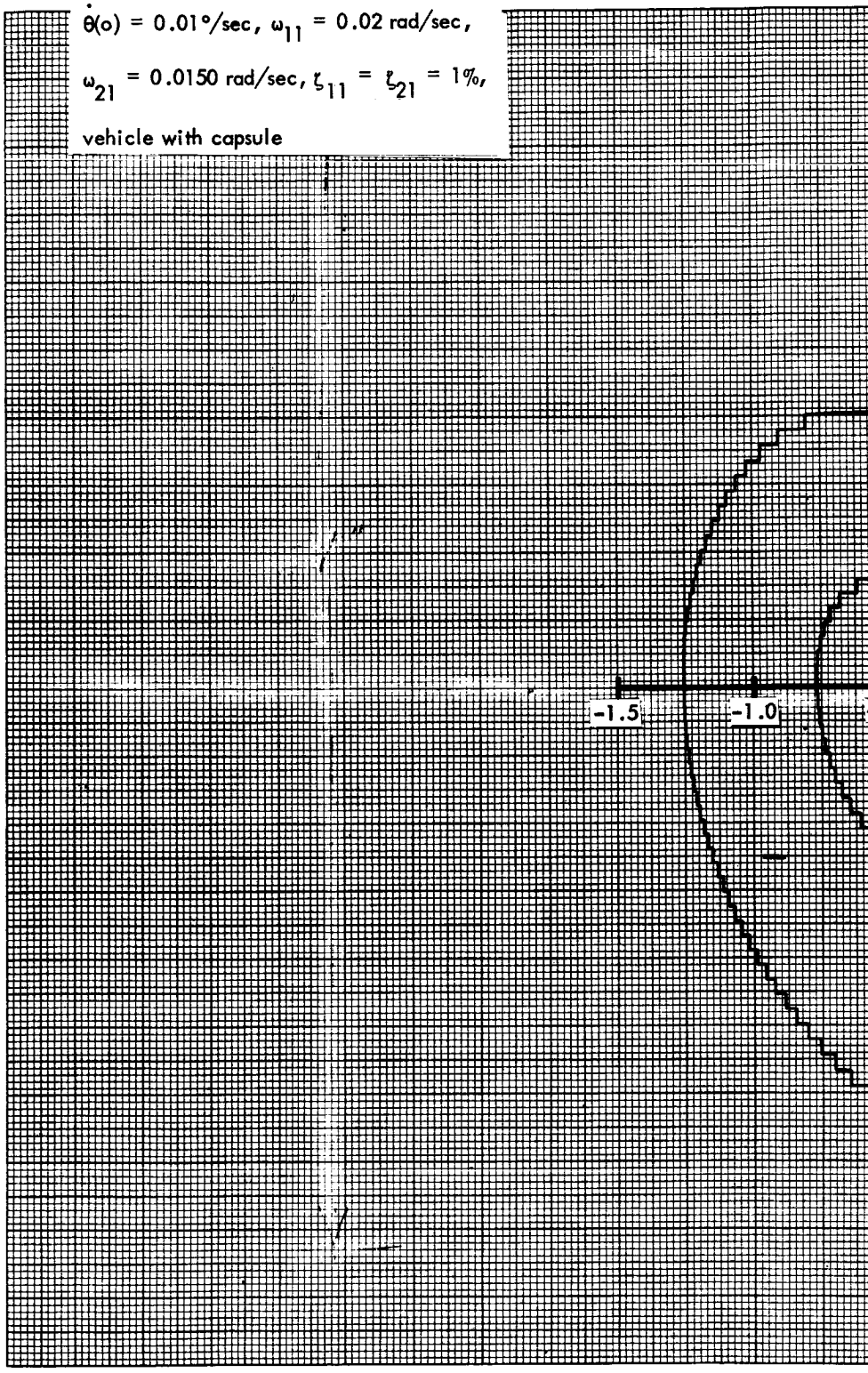
$\dot{\theta}(o) = 0.01°/sec$, $\omega_{11} = 0.02$ rad/sec,
$\omega_{21} = 0.0150$ rad/sec, $\zeta_{11} = \zeta_{21} = 1\%$,
vehicle with capsule
-1.5
-1.0

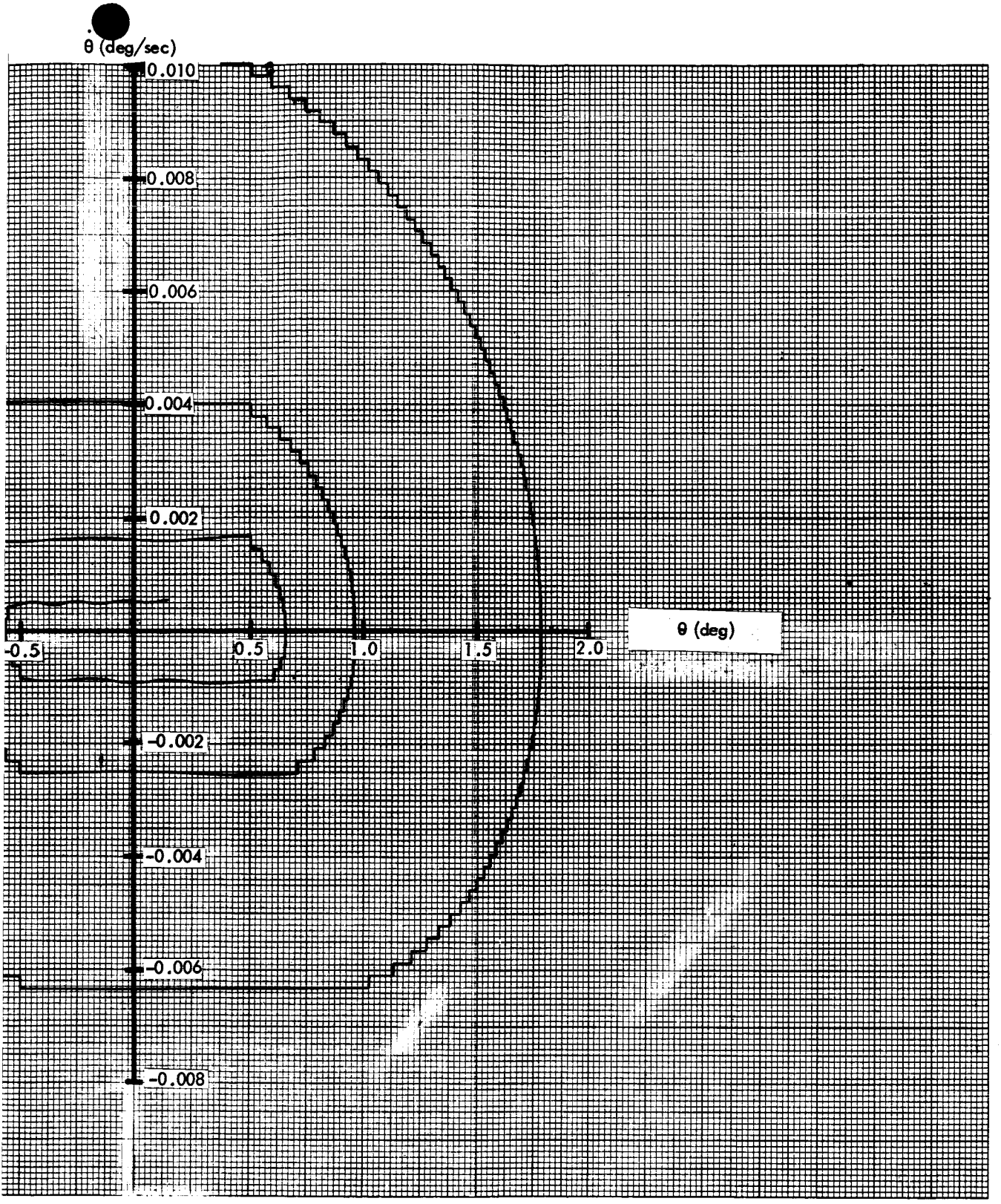

Figure 11. Phase Plane Plot, ω_{11} = 0.02 Rad/Sec

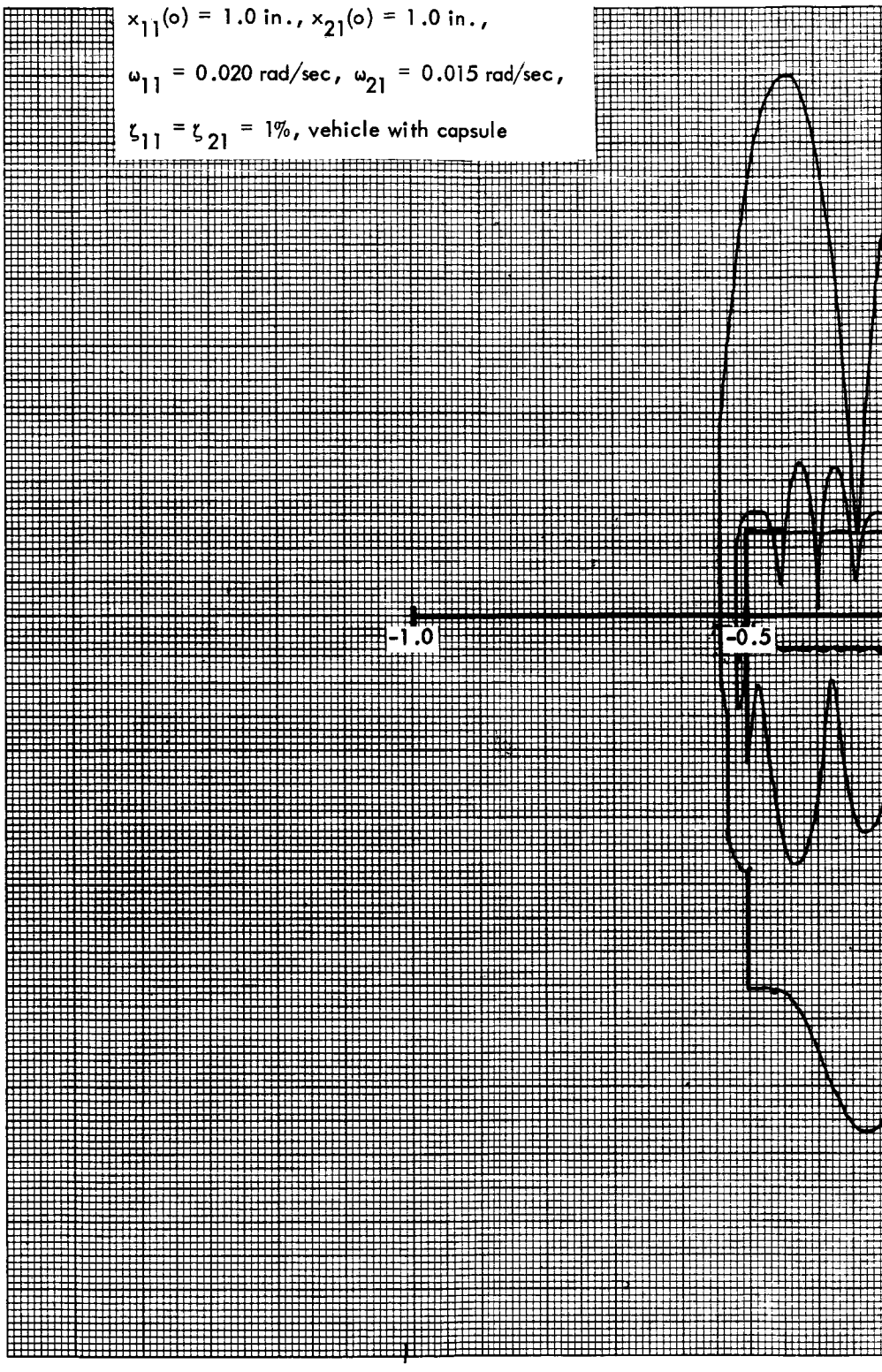
$x_{11}(o)$ = 1.0 in., $x_{21}(o)$ = 1.0 in.,
ω_{11} = 0.020 rad/sec, ω_{21} = 0.015 rad/sec,
$\zeta_{11} = \zeta_{21}$ = 1%, vehicle with capsule
-1.0
-0.5

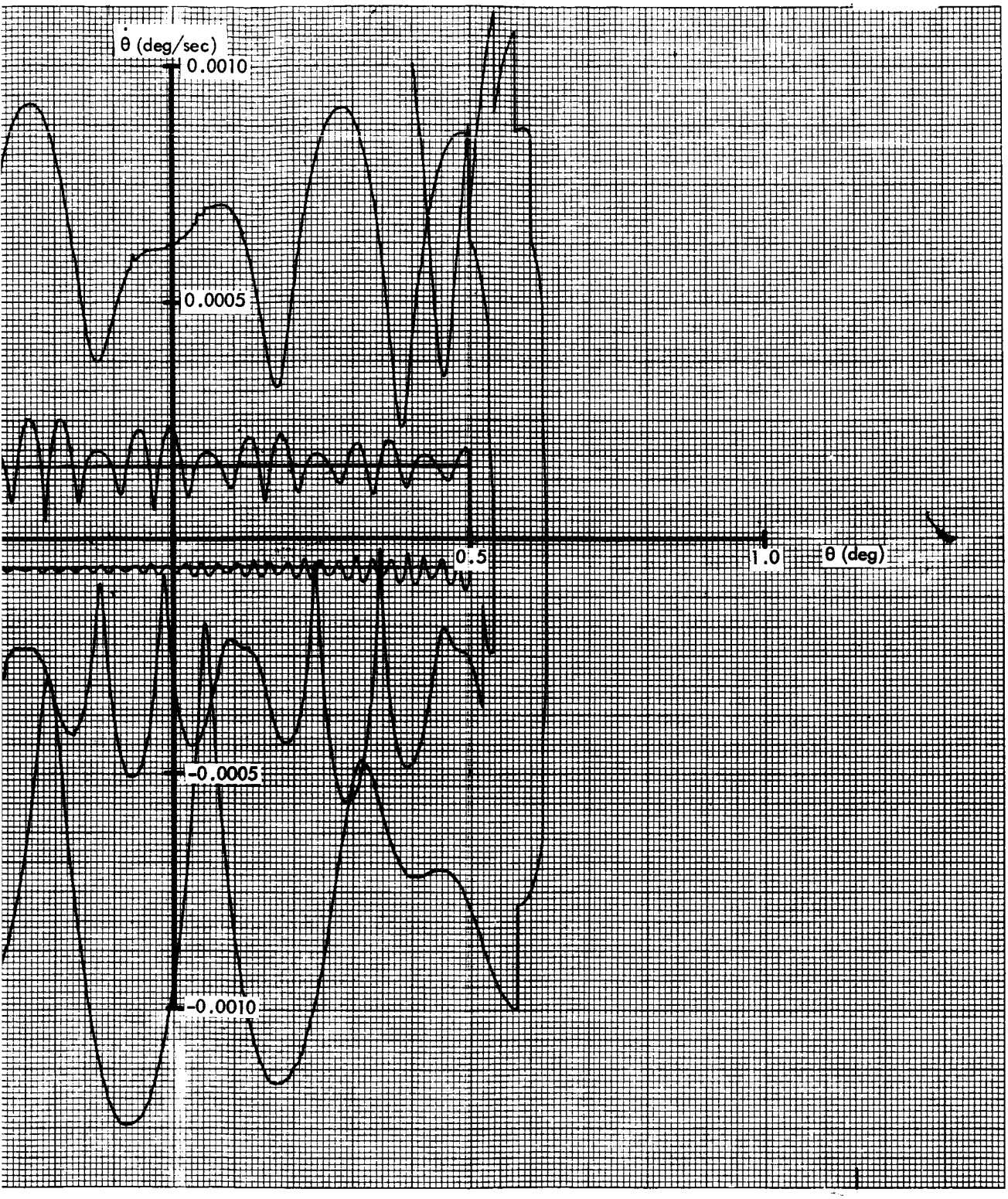

Figure 12. Phase Plane Plot, ω_{11} = 0.020 Rad/Sec

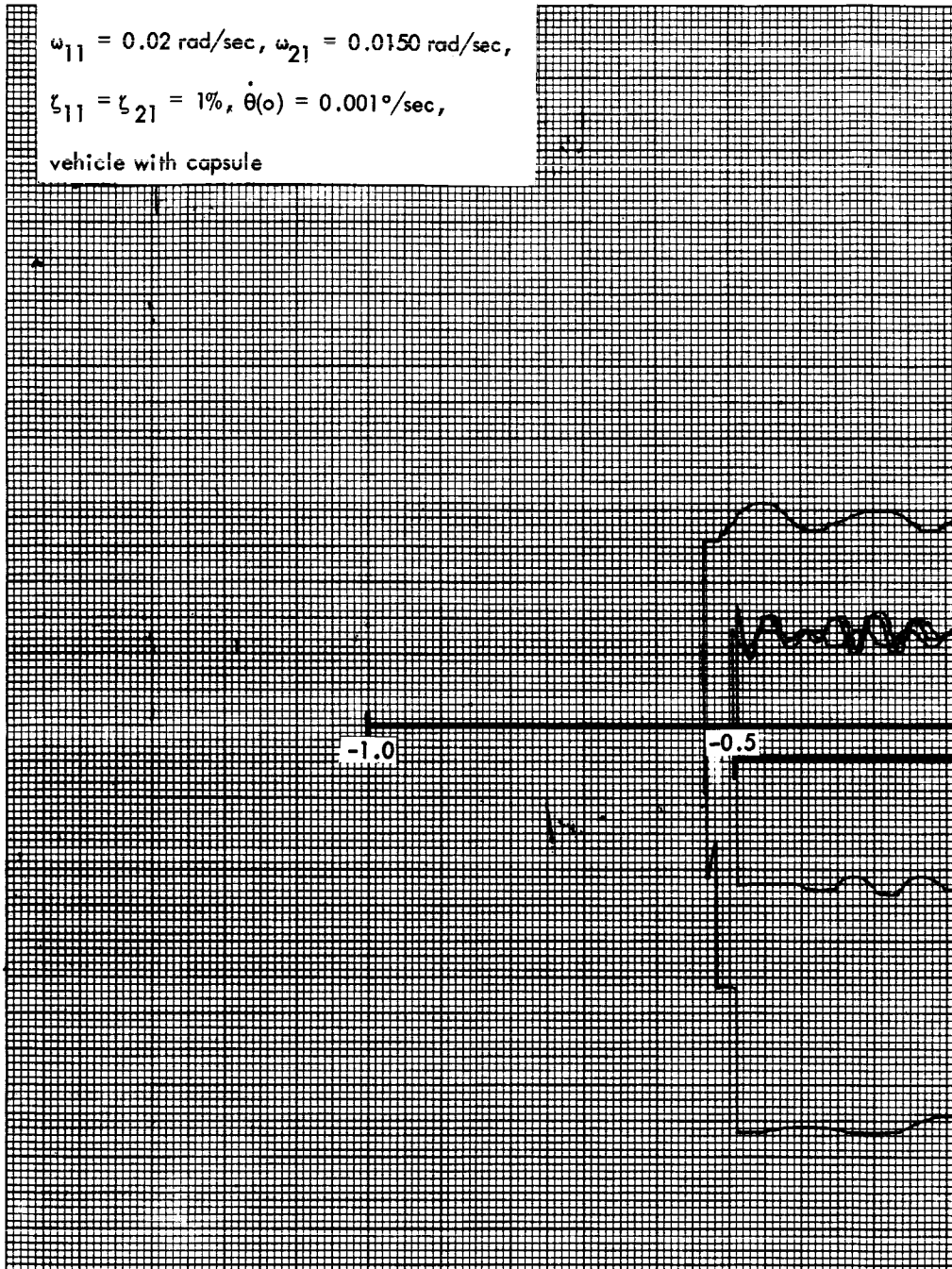
ω_{11} = 0.02 rad/sec, ω_{21} = 0.0150 rad/sec,
$\zeta_{11} = \zeta_{21}$ = 1%, $\dot{\theta}(o)$ = 0.001°/sec,
vehicle with capsule
-1.0
-0.5

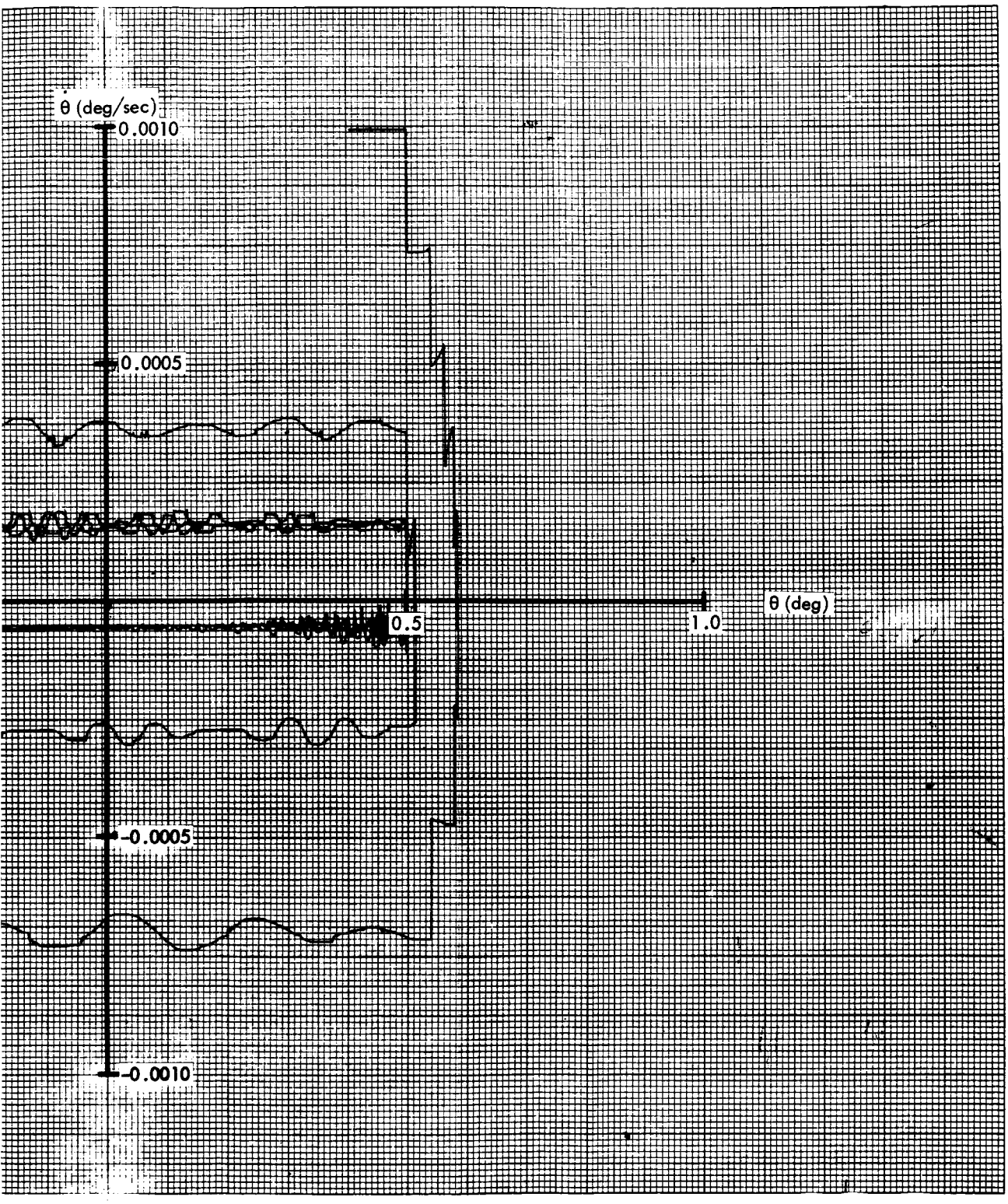

Figure 13. Phase Plane Plot, ω_{11} = 0.02 Rad/Sec

τ = 25 sec, ω_{11} = 0.02 rad/sec, ω_{21} = 0.0159 rad/sec,

$\zeta_{11} = \zeta_{21}$ = 0%, $x_{11}(o)$ = 0.1 in., $x_{21}(o)$ = 0.2 in.,

$\dot{\theta}(o)$ = 0.001°/sec, vehicle with capsule

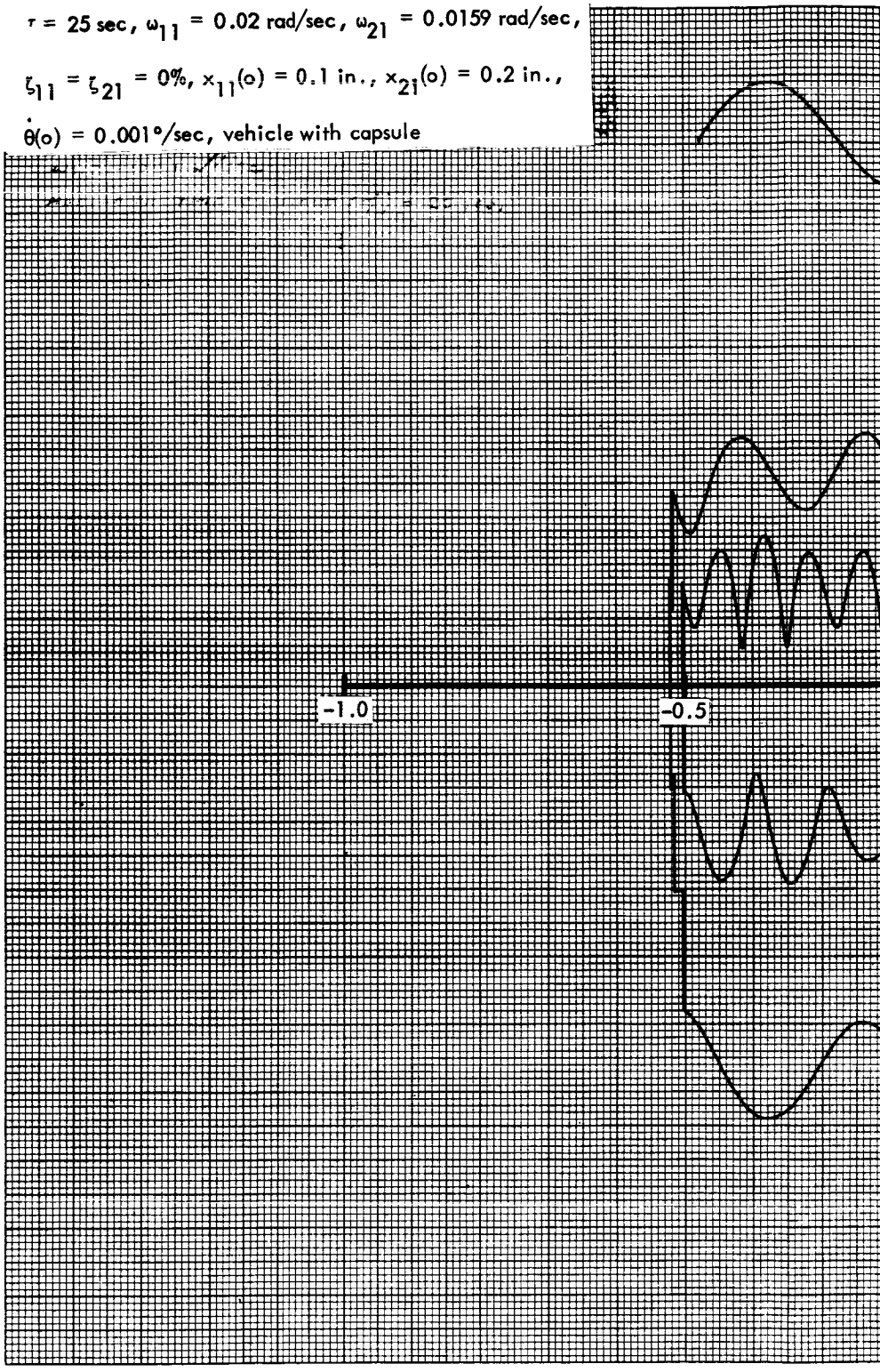

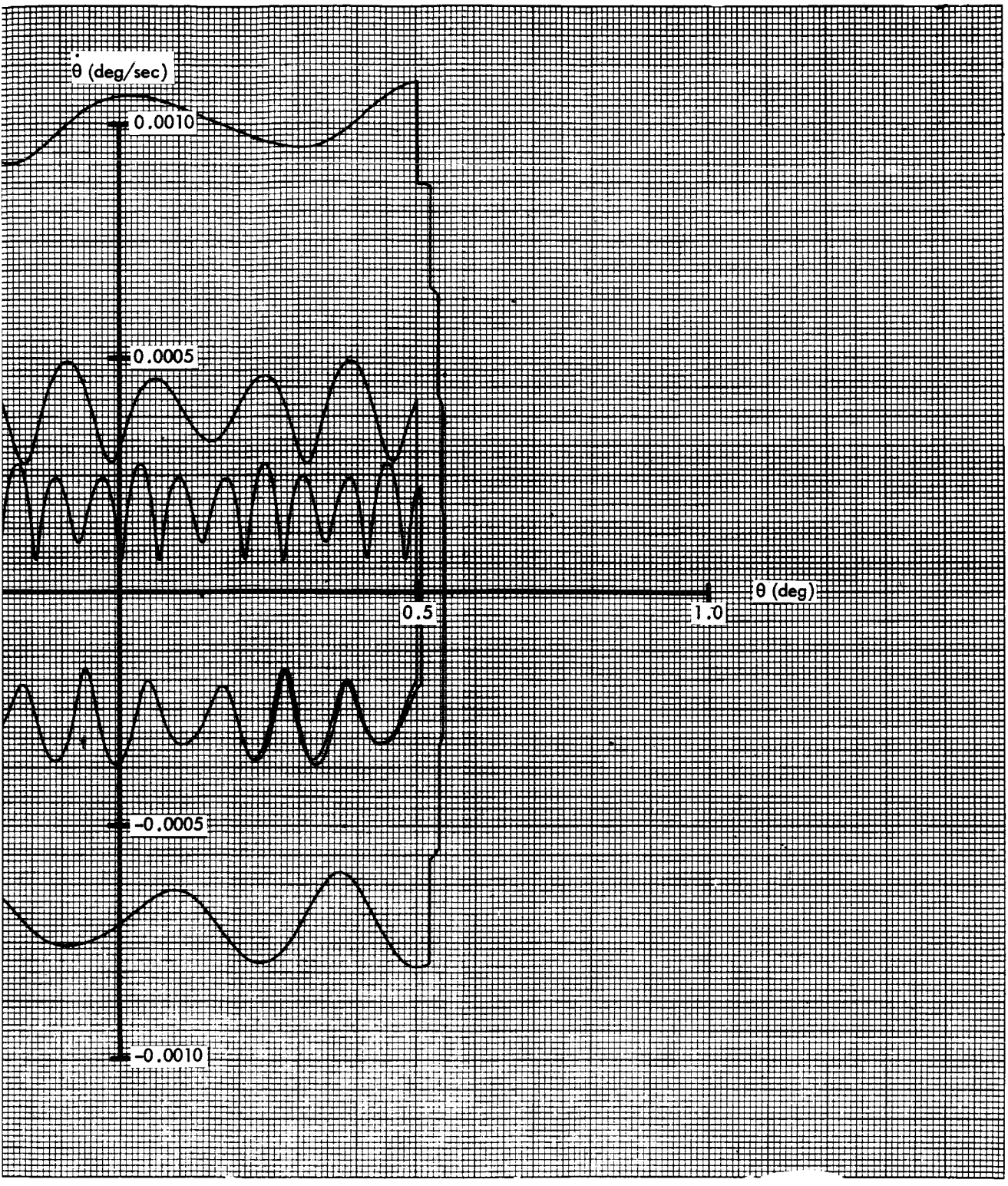

Figure 14. Phase Plane Plot, ω_{11} = 0.02 Rad/Sec

pulse limit cycles occurring is increased when the modulator time constant is decreased. Further evaluation of this effect is desirable.

Increasing τ to 100 seconds resulted in a single pulse limit cycle, although a filter with such a large time constant may be difficult to achieve or maintain electronically.

2.3 CRUISE MODE WITHOUT CAPSULE

The slosh moment arm (distance between the slosh mass attach point and the center of gravity) for the vehicle without capsule is approximately one-fourth of that for the configuration with capsule. The inertia of the vehicle without capsule is reduced to approximately 0.6 of the inertia of the vehicle with capsule. Therefore, for a unit force applied by the slosh mass, the angular acceleration imparted to the vehicle without the capsule is about 40 percent of the angular acceleration that would have been imparted to the vehicle with capsule.

2.3.1 Search for Reinforcement without Disturbance

The objective and basic assumptions were the same as for the configuration with the capsule. The only differences were those due to changes in vehicle mass properties. Both the initial vehicle angular rate and the slosh frequency were selected to induce slosh reinforcement. A slightly different approach from that used previously was followed to select this particular combination.

In order for the control jet firings to continuously increase the fuel and oxidizer slosh amplitudes, the control jet firings should coincide with the occurrence of the peak slosh displacement rates and with a phasing such that each jet firing would increase the slosh rates. Therefore,

$$\frac{2\pi}{\omega'}(N^{+} + 0.5) = \frac{2D}{\dot{\theta}^{+}}$$

and

$$\frac{2\pi}{\omega'}(N^{-} + 0.5) = \frac{-2D}{\dot{\theta}^{-}}$$

where ω' = coupled slosh frequency (slosh coupled with rigid body)

D = deadzone of modulator

$(N^+ + 0.5)$ = number of cycles of oscillation required for slosh reinforcement over the positive limit cycle portion during time = $2D/\dot{\theta}^+$

N^+, N^- = number of full oscillation cycles over positive and negative limit cycle portions

$\dot{\theta}^+, \dot{\theta}^-$ = positive and negative rates during the nominal limit cycle (not necessarily equal in magnitude)

$(N^- + 0.5)$ = number of cycles of oscillation required for slosh reinforcement over the negative limit cycle portion during time = $-2D/\dot{\theta}^-$

For a one-pulse limit cycle, the relationship between the positive and negative limit cycle rates is given by the following equation.

$$\dot{\theta}^+ = \dot{\theta}^- + \Delta\dot{\theta}$$

where $\Delta\dot{\theta}$ = rate change due to attitude engine firing.

Since the change in the vehicle attitude is negligible during the 0.025 second when a single jet fires, $\Delta\dot{\theta}$ is fixed by the pulse rate modulator and performance of the control jets. Neglecting the control jet pulse-to-pulse variations, $\Delta\dot{\theta}$ is determined essentially by the modulator characteristics. Since the modulator filter discharges completely between engine firings, $\Delta\dot{\theta}$ is determined only by the modulator minimum "on" time (a constant).

The above equations were combined to provide the following equations used to select the initial rate, $\dot{\theta}^+$, and the uncoupled slosh mode frequency, ω_{11} (ω_{11} is within a fraction of a percent of ω' and was used primarily to expedite the simulation).

$$\dot{\theta}^+ = \frac{(N^- + 0.5)(\Delta\dot{\theta})}{N^- + N^+ + 1}$$

where $\Delta\dot{\theta} = (F\ell t_{on})/I$

F = force per thruster = 0.2 lb

ℓ = moment arm between thrusters = 19.3 ft

I = inertia = 15.6 slug-ft^2

t_{on} = modulator minimum "on" time = 0.025 sec

$$\omega_{11} = \left[\dot{\theta}^{+}(N^{+} + 0.5)\pi\right]/D$$

Setting $N^{-} = 15$ and $N^{+} = 10$, the required initial rate and slosh frequency were, respectively, 2.258×10^{-4} deg/sec and 0.01489 rad/sec. As Figure 15 illustrates, slosh reinforcement could be induced by these specific conditions. By increasing the slosh damping from 0 to 0.5 percent, the rate of sloshing increase was greatly reduced and limited as indicated by tighter line spacing in Figure 16.

To acquire the sustained slosh reinforcement entailed extremely idealized conditions such as perfect control jet impulse reproducibility, all fuel and oxidizer slosh modes having identical frequencies and moment arms, no fluid damping, no cross-coupling disturbance torques, etc. However, the probability of such perfect conditions occurring simultaneously is zero since control jet pulse-to-pulse variations do exist, small coupling torques are present, some damping is inherent in the sloshing propellant, etc. Therefore, the probability of sustaining slosh reinforcement is equally zero.

2.3.2 Search for Reinforcement with Solar Pressure Disturbance Torque

Since the effects of solar pressure disturbance torques on the configuration with capsule was studied previously in considerable depth, a similar detailed study of the configuration without capsule was not considered necessary. However, simulation runs were conducted in which the solar torque was varied from 0.16×10^{-4} to 2.0×10^{-4} ft-lb. No deleterious effects with regard to slosh reinforcement were found. Figure 17 is a typical run.

2.3.3 Recovery from Initial Conditions

The objectives and assumptions for this study were the same as those for the vehicle with capsule. In Figure 18 the response of the vehicle to the maximum initial rate of 0.01 deg/sec is presented. Figures 19 and 20 present the response of the vehicle to initial 1-inch slosh displacement for 0 and 1 percent slosh damping, respectively. The desired one-pulse limit cycle is shown to result even in the zero damping case.

2.3.4 Slosh Mass Variations

To get an indication of the safety margin inherent in the design, the slosh effects were again arbitrarily increased by a factor of 10. The results are shown in Figure 21. A one-pulse limit cycle still resulted; thus attitude control gas in addition to that used during the normal limit cycling will not be required.

2.3.5 Attitude Control Parameter Variation

The modulator time constant, τ, was varied from 25 to 100 seconds. A single-pulse limit cycle occurred in all cases. Figure 22 is a typical run. The deadzone, D, was decreased to the level switched prior to reorientation maneuvers (0.25 deg per Reference 2). The vehicle response shown in Figure 23 is satisfactory. The modulator minimum "on" time was doubled. No adverse effects were noted except that the nominal limit cycle rates were doubled as expected (Figure 24).

2.4 TRANSITION FROM POWERED FLIGHT TO CRUISE

The initial objective of this study was to investigate the effects of propellant sloshing on vehicle response during the transition from powered flight to the initiation of the cruise mode. (The powered flight phases include pre-booster separation and all Voyager main engine firings.) The control system of Reference 2 and the dynamic equations used for the cruise mode (Sections 2.2 and 2.3) were combined in a single axis simulation. A block diagram of the control system is presented in Figure 25. The high thrust control engines were assumed to provide a pure couple of 57.9 ft-lb (3 pound engines separated by 19.3 feet). The same configurations as in the cruise mode (vehicle with "full" fuel tanks with and without capsule) were studied. After evaluation of the initial transition phase results, it was decided that vehicle performance could be improved through various control system modifications. Therefore, the determination of methods for improving vehicle performance through control system modification and the investigation of the effects of propellant sloshing on vehicle response during the transition phase became additional objectives of the study described below.

$\omega_{11} = \omega_{21} = 0.01489$ rad/sec, $\zeta_{11} = \zeta_{21} = 0\%$

$\dot{\theta}(o) = 2.257 \times 10^{-4}$°/sec, vehicle without capsule

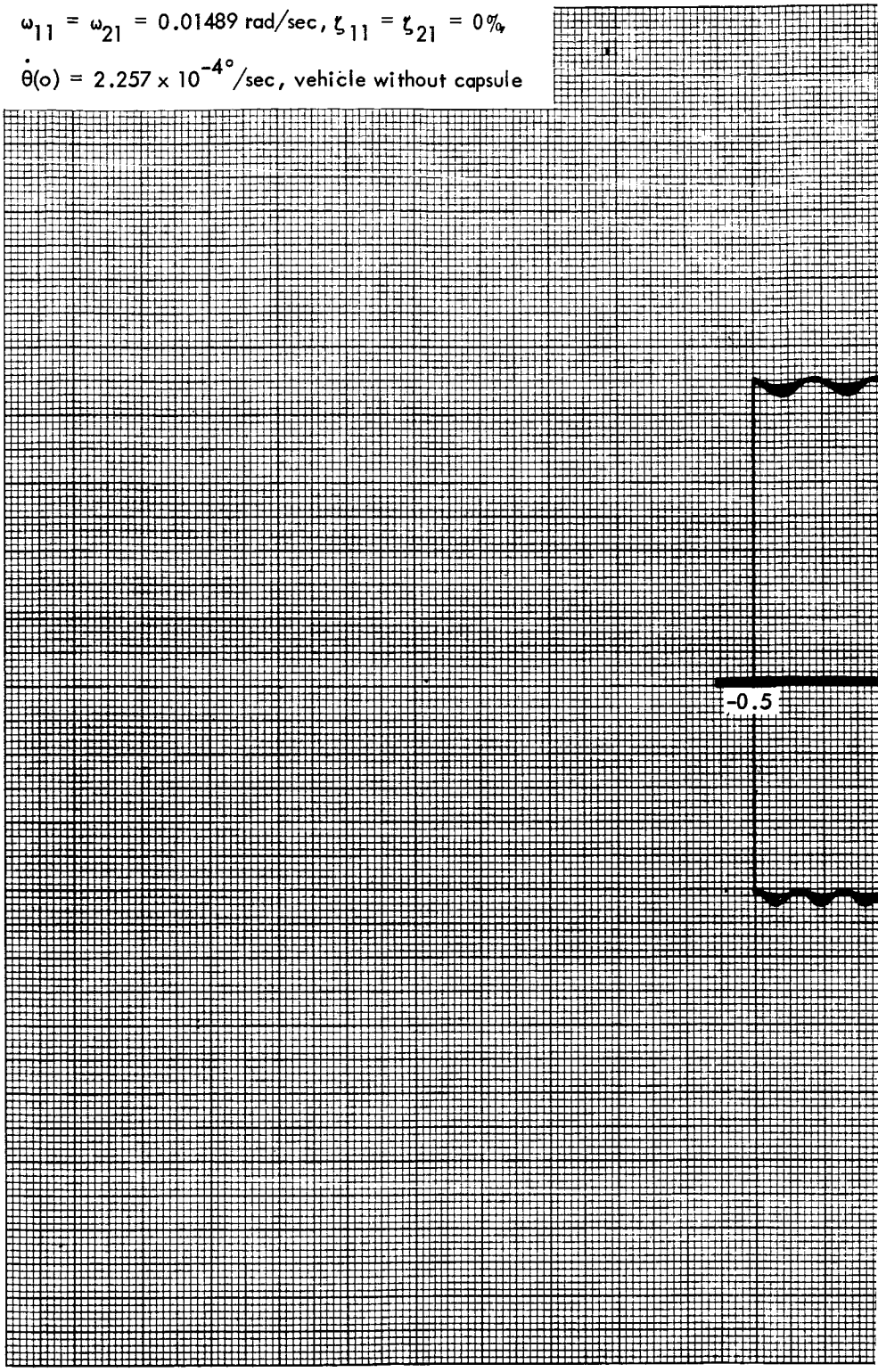

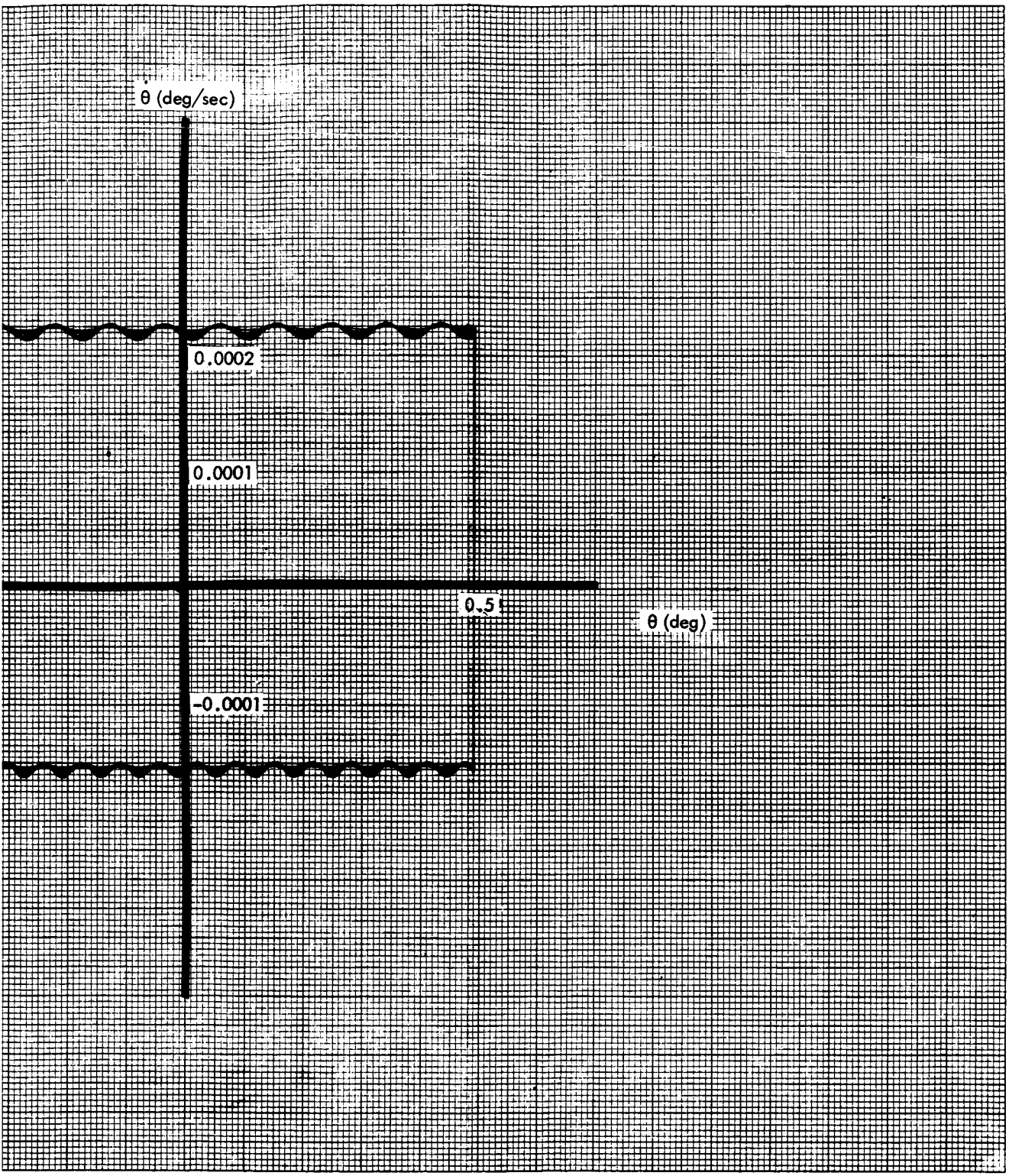

Figure 15. Phase Plane Plot, ω_{11} = 0.01489 Rad/Sec

$\omega_{11} = \omega_{21} = 0.01489$ rad/sec, $\zeta_{11} = \zeta_{21} = 0.05\%$,

$\dot{\theta} = 2.258 \times 10^{-4}$°/sec, vehicle without capsule

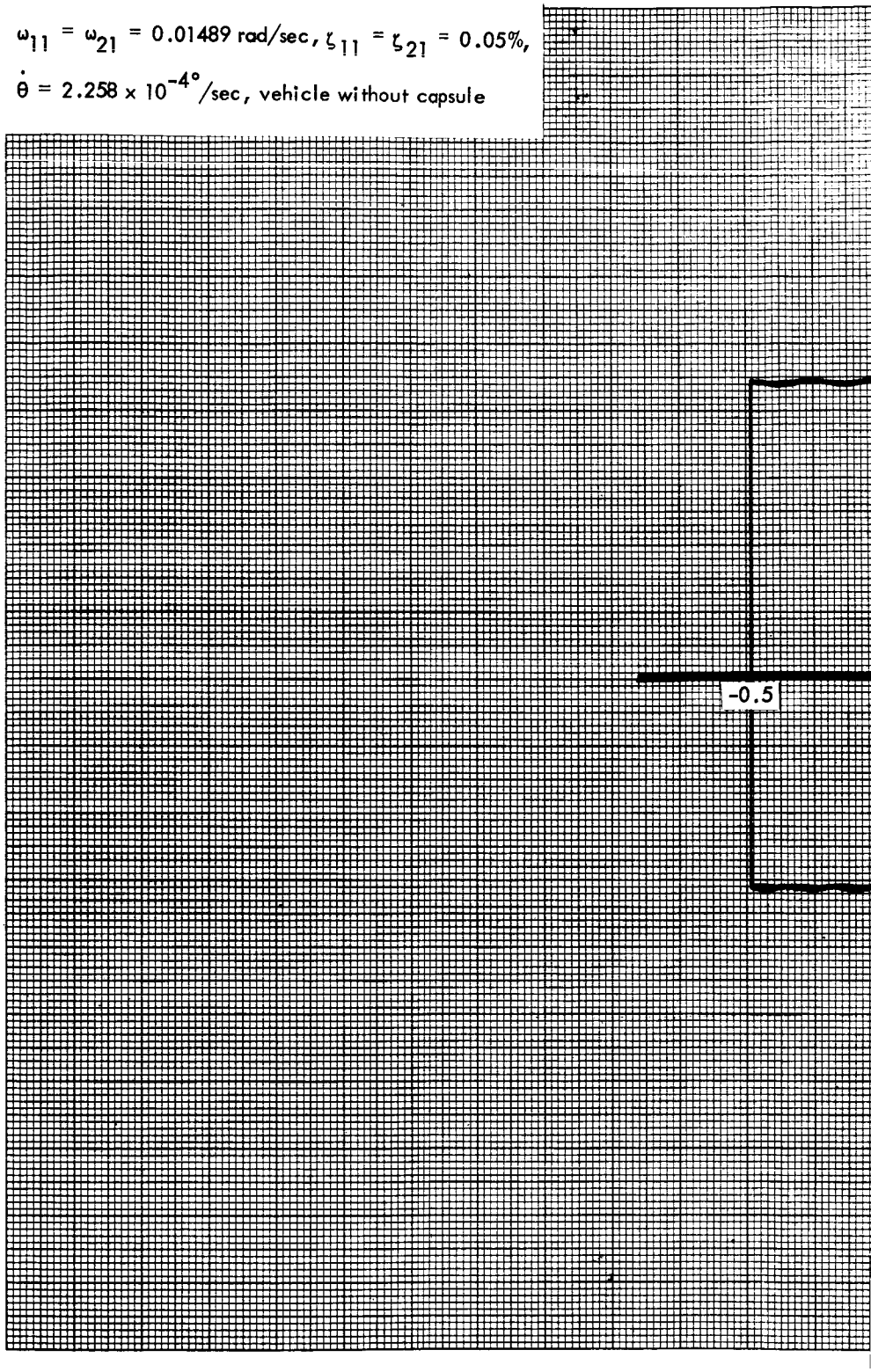

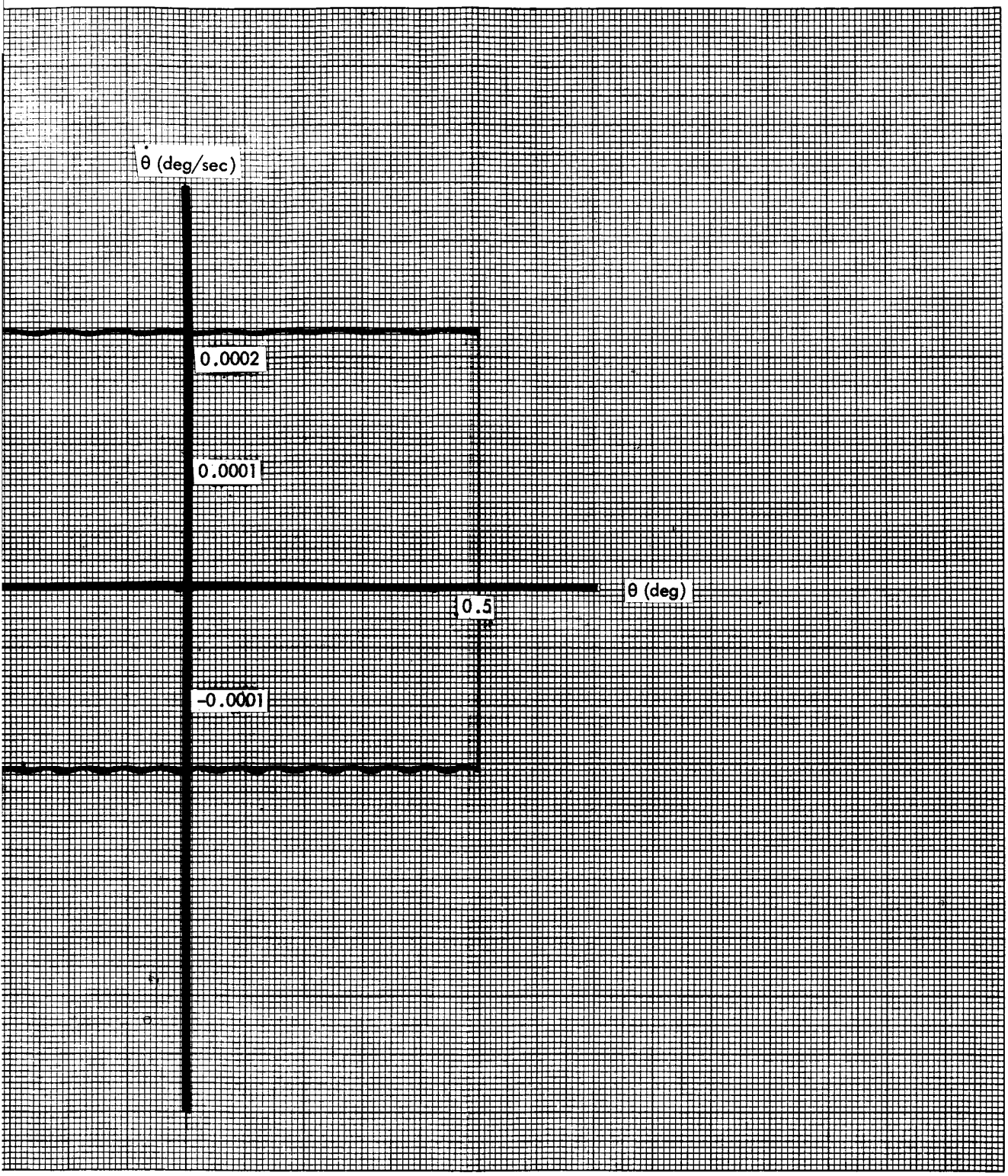

Figure 16. Phase Plane Plot, ω_{11} = 0.01489 Rad/Sec

$T_s = 0.5 \times 10^{-4}$ ft lb, $\omega_{11} = 0.02$ rad/sec, $\omega_{21} = 0.0150$ rad/sec,

$\zeta_{11} = \zeta_{21} = 0\%$, vehicle without capsule

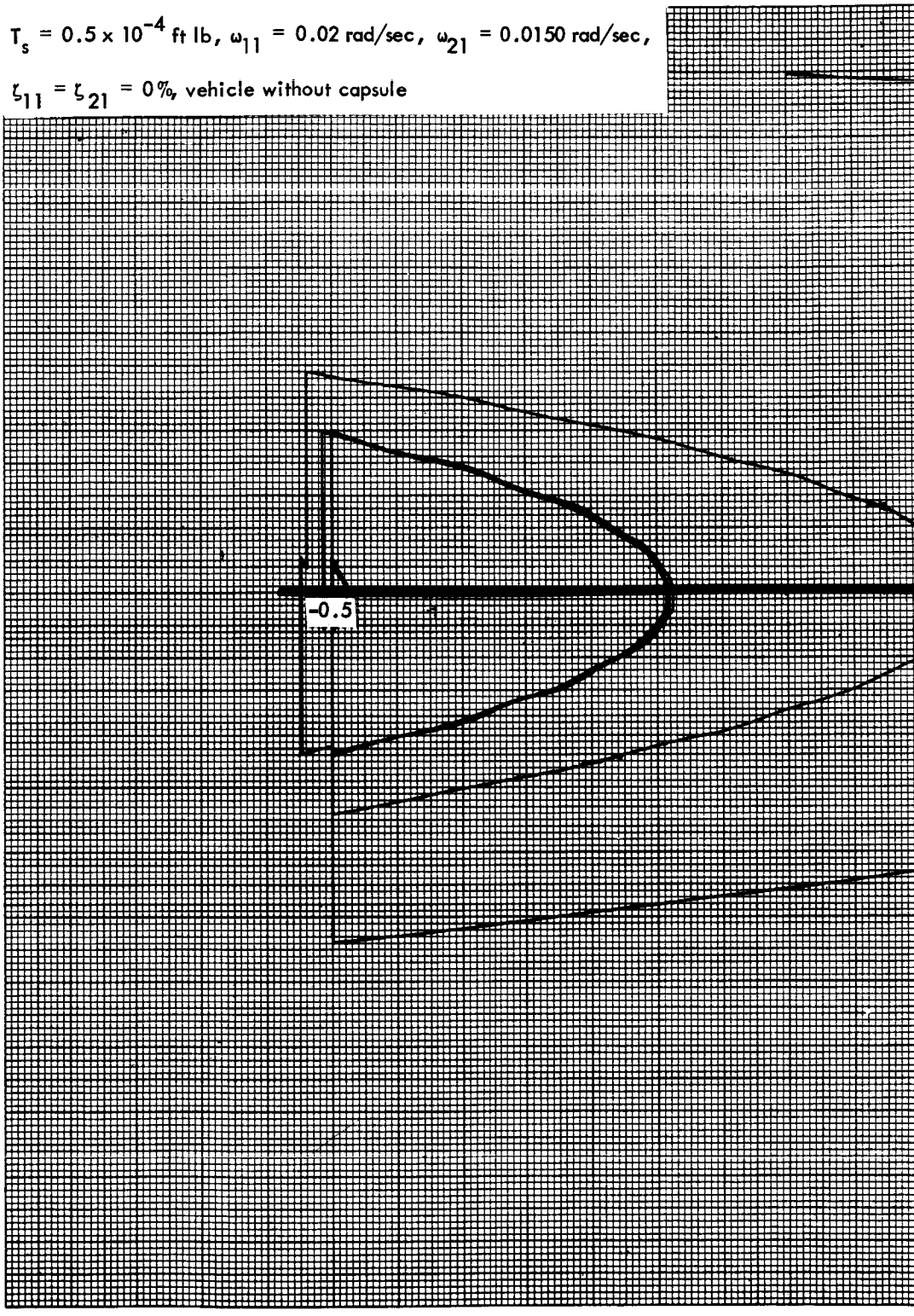

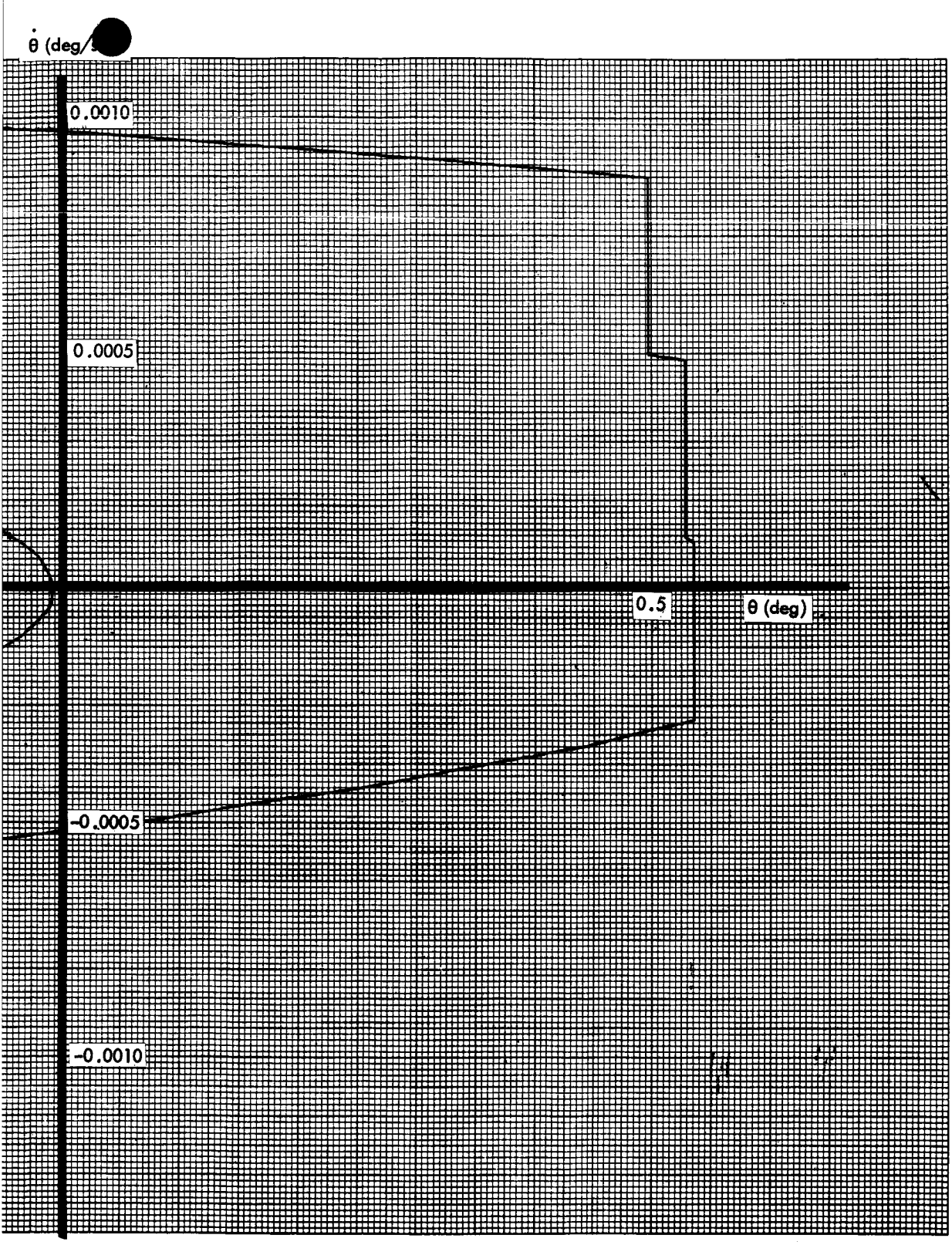

Figure 17. Phase Plane Plot, ω_{11} = 0.02 Rad/Sec

$\dot{\theta}(o) = 0.01°/sec$, $\omega_{11} = 0.02$ rad/sec, $\omega_{21} = 0.015$ rad/sec,

$\zeta_{11} = \zeta_{21} = 1\%$, vehicle without capsule

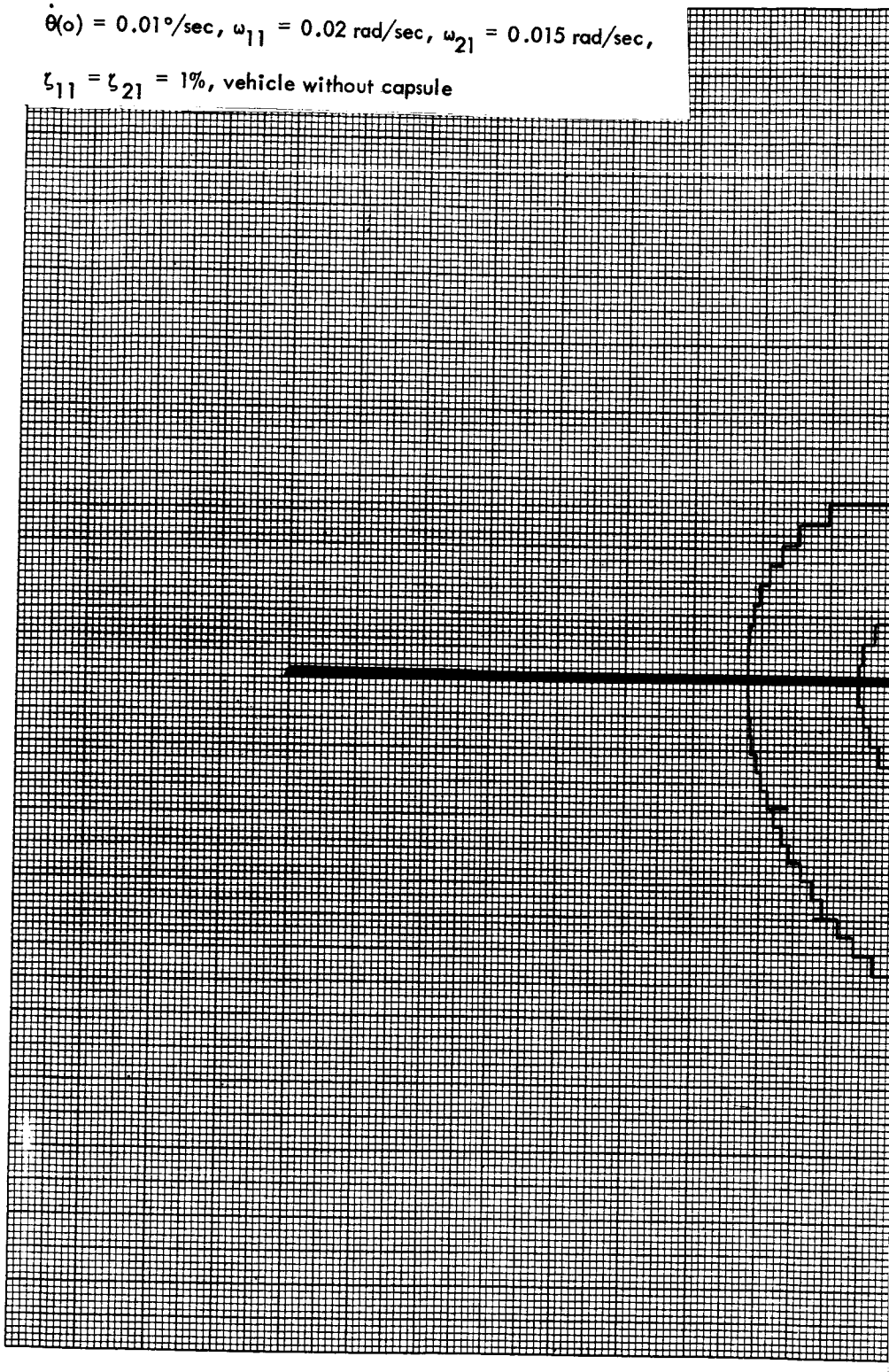

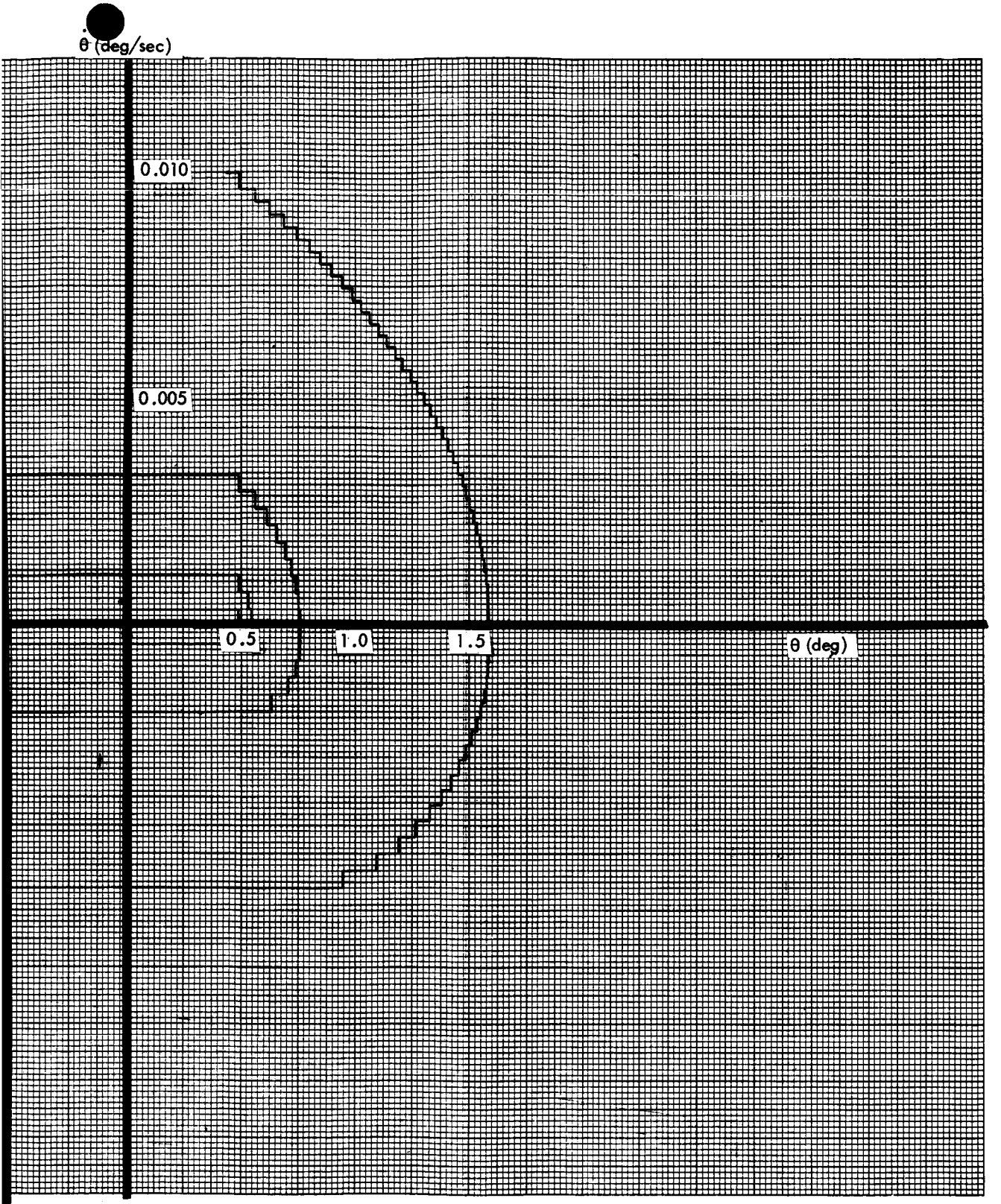

Figure 18. Phase Plane Plot, ω_{11} = 0.02 Rad/Sec

$x_{11}(o) = 1.0$ in., $x_{21}(o) = 1.0$ in., $\omega_{11} = 0.020$ rad/sec,

$\omega_{21} = 0.0150$ rad/sec, $\zeta_{11} = \zeta_{21} = 0\%$, vehicle with capsule

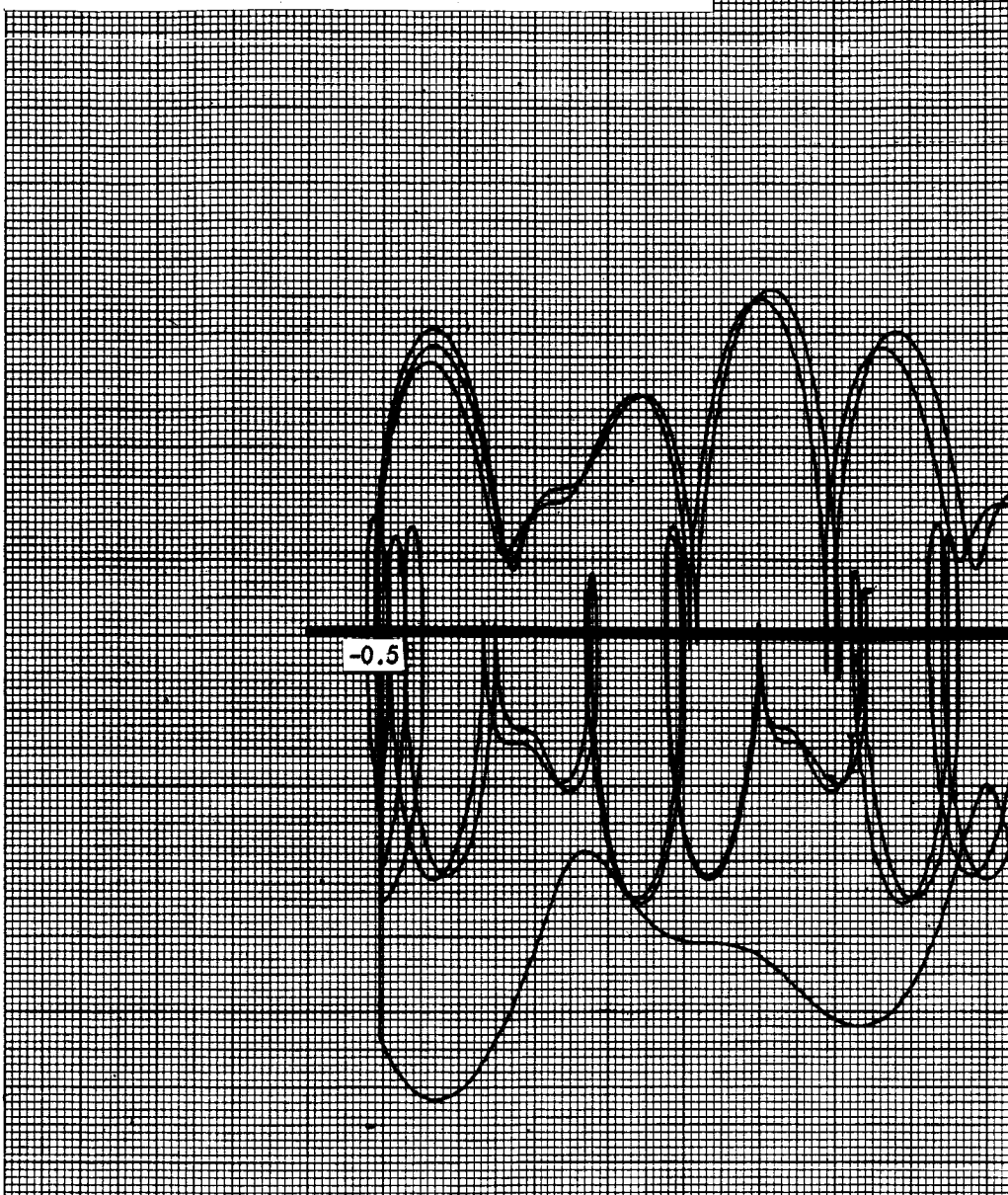

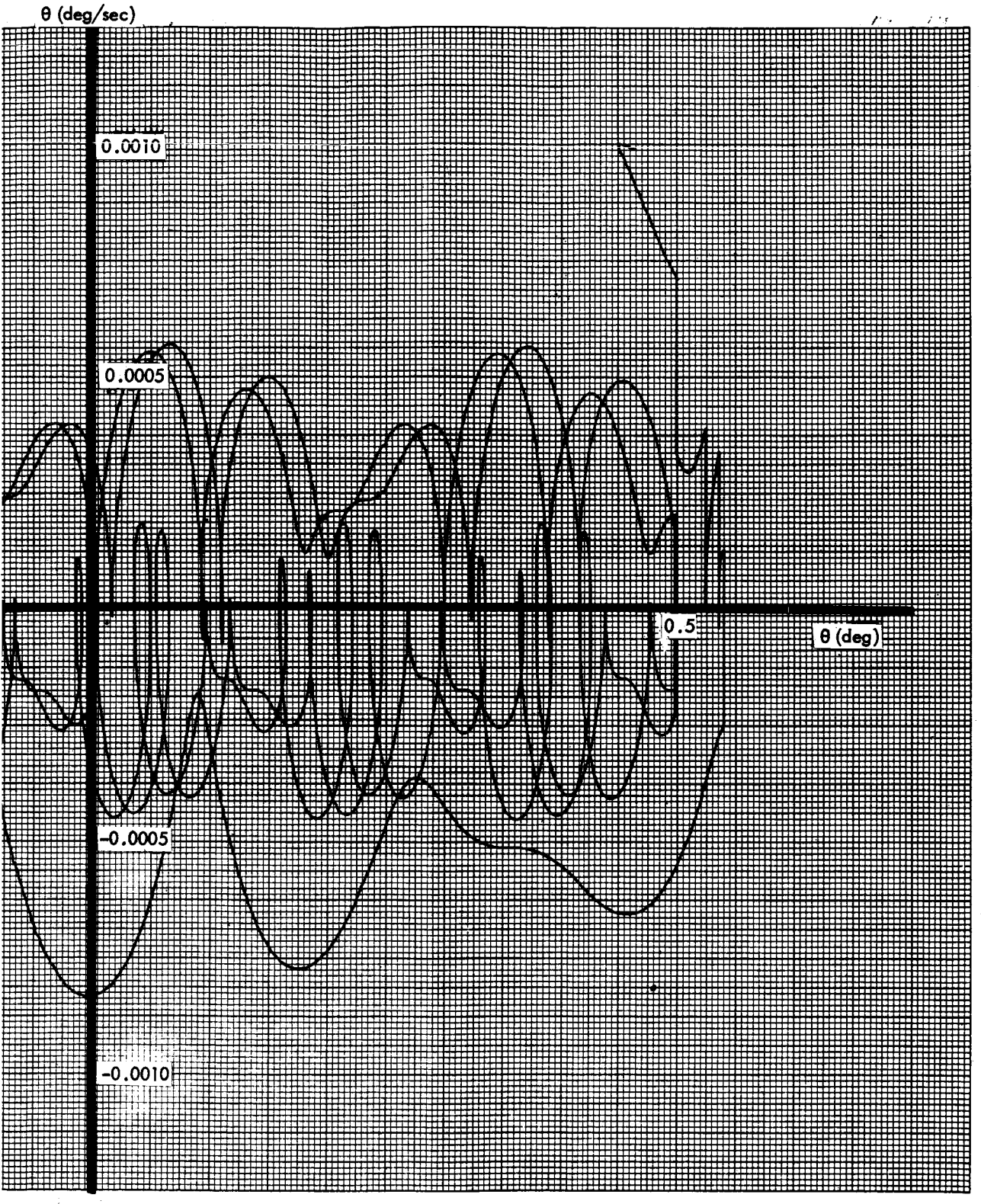

Figure 19. Phase Plane Plot, ω_{11} = 0.020 Rad/Sec

$x_{11}(o) = 1.0$ in., $x_{21}(o) = 1.0$ in., $\omega_{11} = 0.020$ rad/sec, $\omega_{21} = 0.0150$, $\zeta_{11} = \zeta_{21} = 1\%$, vehicle with capsule

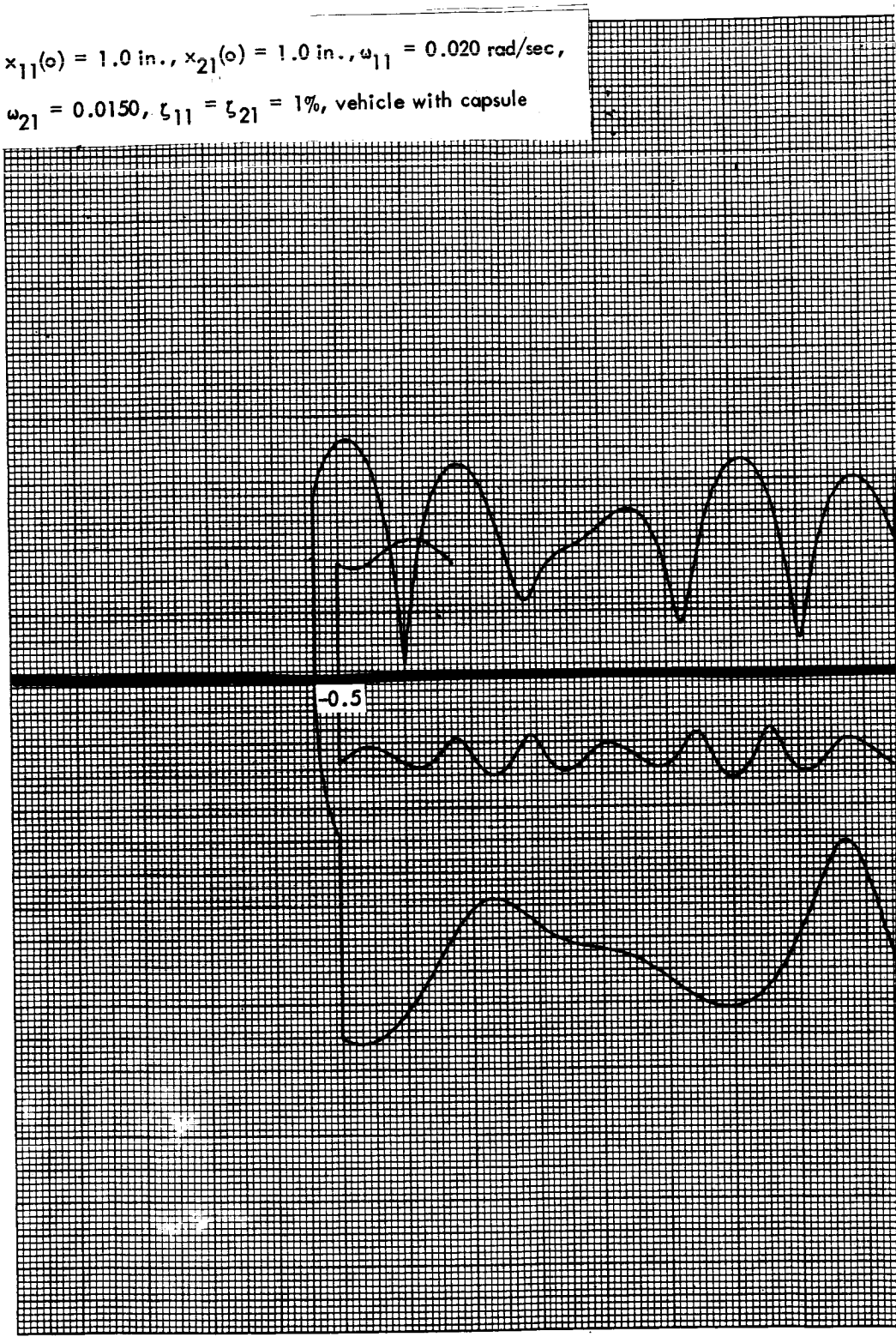

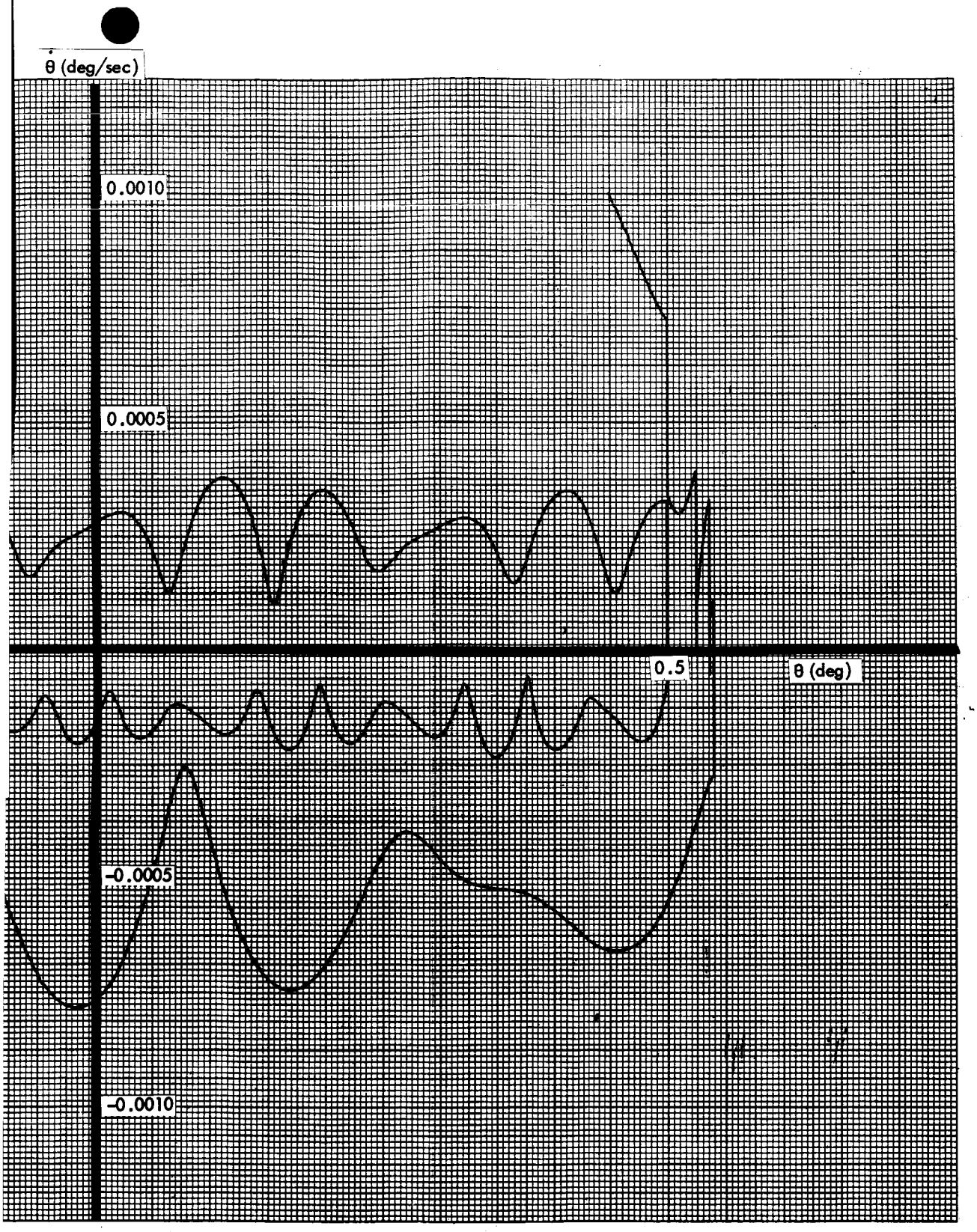

Figure 20. Phase Plane Plot, ω_{11} = 0.020 Rad/Sec

Slosh mass increased by 10, $\omega_{11} = 0.02$ rad/sec,

$\omega_{21} = 0.0150$ rad/sec, $\zeta_{11} = \zeta_{21} = 1\%$, $x_{11}(o) = 0.1$ in.,

$x_{11}(o) = 0.2$ in., vehicle without capsule

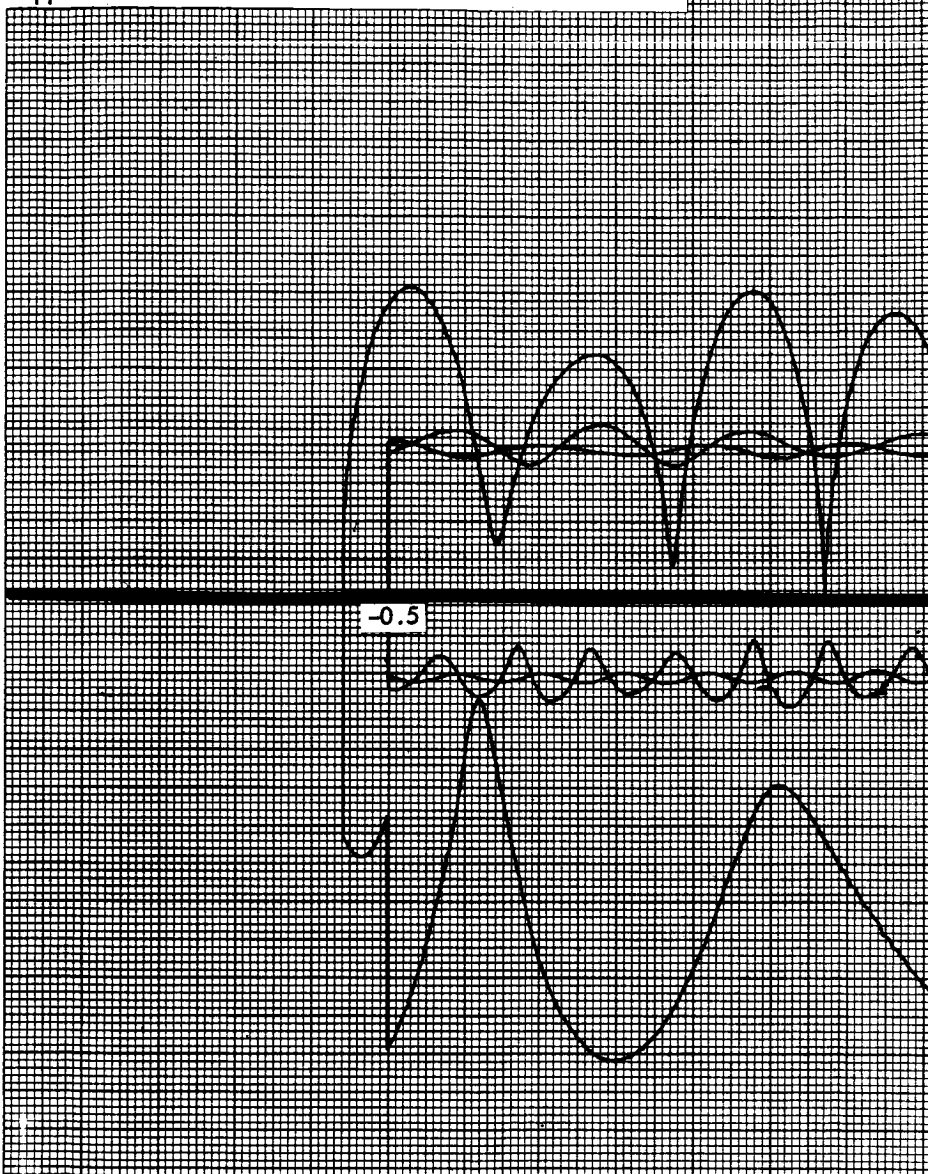

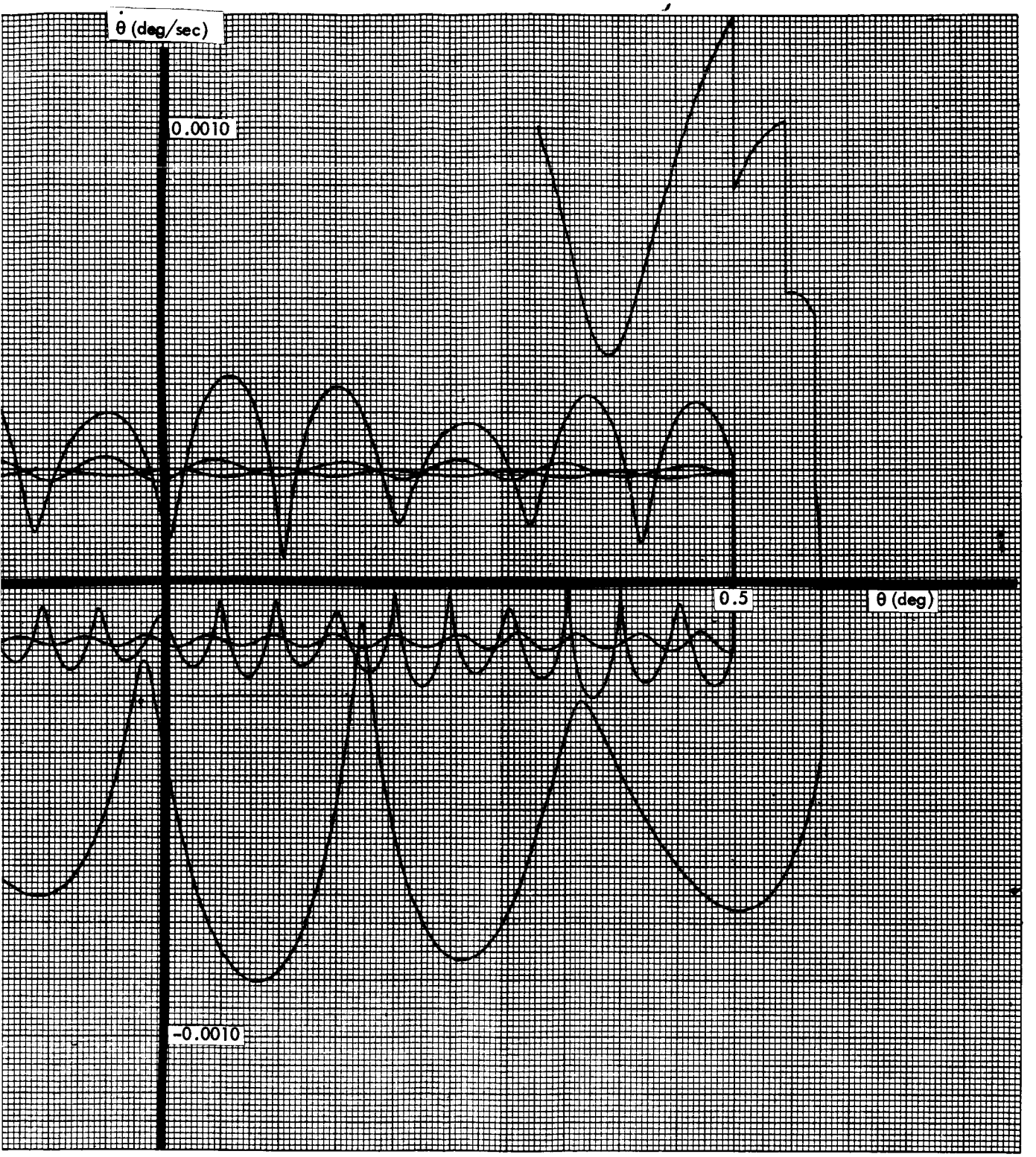

Figure 21. Phase Plane Plot, ω_{11} = 0.02 Rad/Sec

τ = 25 sec, ω_{11} = 0.02 rad/sec, ω_{21} = 0.0150 rad/sec,

$\zeta_{11} = \zeta_{21}$ = 0%, $x_{11}(o)$ = 0.1 in., $x_{21}(o)$ = 0.02 in.,

vehicle without capsule

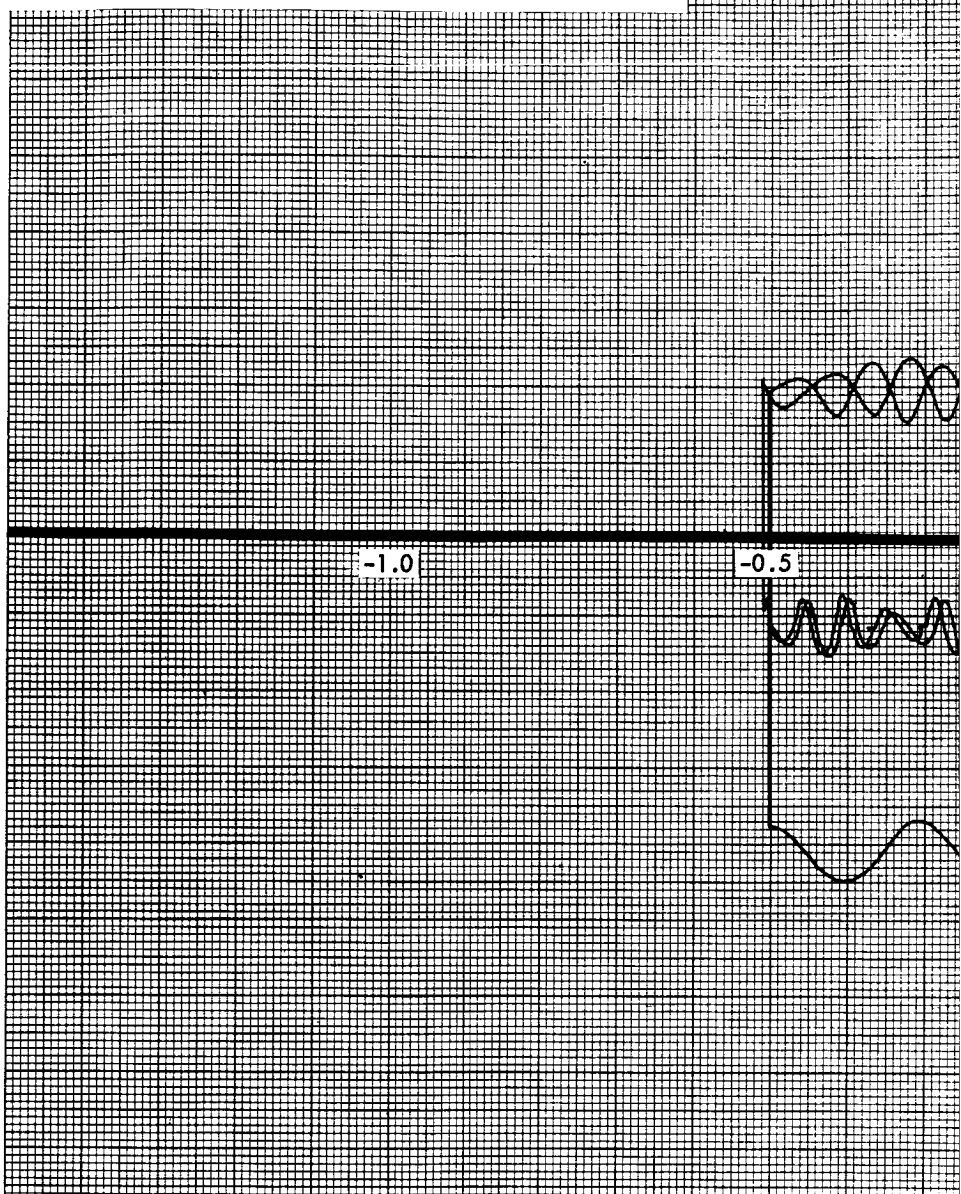

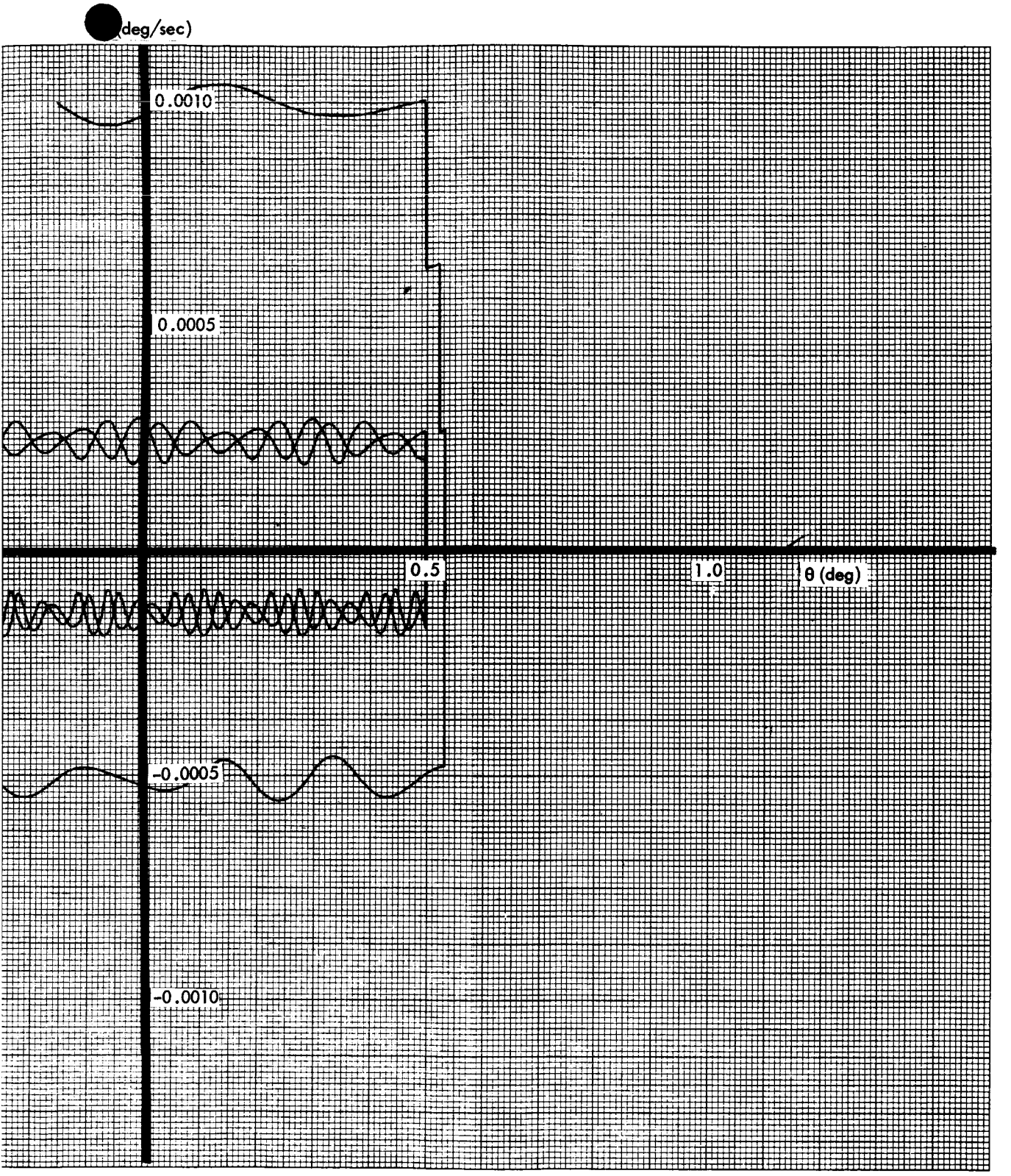

Figure 22. Phase Plane Plot, ω_{11} = 0.02 Rad/Sec

$D = 0.25°$, $\omega_{11} = 0.02$ rad/sec, $\omega_{21} = 0.0150$ rad/sec,

$\zeta_{11} = \zeta_{21} = 0\%$, $x_{11}(o) = 0.1$ in., $x_{21}(o) = 0.2$ in.,

vehicle without capsule

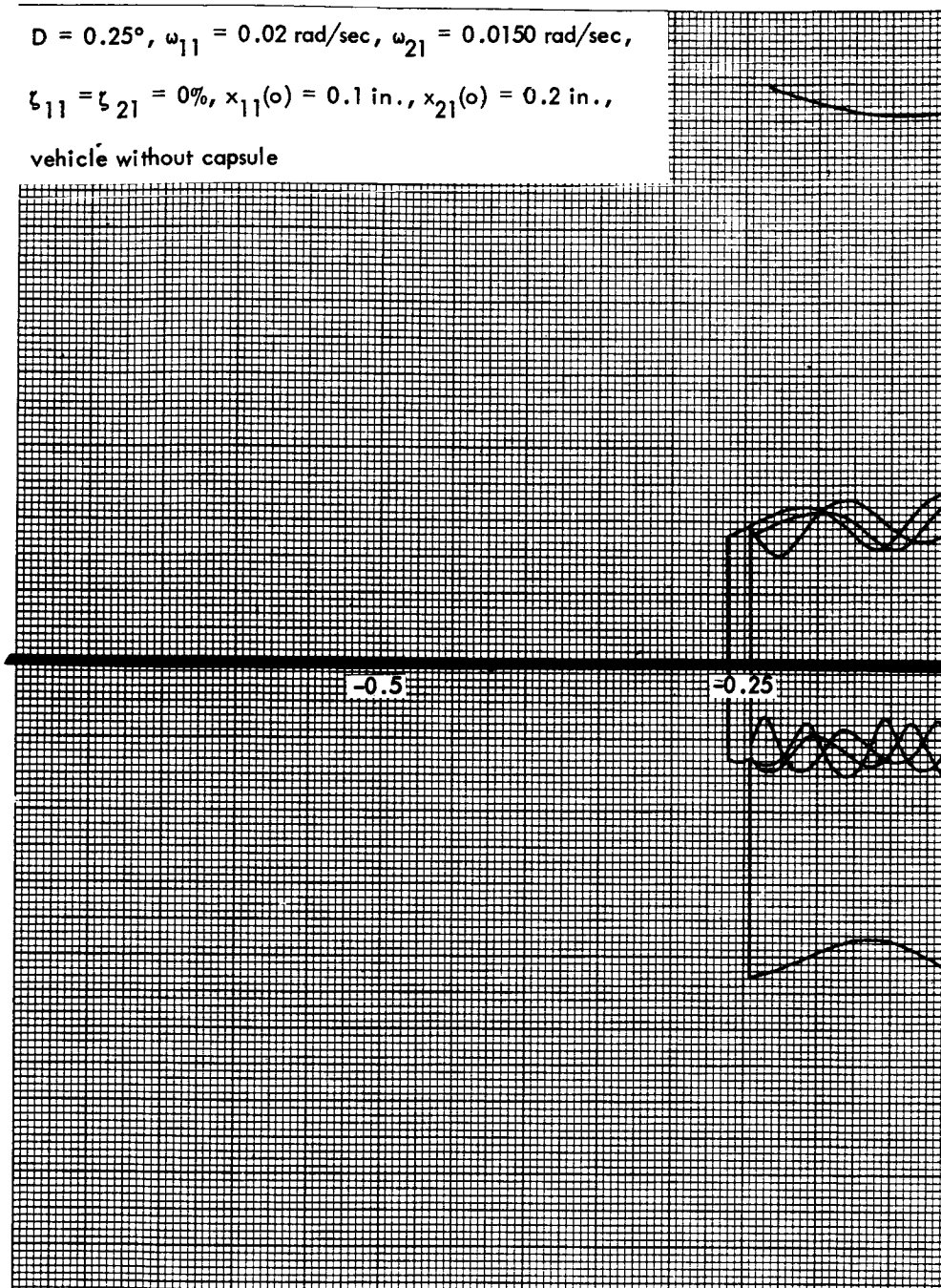

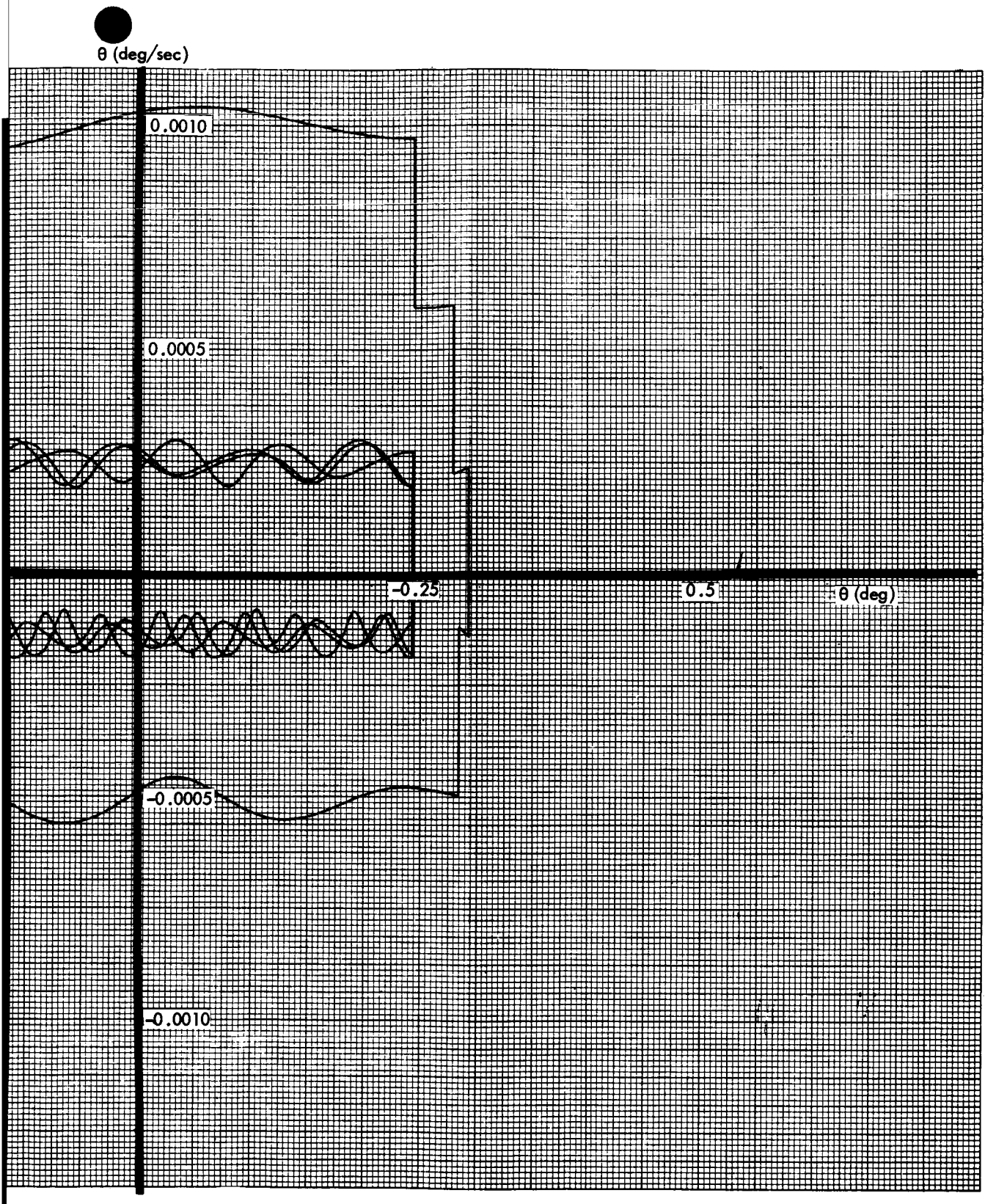

Figure 23. Phase Plane Plot, ω_{11} = 0.02 Rad/Sec

Modulator minimum "on" time doubled, $\omega_{11} = 0.02$ rad/sec

$\omega_{21} = 0.0150$ rad/sec, $\zeta_{11} = \zeta_{21} = 0\%$, $x_{11}(o) = 0.1$ in.,

$x_{21}(o) = 0.2$ in., vehicle without capsule

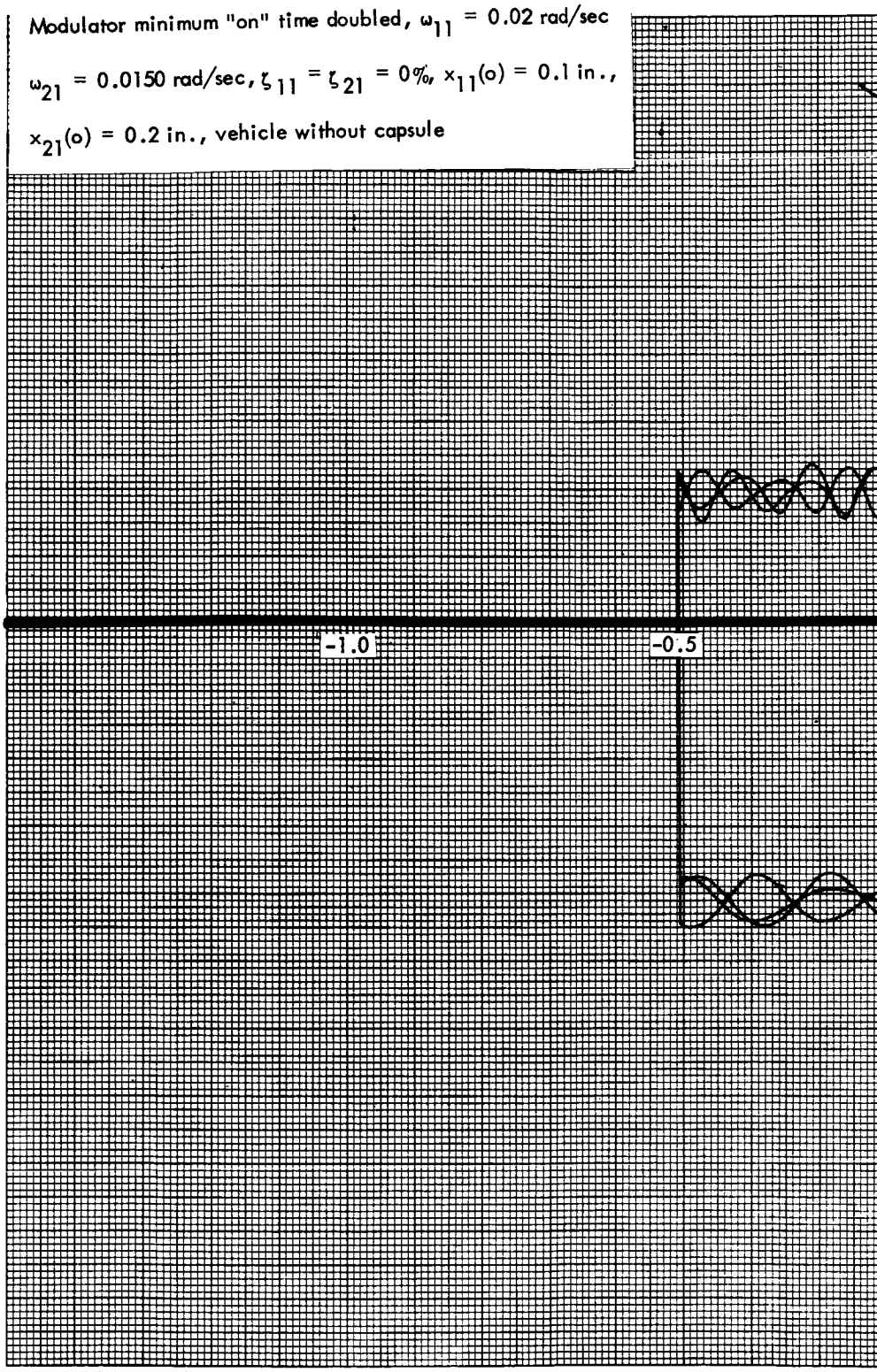

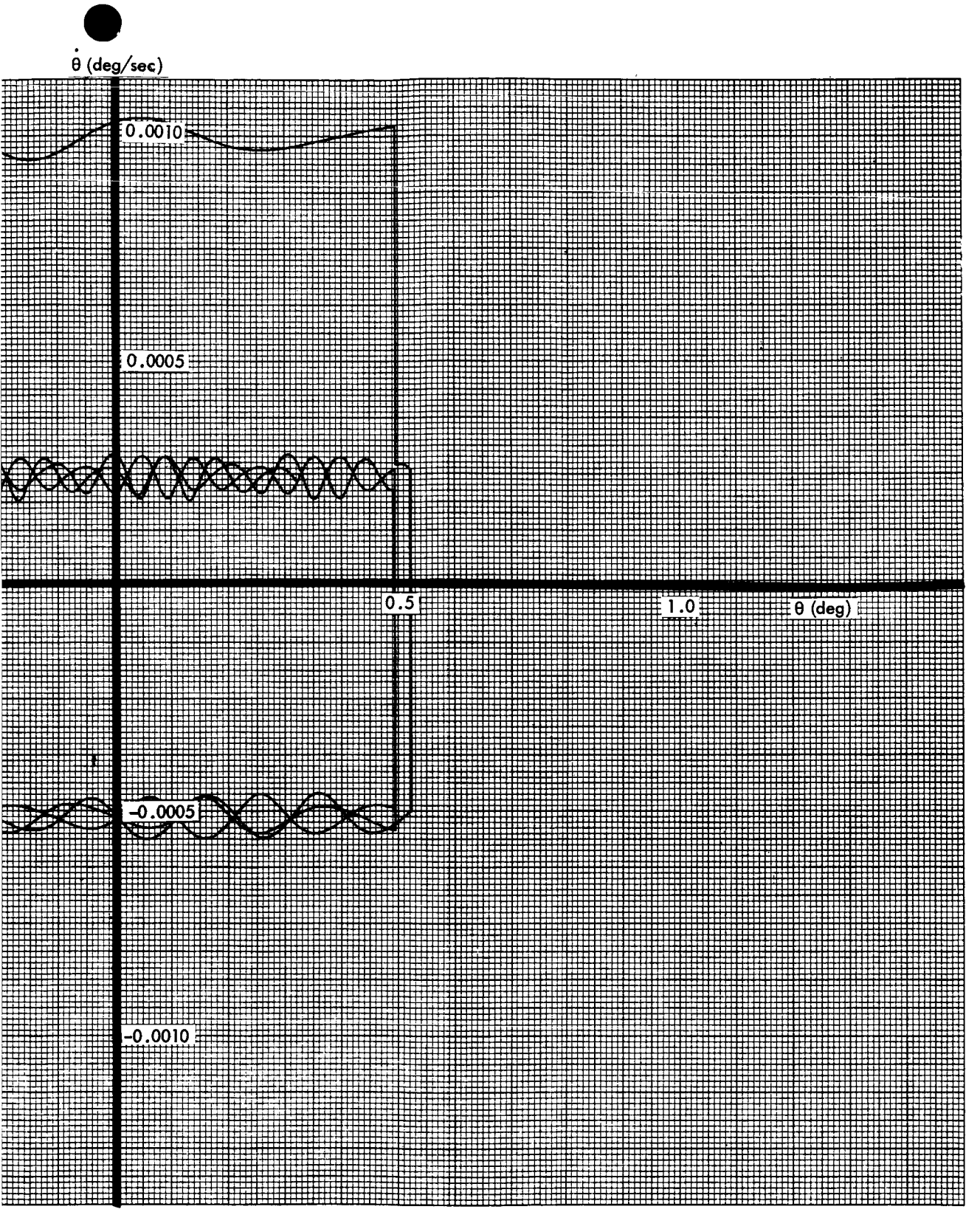

Figure 24. Phase Plane Plot, ω_{11} = 0.02 Rad/Sec

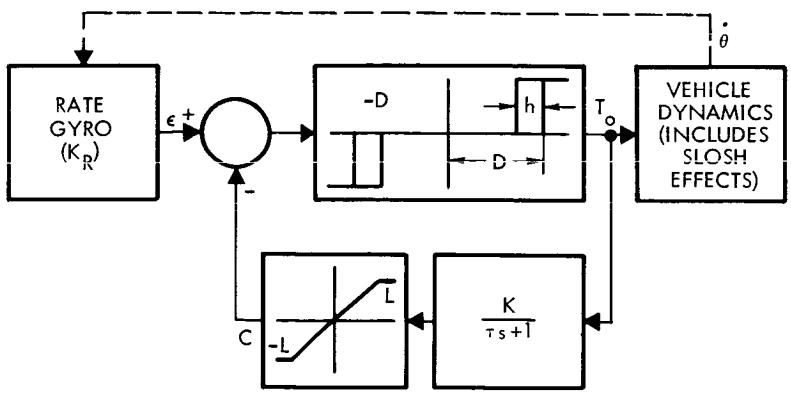

Figure 25. Rate Gyro Mode Block Diagram

2.4.1 Configuration with Capsule

2.4.1.1 Rate Gyro Mode

The variations of vehicle response with parameter changes in the rate gyro mode control system (Figure 25) were investigated. A parameter combination was selected, and the configuration was subjected to large propellant slosh displacements (simulating propellant conditions at booster separation and Voyager main engine thrust cutoff). To provide an indication of the "safety margin" afforded by the design, the vehicle response with the slosh mass increased by a factor of 10 was also investigated.

The nominal control system parameters used for the rate gyro mode (Figure 25) were:

Modulator deadzone, D = 0.5 deg (Reference 2)

Modulator hysteresis, h = 0.1 deg (Reference 2)

Modulator minimum "on" time = 0.025 sec (Reference 2)

Modulator time constant, τ = 50 sec (same on cruise mode, Sections 2.2 and 2.3)

The DRI filter was not limited

A rate gyro gain, K_R, of 50 seconds was used (Reference 2)

The nominal system was subjected to the maximum booster tip-off rate (1.5 deg/sec per Reference 2). The objective of the rate gyro mode

is to reduce the vehicle rate to 0.01 deg/sec before the vehicle attitude changes by more than 10 degrees from the attitude at booster separation. As shown by Figure 26, the vehicle rate was well in excess of 0.01 deg/sec when the attitude excursion exceeded 10 degrees. The seven figures shown in Figure 26 as well as in similar plots to follow are:

ϵ-C = modulator error signal (deg)

T_o = control pulse (on, positive, off, on negative)

C = attitude control command (deg)

$\dot{\theta}$ = vehicle attitude rate (deg/sec)

θ = vehicle attitude (deg)

x_{11} = oxidizer slosh mass displacement (in.)

x_{21} = fuel slosh mass displacement (in.)

The control jets were "on" continuously for about 6 seconds; thereafter, a pulsating control torque was applied and the vehicle attitude increased. The change from a continuous to a pulsating correction torque occurred when the DRI charged up adequately to turn off the modulator.

Increasing the rate gyro gain, or reducing the DRI filter gain, or reducing the DRI filter time constant, increases the duration of continuous torque application, thus reducing the rate of attitude error buildup. Since increasing the rate gyro gain might increase the noise level at the modulator input, this method was not pursued.

As predicted, a reduction in the DRI filter time constant improved vehicle performance (Figures 27 and 28). In fact, with the DRI filter time constant reduced to 1 second, the vehicle rate decreased to 0.01 deg/sec in about 18.7 seconds with an 8.5-degree attitude error (Figure 29).

The modulator minimum "on" time, t_{min}, can be approximately determined by the following equation,

$$t_{min} \approx \frac{h\tau}{K T_o}$$

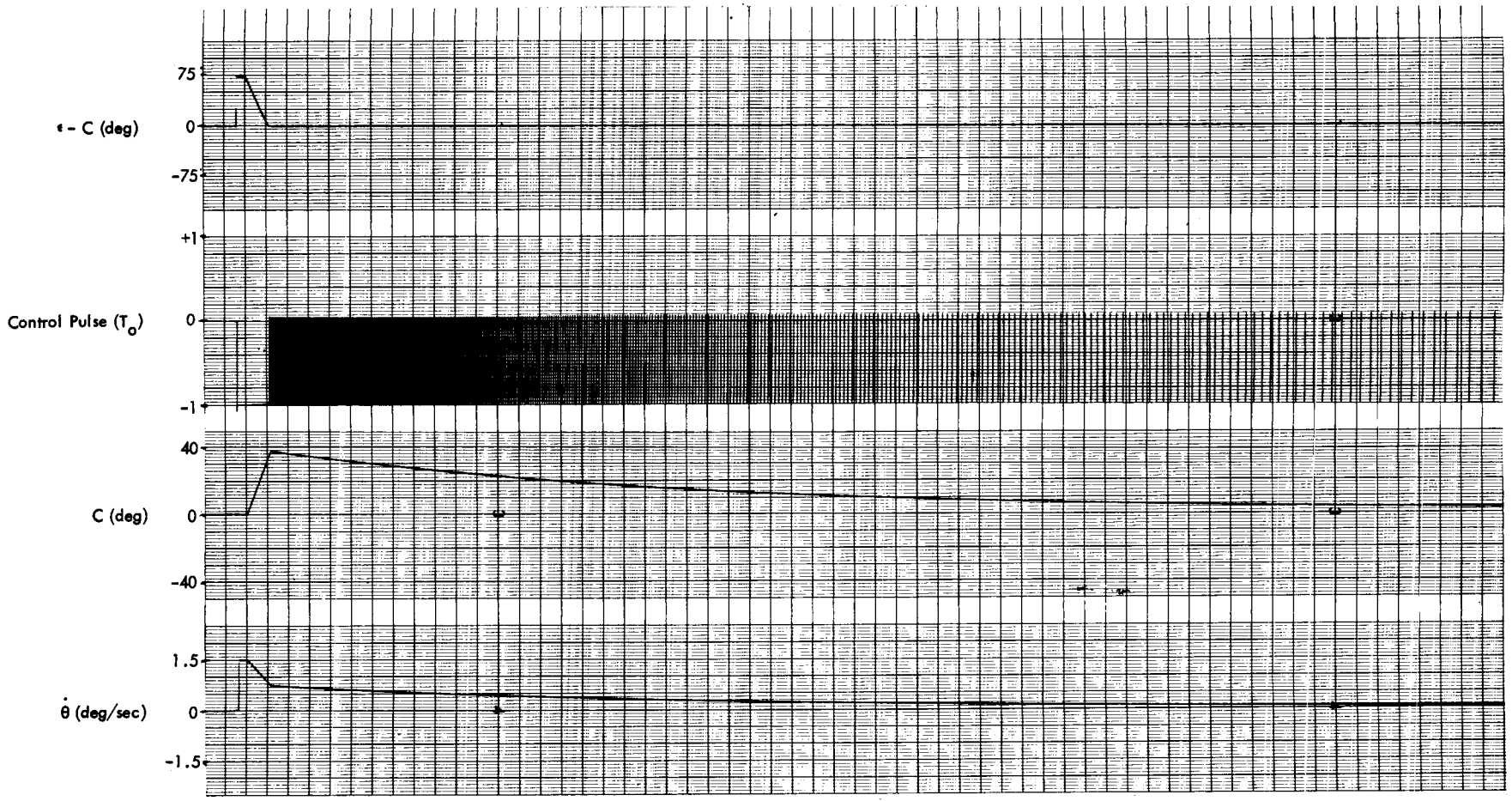
75
0
-75
ε - C (deg)
+1
0
-1
Control Pulse (T_o)
40
0
-40
C (deg)
1.5
0
-1.5
θ̇ (deg/sec)

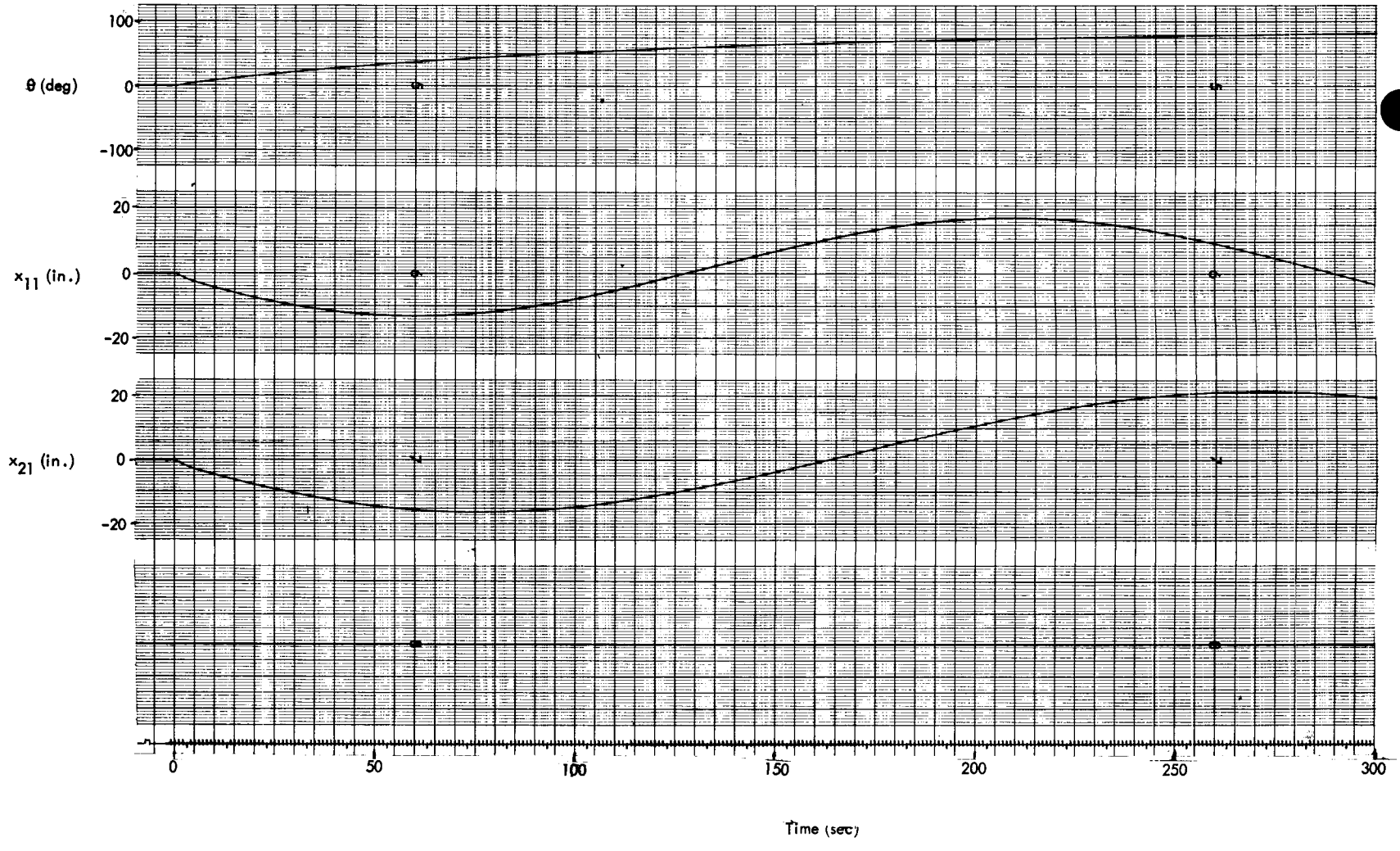

Figure 26. Nominal Rate Gyro Mode Performance, Configuration with Capsule, $\dot{\theta}$ (o) = 1.5 Deg/Sec

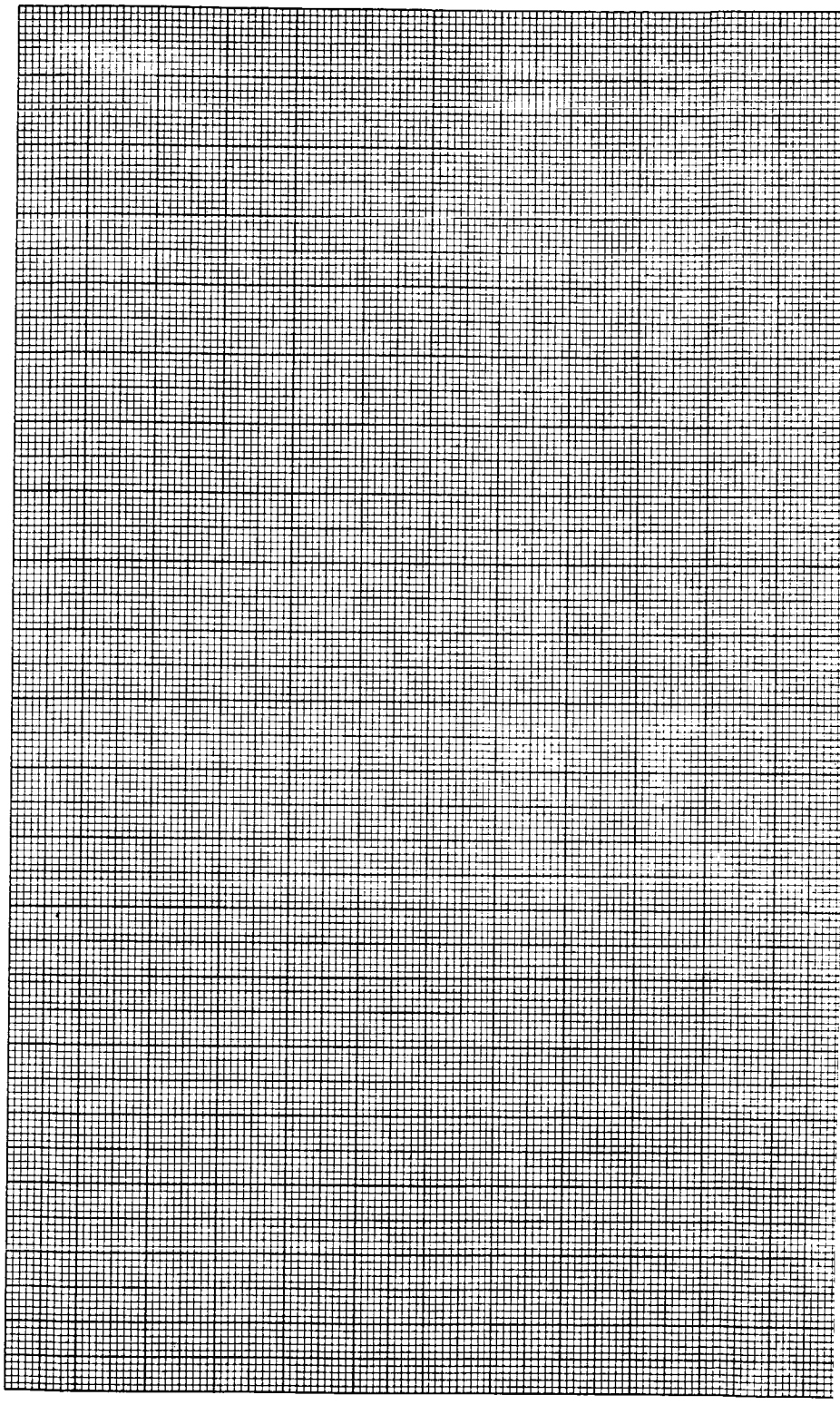

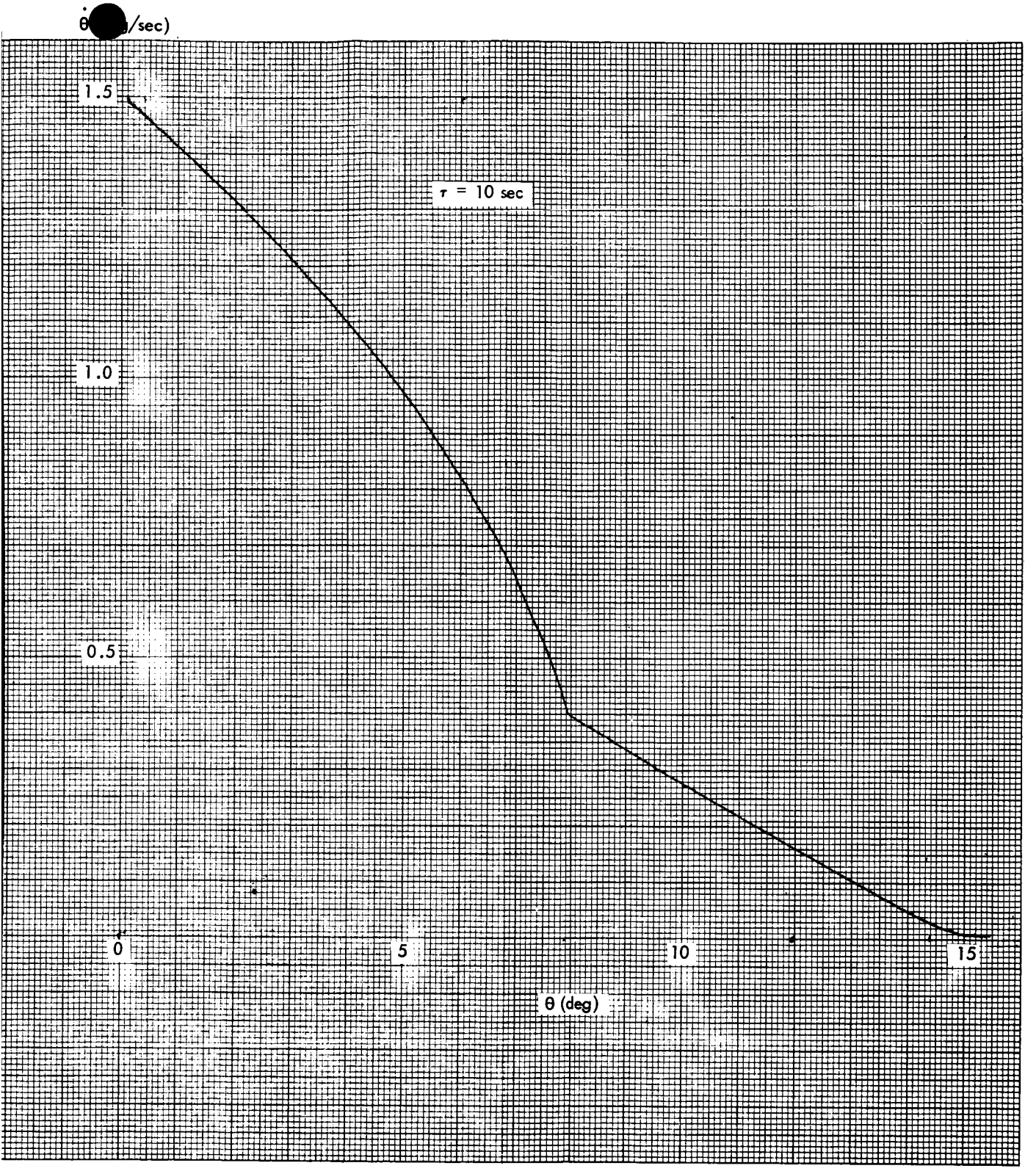

Figure 27. Rate Gyro Mode, Configuration with Capsule, DRI Time Constant = 10 Sec, Rigid Body Representation of Vehicle

θ̇ (deg/sec)
1.5
1.0
0.5
0
1

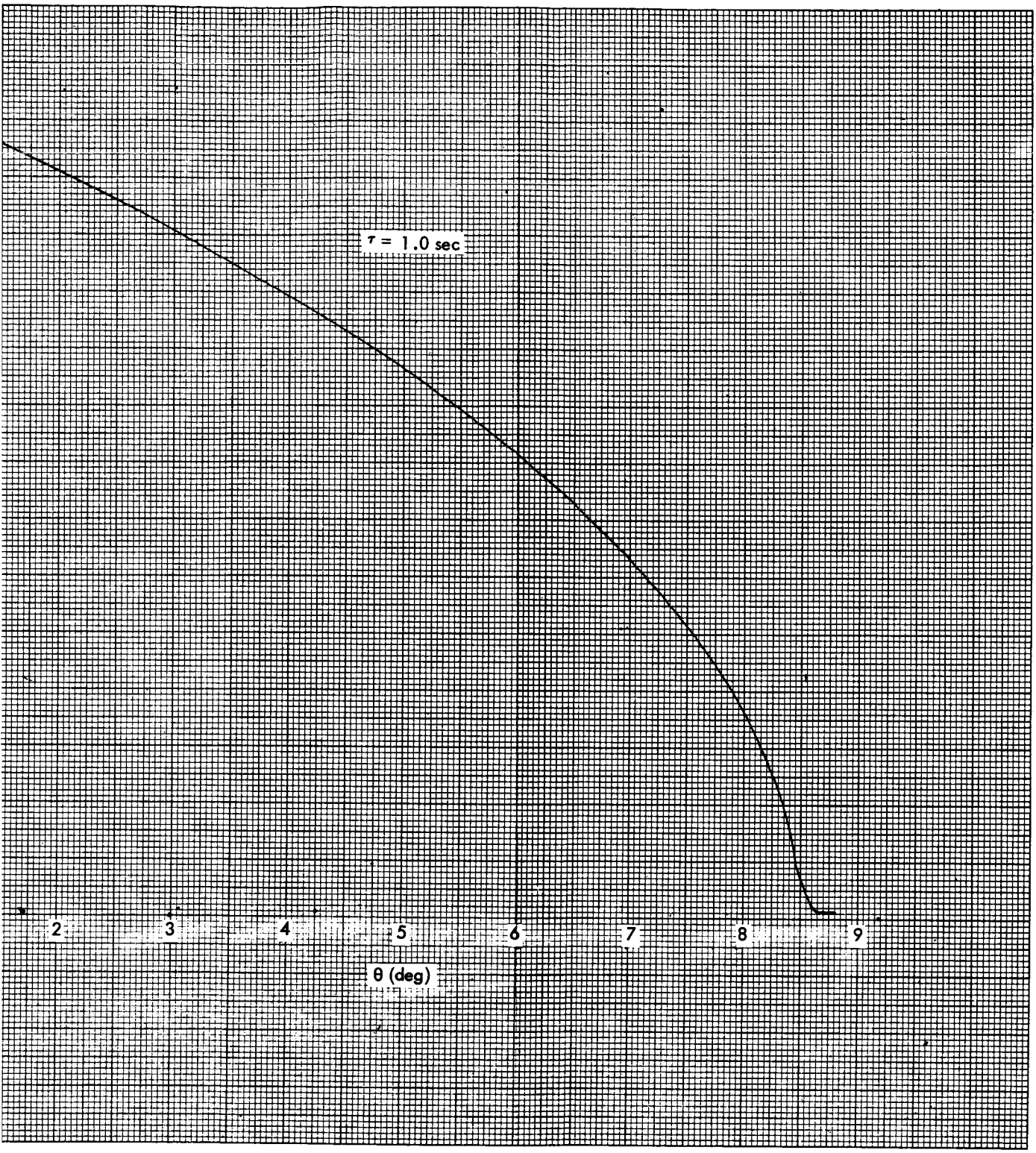

Figure 28. Rate Gyro Mode, Configuration with Capsule, DRI Time Constant = 1 Sec, Rigid Body Representation of Vehicle

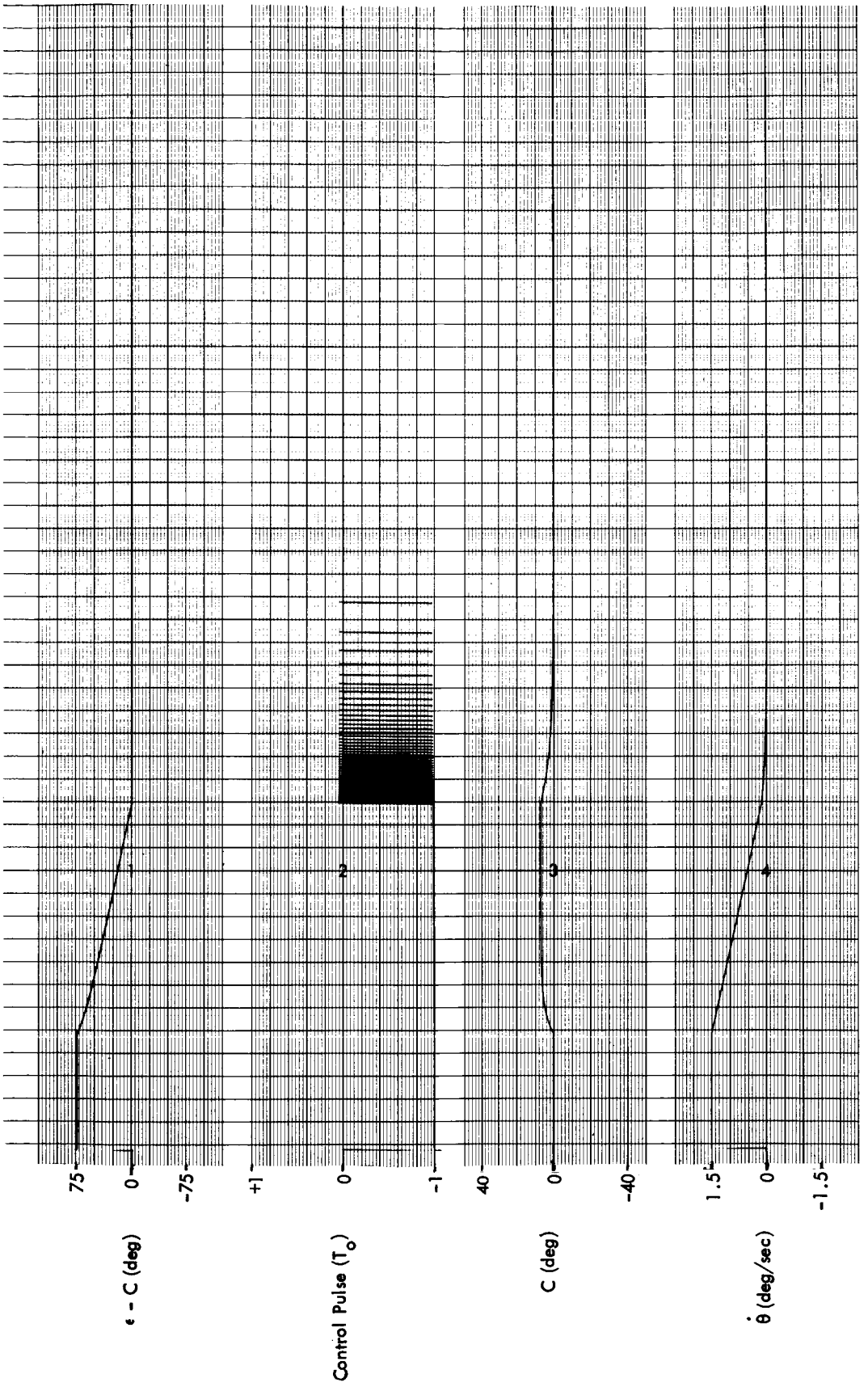
75
0
-75
ε - C (deg)
+1
0
-1
Control Pulse (T_c)
40
0
-40
C (deg)
1.5
0
-1.5
θ̇ (deg/sec)
2
3
4

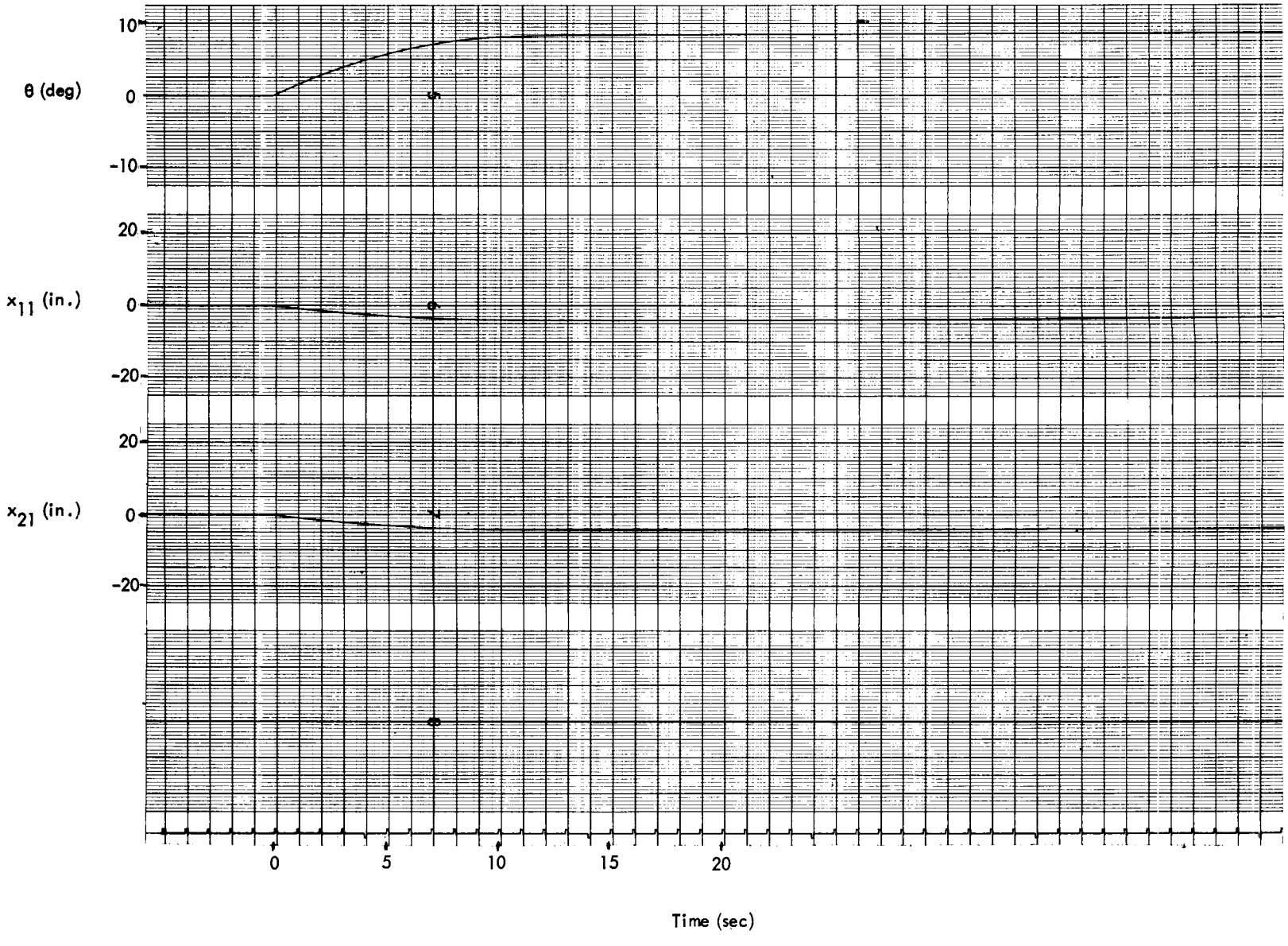

Figure 29. Rate Gyro Mode, Configuration with Capsule, DRI Time Constant = 1 Sec, $\dot{\theta}(o)$ = 1.5 Deg/Sec

Also, the DRI filter output $C = KT_o(1 - e^{-t/\tau})$ assuming the initial filter output was zero. Therefore,

$$C \approx \frac{h\tau}{t_{min}} (1 - e^{-t/\tau})$$

For $t > 5\tau$, $C \approx h\tau/t_{min}$. For the rate gyro mode of Figure 25, the modulator will turn off when $C - K_R \dot{\theta} = D - h$. Therefore, for $t > 5\tau$, the modulator will turn off when

$$\dot{\theta} = \frac{D - h + \frac{h\tau}{t_{min}}}{K_R}$$

Thereafter, until the body rate is reduced to 0.01 deg/sec, the modulator provides approximately minimum control pulses at a rate determined by the vehicle rate and the DRI filter time constant. As shown by the above equation, the rate at which the control torque will change from a continuous to a pulsating torque can be reduced by reducing the filter time constant.

Since the uses of a time constant of about 1 second during cruise (Section 2.2) does not appear advisable, switching of time constants between modes would be required.

The DRI filter was removed (K = 0 in Figure 25). The transition from 1.5 to 0.01 deg/sec was completed in about 11 seconds (Figure 30). The attitude error was approximately 8.2 degrees.

As an alternate to completely removing the filter, the filter limit, L, was reduced. As L was reduced, the response improved (Figures 31 and 32). By reducing L to 0.2 degree, the response obtained (Figure 31) was almost as good as with the filter removed (Figure 30).

To simulate large wave heights in the propellant tanks the slosh masses were initially displaced ±6 inches (Figures 33 and 34). This amplitude corresponds to roughly a 0.5-degree peak rigid body attitude excursion at slosh frequencies. For the -6 inch slosh displacement, the

low frequency sloshing induced three additional minimum pulses after about 20 seconds (Figure 34). The nominal response of the vehicle ($\theta, \dot{\theta}$) was changed only slightly by the sloshing.

To provide an indication of the safety margin inherent in the design, the slosh mass was increased by a factor of 10. The transition time from 1.5 to 0.01 deg/sec was unaffected by the increase in slosh mass (Figure 35). Except for a series of minimum bit pulses induced by the sloshing approximately 160 seconds after the beginning of the run, the vehicle response also was hardly affected by the increase in slosh mass.

2.4.1.2 Position Gyro Modes

The best rate gyro mode responses, previously given, resulted in attitude changes of approximately 8.5 degrees (for initial rates of 1.5 deg/sec) before the rate was reduced to 0.01 deg/sec. Thereafter, the vehicle attitude increased at approximately 0.01 deg/sec. It was hypothesized that using a position gyro in lieu of the rate gyro would result in limit cycling within the deadzone (0.5 deg), thereby improving the antenna look angles.

The effect of DRI filter time constant variations of the position gyro mode of Figure 36 was studied for the configuration without capsule (Figure 37). As the filter time constant was decreased, the maximum attitude excursion during recovery from the initial rate of 1.5 deg/sec decreased; unfortunately, the system response also became more oscillatory. Without the filter the system became unstable (Figure 37a). Since the position gyro has limit stops, the maximum excursions must be constrained. For the configuration with capsule, the maximum attitude excursions would be larger than those shown in Figure 37 (the maximum angular acceleration is smaller since the inertia with the capsule is larger). To avoid hitting the limit stops, small time constants could be used as shown in Figures 37b and 37c for τ = 1 and 10 seconds, respectively. Therefore, in this case, the switching of time constants between modes would be required (τ = 50 seconds for cruise mode).

A position gyro mode with a lead-lag filter to provide system damping was devised (Figure 38). The input to the DRI filter was removed

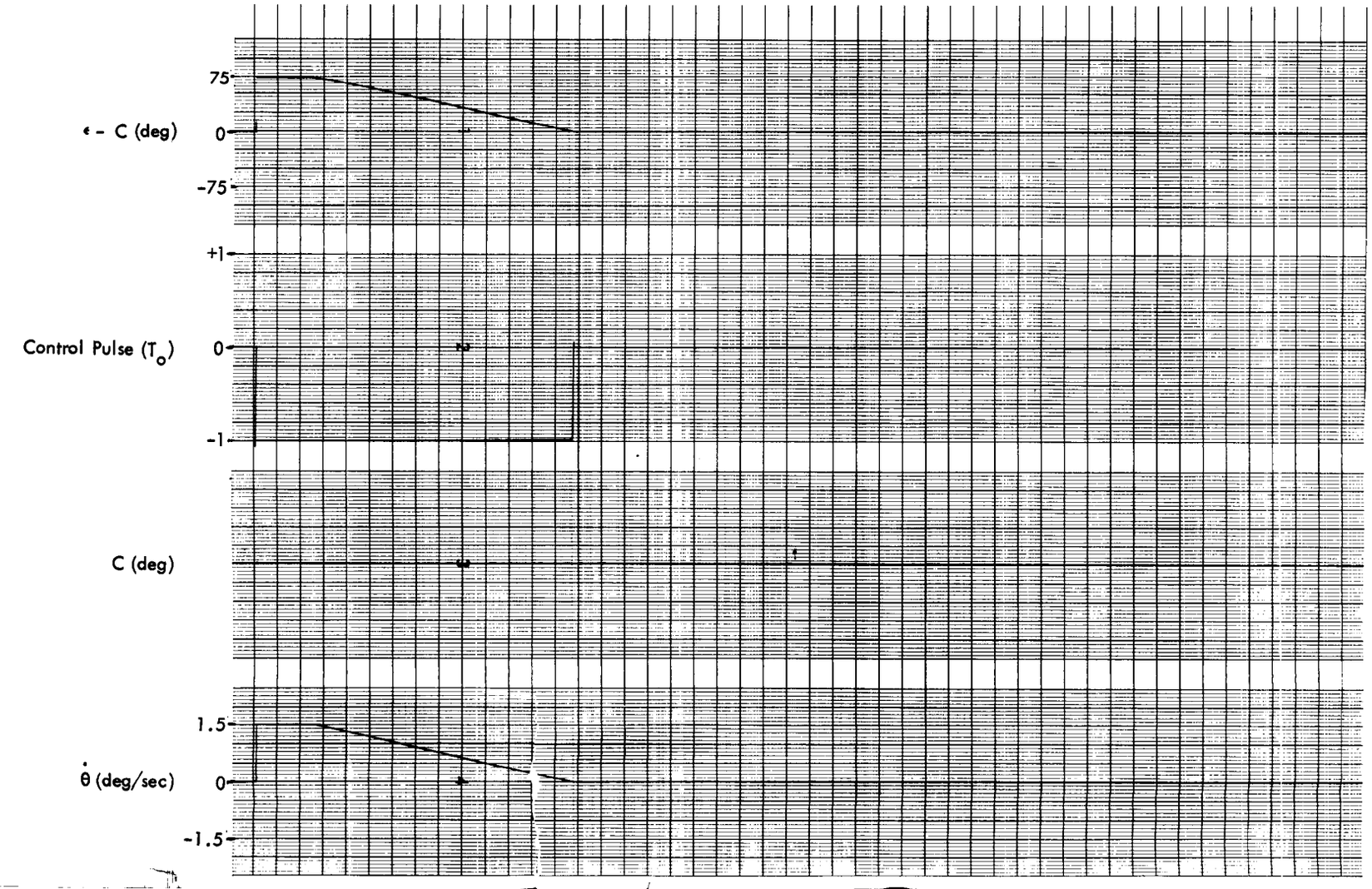
75
ϵ - C (deg)
0
-75
+1
Control Pulse (T_o)
0
-1
C (deg)
1.5
θ̇ (deg/sec)
0
-1.5

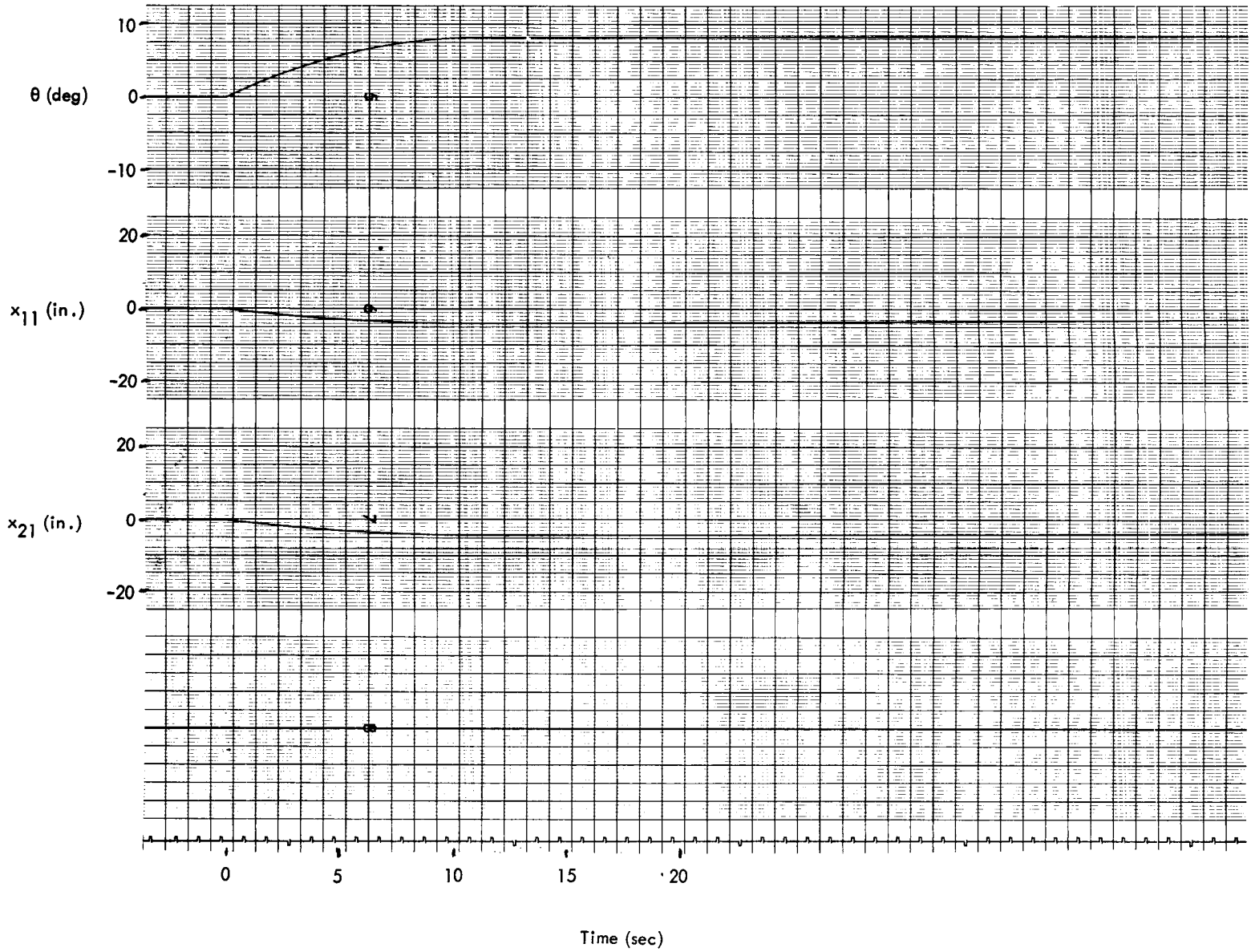

Figure 30. Rate Gyro Mode, Configuration with Capsule, DRI Filter Removed, $\dot{\theta}$ (o) = 1.5 Deg/Sec

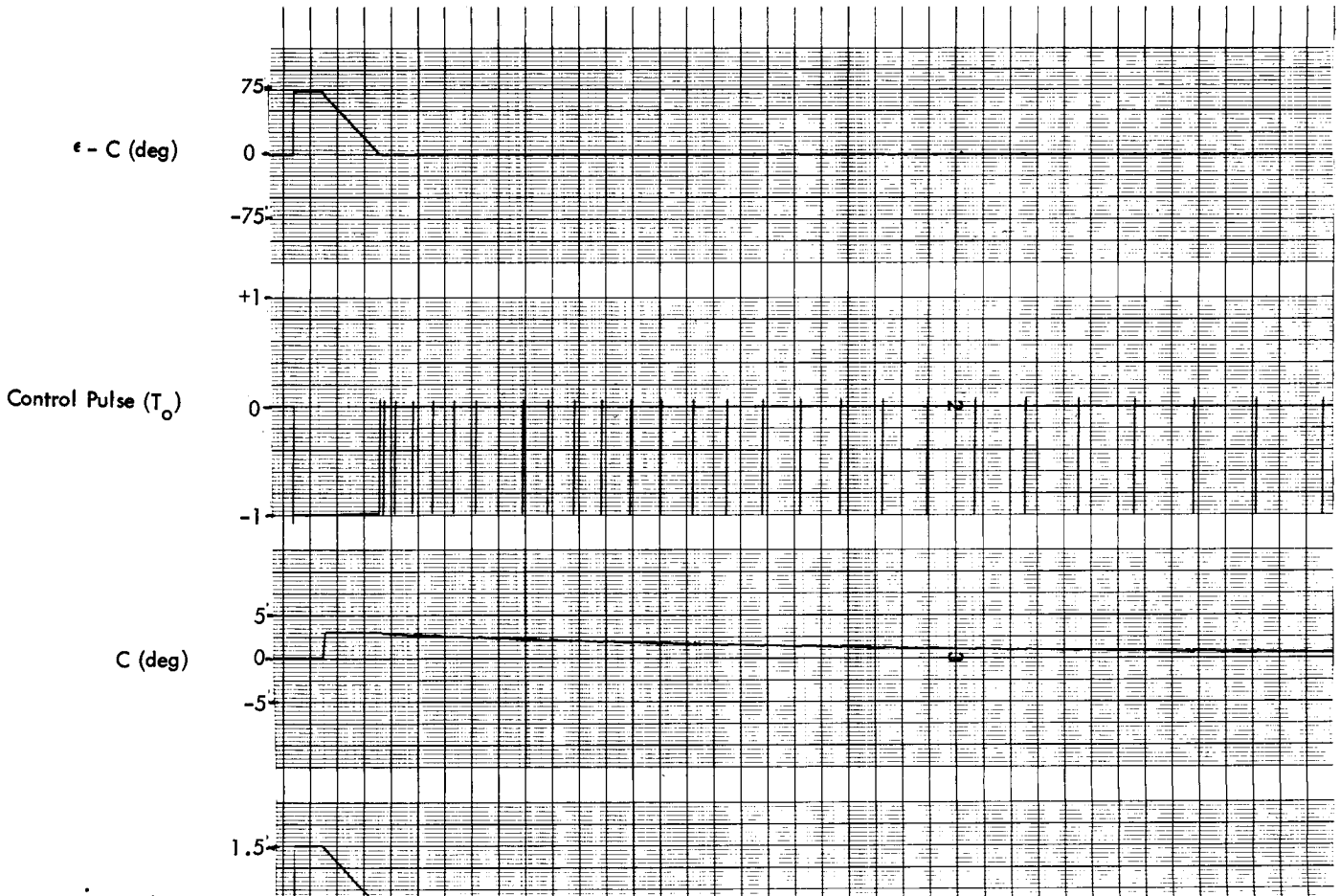
ϵ - C (deg)
75
0
-75
Control Pulse (T_o)
+1
0
-1
C (deg)
5
0
-5
1.5

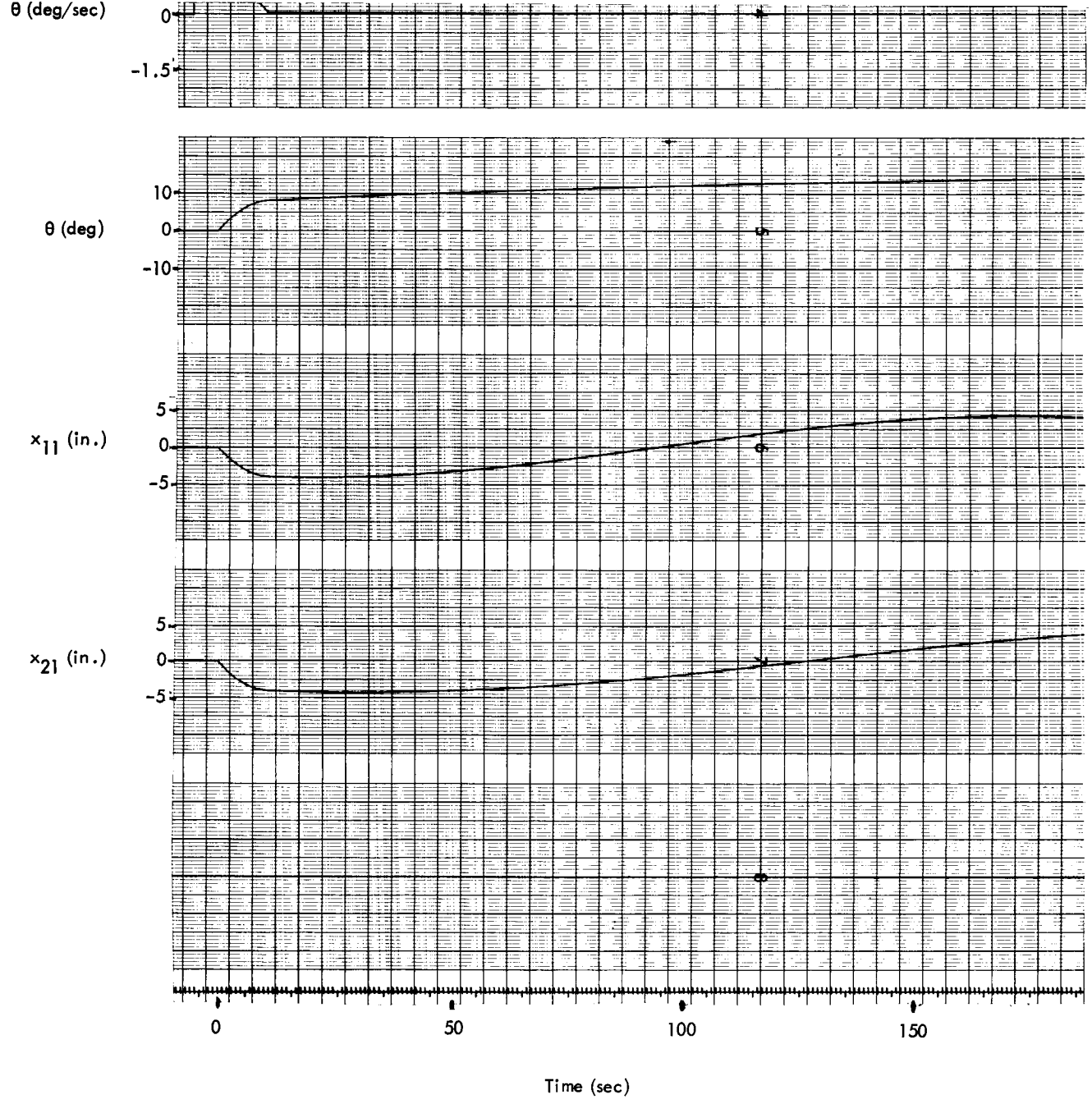

Figure 31. Rate Gyro Mode, Configuration with Capsule, DRI Filter Limit L = 3 Deg, $\dot{\theta}$(o) = 1.5 Deg/Sec

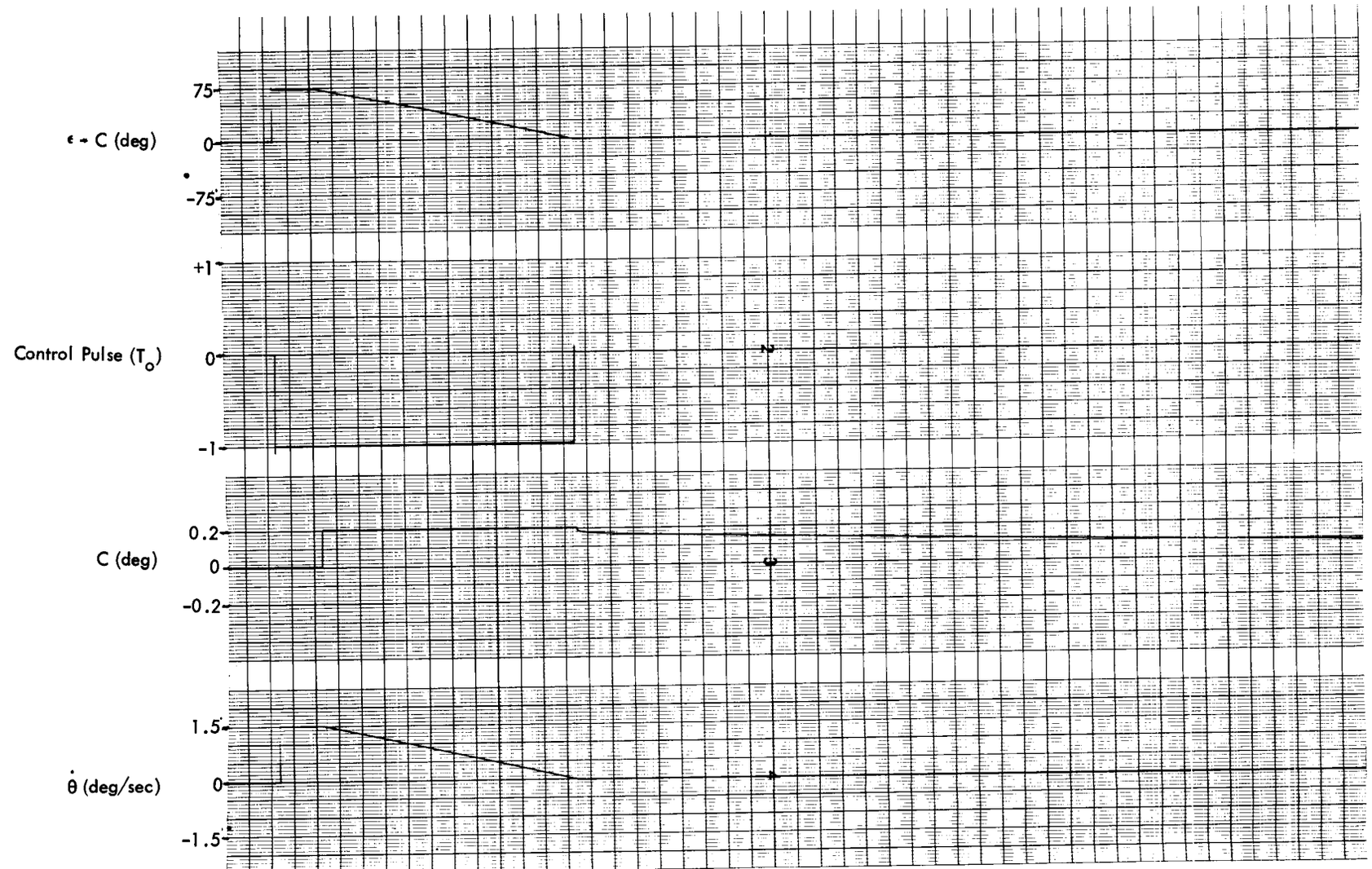
75
0
-75
ϵ → C (deg)
+1
0
-1
Control Pulse (T_o)
0.2
0
-0.2
C (deg)
1.5
0
-1.5
θ̇ (deg/sec)

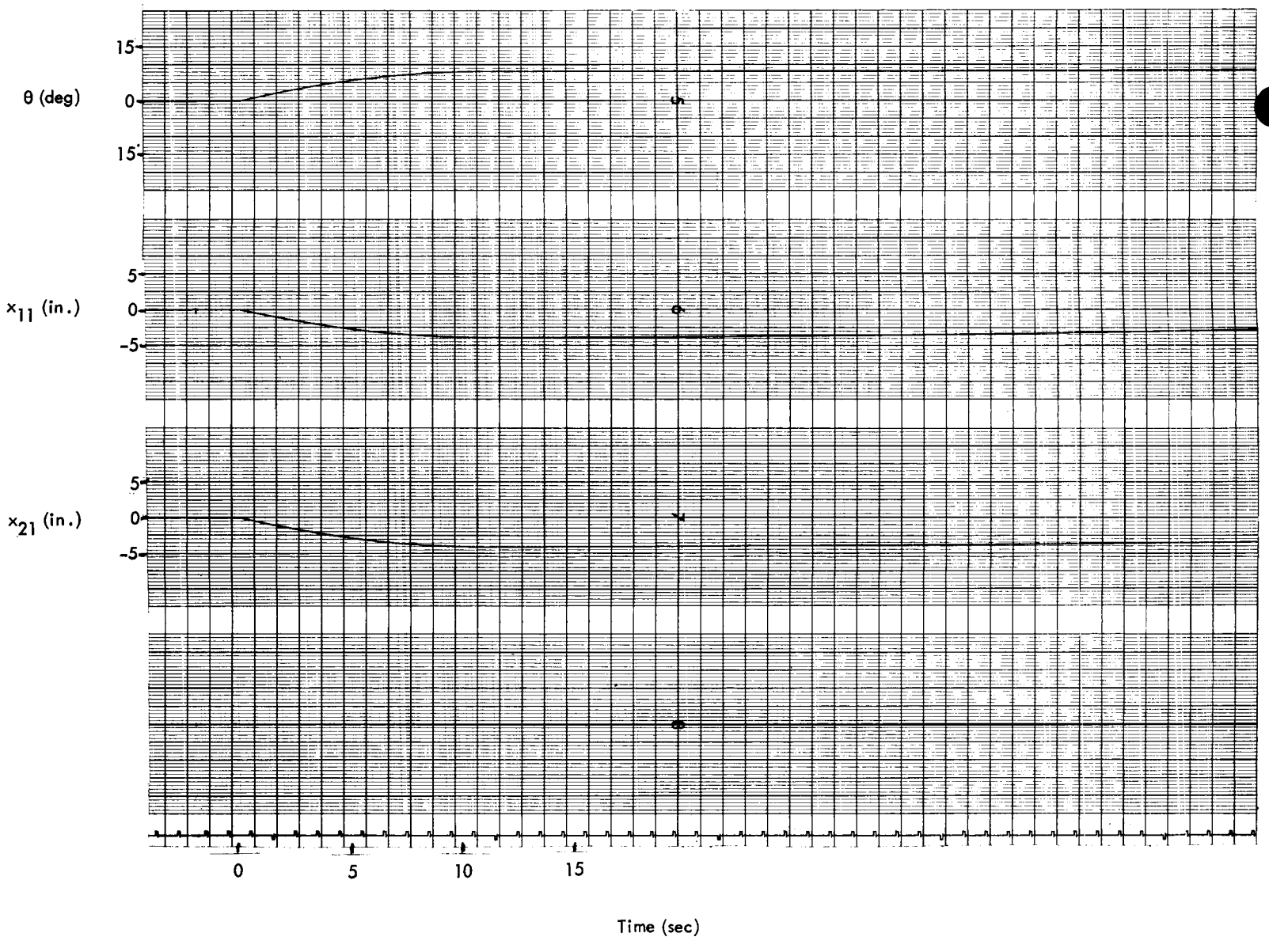

Figure 32. Rate Gyro Mode, Configuration with Capsule, DRI Filter Limit L = 0.2 Deg, $\dot{\theta}$ (o) = 1.5 Deg/Sec

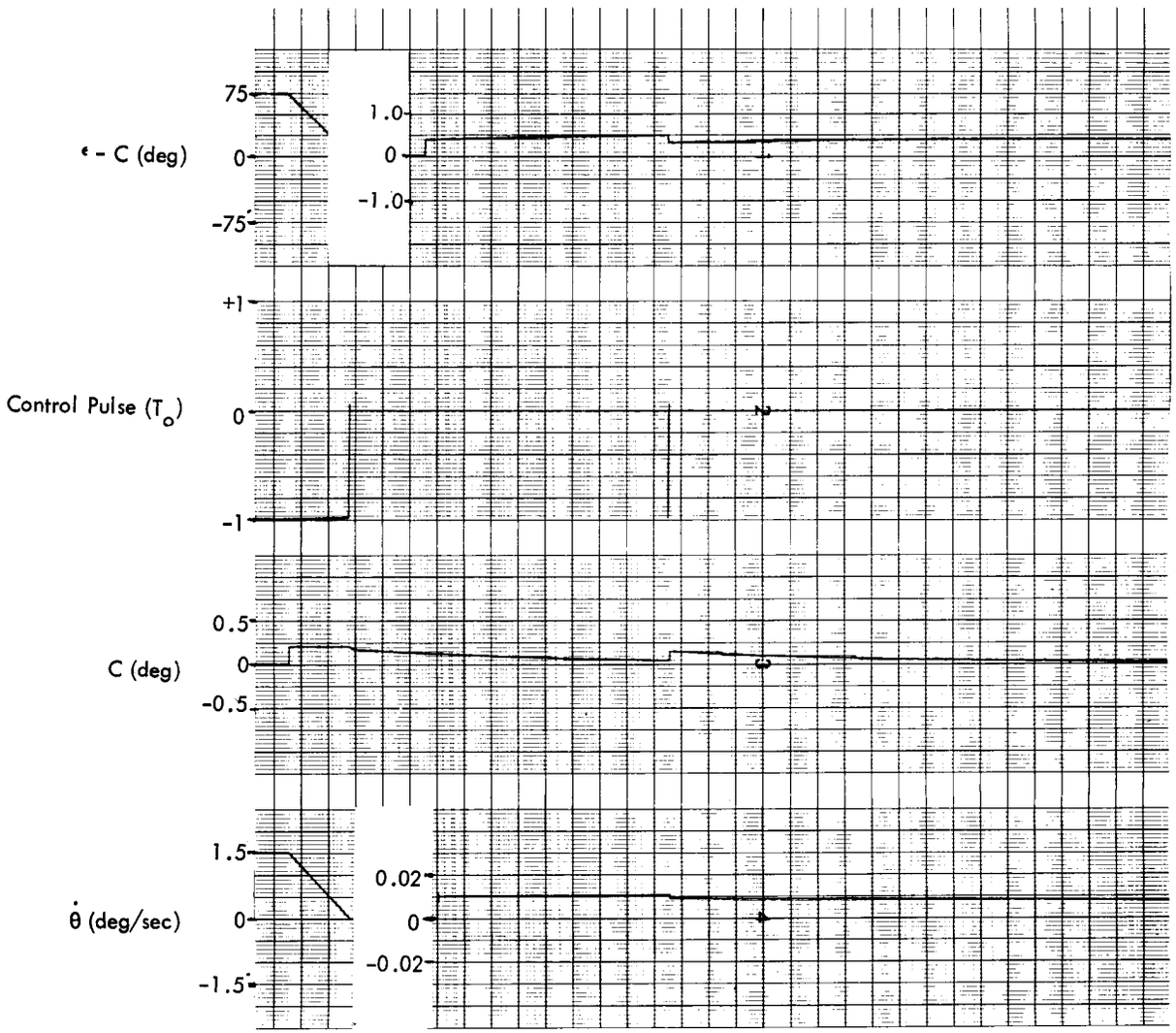
75
0
-75
1.0
0
-1.0
ϵ - C (deg)
+1
0
-1
Control Pulse (T_o)
0.5
0
-0.5
C (deg)
1.5
0
-1.5
0.02
0
-0.02
θ̇ (deg/sec)

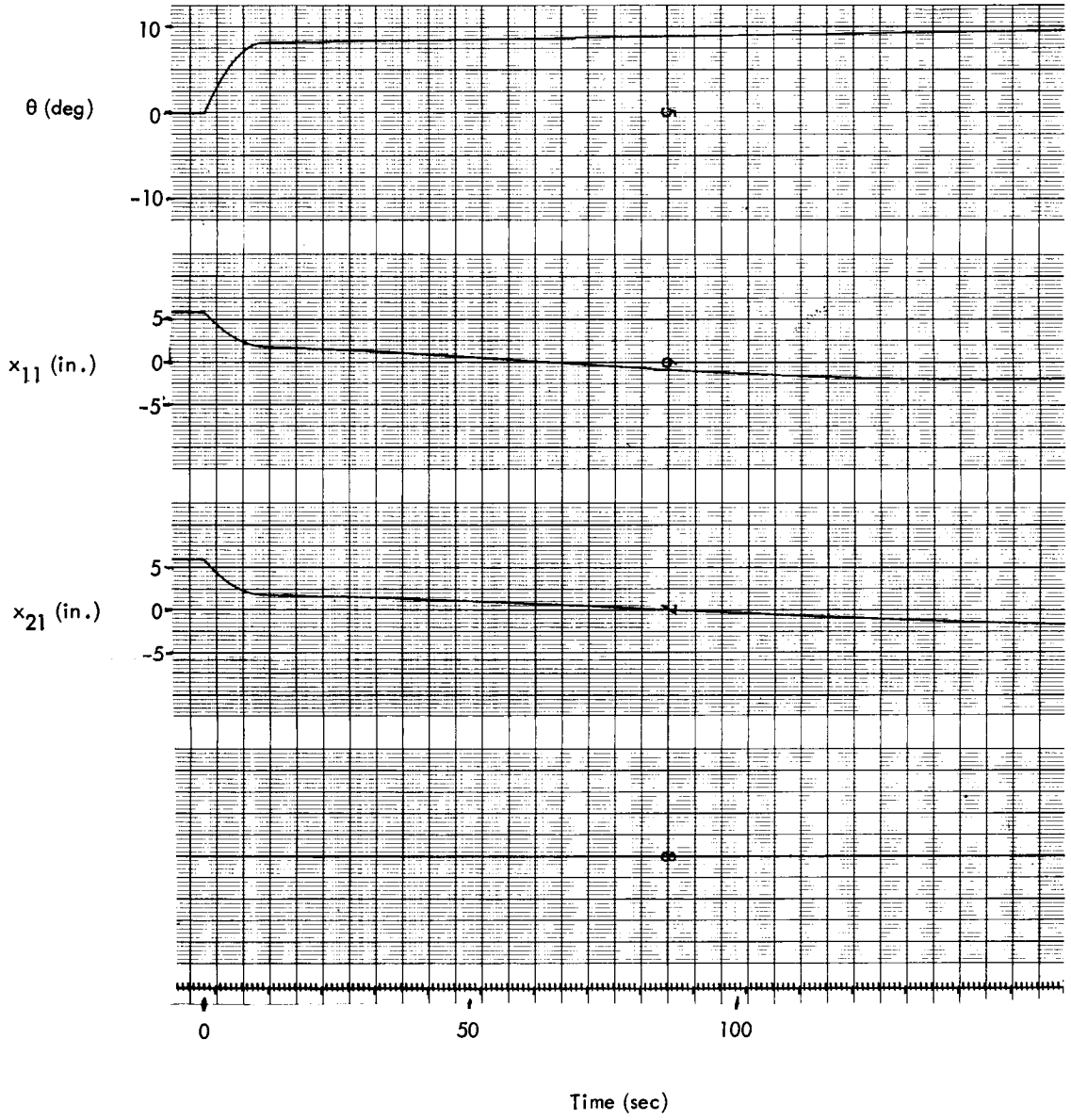

Figure 33. Rate Gyro Mode, Configuration with Capsule, 0.2 Deg Limit DRI, $x_{11}(o) = x_{21}(o) = +6$ In., $\dot{\theta}(o) = 1.5$ Deg/Sec

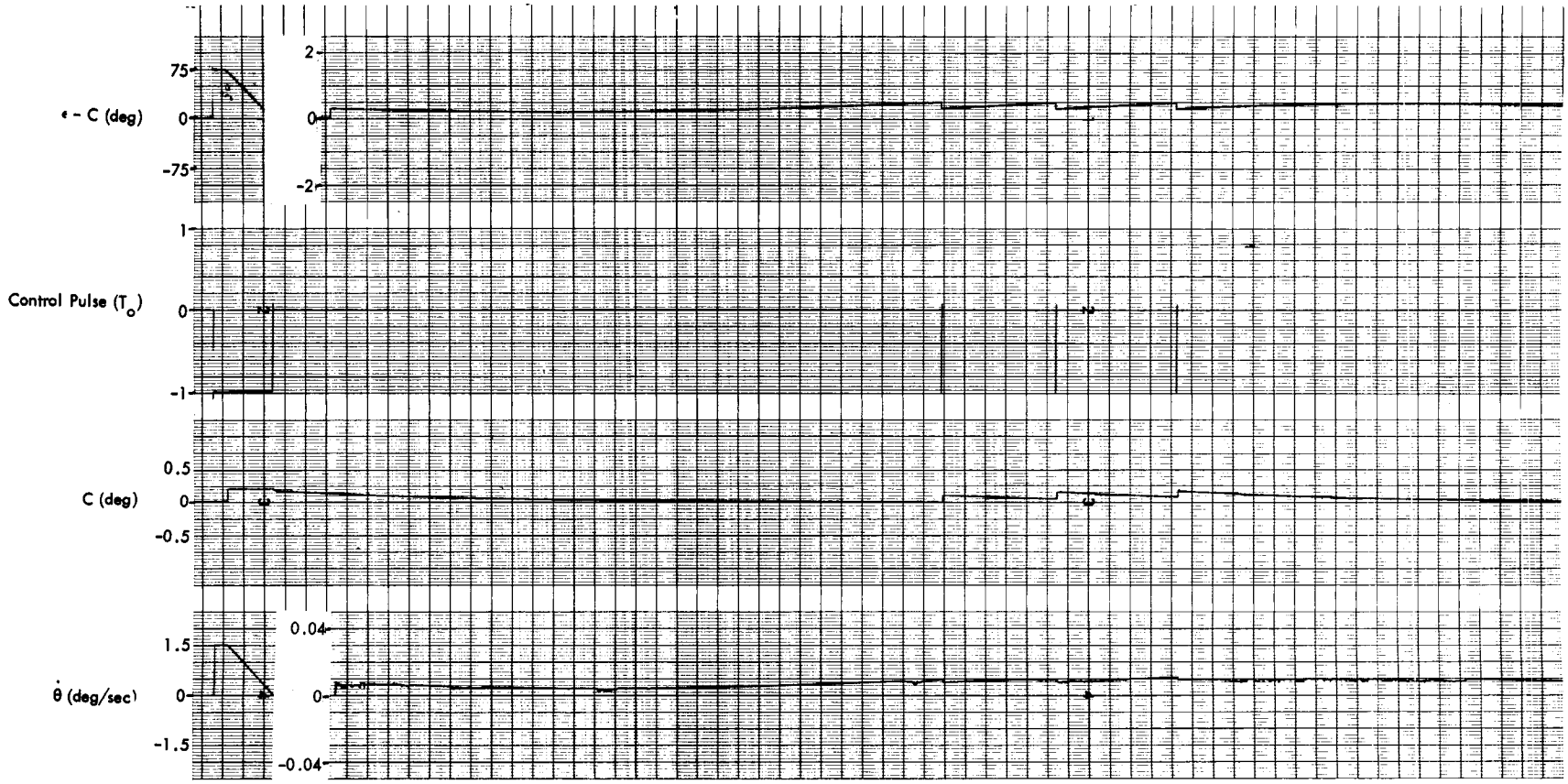
ϵ - C (deg)
75
0
-75
2
0
-2
Control Pulse (T_o)
1
0
-1
C (deg)
0.5
0
-0.5
θ̇ (deg/sec)
1.5
0
-1.5
0.04
0
-0.04

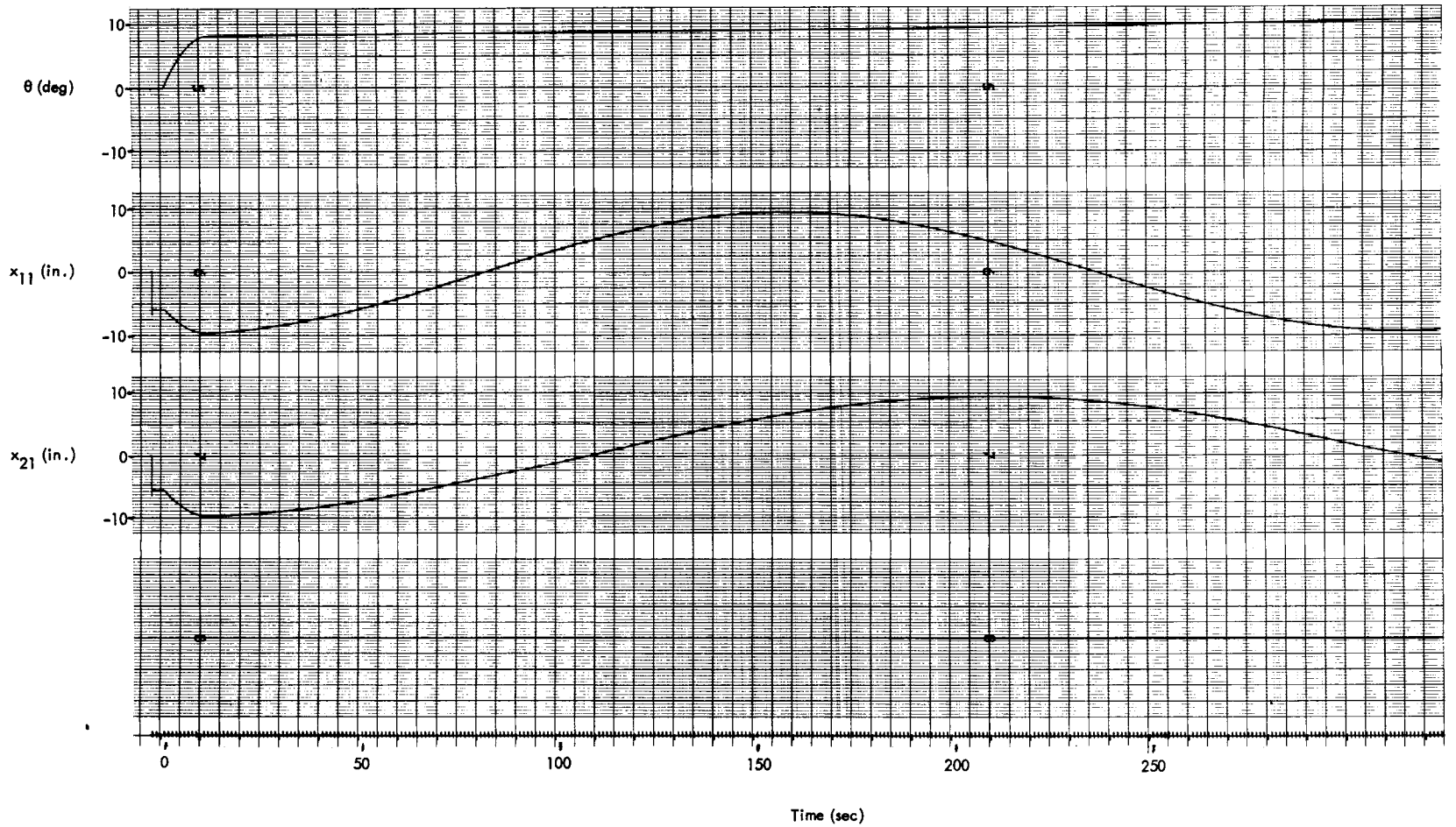

Figure 34. Rate Gyro Mode, Configuration with Capsule, 0.2 Deg Limit DRI, $x_{11}(o) = x_{21}(o) = -6$ In., $\dot{\theta}(o) = 1.5$ Deg/Sec

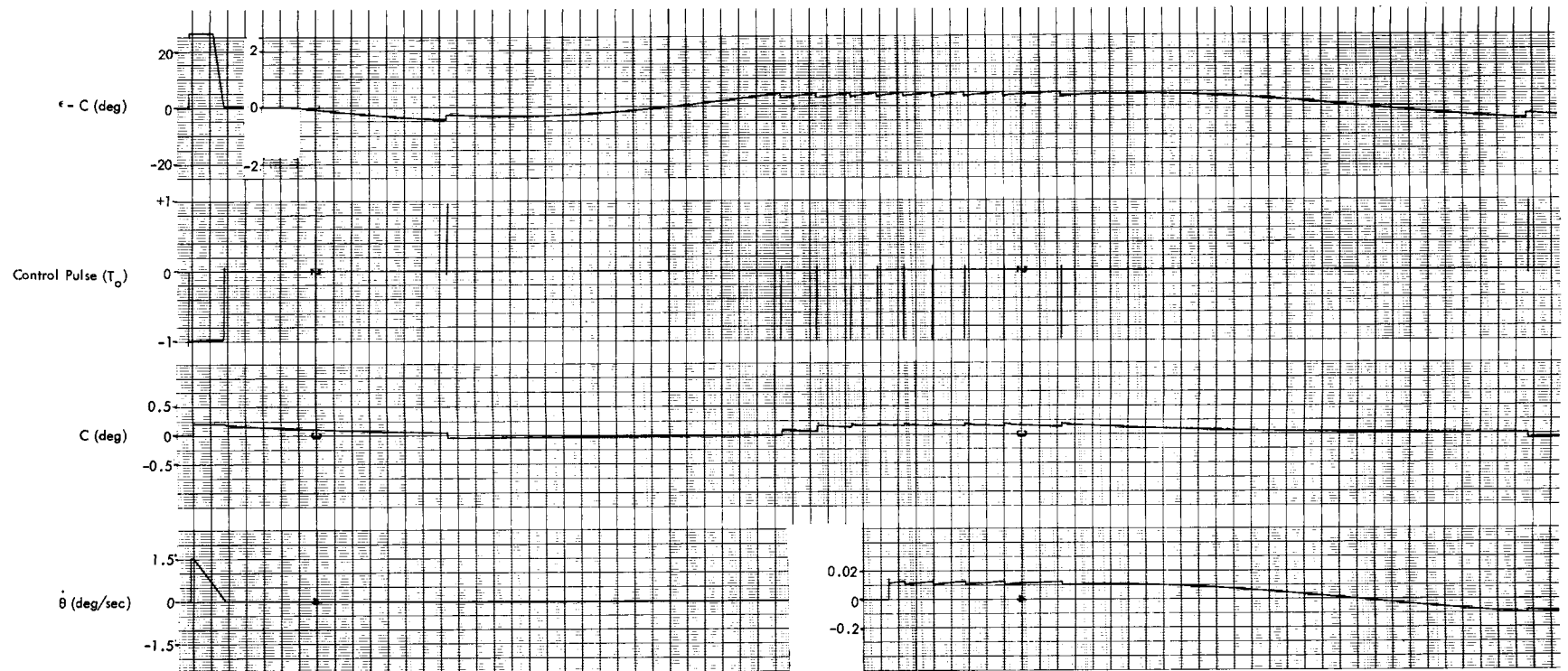
ε - C (deg)
20
0
-20
2
0
-2
Control Pulse (T_o)
+1
0
-1
C (deg)
0.5
0
-0.5
θ̇ (deg/sec)
1.5
0
-1.5
0.02
0
-0.2

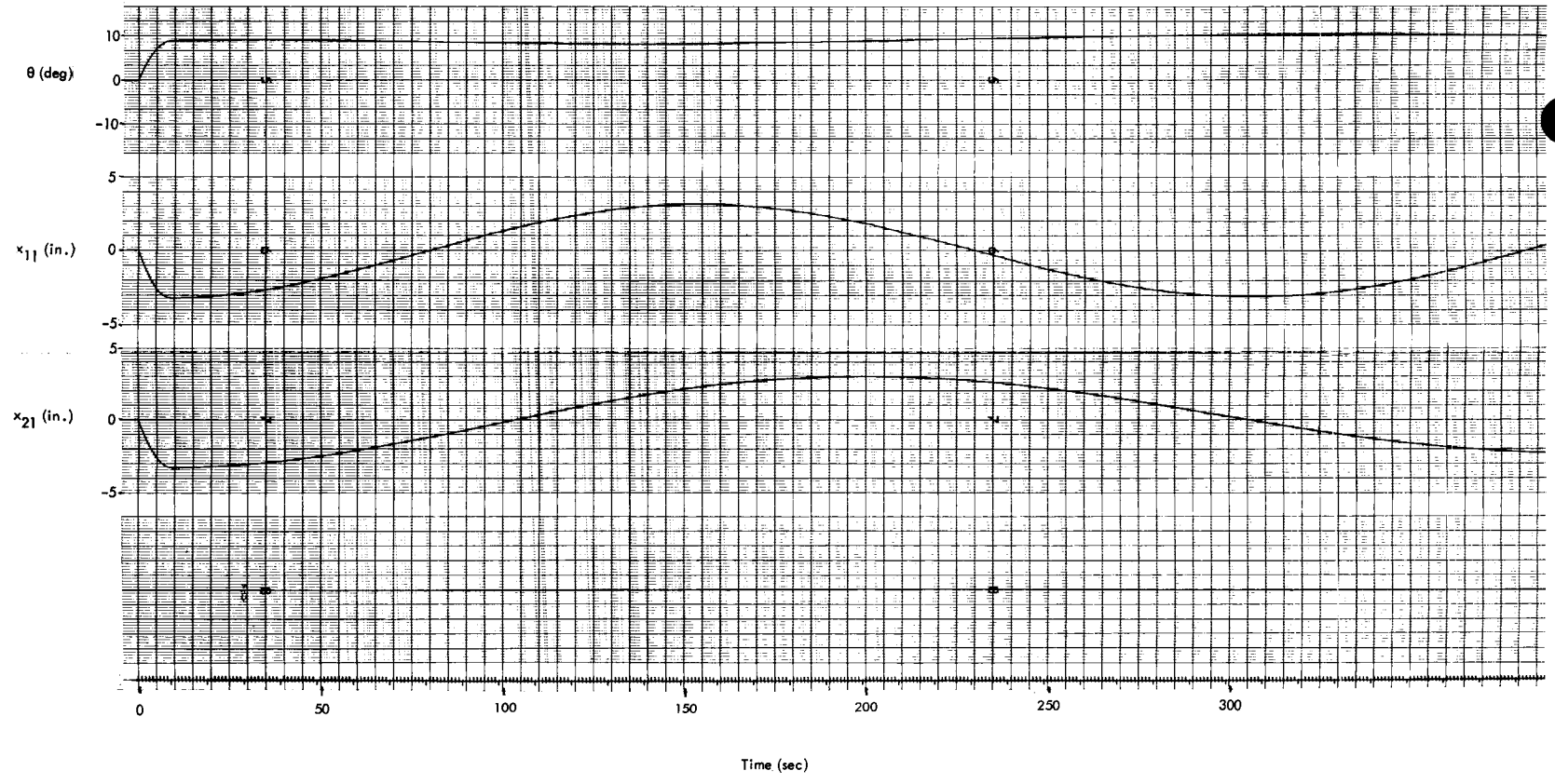

Figure 35. Rate Gyro Mode, Configuration with Capsule, 0.2 Deg Limit DRI, Slosh Mass Increased by 10, $\dot{\theta}$ (o) = 1.5 Deg/Sec

BLANK PAGE

PRECEDING PAGE BLANK NOT FILMED.

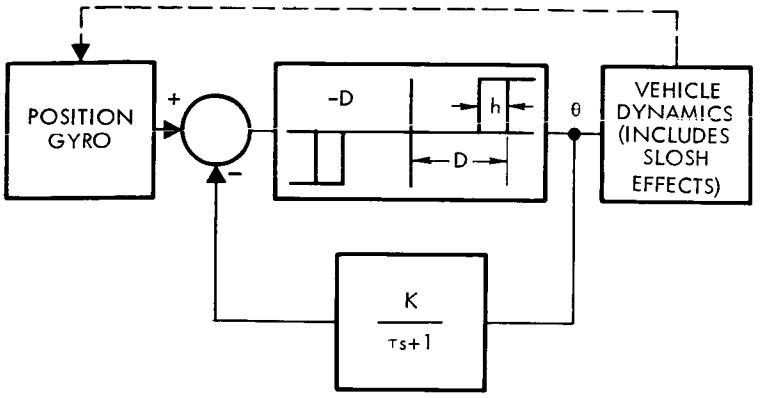

Figure 36. Position Gyro Mode Block Diagram without Lead-Lag Filter

until limit cycling was initiated, then the DRI filter was switched in. The filter parameters selected were: $\alpha_1 = 10$ and $\tau_1 = 1$ second.

The vehicle was subjected to initial rates of 1.5, 1.0, and 0.5 deg/sec. The system responded well in all three cases (Figures 39, 40, 41). As shown by Figure 41, the limit cycle rate is in excess of 0.01 deg/sec until the DRI filter is switched in; then, the rate is reduced in steps of 0.004 deg/sec. Due to the large DRI time constant, the control pulse is not "on" for long periods of time and the attitude error builds up until the vehicle rate changes sign. However, after several minutes the vehicle attitude error will converge to approximately 0.5 degree.

One disadvantage of the position gyro system studied is that for convergence from large initial rates (1.5 deg/sec) about twice as much fuel as for the rate gyro mode is required. A lead limited filter design for the position gyro system would, however, reduce this gas consumption.

The control gas expended, W, can be estimated from the following equation:

$$W = \frac{2F\sum^{n} t_n}{I_{sp}}$$

where F = thrust level (3 lb)

t_n = durations when control jets are on

I_{sp} = specific impulse of gas

Assuming an I_{sp} of 60 seconds (Reference 2), the rate gyro mode (Figure 32) required 1.1 pounds of fuel to attain 0.01 deg/sec and the position gyro mode (Figure 39) required 2.35 pounds of fuel to attain 0.01 deg/sec.

The position gyro mode with lead-lag filter was subjected to initial slosh mass displacements of ±6 inches. The response is shown for an initial -6 inch slosh mass displacement in Figure 42. The vehicle response $(\theta, \dot{\theta})$ wasn't greatly affected by the initial slosh displacements. A few additional minimum pulses occurred after the DRI filter was switched in, due to the sloshing of the propellant.

The slosh mass was increased by a factor of 10 and the position gyro mode with lead-lag filter was subjected to an initial rate of 1.5 deg/sec. No deleterious effects were observed (Figure 43).

The rate gyro mode without DRI was used until the rate was reduced to 0.01 deg/sec; then the position gyro mode with lead-lag filter was switched in. As shown by Figure 44, no advantage was obtained when compared to just using the position gyro mode.

2.4.2 Configuration without Capsule

The configuration without capsule was studied for the most promising rate and position gyro modes; which were the rate gyro mode with 0.2-degree limit and the position gyro mode with lead-lag filter.

2.4.2.1 Rate Gyro Mode with a 0.2-Degree Limit DRI

The vehicle was subjected to an initial rate of 1.5 deg/sec. The rate was reduced to 0.01 deg/sec in approximately 7 seconds. The attitude excursion θ at the end of 7 seconds was 4.8 degrees (Figure 45). The slosh masses were initially displaced ±6 inches (Figures 46 and 47). No adverse effects were found.

To provide an indication of the safety margin in the design, the slosh masses were increased by 10. No deleterious effects resulted as shown in Figure 48.

2.4.2.2 Position Gyro Mode with Lead-Lag Filter

The nominal response of the position gyro mode to an initial rate of 1.5 deg/sec is shown in Figure 49. The maximum attitude excursion

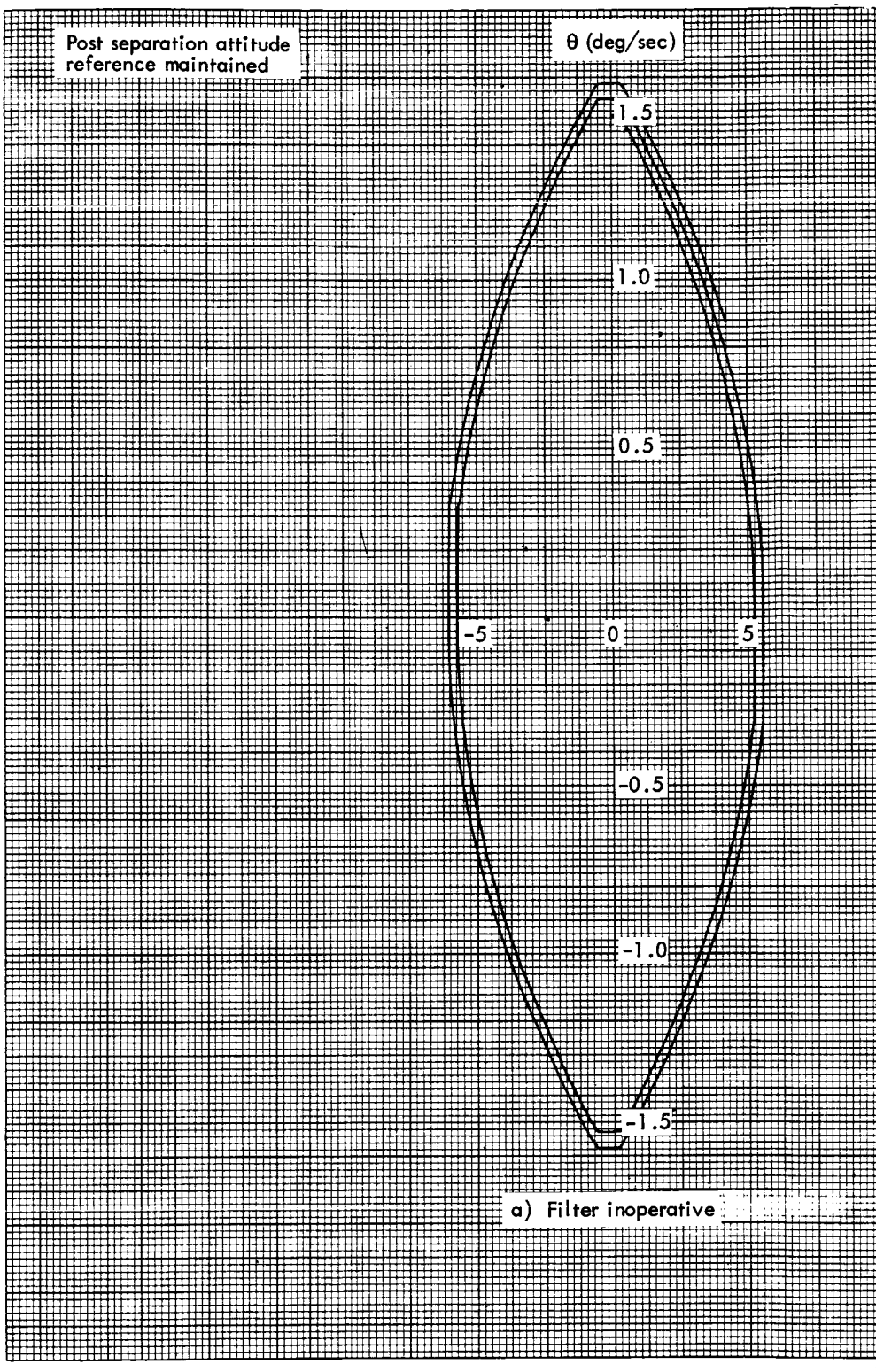
Post separation attitude reference maintained
θ (deg/sec)
1.5
1.0
0.5
-5
0
5
-0.5
-1.0
-1.5
a) Filter inoperative

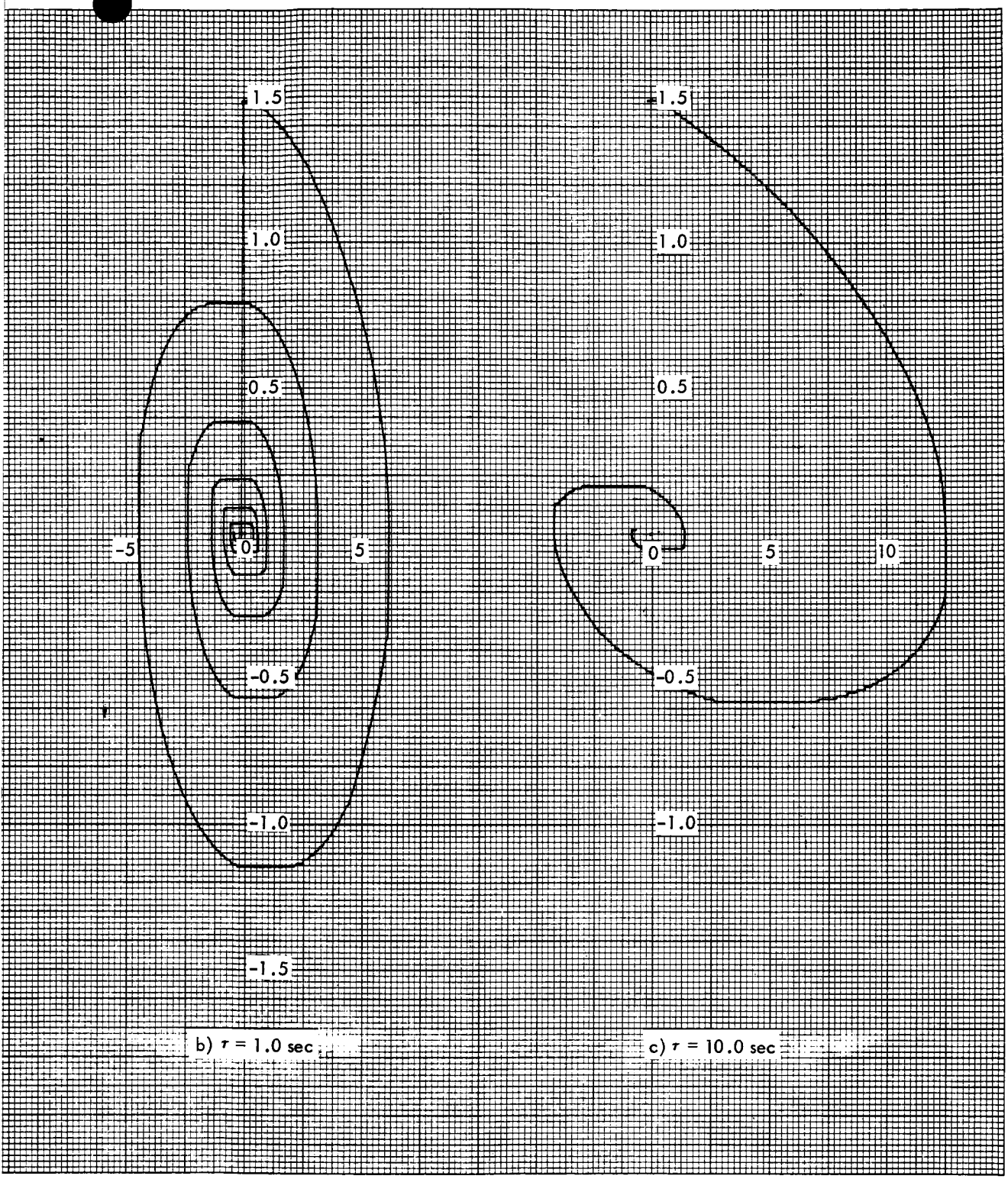

Figure 37. Position Gyro Mode without Lead-Lag Filter, Configuration with Capsule, Variation of DRI Time Constant

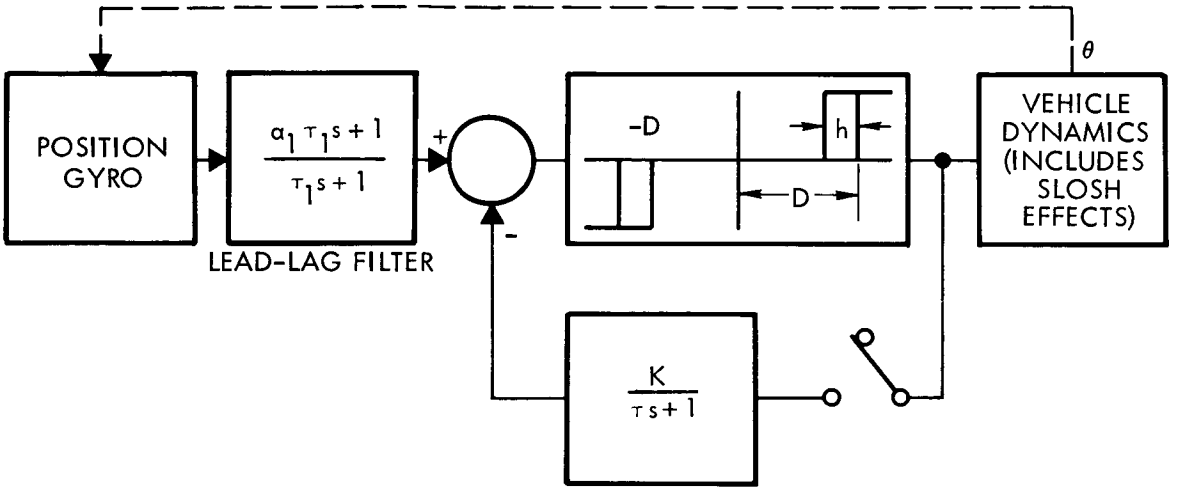

Figure 38. Position Gyro Mode Block Diagram with Lead-Lag Filter

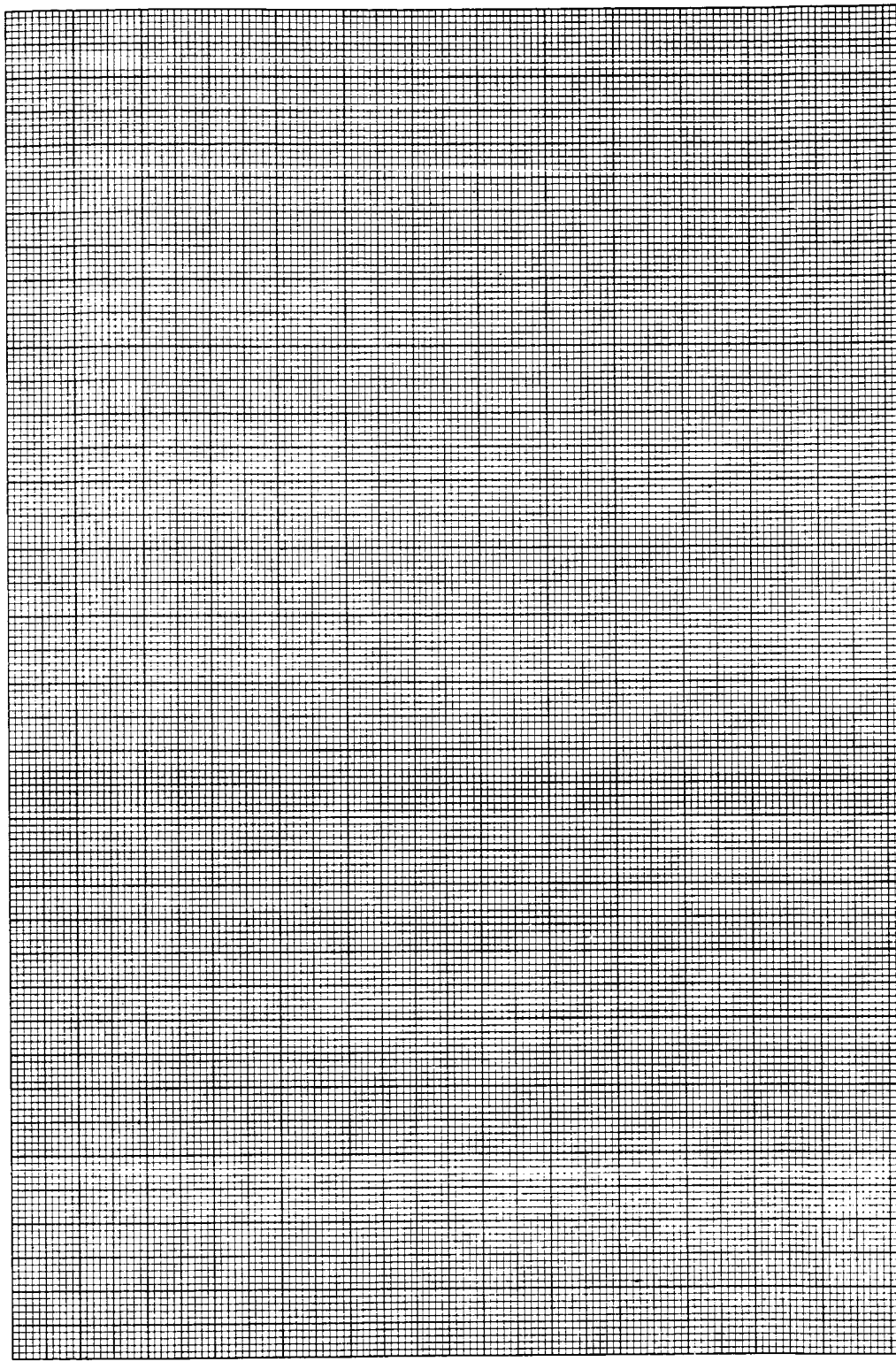

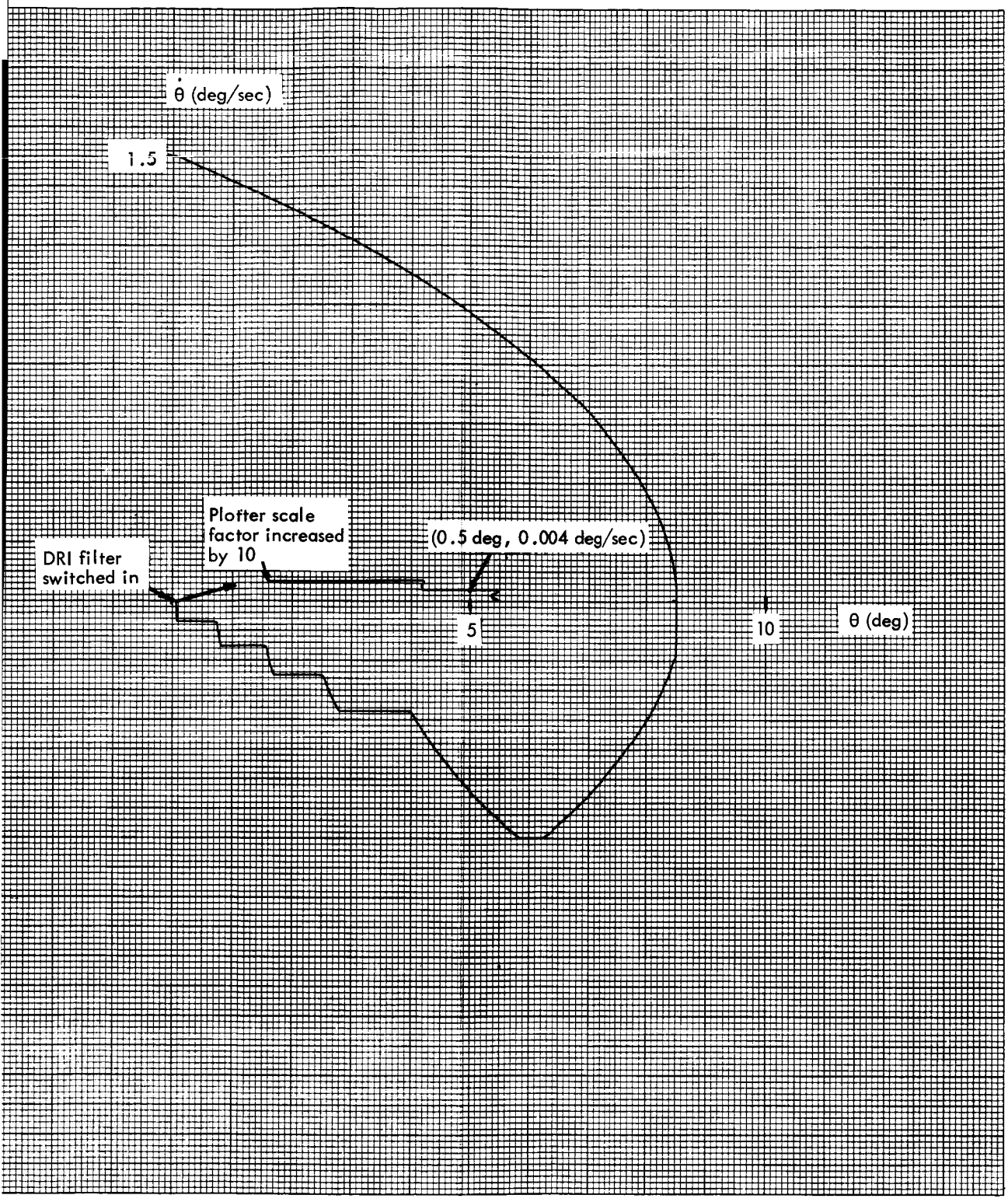

Figure 39. Position Gyro Mode, Configuration with Capsule, Response with Lead-Lag Filter, $\dot{\theta}(o) = 1.5$ Deg/Sec

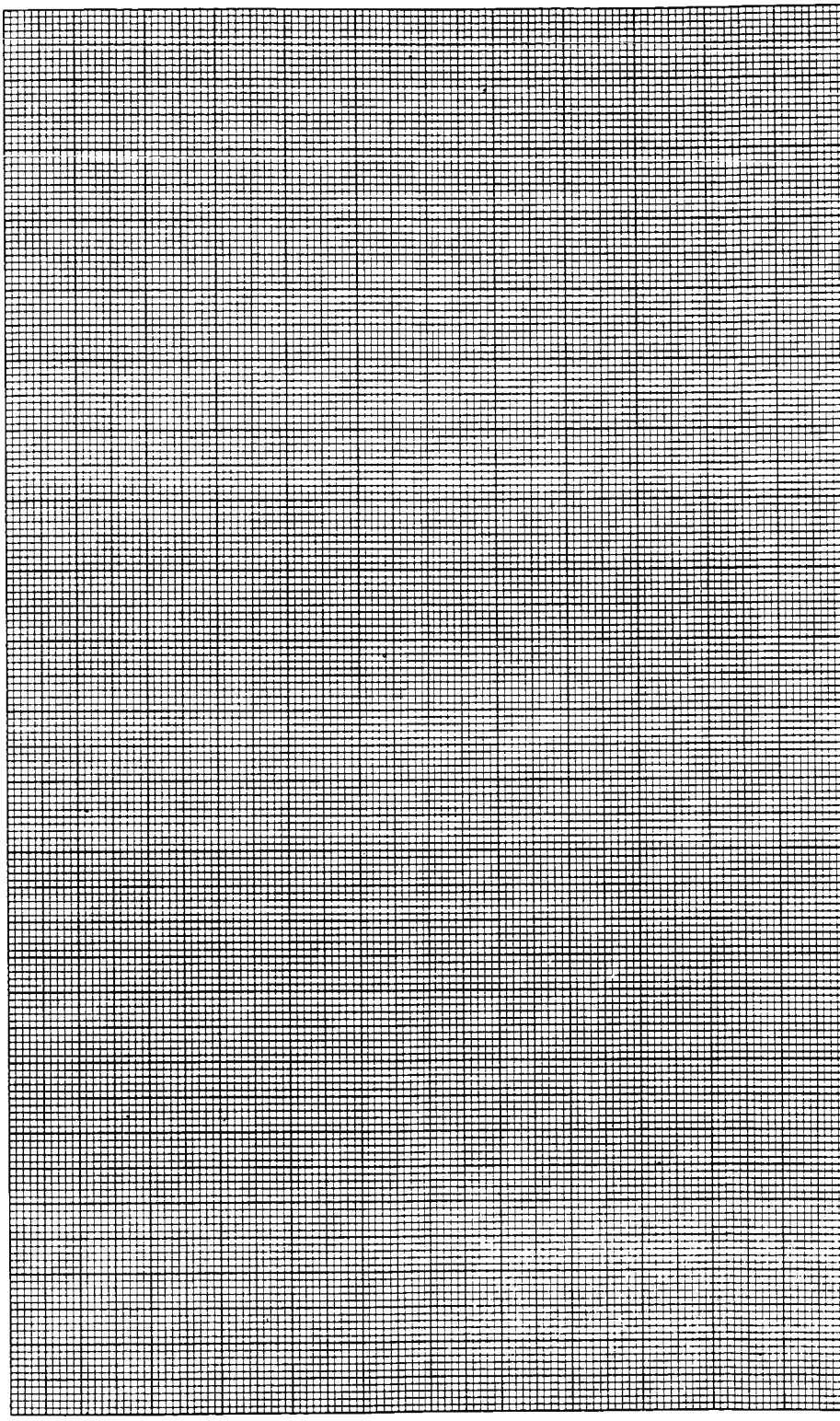

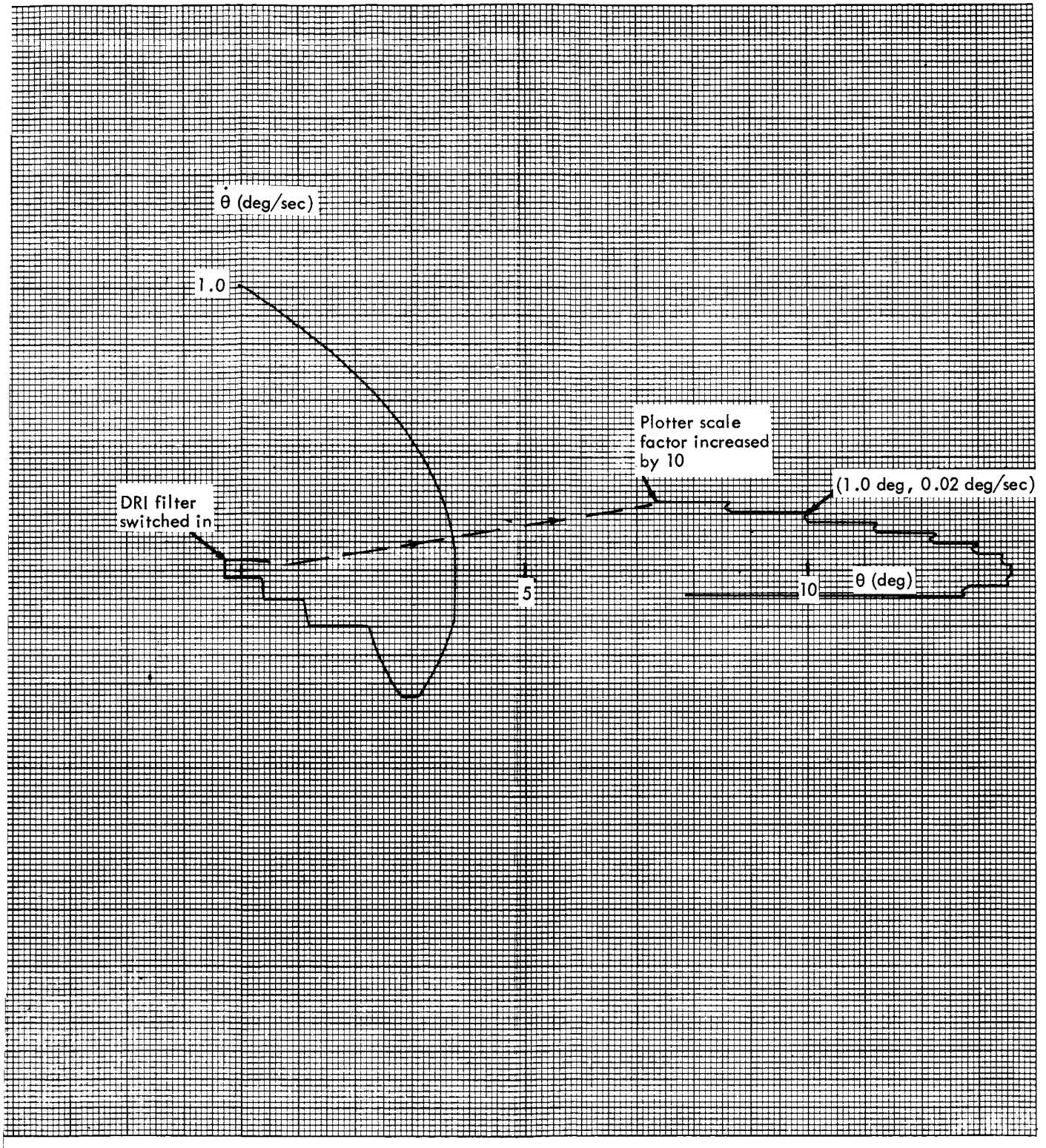

Figure 40. Position Gyro Mode, Configuration with Capsule, Response with Lead-Lag Filter, $\dot{\theta}(o) = 1.0$ Deg/Sec

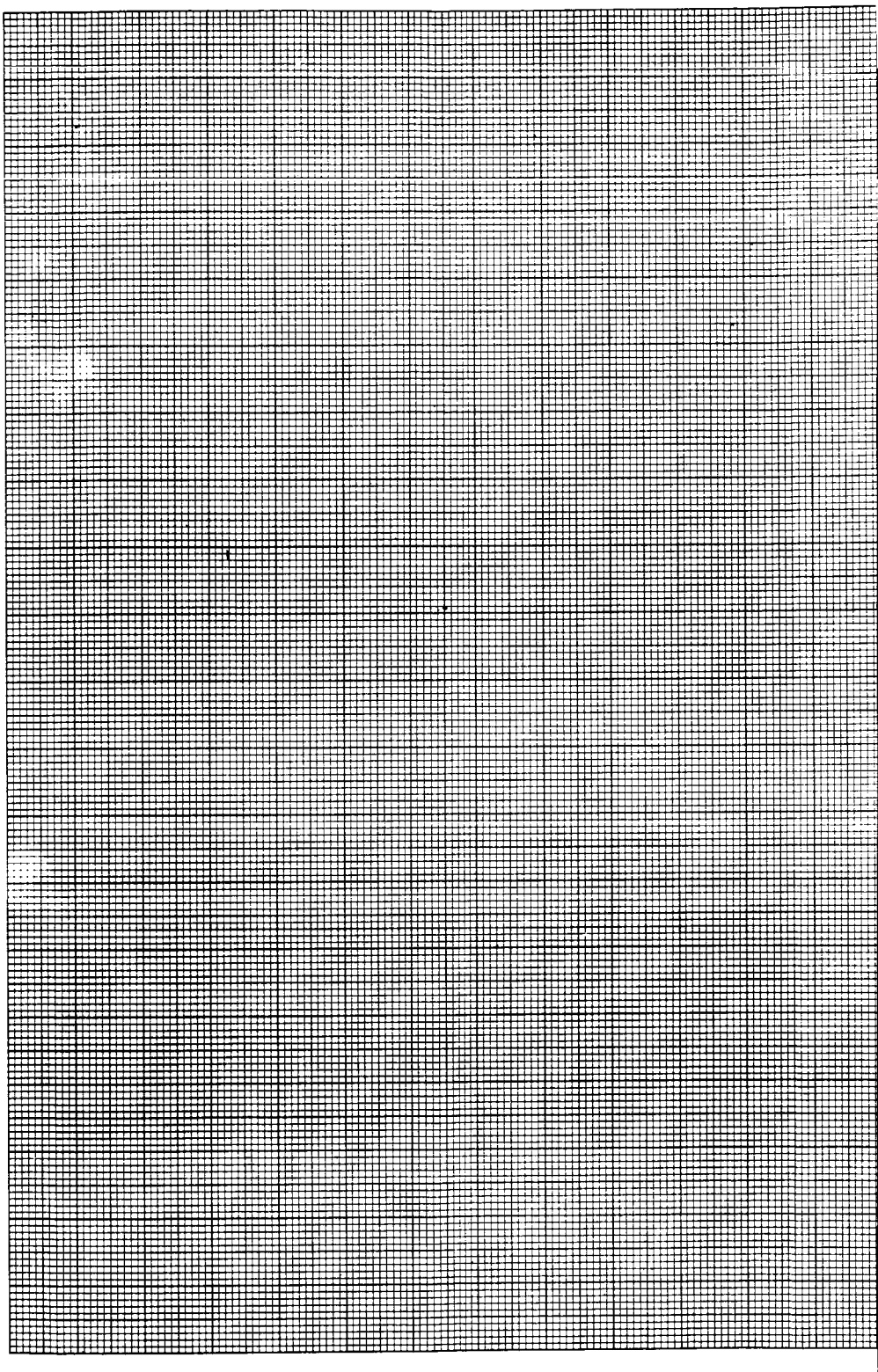

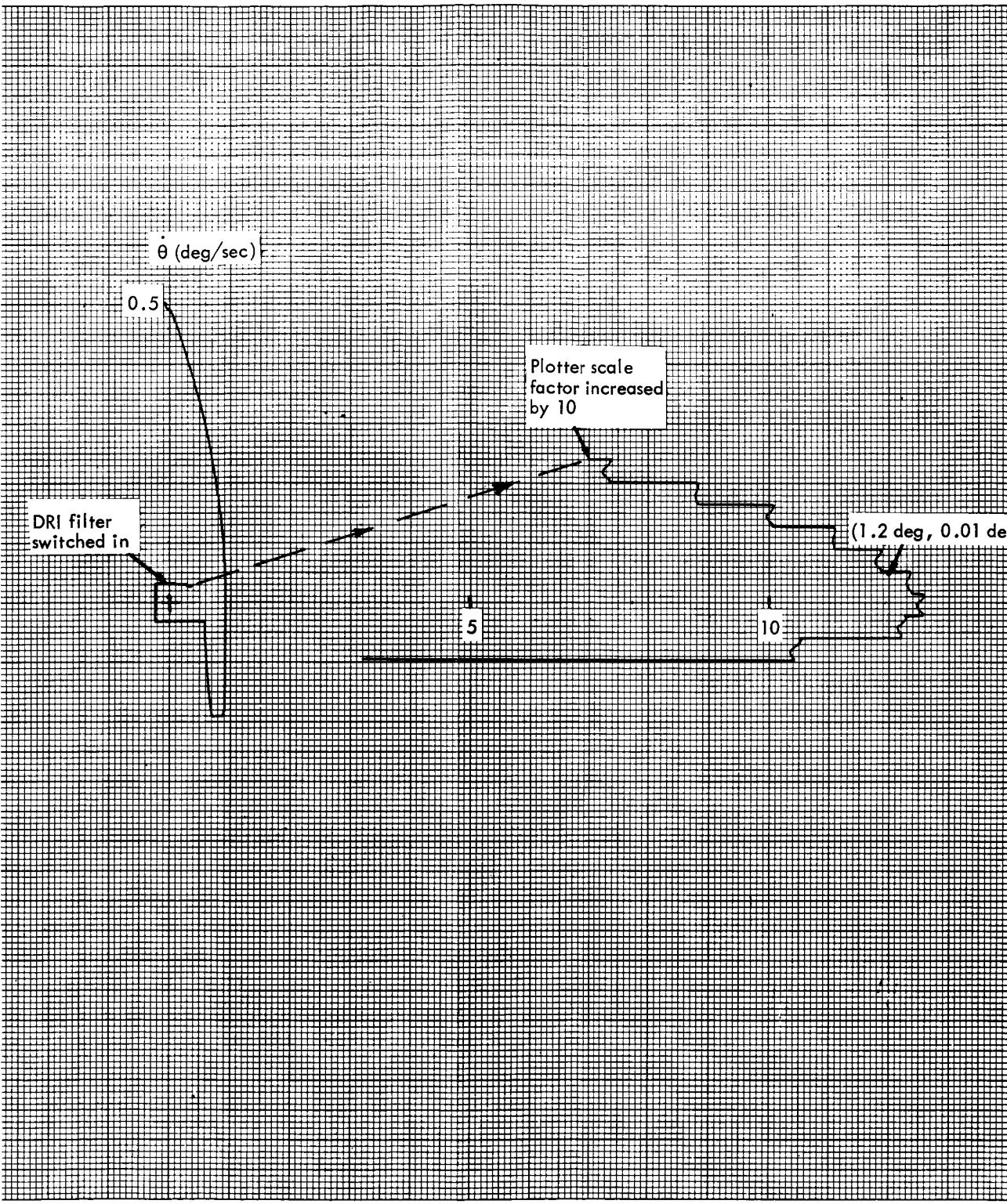

Figure 41. Position Gyro Mode, Configuration with Capsule, Response with Lead-Lag Filter, $\dot{\theta}$ (o) = 0.5 Deg/Sec

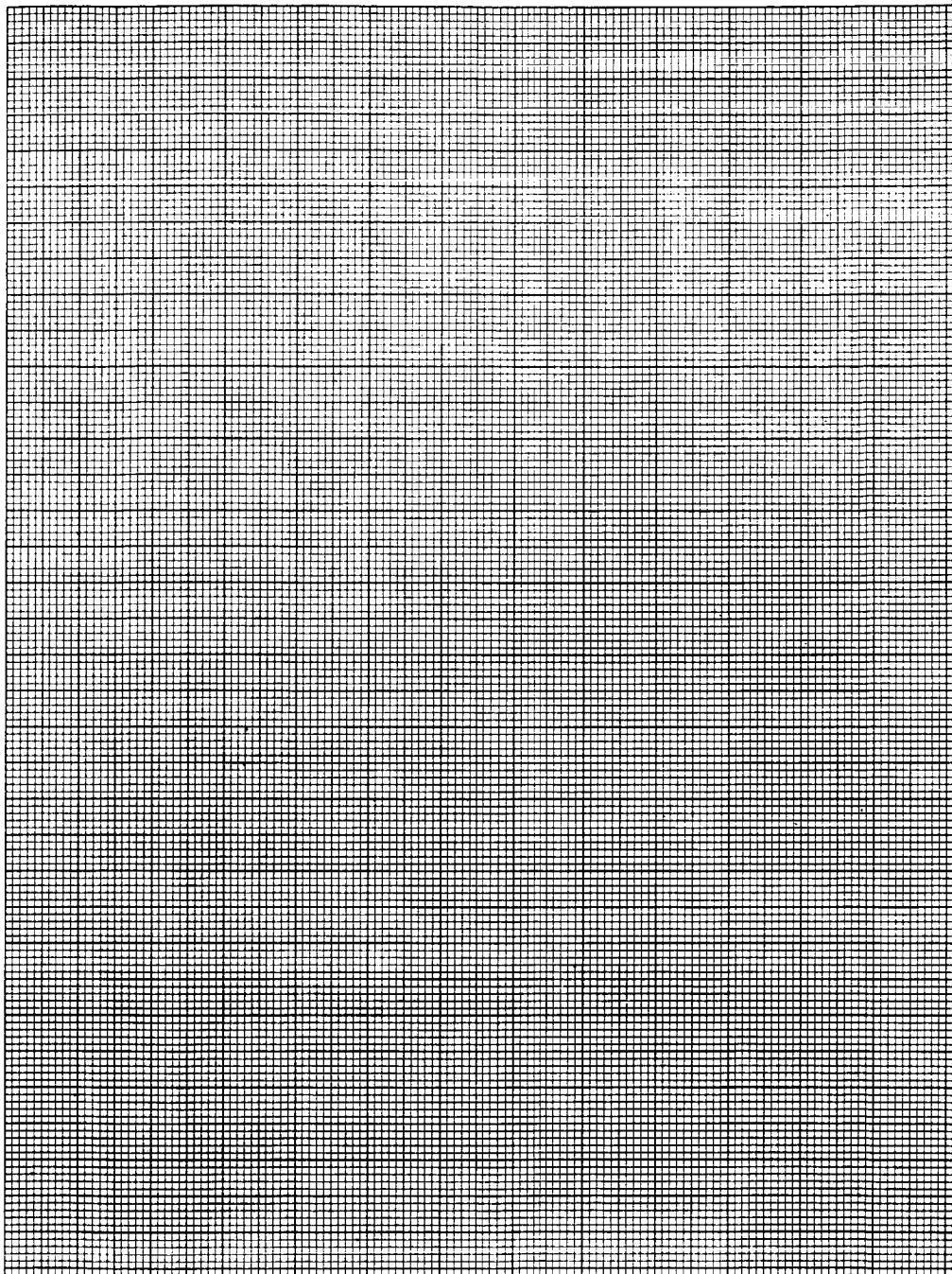

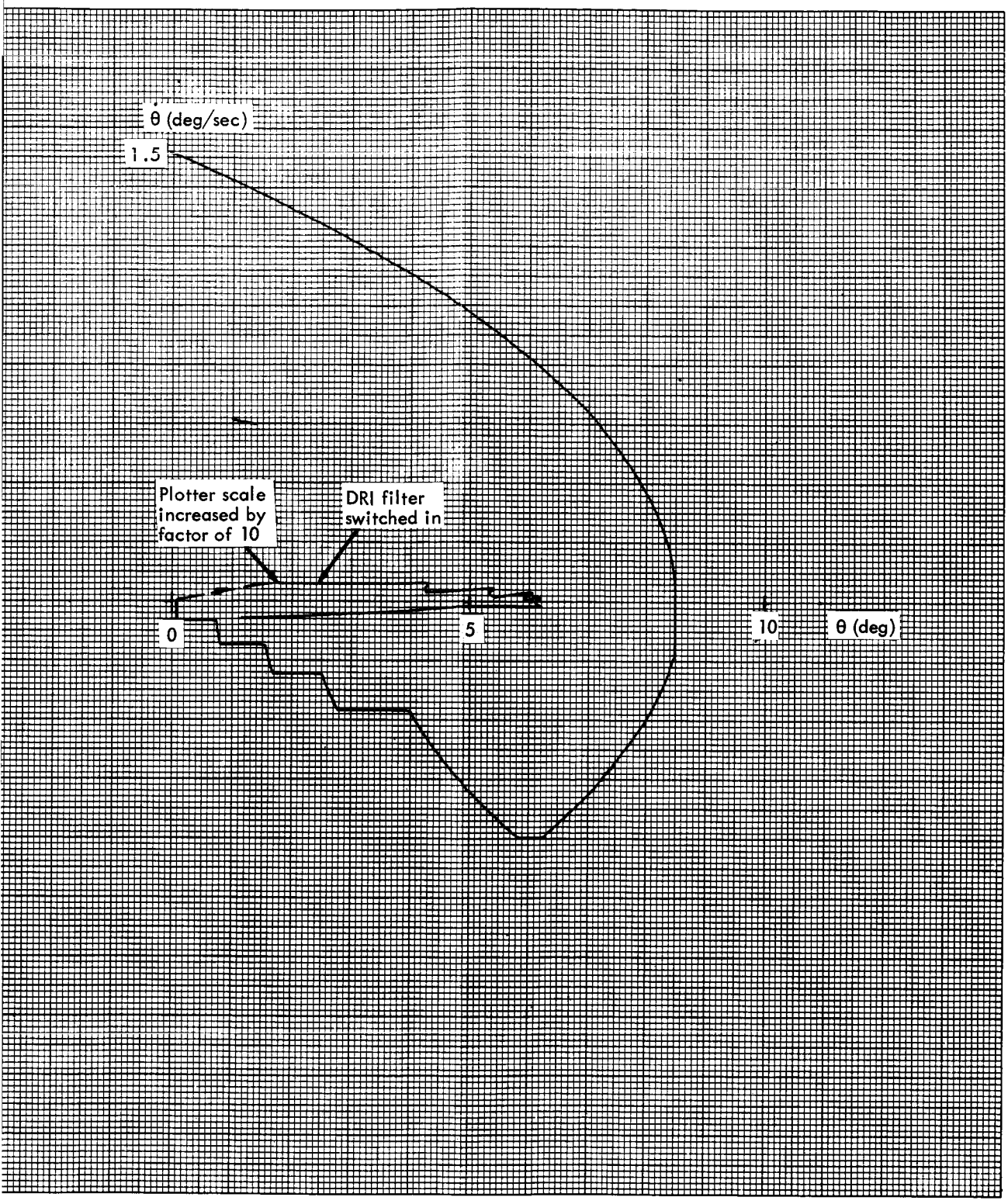

Figure 42. Position Gyro Mode, Configuration with Capsule, Response with Lead-Lag Filter, $x_{11}(o) = x_{21}(o) = -6$ In., $\dot{\theta}(o) = 1.5$ Deg/Sec

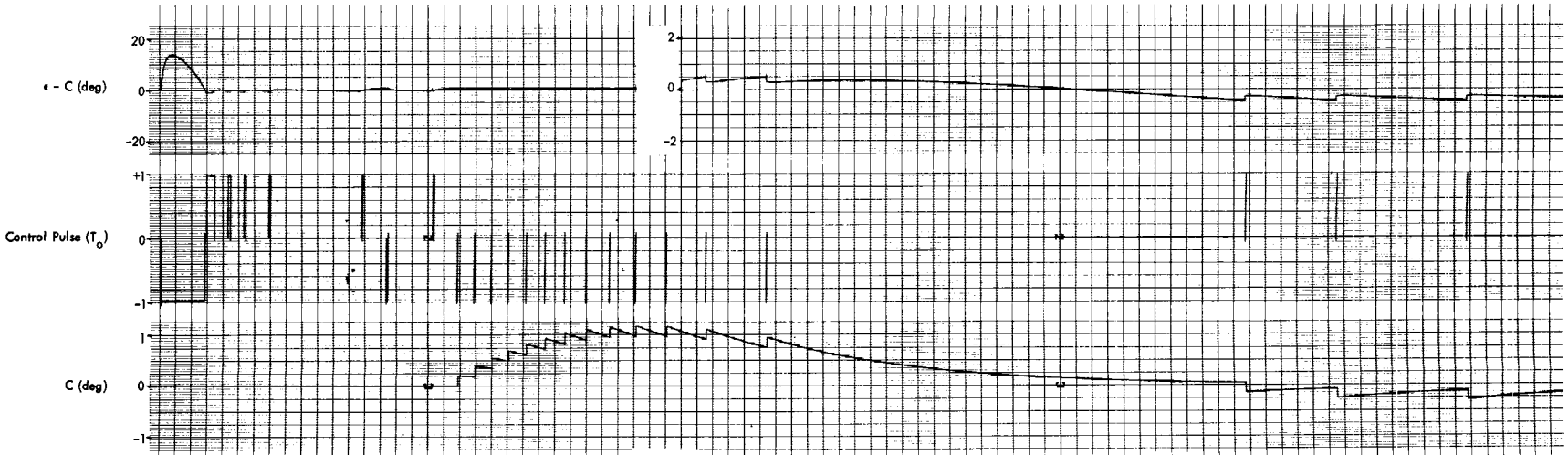
ε - C (deg)
20
0
-20
2
0
-2
Control Pulse (T_o)
+1
0
-1
C (deg)
1
0
-1

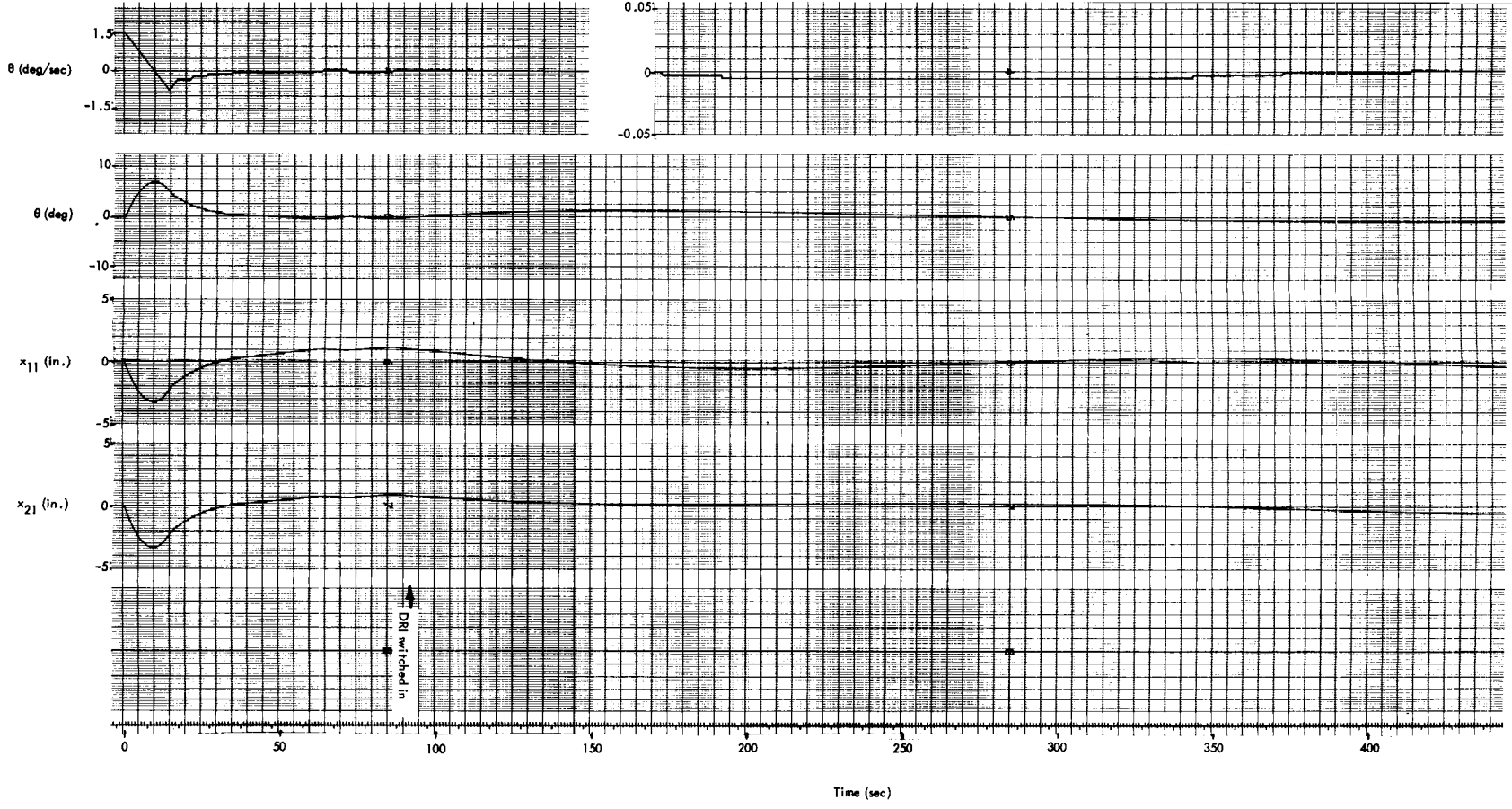

Figure 43. Position Gyro Mode, Configuration with Capsule, Response with Lead-Lag Filter, Slosh Mass Increased by Factor of 10, $\dot{\theta}$ (o) = 1.5 Deg/Sec

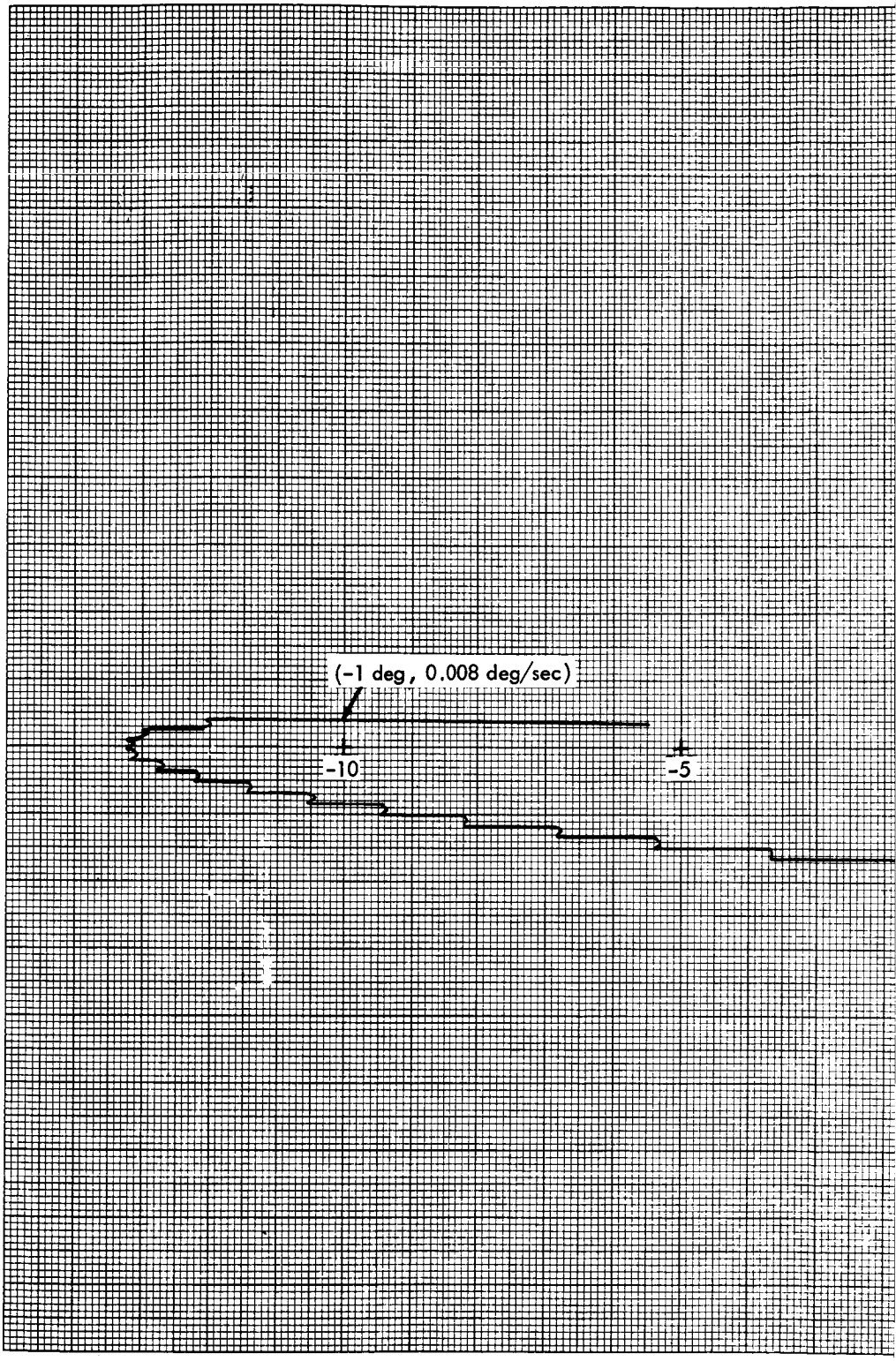
(-1 deg, 0.008 deg/sec)
-10
-5

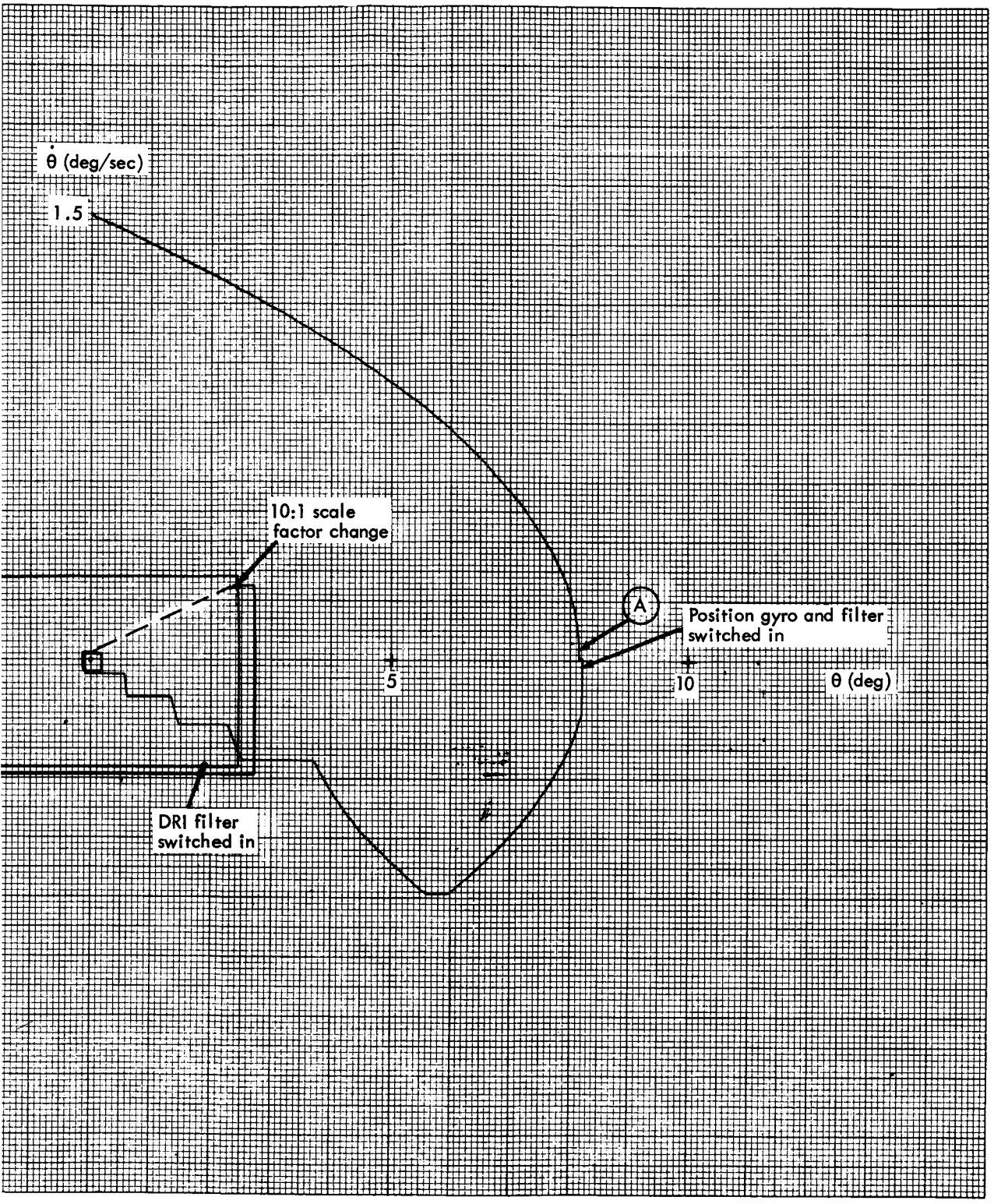

Figure 44. Rate Gyro Mode to Position Gyro Mode Sequence, Configuration with Capsule, $\dot{\theta}$ (o) = 1.5 Deg/Sec

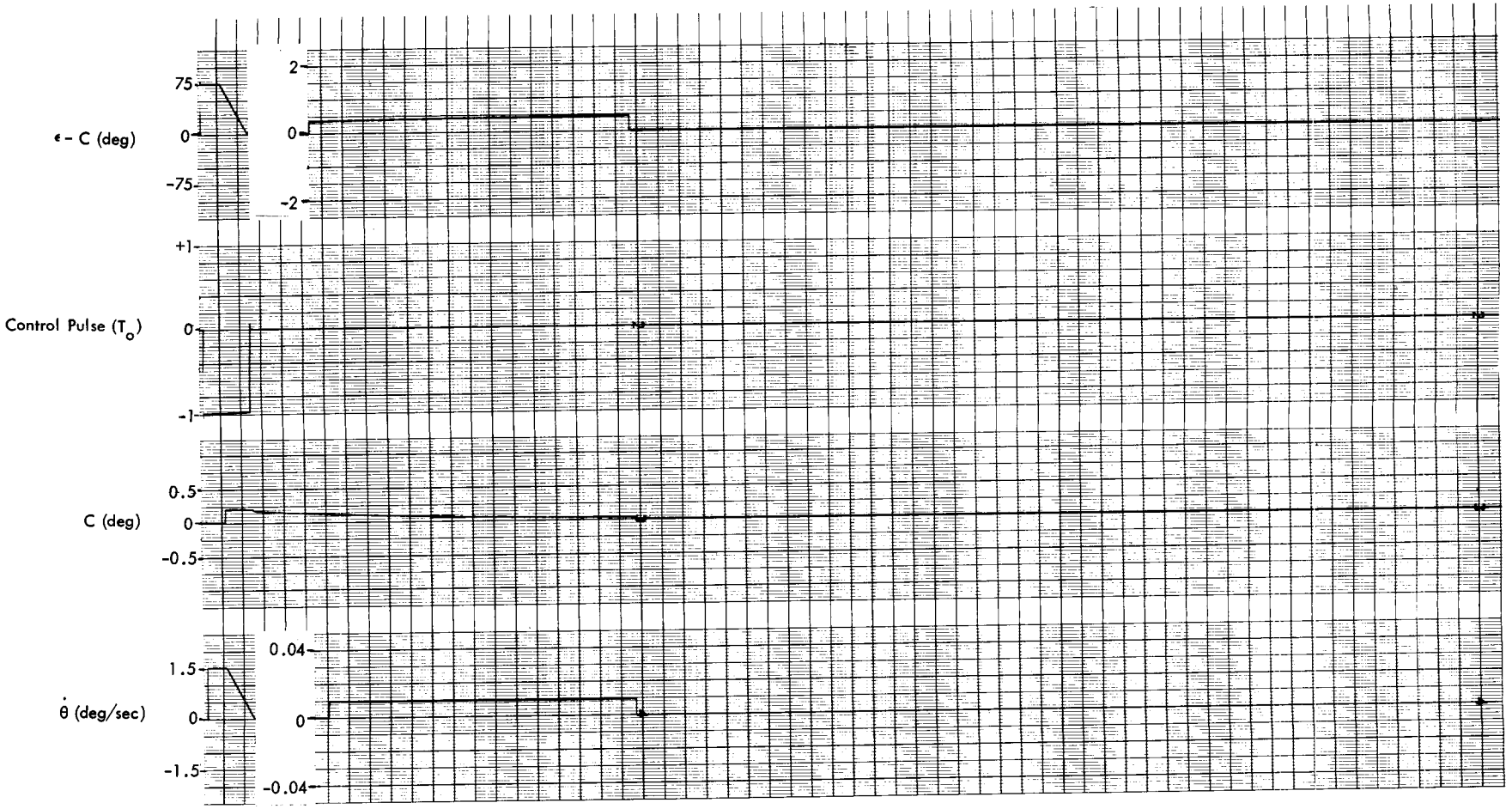
75
0
-75
2
0
-2
ϵ - C (deg)
+1
0
-1
Control Pulse (T_o)
0.5
0
-0.5
C (deg)
1.5
0
-1.5
0.04
0
-0.04
$\dot{\theta}$ (deg/sec)

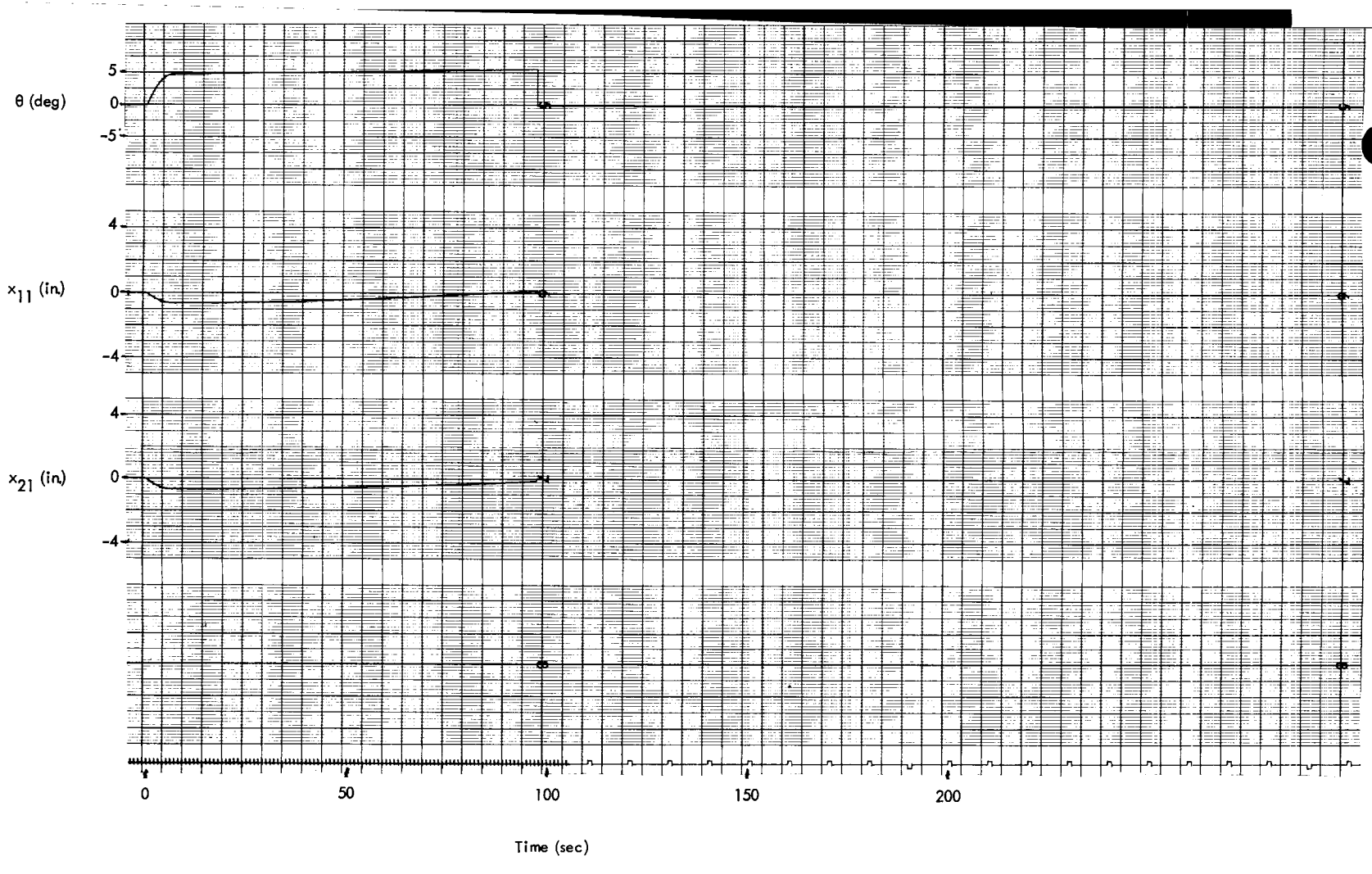

Figure 45. Rate Gyro Mode, Configuration without Capsule, DRI Filter
L = 0.2 Deg, $\dot{\theta}$ (o) = 1.5 Deg/Sec

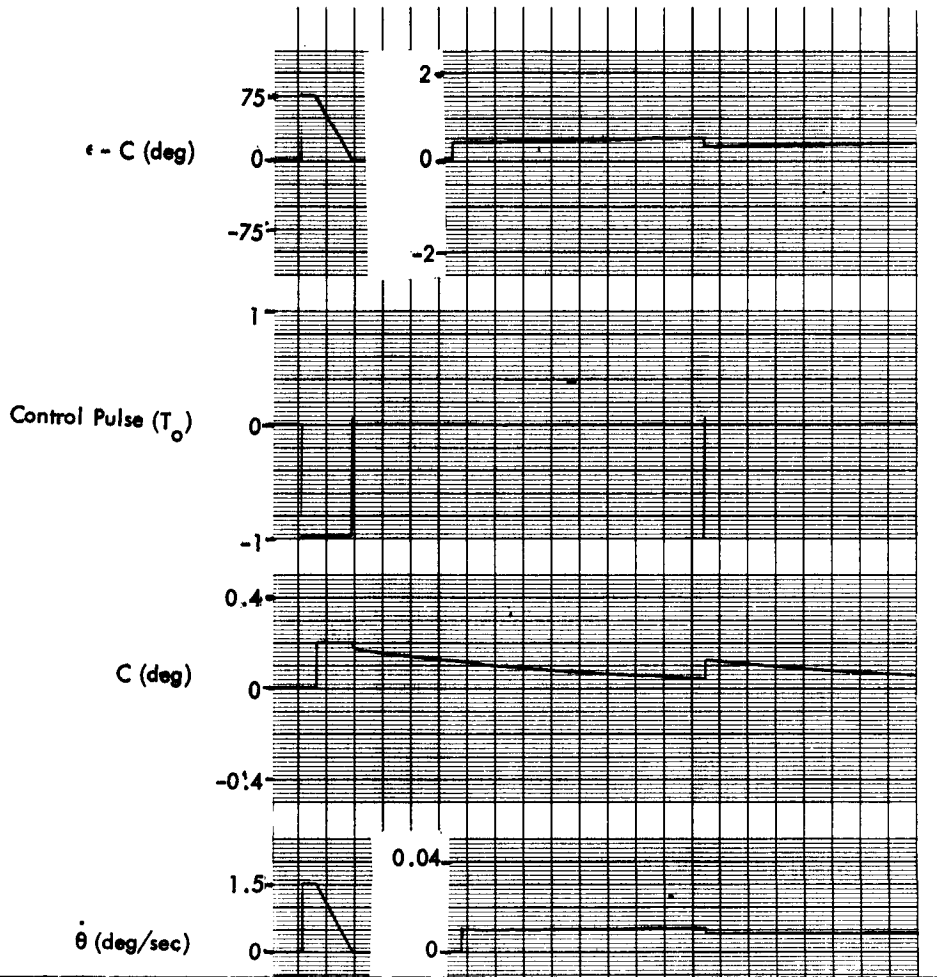
ε - C (deg)
75
0
-75
2
0
-2
Control Pulse (T_o)
1
0
-1
C (deg)
0.4
0
-0.4
θ̇ (deg/sec)
1.5
0
0.04
0

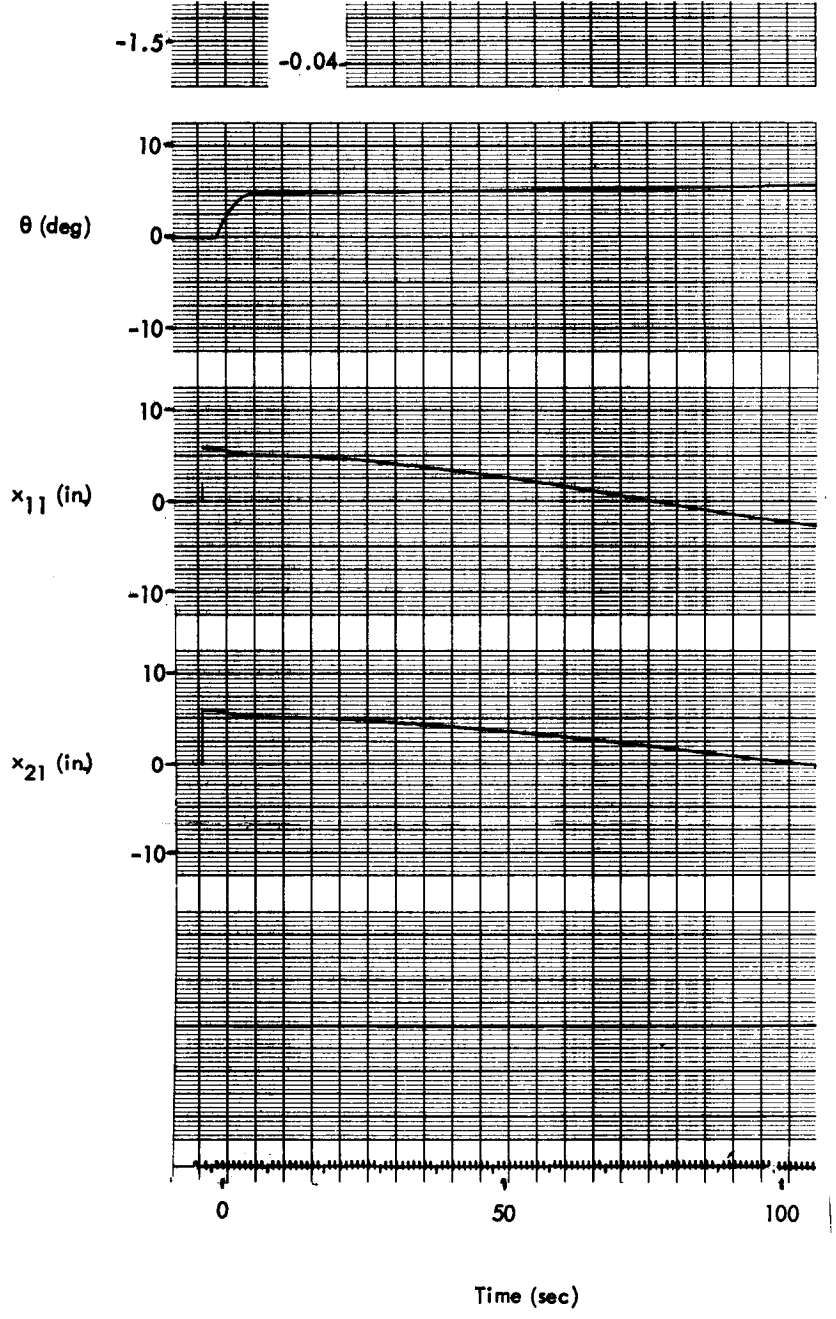

Figure 46. Rate Gyro Mode, Configuration without Capsule, DRI Filter
L = 0.2 Deg, $x_{11}(o) = x_{21}(o) = +6$ In., $\dot{\theta}(o) = 1.5$ Deg/Sec

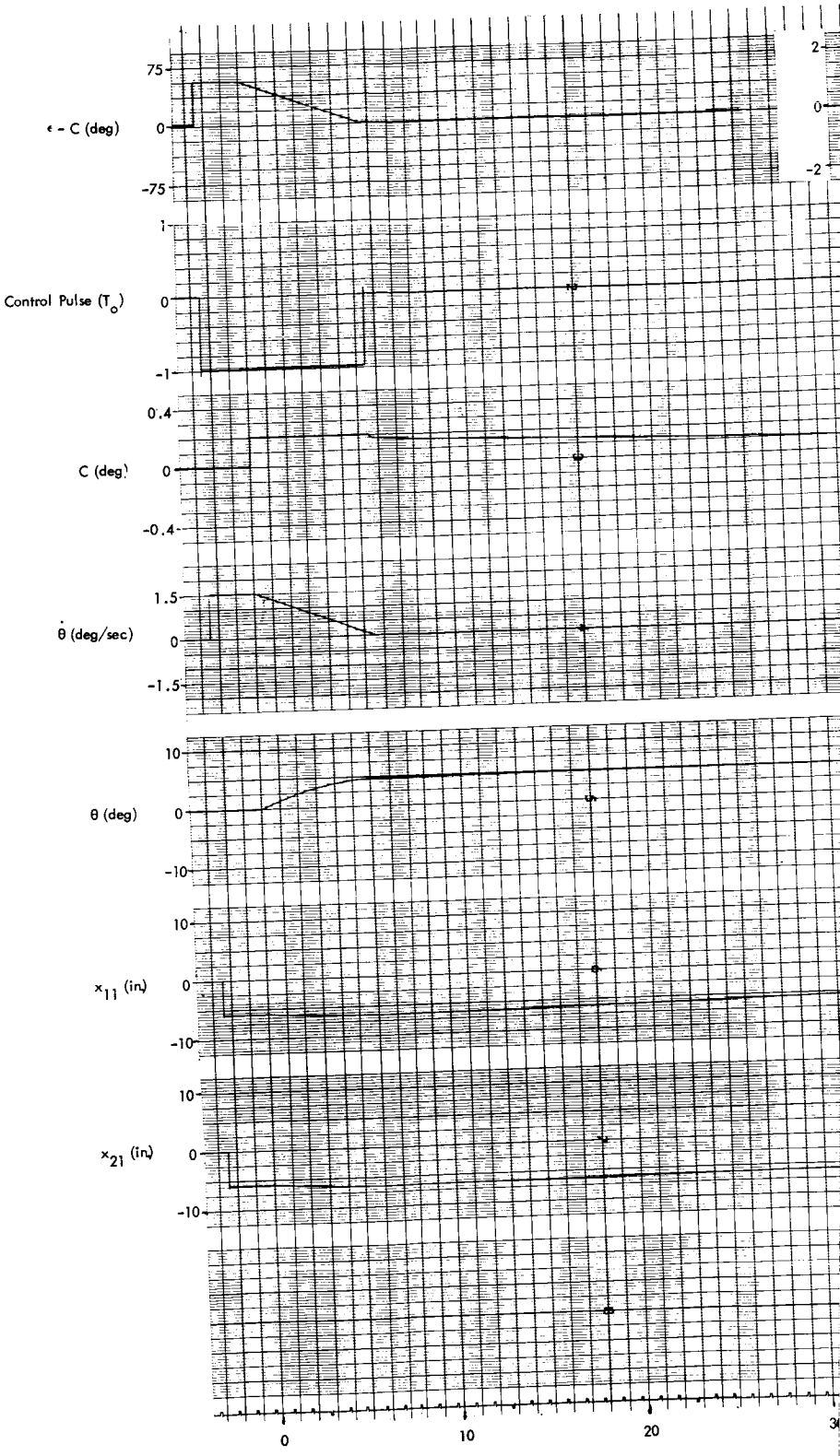
ϵ - C (deg)
75
0
-75
Control Pulse (T_o)
1
0
-1
C (deg)
0.4
0
-0.4
θ̇ (deg/sec)
1.5
0
-1.5
θ (deg)
10
0
-10
x_{11} (in)
10
0
-10
x_{21} (in)
10
0
-10
2
0
-2
0
10
20
30

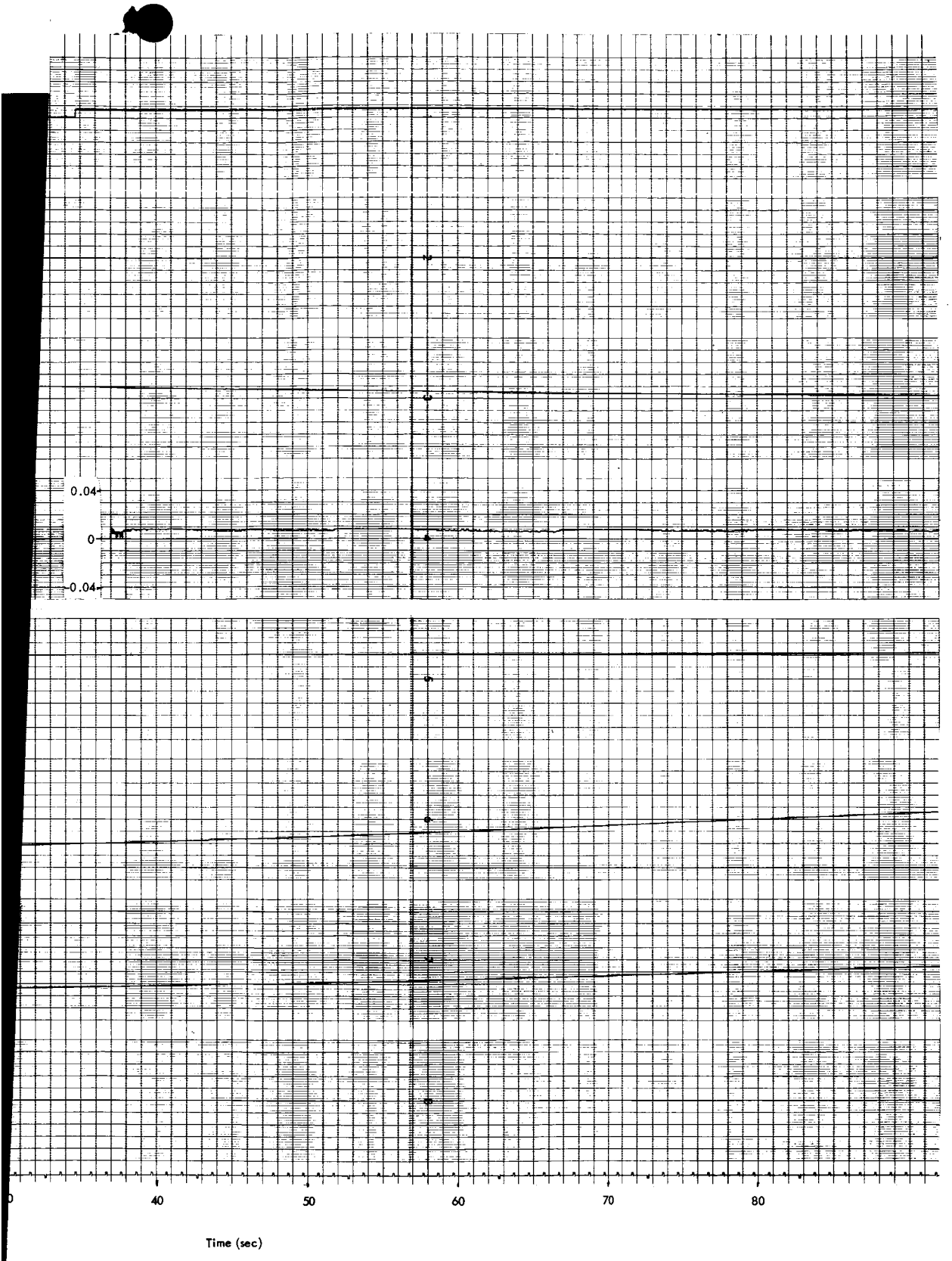

Figure 47. Rate Gyro Mode, Configuration without Capsule, DRI Filter L = 0.2 Deg, $x_{11}(o) = x_{21}(o) = -6$ In., $\dot{\theta}(o) = 1.5$ Deg/Sec

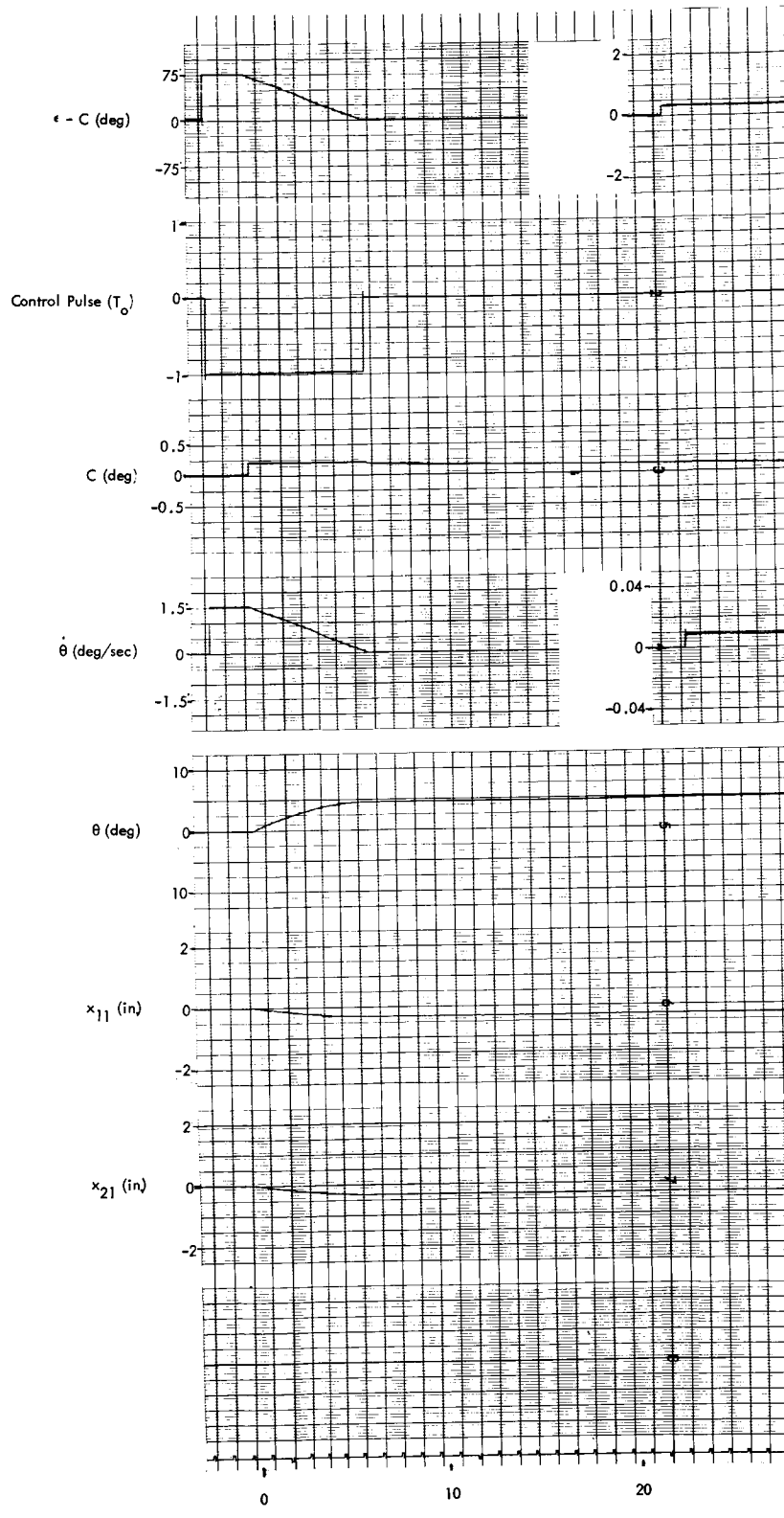
ϵ - C (deg)
75
0
-75
2
0
-2
Control Pulse (T_o)
1
0
-1
C (deg)
0.5
0
-0.5
θ̇ (deg/sec)
1.5
0
-1.5
0.04
0
-0.04
θ (deg)
10
0
10
x_{11} (in)
2
0
-2
x_{21} (in)
2
0
-2
0
10
20

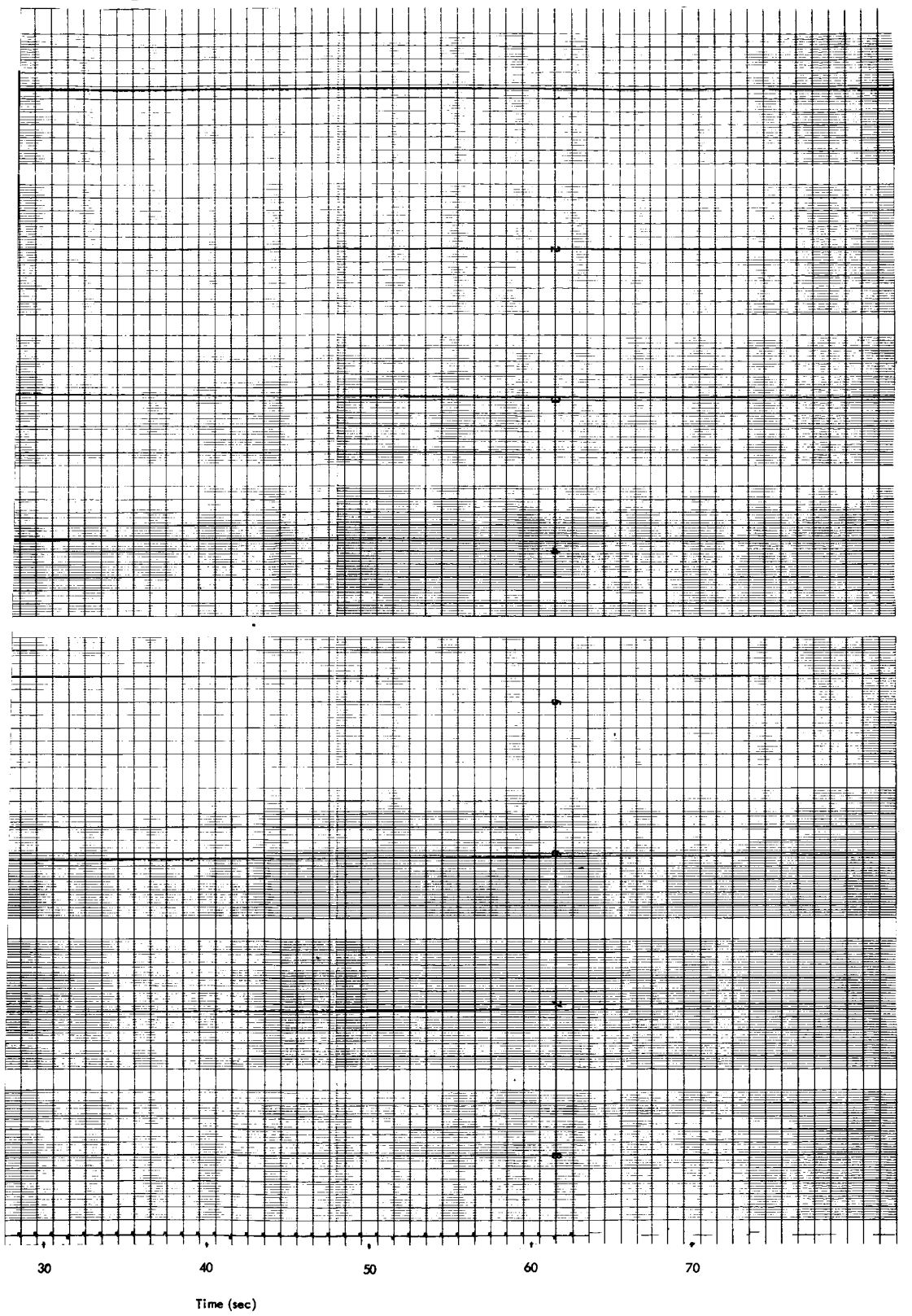

Figure 48. Rate Gyro Mode, Configuration without Capsule, DRI Filter L = 0.2 Deg, Slosh Mass Increased by Factor of 10

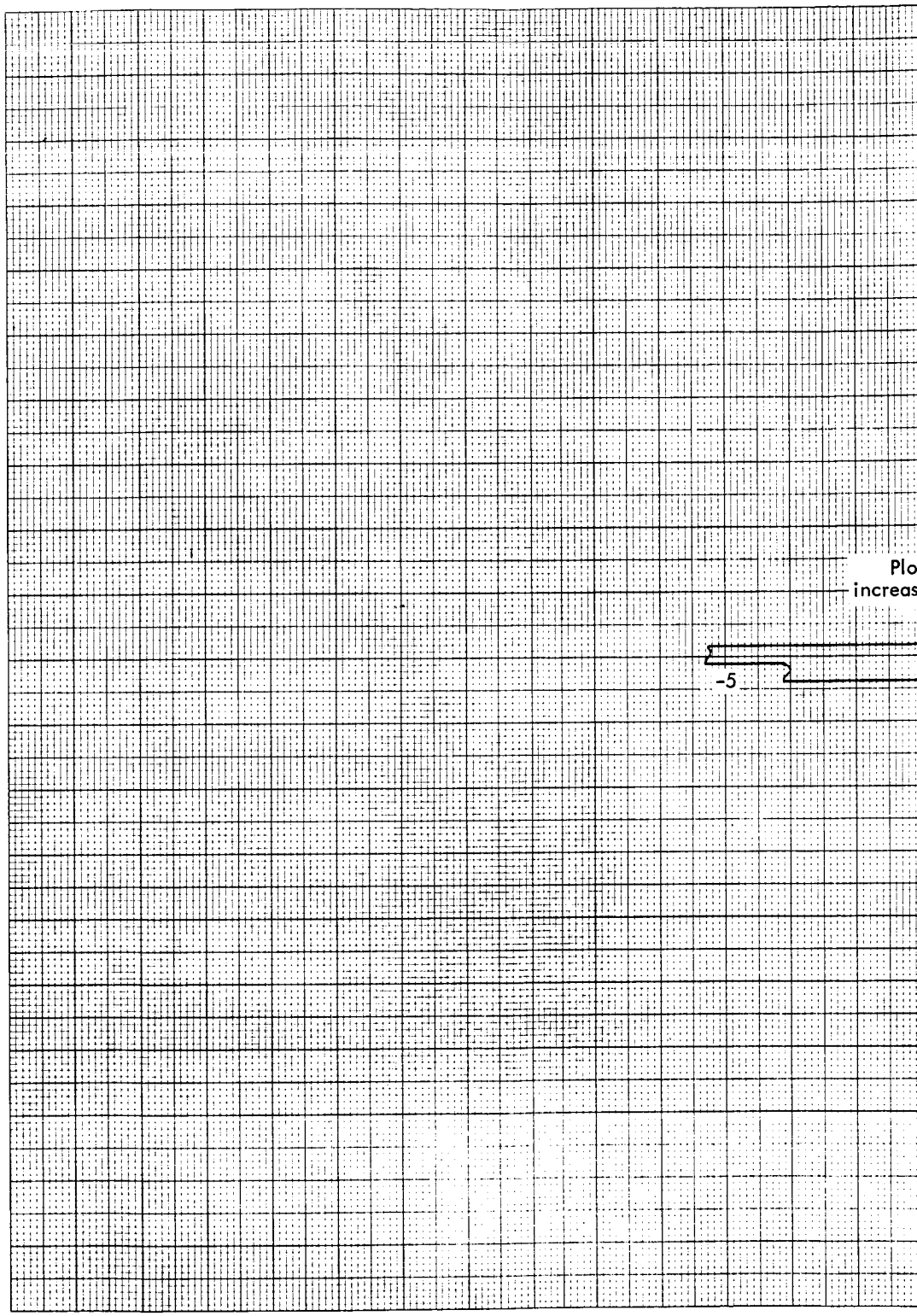
Plo
increas
-5

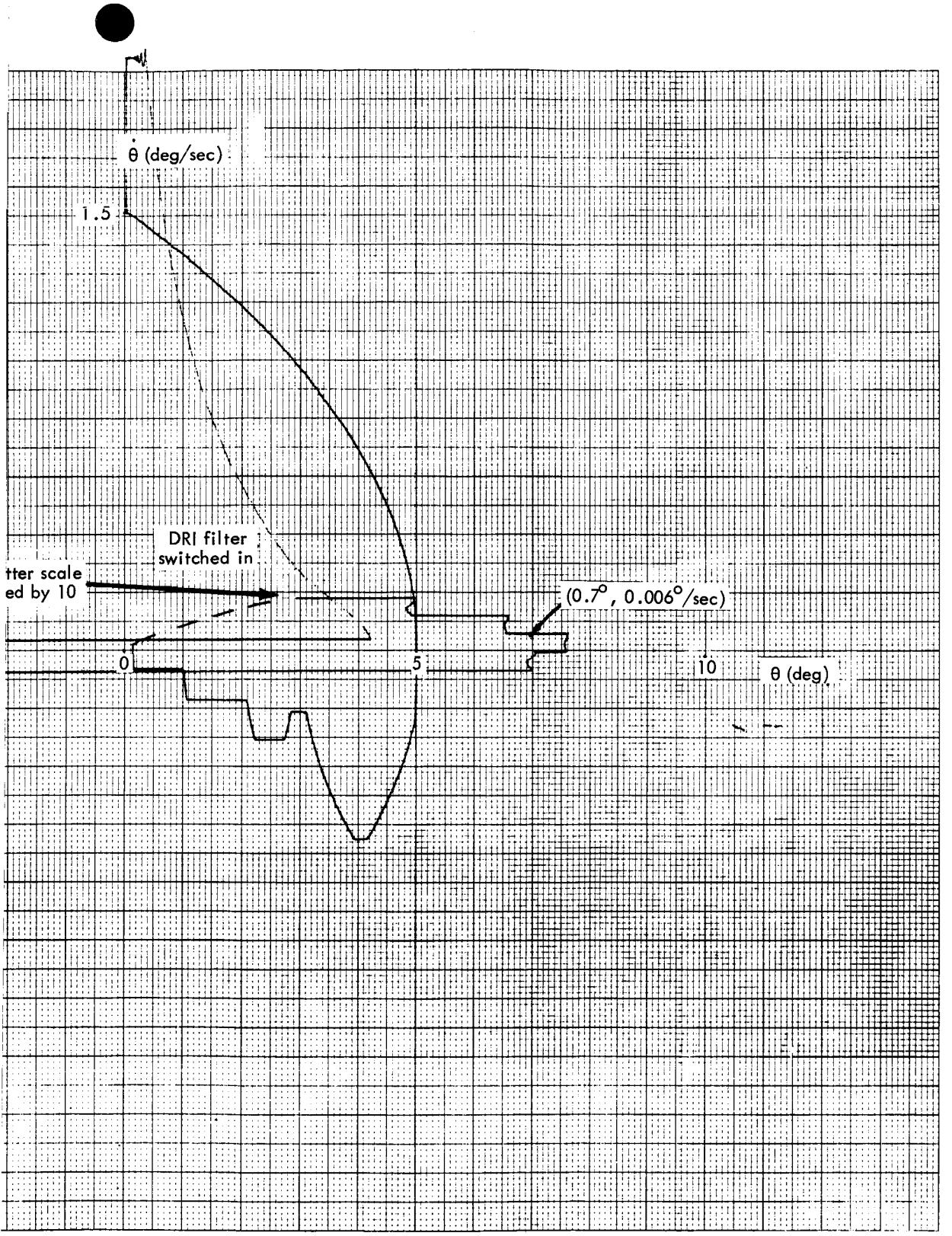

Figure 49. Position Gyro Mode, Configuration without Capsule, Response with Lead-Lag Filter, $\dot{\theta}(o) = 1.5$ Deg/Sec

during transition was 5 degrees. As shown in Figure 49, by waiting long enough the vehicle rates become less than 0.01 deg/sec and attitude excursion becomes limited to ±0.5 degree.

Initial slosh mass displacements of ±6 inches did not greatly affect the vehicle performance (Figures 50 and 51). Good vehicle response was obtained even when the slosh mass was increased by a factor of 10. (Figure 52).

2.5 CONCLUSIONS

With the same DRI time constant used for the cruise mode (50 sec), the performance of the rate gyro mode during the S-IVB separation phase (Figure 25) was not acceptable. Switching to a 1-second DRI time constant during the transition phase from powered flight to cruise reduced the vehicle rate from 1.5 to 0.01 deg/sec in about 19 seconds for the configuration with capsule. Further reduction in τ would decrease the transition time. By removing the DRI filter or limiting the DRI filter output to 0.2 degree, the vehicle rate was reduced from 1.5 to 0.01 deg/sec in approximately 11 seconds for the configuration with capsule. For the three modifications, the attitude excursions were approximately 8.5 to 9.0 degrees for the configuration with capsule at the instant when the vehicle rate was reduced to 0.01 deg/sec. For the configuration without capsule and with the DRI filter limited to 0.2 degree, the vehicle rate was reduced from 1.5 to 0.01 deg/sec in approximately 6 seconds with a corresponding attitude excursion of 5 degrees.

For both vehicle configurations with a 0.2-degree limited DRI filter output, the vehicle response was not greatly affected by large slosh mass displacements (±6 inches) or an increase in slosh mass by a factor of 10. The terminal attitude error with this filter could be reduced to 1.0 degree and the vehicle rate to 0.01 deg/sec in 100 seconds. After a few minutes the vehicle attitude is reduced to within ±0.5 degree with a single minimum pulse limit cycle achieved. In the configurations with and without capsule, the vehicle responses were not greatly affected by larger slosh mass displacements or by increasing the slosh mass by a factor of 10.

Switching from a rate gyro mode to the position gyro mode was attempted at an instant when the vehicle rate was reduced to 0.01 deg/sec. No benefits were found from this mode sequencing.

The rate gyro mode with any of the three modifications mentioned uses less fuel but produces larger steady-state attitude errors than the position gyro mode. The position gyro mode requires more time to reach steady state and uses over twice as much gas due to overshoots, but retains the inertial attitude reference. A lead-lag filter design in which lead signal limiting is included would, however, rectify these two disadvantages and provide the more ideal design. This design improvement was reserved for further investigation.

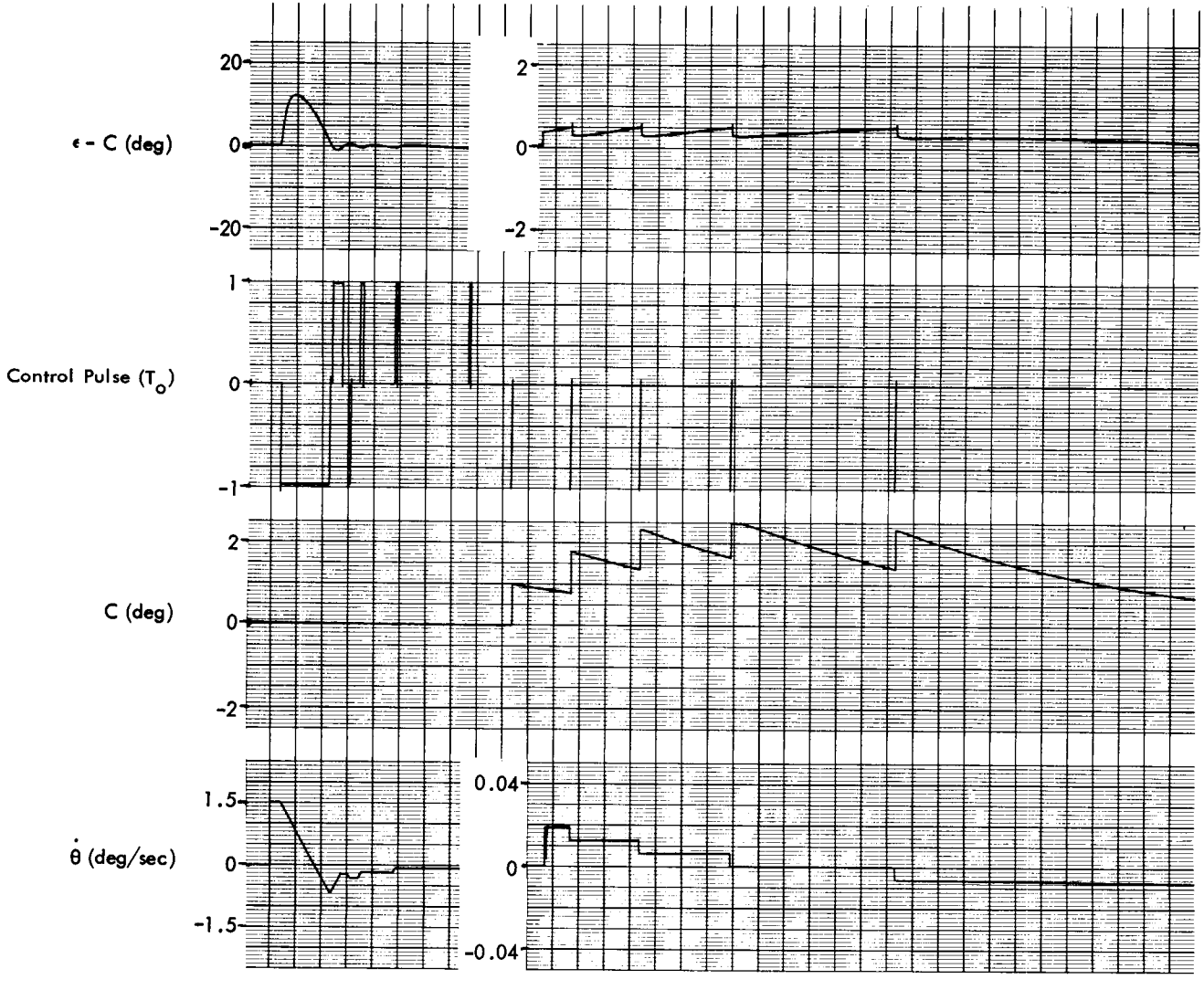
ϵ - C (deg)
20
0
-20
2
0
-2
Control Pulse (T_o)
1
0
-1
C (deg)
2
0
-2
θ̇ (deg/sec)
1.5
0
-1.5
0.04
0
-0.04

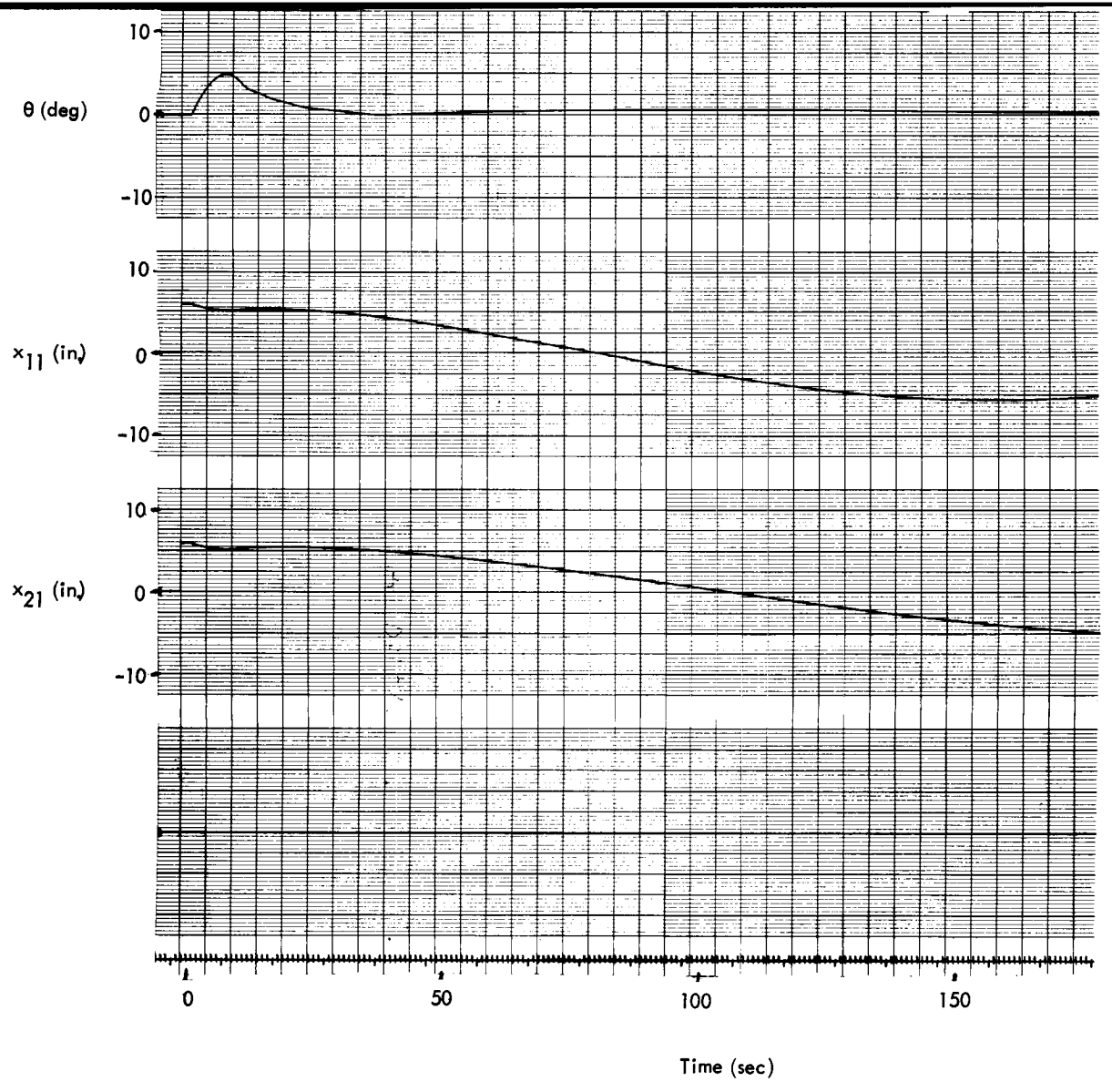

Figure 50. Position Gyro Mode, Configuration without Capsule, Response with Lead-Lag Filter, $x_{11}(o) = x_{21}(o) = +6$ In.

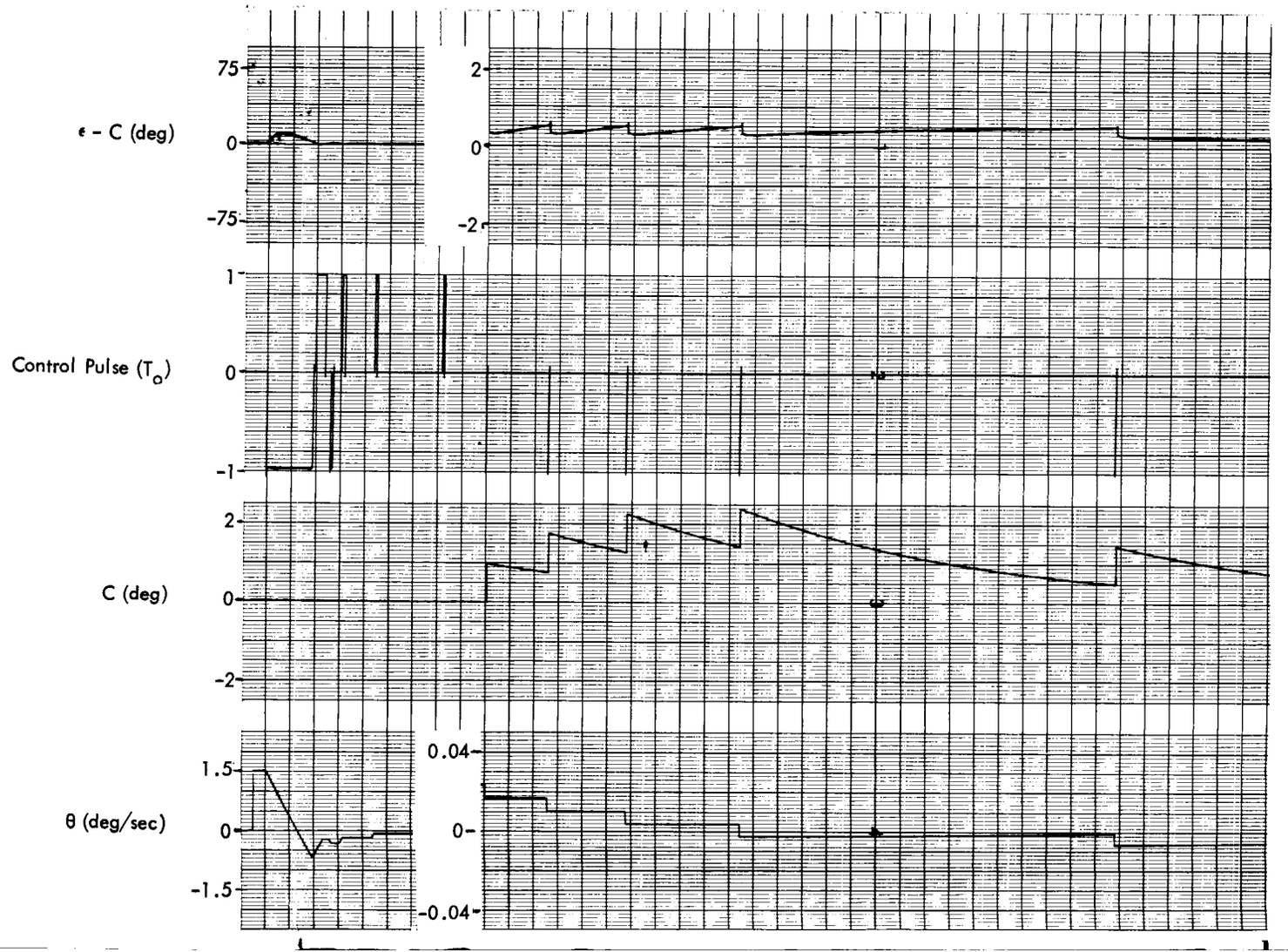
ϵ - C (deg)
75
0
-75
2
0
-2
Control Pulse (T_o)
1
0
-1
C (deg)
2
0
-2
θ (deg/sec)
1.5
0
-1.5
0.04
0
-0.04

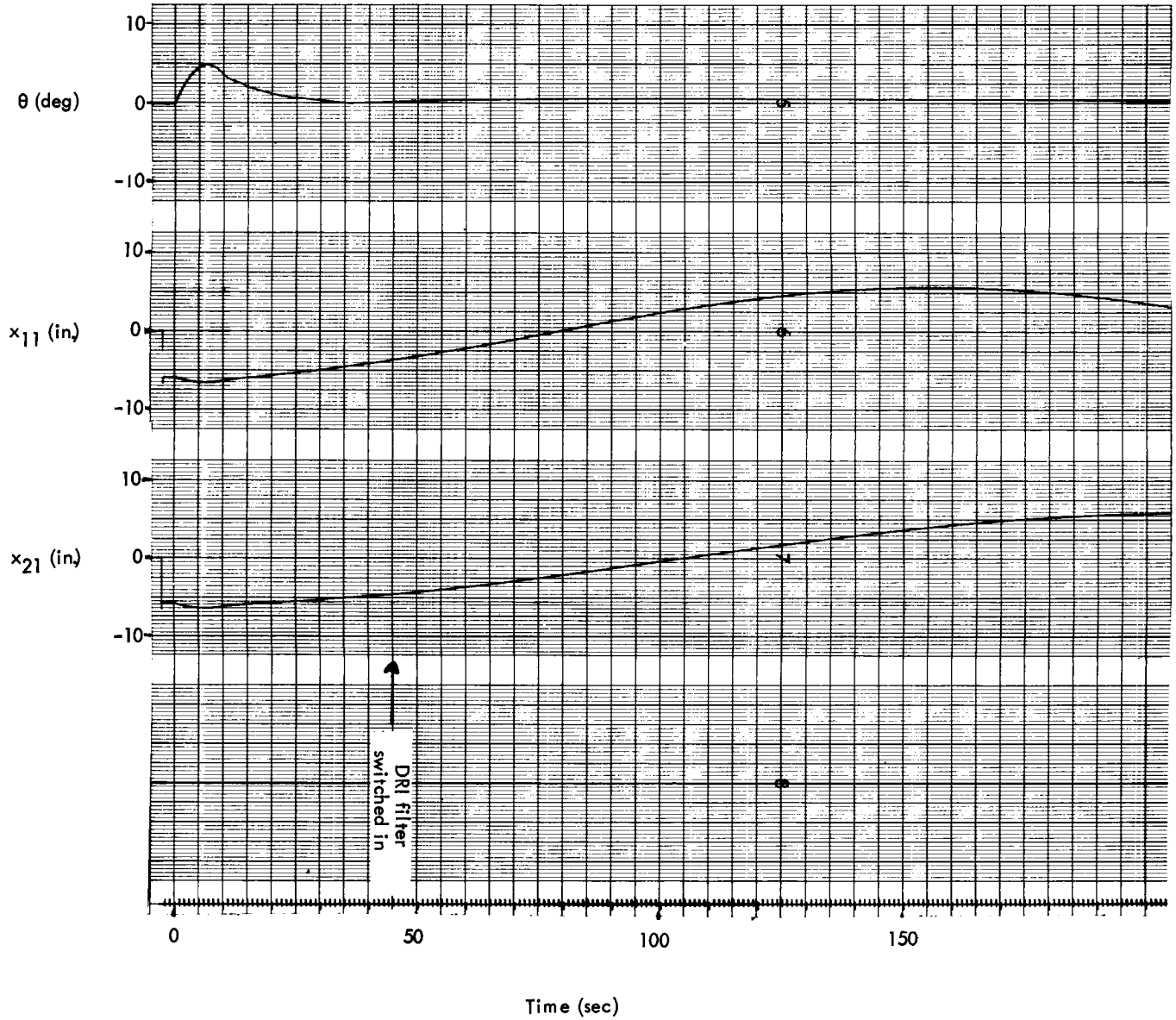

Figure 51. Position Gyro Mode, Configuration without Capsule, Response with Lead-Lag Filter, $x_{11}(o) = x_{21}(o) = -6$ In.

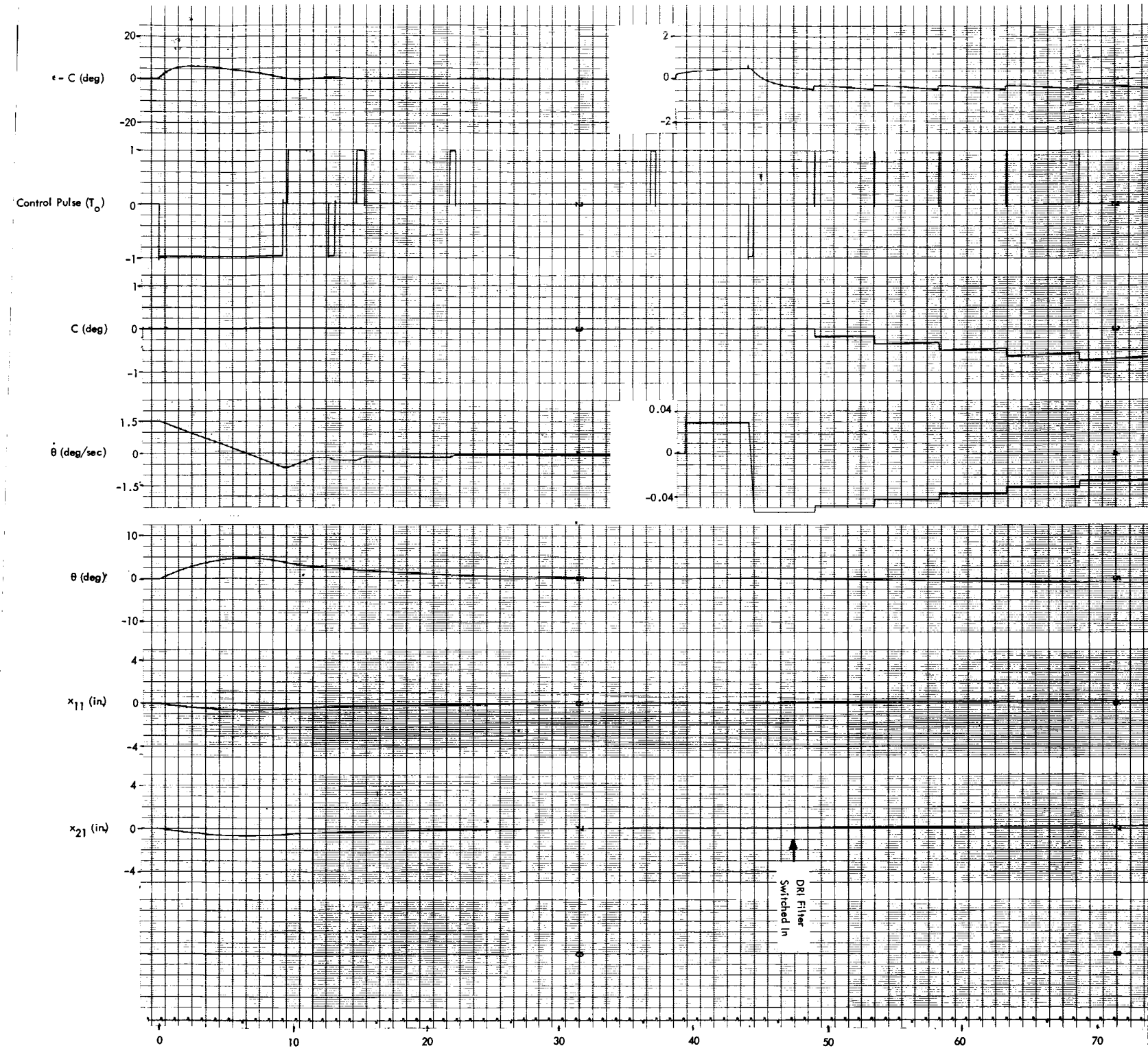
ε - C (deg)
Control Pulse (T_o)
C (deg)
θ̇ (deg/sec)
θ (deg)
x_{11} (in)
x_{21} (in)
DRI Filter Switched In
0
10
20
30
40
50
60
70

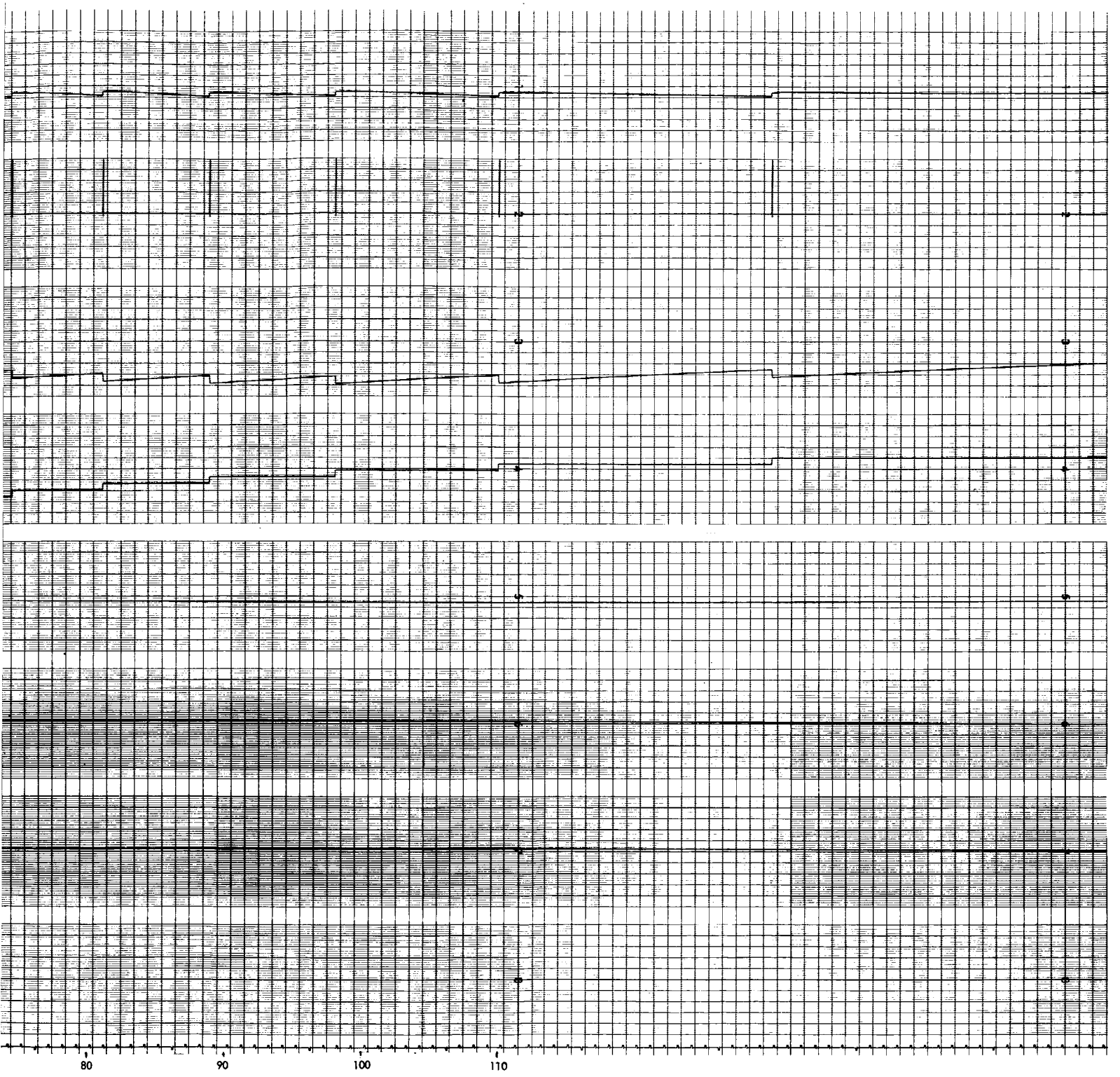

Figure 52. Position Gyro Mode, Configuration without Capsule, Response with Lead-Lag Filter, Slosh Mass Increased by Factor of 10, $\dot{\theta}$ (o) = 1.5 Deg/Sec

PRECEDING PAGE BLANK NOT FILMED.

3. POWERED FLIGHT STABILITY

3.1 INTRODUCTION

The powered flight control system stability analyses employed linear control system models for the determination of gain and phase stability margins for rigid body operation propellant slosh modes and spacecraft body bending modes. The slosh modes included those for both the bus and capsule. The primary body bending modes (described in the Appendix to this report) were those due to coupling of the bus with the aft equipment module, high-gain antenna, landing capsule, and planetary scan platform, these modes being given in increasing order of resonant frequency. Very little deformation of the bus resulted in these modes, the bus acting essentially as a rigid beam. The true bus bending modes in which bus model shapes were obtained were of much higher frequency and safely ignored.

The primary bending mode stability problem encountered was that of the aft equipment module (or solar array) mode. The addition of solar array struts to stiffen (by a factor of 6) its attachment to the bus was investigated. The effects of additional autopilot filtering in conjunction with the added solar array struts were also studied.

Four mission phases were studied:

- Midcourse correction (MCC)
- Start of Mars orbit insertion (start MOI)
- End of Mars orbit insertion (end MOI)
- Mars orbit trim (MOT)

Spacecraft configurations with capsule on and off were analyzed. Except for the Mars orbit trim, all other phases with the capsule off represented an abort or contingency configuration in which the capsule is either ejected prematurely during the flight or not initially included.

Propellant damping variations were made to determine how much damping would be required to stabilize unstable slosh modes or to determine how little damping would be required to unstabilize stable

slosh modes. The primary slosh modes of concern were the capsule slosh modes for the capsule-on configuration and the bus slosh modes for the capsule-off configuration.

The use of electronic integrators to reduce trajectory errors due to thrust misalignments or cg offsets was studied (see Section 4), and the effects of these integrators upon the control system stability margins are presented in Section 3.8. Two types of integral feedback designs were considered, integral attitude feedback with and without integral engine angle feedback. The use of integral attitude feedback would null trajectory errors due only to cg offsets and thrust vector offsets. The use of both integral attitude and integral engine angle feedback would null trajectory errors due only to thrust vector misalignments. The design selection would therefore be dependent upon the relative magnitudes of these anomalies.

A block diagram of the spacecraft powered flight control system is given in Figure 53. The actuation system model shown is a simplification of the Apollo actuation system.

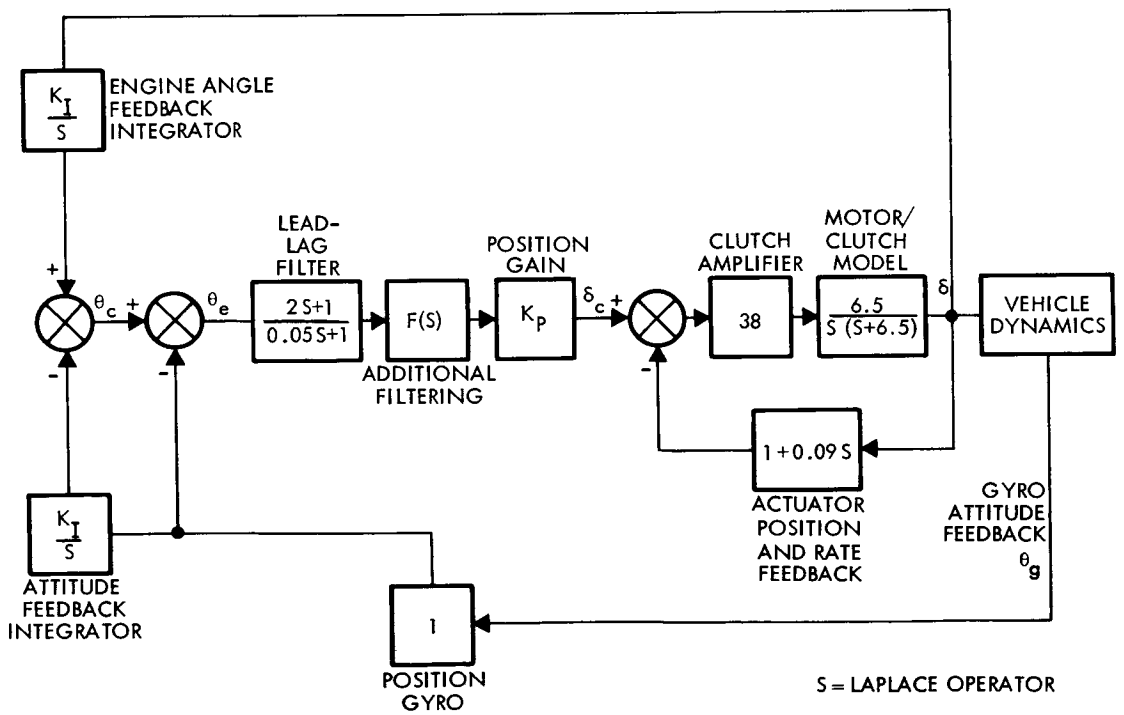

Figure 53. Block Diagram of the Powered Flight Control System Model

The control system angular rate information is obtained through use of a lead-lag filter. The filter configuration shown in Figure 53 was employed throughout the analyses with the exception of the filter variation studies presented in Section 3.7.

The equations employed are represented by the matrix of homogeneous equations given in Figure 54. The terminology associated with the block diagram and equation matrix is given in Table 2.

Tables 3 and 4 list parameter values employed for the four mission phases with and without the capsule, respectively. The bending data were obtained from the attachment included in the Appendix.

The conclusions reached from this analysis are as follows:

1) The bus propellant slosh modes for the nominal mission configurations are stable assuming that considerable propellant damping exists at the tank bottom for the Mars orbit trim firings after capsule ejection. The use of anti-geysering and anti-vortexing baffles are expected to provide more than adequate damping. Additional damping aids would be helpful, particularly, vertical baffles to damp nonlinear (rotational) slosh effects.

2) The bus propellant slosh modes are unstable for the abort or contingency configuration in which the capsule is prematurely ejected or not included in the mission. The aftward shift of the vehicle cg coupled with fairly full propellant tank configurations produces the instability. Damping aids would be required for this abort or contingency configuration, if intended for use.

3) The capsule slosh modes, although in an unstable mode configuration, have little impact on the bus control system, primarily because of the small capsule slosh masses involved. Again, inclusion of damping aids in the capsule tanks, although not required, would be helpful. A recommended design feature, however, is to fill the oxidizer tank to 90 percent or more instead of the present 75 percent, thereby reducing the slosh mass even further. The fuel tank is to be filled near 90 percent.

4) The solar array or aft equipment module in the Task B design poses concern for control system stability; the addition of solar array struts to stiffen its attachment to the bus is recommended.

5) The use of electronic integrators to reduce trajectory errors is acceptable from stability considerations provided that the integrator gains are maintained at a reasonably low level. Thrust vector pointing error analyses discussed in Section 4 show the desirability of their inclusion. The type of integral feedback desired will depend upon the vehicle cg offsets, engine thrust offsets, and engine thrust misalignment angles expected in the final vehicle. The use of switching between these integral feedback designs on a mission phase basis should also be considered.

3.2 STABILITY WITH CAPSULE ON

The control system stability margins for the spacecraft with landing capsule on is given by the gain-phase plots for the four mission phases in Figures 55 through 58. Three slosh modes and four bending modes are apparent in these frequency response figures. Employing Figure 55 as an example, the lowest frequency point on the plot occurs at +65 db. The system gain is reduced as the frequency increases, and the first resonance encountered is that from the bus slosh mode. Since all four bus propellant tanks are identical, with assumed identical fluid levels, the four slosh modes occur at the same frequency and combine into the one large modal loop shown. Next, as the frequency is increased, two capsule slosh modes are encountered. Two separate modes are shown, corresponding to the capsule fuel and oxidizer modes; since the propellant tanks are spherical bottles of different diameter different capsule slosh frequencies result. This mode is discussed further in Section 3.5

The resonant modes encountered next are those from the aft equipment module, high-gain antenna, landing capsule, and planetary scan platform (PSP) as shown by the four separate loops. For this midcourse correction case, a higher system gain than unity (represented by the 0 db point) can be tolerated. Increasing the gain by as much as 12 db or $K_p = 4$, to compensate for the reduced thrust during this phase, would still produce an 11 db high frequency gain margin. The phase margin at $K_p = 4$ is shown to be larger than 50 degrees.

In Figure 56 for the case representing the start of MOI, the increased engine thrust during this phase is manifested by a general shift in the gain-phase plot upward along the positive db axis. The

	Rigid Body Attitude Angle (Radians) θ	Bus Oxidizer Slosh Mass Displacement (Feet) λ_{BO}	Bus Fuel Slosh Mass Displacement (Feet) λ_{BF}	Capsule Oxidizer Slosh Mass Displacement (Feet) λ_{CO}
Rigid Body Moment Equation	IS^2	$K_{BO} L_{BO} - M_{BO} \frac{T}{M}$	$K_{BF} L_{BF} - M_{BF} \frac{T}{M}$	$K_{CO} L_{CO} - M_{CO} \frac{T}{M}$
Bus Oxidizer Slosh Equation	$- L_{BO} S^2$	$\left(1 - \frac{M_{BO}}{M}\right) S^2 + 2\zeta_{BO} \omega_{BO} S + \omega_{BO}^2$	$\frac{K_{BF}}{M}$	$\frac{K_{CO}}{M}$
Bus Fuel Slosh Equation	$- L_{BF} S^2$	$\frac{K_{BO}}{M}$	$\left(1 - \frac{M_{BF}}{M}\right) S^2 + 2\zeta_{BF} \omega_{BF} S + \omega_{BF}^2$	$\frac{K_{CO}}{M}$
Capsule Oxidizer Slosh Equation	$- L_{CO} S^2$	$\frac{K_{BO}}{M}$	$\frac{K_{BF}}{M}$	$\left(1 - \frac{M_{CO}}{M}\right) S^2 + 2\zeta_{CO} \omega_{CO} S + \omega_{CO}^2$
Capsule Fuel Slosh Equation	$- L_{CF} S^2$	$\frac{K_{BO}}{M}$	$\frac{K_{BF}}{M}$	$\frac{K_{CO}}{M}$
First Bending Mode Equation				
Second Bending Mode Equation				
Third Bending Mode Equation				
Fourth Bending Mode Equation				
Actuation Loop Equation				
Autopilot Filter Equation				
Attitude Error Equation	- 1			
Integrator Feedback Equation				

Capsule Fuel Slosh Mass Displacement (Feet) λ_{CF}	First Bending Mode Amplitude (Radians) Q_1	Second Bending Mode Amplitude (Radians) Q_2	Third Bending Mode Amplitude (Radians) Q_3	Fourth Bending Mode Amplitude (Radians) Q_4
$K_{CF} L_{CF} - M_{CF} \frac{\bar{I}}{M}$	$T\left[\phi_{1T} - \phi_{1T}' L_T\right]$	$T\left[\phi_{2T} - \phi_{2T}' L_T\right]$	$T\left[\phi_{3T} - \phi_{3T}' L_T\right]$	$T\left[\phi_{4T} - \phi_{4T}' L_T\right]$
$\frac{K_{CF}}{M}$	$\phi_{BO1} S^2$	$\phi_{BO2} S^2$	$\phi_{BO3} S^2$	$\phi_{BO4} S^2$
$\frac{K_{CF}}{M}$	$\phi_{BF1} S^2$	$\phi_{BF2} S^2$	$\phi_{BF3} S^2$	$\phi_{BF4} S^2$
$\frac{K_{CF}}{M}$	$\phi_{CO1} S^2$	$\phi_{CO2} S^2$	$\phi_{CO3} S^2$	$\phi_{CO4} S^2$
$\left(1 - \frac{M_{CF}}{M}\right) S^2$ $+ 2\zeta_{CF} \omega_{CF} S + \omega_{CF}^2$	$\phi_{CF1} S^2$	$\phi_{CF2} S^2$	$\phi_{CF3} S^2$	$\phi_{CF4} S^2$
	$M_1 \left(S^2 + 2\zeta_1 \omega_1 S + \omega_1^2\right)$ $+ T \phi_{1T}' \phi_{1T}$	$T\phi_{2T}' \phi_{2T}$	$T \phi_{3T}' \phi_{3T}$	$T \phi_{4T}' \phi_{4T}$
	$T \phi_{1T}' \phi_{1T}$	$M_2 (S^2 + 2\zeta_2 \omega_2 S +$ $+ T\phi_{2T}' \phi_{2T}$	$T \phi_{3T}' \phi_{3T}$	$T\phi_{4T}' \phi_{4T}$
	$T\phi_{1T}' \phi_{1T}$	$T\phi_{2T}' \phi_{2T}$	$M_3 \left(S^2 + 2\zeta_3 \omega_3 S + \omega_3^2\right)$ $+ T\phi_{3T}' \phi_{3T}$	$T\phi_{4T}' \phi_{4T}$
	$T\phi_{1T}' \phi_{1T}$	$T\phi_{2T}' \phi_{2T}$	$T\phi_{3T}' \phi_{3T}$	$M_4 \left(S^2 + 2S_4 \omega_4 S + \omega_4^2\right)$ $+ T\phi_{4T}' \phi_{4T}$
	ϕ_{1G}'	ϕ_{2G}'	ϕ_{3G}'	ϕ_{4G}'
	$K_I \phi_{1G}'$	$K_I \phi_{2G}'$	$K_I \phi_{3G}'$	$K_I \phi_{3G}'$

Engine Angle (Radians) δ	Engine Angle Command (Radians) δ_c	Attitude Command Error (Radians) θ_e	Integral Feedback Attitude Command (Radians) θ_C
$-\left[TL_T\left(1+\frac{M_e L_e}{ML_T}\right) + S^2\left(I_H + M_e L_e L_T\right)\right]$			
$-\frac{T}{M}$			
$-\frac{T}{M}$			
$-\frac{T}{M}$			
$-\frac{T}{M}$			
$T\phi_{1T}\left(1-\frac{I_H + M_e L_e L_T}{I}\right) - S^2\left(I_H \phi_{1T}' - M_e L_e \phi_{1T}\right)$			
$T\phi_{2T}\left(1-\frac{I_H + M_e L_e L_T}{I}\right) - S^2\left(I_H \phi_{2T}' - M_e L_e \phi_{2T}\right)$			
$T\phi_{3T}\left(1-\frac{I_H + M_e L_e L_T}{I}\right) - S^2\left(I_H \phi_{3T}' - M_e L_e \phi_{3T}\right)$			
$T\phi_{4T}\left(1-\frac{I_H + M_e L_e L_T}{I}\right) - S^2\left(I_H \phi_{4T}' - M_e L_e \phi_{4T}\right)$			
$38\,(1 + 0.09S) + S\left(\frac{S}{6.5}+1\right)$	-38		
	$(0.05S + 1)\,F\,(S)$	$-K_p\,(2S+1)$	
		-1	1
K_I			$-S$

Figure 54. Matrix of Homogeneous Equations

Table 2. Matrix of Homogeneous Equations Terminology

Mass Parameters

I = vehicle moment of inertia, slug ft^2

M = vehicle mass, slugs

Engine Parameters

T = engine thrust, lb

M_e = engine mass, slugs

L_e = distance between engine cg and vehicle cg ft

L_T = distance between engine gimbal and vehicle cg ft

I_H = inertia of engine about the gimbal point, slug ft^2

Slosh Parameters

$L_{BO}, L_{BF}, L_{CO}, L_{CF}$ = bus and capsule, fuel and oxidizer, slosh mass distances from vehicle cg (positive aft of cg, towards gimbal), ft

$M_{BO}, M_{BF}, M_{CO}, M_{CF}$ = slosh masses, slugs

$K_{BO}, K_{BF}, K_{CO}, K_{CF}$ = slosh mode spring constants, $lb\text{-}ft^{-1}$

$\omega_{BO}, \omega_{BF}, \omega_{CO}, \omega_{CF}$ = slosh mode frequencies, rad/sec

$\zeta_{BO}, \zeta_{BF}, \zeta_{CO}, \zeta_{CF}$ = slosh mode damping, no dimensions

Bending Parameters

M_1, M_2, M_3, M_4 = bending mode masses (four modes), slugs

$\omega_1, \omega_2, \omega_3, \omega_4$ = bending mode frequencies, rad/sec

$\zeta_1, \zeta_2, \zeta_3, \zeta_4$ = bending mode damping, no dimensions

$\phi_{1T}, \phi_{2T}, \phi_{3T}, \phi_{4T}$ = bending displacements at the gimbal point (positive values), ft

$\phi'_{1T}, \phi'_{2T}, \phi'_{3T}, \phi'_{4T}$ = bending slopes at the gimbal point (positive values), ft/ft

Table 2. Matrix of Homogeneous Equations Terminology (Continued)

$\phi_{BO1}, \phi_{BO2}, \phi_{BO3}, \phi_{BO4}$	=	bending displacements at bus oxidizer slosh mass station, ft
$\phi_{BF1}, \phi_{BF2}, \phi_{BF3}, \phi_{BF4}$	=	bending displacements at bus fuel slosh
$\phi_{CO1}, \phi_{CO2}, \phi_{CO3}, \phi_{CO4}$	=	bending displacements at capsule oxidizer slosh mass station, ft
$\phi_{1G}', \phi_{2G}', \phi_{3G}', \phi_{4G}'$	=	bending slopes at the position gyro station, ft/ft

Variables

θ	rigid body vehicle attitude angle, rad
λ_{BO}	bus oxidizer slosh mass displacement, ft
λ_{BF}	bus fuel slosh mass displacement, ft
λ_{CO}	capsule oxidizer slosh mass displacement, ft
λ_{CF}	capsule fuel slosh mass displacement, ft
Q_1	first bending mode amplitude, rad
Q_2	second bending mode amplitude, rad
Q_3	third bending mode amplitude, rad
Q_4	fourth bending mode amplitude, rad
δ	engine displacement angle, rad
δ_C	engine command angle, rad
θ_e	attitude error angle, rad
θ_C	integrator feedback attitude command, rad

Station Numbers

Engine gimbal point	111 in.
Bottom of bus propellant tanks	118.25 in.
Gyro location	136 in.
Capsule slosh mass attach points	280 in.

Table 3. Parameter Values, Vehicle With Capsule On

	MCC	Start MOI	End MOI	MOT
I, slug ft^2	26,157	26,623	19,094	19,094
M, slugs	636	595	286	286
T, lb	1,050	7,750	7,750	1,050
M_e, slugs	12.4	12.4	12.4	12.4
L_e, ft	4.91	4.91	4.91	4.91
L_T, ft	4.91	4.91	4.91	4.91
I_H, slug ft^2	50	50	50	50
$L_{BO} = L_{BF}$, ft	1.68	1.68	5.8	5.8
$L_{CO} = L_{CF}$, ft	-9.15	-9.15	-7.35	-7.35
M_{BO}, slugs	75.6	75.6	6.23	6.23
M_{BF}, slugs	47.2	47.0	3.87	3.87
M_{CO}, slugs	2.7	2.7	2.7	2.7
M_{CF}, slugs	0.9	0.9	0.9	0.9
K_{BO}, lb-ft	105	840	76	10.4
K_{BF}, lb-ft	66	555	47	6.4
K_{CO}, lb-ft	9.7	78	160	22
K_{CF}, lb-ft	3.2	26	53	7.4
$\omega_{BO} = \omega_{BF}$, rad/sec	1.18	3.35	3.48	1.29
ω_{CO}, rad/sec	1.89	5.37	7.69	2.87
ω_{CF}, rad/sec	2.30	6.55	9.40	3.49
$\zeta_{BO} = \zeta_{BF}$	0.001	0.001	0.001	0.001
$\zeta_{CO} = \zeta_{CF}$	0.01	0.01	0.01	0.01

Table 3. Parameter Values, Vehicle with Capsule On (Continued)

	MCC	Start MOI	End MOI	MOT
$M_1 = M_2 = M_3 = M_4$, slug ft^2	1	1	1	1
ω_1, rad/sec	10.07	10.07	10.75	10.75
ω_2, rad/sec	24.97	24.97	25.16	25.16
ω_3, rad/sec	37.50	37.50	39.21	39.21
ω_4, rad/sec	47.13	47.13	47.89	47.89
$\zeta_1 = \zeta_2 = \zeta_3 = \zeta_4$	0.01	0.01	0.01	0.01
ϕ_{1T}, ft	0.00506	0.00506	0.0117	0.0117
ϕ_{2T}, ft	0.00216	0.00216	0.00431	0.00431
ϕ_{3T}, ft	0.00347	0.00347	0.00958	0.00958
ϕ_{4T}, ft	0.00262	0.00262	0.00706	0.00706
ϕ_{1T}'	0.000592	0.000592	0.001089	0.001989
ϕ_{2T}'	0.000480	0.000480	0.00070	0.00070
ϕ_{3T}'	0.000254	0.000254	0.00068	0.00068
ϕ_{4T}'	0.000543	0.000543	0.00094	0.00094
$\phi_{BO1} = \phi_{BF1}$, ft	0.00353	0.00353	0.00885	0.00885
$\phi_{BO2} = \phi_{BF2}$, ft	0.000092	0.000092	0.0025	0.0025
$\phi_{BO3} = \phi_{BF3}$, ft	0.00282	0.00282	0.00781	0.00781
$\phi_{BO4} = \phi_{BF4}$, ft	0.00122	0.00122	0.0046	0.0046
ϕ_{CO1}, ϕ_{CF1}, ft	-.00332	-.00332	-.00366	-.00366
ϕ_{CO2}, ϕ_{CF2}, ft	-.00466	-.00466	-.0056	-.0056
ϕ_{CO3}, ϕ_{CF3}, ft	-.000025	-.000025	0.00013	0.00013
ϕ_{CO4}, ϕ_{CF4}, ft	-.00525	-.00525	-.00648	-.00648
ϕ_{1G}'	0.000595	0.000595	0.00109	0.00109

Table 3. Parameter Values, Vehicle with Capsule On (Continued)

	MCC	Start MOI	End MOI	MOT
ϕ_{2G}'	0.00048	0.00048	0.000070	0.000070
ϕ_{3G}'	0.00025	0.00025	0.000068	0.000068
ϕ_{4G}'	0.00054	0.00054	0.000094	0.000094
ϕ_{3T}'	0.00129	0.00129	0.00172	0.00172
$\phi_{BO1} = \phi_{BF1}'$, ft	0.0058	0.0058	0.01112	0.01112
$\phi_{BO2} = \phi_{BF2}'$, ft	0.00348	0.00348	0.00107	0.00107
$\phi_{BO3} = \phi_{BF3}'$, ft	0.00382	0.00382	0.00118	0.00118
α_{1G}'	0.000626	0.000626	0.00112	0.00112
ϕ_{2G}'	0.00159	0.00159	0.00137	0.00137
ϕ_{3G}'	0.00129	0.00129	0.00172	0.00172

Table 4. Parameter Values, Vehicle with Capsule Off

	MCC	Start MOI	End MOI	MOT
I, slug-ft^2	14,500	13,523	4,547	4,547
M, slugs	550	500	208	208
T, lb	1,040	7,750	7,750	1,040
M_e, slugs	12.4	12.4	12.4	12.4
L_e, ft	3.19	3.05	2.5	2.5
L_T, ft	3.19	3.05	2.5	2.5
I_H, slug ft^2	50	50	50	50
$L_{BO} = L_{BF}$, ft	0.995	1.142	1.71	1.71
M_{BO}, slugs	75.6	75.6	6.23	6.23
M_{BF}, slugs	47.2	47.0	3.87	3.87
K_{BO}, slugs	121	997	104	14
K_{BF}, slugs	76	624	63	8.7
$\omega_{BO} = \omega_{BF}$, rad/sec	1.26	3.65	4.07	1.50
$\zeta_{BO} = \zeta_{BF}$	0.001	0.001	0.001	0.001
$M_1 = M_2 = M_3 = M_4$	1	1	1	1
ω_1, rad/sec	10.96	10.96	10.96	10.96
ω_2, rad/sec	25.76	25.76	25.76	25.76
ω_3, rad/sec	49.27	49.27	49.27	49.27
$\zeta_1 = \zeta_2 = \zeta_3$	0.01	0.01	0.01	0.01
ϕ_{1T}, ft	0.00741	0.00741	0.0140	0.0140
ϕ_{2T}, ft	0.00678	0.00678	0.00462	0.00462
ϕ_{3T}, ft	0.00118	0.00118	0.00563	0.00563
ϕ_{1T}'	0.000626	0.000626	0.00112	0.00112
ϕ_{2T}'	0.00159	0.00159	0.00137	0.00137

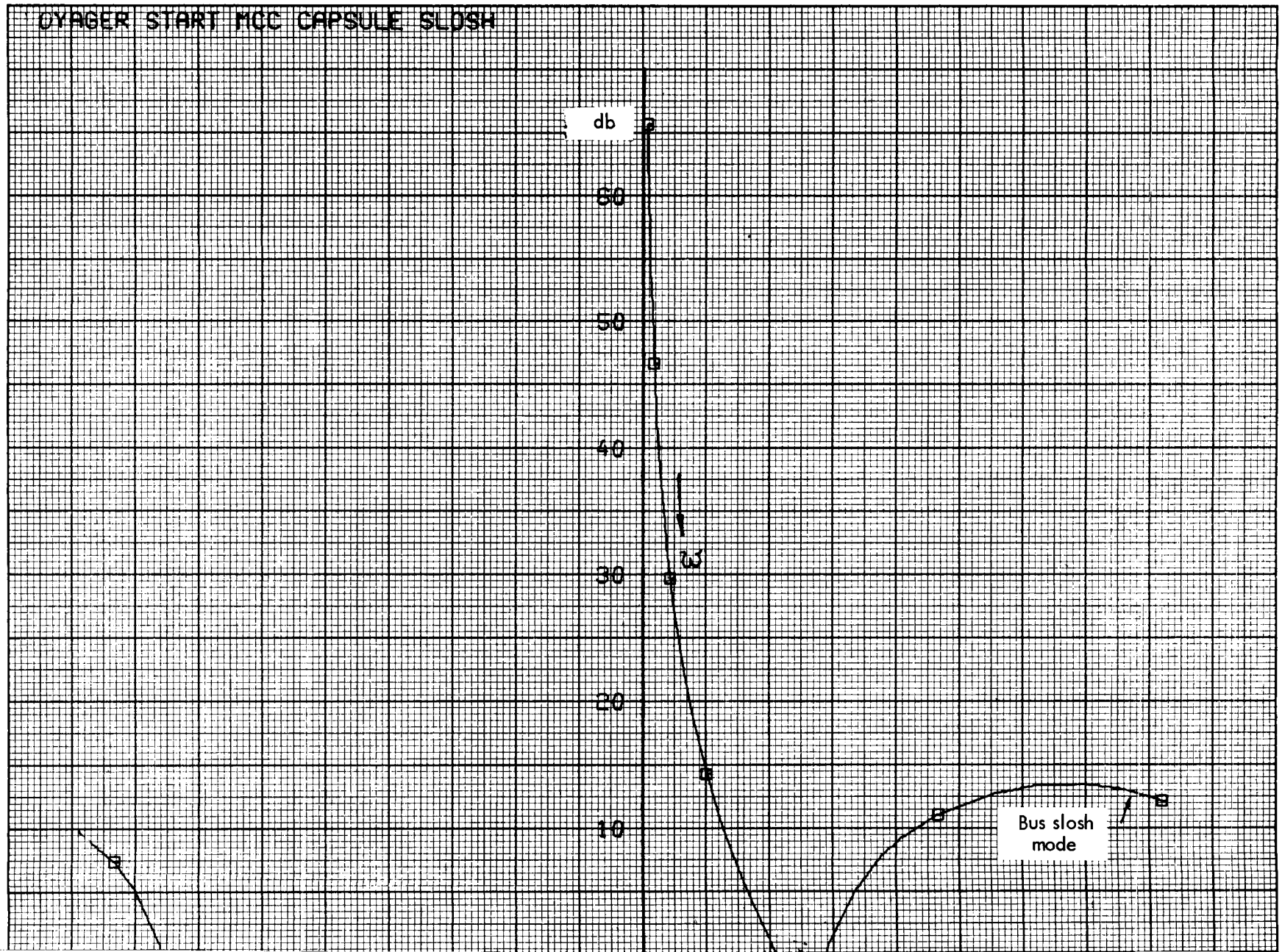
VOYAGER START MCC CAPSULE SLOSH
db
60
50
40
30
20
10
Bus slosh mode

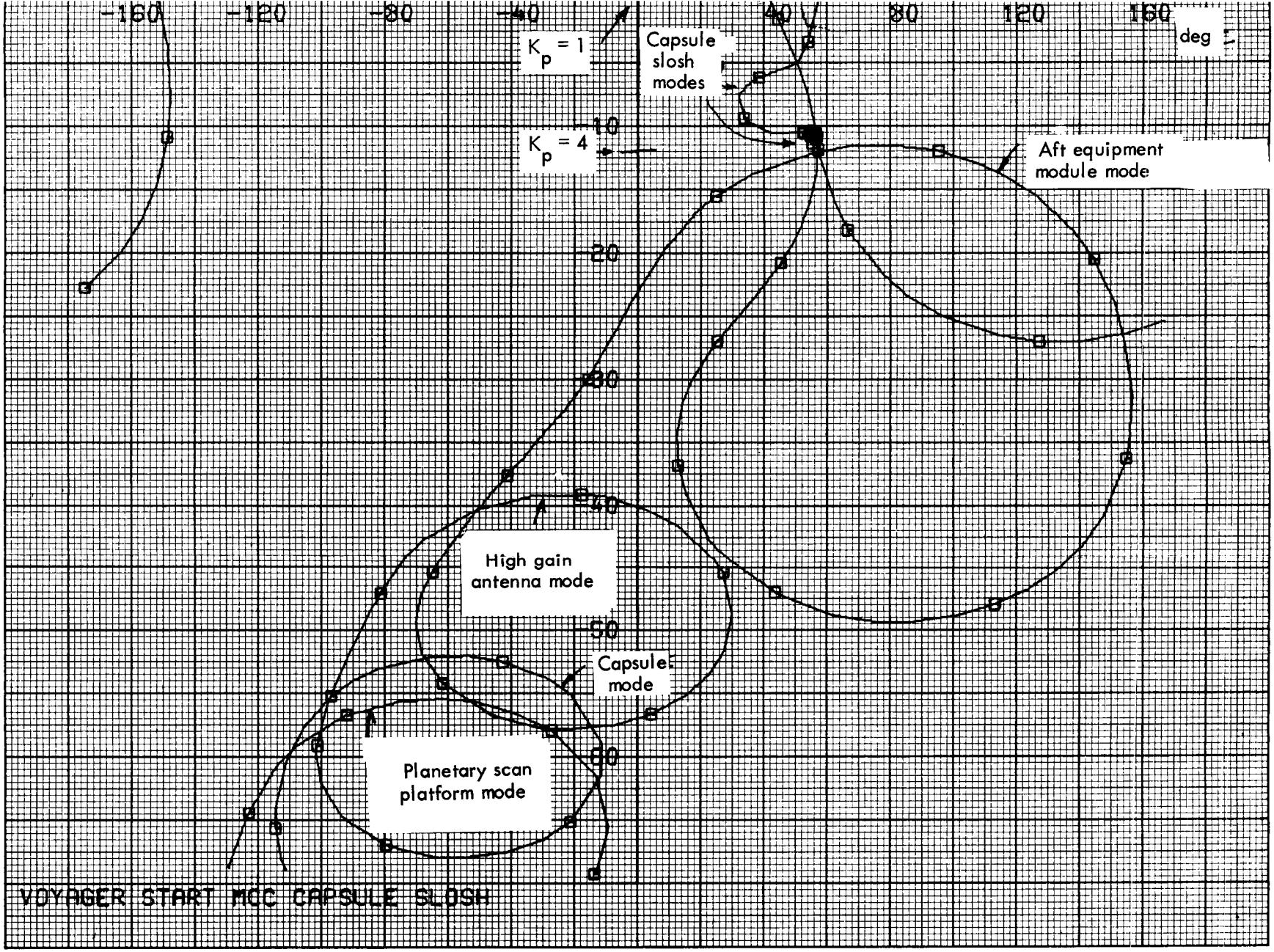

Figure 55. Gain-Phase Plot, Start MCC, with Capsule

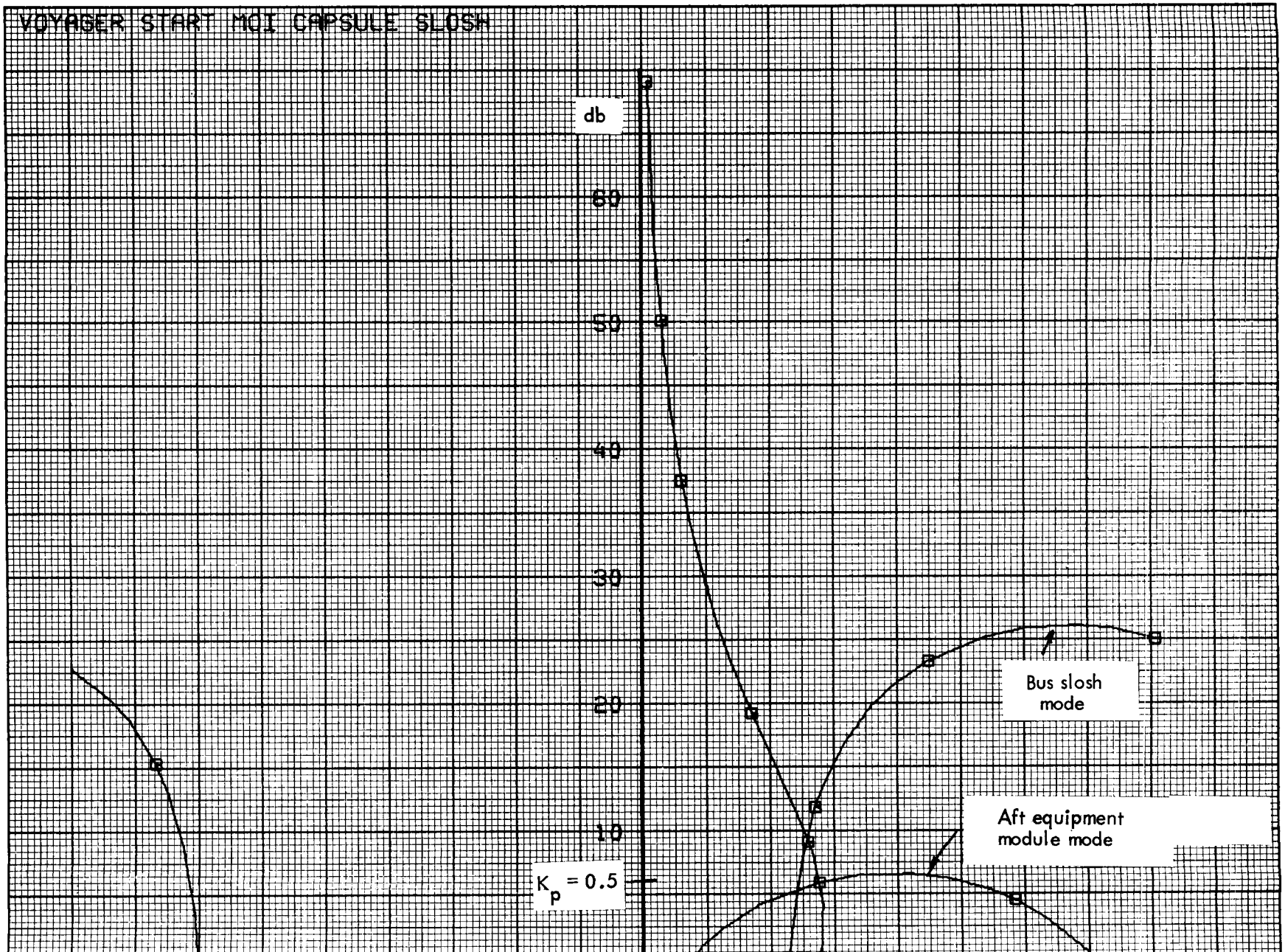
VOYAGER START MOI CAPSULE SLOSH
db
60
50
40
30
20
10
$K_p = 0.5$
Bus slosh mode
Aft equipment module mode

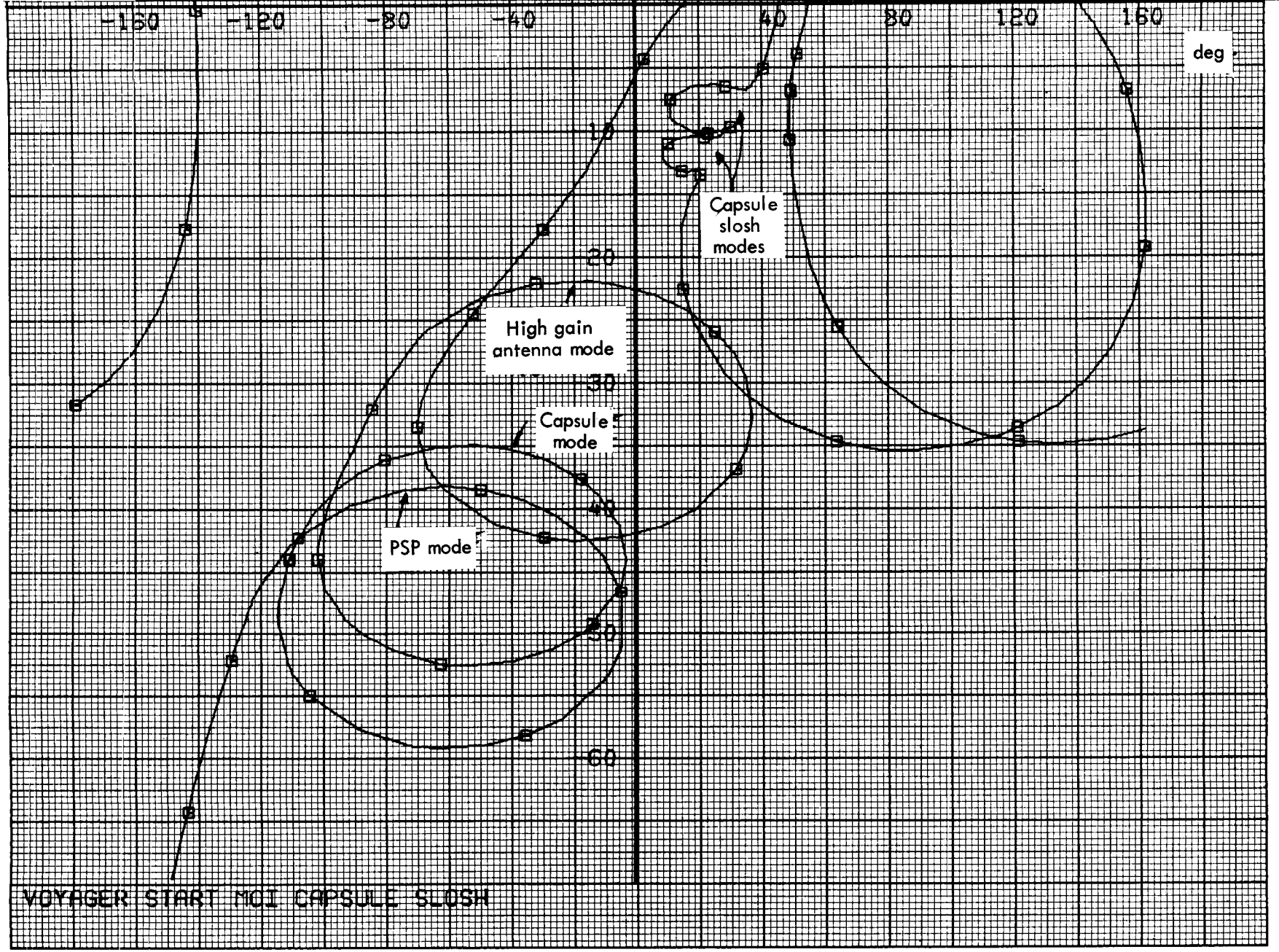

Figure 56. Gain-Phase Plot, Start MOI, with Capsule

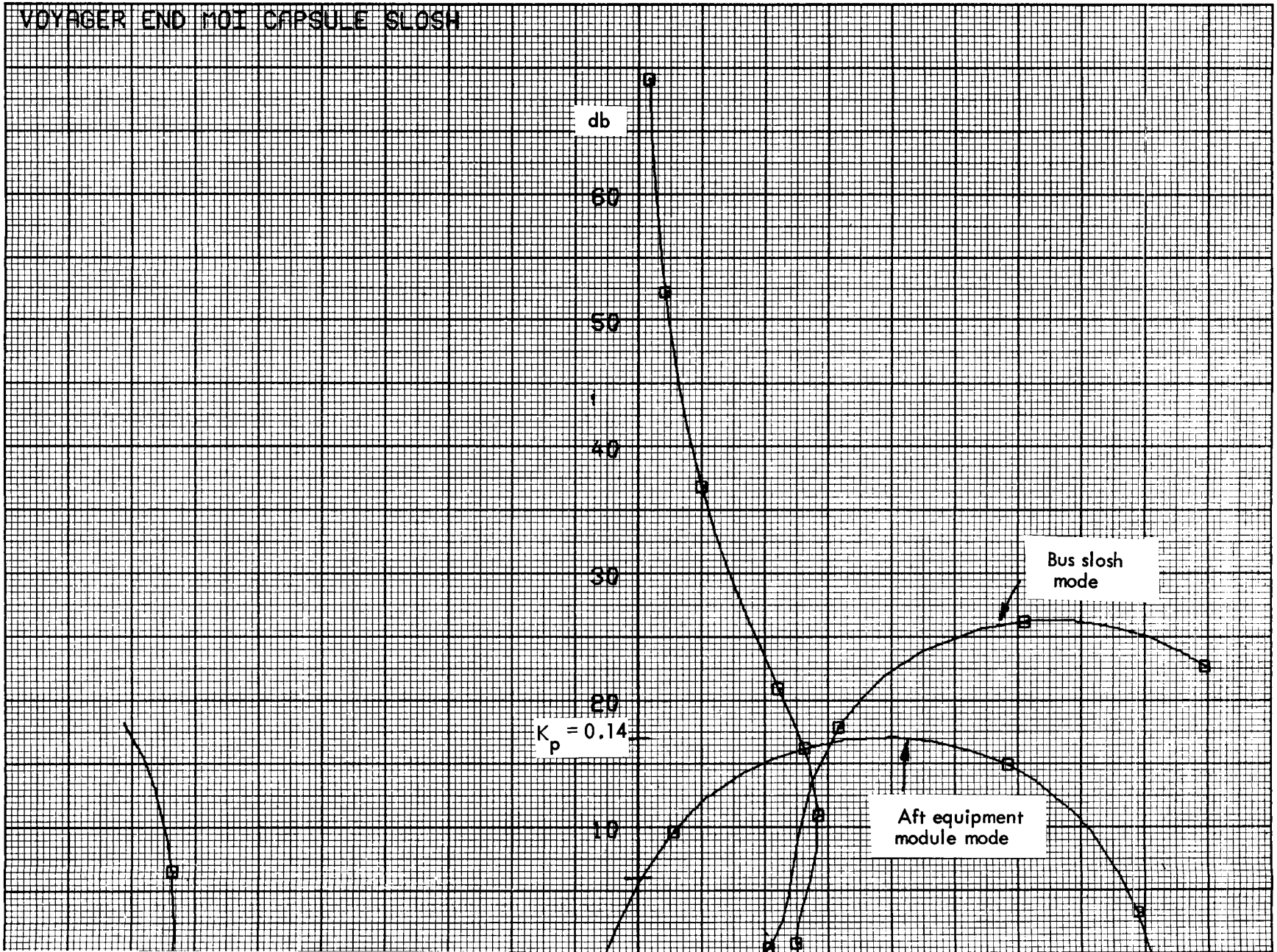
VOYAGER END MOI CAPSULE SLOSH
db
60
50
40
30
20
10
$K_p = 0.14$
Bus slosh mode
Aft equipment module mode

190

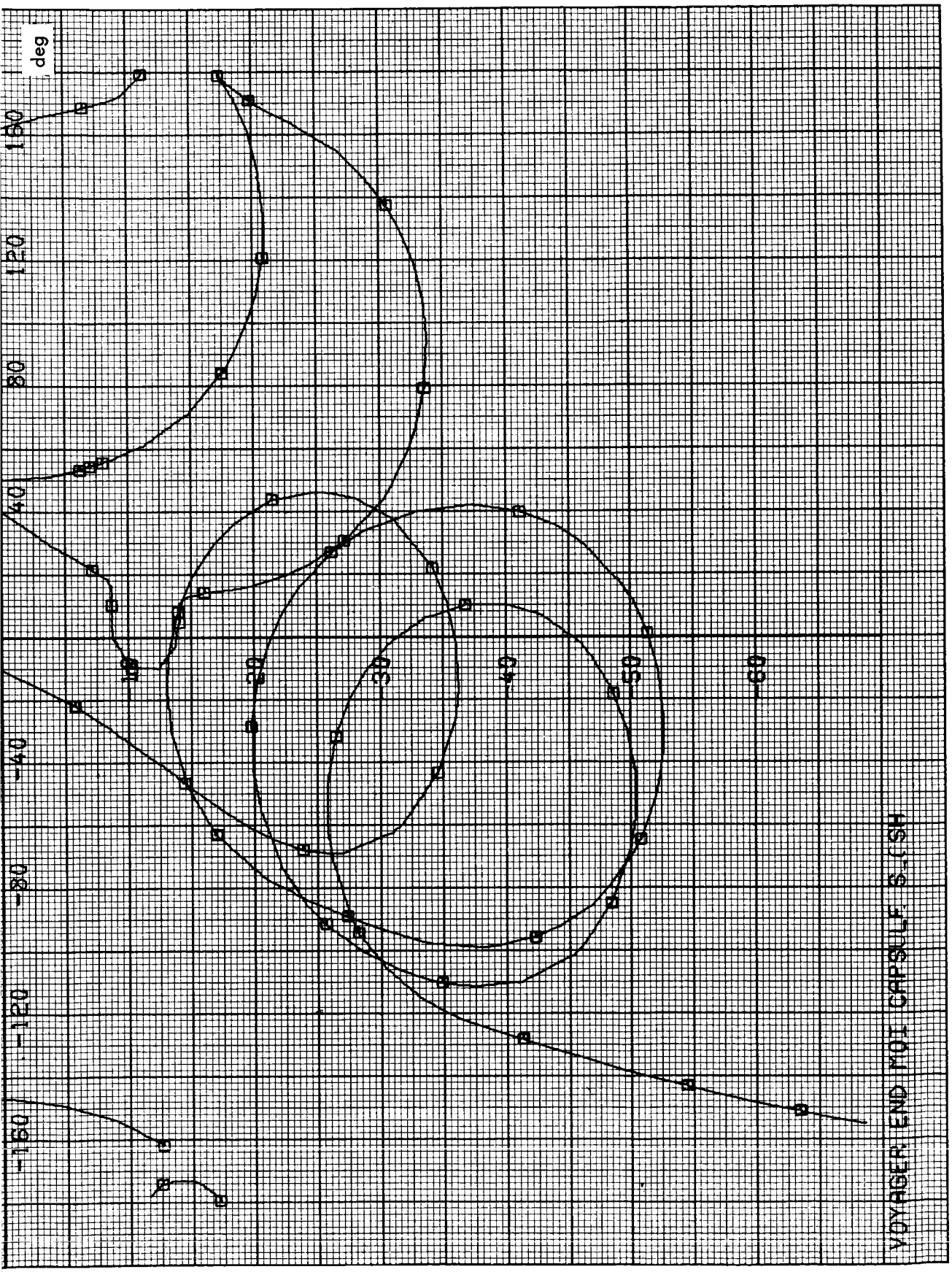

Figure 57. Gain-Phase Plot, End MOI, with Capsule

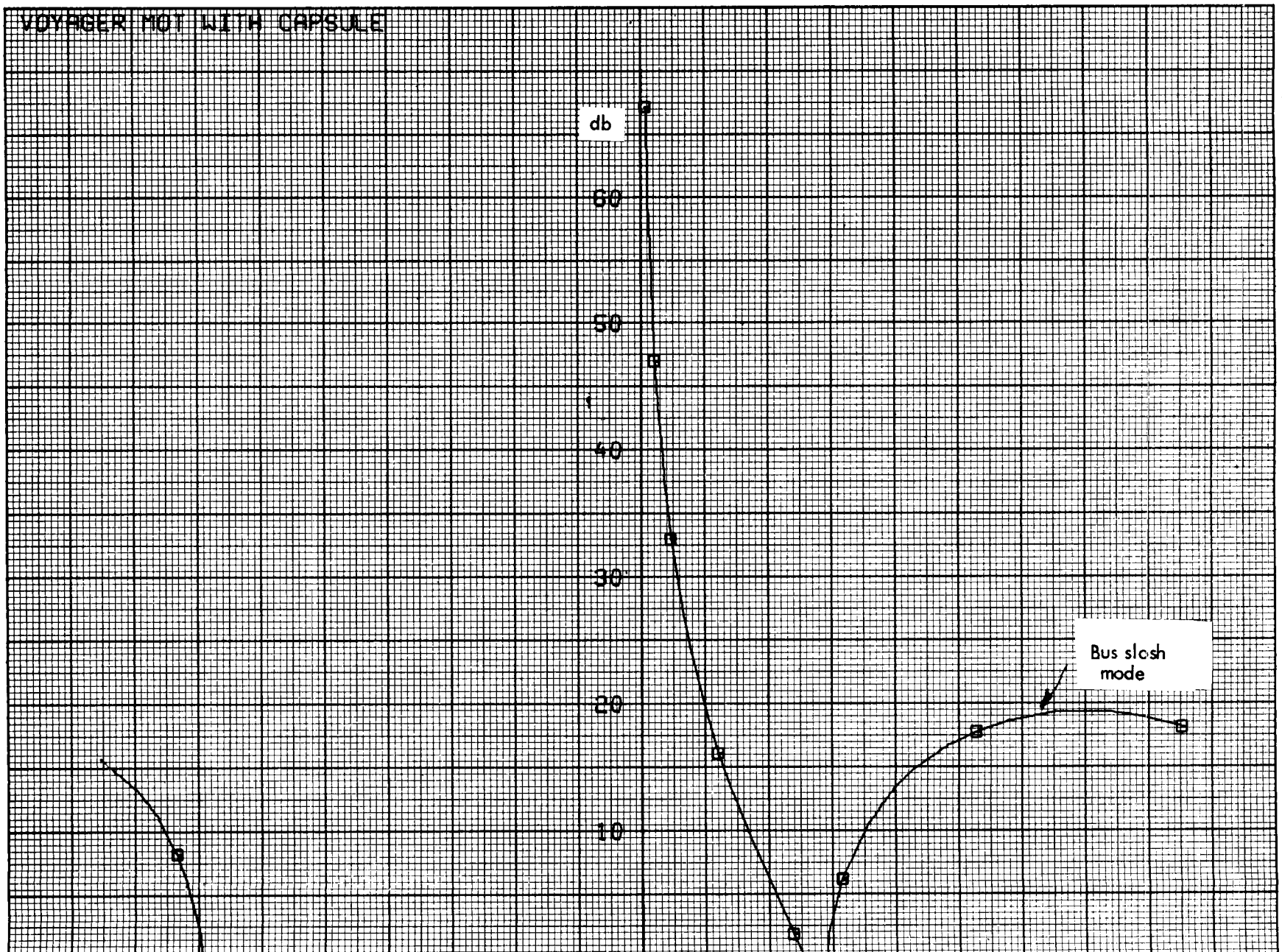
VOYAGER MOT WITH CAPSULE
db
60
50
40
30
20
10
Bus slosh mode

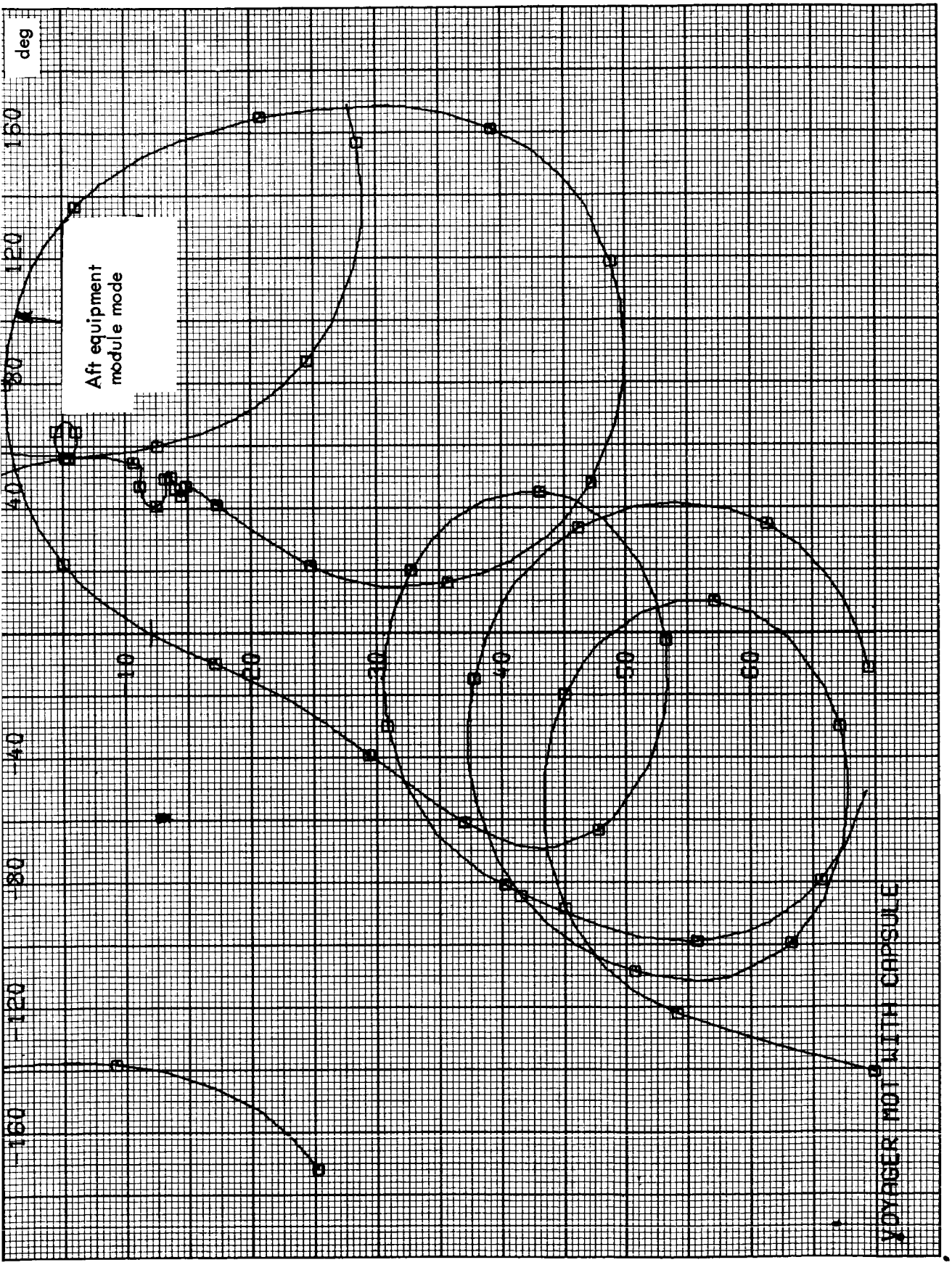

Figure 58. Gain-Phase Plot, MOT, with Capsule

slosh mode loops are larger due to the higher energy vehicle state, and both of the capsule slosh mode loops are clearly visible. Because of the higher thrust of the system, the desirable control system position gain is reduced 6 db from unity or $K_p = 0.5$.

The stability margins at the end of MOI are shown in Figure 57. The effects of the aft equipment module resonance is shown to be more pronounced than at the start of MOI. To obtain the same stability margins that were present in the previous two figures, a reduction in position gain to $K_p = 0.14$ is indicated. Such a reduction, however, is not altogether desirable since the consequences of employing low gains manifests itself in larger thrust vector pointing errors. The electronic or mechanical filtering of this mode to achieve the desired stability margins is preferable to the selection of such a low position gain. Several unsuccessful attempts were made to find a suitable electronic filter design; however, it was discovered that the addition of solar array struts to stiffen the linkage between the aft equipment module and the spacecraft bus could be accomplished quite readily. The addition of these struts could easily increase the stiffness by a factor of 6, hence the modal frequency could be increased by approximately the square root of 6 which would place it approximately at the high-gain antenna modal frequency. The results of this addition are described in Section 3.6.

Figure 58 shows the stability margins for the Mars orbit trim phase before capsule separation. A gain of approximately unity is indicated to be desirable due to the presence of the aft equipment module mode.

3.3 STABILITY WITH CAPSULE OFF

There remains a possibility that a Mars orbit trim firing may occur after the landing capsule has been ejected; therefore, the gain-phase plot shown in Figure 62 can be considered pertinent to the nominal mission. However, the three cases represented by Figure 59 through 61 are abort or contingency cases in which the landing capsule is ejected or is not included in the mission.

The absence of the capsule results in an aftward shift of the vehicle center of gravity. The previously stable bus slosh modes become

unstable as a result, requiring increased damping to produce stability. The amount of damping required is discussed in Section 3.4 The absence of the capsule slosh mode and bending mode is apparent in the gain phase plots.

3.4 BUS PROPELLANT SLOSH DAMPING

In the previous discussion, unstable bus slosh modes were shown. If it is desirable to stabilize these modes, the addition of damping aids such as baffles or screens is required. These devices generally do not remove the unstable condition but aid in limiting the propellant slosh limit cycle amplitudes. However, if a screen is used with a mesh so dense as to be more solid than porous, it is conceivable that the tank geometry would be altered sufficiently to change the slosh frequency, perhaps even to remove the unstable slosh modes.

The use of annular ring baffles as commonly used in boost vehicles results in a propellant slosh limit cycle since propellant motion is required to obtain the dissipative effects. Therefore, regardless of the size of the baffle, some propellant motion will exist for an unstable mode.

The larger the baffle, of course, the smaller the slosh amplitude will be. If the slosh oscillation is sustained for any length of time and if the pitch and yaw control systems are similar in design, the pitch slosh oscillations will become quadrature phase-locked with the yaw slosh oscillations due to the natural tendency of the slosh oscillation nodal line to rotate when driven near its resonant frequency. With this occurrence, rotation of the fluid particles results. The rotary fluid motion decreases the effectiveness of the baffles, thereby further increasing the slosh amplitude. To overcome this problem, vertical baffles are often used with annular baffles to dampen fluid rotation. One of the important consequences of the fluid rotation is that the rotary fluid momentum is imparted to the vehicle roll control system either through impingement upon the vertical baffles or through drainage into the propellant supply lines. In either case, additional roll control propellant requirements would result.

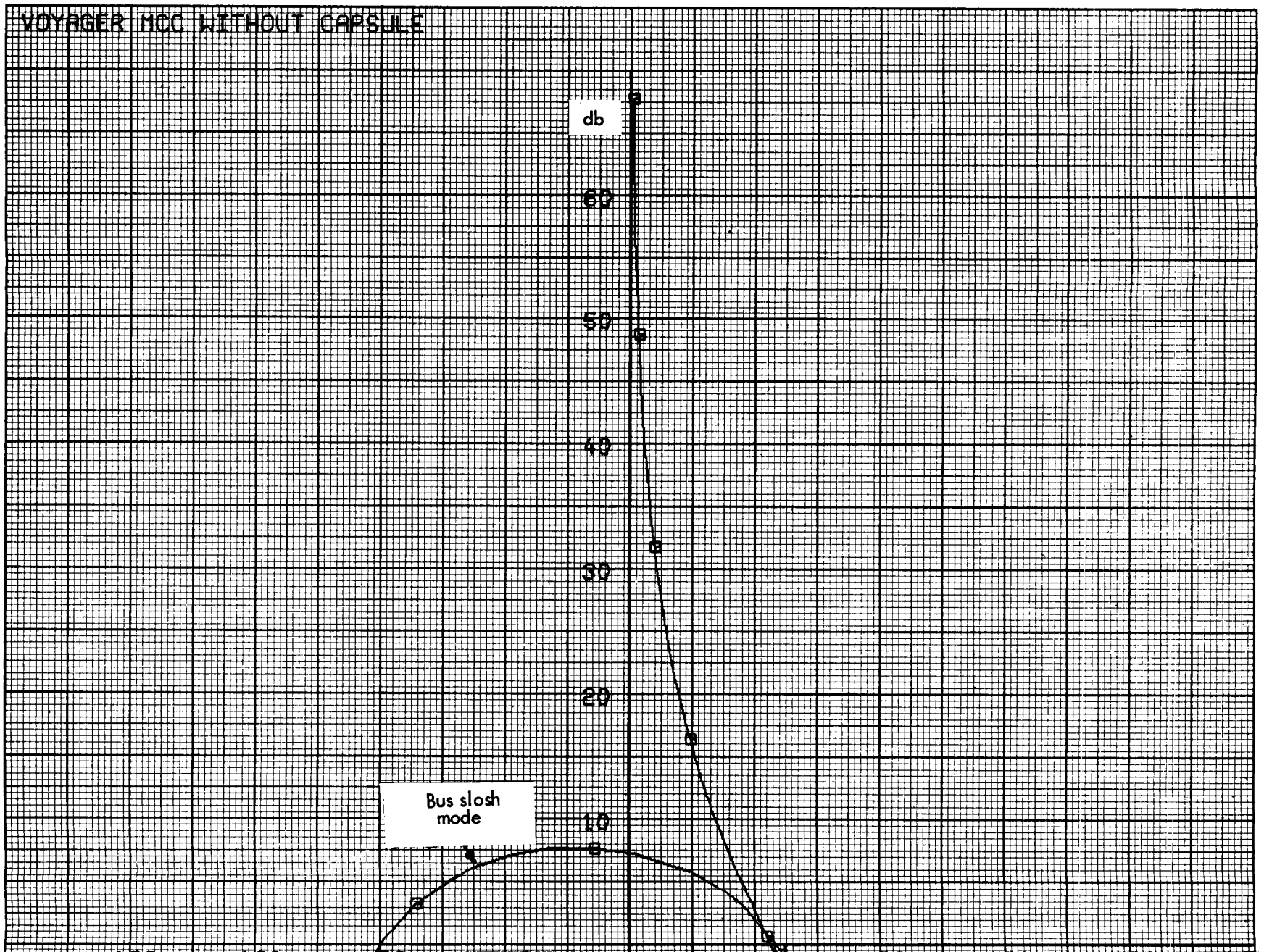
VOYAGER MCC WITHOUT CAPSULE
db
60
50
40
30
20
10
0
Bus slosh mode

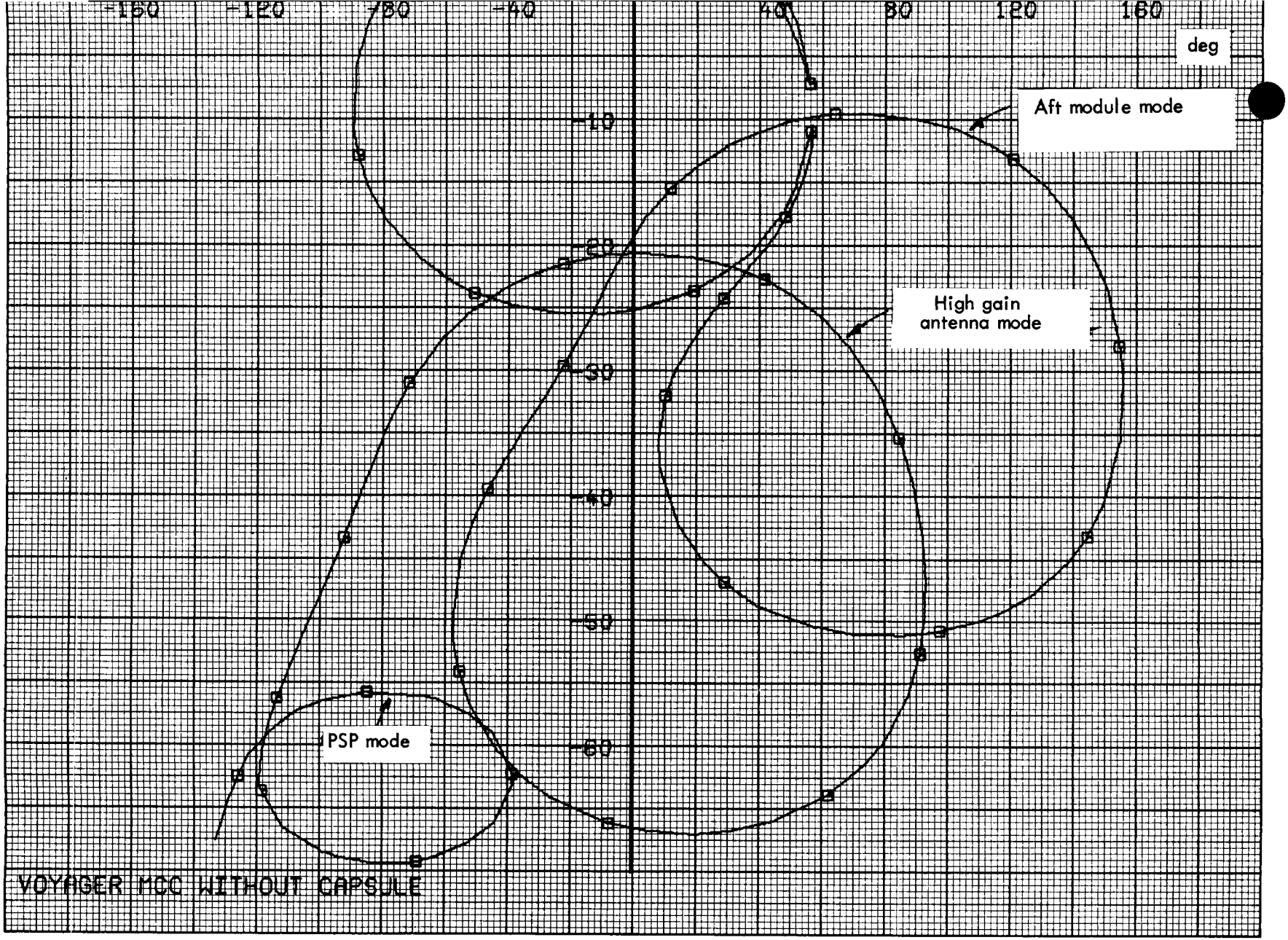

Figure 59. Gain-Phase Plot, MCC, without Capsule

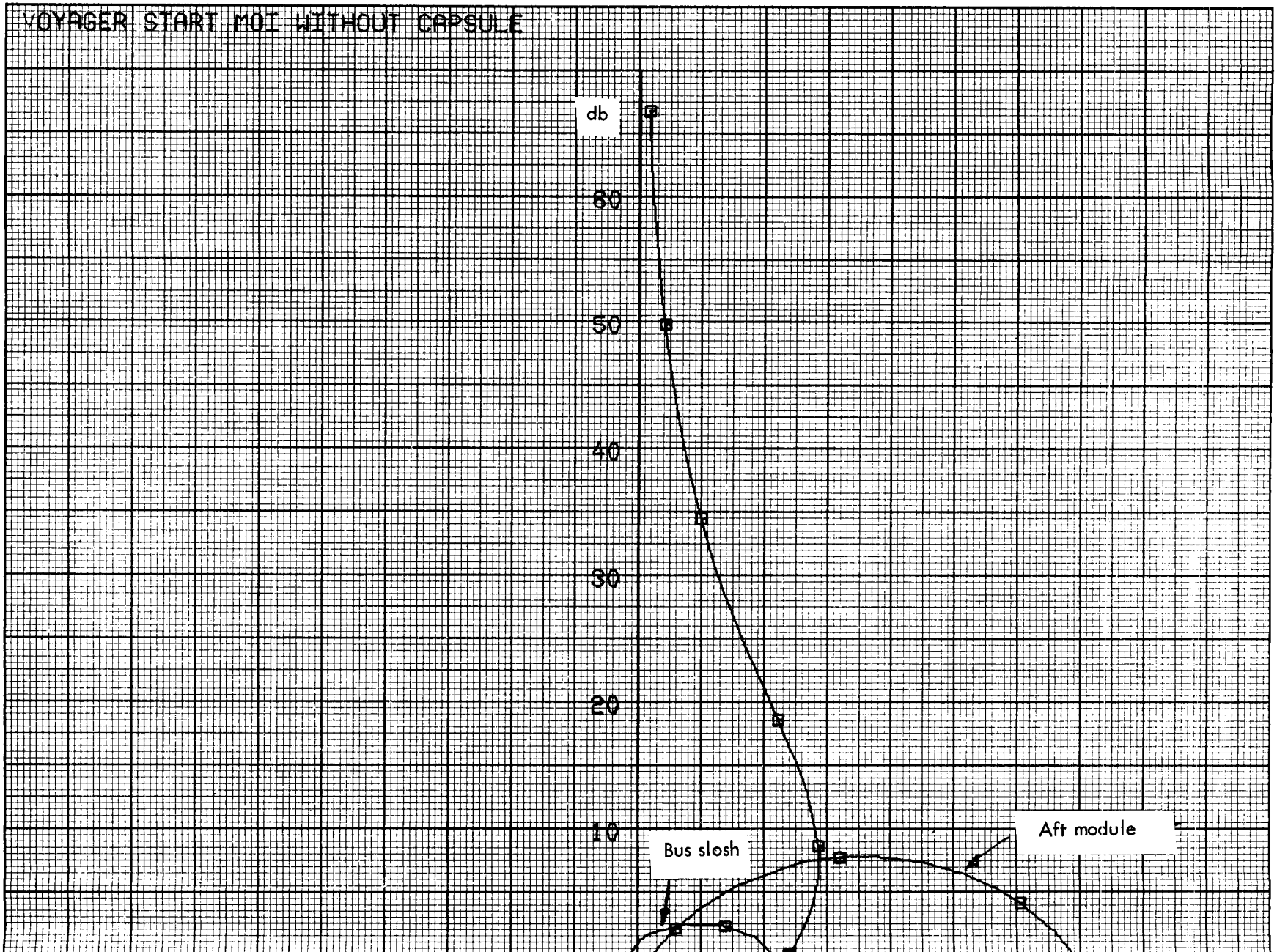
VOYAGER START MOI WITHOUT CAPSULE
db
60
50
40
30
20
10
Bus slosh
Aft module

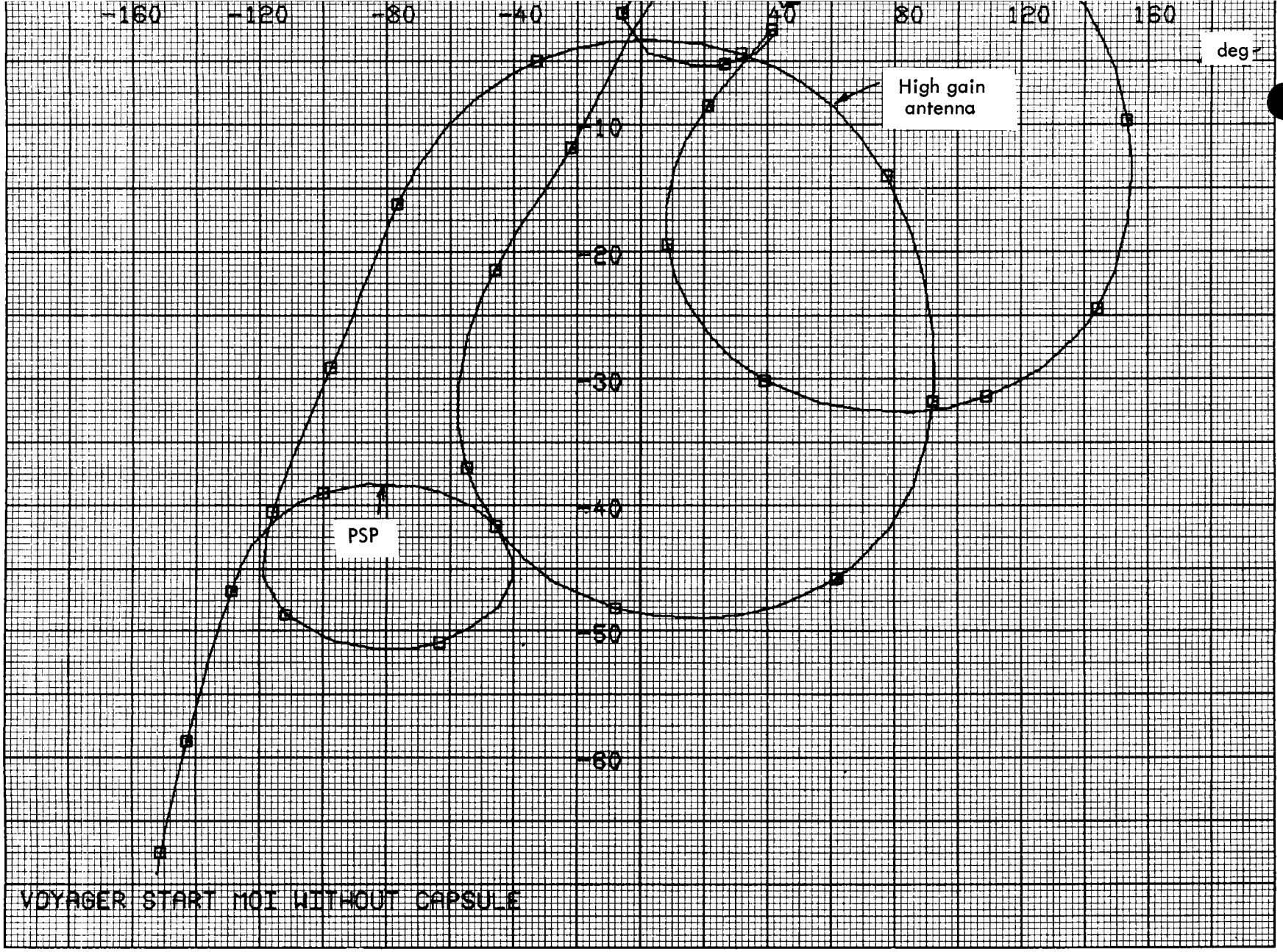

Figure 60. Gain-Phase Plot, Start MOI, without Capsule

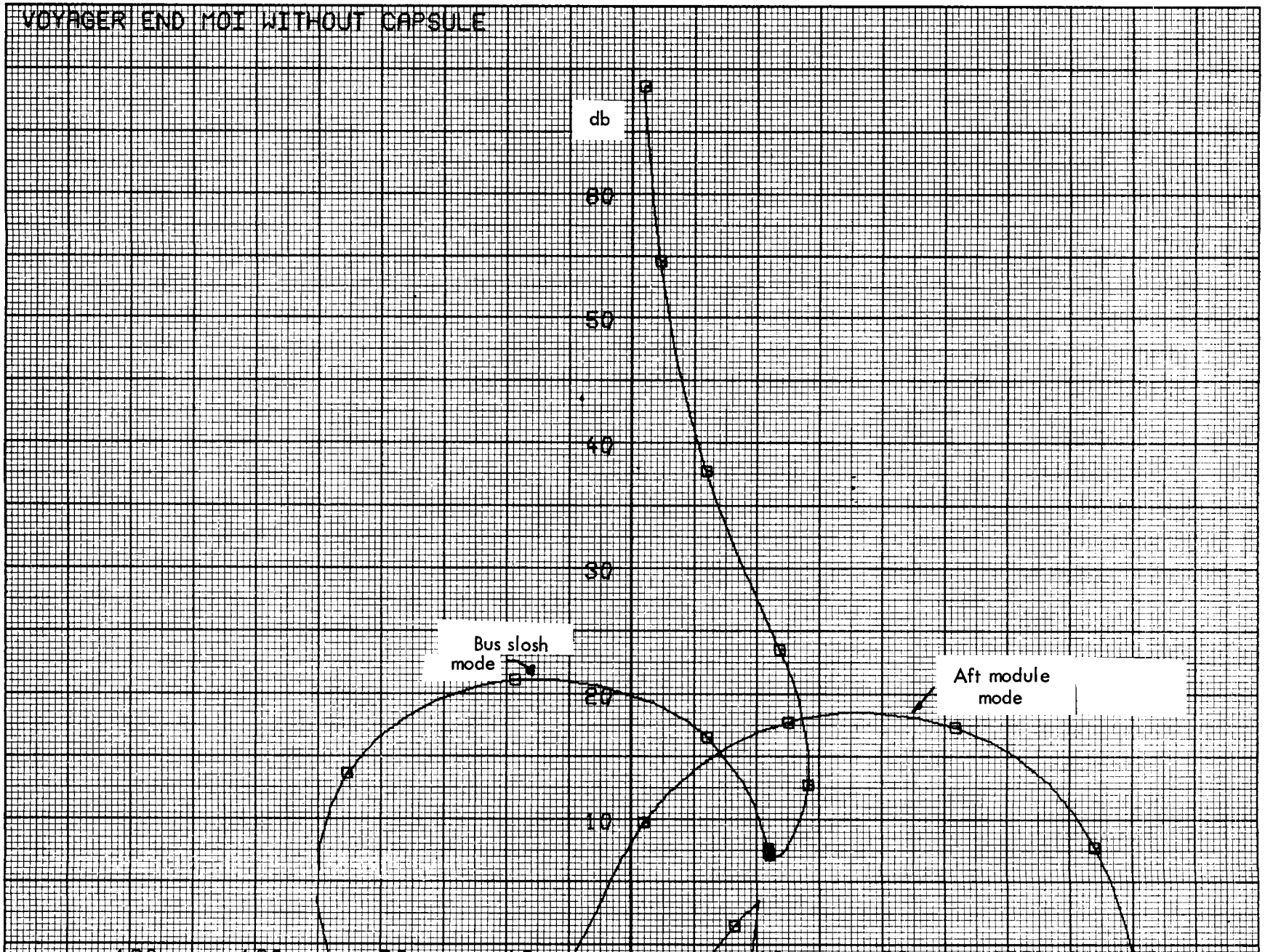
VOYAGER END MOI WITHOUT CAPSULE
db
60
50
40
30
20
10
Bus slosh mode
Aft module mode

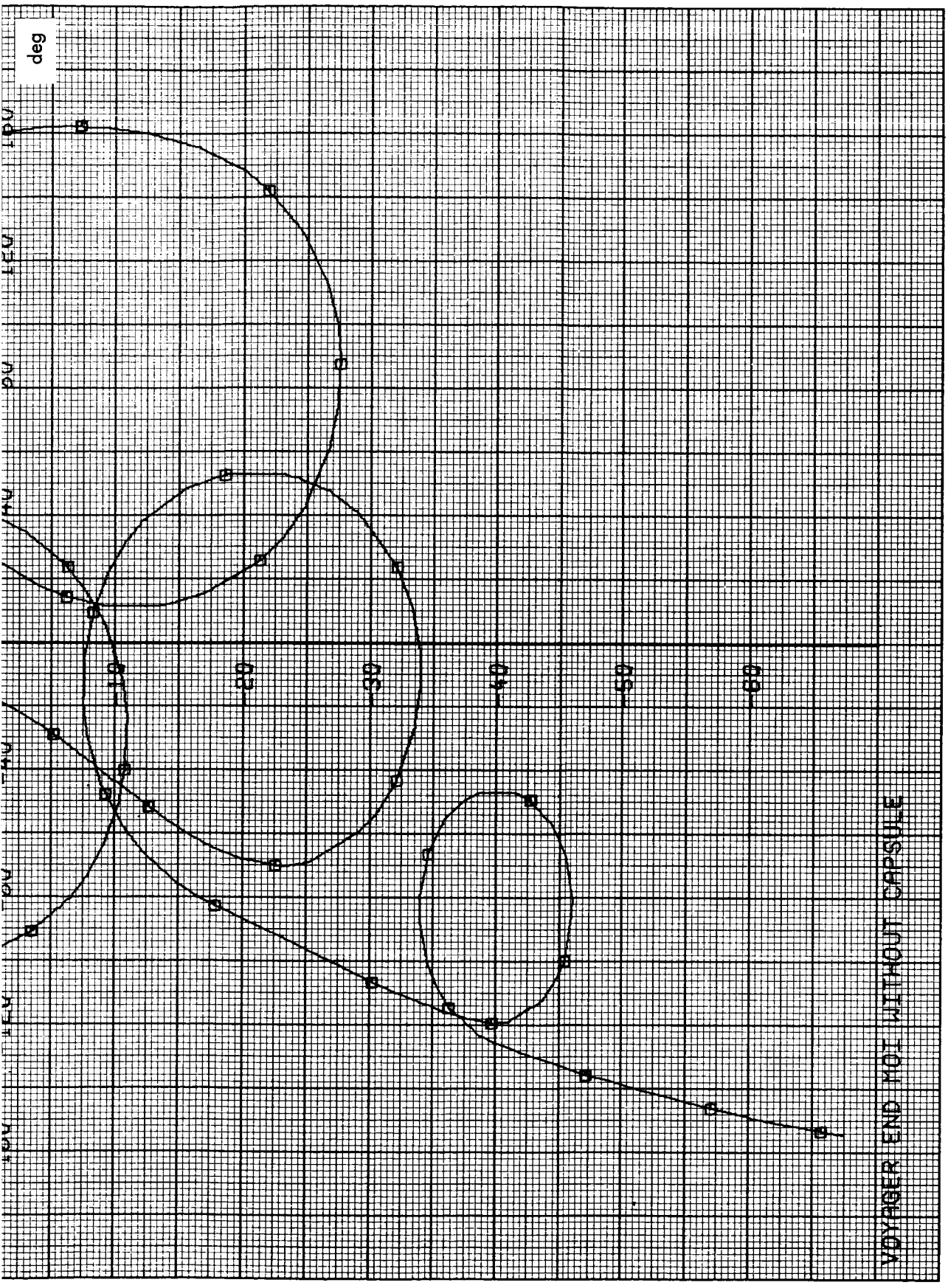

Figure 61. Gain-Phase Plot, End MOI, without Capsule

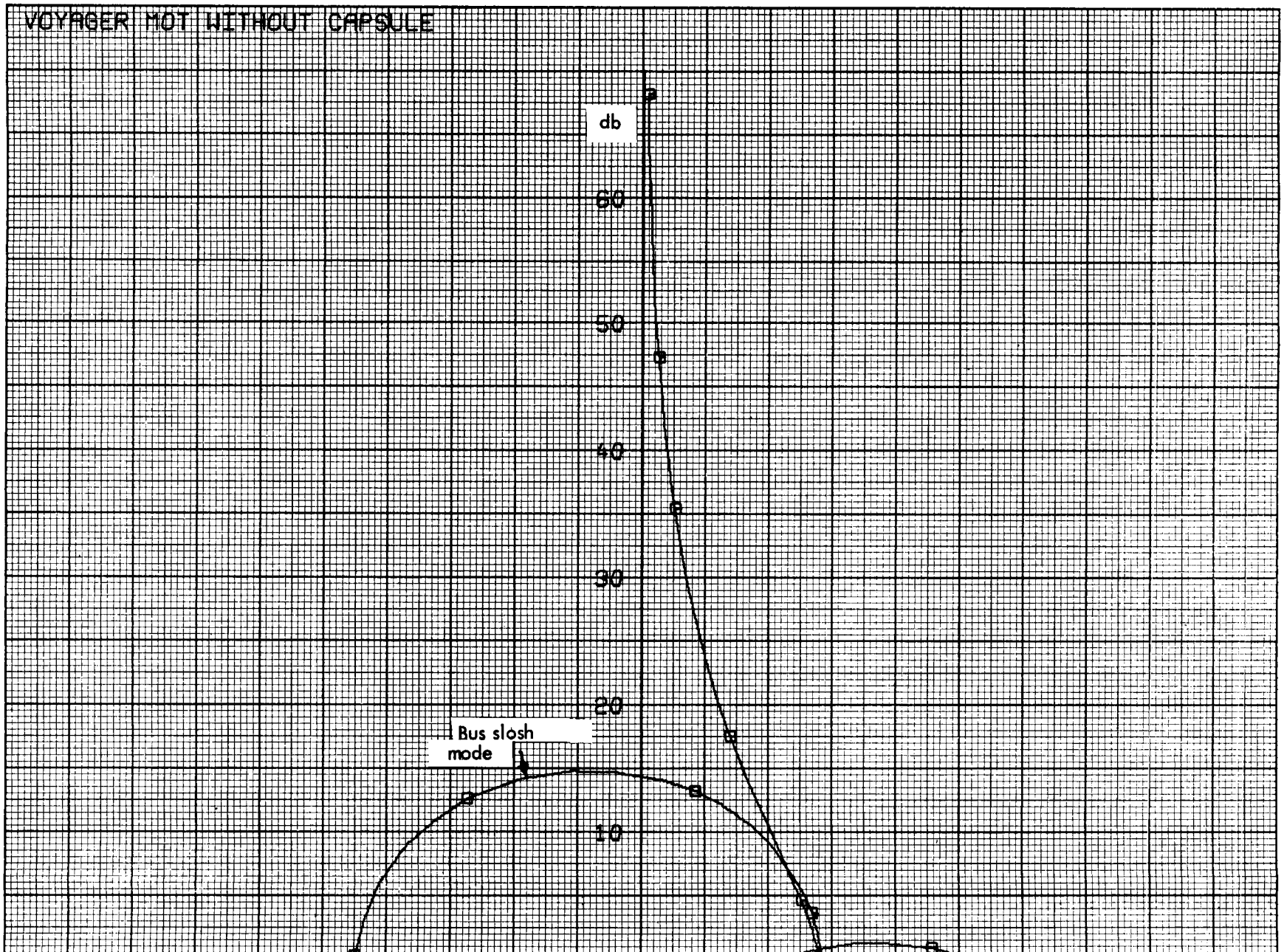
VOYAGER MOT WITHOUT CAPSULE
db
60
50
40
30
20
10
Bus slosh mode

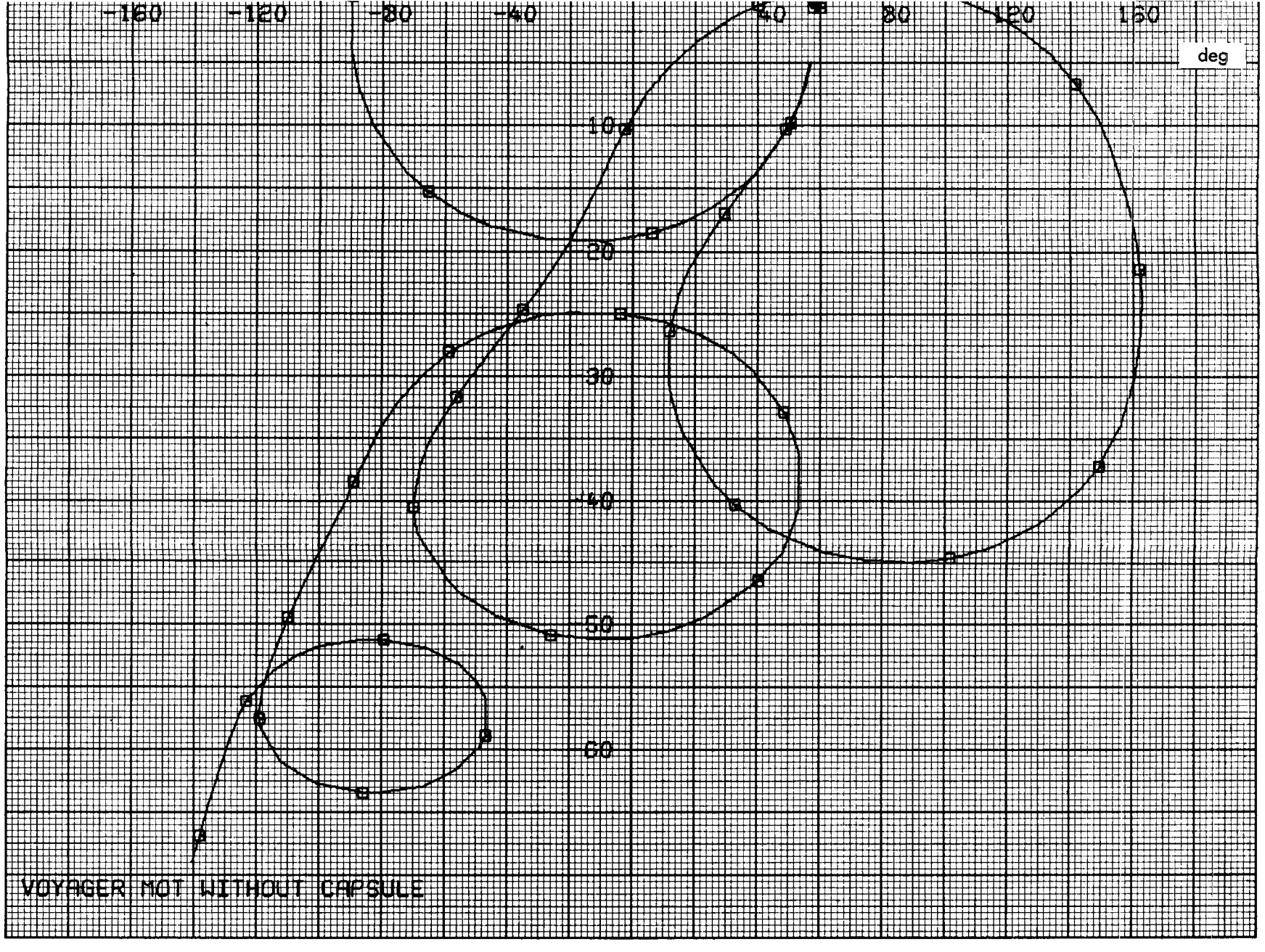

Figure 62. Gain-Phase Plot, MOT, without Capsule

3.4.1 Mars Orbit Insertion

The unstable slosh case at the end of MOI was selected to determine the amount of damping required to stabilize this mode. Figures 63 through 65 show three values of damping applied to the slosh mode. The nominal damping employed was 0.1 percent, corresponding to damping expected from smooth wall cylindrical tanks. Figure 65 shows that a damping of 0.8 percent will just produce (neutral) stability. With the knowledge of the quiescent fluid level above an annular ring baffle and the damping required to produce neutral stability, application of standard baffle equations will determine the propellant slosh limit cycle amplitude as a function of baffle width.

3.4.2 Mars Orbit Trim

Figures 66 and 67 for the Mars orbit trim phase show that a damping value approximately six times nominal or 0.6 percent is required to produce neutral slosh stability. This amount of damping may exist near the bottom of the tanks since anti-geysering and drainage screens and perhaps anti-vortexing baffles are contemplated for the spacecraft design.

3.5 CAPSULE PROPELLANT SLOSH DAMPING

In the stability plots given in Section 3.2 with capsule sloshing included, the capsule slosh mode loops were shown to be smaller than the bus slosh loops because the slosh masses were less than 1/25th of those for the bus slosh modes and because a larger slosh damping value of 1 percent was employed. Because the capsule spherical bottles are to be filled such that the quiescent fluid level is in the upper dome, considerable dome damping effects are to be expected from motion of the propellants. Figure 68 shows an approximate relationship between the propellant damping factor and slosh mass displacement at different propellant loading conditions. The curves for the capsule fuel tank (20.5-inch diameter, 90 percent full) and oxidizer tank (22-inch diameter, 73 percent full) are shown in the figure. The curves were obtained from experimental slosh damping results with a hemispherical domed tank as presented in Reference 9. The results were adjusted for the propellant densities and tank radius corresponding to the capsule tanks.

BLANK PAGE

155

PRECEDING PAGE BLANK NOT FILMED.

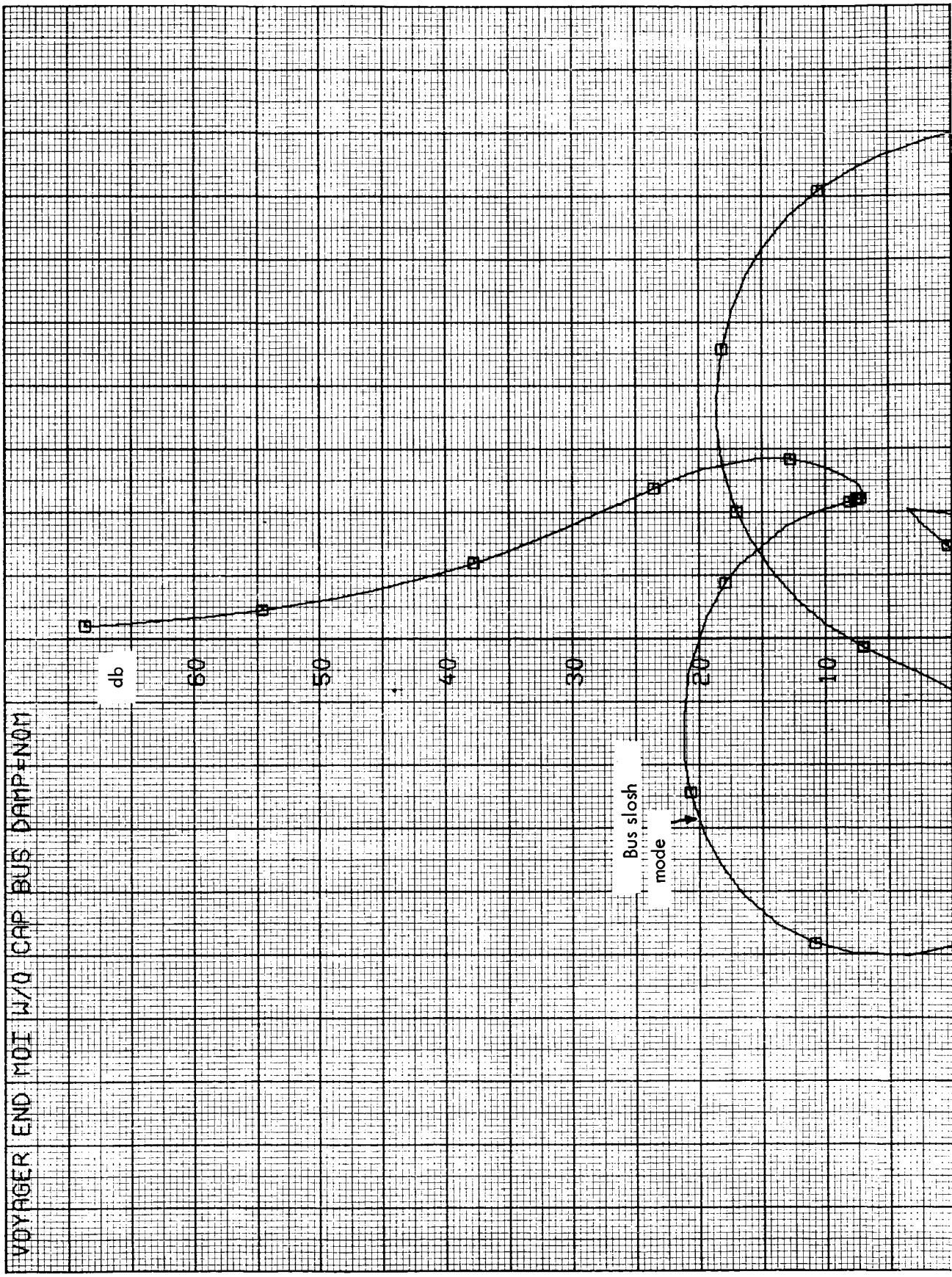

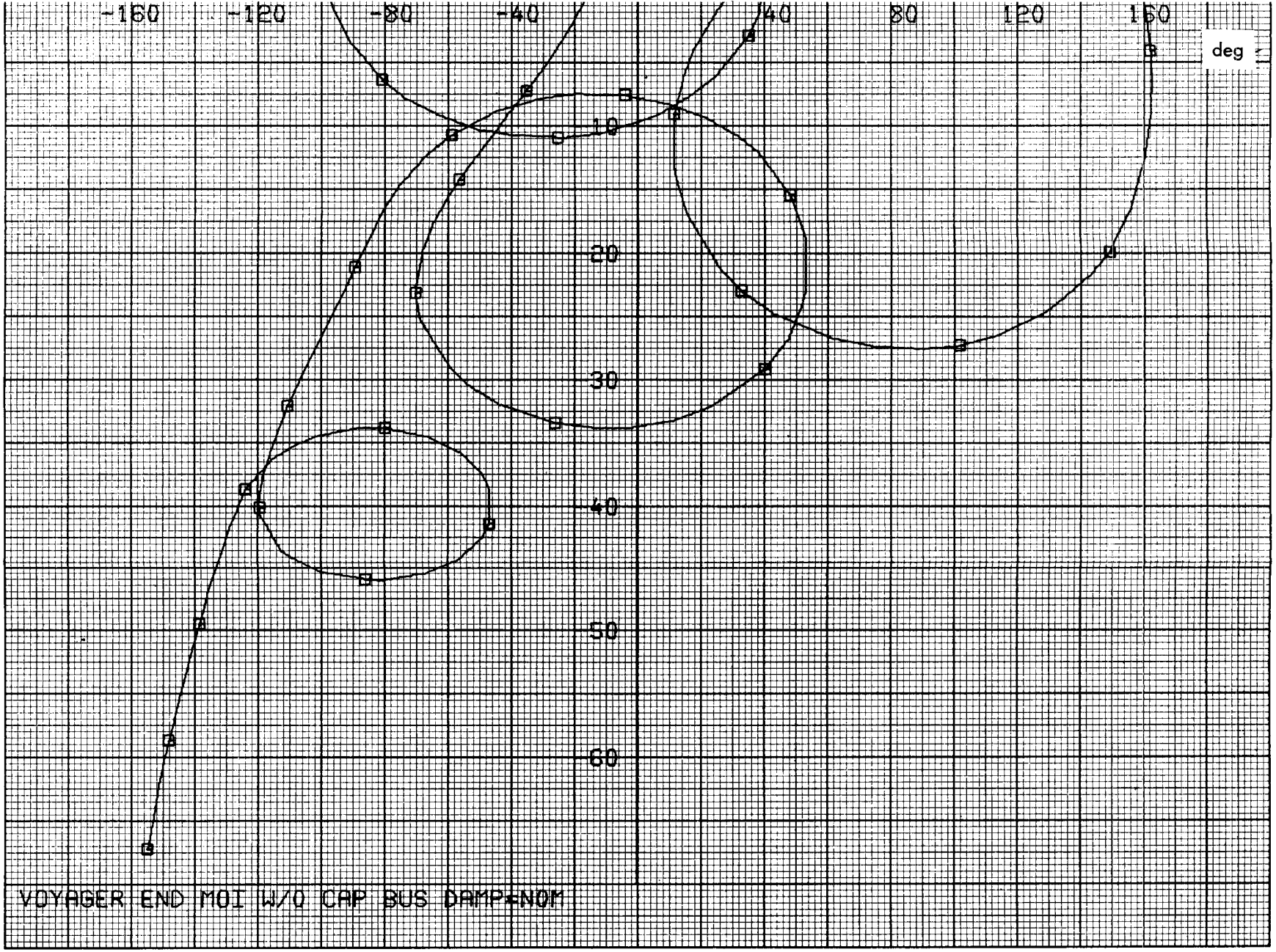

Figure 63. Gain-Phase Plot, End MOI, without Capsule, Nominal Bus Slosh Damping

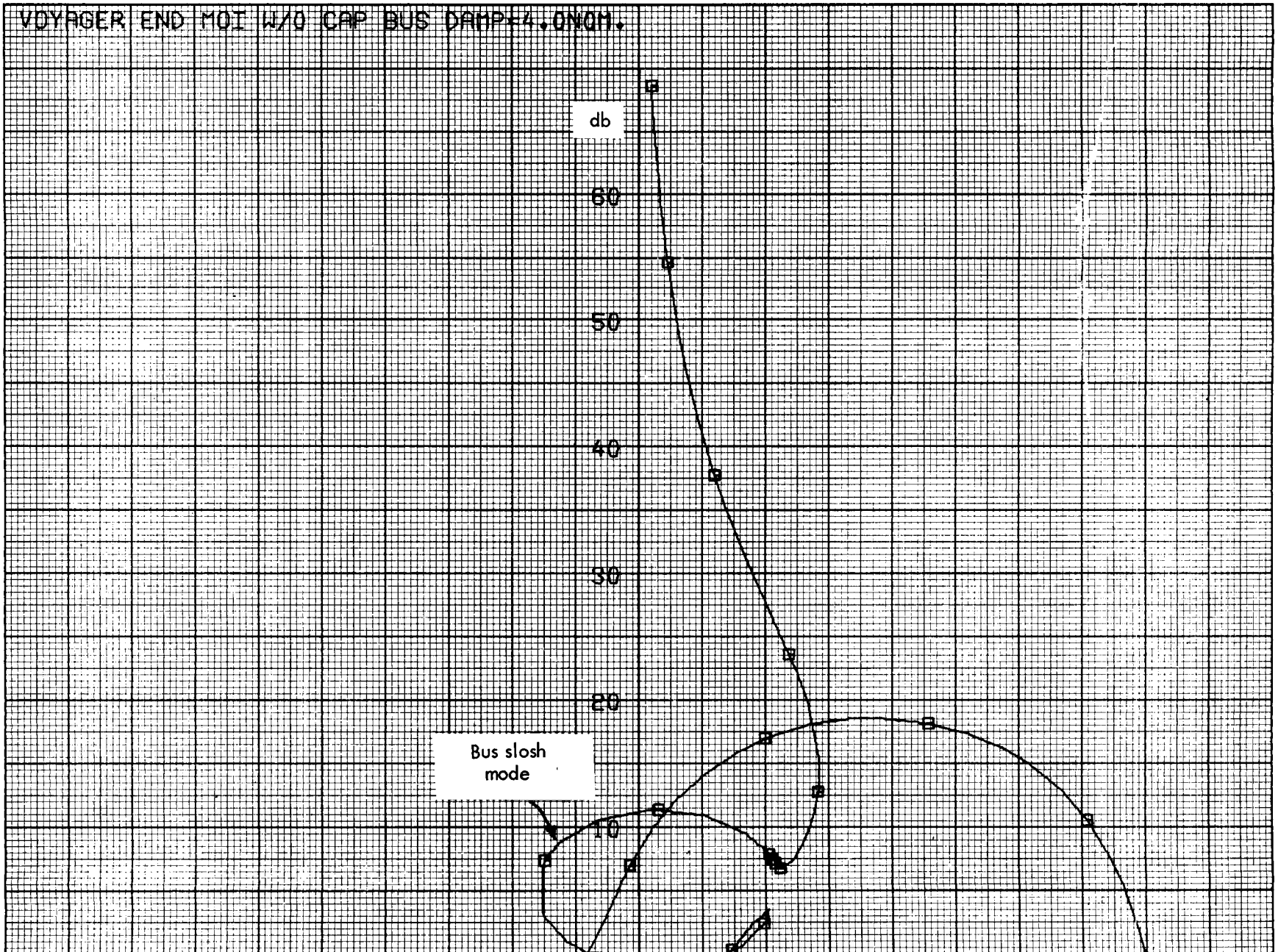
VOYAGER END MOI W/O CAP BUS DAMP=4.0NOM.
db
60
50
40
30
20
10
Bus slosh mode

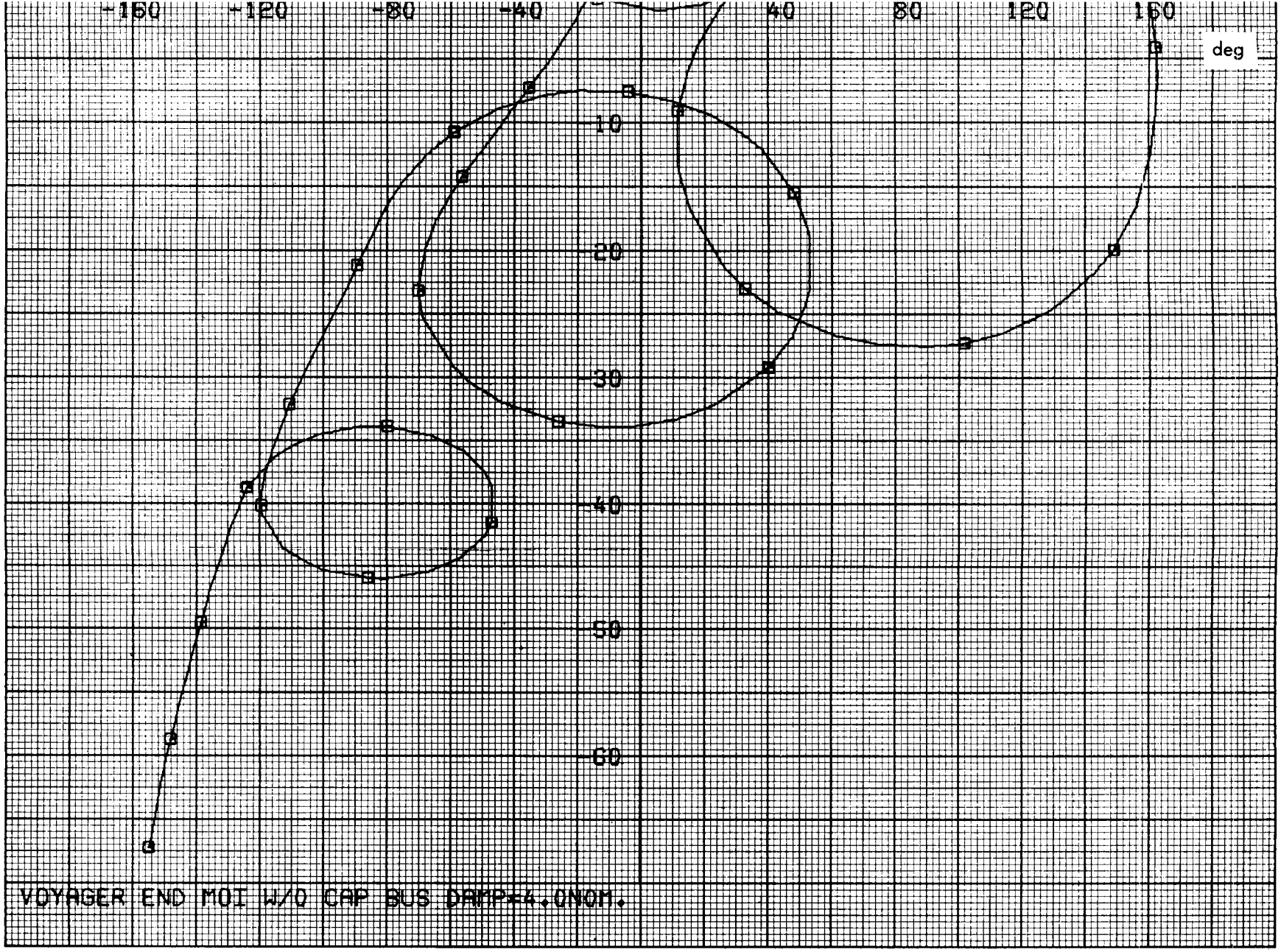

Figure 64. Gain-Phase Plot, End MOI, without Capsule, 4× Nominal Bus Slosh Damping

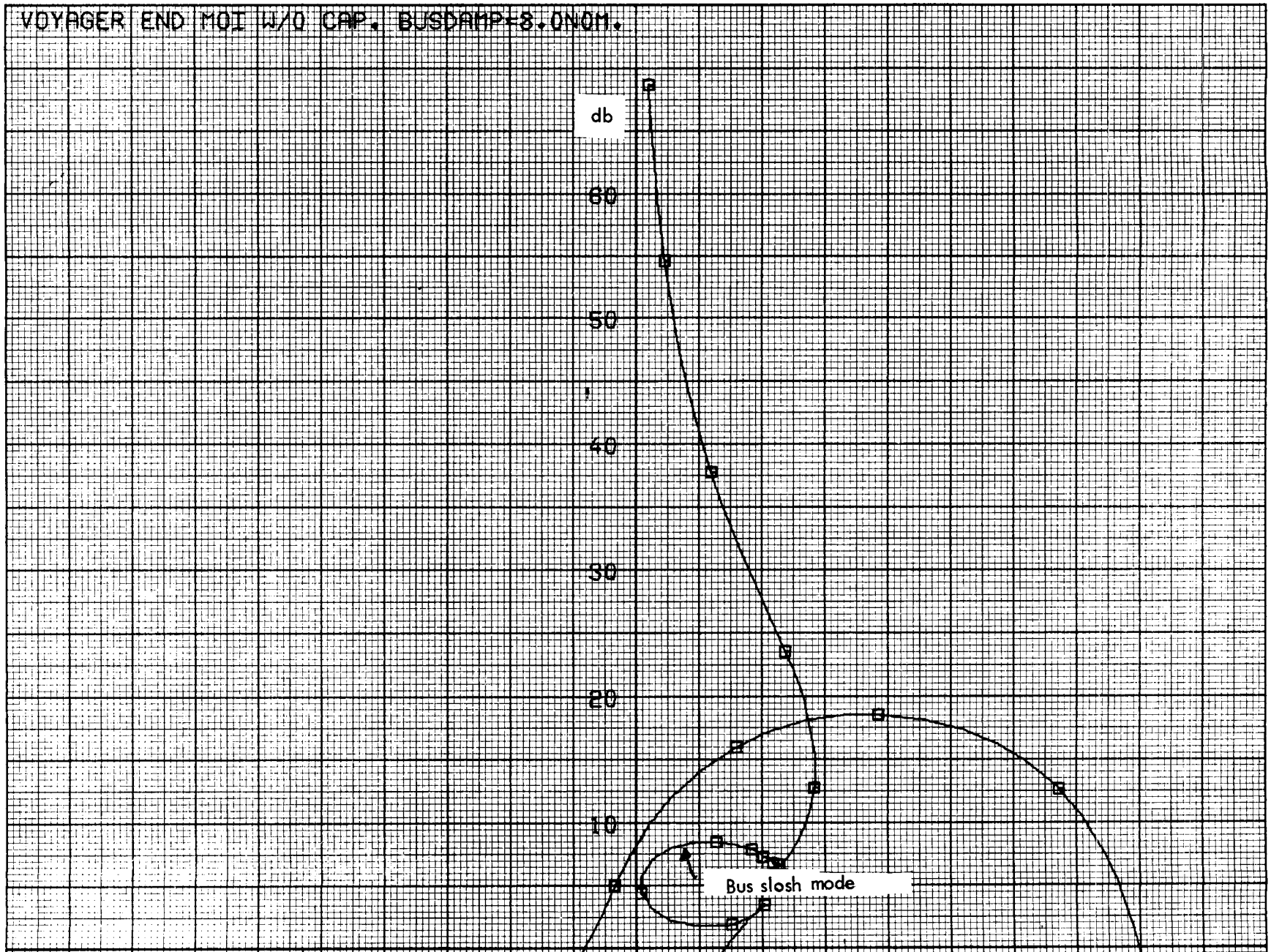
VOYAGER END MOI W/O CAP. BUSDAMP=3.0NOM.
db
60
50
40
30
20
10
Bus slosh mode

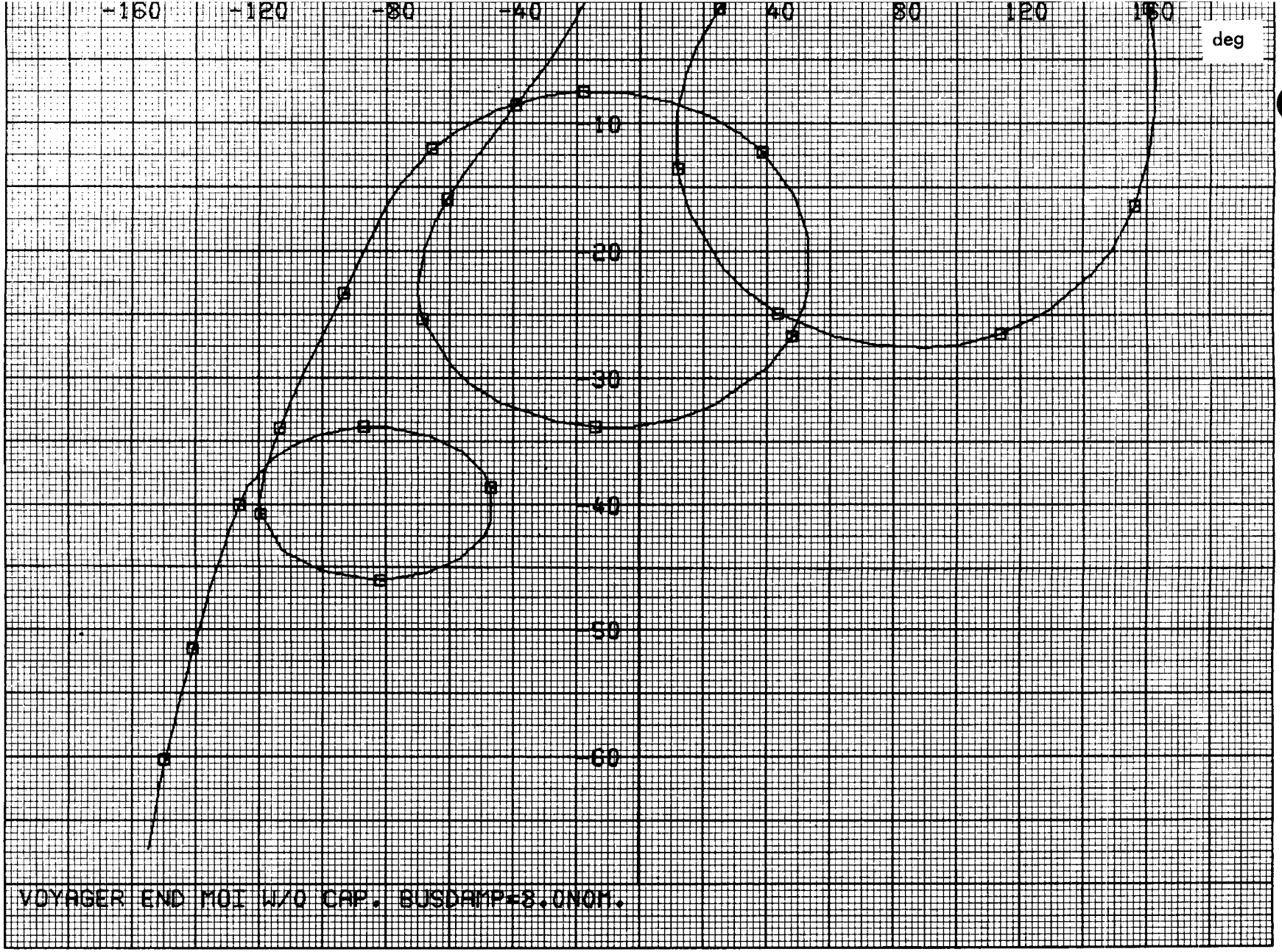

Figure 65. Gain-Phase Plot, End MOI, without Capsule, 8× Nominal Bus Slosh Damping

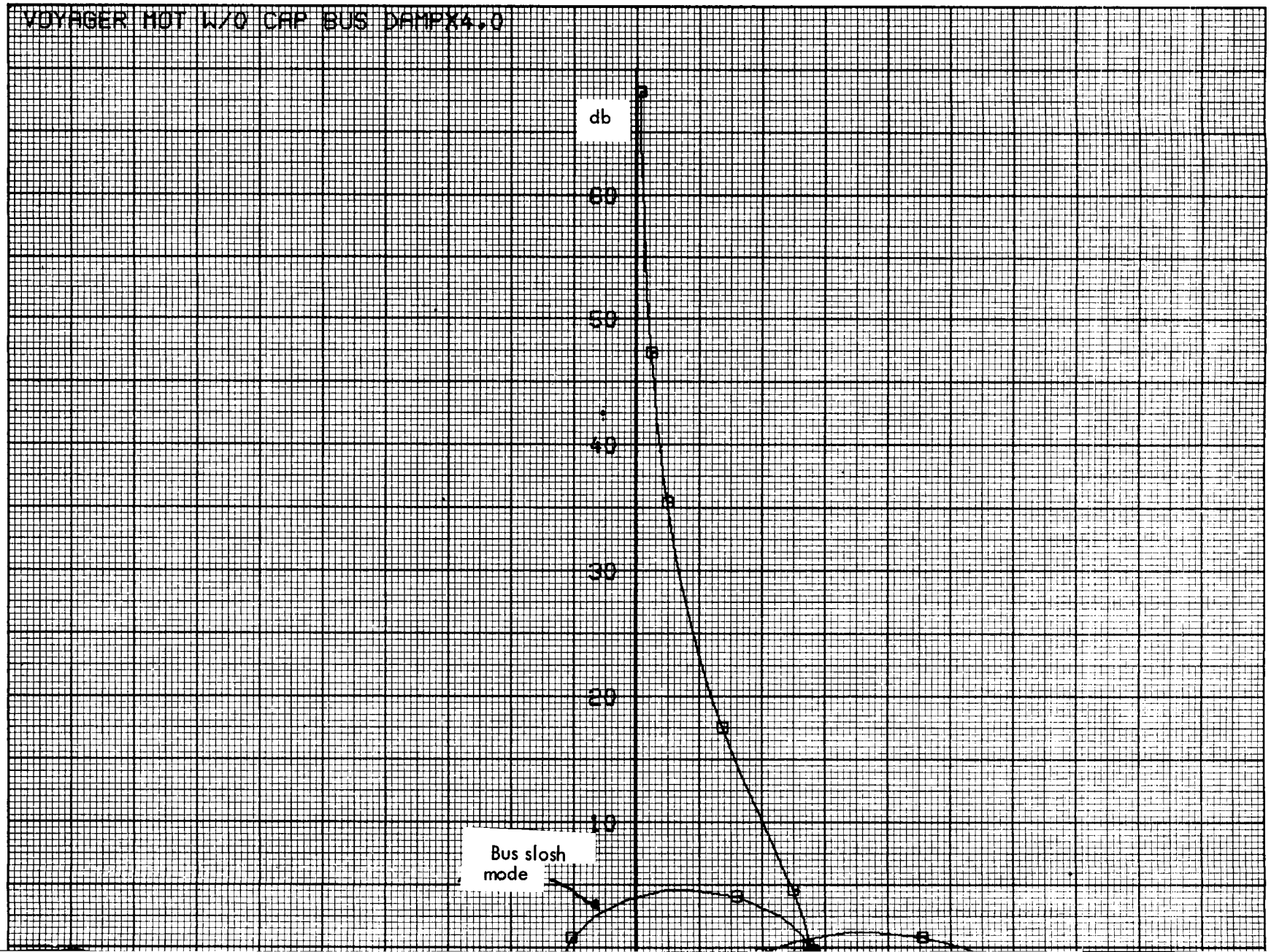
VOYAGER HOT W/O CAP BUS DAMPX4.0
db
60
50
40
30
20
10
Bus slosh mode

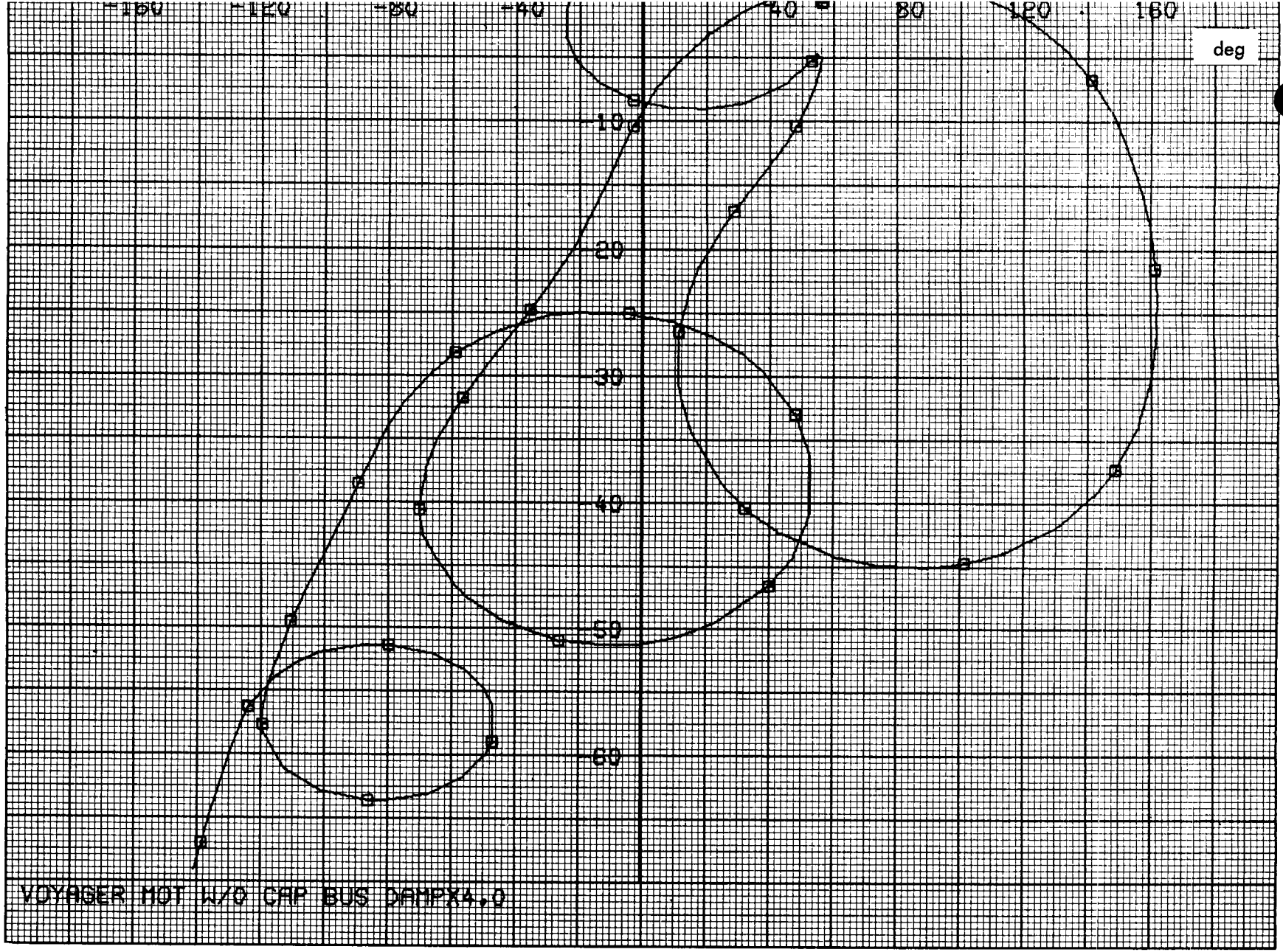

Figure 66. Gain-Phase Plot, MOT, without Capsule, 4X Nominal Bus Slosh Damping

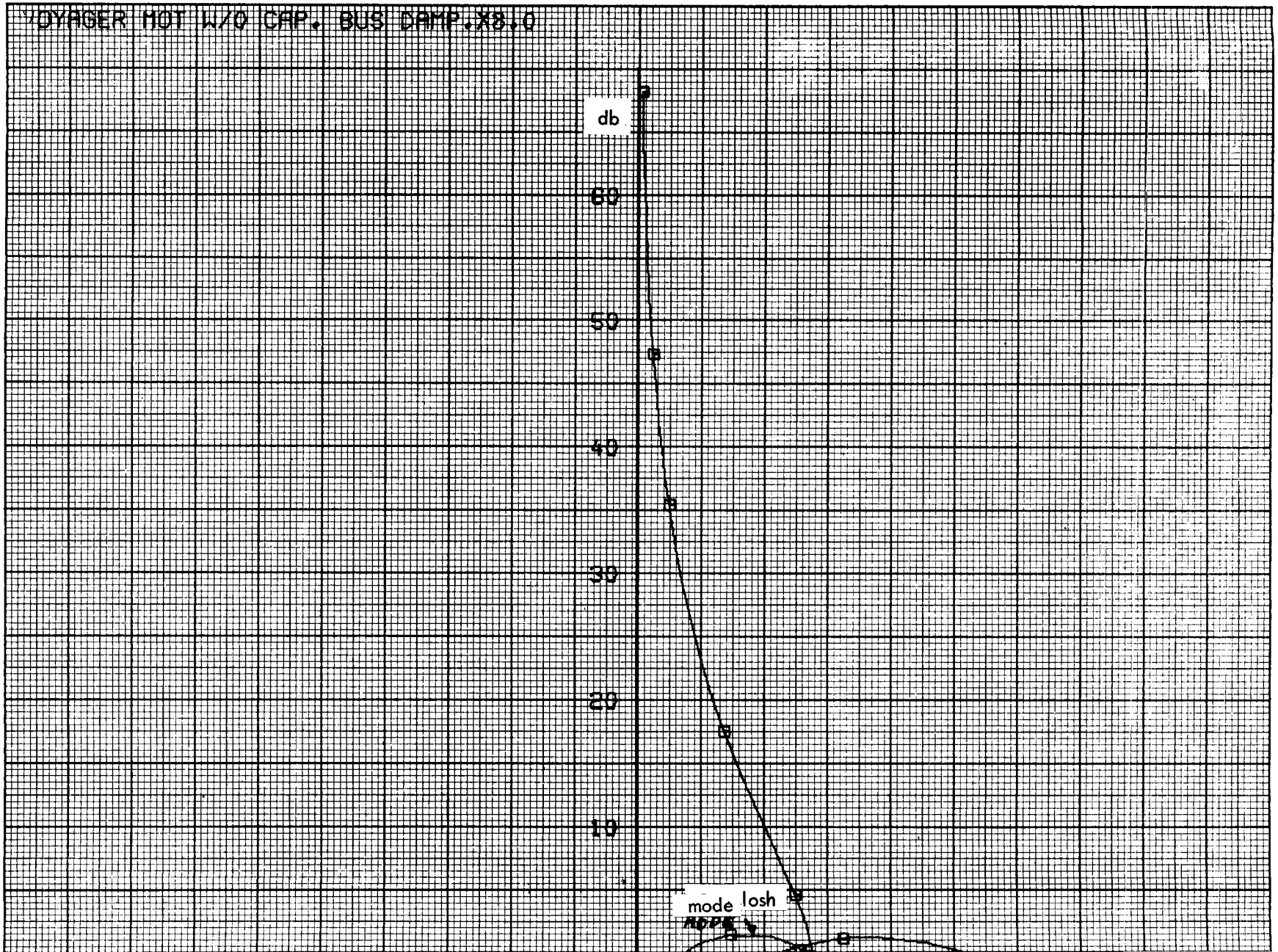
VOYAGER HOT W/O CAP. BUS CAMP.X8.0
db
60
50
40
30
20
10
mode losh
ROPE

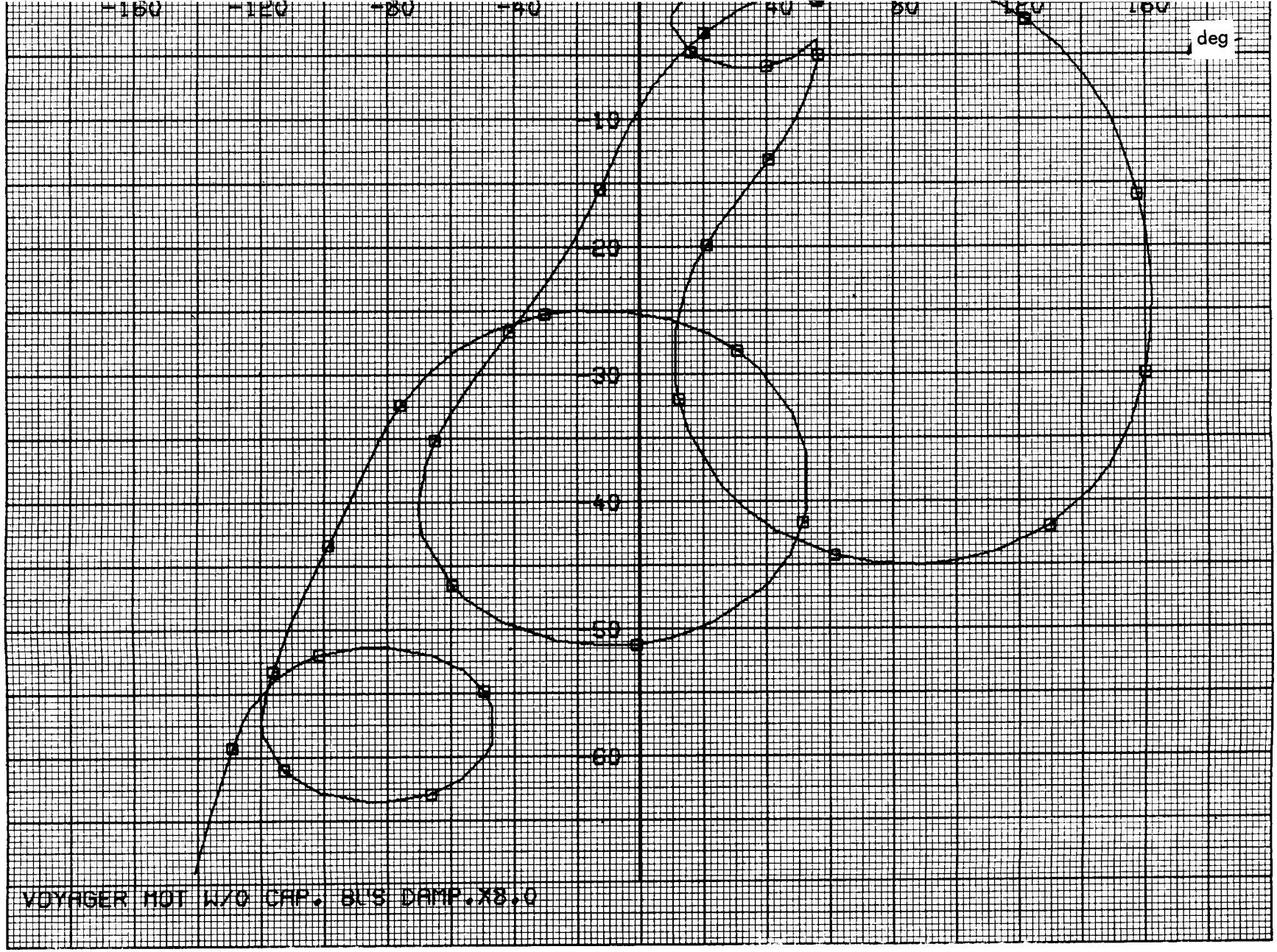

Figure 67. Gain-Phase Plot, MOT, without Capsule, 8× Nominal Bus Slosh Damping

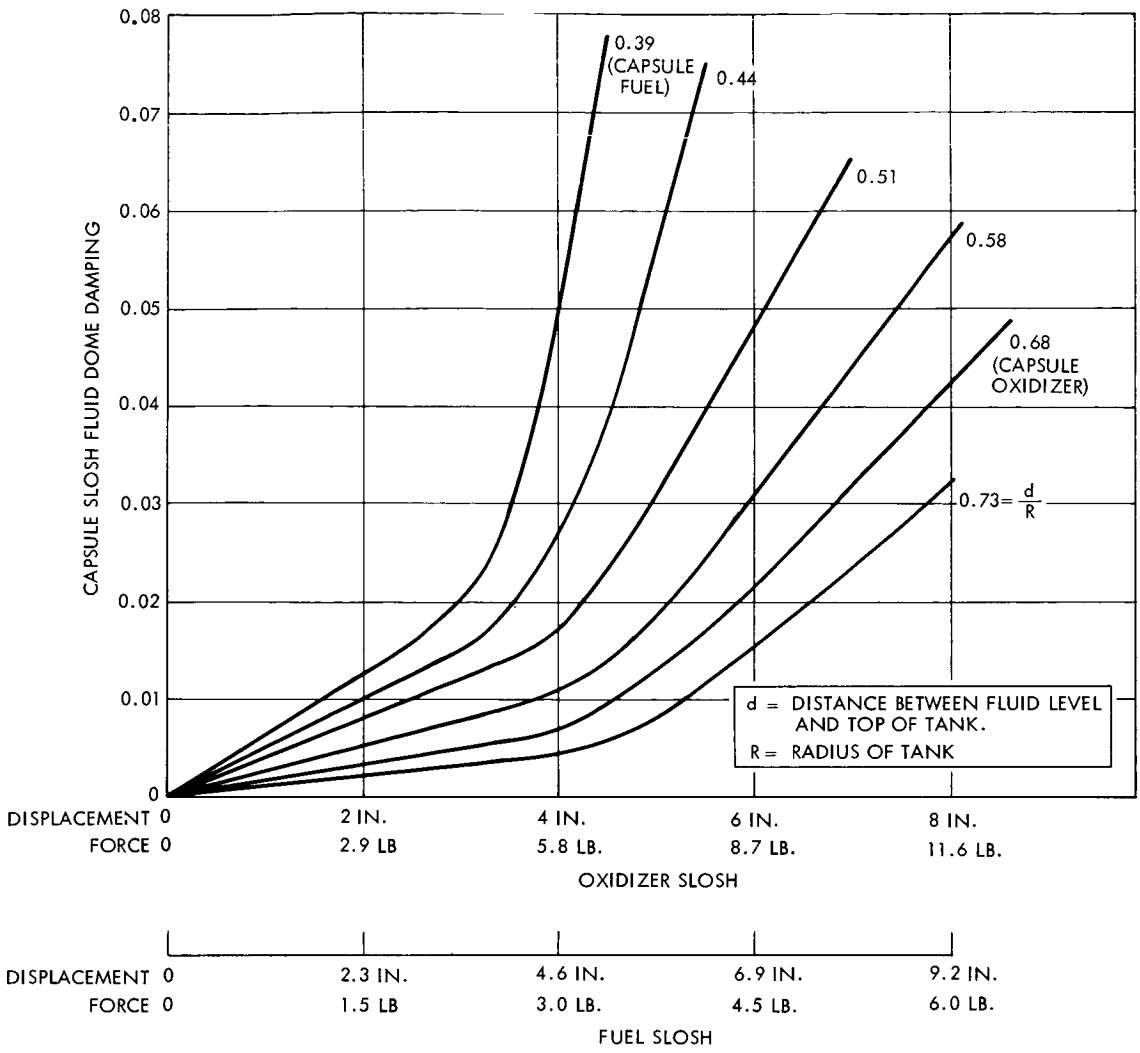

Figure 68. Slosh Dome Damping Versus Slosh Mass Displacement

The relationship between slosh mass displacements and slosh forces on the vehicle are also shown in Figure 68. For a 2-inch oxidizer slosh mass displacement, a 2.9-pound slosh force on the vehicle results. The fluid wave heights are approximately 1.6 times the slosh mass displacements for the fluid levels under consideration. The ratio of wave height to slosh mass displacement decreases as the fluid level is decreased in a spherical tank.

The necessary amount of reduction in the capsule slosh mode damping to obtain a neutrally stable limit cycle is indicated in Figures 69 to 71 for 0.5, 0.25, and 0.125 times nominal damping values.

Figure 70 shows that a damping of one-fourth of nominal or 0.0025 is required to reduce the phase margin to zero. If an operating gain of 0.5 is employed, the gain margin for this case would be 13 db. Figure 71 shows that only gain margin exists if the damping is reduced by one-eighth or a value of 0.00125. With an operating gain of 0.5, the margin is 8 db. With an operating gain of unity the margin is 2 db. Figure 68 shows that these low damping values are obtained with little propellant motion and with negligible force effects on the spacecraft; hence the capsule slosh modes do not appear to be of serious consequence.

3.6 SOLAR ARRAY STRUTS

The previous stability plots have shown that the stability margins for the solar array (or aft equipment module) mode was unsatisfactory. It was also mentioned in Section 3.2 that the addition of simple struts to stiffen the linkage between the solar array and the bus would increase the mode frequency by approximately the square root of 6. Although bending modes including the effects of added struts were not available, the stability plots of Section 3.2 were rerun by changing the modal frequency as indicated. The results are given in Figures 72 through 75 for the four mission phases. The first two cases show the solar array mode slightly lower in frequency than the high-gain antenna mode. The last two cases show the solar array mode slightly higher than the antenna mode.

The selection of one position gain for the low thrust phases and another position gain for the high thrust phase is possible due to the reduction in the solar array resonance effects. If a low thrust gain is selected to be $K_p = 4$, a high frequency gain margin of 18 db at MCC and 8 db at MOT results. If a high thrust gain of $K_p = 0.5$ is selected, the gain margin at the start of MOI is 17 db and at the end of MOI is 8 db. The phase margins at these operating points are in excess of 40 degrees.

Needless to say, the reduction in the number of gain changes is desirable for simplicity of equipment and reliability. Since the addition of the solar array struts were determined to pose no structural implementation problems, the desirability of their inclusion is indicated.

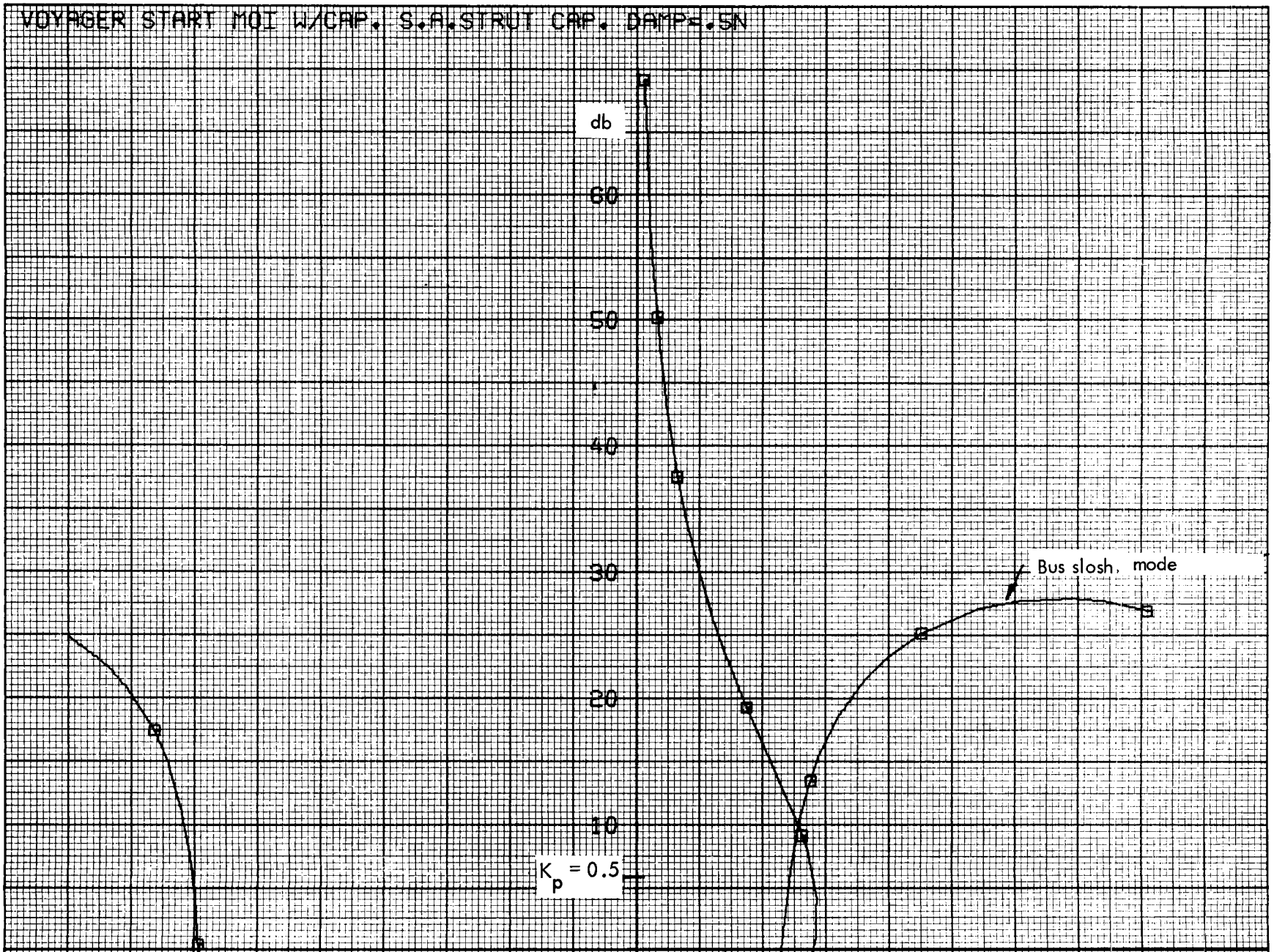
VOYAGER START MOI W/CAP. S.A.STRUT CAP. DAMP=.5N
db
60
50
40
30
20
10
Bus slosh. mode
$K_p = 0.5$

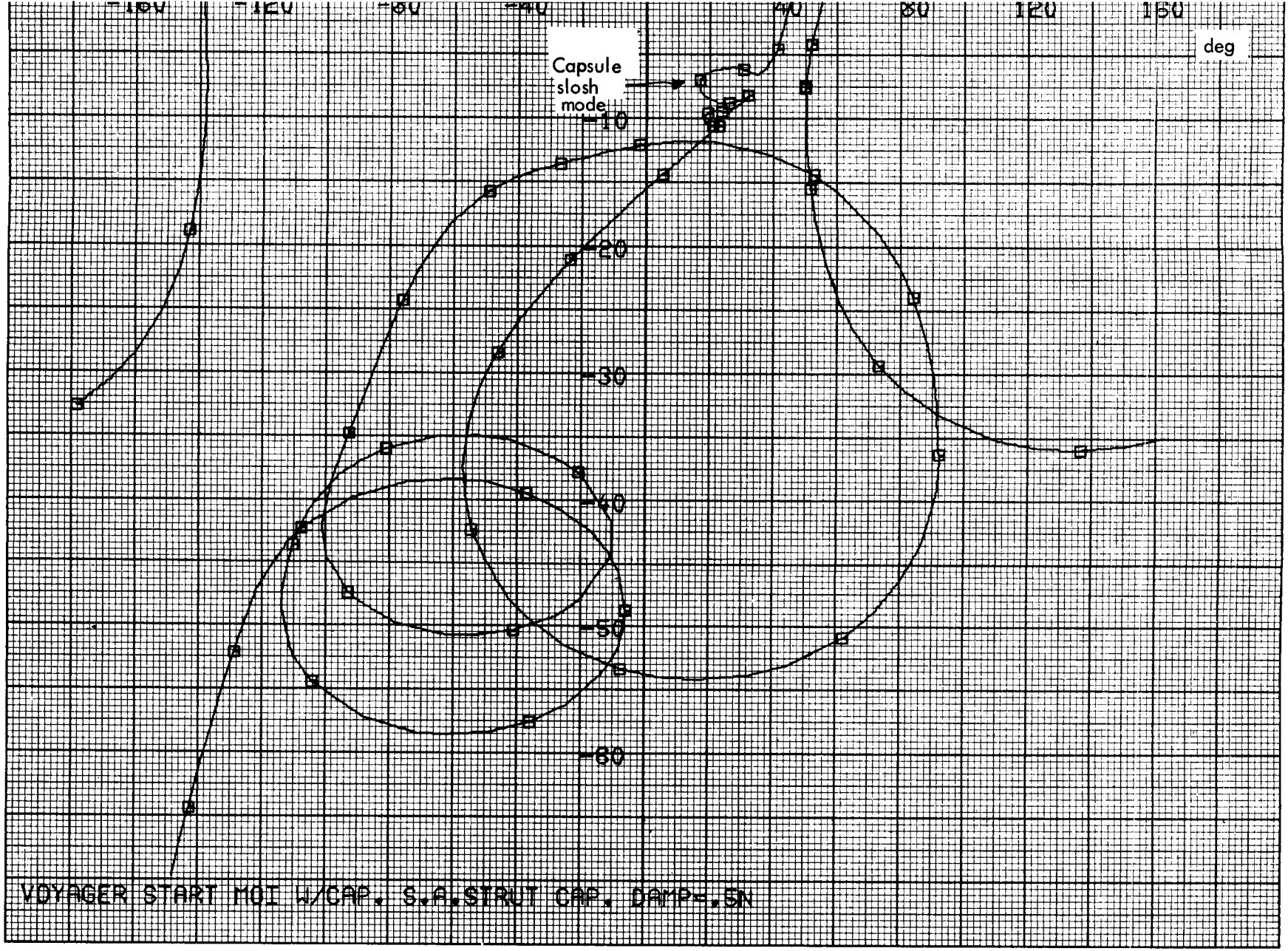

Figure 69. Gain-Phase Plot, Start MOI, with Capsule, 0.5× Nominal Capsule Slosh Damping

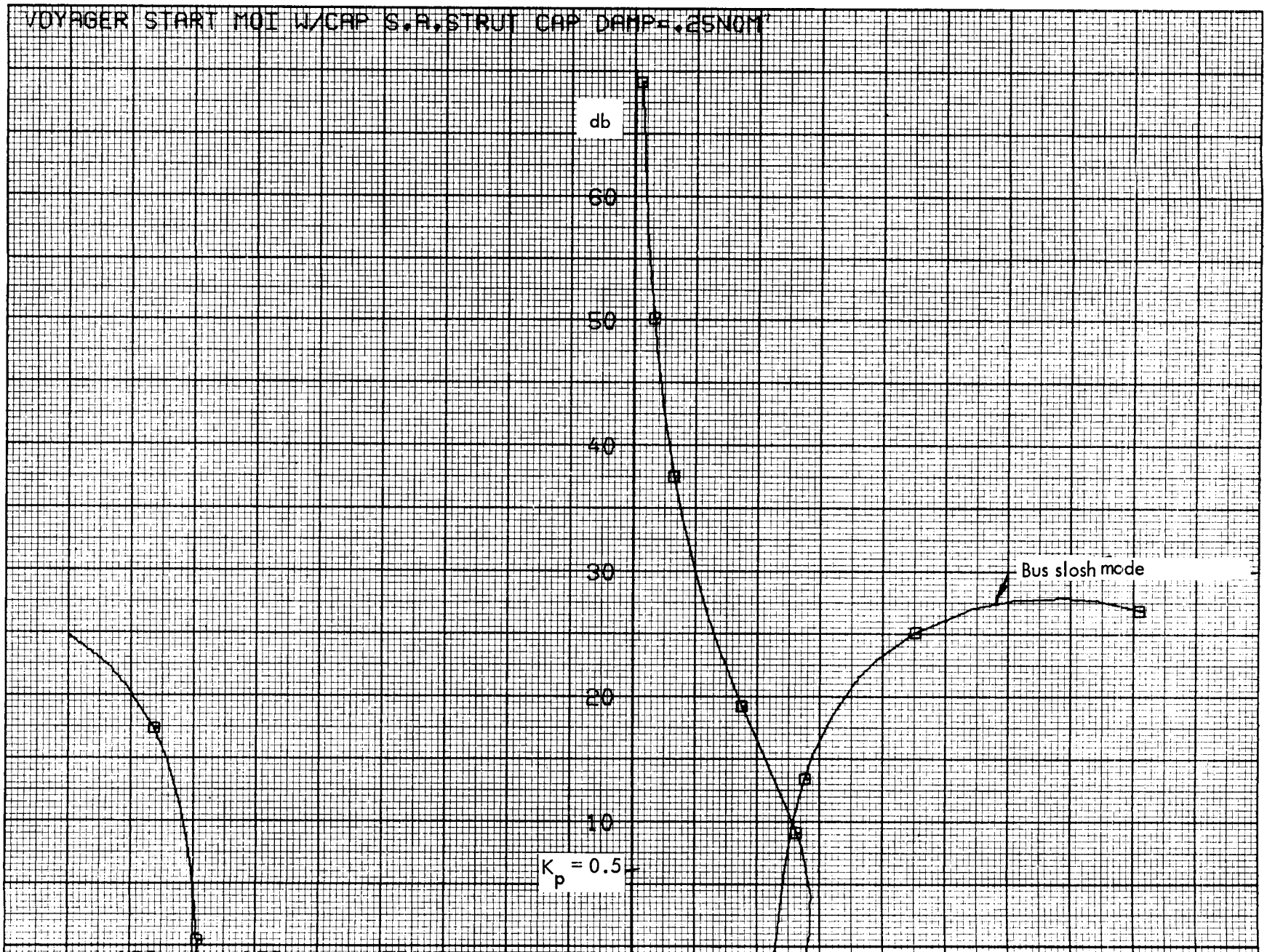
VOYAGER START MOI W/CAP S.A.STRUT CAP DAMP=.25NOM
db
60
50
40
30
20
10
Bus slosh mode
$K_p = 0.5$

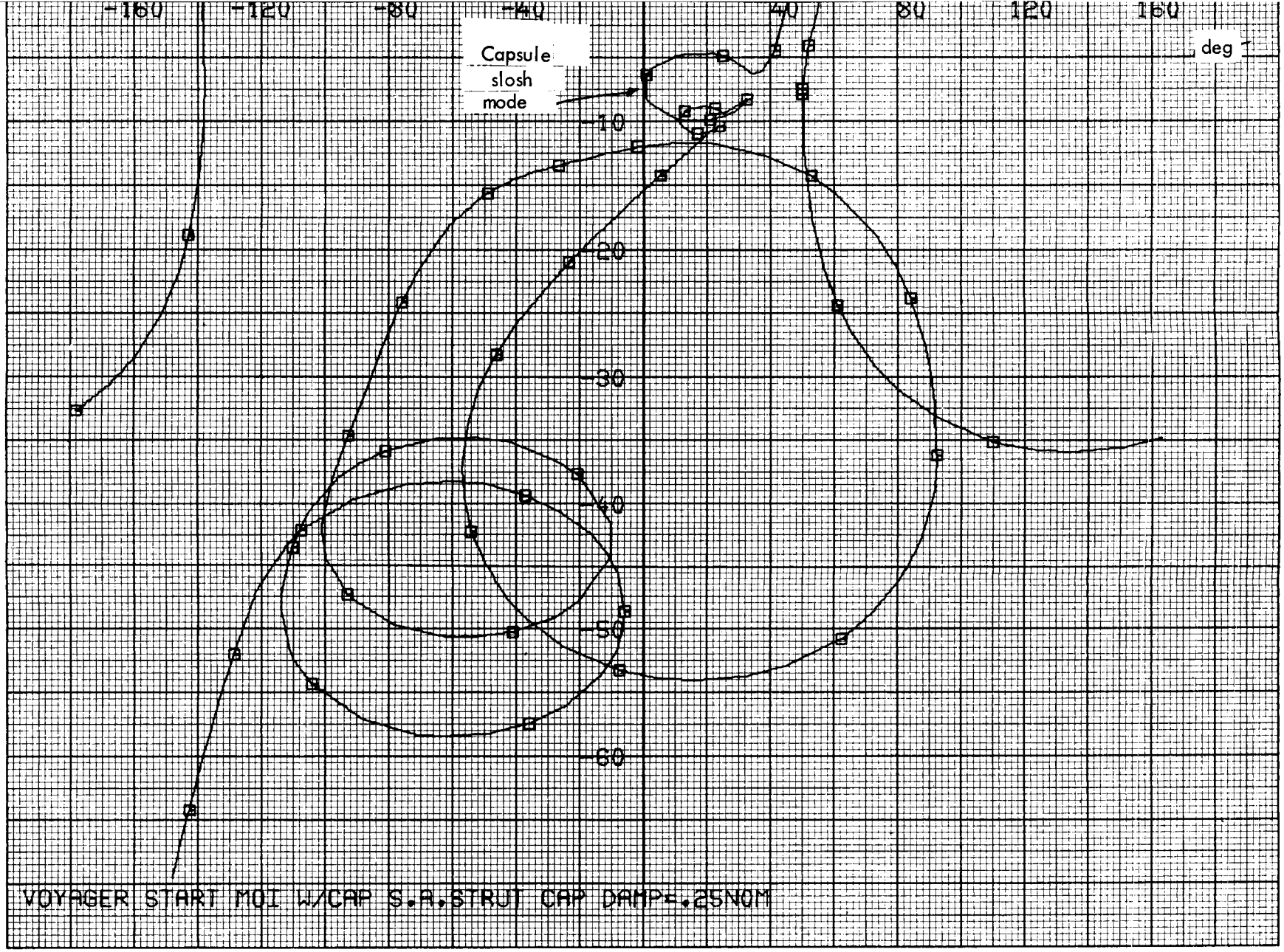

Figure 70. Gain-Phase Plot, Start MOI, with Capsule, 0.25× Nominal Capsule Slosh Damping

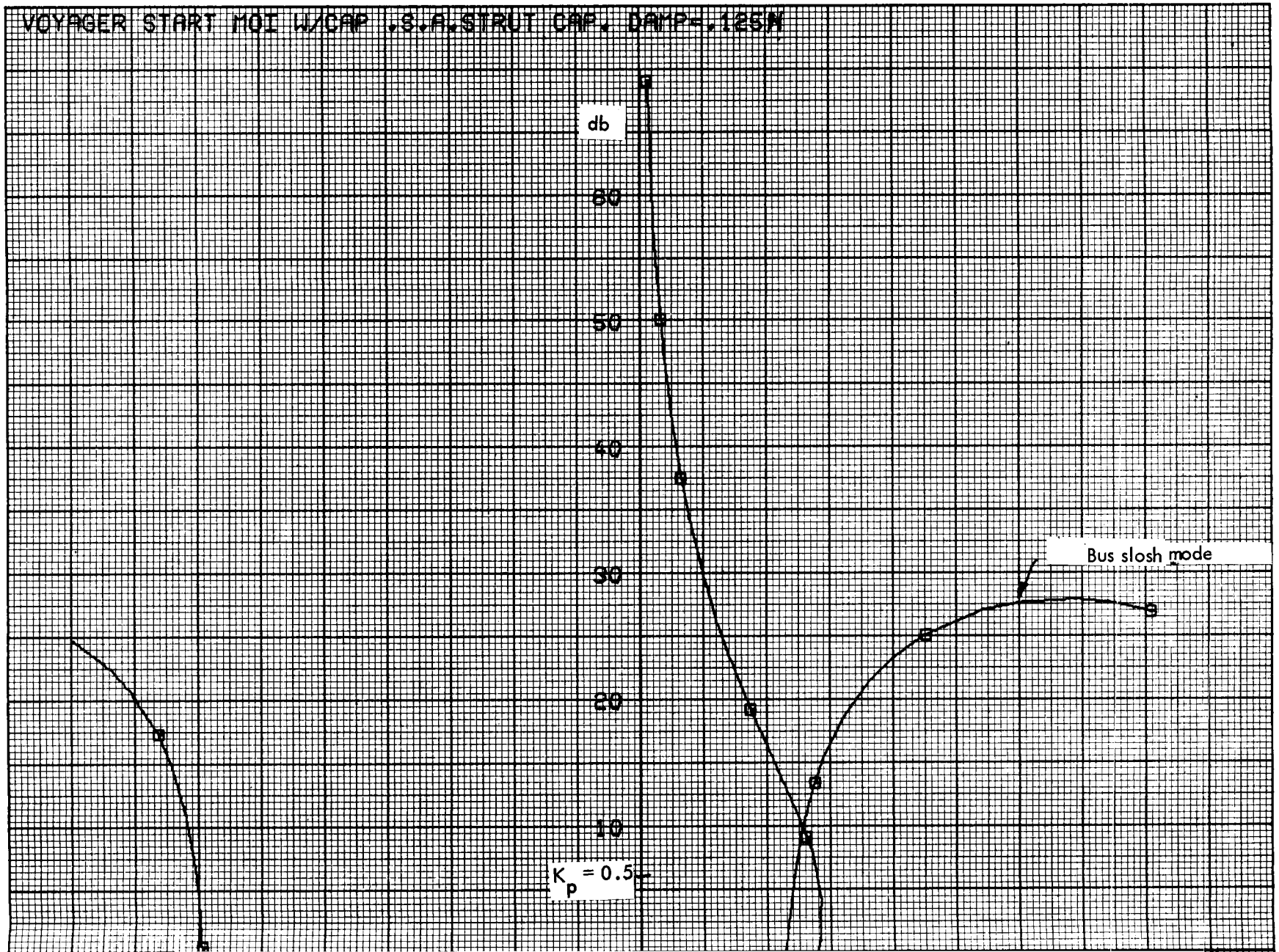
VOYAGER START MOI W/CAP .S.A.STRUT CAP. DAMP=.125N
db
60
50
40
30
20
10
Bus slosh mode
$K_p = 0.5$

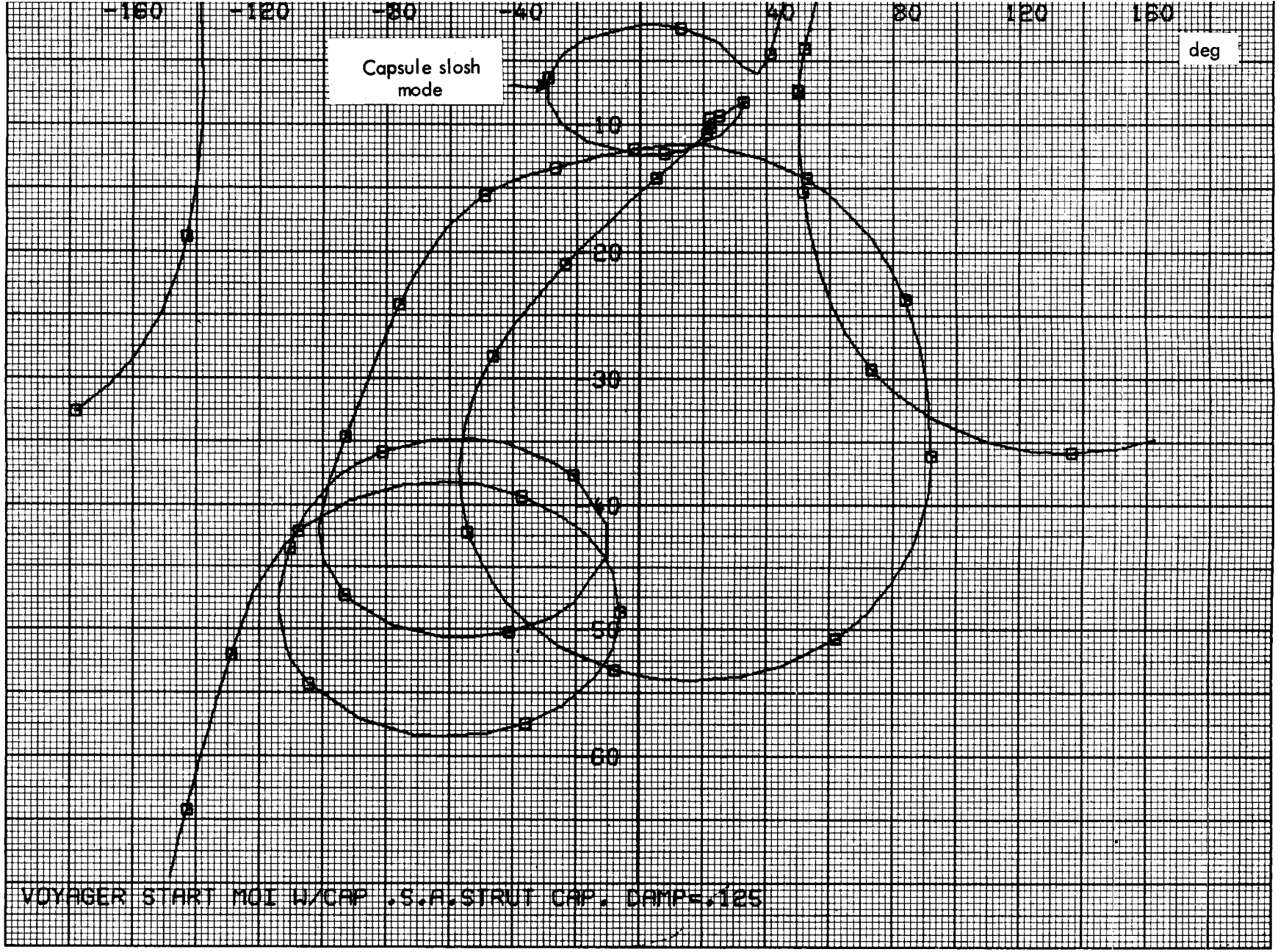

Figure 71. Gain-Phase Plot, Start MOI, with Capsule, 0.125X Nominal Capsule Slosh Damping

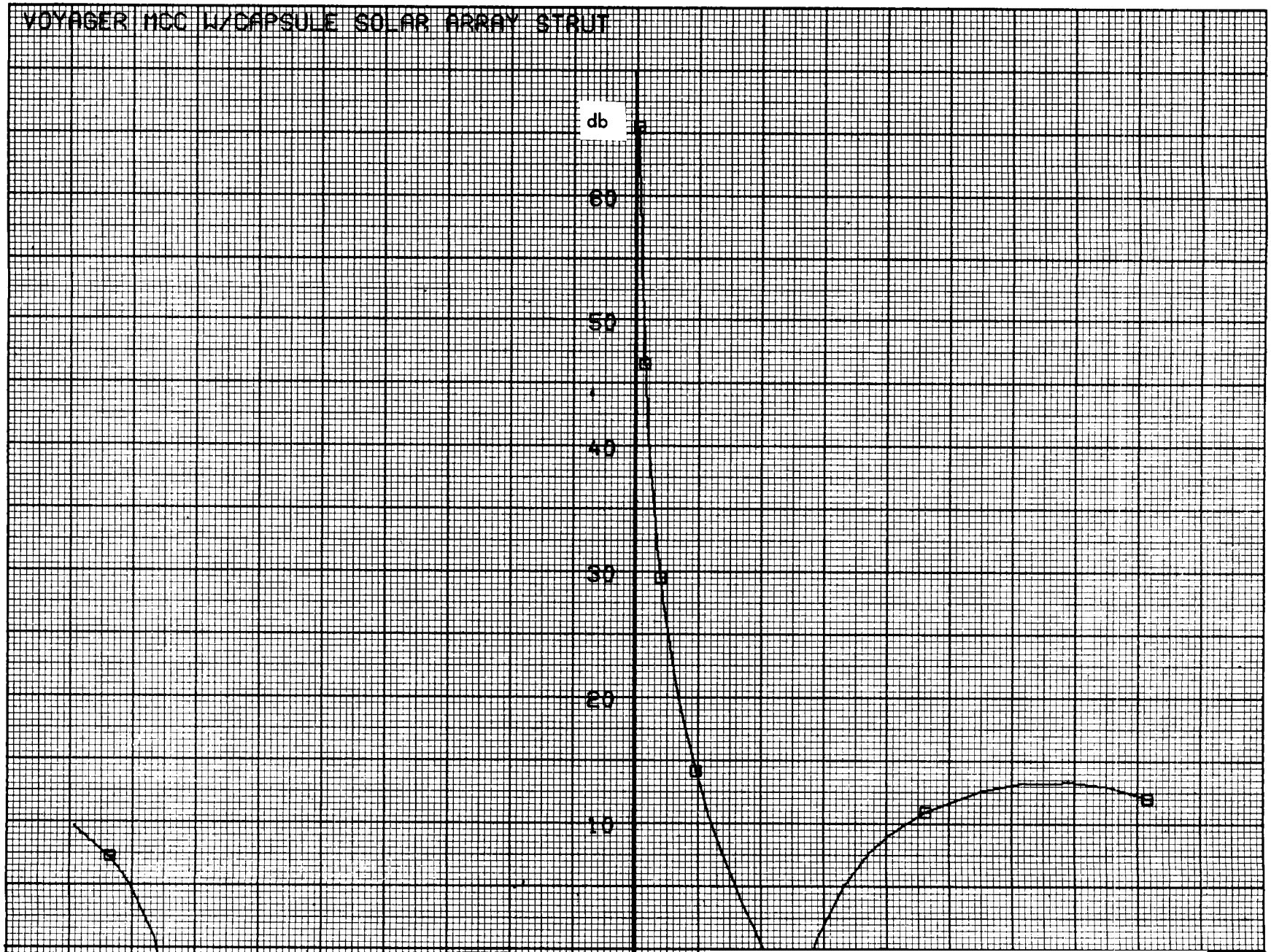
VOYAGER HCC W/CAPSULE SOLAR ARRAY STRUT
db
60
50
40
30
20
10

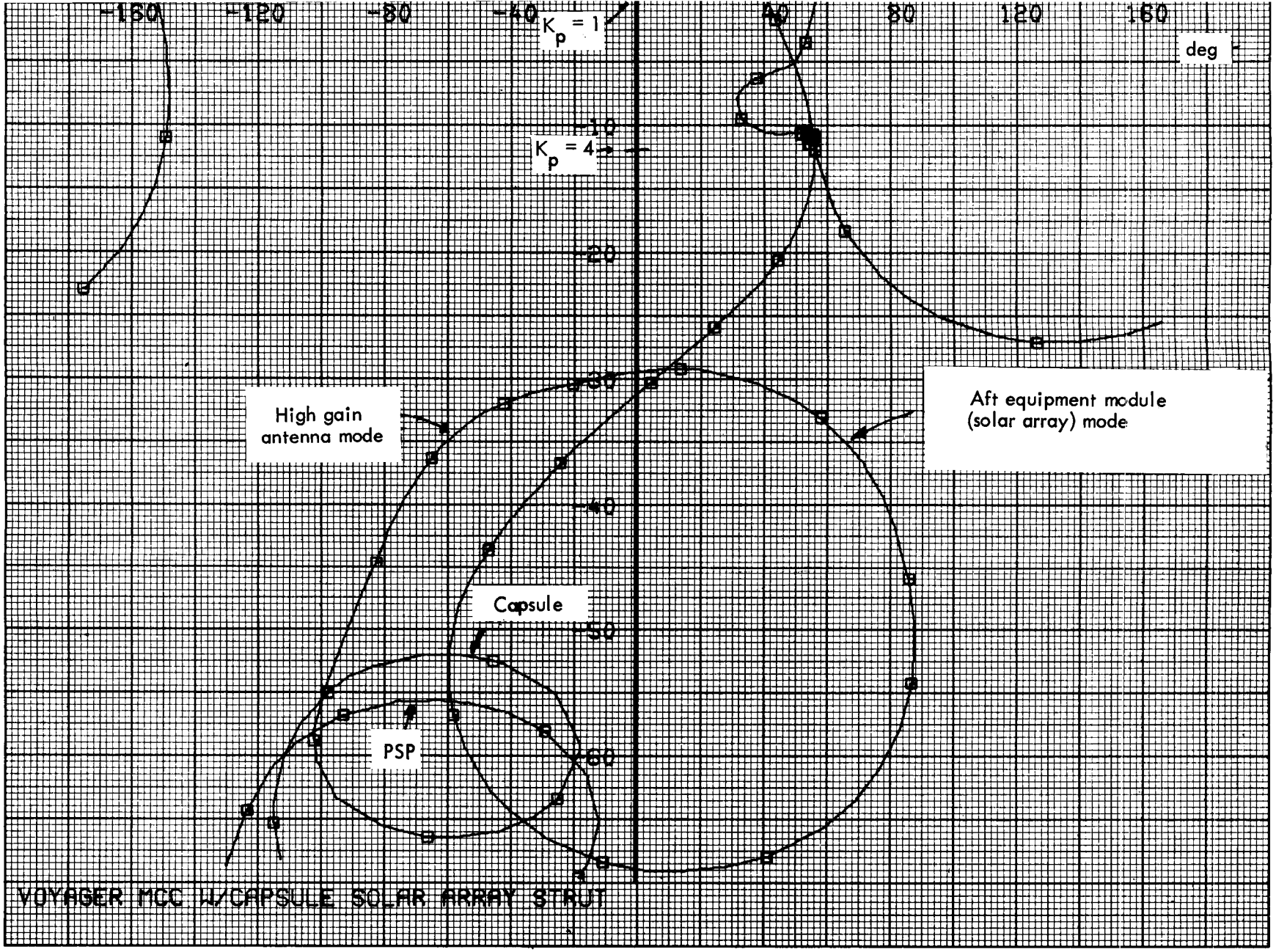

Figure 72. Gain-Phase Plot, MCC, with Capsule, Solar Array Struts Added

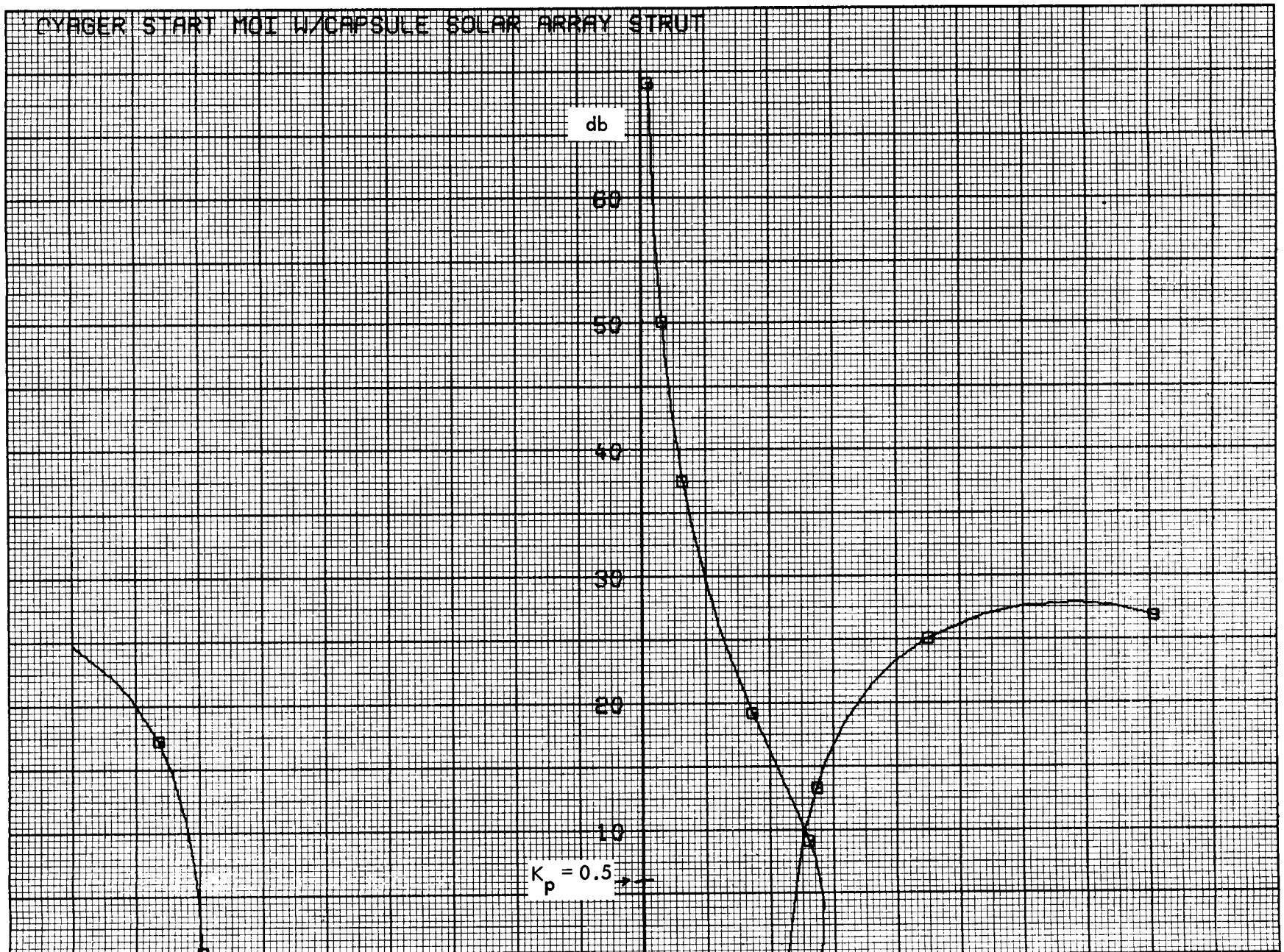
VOYAGER START MOI W/CAPSULE SOLAR ARRAY STRUT
db
60
50
40
30
20
10
K_p = 0.5

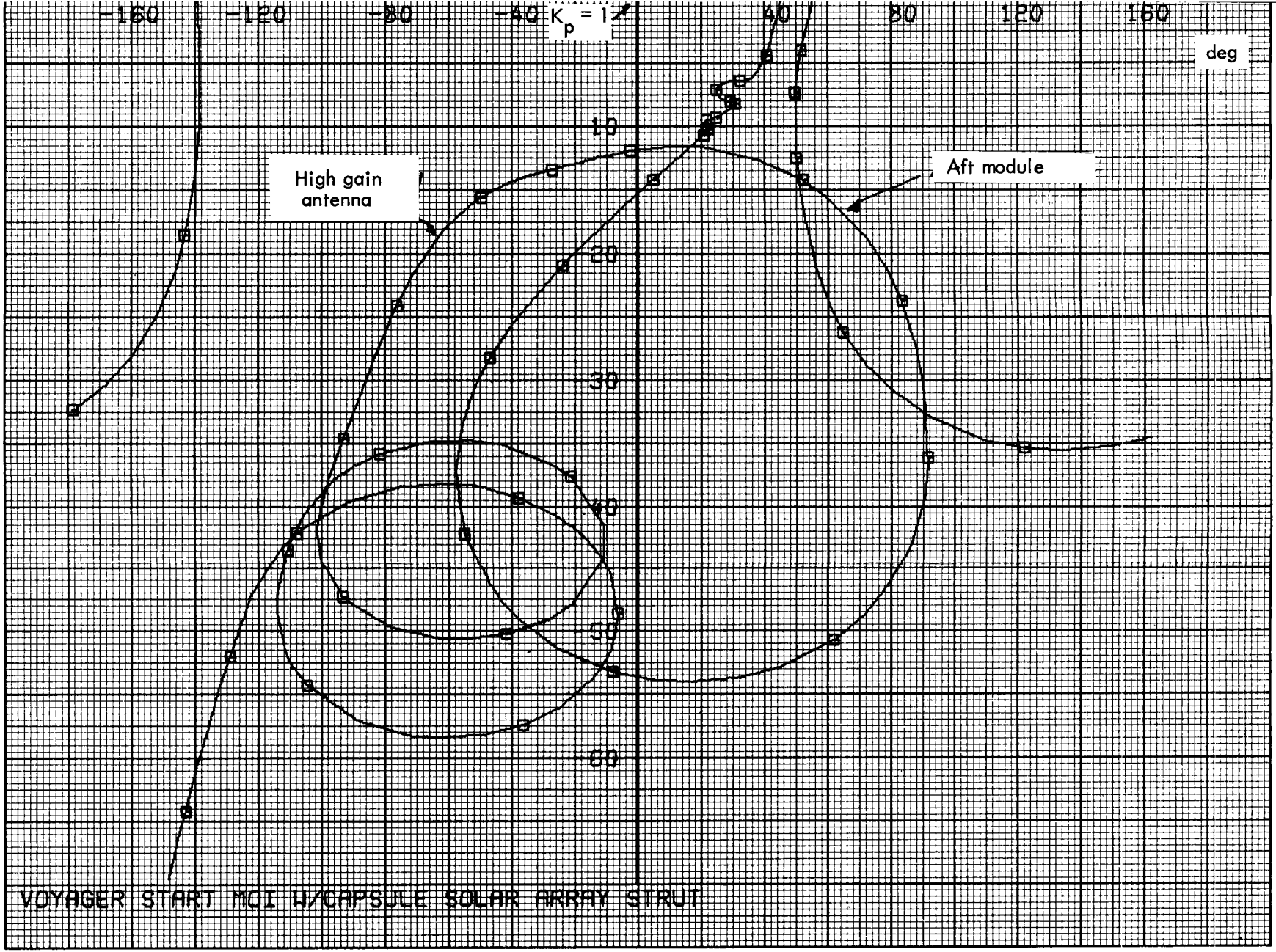

Figure 73. Gain-Phase Plot, Start MOI, with Capsule, Solar Array Struts Added

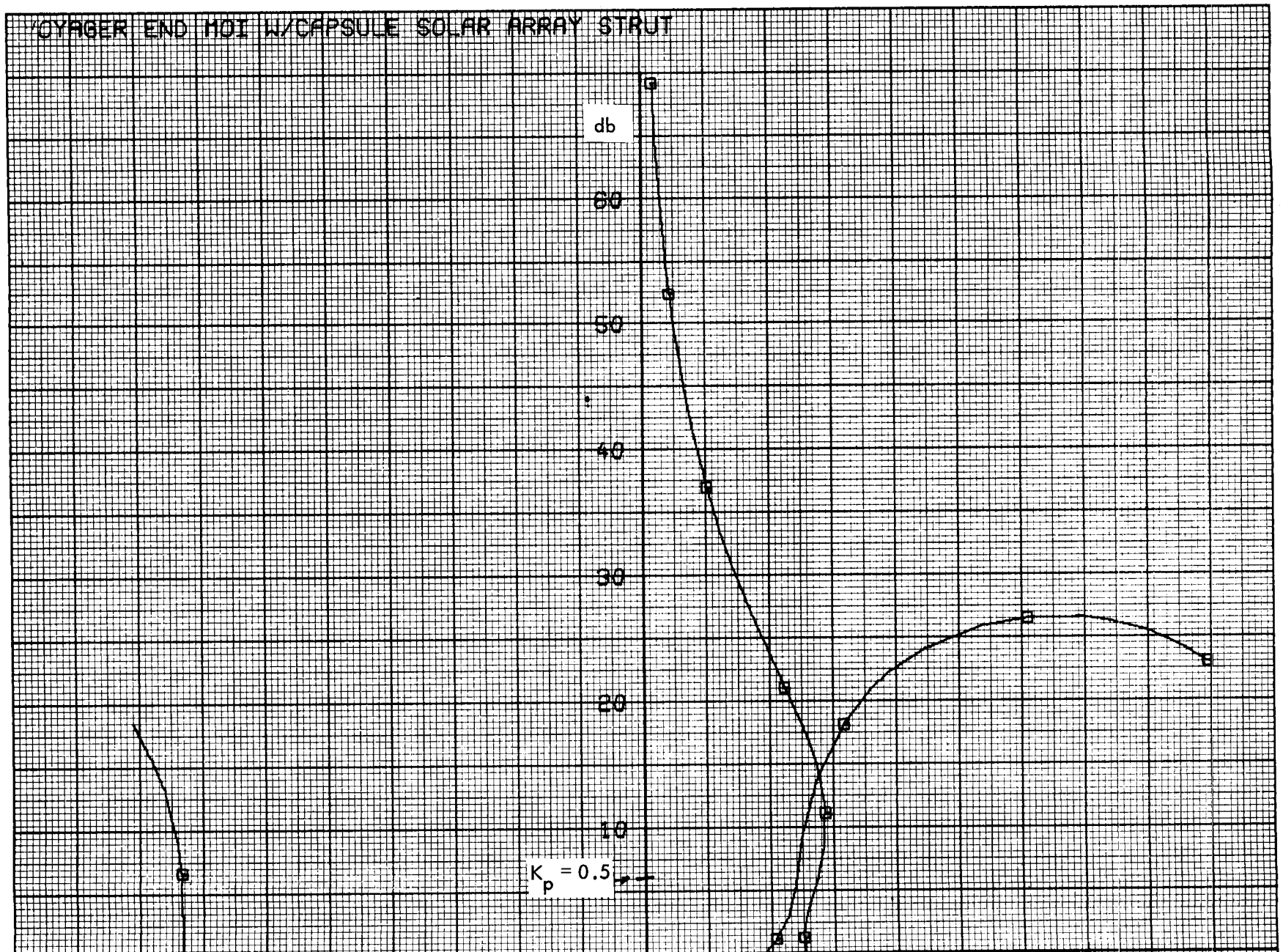
'OYAGER END HOI W/CAPSULE SOLAR ARRAY STRUT
db
60
50
40
30
20
10
$K_p = 0.5$

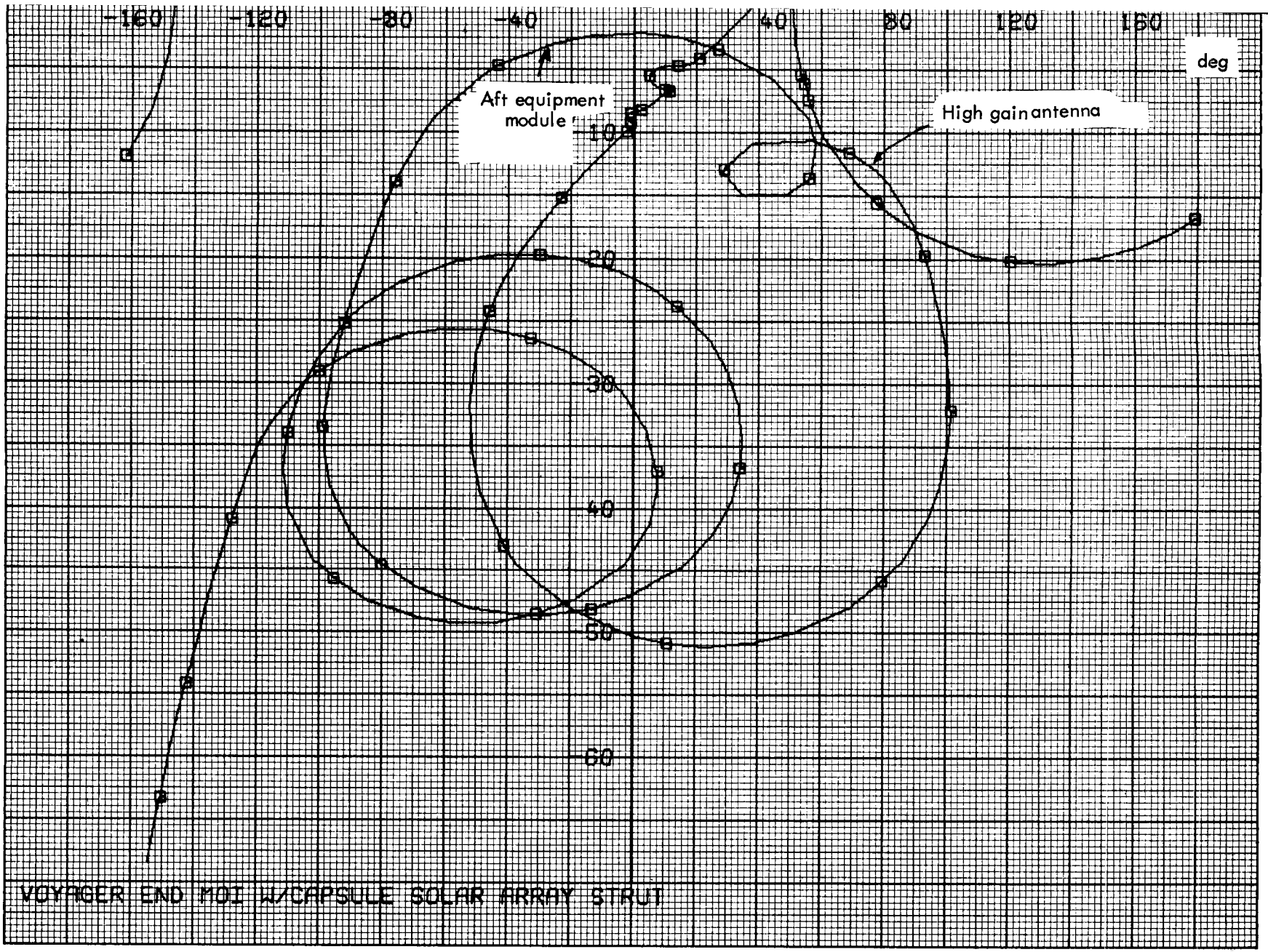

Figure 74. Gain-Phase Plot, End MOI, with Capsule, Solar Array Struts Added

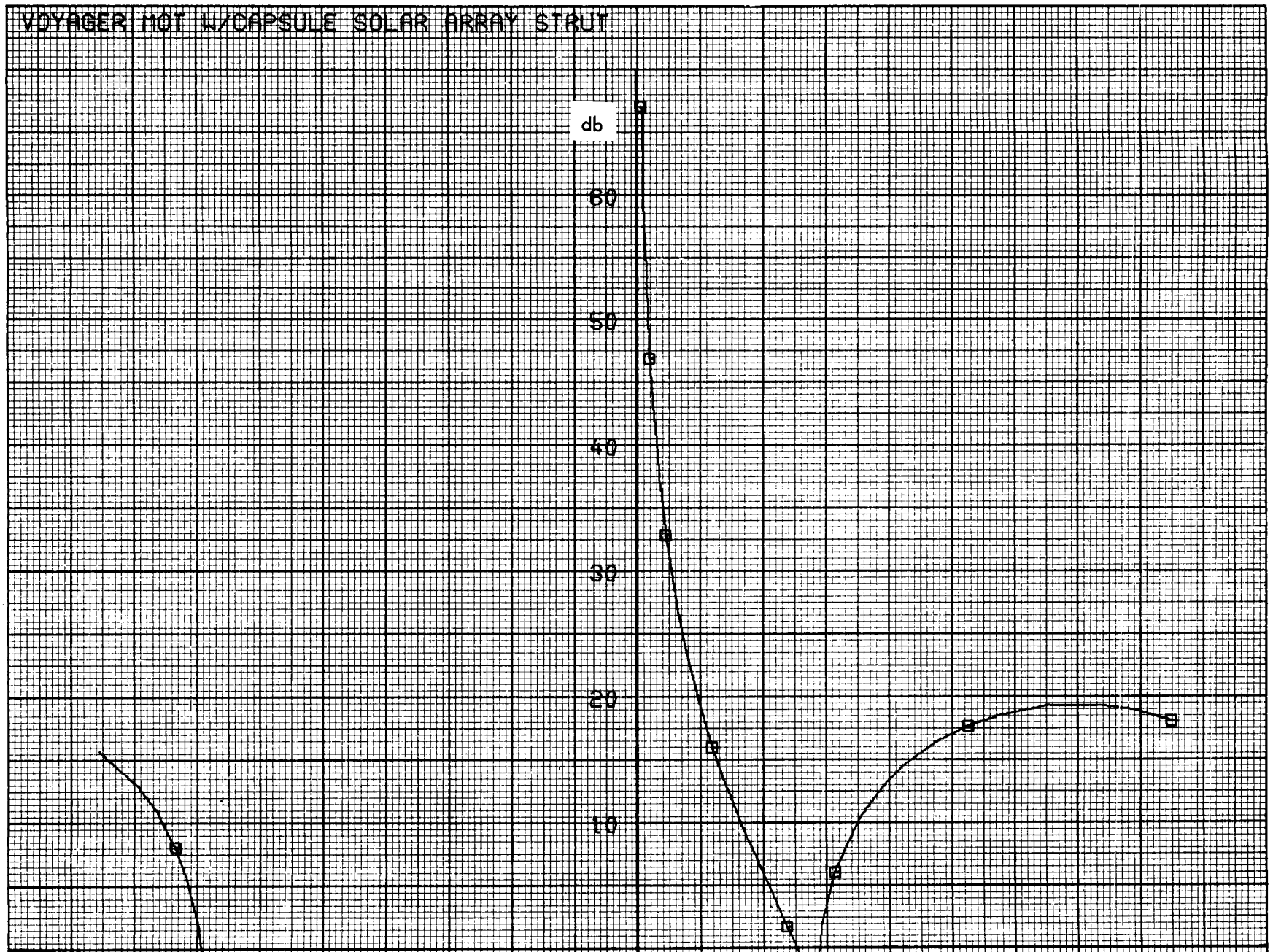

081

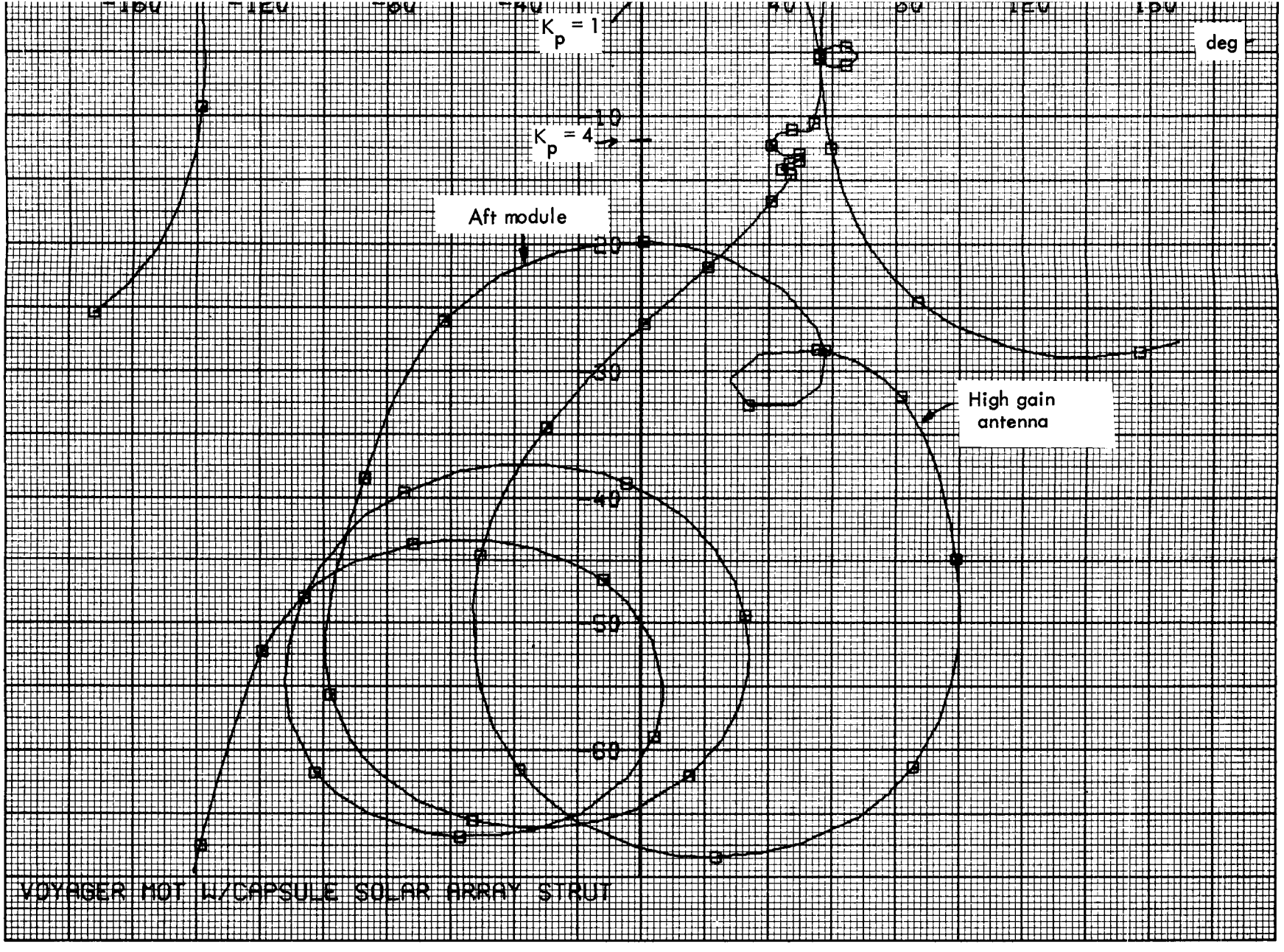

Figure 75. Gain-Phase Plot, MOT, with Capsule, Solar Array Struts Added

BLANK PAGE

PRECEDING PAGE BLANK NOT FILMED.

3.7 AUTOPILOT FILTERING

3.7.1 Noise Filtering

All of the previous stability plots employed a simple lead-lag filter for control system rate compensation without additional filtering to remove any high frequency noise in the control signals. Such noise filtering would be even more desirable if it attenuates or further stabilizes body bending modes without affecting the rigid body control stability margins. One possible filter configuration was studied.

To achieve greater noise attenuation by the filter, it is desirable that its frequency be as low as possible. On the other hand, the phase lags introduced into the rigid body frequencies by the attenuator must be kept to a minimum to retain good stability margins. An ideal compromise design to satisfy both requirements entails the use of complex pole filters (or quadratic pole filters) with a damping factor ranging between 0.5 to 0.7. A design with a damping factor of 0.5 was selected to illustrate the effects of this filter configuration upon the control system stability margins.

The end MOI case with solar array struts included was employed for the illustration and the filter frequency was varied. Figure 75 shows the filter frequency at 10 rad/sec. The rigid body margins are shown to be unsatisfactorily degraded when compared to Figure 74 (without the filter). The solar array mode is shown to be overly attenuated and indicates that a higher frequency filter is desirable. Figure 77 corresponds to a filter frequency of 20 rad/sec. The recovery of much of the rigid body margins is shown with a high frequency gain margin of 10 db and a phase margin of 26 degrees. Figure 78 shows a further increase in the filter frequency to 30 rad/sec. The high frequency gain margin is shown to be 10.5 db with a 41-degree phase margin. The increased rigid body gain margin over that shown in Figure 77 was obtained at the expense of a 4-db loss in attenuation of the aft module mode as shown and perhaps the best frequency to be selected would occur near 25 rad/sec.

The 30-rad/sec filter was employed with the start MOI condition, and the results given in Figure 79 can be compared with Figure 73 (without the filter). The stability margins for both cases are shown to be

acceptable. Figure 80 with the MOT vehicle configuration shows a marked improvement in stability margins over Figure 75. The aft module mode is shown to contain a 70-degree phase lag margin in addition to a 7-db gain margin.

3.7.2 Lead-Lag Filter Change

All of the previous gain phase plots employed the lead-lag filter shown in Figure 53. This design was found to be satisfactory; hence, the problems of propellant slosh and body bending stability were next given immediate attention. When these problem areas were analyzed in sufficient depth, the question as to whether changes in the lead-lag filter design would offer improvements in stability margins was posed. Since the rigid body margins were, in general, quite ample, the possibility of reducing the rate information was considered. The lag shown in Figure 53 was retained at 20 rad/sec, and the lead root was increased in frequency to 1 rad/sec rather than the previous 0.5 rad/sec. Figures 81 through 84 show gain-phase plots for the four mission configurations. Comparison with Figures 72 through 75 shows that although the phase margins have been reduced by as much as 10 degrees they are still satisfactory, and, more significantly, that the operating gain could be increased by 6 db (factor of 2) from those given before. Since smaller attitude errors result to counteract thrust vector misalignment and offsets and cg offset effects, the higher operating gains are preferable from thrust vector pointing error considerations. Therefore, the revised lead-lag filter appears at first glance to be desirable. Since it is also wise to add a noise attenuating filter which further reduces the phase margin, the better design would have a lead at a slightly lower frequency than 1 rad/sec and would include a noise filter at approximately 25 rad/sec as discussed previously.

3.8 ELECTRONIC INTEGRATORS

In powered flight phases of fairly long duration, the effects of either thrust vector misalignments or thrust vector offsets and cg offsets can be nullified with respect to thrust vector pointing errors through the use of mechanical or electrical integrators in the control system. These integrators nullify cross velocity errors due to thrust

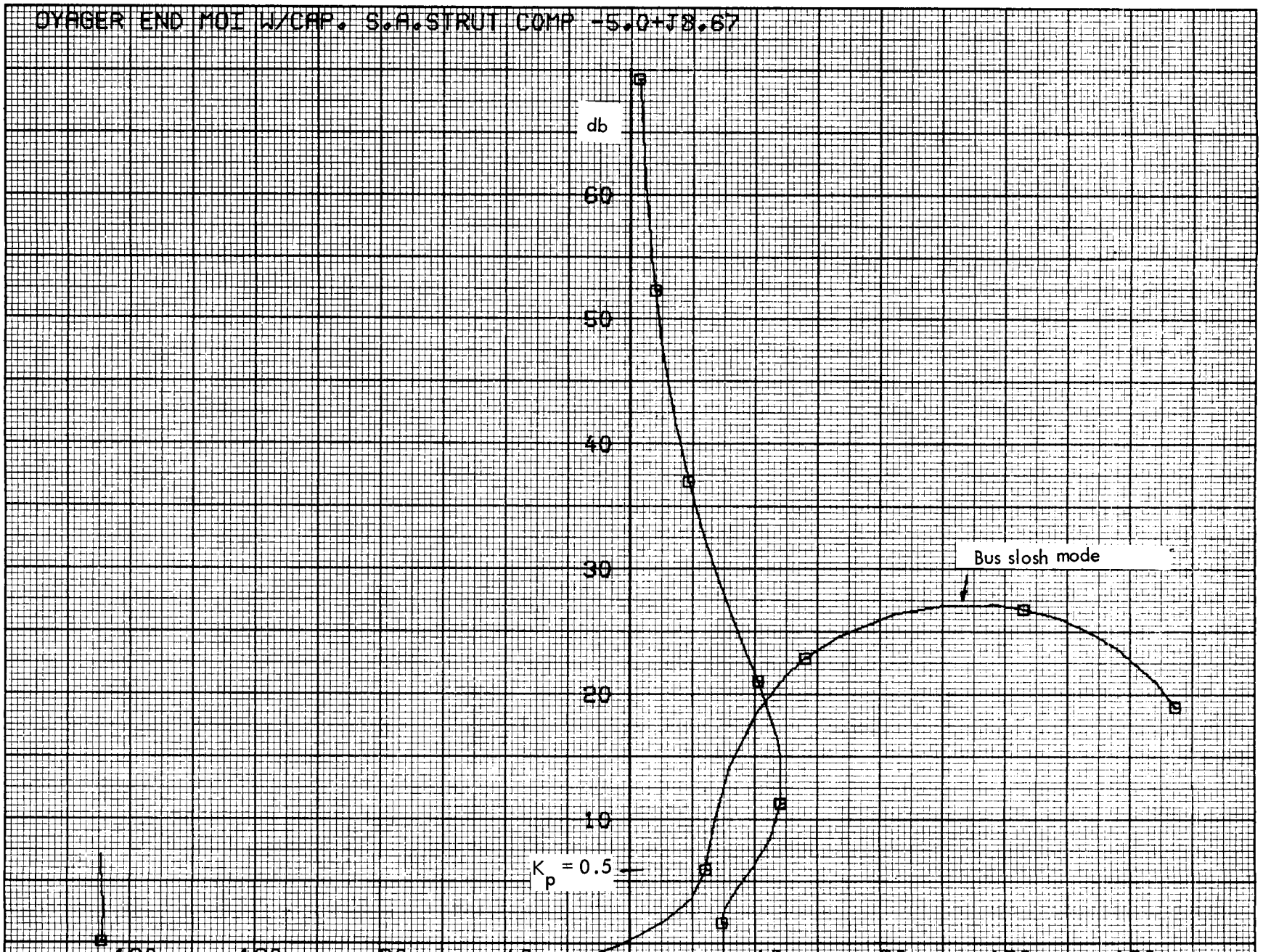
VOYAGER END MOI W/CAP. S.A.STRUT COMP -5.0+J8.67
db
60
50
40
30
20
10
Bus slosh mode
K_p = 0.5

1-58

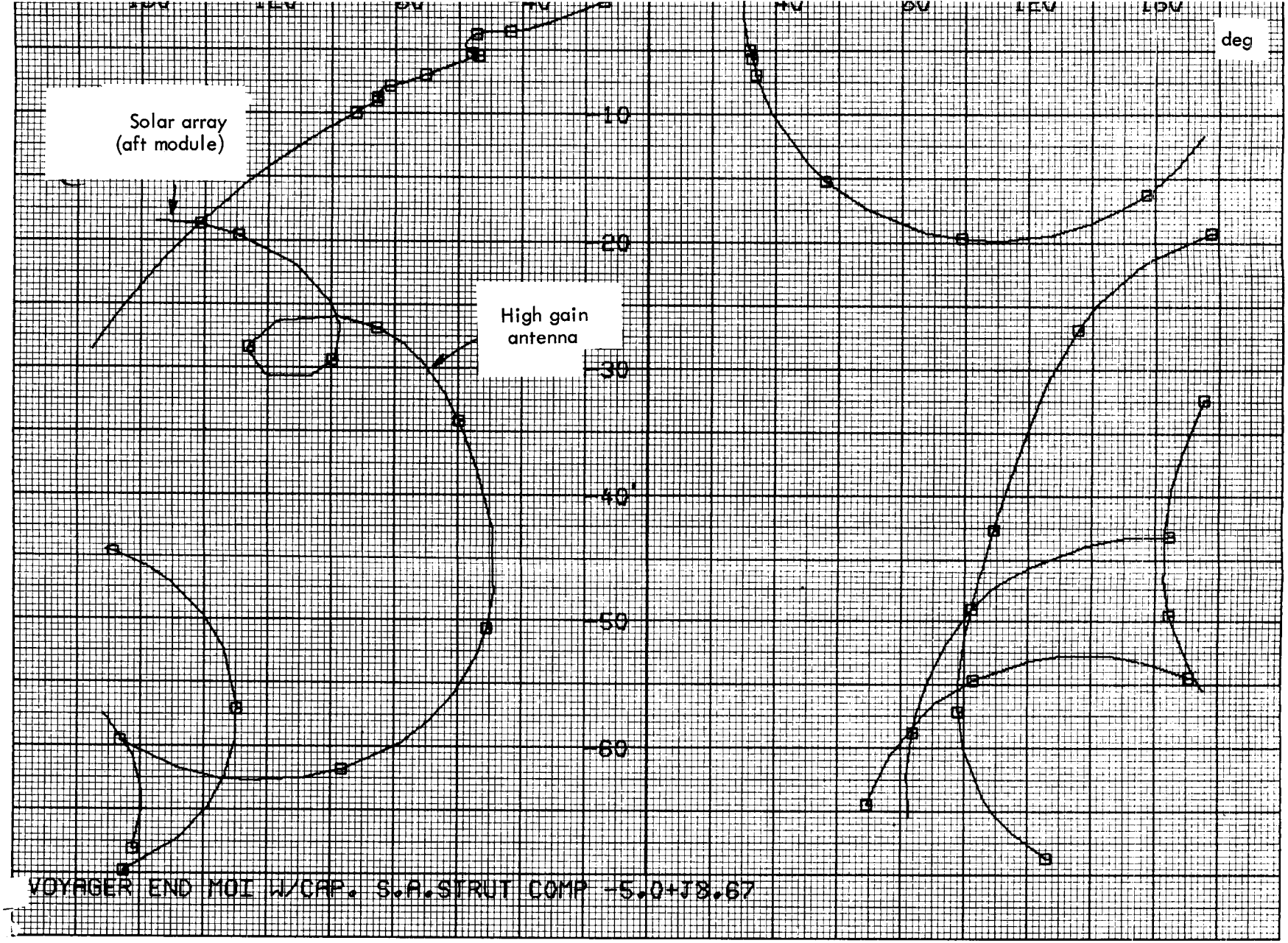

Figure 76. Gain-Phase Plot, End MOI, with Capsule, Solar Array Struts Added, Noise Filter Added at $\omega = 10$ Rad/Sec

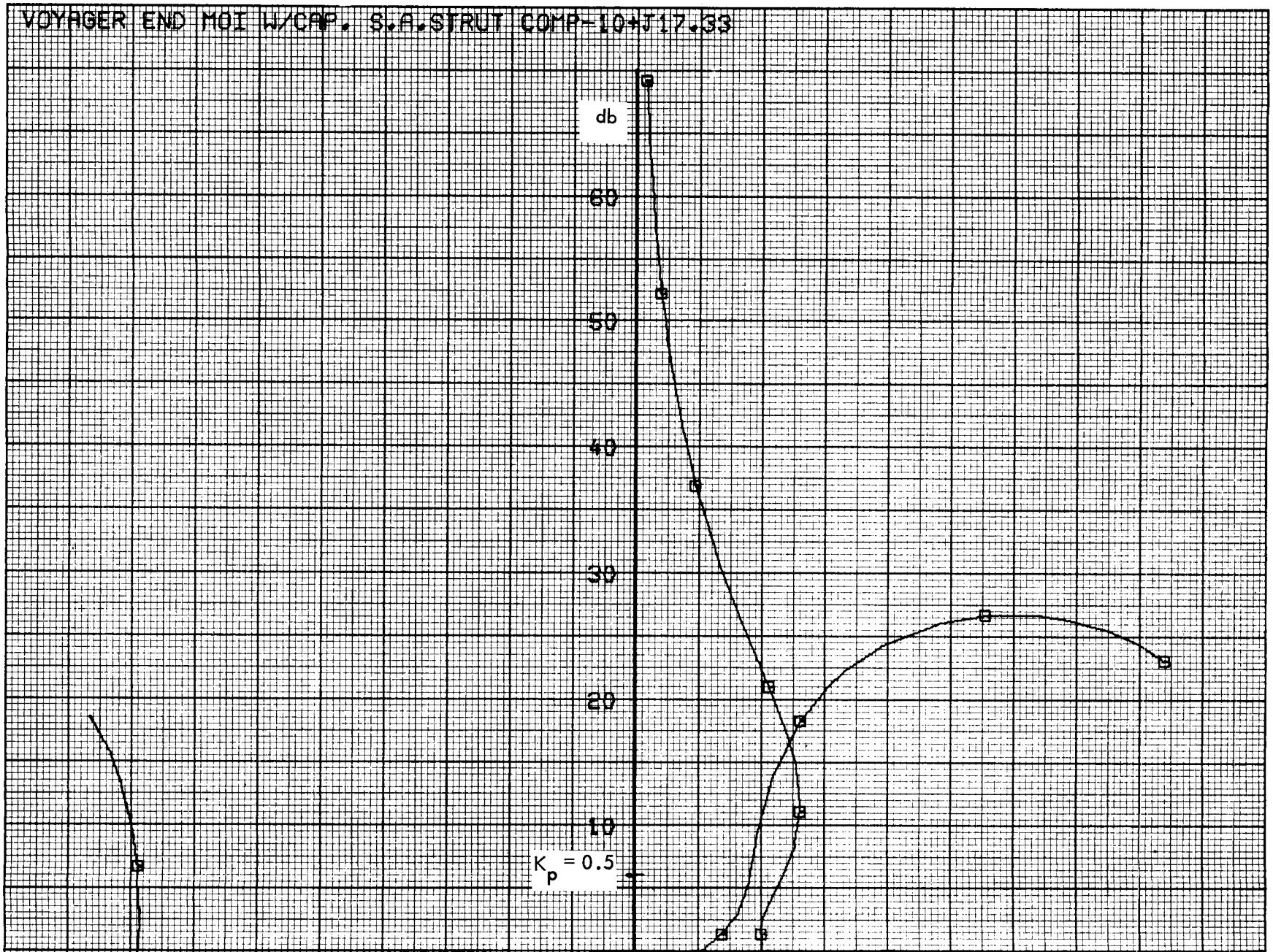
VOYAGER END MOI W/CAP. S.A.STRUT COMP-10+J17.33
db
60
50
40
30
20
10
$K_p = 0.5$

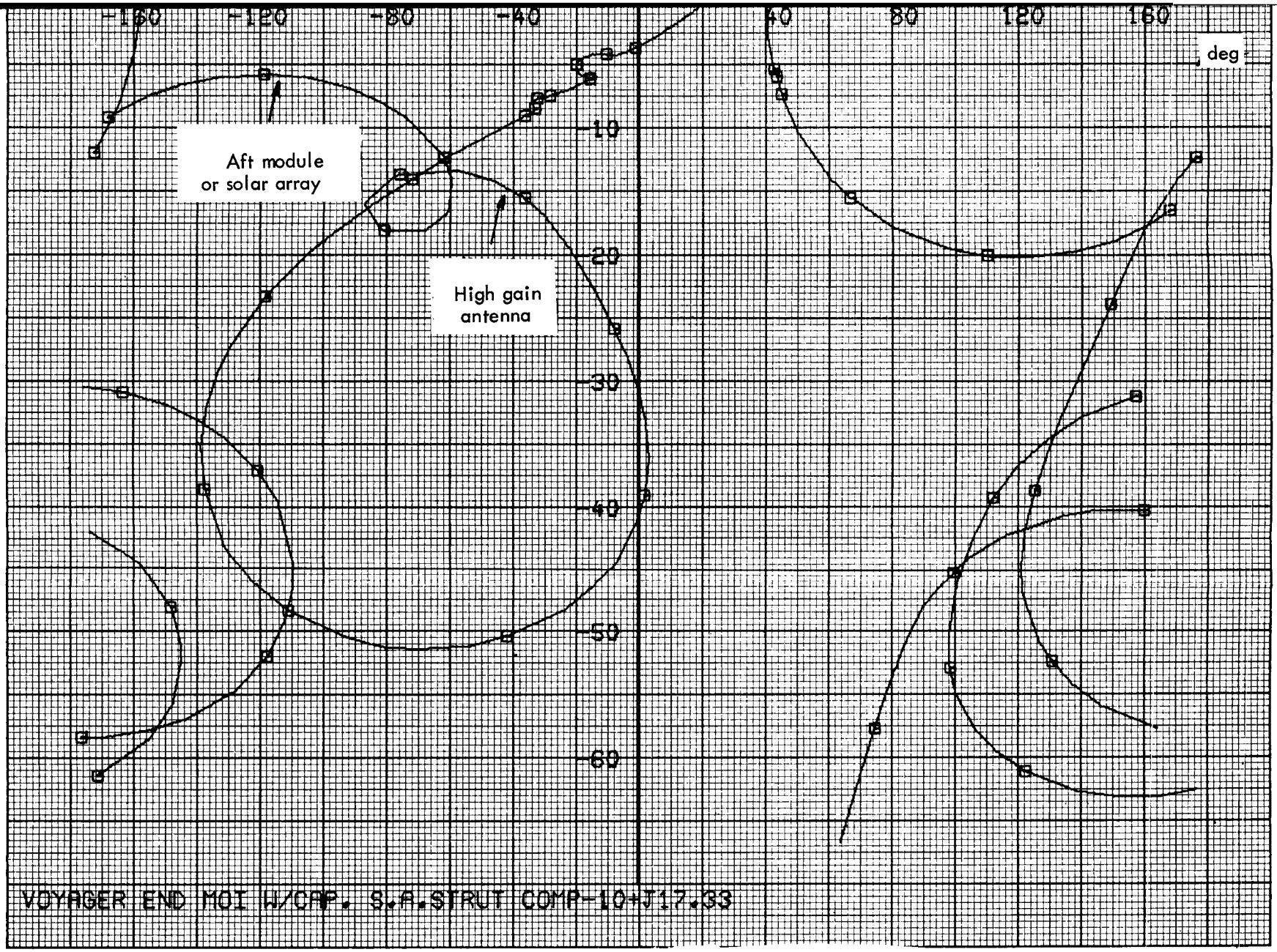

Figure 77. Gain-Phase Plot, End MOI, with Capsule, Solar Array Struts Added, Noise Filter Added at ω = 20 Rad/Sec

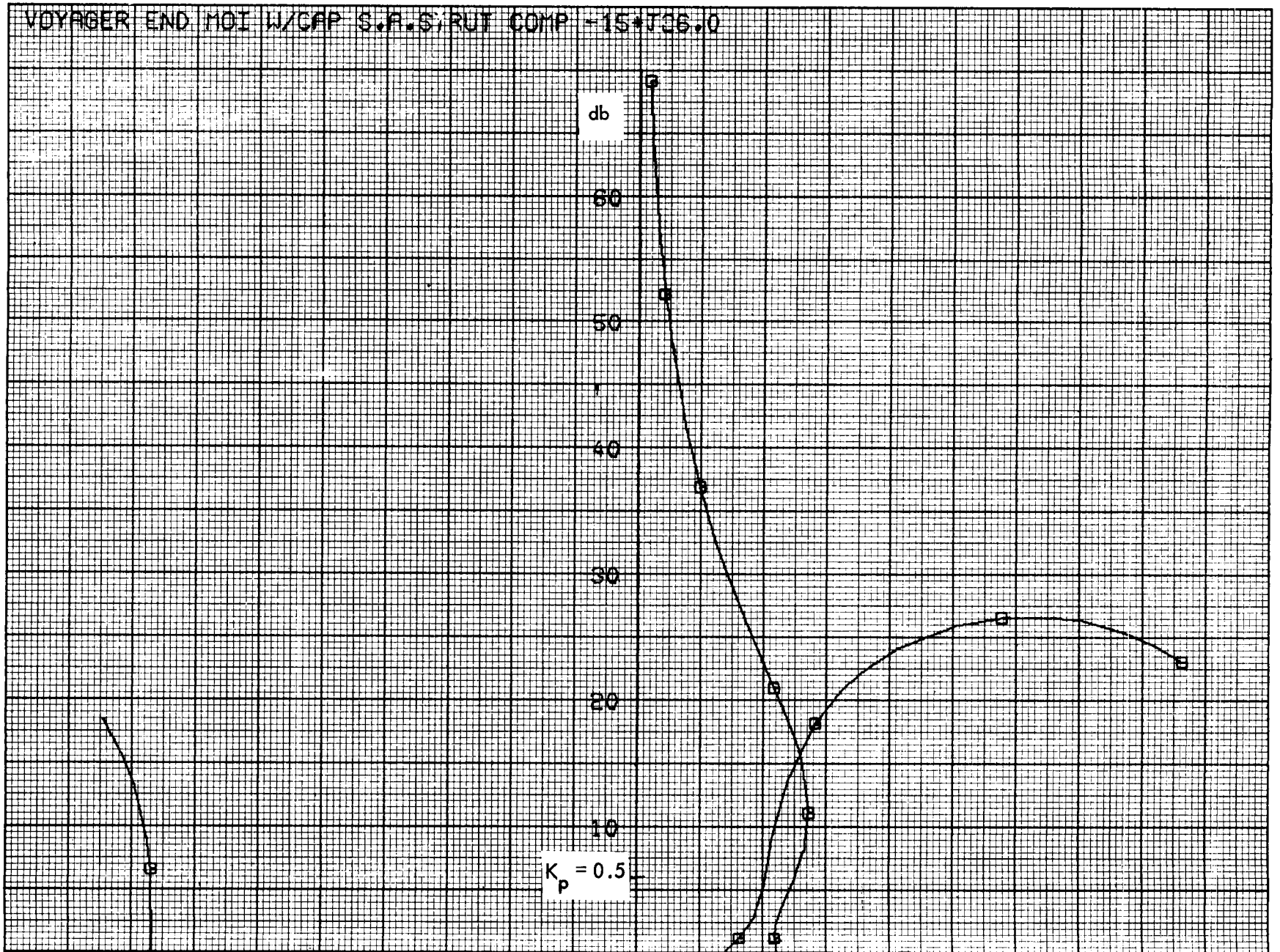
VOYAGER END MOI W/CAP S.R.S/RUT COMP -15*T36.0
db
60
50
40
30
20
10
K_p = 0.5

881

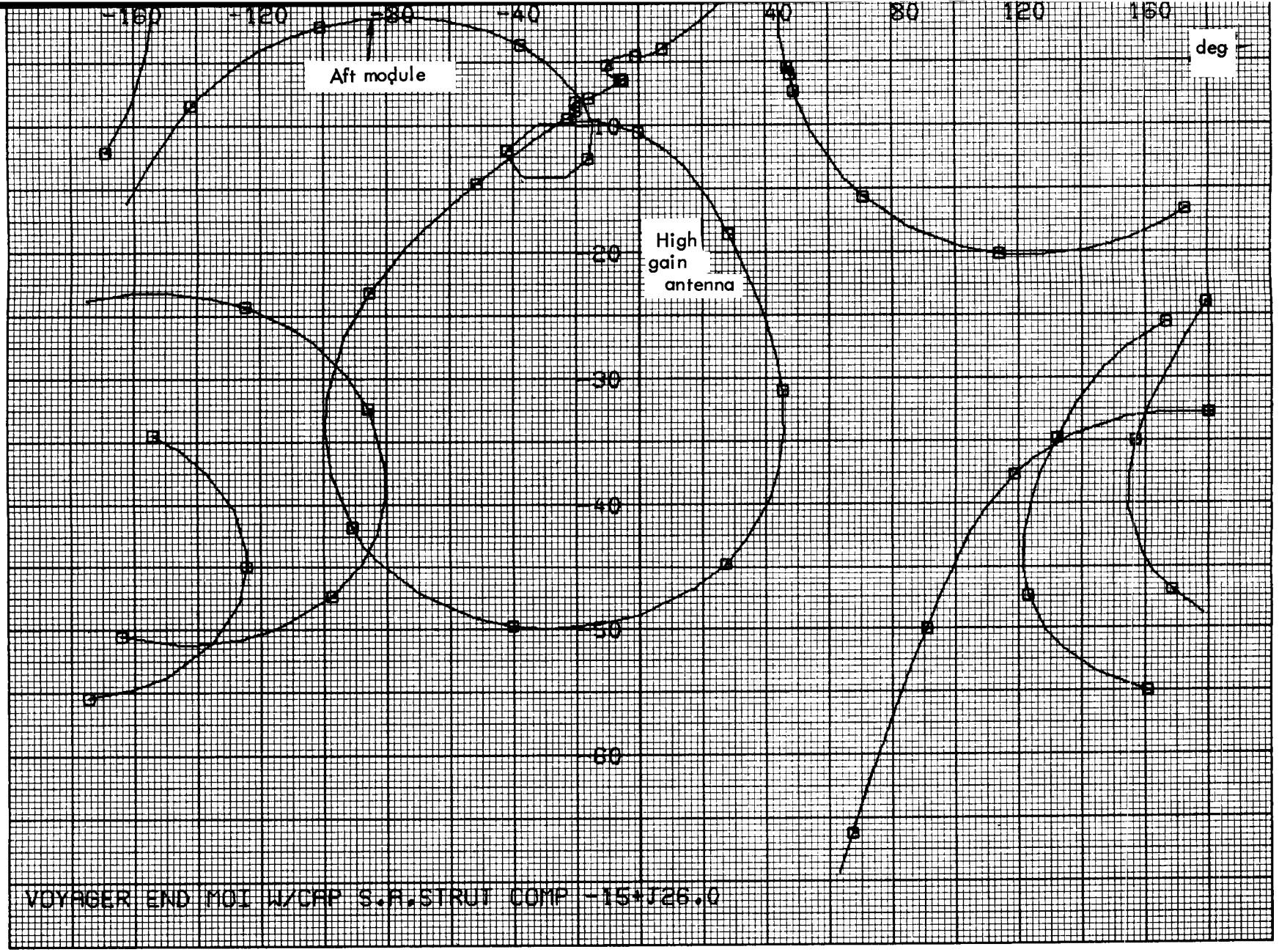

Figure 78. Gain-Phase Plot, End MOI, with Capsule, Solar Array Struts Added, Noise Filter Added at ω = 30 Rad/Sec

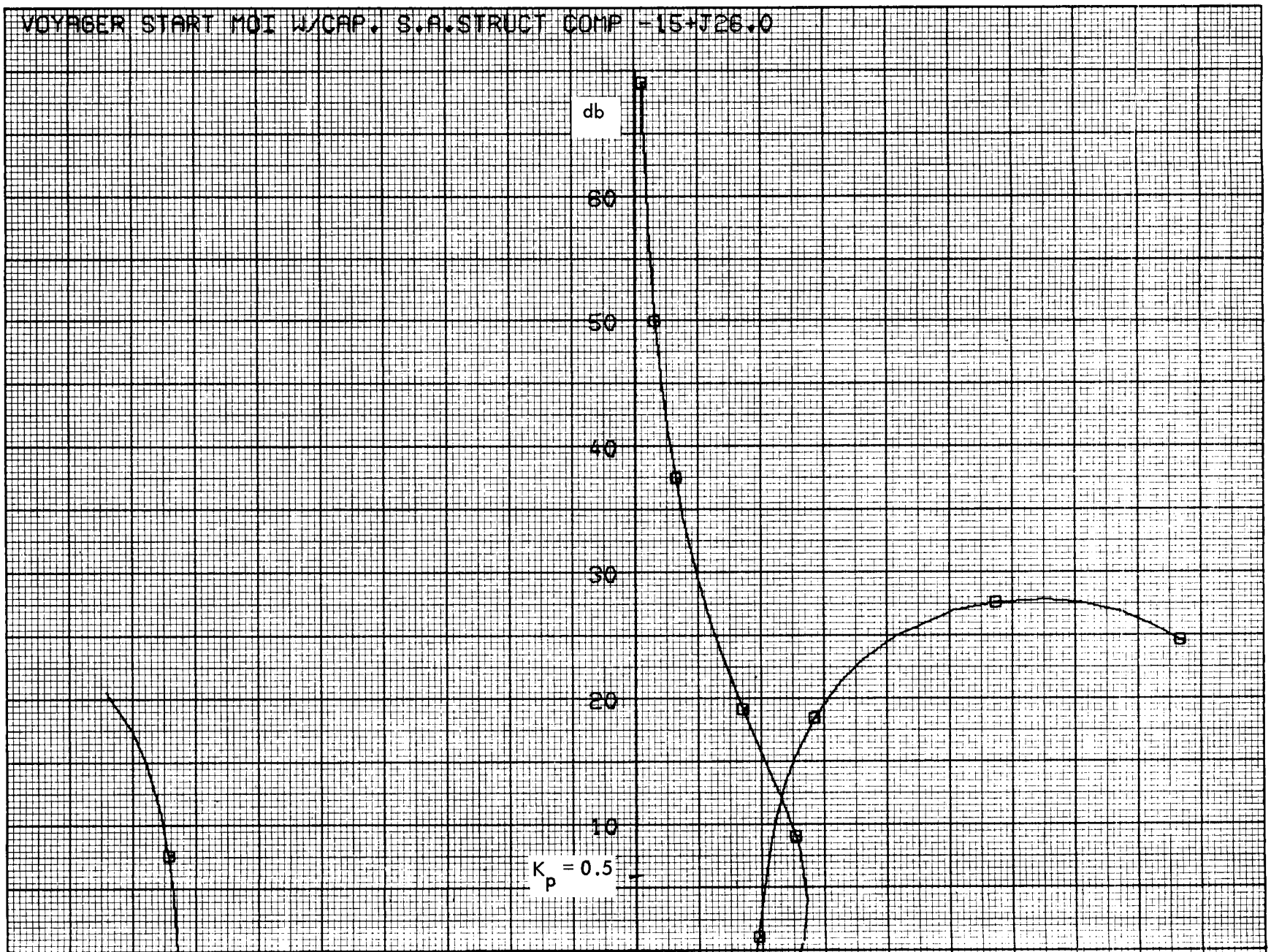
VOYAGER START MOI W/CAP. S.A. STRUCT COMP -15+J26.0
db
60
50
40
30
20
10
$K_p = 0.5$

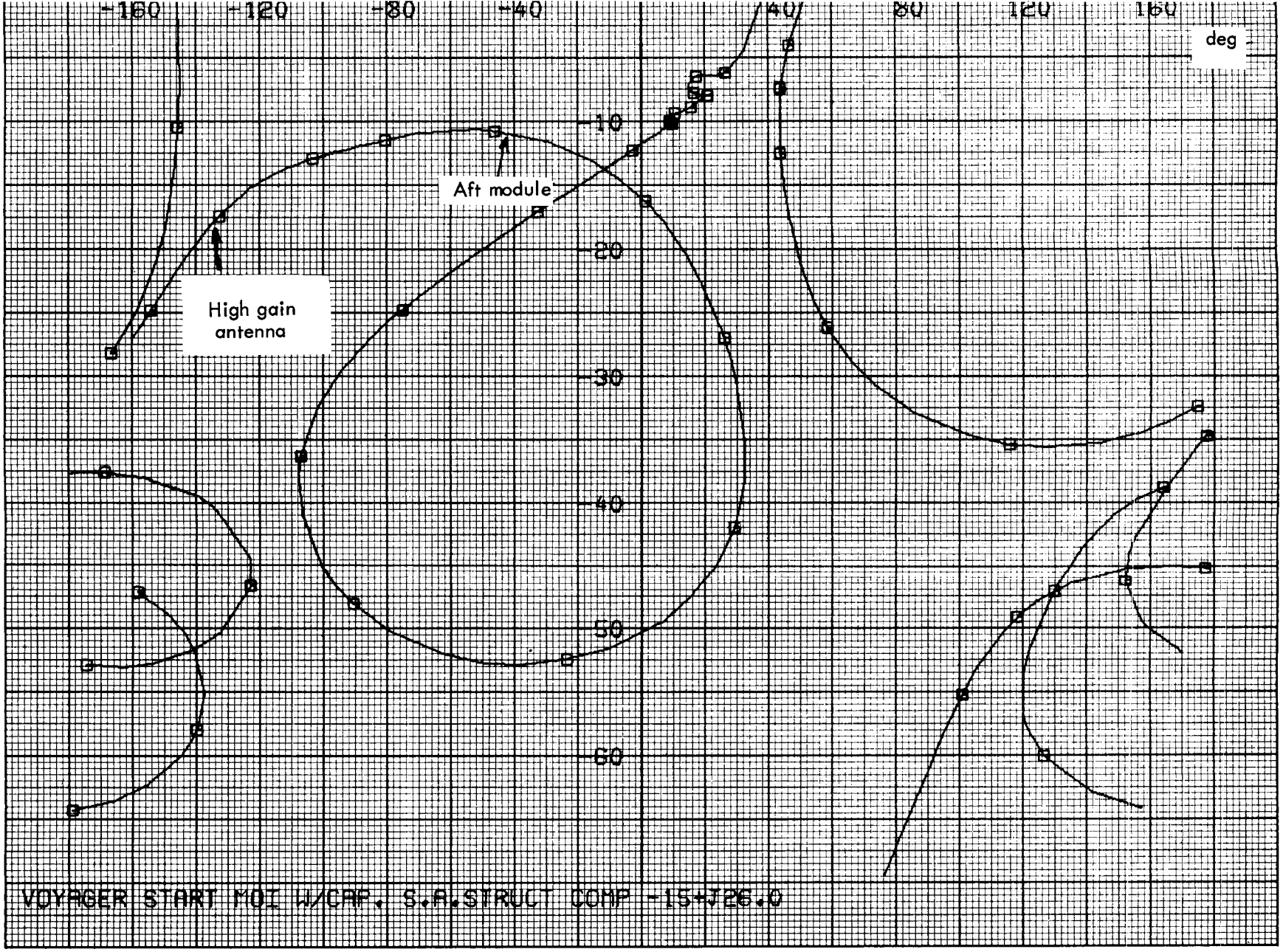

Figure 79. Gain-Phase Plot, Start MOI, with Capsule, Solar Array Struts Added, Noise Filter Added at ω = 30 Rad/Sec

dB
60
50
40
30
20
10

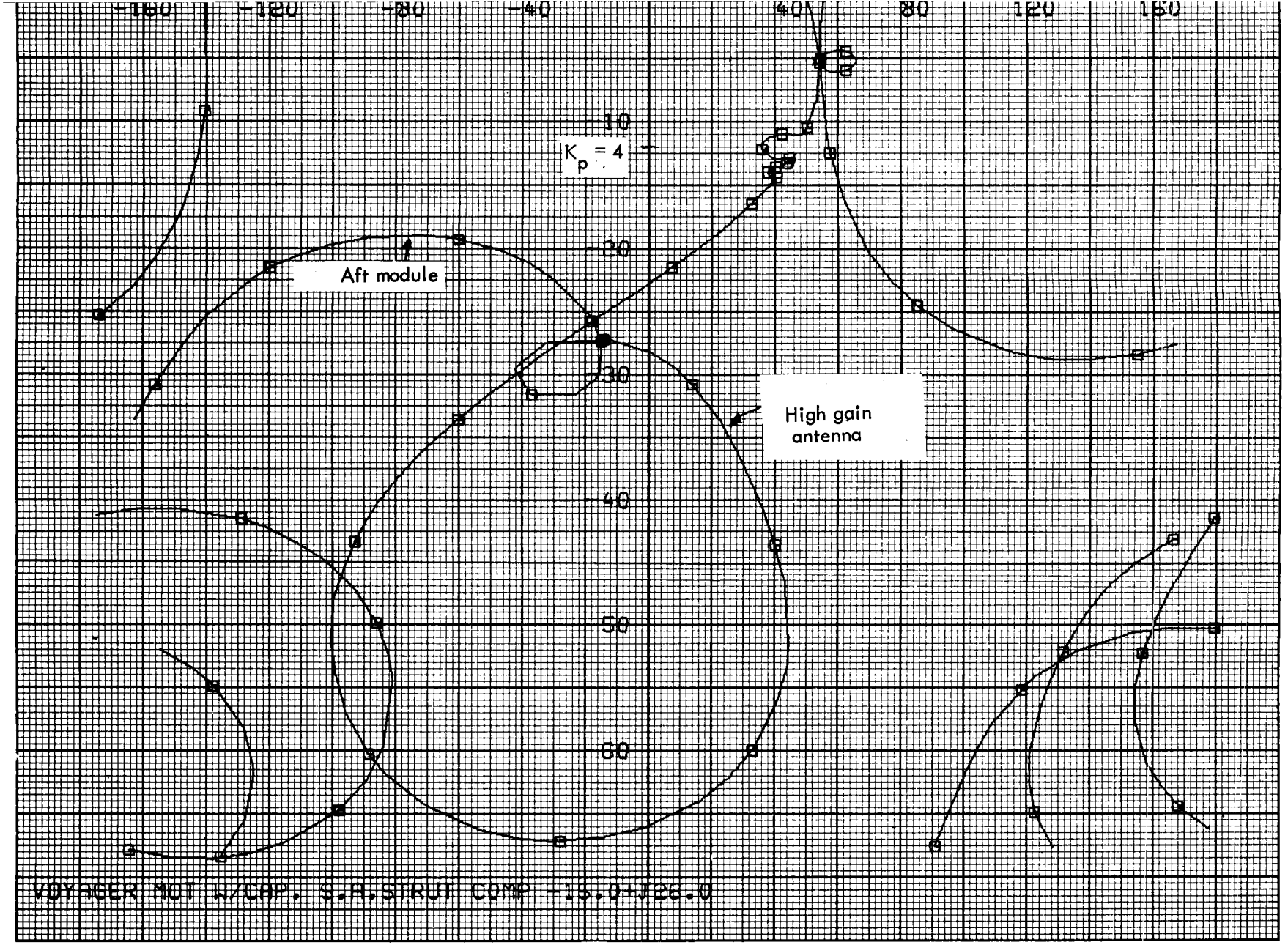

Figure 80. Gain-Phase Plot, MOT, with Capsule, Solar Array Struts Added, Noise Filter Added at ω = 30 Rad/Sec

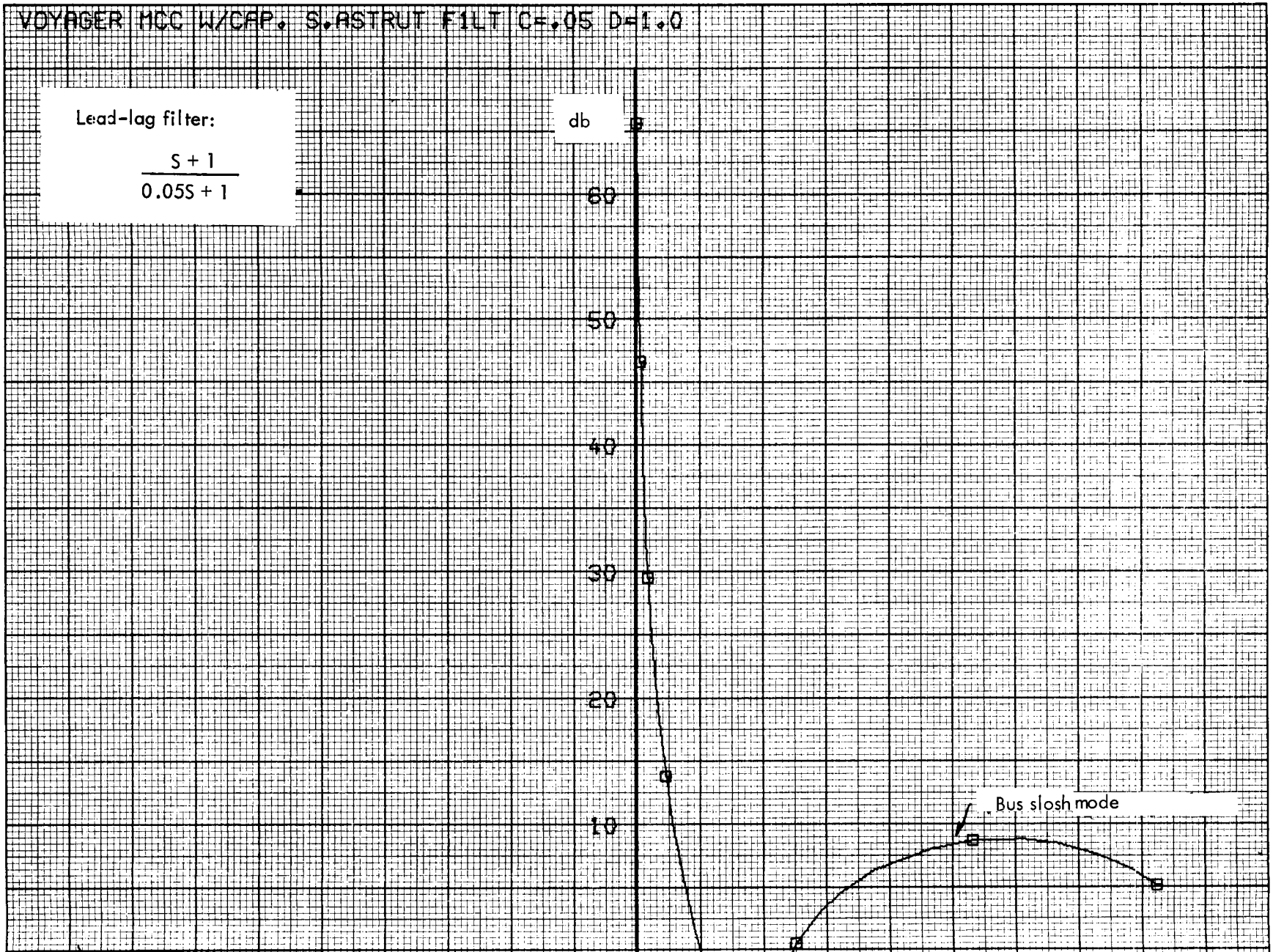
VOYAGER MCC W/CAP. S.ASTRUT FILT C=.05 D=1.0
Lead-lag filter:
S + 1
0.05S + 1
db
60
50
40
30
20
10
Bus slosh mode

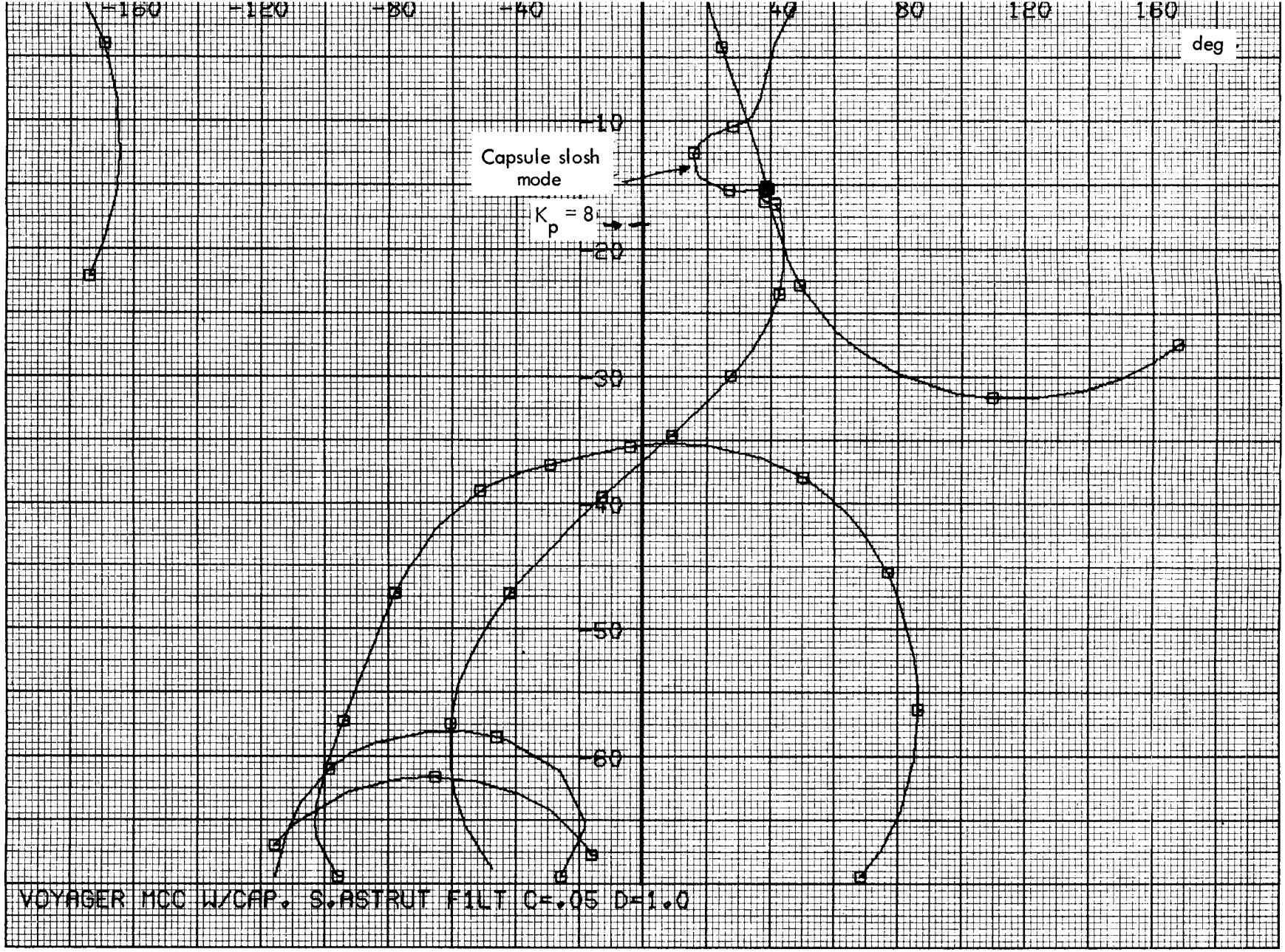

Figure 81. Gain-Phase Plot, MCC, with Capsule, Solar Array Struts Added, Lead-Lag Filter Change

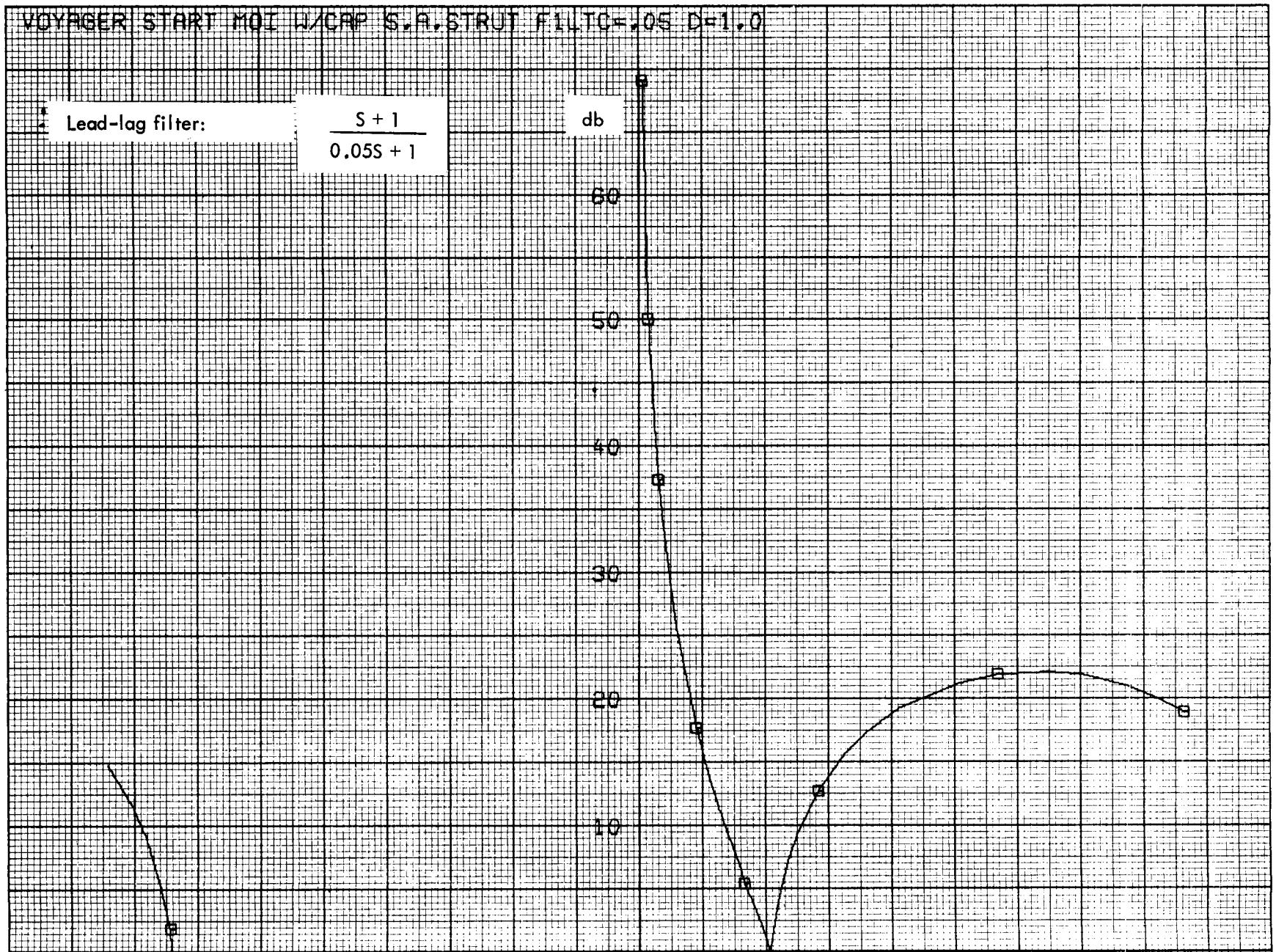
VOYAGER START MOT W/CAP S.A.STRUT FILTC=.05 D=1.0
Lead-lag filter:
S + 1
0.05S + 1
db
60
50
40
30
20
10

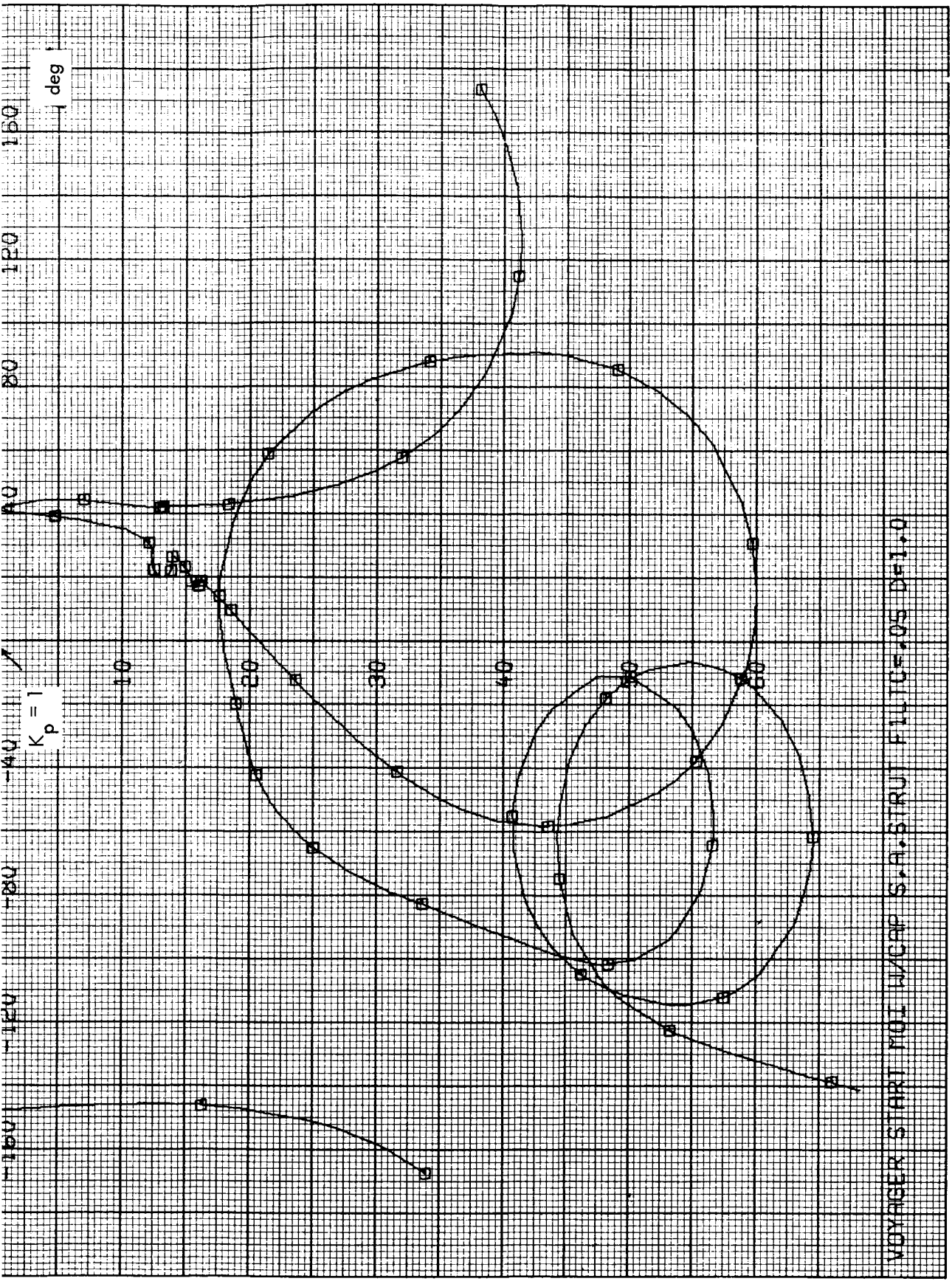

Figure 82. Gain-Phase Plot, Start MOI, with Capsule, Solar Array Struts Added, Lead-Lag Filter Change

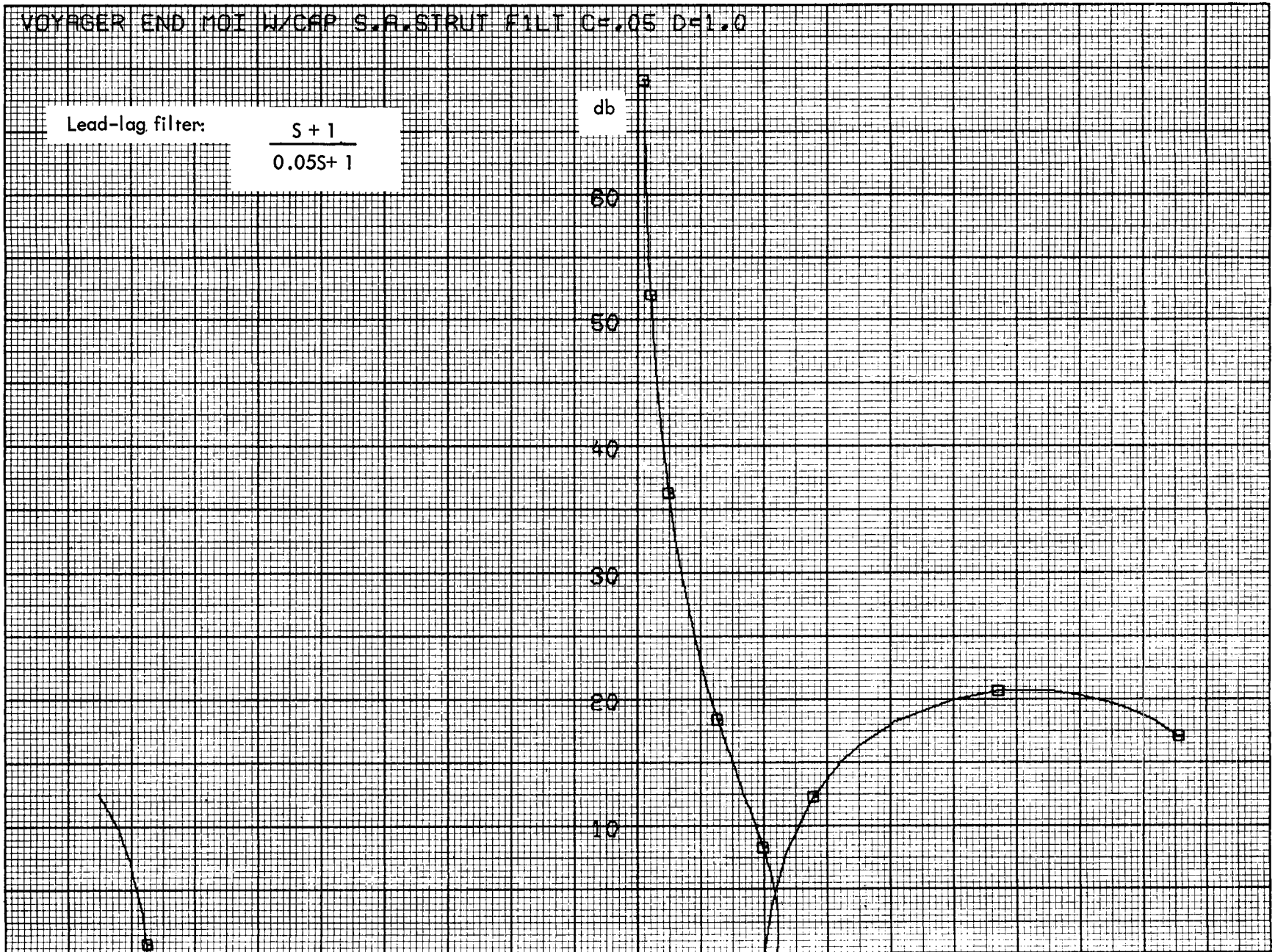
VOYAGER END MOI W/CAP S.A.STRUT FILT C=.05 D=1.0
Lead-lag filter:
S + 1
0.05S+ 1
db
60
50
40
30
20
10

181

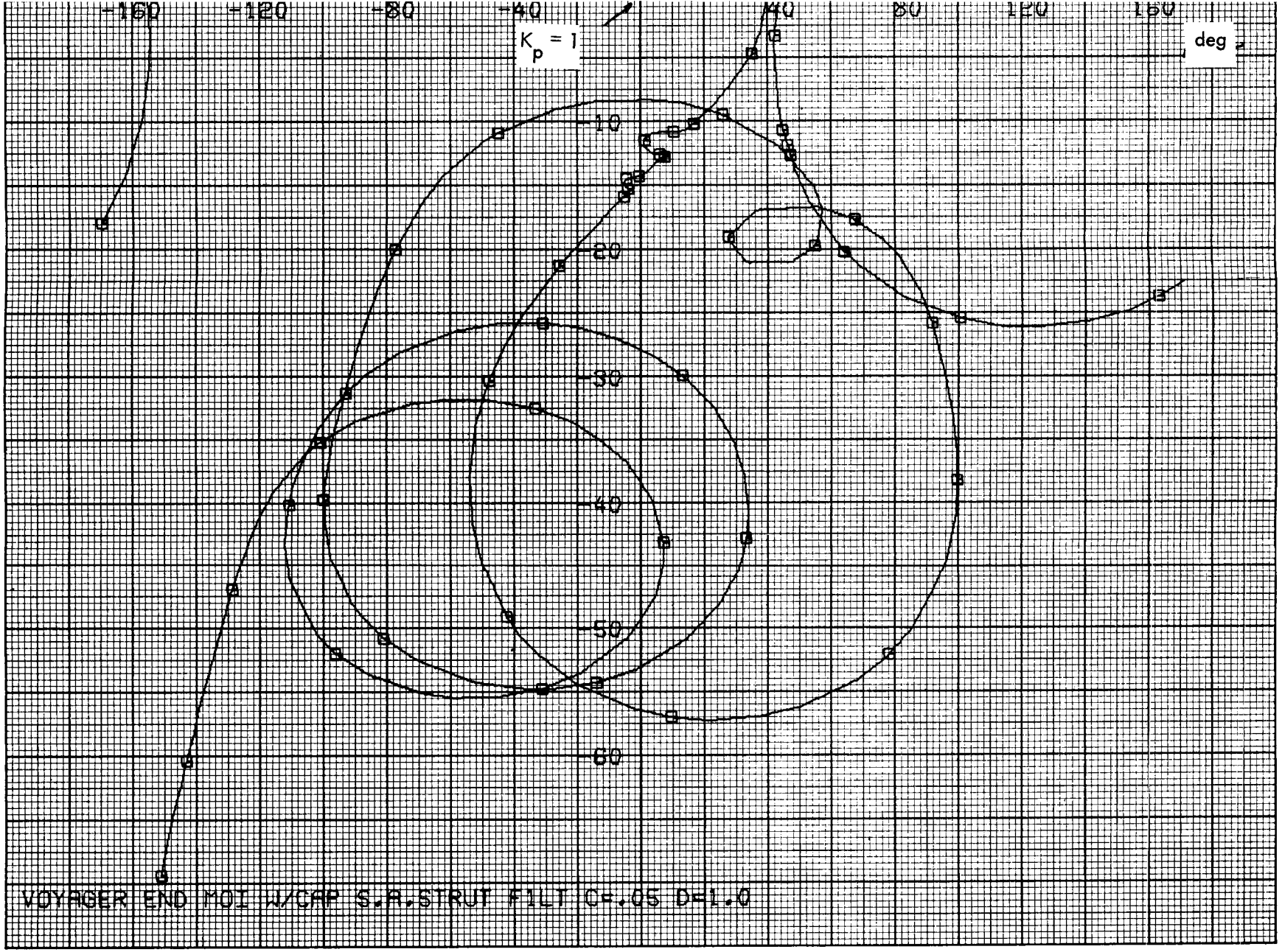

Figure 83. Gain-Phase Plot, End MOI, with Capsule, Solar Array Struts Added, Lead-Lag Filter Change

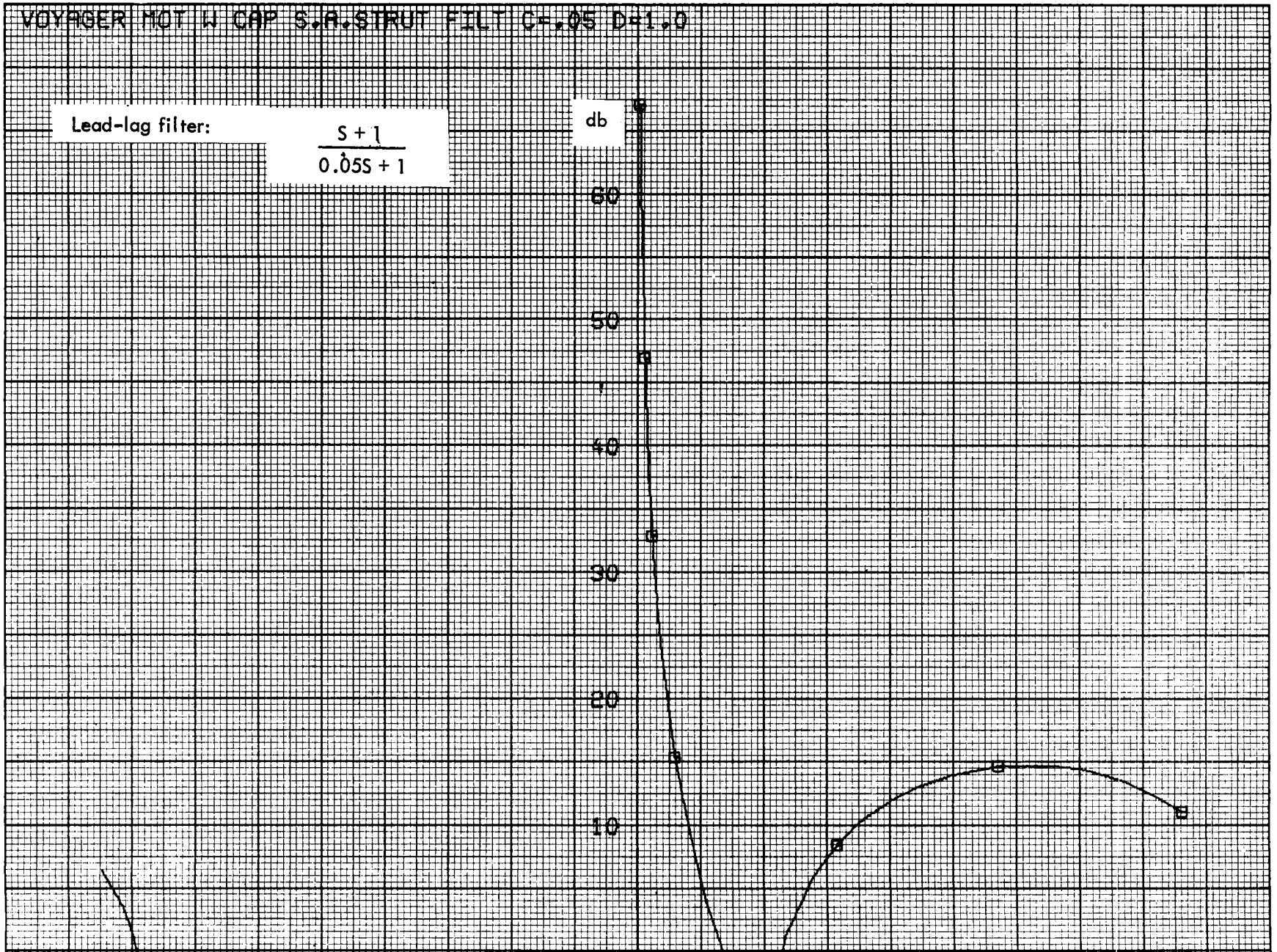
VOYAGER MOT W CAP S.A.STRUT FILT C=.05 D=1.0
Lead-lag filter:
S + 1
0.05S + 1
db
60
50
40
30
20
10

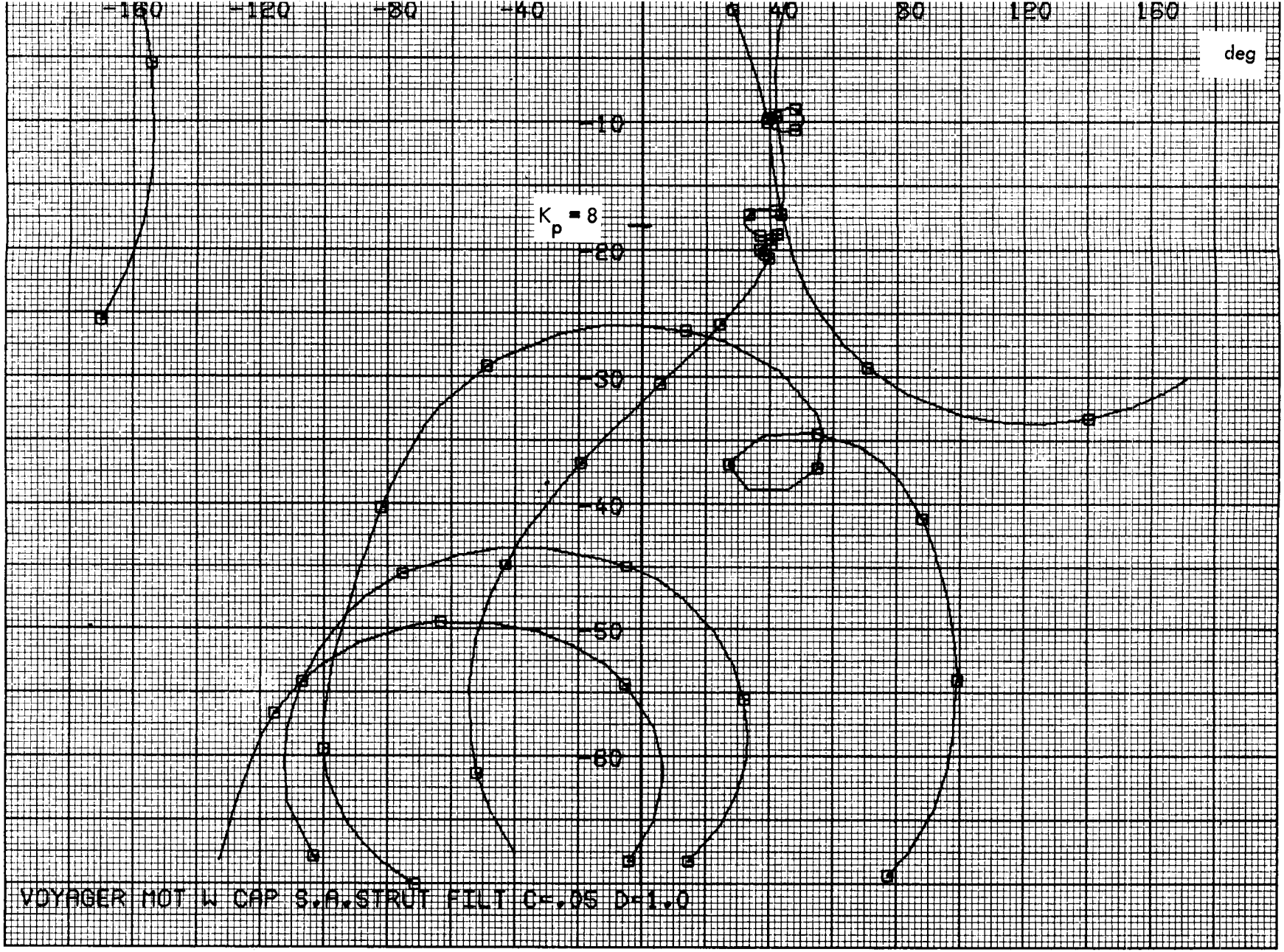

Figure 84. Gain-Phase Plot, MOT, with Capsule, Solar Array Struts Added, Lead-Lag Filter Change

vector misalignments only, if an integral attitude feedback loop were employed. Similarly, the cross velocity errors due to offsets alone are nullified if an integral engine angle feedback loop were also included with the integral attitude feedback loop. These possibilities are shown in Figure 53 where the two feedback loops could be excluded by setting the integrator gains to zero.

The magnitude of the integrator gain determines how quickly the cross velocity errors were nullified, the larger gain giving faster nulling response. However, degradation of the rigid body phase margin and low frequency gain margin results as the integrator gain is increased, as evaluated in this section; therefore, a constraint upon the maximum integrator gain is established. In powered flight phases of shorter duration, relative to the integrator loop time constant, the integrator will be only partially effective in reducing cross velocity errors. For the Voyager mission, however, two sizable powered flight phases are certain to occur (MOI and the part of MCC in which separation of the two Voyager spacecraft are achieved to preclude simultaneous planetary arrival). The second (or possibly third) MCC firing phase and the MOT phase may also be of long duration relative to the integrator loop time constant. Because of at least two long duration firings, the use of integral feedback within the control system is desirable.

The suitable type of integral feedback will depend on the expected magnitudes of misalignments and offsets throughout the mission. One powered flight phase may require only integral attitude feedback. A different phase may require additional switching-in of the integral engine angle feedback loop. Evaluation of the thrust vector pointing errors with and without these integrators is given in Section 4.

3.8.1 Attitude and Engine Angle Integration

The set of start MOI gain-phase plots given in Figure 85 to 88 pertain to the integral attitude and engine angle feedback with integrator gains set at 0.125, 0.25, 0.5 and 1. The high frequency portion of the gain-phase plot is shown to be considerably distorted from those given before due primarily to the addition of integral engine angle feedback. The engine angle feedback represents a form of angular acceleration

feedback thereby having a pronounced effect upon the high frequency crossover on the gain-phase plot as shown in the figures. A low frequency rigid body gain constraint is therefore imposed where previously it was nonexistent as shown in Figures 72 to 75. Figure 85 shows that an integration gain of 0.125 for both engine angle and attitude feedback integrators is satisfactory. (There presently appears to be no clear advantage in setting these gains at different values.) Figure 86 shows that an integrator gain of 0.25 is barely tolerable. The next two figures show that integrator gains of 0.5 and 1 are completely out of the question.

Figure 89 shows the end of MOI stability margins with an integrator gain of 0.125. It is clear from this result that a lower gain for the low thrust powered flight phases is required. The integrator gain was reduced by the ratio of thrust levels to a value of 0.025. The results are shown in Figure 91. It is clear that this rationale for selection of the integrator gain is not accurate and that a larger gain is permissible. It is suspected that the correct adjustment in integrator gain due to a change only in thrust level may entail reduction of the gain by the square root of the ratio rather than direct application of it. This point was set aside for future evaluation.

Figures 92 and 93 show the gain-phase plots for the MOT phase with integrator gains of 0.125 and 0.02, respectively. A gain of 0.125 is again shown to be unsatisfactory and a gain of 0.025 is shown to be acceptable but less than the maximum allowable.

3.8.2 Attitude Integration Only

The results of adding only an integral attitude feedback loop is contained herein. A gain of 0.125 and 0.25 were employed in the start MOI case and are shown to be identical at high frequencies when compared to Figure 73. The basic difference occurs at the low frequencies with a crossover of the stability boundary thereby imposing a lower gain margin on the control system. Both plots appeared to have acceptable stability margins. A gain of 0.125 was employed for the other three mission phases and are shown in Figures 96 through 98. It is interesting to note that a change in thrust level does not require a change in integrator gain for the integral attitude feedback design, this being contrary to the results for the added integral engine angle feedback design.

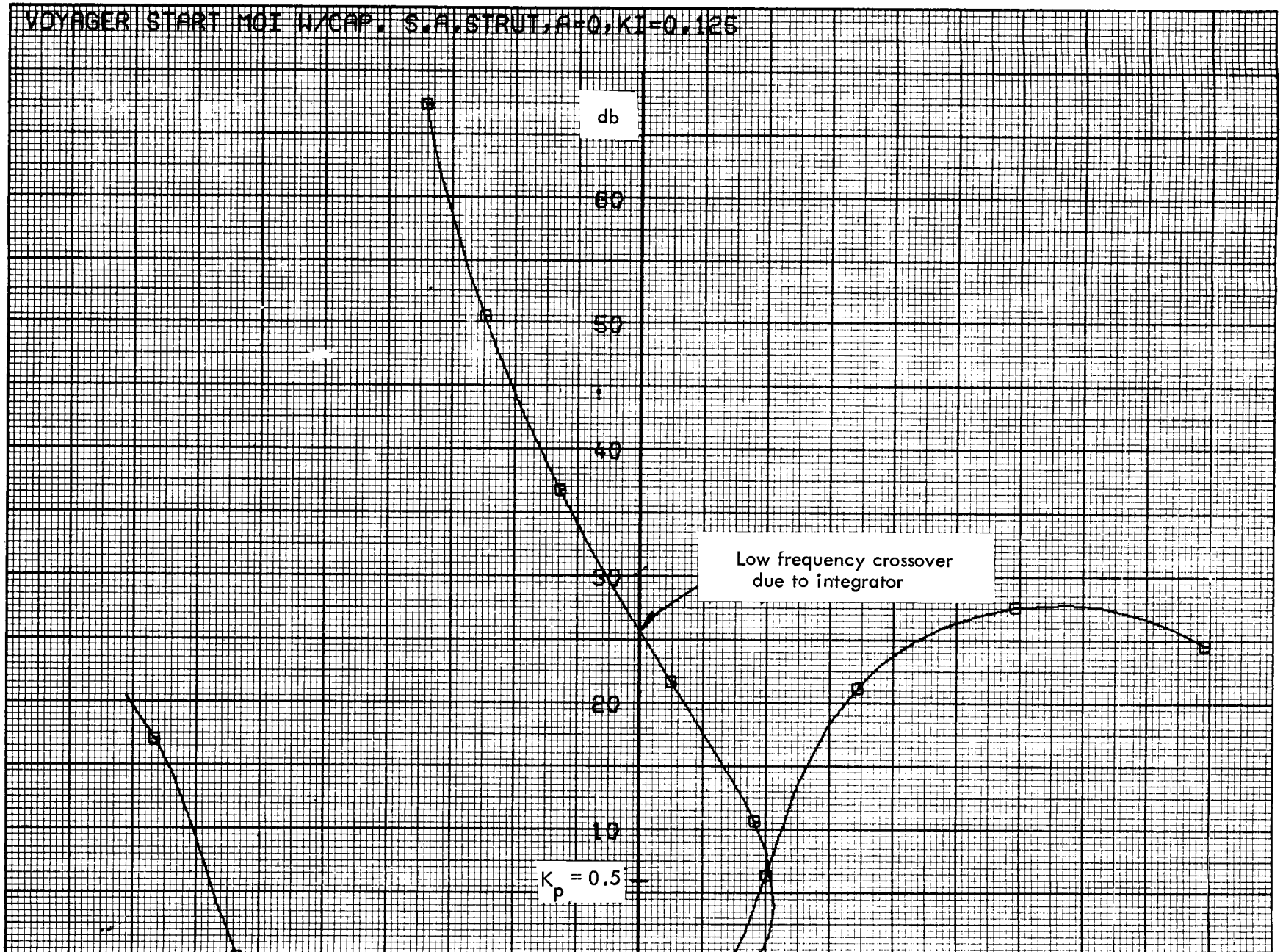
VOYAGER START MOI W/CAP. S.A.STRUT, A=0, KI=0.125
db
60
50
40
30
20
10
Low frequency crossover
due to integrator
$K_p = 0.5$

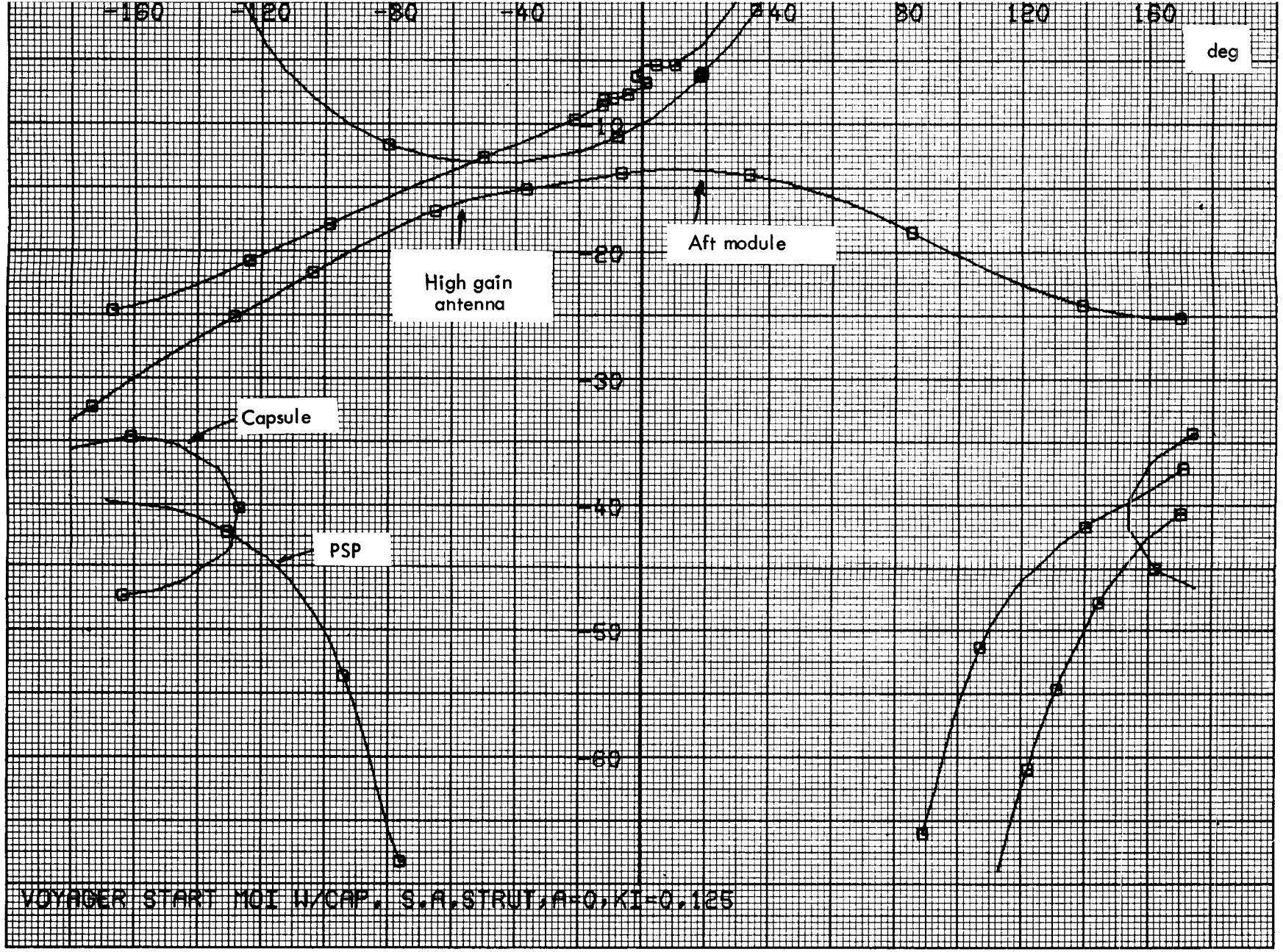

Figure 85. Gain-Phase Plot, Start MOI, with Capsule, Solar Array Struts Added, Integral Attitude and Engine Angle Feedback, K_I = 0.125

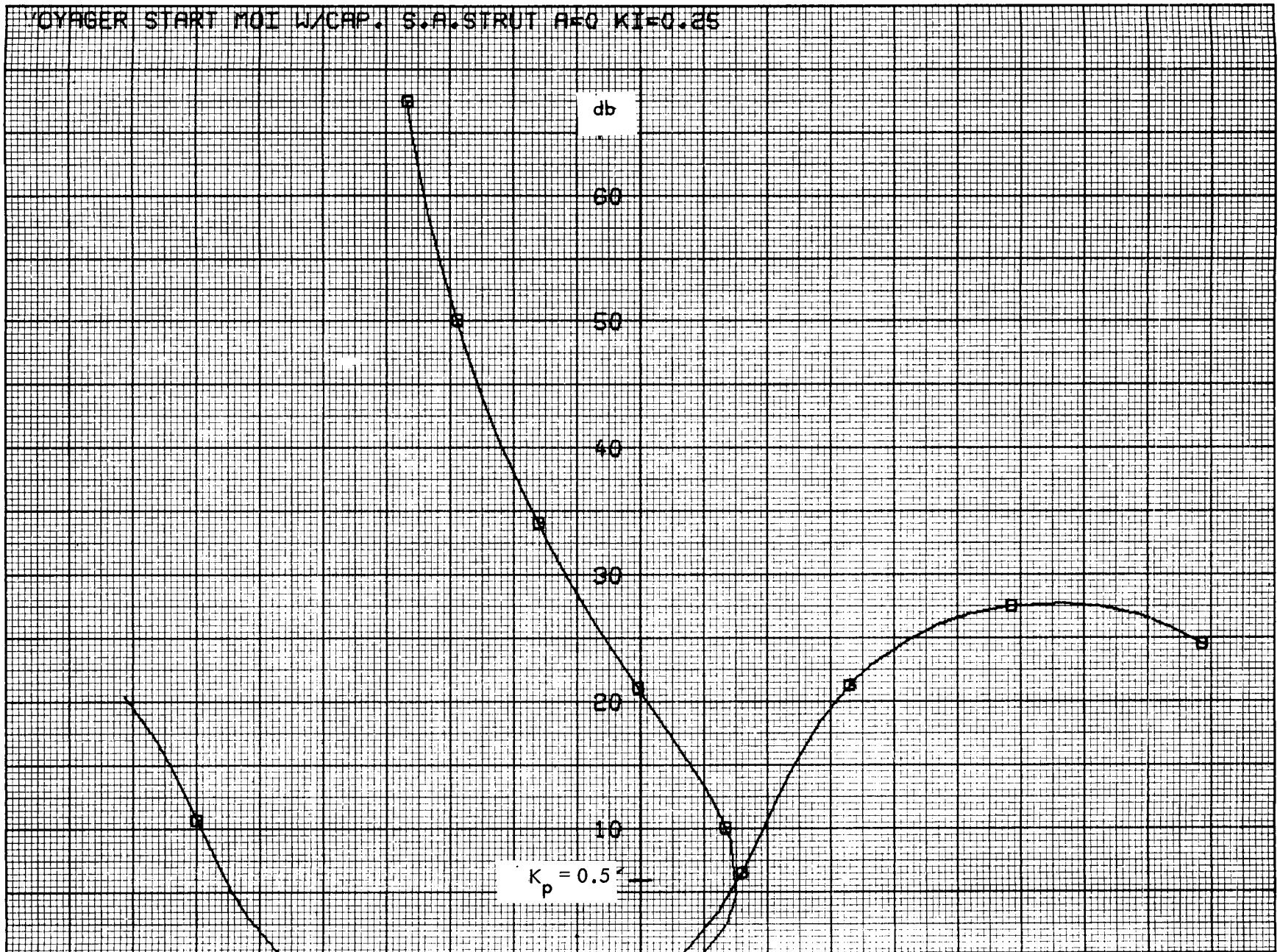
VOYAGER START MOI W/CAP. S.A.STRUT A=0 KI=0.25
db
60
50
40
30
20
10
$K_p = 0.5$

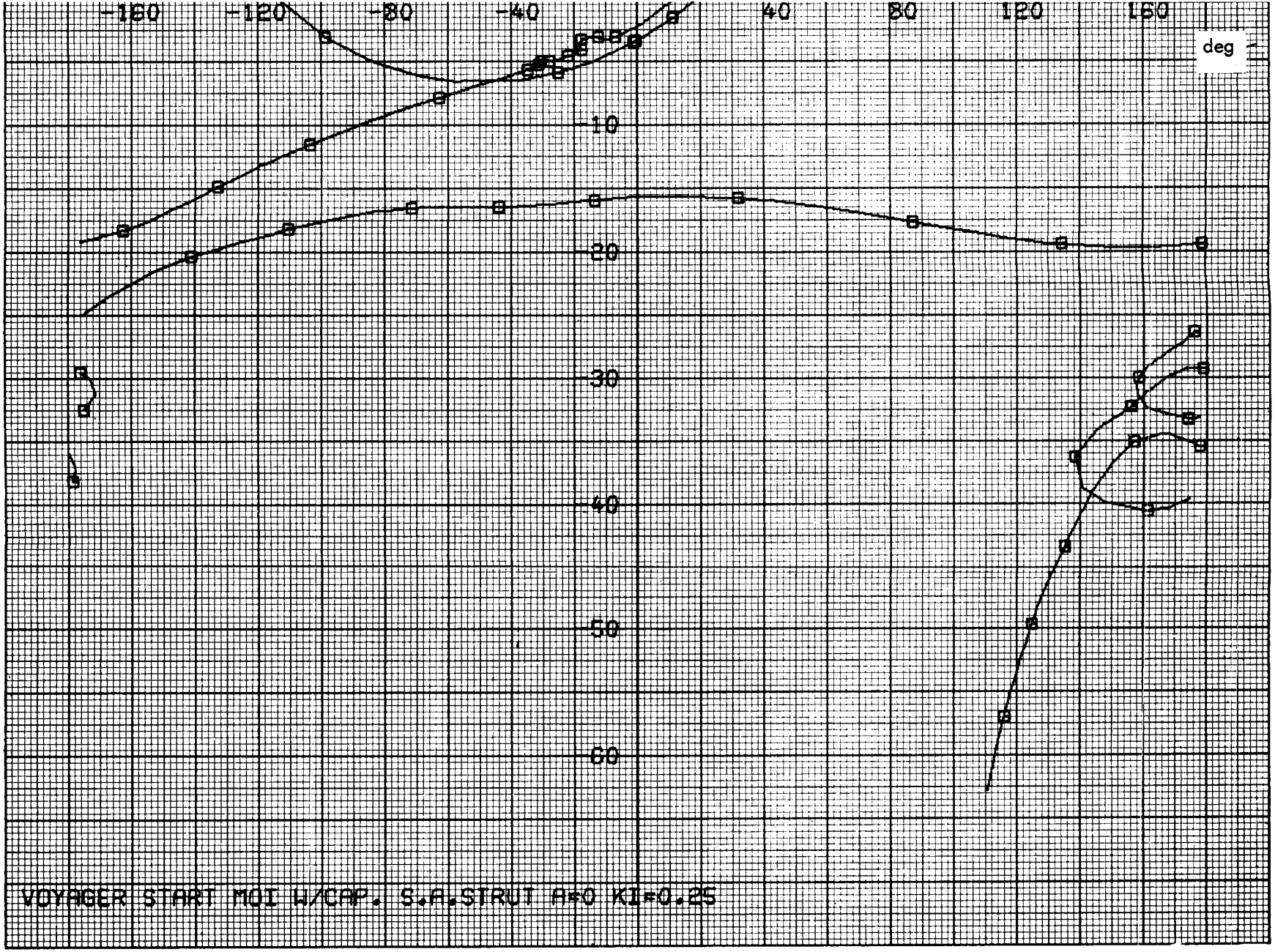

Figure 86. Gain-Phase Plot, Start MOI, with Capsule, Solar Array Struts Added, Integral Attitude and Engine Angle Feedback, K_I = 0.25

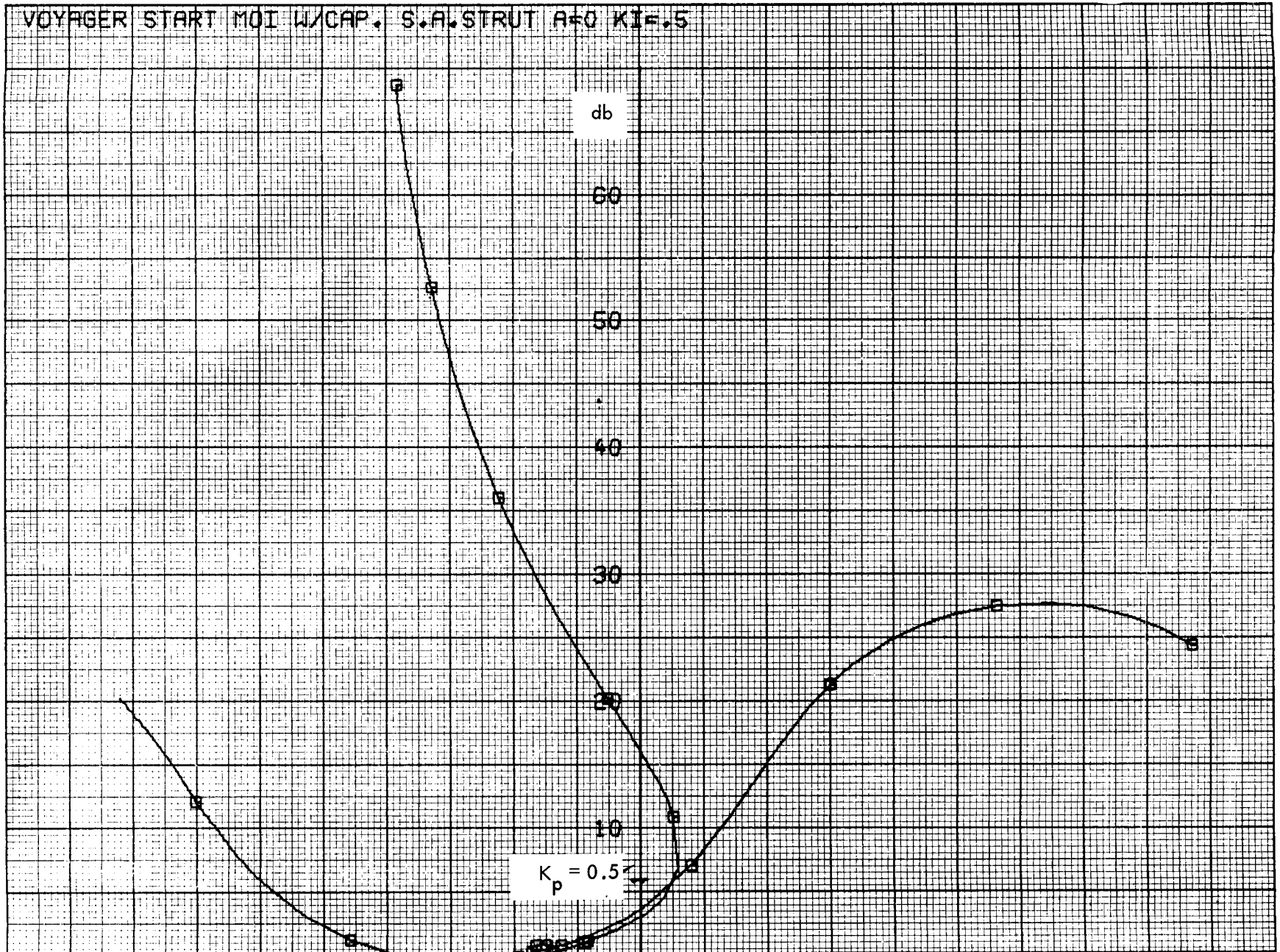
VOYAGER START MOI W/CAP. S.A.STRUT A=0 KI=.5
db
60
50
40
30
20
10
$K_p = 0.5$

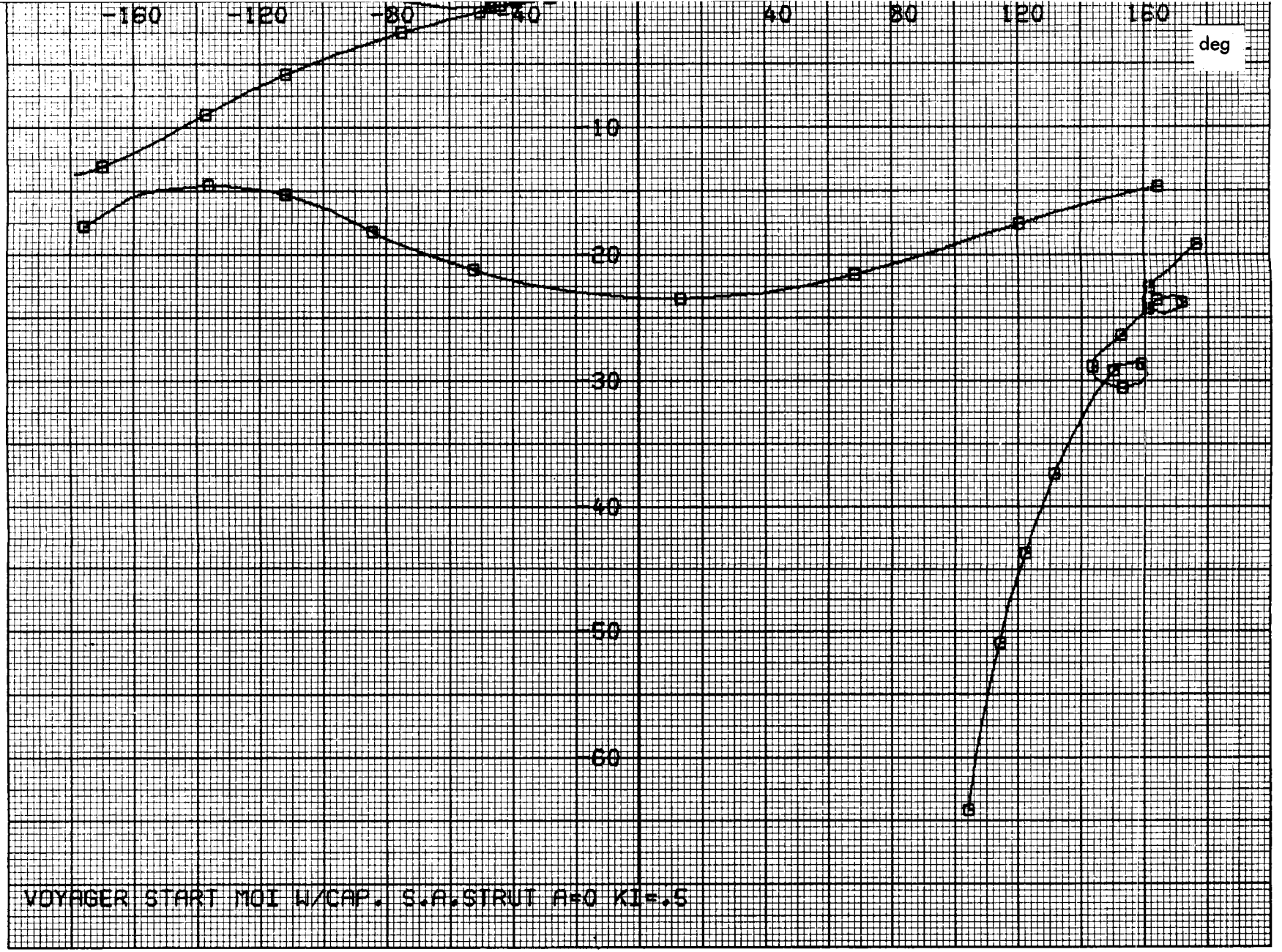

Figure 87. Gain-Phase Plot, Start MOI, with Capsule, Solar Array Struts Added, Integral Attitude and Engine Angle Feedback, K_I = 0.5

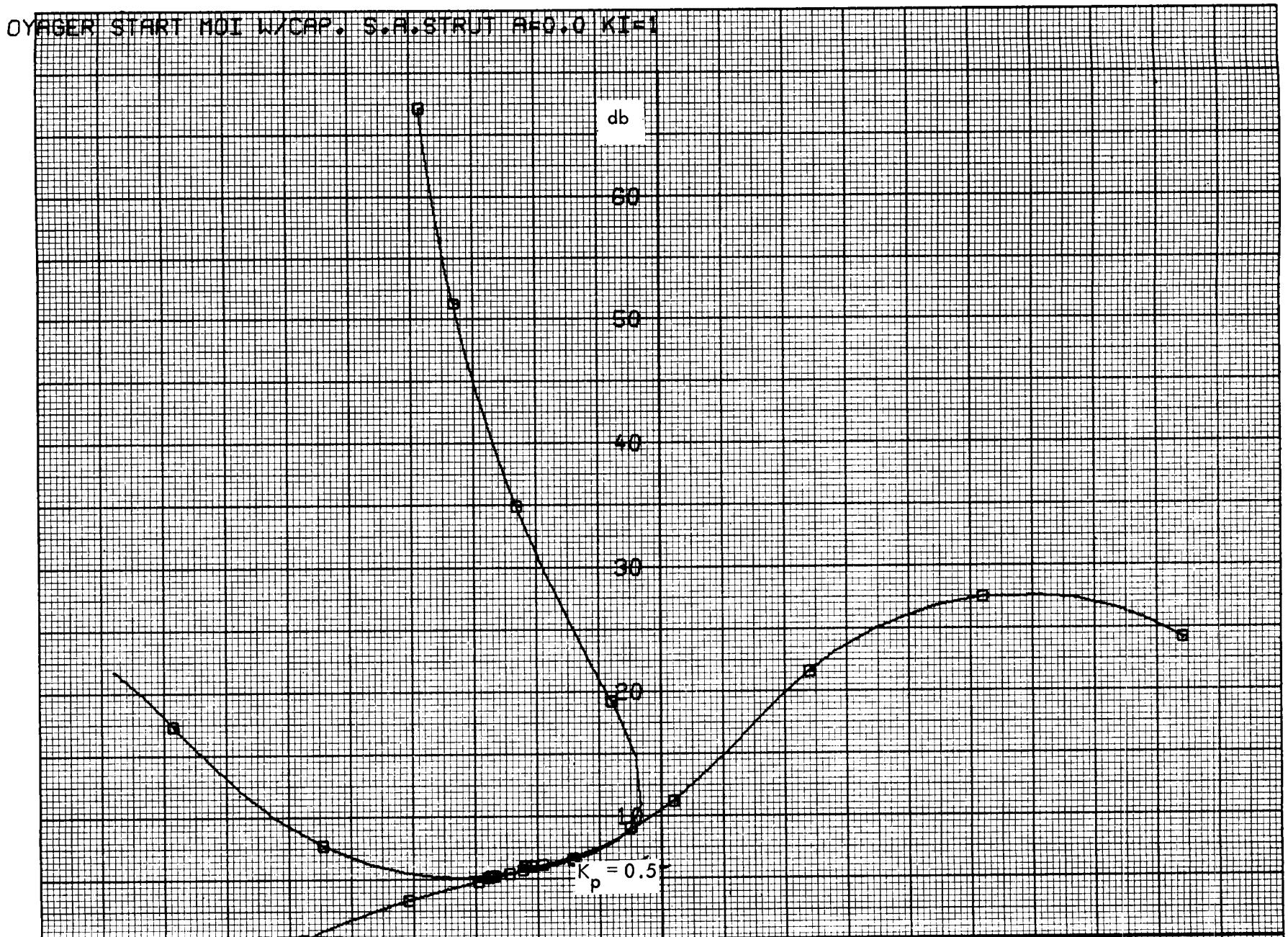
OYAGER START MOI W/CAP. S.R.STRUT A=0.0 KI=1
db
60
50
40
30
20
10
$K_p = 0.5$

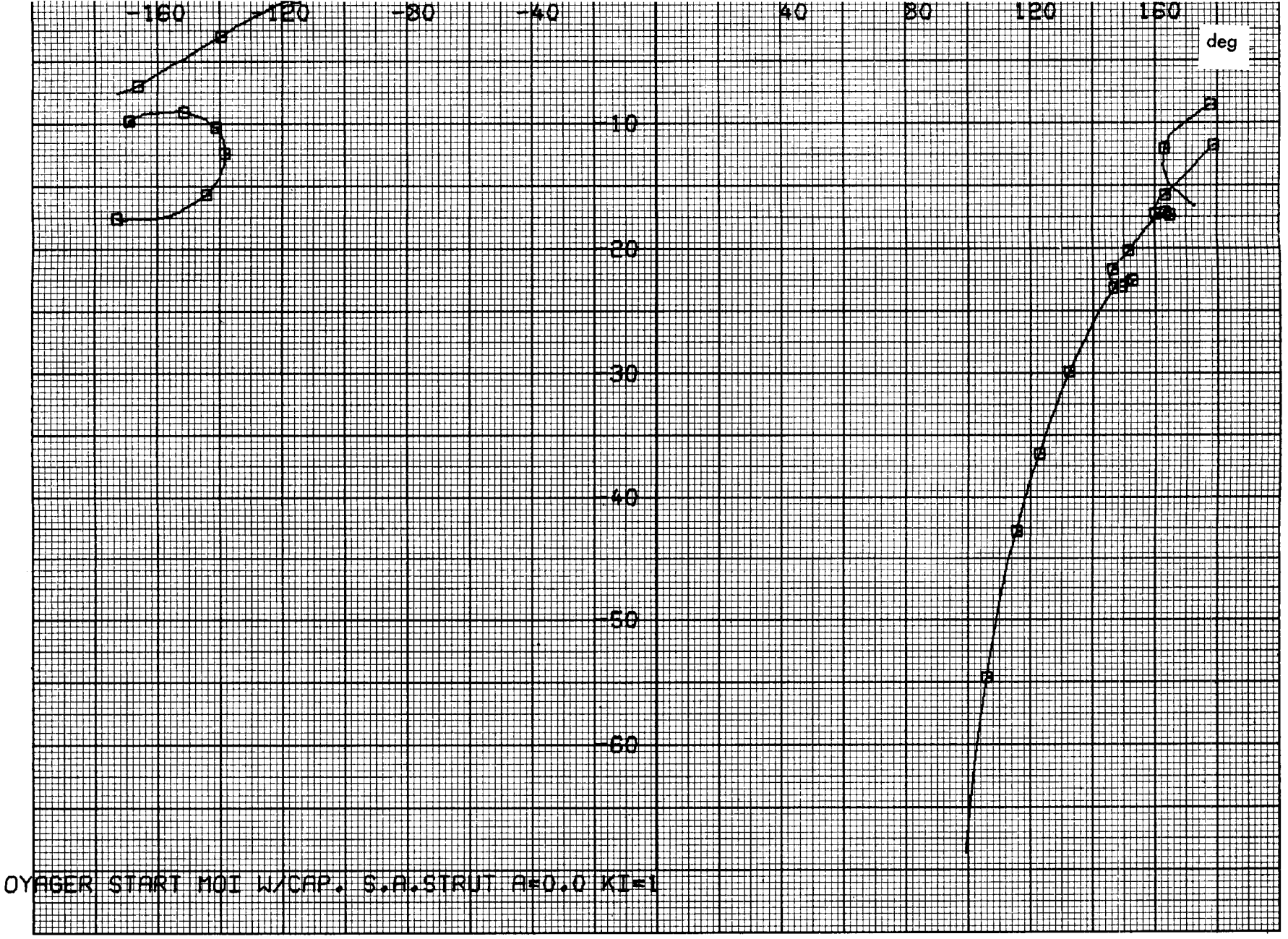

Figure 88. Gain-Phase Plot, Start MOI, with Capsule, Solar Array Struts Added, Integral Attitude and Engine Angle Feedback, K_I = 1.0

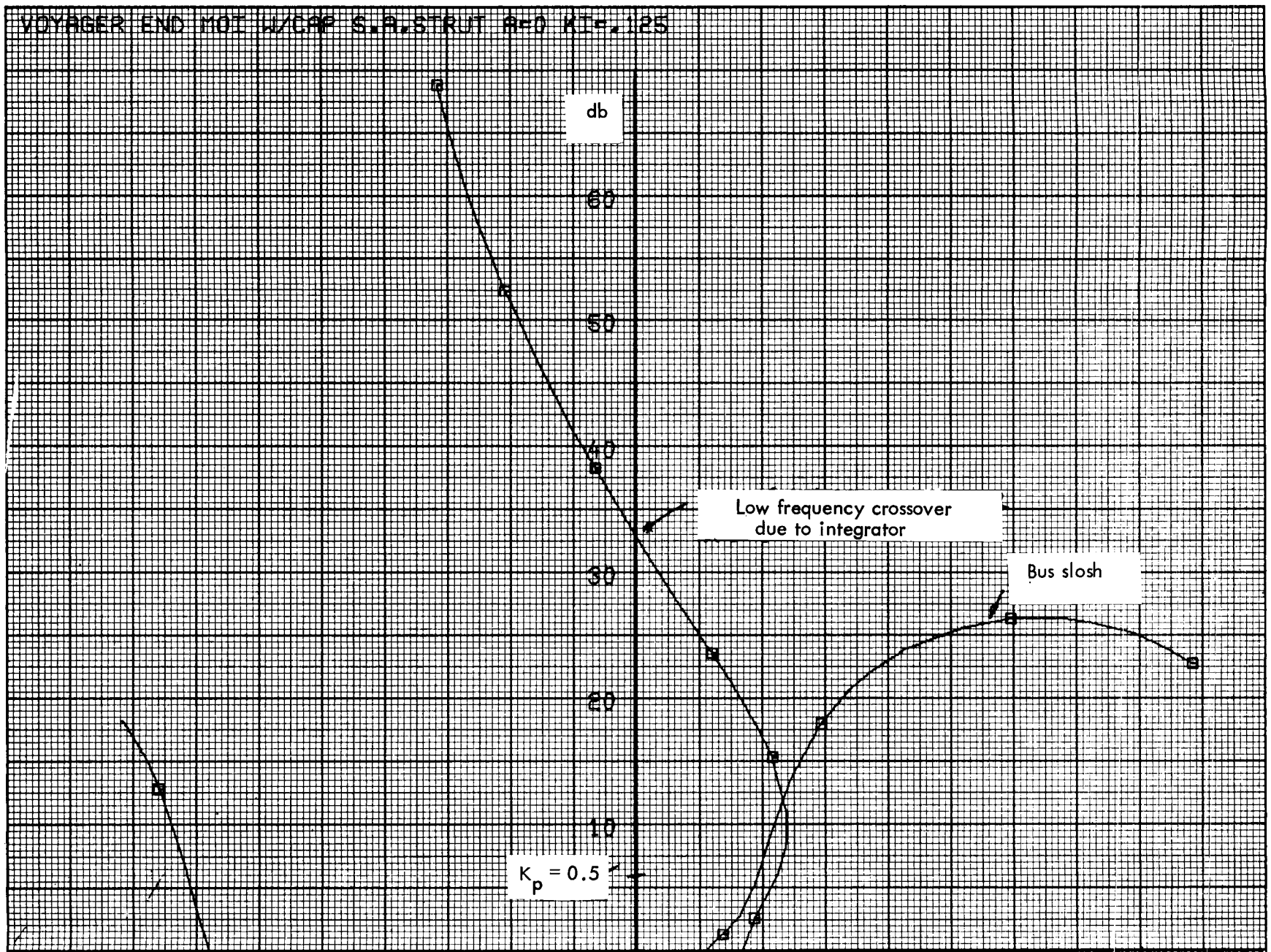
VOYAGER END MOI W/CAP S.A.STRUT A=0 KI=.125
db
60
50
40
30
20
10
Low frequency crossover
due to integrator
Bus slosh
$K_p = 0.5$

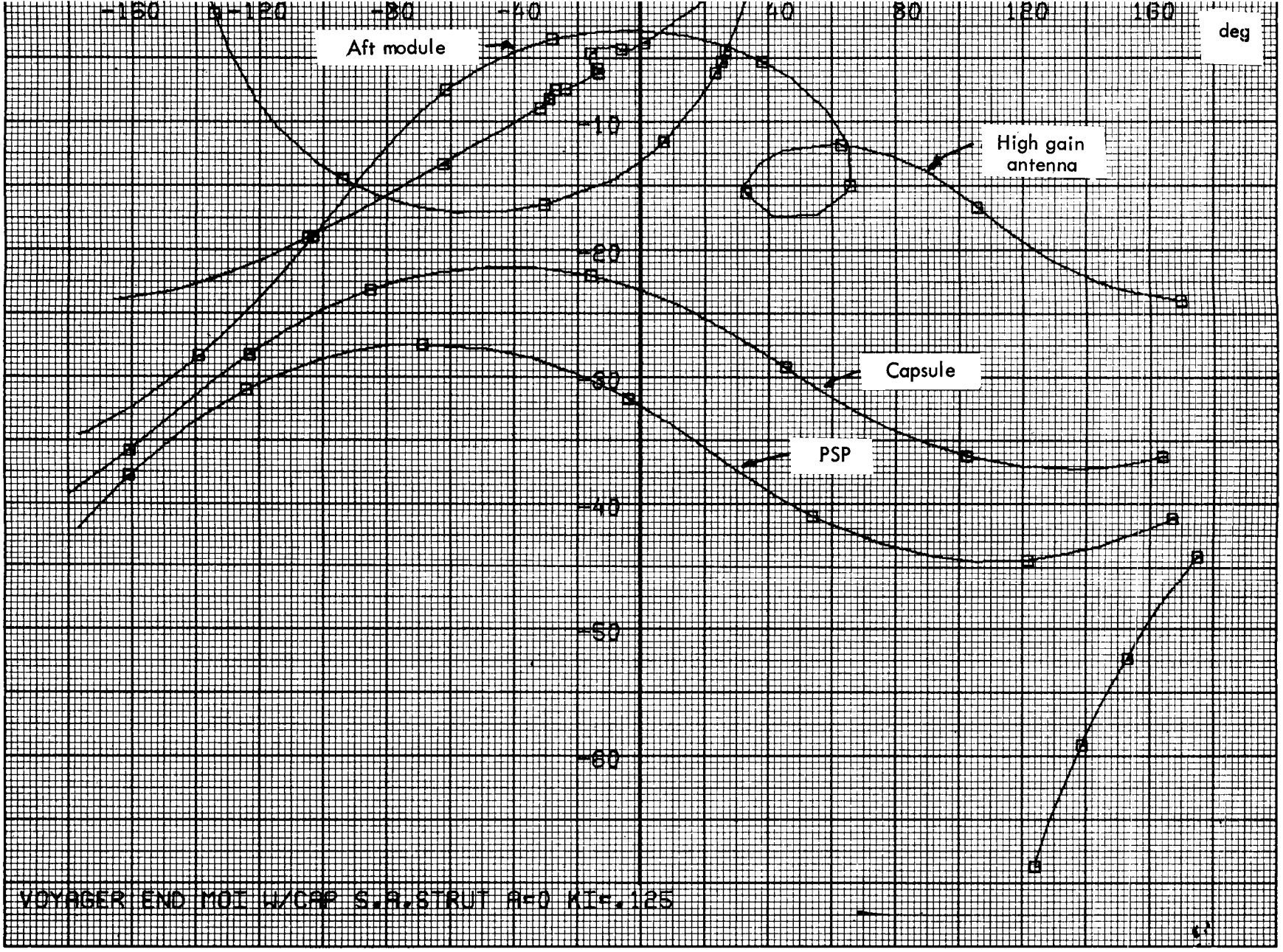

Figure 89. Gain-Phase Plot, End MOI, with Capsule, Solar Array Struts Added, Integral Attitude and Engine Angle Feedback, K_I = 0.125

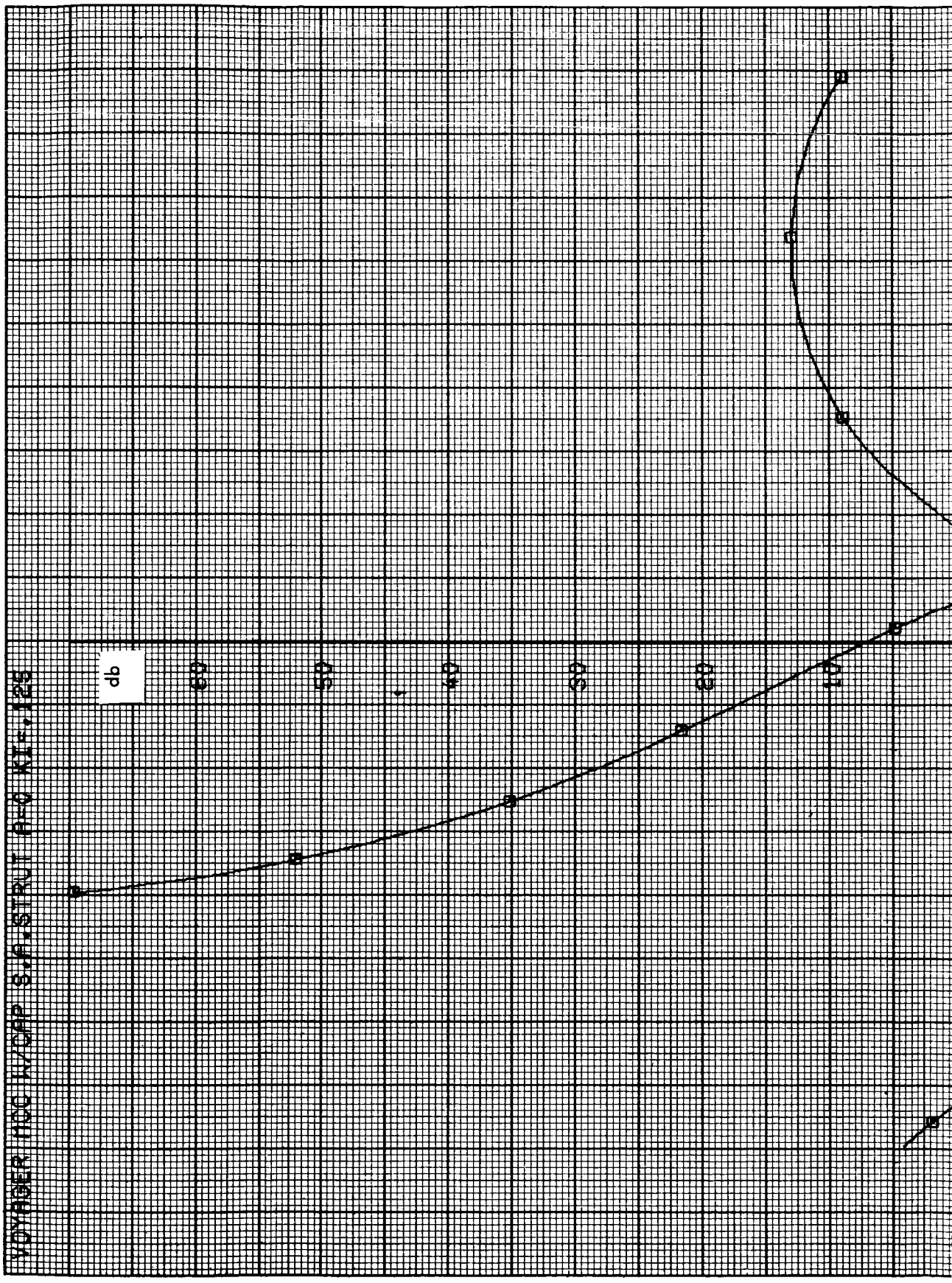
db
60
50
40
30
20
VOYAGER HGC IK/SAP S.F. STRUT PRE KIT #125

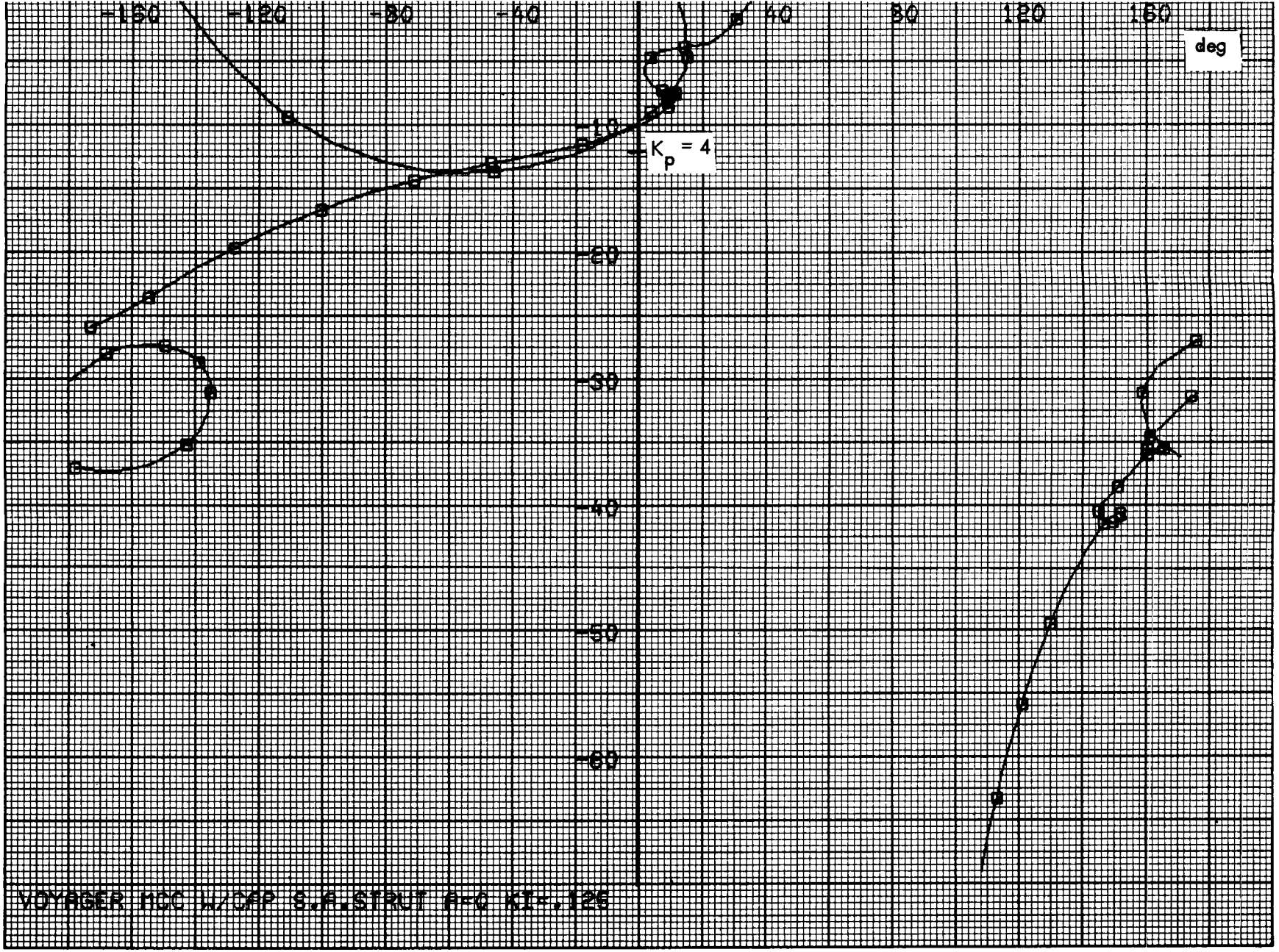

Figure 90. Gain-Phase Plot, MCC, with Capsule, Solar Array Struts Added, Integral Attitude and Engine Angle Feedback, K_I = 0.125

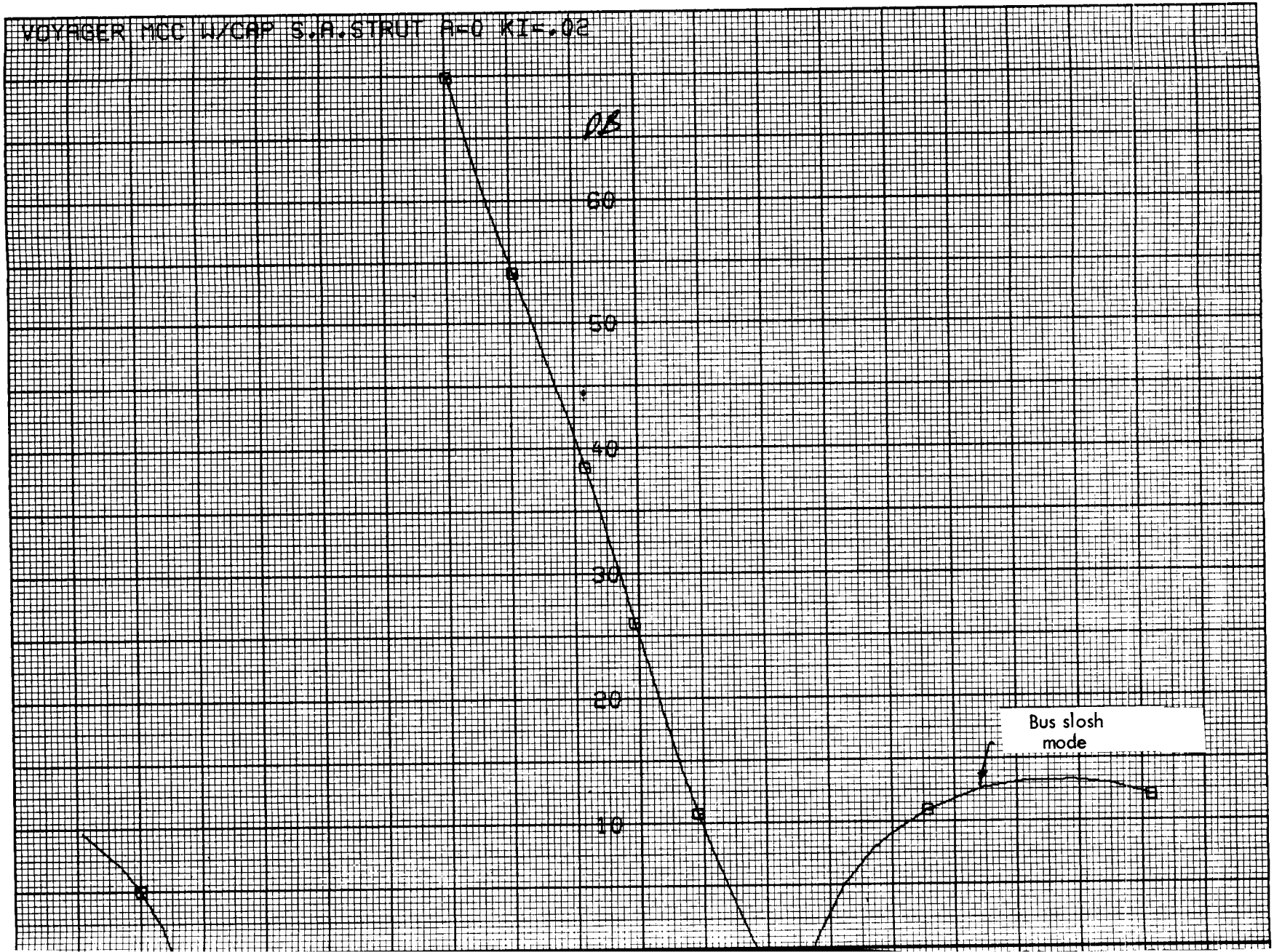
VOYAGER MCC W/CAP S.A.STRUT A=0 KI=.02
60
50
40
30
20
10
Bus slosh mode

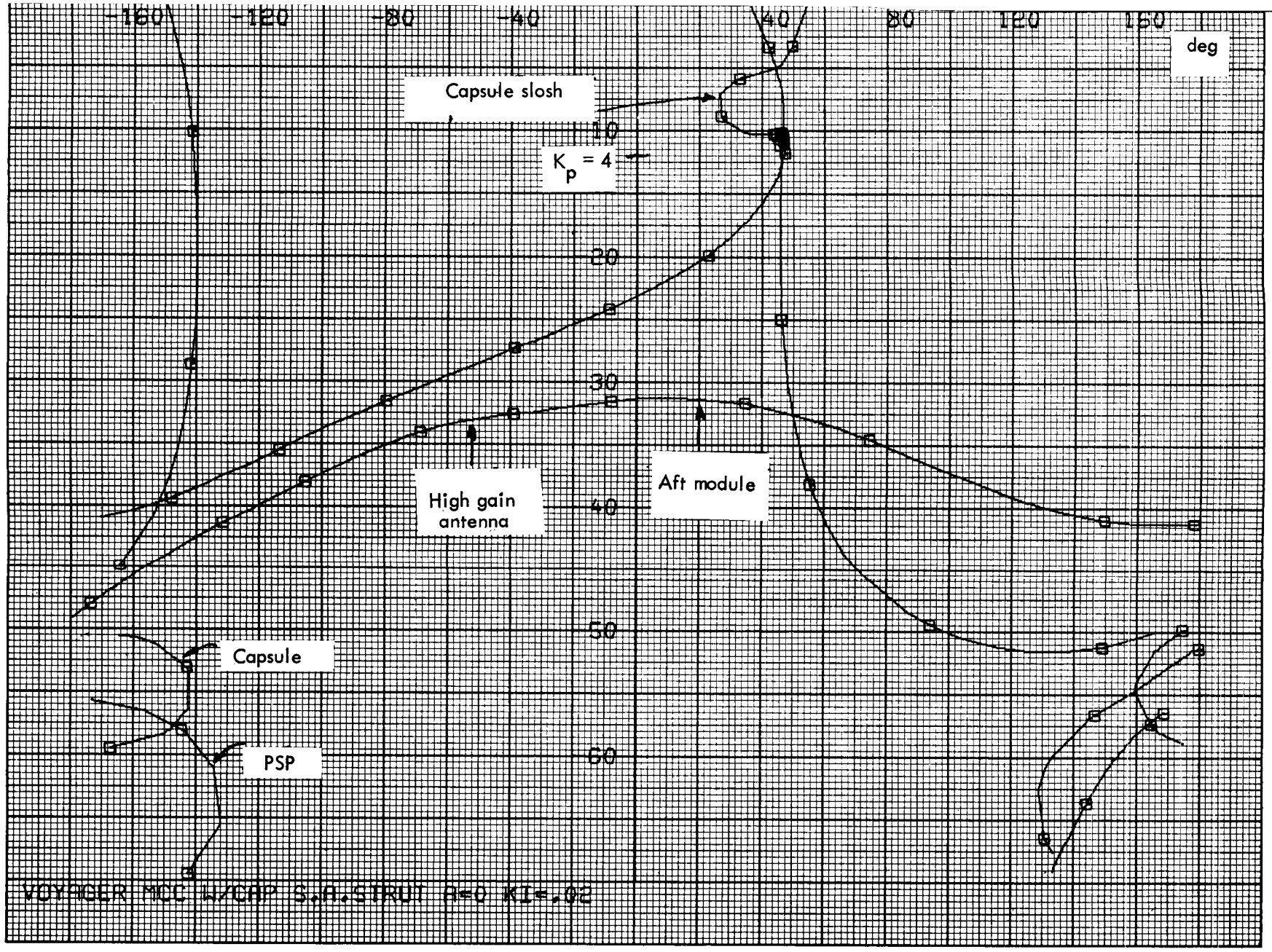

Figure 91. Gain-Phase Plot, MCC, with Capsule, Solar Array Struts Added, Integral Attitude and Engine Angle Feedback, $K_I = 0.02$

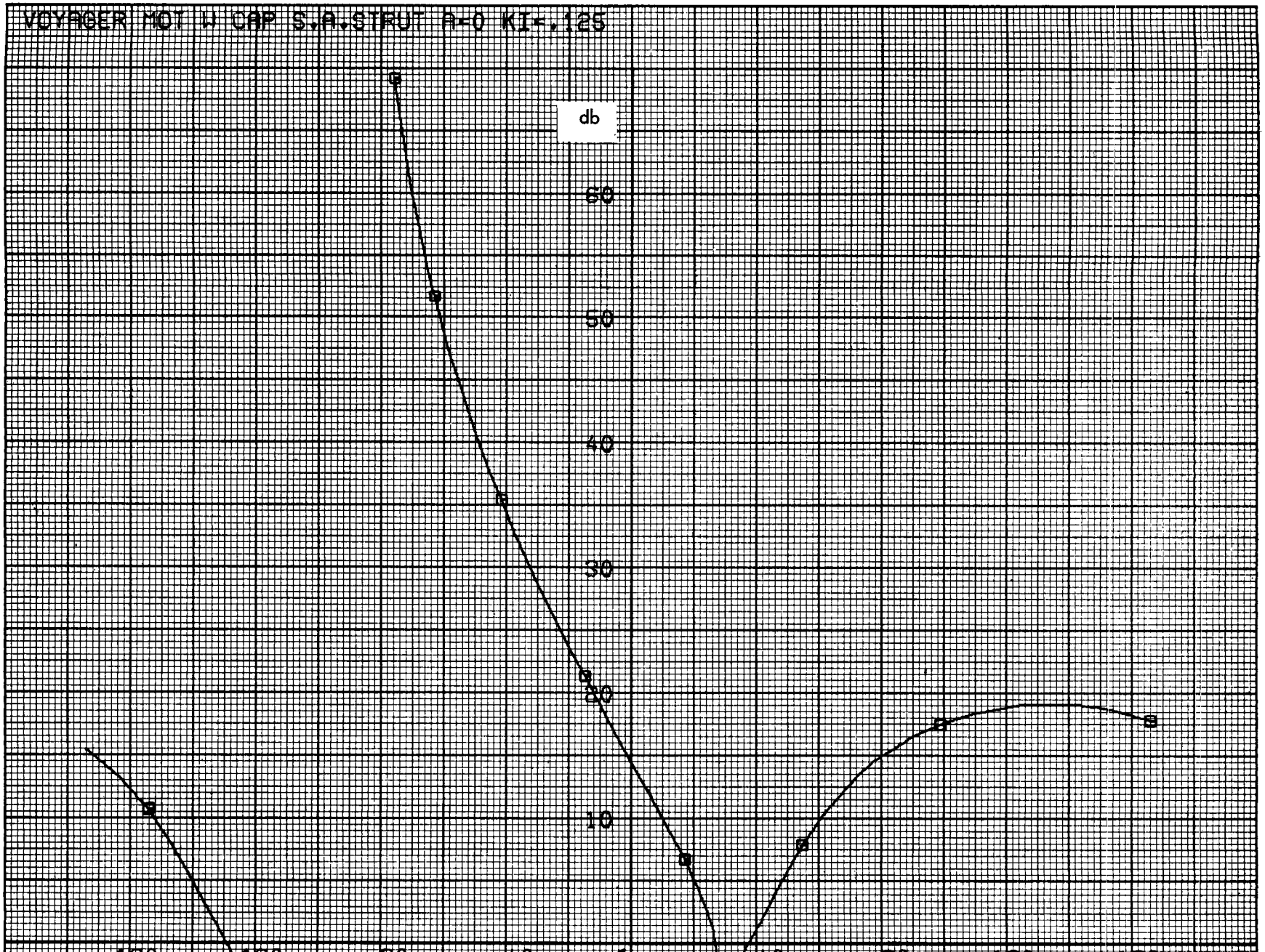
VOYAGER HGT W CAP S.A.STRUT A=0 KI=.125
db
60
50
40
30
20
10

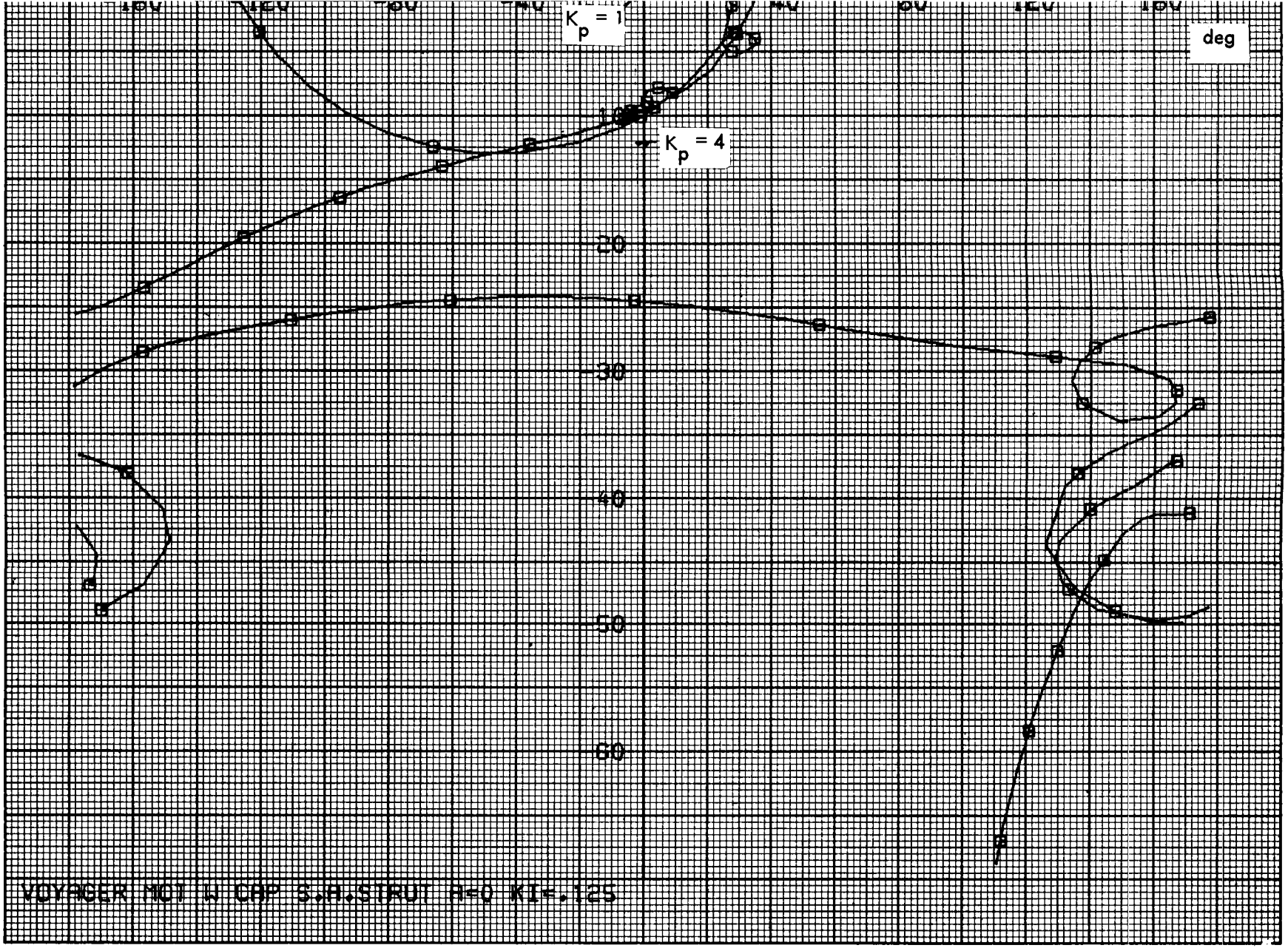

Figure 92. Gain-Phase Plot, MOT, with Capsule, Solar Array Struts Added, Integral Attitude and Engine Angle Feedback, $K_I = 0.125$

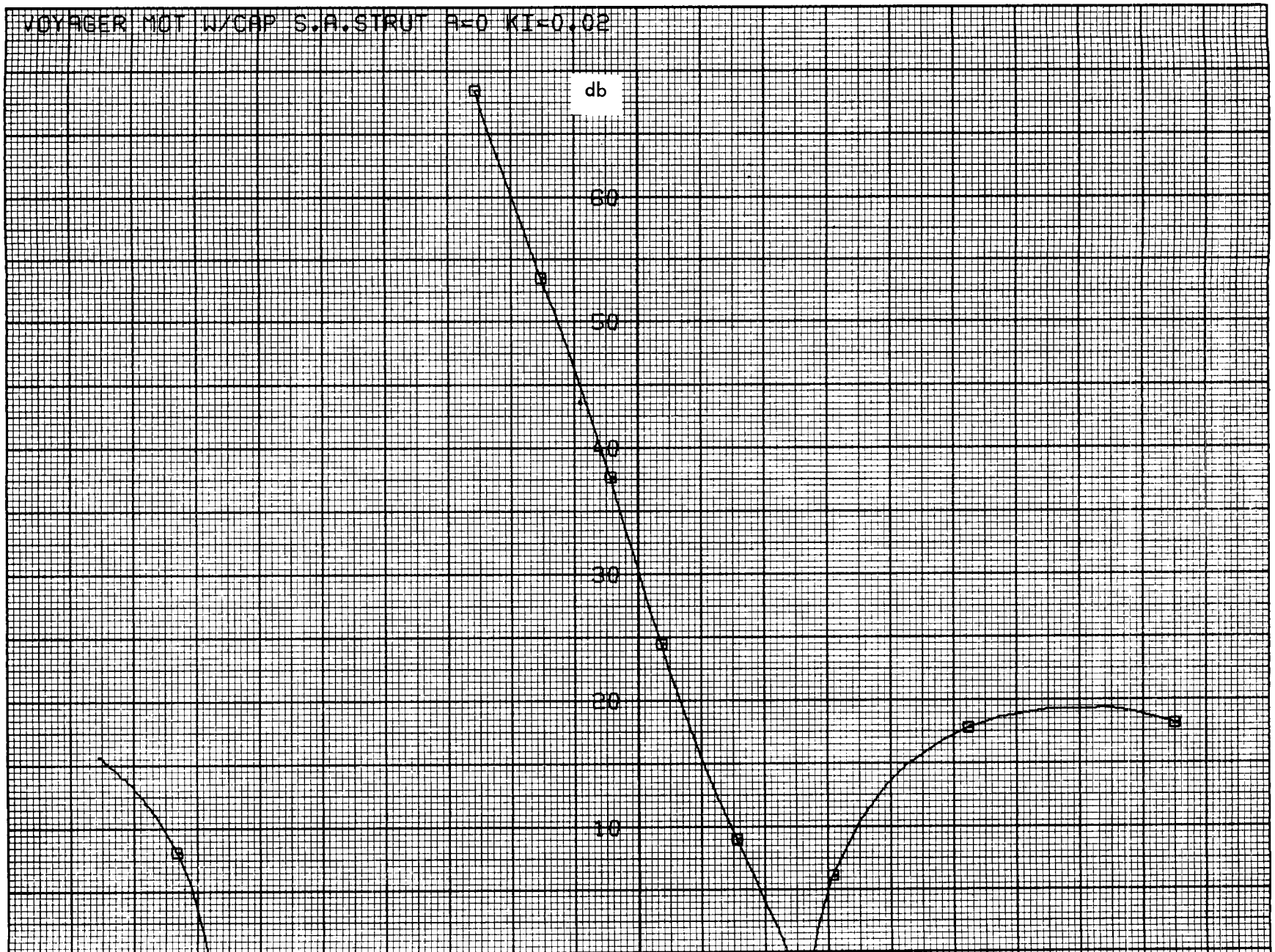
VOYAGER MOT W/CAP S.A.STRUT A=0 KI=0.02
db
60
50
40
30
20
10

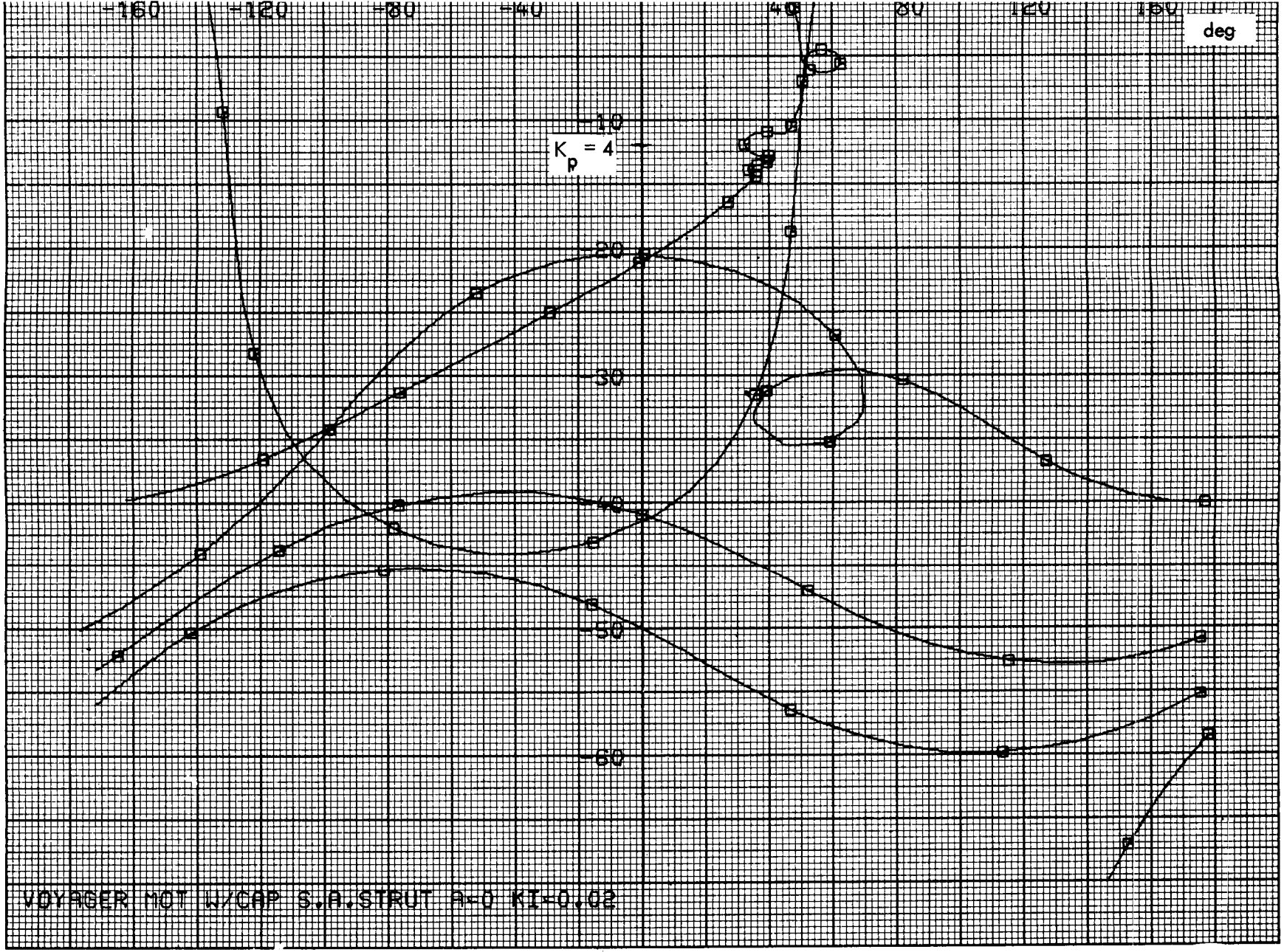

Figure 93. Gain-Phase Plot, MOT, with Capsule, Solar Array Struts Added, Integral Attitude and Engine Angle Feedback, $K_I = 0.02$

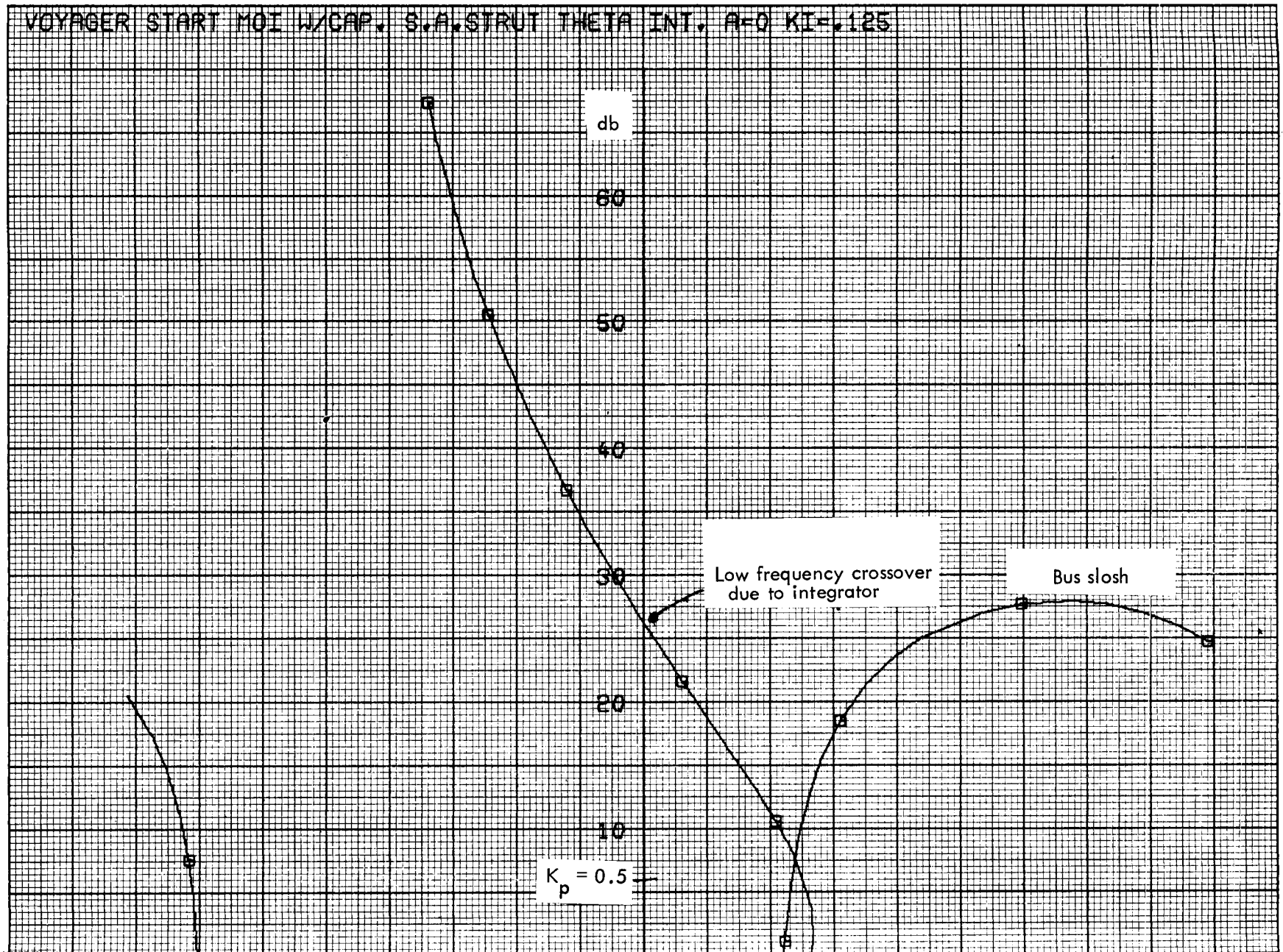
VOYAGER START MOI W/CAP. S.A.STRUT THETA INT. A=0 KI=.125
db
60
50
40
30
20
10
Low frequency crossover due to integrator
Bus slosh
$K_p = 0.5$

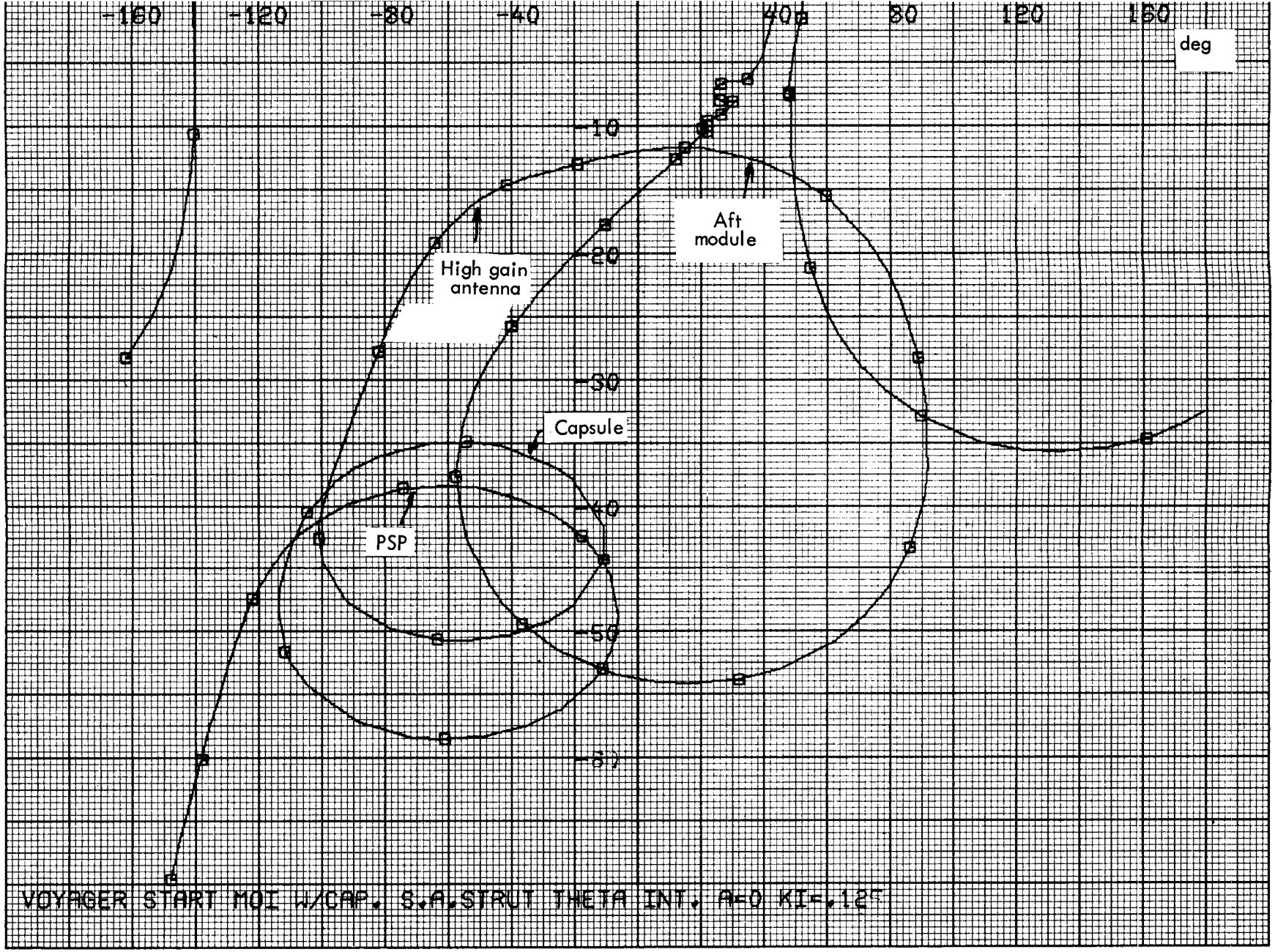

Figure 94. Gain-Phase Plot, Start MOI, with Capsule, Solar Array Struts Added, Integral Attitude Feedback, $K_I = 0.125$

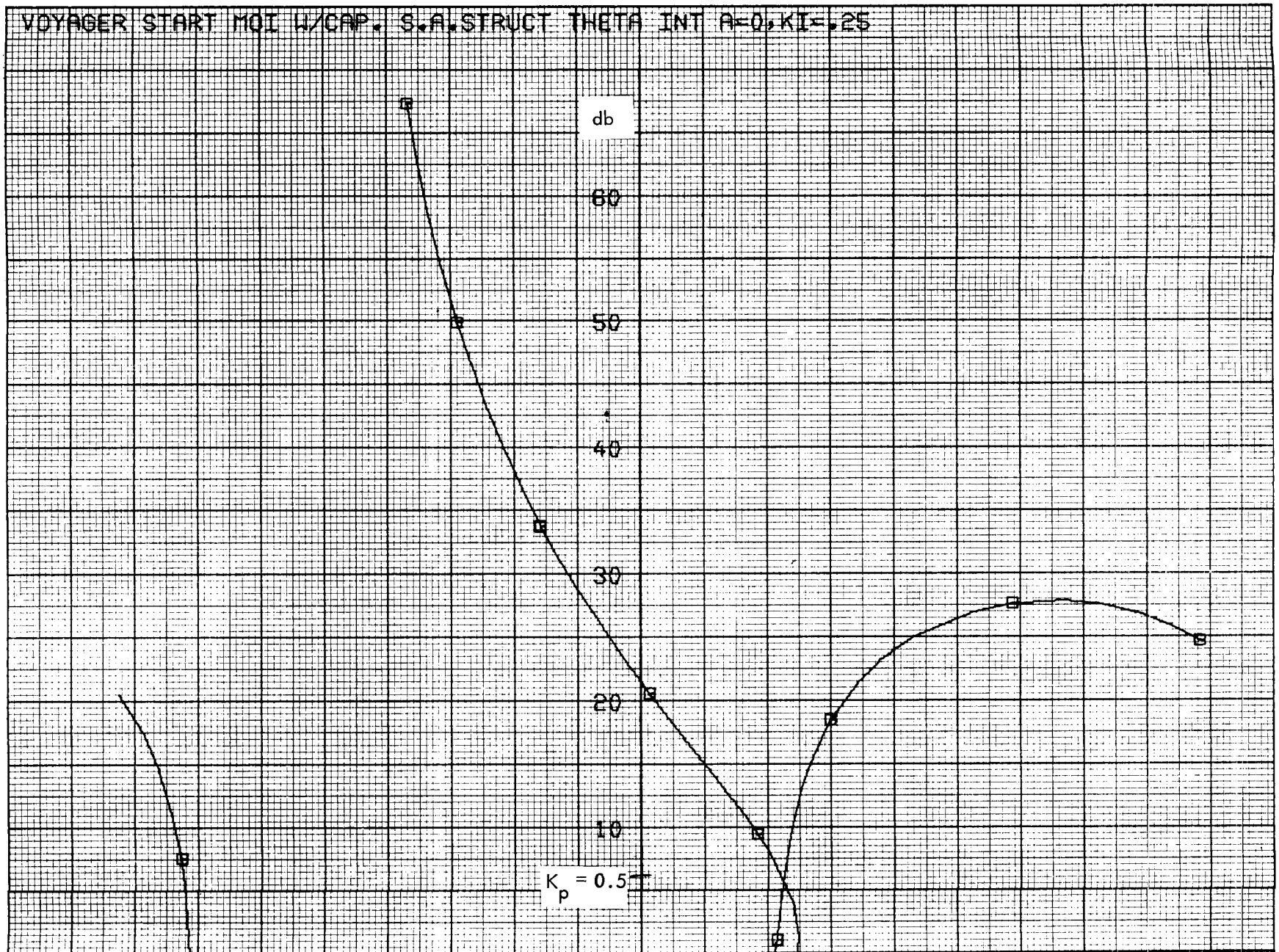
VOYAGER START MOI W/CAP. S.A.STRUCT THETA INT A=0,KI=.25
db
60
50
40
30
20
10
$K_p = 0.5$

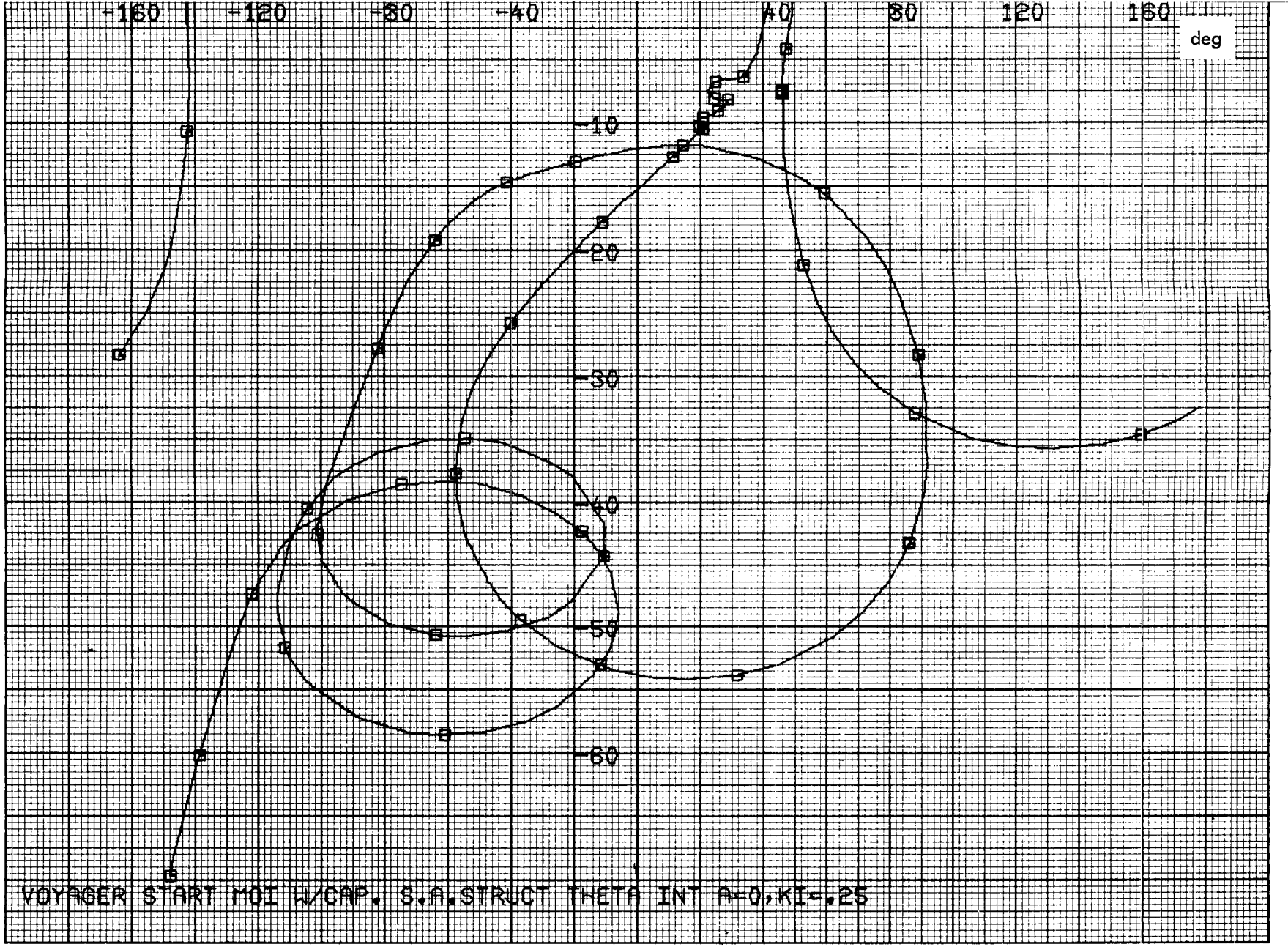

Figure 95. Gain-Phase Plot, Start MOI, with Capsule, Solar Array Struts Added, Integral Attitude Feedback, $K_I = 0.25$

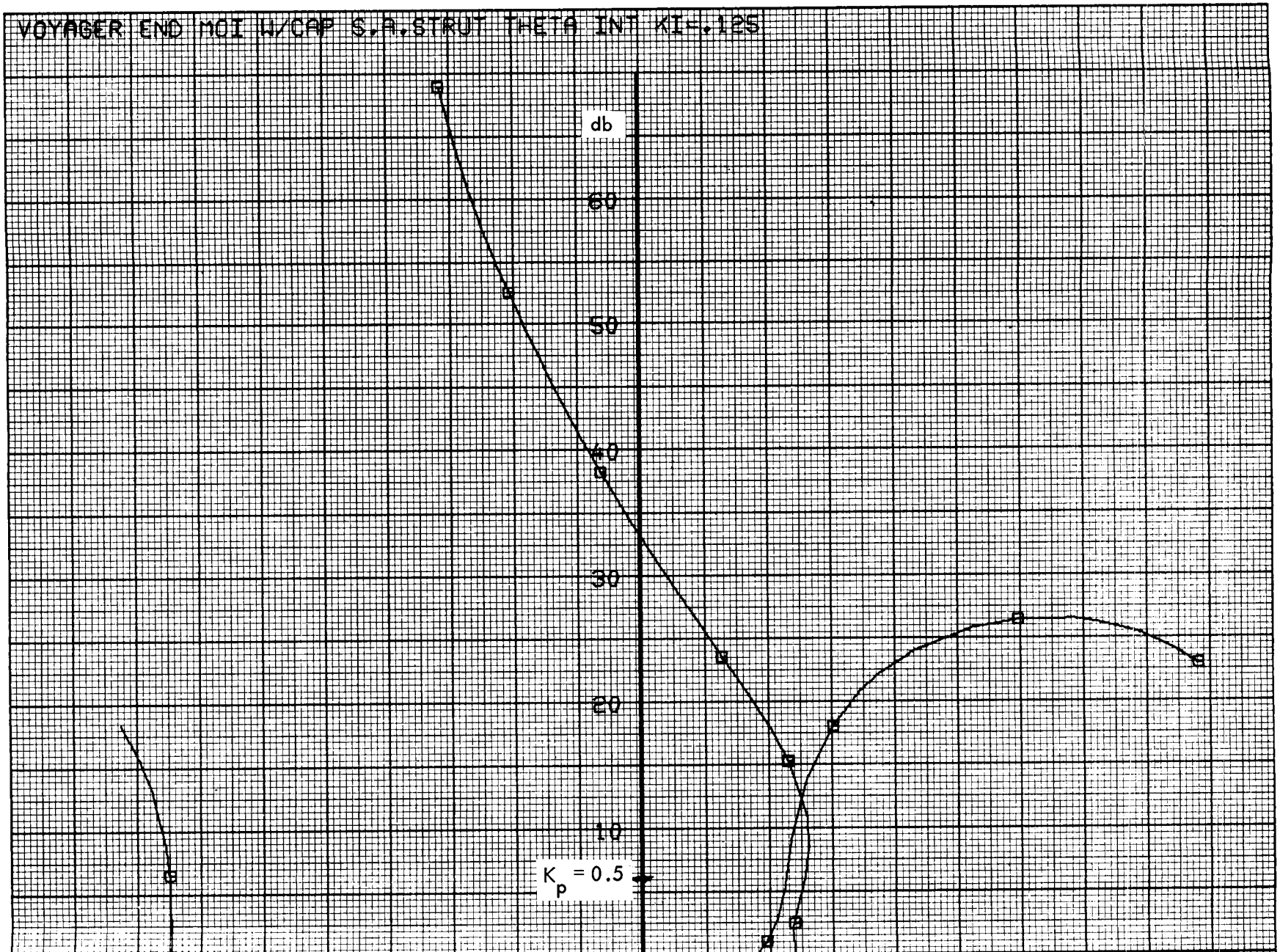
VOYAGER END MOI W/CAP S.A.STRUT THETA INT KI=.125
db
60
50
40
30
20
10
$K_p = 0.5$

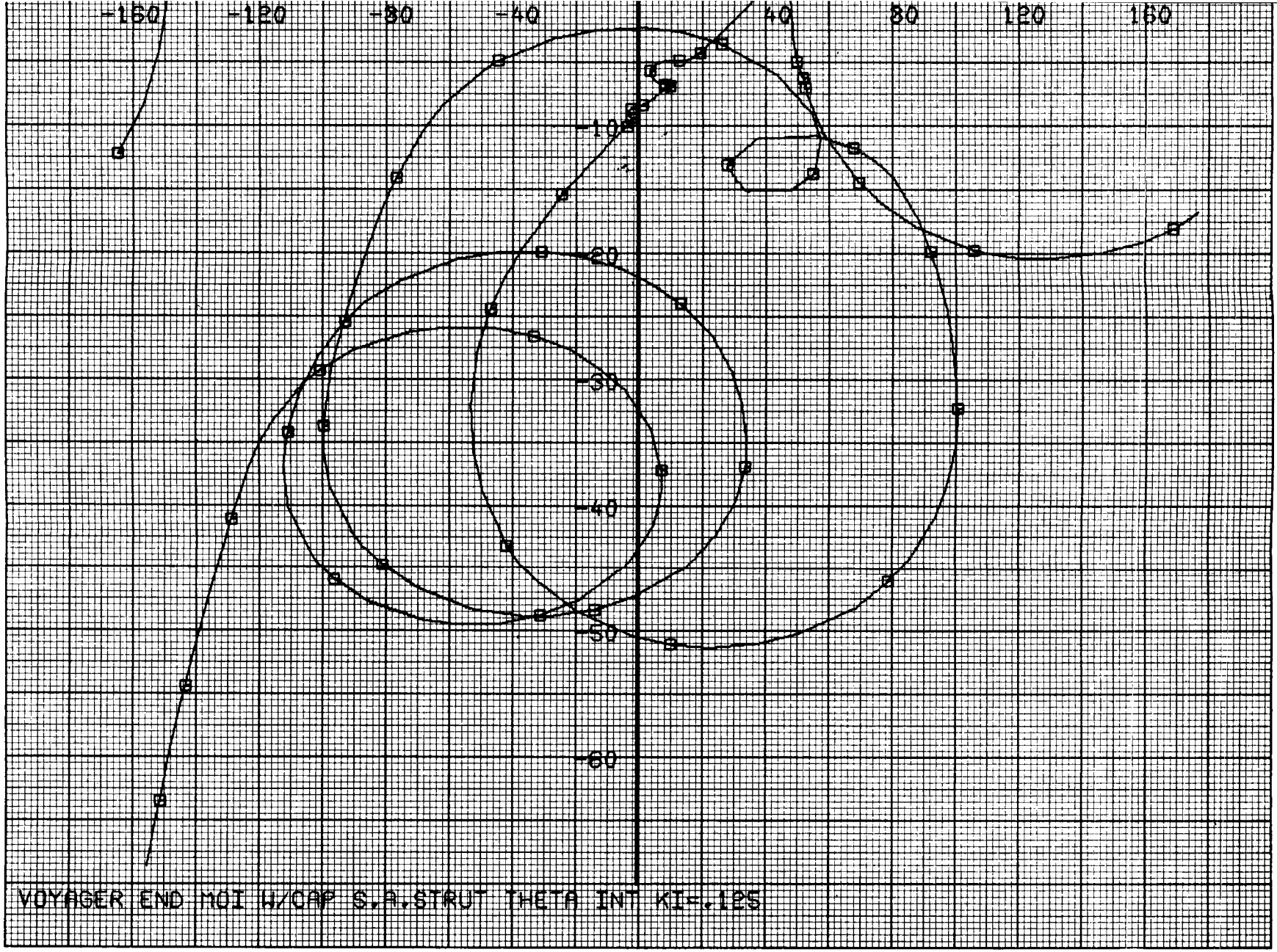

Figure 96. Gain-Phase Plot, End MOI, with Capsule, Solar Array Struts Added, Integral Attitude Feedback, $K_I = 0.125$

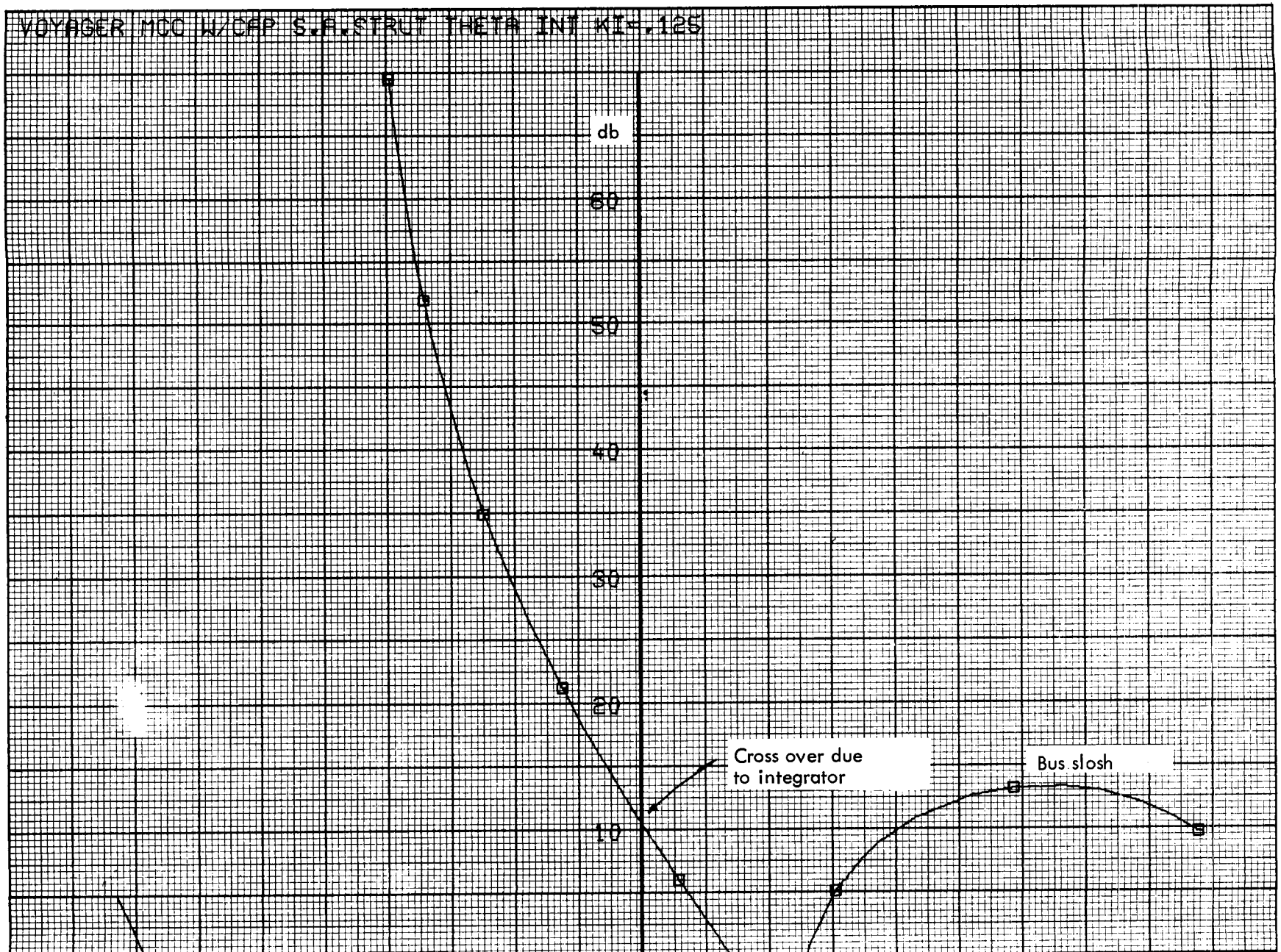
VOYAGER MCC W/CAP S.A.STRUT THETA INT KI=.125
db
60
50
40
30
20
10
Cross over due
to integrator
Bus slosh

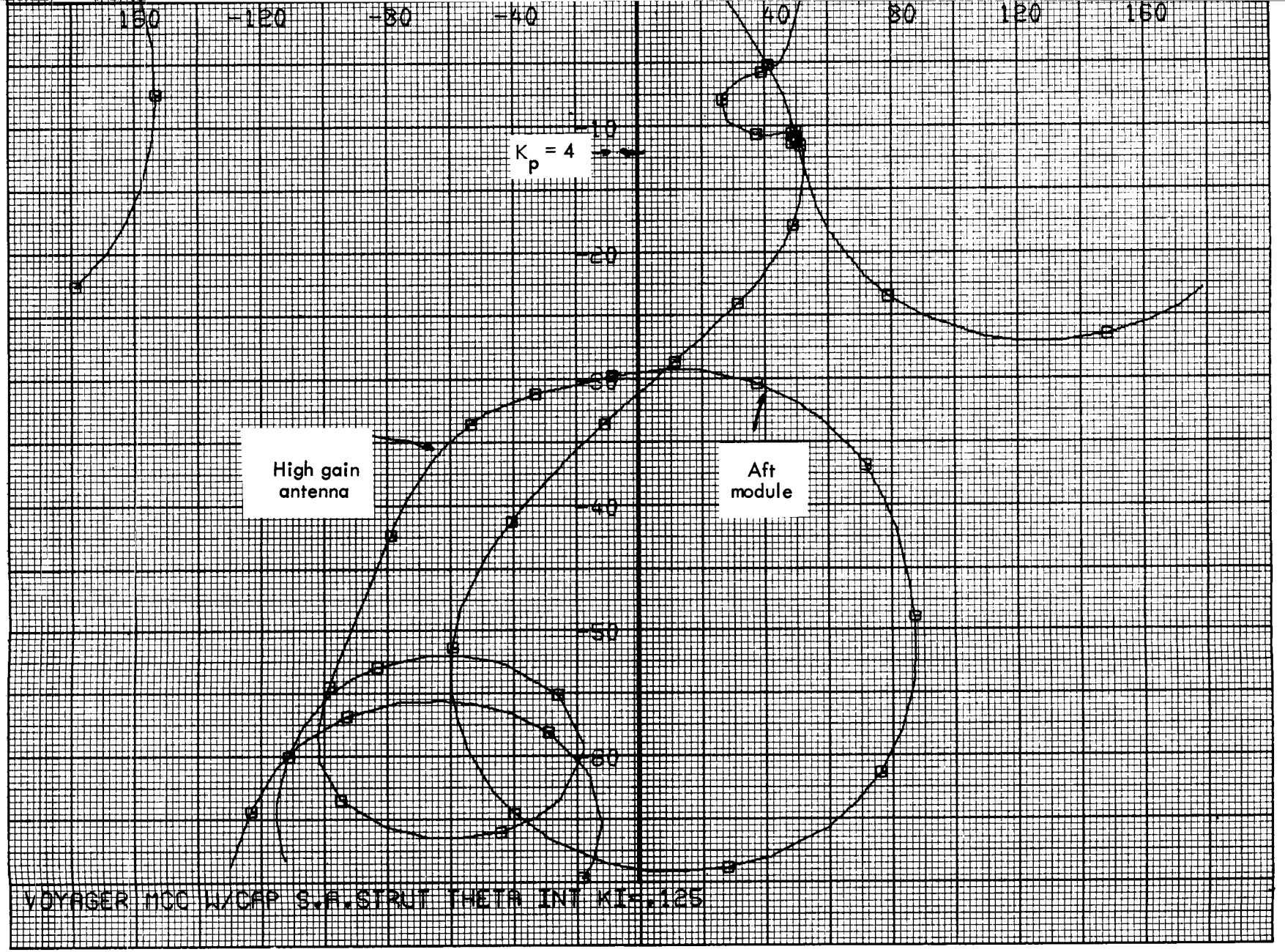

Figure 97. Gain-Phase Plot, MCC, with Capsule, Solar Array Struts Added, Integral Attitude Feedback, $K_I = 0.125$

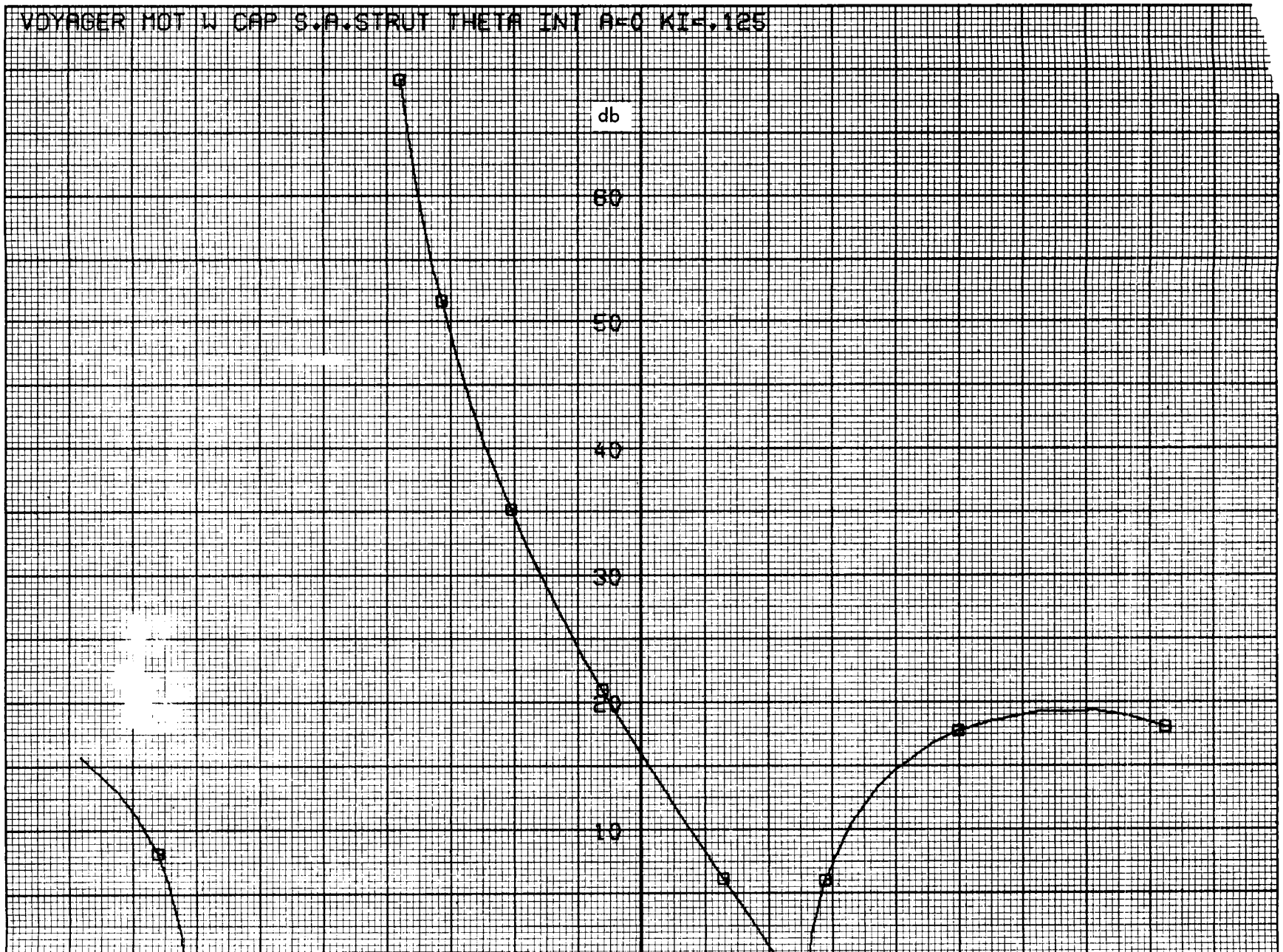
VOYAGER MOT W CAP S.A.STRUT THETA INT A=0 KI=.125
db
60
50
40
30
20
10

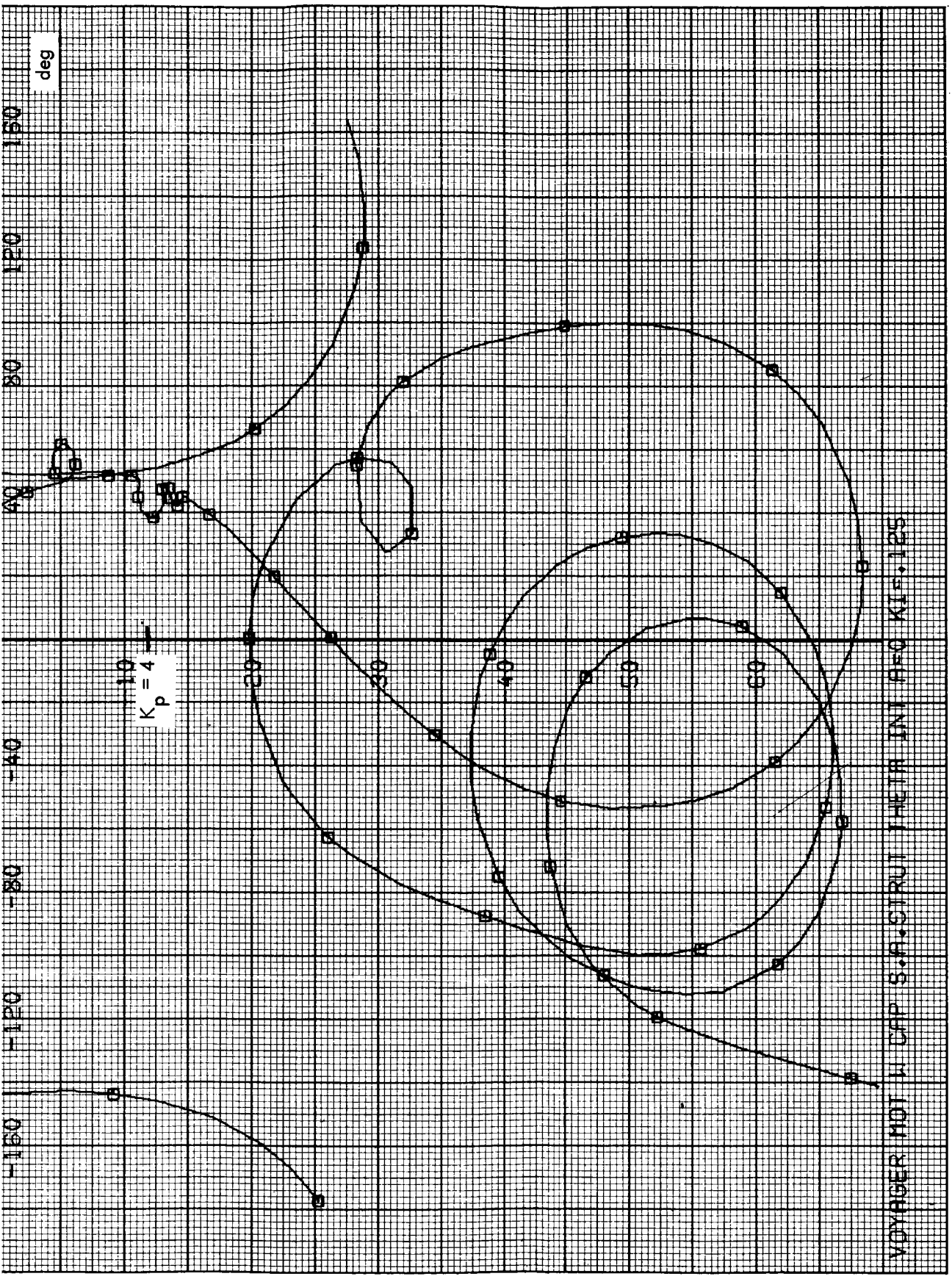

Figure 98. Gain-Phase Plot, MOT, with Capsule, Solar Array Struts Added, Integral Attitude Feedback, $K_I = 0.125$

BLANK PAGE

PRECEDING PAGE BLANK NOT FILMED.

4. THRUST VECTOR POINTING ERROR

4.1 INTRODUCTION

To estimate the thrust vector control (TVC) pointing errors and crossrange velocity errors incurred during midcourse correction (MCC), Mars orbit insertion (MOI), and Mars orbit trim (MOT), the errors introduced by the gyro, attitude control system, limit cycle, and reference misalignments were combined with TVC-induced pointing errors to obtain total powered flight pointing errors. The thrust vector error sources considered were cg offsets, thrust vector offsets, and thrust vector misalignments. The effects of three control system designs on the thrust-vector-induced pointing errors were evaluated. The three control system designs studied were:

- Without electronic integrators
- With attitude feedback integration
- With attitude and engine angle feedback integration

A 380-second main engine firing (ΔV = 200 m/sec) was assumed for MCC and a 330-second firing (ΔV = 2 km/sec) for MOI. Total pointing error angle and cross velocity error at the end of engine firing is provided for each of the control systems. The results are based on a constant coefficient simulation. Since the mass and inertia properties change radically from the start to the end of MOI, these results should be considered preliminary.

It was determined that the use of integrators considerably improved the steady-state total pointing angle and cross-velocity accuracy. For each of the control systems, the total pointing angle errors, after reaching steady state, were:

	Total Steady State Pointing Angle Error (deg)			
	MCC		MOI	
	Mean	3σ	Mean	3σ
Without electronic integrators	0.28	0.87	1.5	1.52
With attitude feedback integration	0.22	0.73	0.5	0.67
With attitude and engine angle feedback integration	0	0.76	0	0.76

The non-zero mean values occur because of a non-zero mean cg offset. The mean pointing errors can be removed if the motion of the cg with flight time can be accurately determined. The thrust vector can be pointed through the mean cg by providing a programmed bias to the actuator. This program is not needed with attitude plus engine angle feedback integration since this compensation scheme removes the steady state thrust pointing errors incurred from thrust vector offsets and cg offsets. Attitude integration feedback, on the other hand, removes the steady state thrust vector pointing error induced by a thrust vector misalignment. Attitude integration feedback appears to provide the smallest variance in pointing error because the dominant thrust vector pointing error source was that due to the thrust vector misalignment (0.5 degree). If the thrust vector misalignment is reduced to 0.25 degree, for example, the pointing error with attitude and engine angle feedback would show the smallest 3σ value of 0.62 degree.

The cross velocity errors were

	Cross Velocity (ft/sec)			
	MCC (end of 380 sec)		MOI (end of 330 sec)	
	Mean	3σ	Mean	3σ
Without electronic integrators	2.92	18.75	192	203
With attitude feedback integration	2.35	7.85	60	67
With attitude and engine angle feedback integration	0.47	7.85	4.2	67

The cross velocity error is the product of the "constant" acceleration times the time integral of the pointing error. The velocity error can be predicted very closely through the use of the steady-state pointing error but not exactly because of the effect of transients. In all cases the mean cross velocity error can be removed by proper programming, if the motion of the nominal cg with flight is accurately determined.

MOT pointing errors were not investigated as thoroughly as MCC and MOI errors. Only the steady state pointing errors were obtained. They are:

	Total Steady State Pointing Angle Error (deg), MOT	
	Mean	3σ
Without integrators	0.5	2.04
With attitude feedback integration	1	1.98
With attitude and engine angle feedback integration	0	0.76

The larger cg uncertainty and the small distance between the engine and cg locations at MOT produce a large offset angle. Attitude and engine angle feedback integration reduce the steady state pointing error for these effects to zero.

In obtaining these results, the approach was as follows:

1) The thrust vector pointing errors incurred from thrust vector misalignment δ_m, thrust vector offsets, or cg offsets were determined with the cg or thrust vector offsets combined into an equivalent thrust vector offset angle δ_{off}. To provide sensitivity coefficients the steady state thrust vector pointing error angle ϵ_T and velocity error V_T for a unit thrust vector misalignment δ_m and a unit thrust vector offset δ_{off}, were determined.

2) For the control system the thrust vector pointing errors produced by unit thrust vector misalignments and offset angles were scaled by the offsets and misalignments in the Task B report to determine the control thrust vector pointing errors.

3) The thrust vector pointing errors were combined with the pointing errors introduced by the gyro, limit cycle, and reference misalignments to determine the total pointing errors.

The coordinates and angles used in the analysis are illustrated in Figure 99. Definitions and nomenclature are presented in Table 5. The model used to determine the pointing errors introduced by the thrust vector is presented in Figure 100. The assumptions for this model were:

Filter:	d = 2.0 sec, c = 0.05 sec (identical to Section 3)
Actuator:	Operation is linear and actuator dynamics are negligible

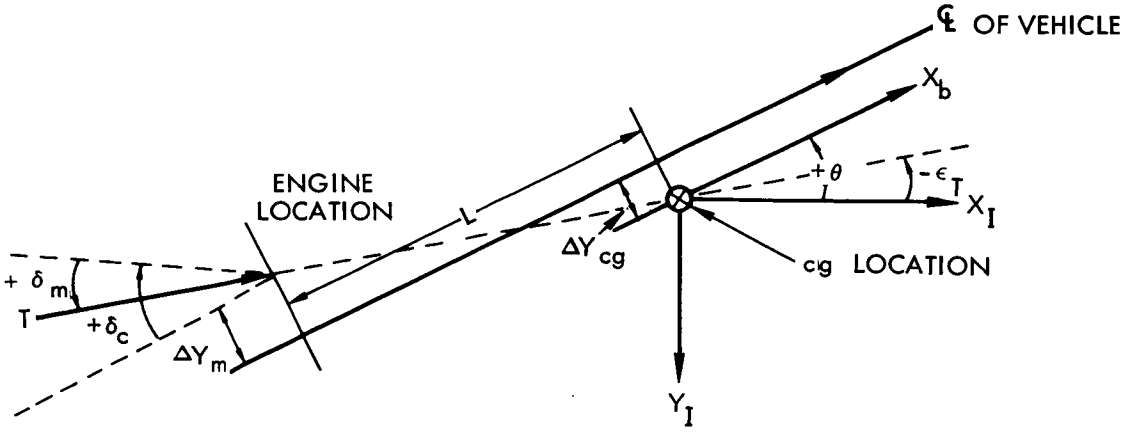

Figure 99. Coordinates and Angles Used in Analysis
(Refer to Table 5 for Nomenclature)

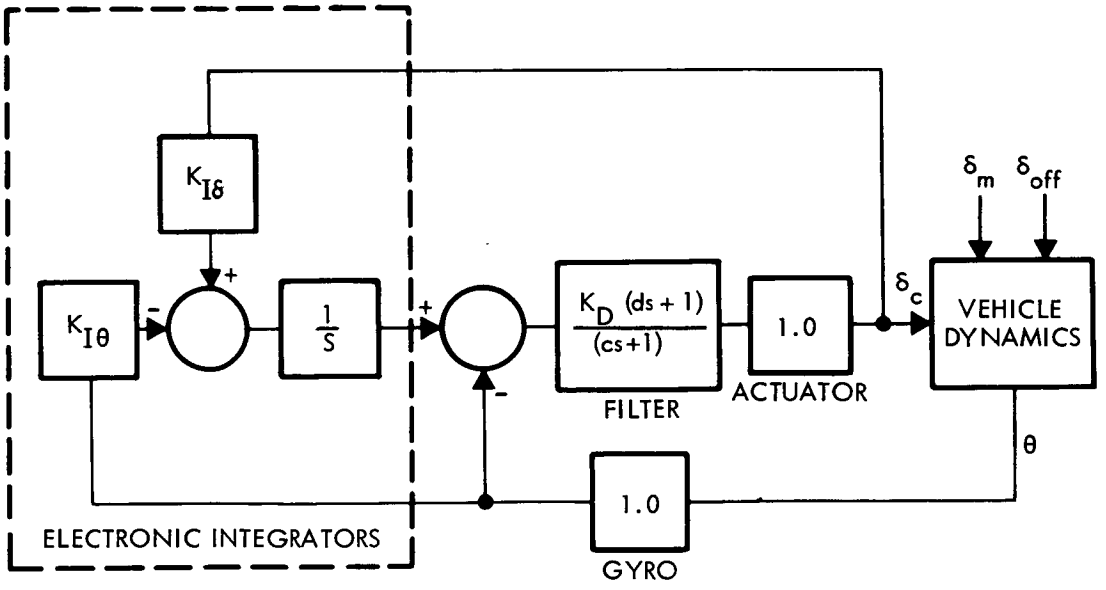

Figure 100. Thrust Vector Pointing Error Model
(Refer to Table 5 for Nomenclature)

Table 5. Definitions and Nomenclature

Symbol	Definition
δ_c	Actuator angle (engine angle)
δ_m	Thrust vector misalignment
ΔY_m	Thrust vector offset
ΔY_{cg}	Cg offset
L	Distance from cg to engine gimbal point
δ_{off}	Thrust vector offset angle
	$\delta_{off} \triangleq \frac{\Delta Y_m + \Delta Y_{cg}}{L}$ (small angles assumed)
θ	Attitude reference angle (gyro angle)
ϵ_T	Instantaneous thrust vector pointing error angle
	$\epsilon_T \triangleq \delta_c - \delta_m - \theta$. The positive direction of ϵ_T is shown below
	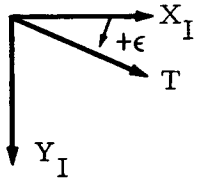
V_T	Velocity error due to thrust vector $V_T \triangleq \int A_T \epsilon \, dt$ (small angles assumed)
ϵ_{Ts}	Final value of ϵ_T ($\epsilon_{Ts} = \epsilon_T$ as $t \rightarrow \infty$)
ϵ	Total pointing error angle
V	Total velocity error
$K_{I\delta}$	Engine angle feedback integrator gain (Figure 100)
$K_{I\theta}$	Attitude feedback integrator gain (Figure 100)
d, c	Filter parameters
K_D	Control loop gain
μ_c	Control moment coefficient
A_T	Linear acceleration provided by main engine thrust

Gyro: Dynamics can be neglected

Vehicle Dynamics: Rigid body representation of vehicle

A fixed coefficient study was conducted. For MOI, the average of the values for the start and end of MOI was used for the linear acceleration, A_T, and the torque coefficient, μ_c. The values of A_T and μ_c used for MCC and MOI were:

μ_c = 0.193 rad/sec^2 for MCC and 2.08 rad/sec^2 for MOI (derived from Section 3)

A_T = 1.63 ft/sec^2 for MCC and 20.0 ft/sec^2 for MOI (derived from Section 3)

4.2 TVC ERRORS WITHOUT ELECTRONIC INTEGRATORS

The integrator gains $K_{I\theta}$ and $K_{I\delta}$ were set to zero, thereby removing the electronic integrators (Figure 100). The gain and phase margin with a K_D of 1.0 were determined in Section 3; the gain-phase plots in the vicinity of the origin are presented in Figure 101. The control loop gain K_D was selected to provide a minimum gain and phase margin of 30 degrees and 6 db, respectively. This resulted in loop gains of 4.0 and 0.5 for MCC and MOI, respectively (Figure 101).

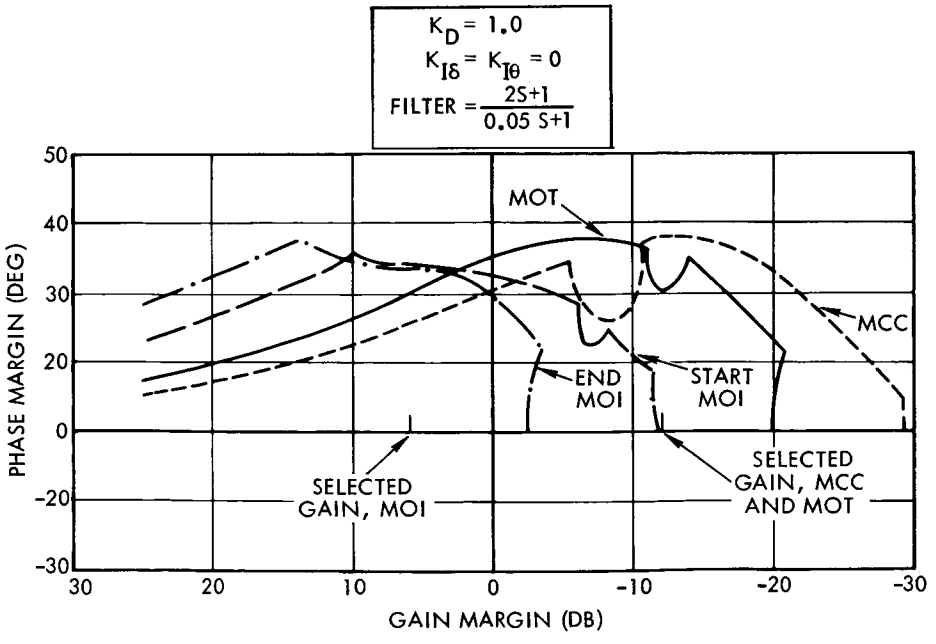

Figure 101. Gain and Phase Margins without Electronic Integrators

The steady state pointing error, ϵ_T, and resulting velocity error, V_T, for a 1-degree thrust vector misalignment was determined for MOI and MCC. The results are presented in Figures 102 and 103. For constant thrust levels, the velocity error curve can be obtained from the pointing error curve by multiplying the thrust by the integral of ϵ_T.

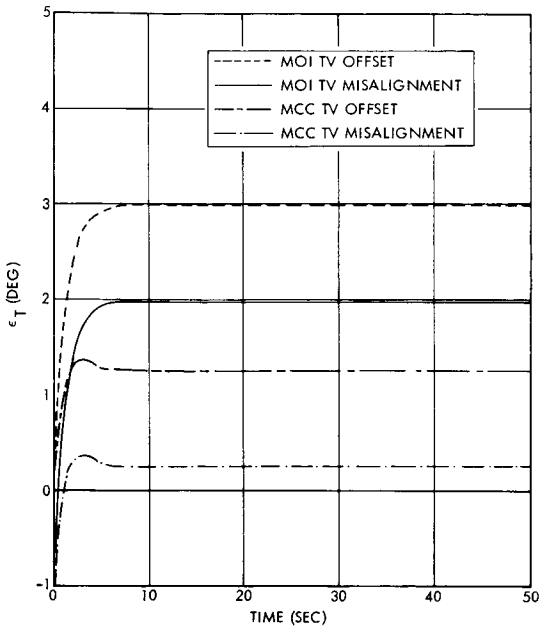

Figure 102. ϵ_T without Electronic Integrators

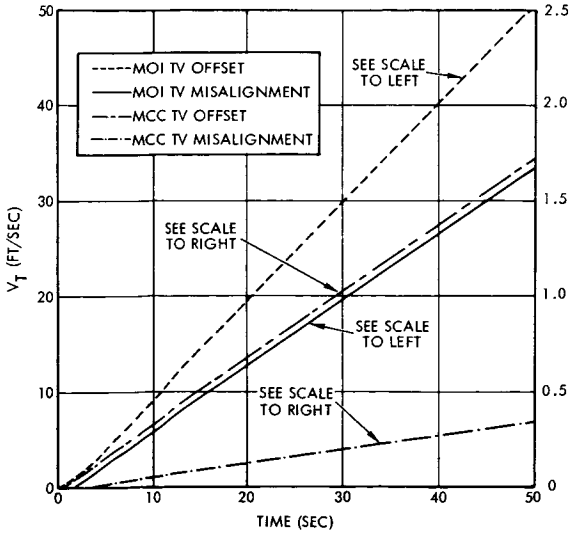

Figure 103. V_T without Electronic Integrators

The steady state values of θ and δ_c determined by the final value theorem, are

$$\delta_c = \delta_m$$

$$\theta = \frac{\delta_m}{K_D}$$

Since $\epsilon = \delta_c - \delta_m - \theta$,

$$\epsilon_{Ts} = \frac{\delta_m}{K_D} .$$

An illustration of the final orientation of the vehicle with only a thrust vector misalignment is presented in Figure 104a.

For a 1-degree thrust vector misalignment, the steady state pointing errors were predicted for MCC and MOI to be 0.25 and 2.0 degrees, respectively. This agrees with the computer results of Figure 102. Assuming a 380-second firing time for MCC and a 330-second firing time for MOI, the velocity error due to a 1-degree thrust vector misalignment for MCC and MOI are 2.8 and 227 ft/sec, respectively.

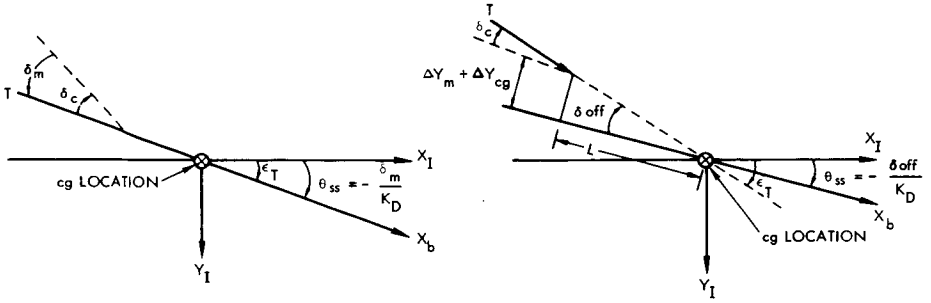

Figure 104. Steady-State Orientation without Electronic Integrators

For a 1-degree thrust vector offset angle, ϵ_T and V_T were determined for MOI and MCC. The results are presented in Figures 102 and 103. The steady state orientation of the vehicle is illustrated in Figure 104b.

$$\epsilon_{Ts} = \left(\frac{1 + K_D}{K_D}\right) \delta_{off}$$

For a 1-degree thrust vector offset, the steady state pointing errors for MCC and MOI are 1.25 and 3.0 degrees, respectively. Assuming a 380-second firing time for MCC and a 330-second firing time for MOI, the velocity error for MCC and MOI due to a 1-degree thrust vector effect are 13.28 and 395 ft-sec, respectively.

4.3 TVC ERRORS WITH ATTITUDE FEEDBACK INTEGRATION

With the integrator gains $K_{I\theta} = 0.125$ and $K_{I\delta} = 0$, the gain and phase margin plot of Figure 105 was determined. By setting K_D equal to 4.0 and 0.5 for MCC and MOI, respectively, gain and phase margins of 40 degrees and 6 db could be obtained.

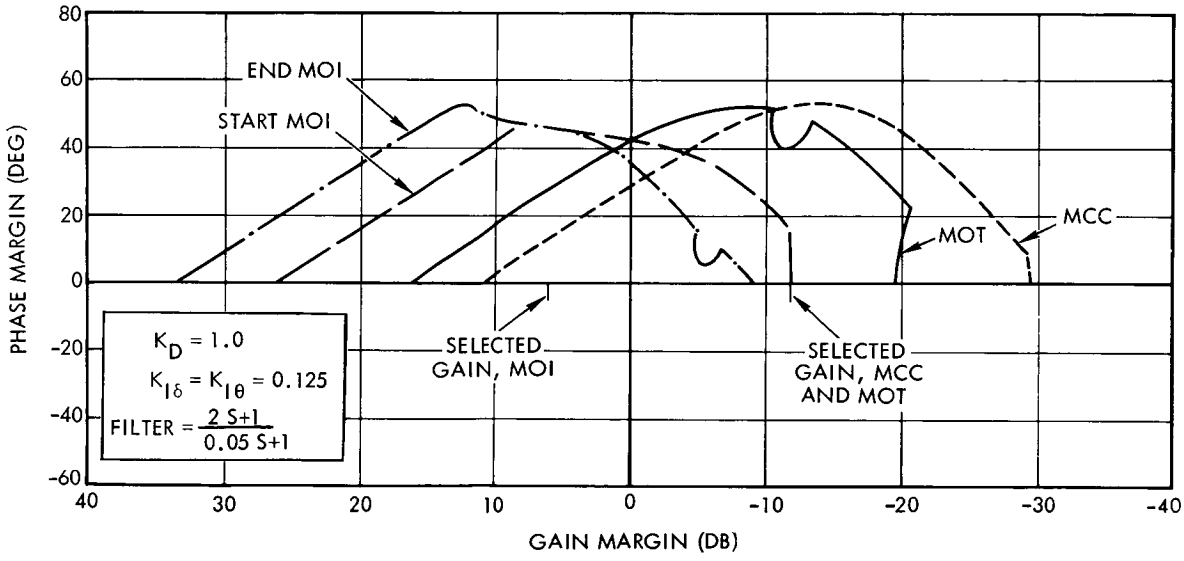

Figure 105. Gain and Phase Margins with Attitude Feedback Integration

The same procedure was followed as without integrators. The responses to a 1-degree thrust vector misalignment is presented in Figures 106 and 107. The pointing error angle is driven to approximately zero in 50 seconds. The final orientation of the model is presented in Figure 108a.

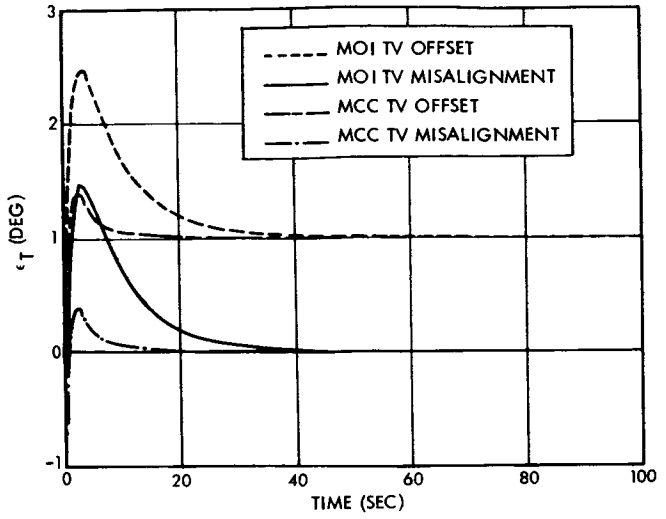

Figure 106. ϵ_T with Attitude Feedback Integration

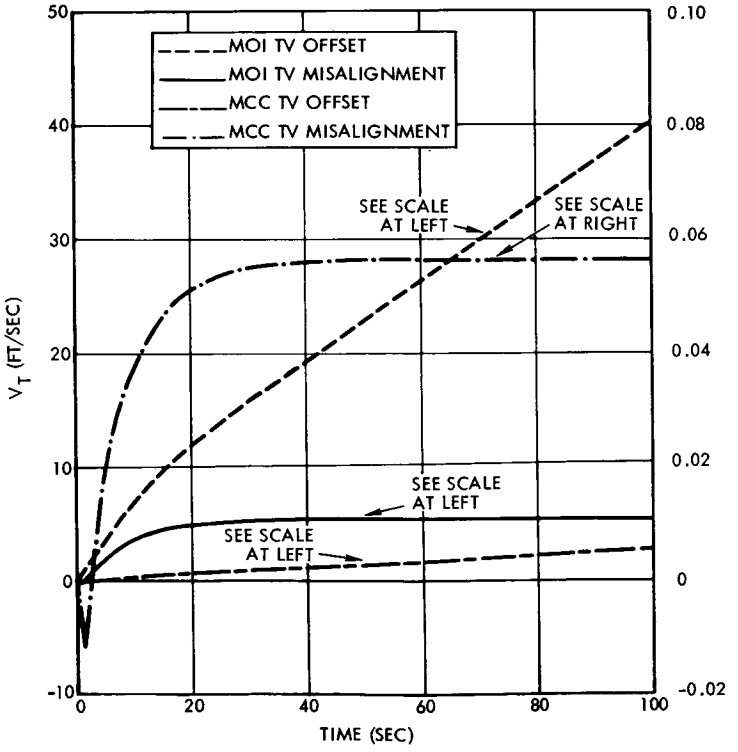

Figure 107. V_T with Attitude Feedback Integration

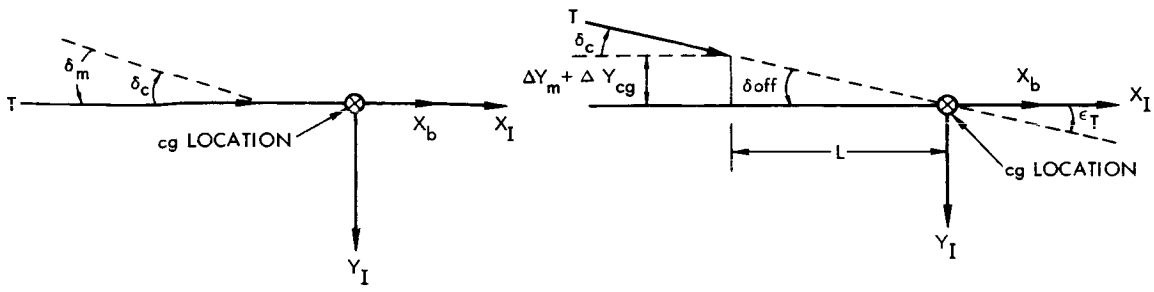

A. THRUST VECTOR MISALIGNMENT

B. THRUST VECTOR OFFSET

Figure 108. Steady-State Orientation with Attitude Feedback Integration

The velocity error due to a 1-degree thrust vector misalignment at the end of a 380-second firing time for MCC is 0.06. At the end of a 330-second main engine ignition for MOI, the velocity error due to a 1-degree thrust vector offset is 5.6 ft/sec.

The pointing errors for a 1-degree thrust vector offset are presented in Figures 106 and 107. The steady-state pointing error equalled the thrust vector offset angle (Figure 106). The final orientation of the model is presented in Figure 108b.

4.4 TVC ERRORS WITH ATTITUDE AND ENGINE ANGLE FEEDBACK INTEGRATION

With integrator gains $K_{I\theta} = K_{\delta} = 0.125$, the gain and phase margin plot of Figure 109 was developed. As shown by Figure 110, a K_D of 0.5 could be used for MOI, but no control loop gain would provide adequate gain and phase margin for MCC. This necessitates a different integrator gain for MCC. With $K_{I\theta} = K_{I\delta} = 0.02$, a K_D of 4.0 provided adequate gain and phase margin (Figure 110).

For $K_{I\delta} = K_{I\theta}$, $\epsilon_{TS} = \delta_m$. The steady state orientation is shown in Figure 113a. The velocity errors, V_T, after a 380-second engine firing are 9.65 and 125 ft/sec for MCC and MOI, respectively.

The thrust vector pointing errors for a thrust vector offset of 1 degree are shown in Figures 111 and 112. The thrust vector pointing angle was reduced to zero in approximately 200 seconds for the MCC and 50 seconds for MOI. The steady-state orientation of the vehicle is

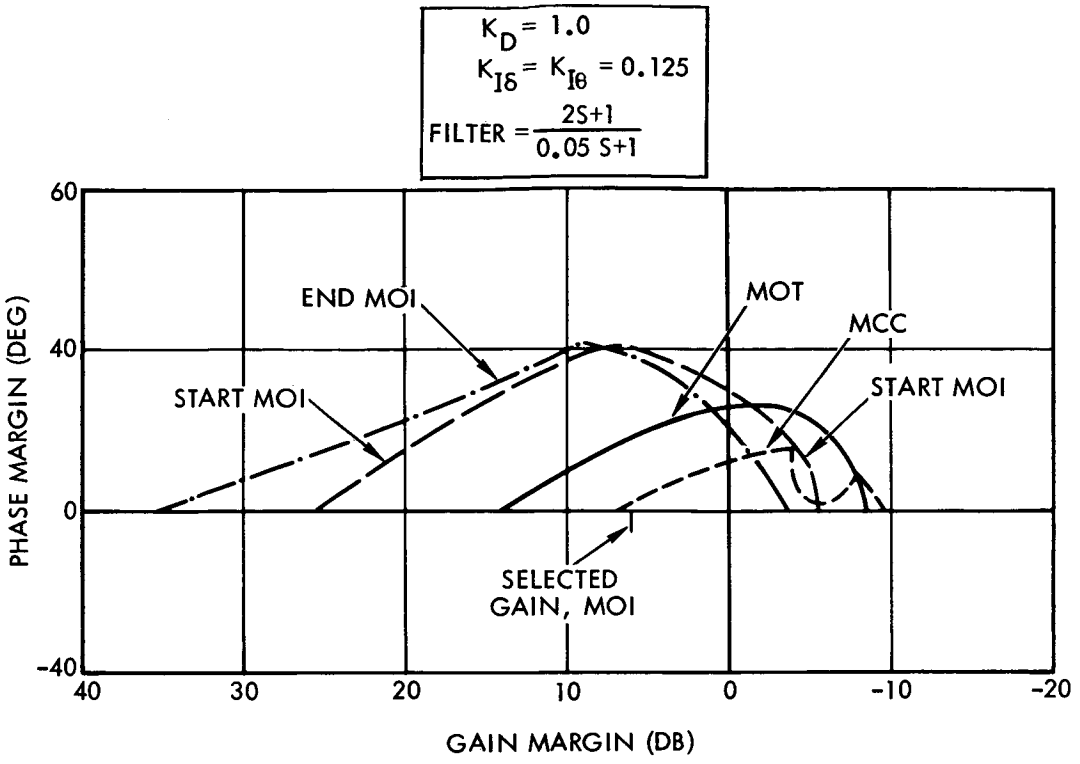

Figure 109. Gain and Phase Margins with Attitude and Engine Angle Feedback Integration, $K_{I\delta} = 0.125$

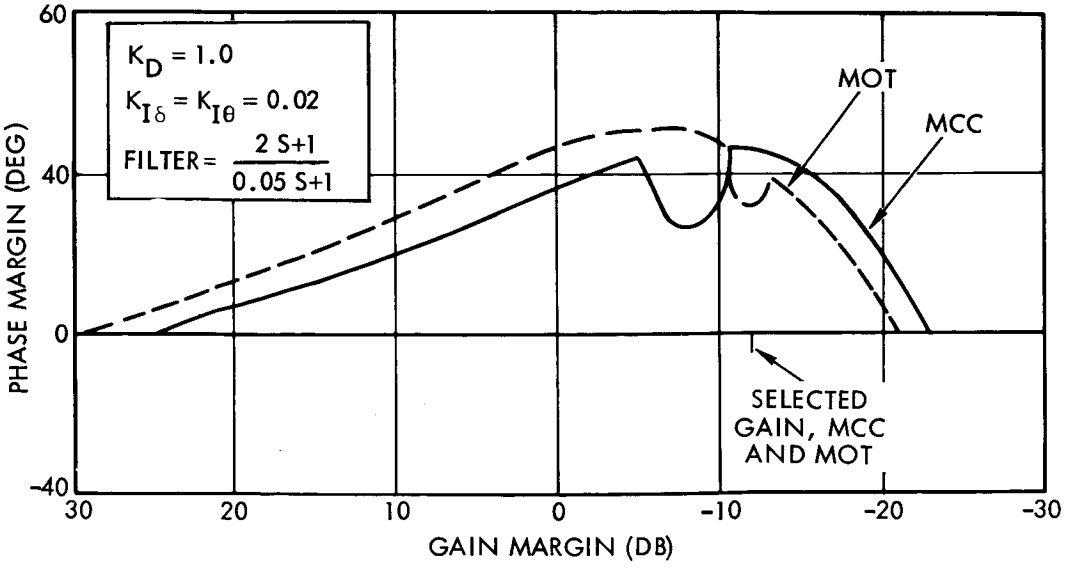

Figure 110. Gain and Phase Margins with Attitude and Engine Angle Feedback Integration, $K_{I\delta} = 0.02$

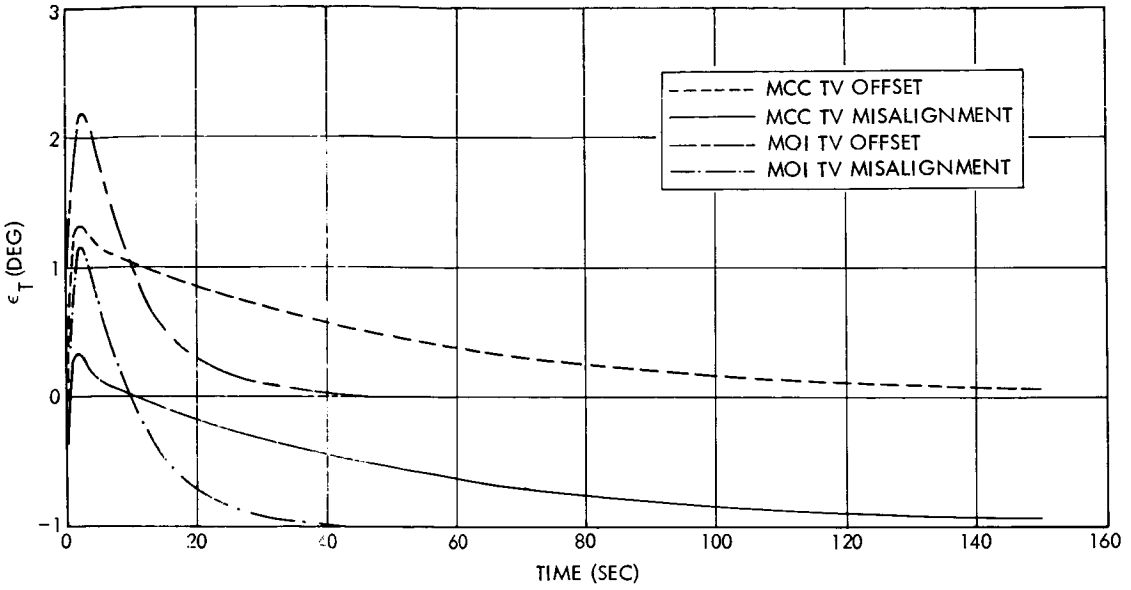

Figure 111. ϵ_T with Attitude and Engine Angle Feedback Integration

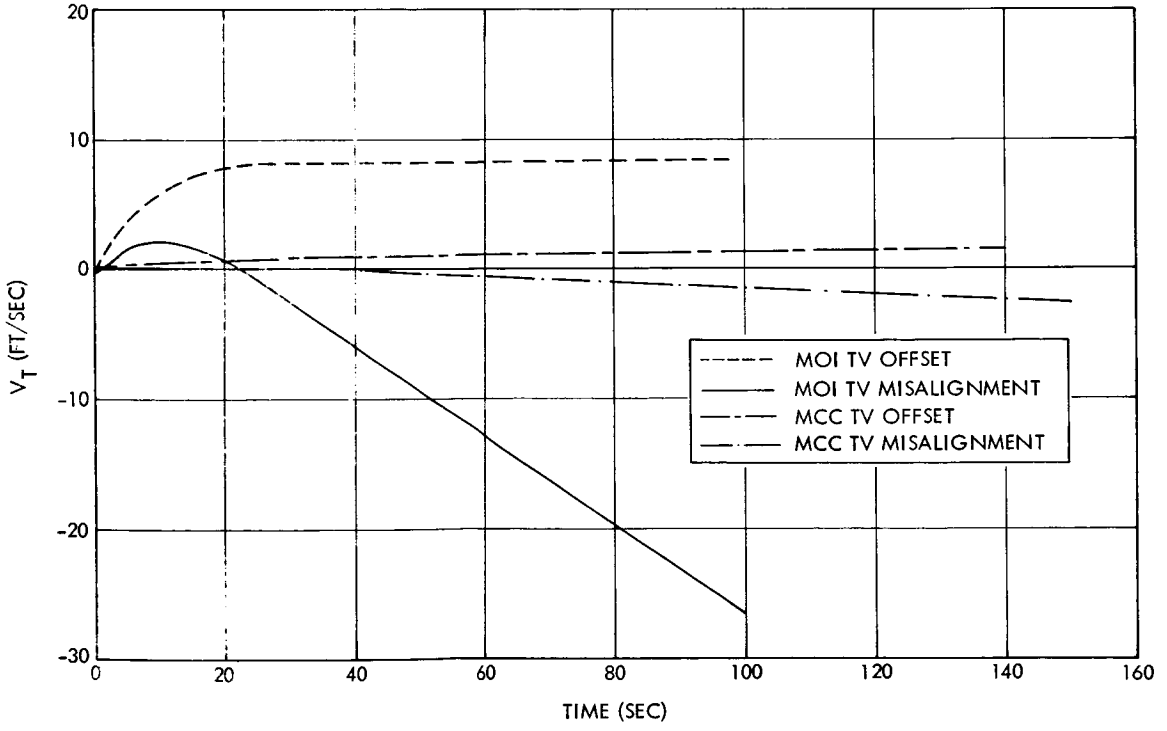

Figure 112. V_T with Attitude and Engine Angle Feedback Integration

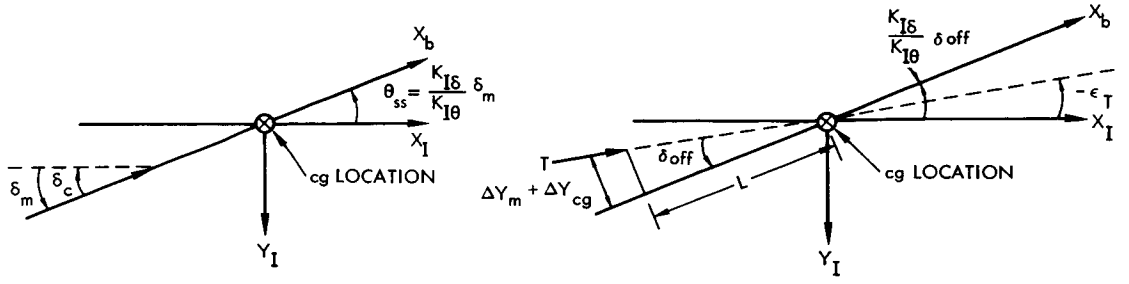

A. THRUST VECTOR MISALIGNMENT B. THRUST VECTOR OFFSET

Figure 113. Steady-State Orientation with Attitude and Engine Angle Feedback Integration

illustrated in Figure 113b. The velocity error for a 380-second engine firing time is 2.1 and 8.4 ft/sec for MCC and MOI, respectively.

The following 3σ errors were used to predict the overall accuracy for midcourse correction (Reference 2).

Attitude reference accuracy	±0.1 deg
Gyro torquing error	±0.2 deg
Gyro alignment error	±0.1 deg
Gyro drift error, 0.4 deg/hr for 1 hr	±0.4 deg
Gyro g-sensitive error	±0.003 deg (MCC) and ±0.042 (MOI)
Limit cycle error (at gyro uncage)	±0.25 deg
TVC limit cycle error	±0.2 deg

Throughout flight the thrust vector offset (3σ) and thrust vector misalignment were assumed to be 0.25 inch and 0.5 degree, respectively. From the reference the radial offset of the cg at MCC is 0.23 ±0.4 inch; for MOI the radial offset of the cg is 0.6 ±0.35 inch. The mean value can be removed if the motion of cg location with flight can be accurately determined. The equivalent offset angles are given below.

Time of Flight	L (in)	Thrust Vector Offset Angle (3σ) (deg)	CG Offset Angle (deg) Mean	(3σ)
MCC	59	±0.24	0.22	±0.39
MOI	69	±0.21	0.5	±0.29

The resulting thrust vector pointing errors are presented in Table 6; the thrust vector velocity errors are presented in Table 7.

All 3σ pointing error angle values were RSS'd to determine the 3σ pointing error. These were added to the mean offset error to provide the total pointing error. The results are presented in Table 8. The same procedure was followed for the total velocity error. The results are presented in Table 9.

The mean pointing and velocity errors can be removed in the nominal cg motion, when flight time is known accurately, by providing a bias command to the actuator such that the assumed nominal thrust vector points through the nominal cg location throughout main engine ignition.

Table 6. Thrust Vector Pointing Angle Errors (ϵ_T)

Time of Flight	Source of Error	Without Electronic Integrators (deg)	With Attitude Feedback Integrators (deg)	With Attitude and Engine Angle Feedback Integrators (deg)
MCC	Thrust vector offset angle	±0.30 (3σ)	±0.24 (3σ)	0
MCC	cg offset angle	0.275 ± 0.49 (mean) ± (3σ)	0.22 ± 0.39 (mean) ± (3σ)	0
MCC	Thrust vector misalignment	±0.312 (3σ)	0	±0.5 (3σ)
MOI	Thrust vector offset angle	±0.63 (3σ)	±0.21 (3σ)	0
MOI	cg offset angle	1.5 ± 0.79 (mean) ± (3σ)	0.5 ±0.29 (mean) ± (3σ)	0
MOI	Thrust vector misalignment	1.0 (3σ)	0	±0.5 (3σ)

Table 7. Thrust Vector Velocity Error

Time of Flight	Source of Error	Without Electronic Integrators (ft/sec)	With Attitude Feedback (ft/sec)	With Attitude and Engine Angle Integration (ft/sec)
MCC	Thrust vector offset angle	$\pm$3.17 (3σ)	$\pm$2.58 (3σ)	$\pm$0.50 (3σ)
MCC	cg offset angle	2.92 + 5.17 (mean) $\pm$ (3σ)	2.35 + 4.15 (mean) $\pm$ (3σ)	0.47 + 0.83 (mean) $\pm$ (3σ)
MCC	Thrust vector misalignment	$\pm$1.42 (3σ)	$\pm$0.03 (3σ)	$\pm$4.82 (3σ)
MOI	Thrust vector offset angle	+83 (3σ)	25.1 (3σ)	$\pm$1.76 (3σ)
MOI	cg offset angle	192 + 57 (mean) $\pm$ (3σ)	60.0 + 35.0 (mean) $\pm$ (3σ)	4.2 + 2.45 (mean) $\pm$ (3σ)
MOI	Thrust vector misalignment	113.7 (3σ)	2.8	53.7 (3σ)

Table 8. Total Pointing Angle Error Angles

Time of Flight	Without Electronic Integrators (deg)		With Attitude Feedback Integrators (deg)		With Attitude and Engine Angle Feedback Integration (deg)	
	Mean	3δ	Mean	3δ	Mean	3δ
MCC	0.28	$\pm$0.87	0.22	$\pm$0.73	0	$\pm$0.76
MOI	1.5	$\pm$1.52	0.5	$\pm$0.67	0	$\pm$0.76

Table 9. Total Velocity Error

Time of Flight	Without Electronic Integrators (ft/sec)		With Attitude Feedback Integration (ft/sec)		With Attitude and Engine Angle Feedback Integration (ft/sec)	
	Mean	3δ	Mean	3δ	Mean	3δ
MCC	2.92	18.75	2.35	±7.85	0.47	±7.85
MOI	192	203	60.0	±67.0	4.2	±67.0

5. ACTUATOR DESIGN

5.1 INTRODUCTION

The electromechanical clutch-driven actuator specified in the Task B study report was investigated for suitability in the Voyager spacecraft employing the modified LM descent engine. This actuator design is essentially identical to that used for thrust vector control on the Apollo Service Module. Since the engine loads are considerably reduced from those on the service module, the actuation system gave more than ample control of the Voyager thrust vector. The control system performance with the selected actuation system was evaluated and found to be satisfactory. The actuator torque and rate limits were varied and found to be more than sufficient. The actuator design requirements and engine parameters are given below:

Engine Parameters

Engine inertia about gimbal point = 50 slug-ft^2

Constant load torque due to thrust vector offset, 3σ = 155 ft-lb at 7750-lb thrust

Thrust vector misalignment, 3σ = 0.5 deg

Actuator moment arm = 1.5 ft

Gimbal friction, 3σ = 67 ft-lb at 10,000-lb thrust

Engine deflection limit = ±6 deg

Engine flexline restraint = 11 ft-lb/deg

Engine thrust: low level, 1040-lb nominal for 380 sec total
high level, 7750-lb nominal for 380 sec (one firing)

Actuator Design Requirements

Minimum engine acceleration = 50 deg/sec^2

Minimum actuator rate limit = 10 deg/sec

Maximum actuator extended length = 18 in.

Actuator maximum stroke capability = 4.1 in.

Positive lock when de-energized at engine zero or sufficient restraint to prevent free movement when de-energized

5.2 DESIGN DESCRIPTION

The Task C thrust vector control actuator system follows the recommendation of Task B. A magnetic particle clutch actuator is used to gimbal the thrusting engine. The actuator is similar to that used in the Apollo Service Module engine system, but scaled down to meet the requirements of Voyager. Counterrotating magnetic particle clutches are driven by DC motors which transmit power through precision gear trains to a ballscrew. The ballscrew converts the rotation of the motor into the linear motion of the actuator shaft.

Shaft motion is commanded by excitation of the appropriate clutch. The clutches are normally disengaged, except for a bias to reduce deadband. The clutch current, which is provided by an amplifier, determines the output torque. Feedback is provided for position control and for dynamic stability.

5.2.1 Mathematical Model

In order to understand the operation of the actuator control system, a mathematical model was derived. Parameter values were derived from literature obtained through Lear-Siegler, manufacturer of the Apollo Service Module actuator.

A block diagram of the actuator control subsystem is shown in Figure 114. Amplifier gains and clutch-motor dynamics are also given. The feedback signal is derived from the LVDT position transducer and the velocity generator. The feedback signal is combined with the command signal to yield the error signal.

$$\text{Error, } V_e = V_c - V_{fp} - V_{fr}$$

$$\text{Rate Feedback, } V_{fr} = K_r \dot{\theta}$$

$$\text{Position Feedback, } V_{fp} = K_p \theta$$

where V_e = error signal (volt)

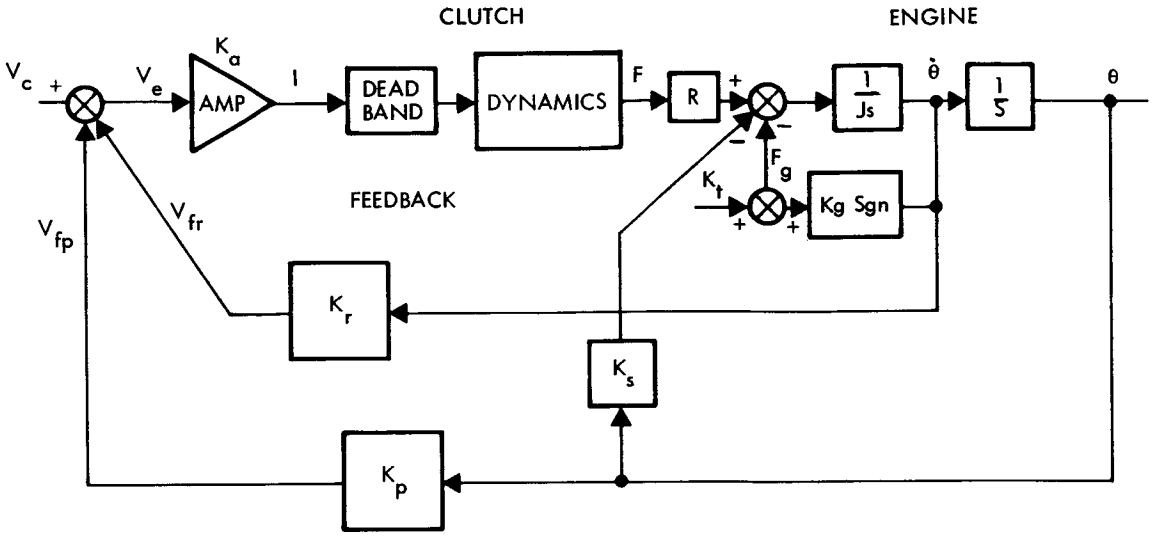

K_a = 228 MA/VOLT
K_c = 2.6 LB/MA
D = 30 MA
T_i = 25 MS
R = 1.5 FT
J = 50 SLUG-FT^2
K_s = 630 FT-LB/RAD
K_t = 155 FT-LB
K_g = 67 FT-LB
K_r = 9 VOLT PER RAD/SEC
K_p = 86 VOLT/RAD

Figure 114. Block Diagram of Thrust Vector Control Actuator

V_c = command signal (volt)

V_{fp} = position feedback signal (volt)

V_{fr} = rate feedback signal (volt)

K_r = rate feedback gain (volt/rad/sec)

K_p = position feedback gain (volt/rad)

The error is fed to an amplifier with an output current proportional to input. This current flows through a clutch which engages the ballscrew to a motor output. The output force at the ballscrew shaft is proportional to clutch current except for a deadband. The reaction from the driving motor produces a lag in force output.

Amplifier, $I = K_a V_e$

Clutch Deadband, $F_d = K_c (I \pm D)$

Clutch Dynamics, $F = F_d/(T_1 s + 1)$

where I = clutch current (ma)

K_a = amplifier gain (ma/volt)

F_d = clutch torque (lb)

K_c = clutch gain (lb/ma)

D = clutch deadband (ma)

F = output force (lb)

T_1 = clutch time constant (sec)

The actuator is attached to the engine and rotates it with the torque, FR. The loads are made up of engine dynamic loads and steady-state (static loads).

Engine Dynamics, $FR = J\ddot{\theta} + K_s \theta + F_g$

Steady-State Load, $F_g = K_t + K_g \operatorname{sgn} \theta$

where R = radius arm (ft)

J = engine inertia (slug-ft^2)

K_s = flexline spring load (ft-lb/rad)

F_g = total steady-state load (ft-lb)

K_t = side load due to thrust misalignment (ft-lb)

K_g = gimbal friction (ft-lb)

The resulting peak acceleration for the selected design was 680 deg/sec^2 with a total force output of the actuator of 900 ft-lb.

5.2.2 Reliability

The reliability analysis of the magnetic particle clutch actuator system can be divided into two parts: one for the actuator and another

for the electronic section. This study will consider only the actuator itself since electronic parameters have been assumed unchanged from the Task B study. In this study, the electronic section with triple redundant preamplifiers and double redundant power amplifiers is assumed to have a reliability (per Task B study) of 0.9983589.

The reliability of the actuator system using a nonredundant actuator with redundant electronics is 0.997724. For a double-size motor the system reliability increases to 0.997886. For the system with redundant motors, the reliability further improves to 0.9982656.

5.2.3 Power

The peak input power for the redundant motor actuator system for two actuators (pitch and Yaw) is 1300 watts. Slewing power is 828 watts. Minimum power (standby power is used to reduce deadband) is 400 watts.

5.2.4 Size and Weight

Since power requirements are essentially the same as in Task B, the same considerations are valid for the sizing of the actuator motor and mechanical parts. The total weights are as follows:

Clutch (4)	3.8 lb
Motor (2)	7.0
Structure, gears, ballscrew	7.2
	18.0 lb

The size would be essentially the same: 5.5 × 8 × 16 inches (at midstroke).

5.3 CONTROL SYSTEM PERFORMANCE

The nonlinear model of the Task B actuation system was employed in simulation studies to determine the performance of the Voyager powered flight control system. The performance of the nominal system was initially investigated. Variations in the actuation system design and initial vehicle attitude rates were next made to determine if stability boundaries existed.

5.3.1 Control System Nonlinear Model

The basic nonlinearities of the actuation system were included in the simulation study. These nonlinearities were engine angle limits (±6 degrees), actuator rate limits, and actuator torque limits. The electromagnetic clutch deadzone was not included with the assumption that clutch bias currents are employed to eliminate this effect. A constant thrust vector offset torque upon the engine actuator was included as well as the effects of a 3σ thrust misalignment angle upon the vehicle control system. A thrust offset of 200 ft-lb was employed. The coulomb friction torque of ±52 ft-lb (at a thrust of 7750 pounds) was not included due to excessive computational time required in the digital simulation program. This exclusion was considered harmless since it represents a small fraction of the design actuator torque capability.

In the study, the actuator torque limits were varied from a minimum of 360 ft-lb to the assumed nominal redundant design value of 1800 ft-lb. The actuator rate limits were varied from a minimum of 1 deg/sec to the nominal design value of 10 deg/sec.

A control system position gain of 0.5 was employed throughout the analysis. The lead-lag filter given previously in Figure 53, containing a lead root at -0.5 rad/sec, was also used in all of the simulation cases. Only the start MOI with capsule on case was studied and the data employed are those previously given in Table 3. Propellant slosh effects were included and body bending effects were excluded in order to retain a low frequency simulation.

The actuation loop natural frequency for the Voyager design is approximately a factor of 2 higher than for the Apollo Service Module since the engine inertia is approximately a factor of 4 smaller. If the same actuator dynamic model is desired, the clutch or clutch amplifier gain could be decreased appropriately. Without any change, this design would contribute less phase lag and attenuation at rigid body and bending frequencies.

To obtain the same attenuation at the first (aft equipment module) bending mode frequency, the noise filter included should be reduced in frequency or additional filtering should be included.

In the simulation study a high clutch-amplifier gain of 1000 ft-lb/deg was employed. The actuator rate feedback gain was reduced to 0.04 second, producing poles for the linear actuator loop at -20 ±25.

5.3.2 Nominal Actuator Design

Performance of the control system with the nominal actuator design was evaluated. The nominal design is defined as having a rate limit of 10 deg/sec and an actuator torque limit of 1800 ft-lb. These two limits were essentially the only actuation system design parameters varied in the study. The powered flight phases are to be unguided, that is, an attitude hold operation is employed; therefore, excitation to the powered flight control system in the form of guidance command will not result. The primary disturbances to the vehicle control system are those arising from thrust vector misalignments and offsets, cg offsets, and, to a lesser degree, initial attitude and rate conditions from the coast phase.

The initial attitude errors to be expected are less than 0.25 degree and the initial attitude rates to be expected are much less than 0.1 deg/sec, hence, use of these values would cause little system response. The 3σ thrust vector misalignment of 0.5 degree, however, would perturb the control system significantly; therefore, this effect was retained throughout the simulation runs. The response of the vehicle to thrust vector offsets and cg offsets would be similar in characteristics to the thrust misalignment response with the exception of the final attitude error; therefore, only the thrust misalignment cases were studied. Figures 115 to 120 show the response of the control system to a 0.5-degree thrust misalignment and Figures 121 to 126 show the response to a -0.5-degree thrust misalignment.

The sizable attitude error shows results from the combined effects of thrust vector misalignments (DM), a thrust offset torque on the actuator (TM), a position gain of 0.5 and engine hose restraint effects, K_G. The steady-state value, θ_{ss}, would be:

$$\theta_{ss} = \frac{1}{K_p}\left(\frac{K_A + K_G}{K_A}\right)\left(\frac{TM}{K_A} + DM\right)$$

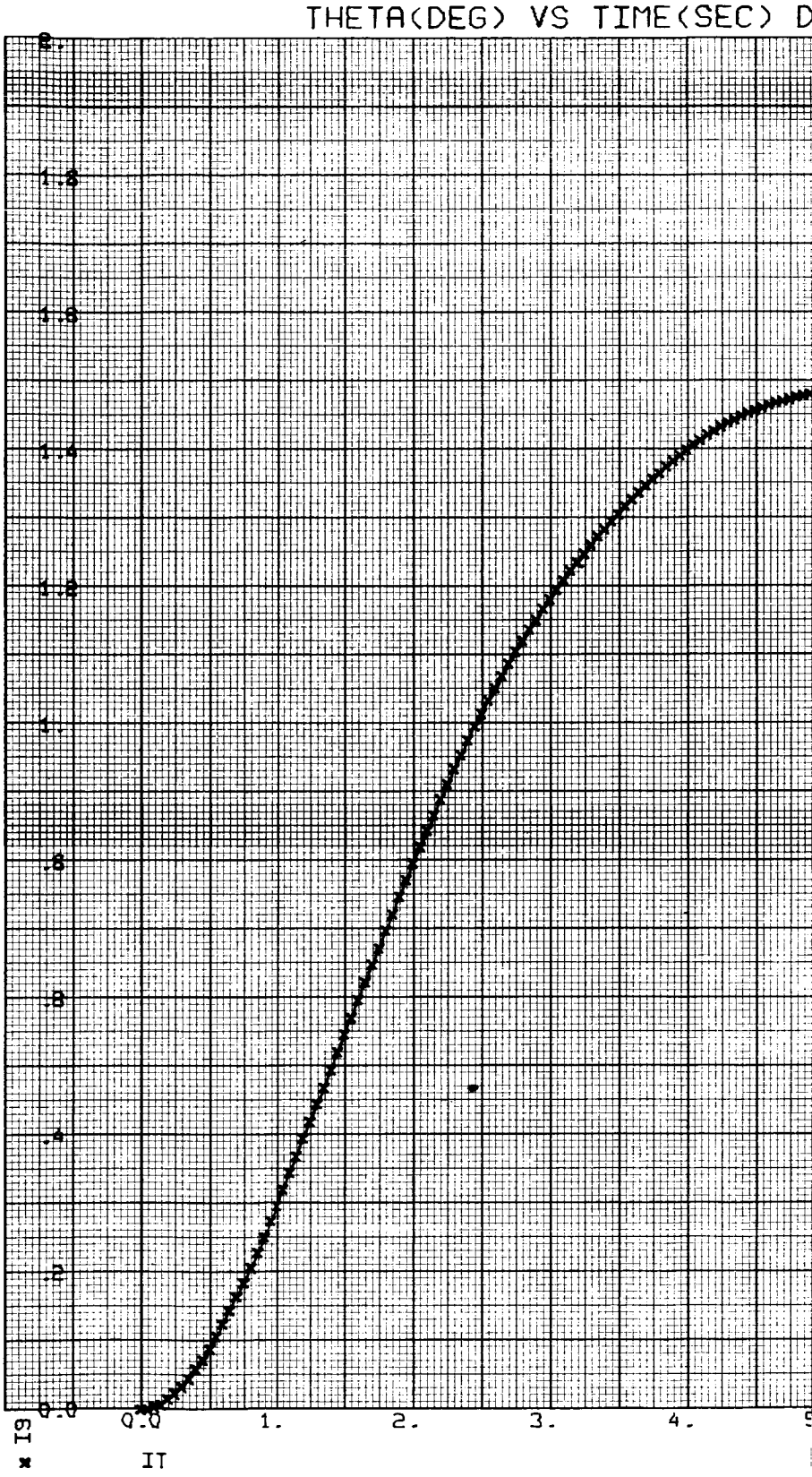
THETA(DEG) VS TIME(SEC) D
2.
1.8
1.6
1.4
1.2
1.
.8
.6
.4
.2
0.0
0.0
1.
2.
3.
4.
SIG
IT

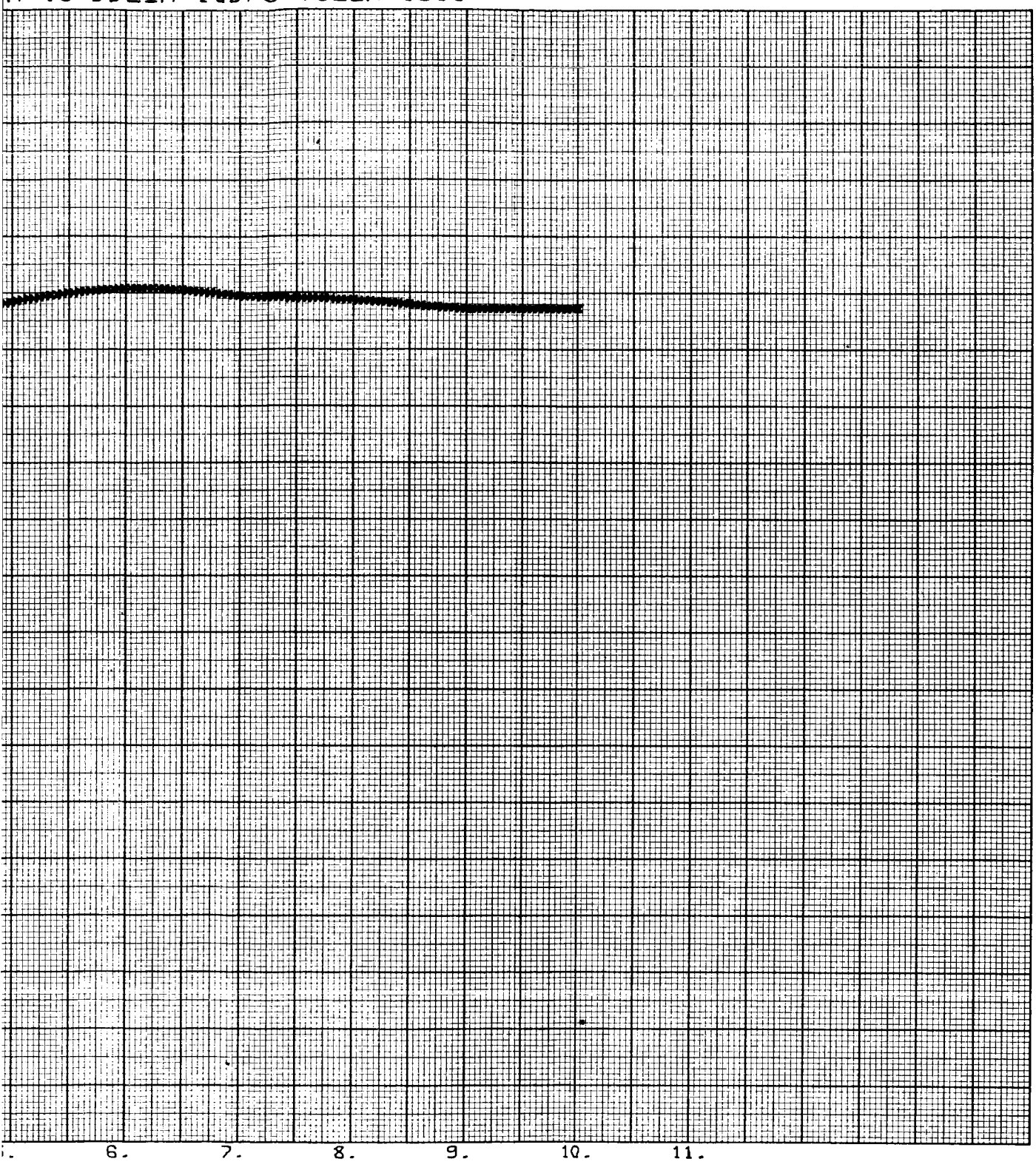

Figure 115. Nominal Actuation System, Vehicle Attitude Versus Time, DM = 0.5 Deg

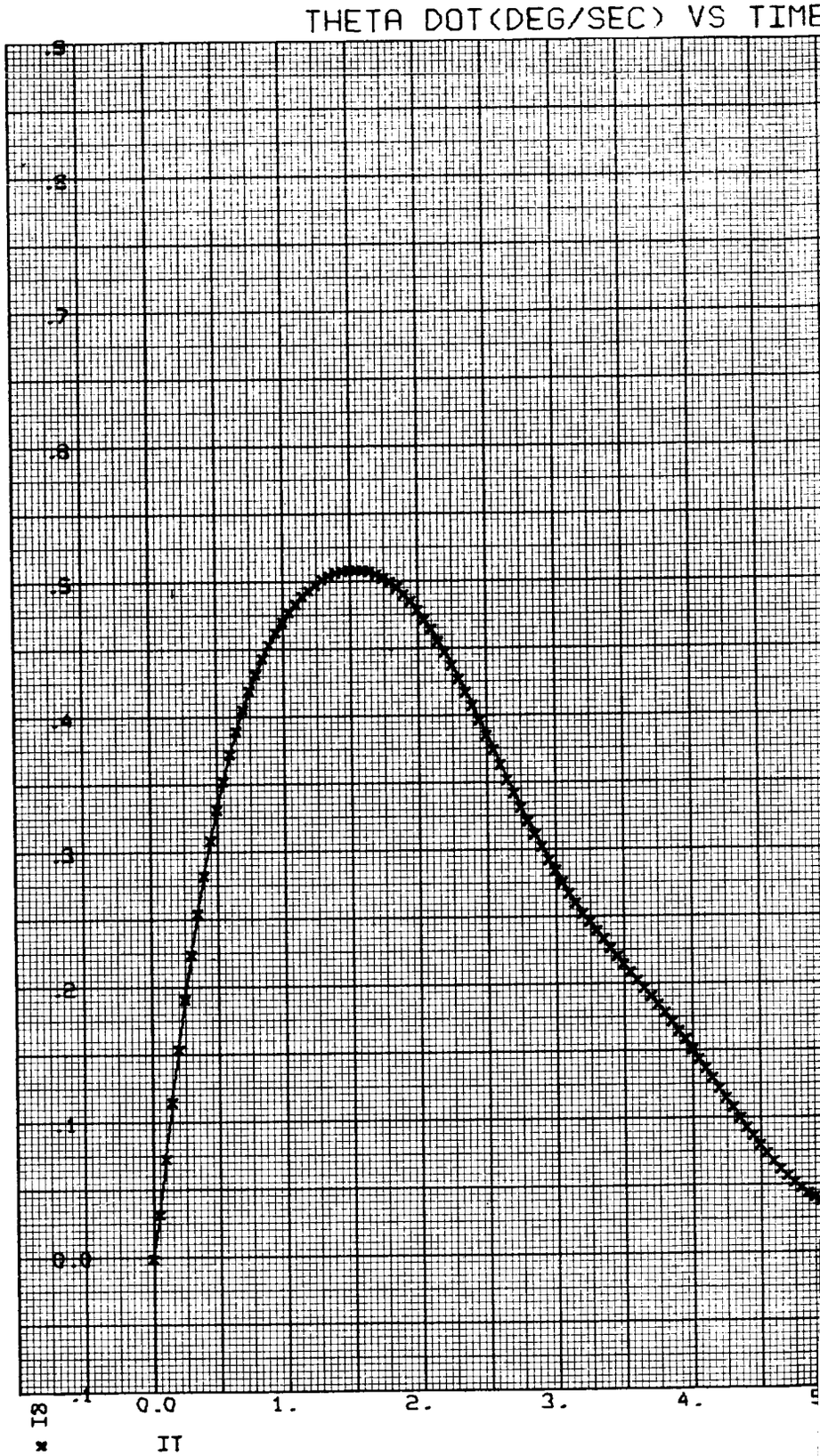
THETA DOT(DEG/SEC) VS TIME
.9
.8
.7
.6
.5
.4
.3
.2
.1
0.0
-.1
0.0
1.
2.
3.
4.
I8
IT

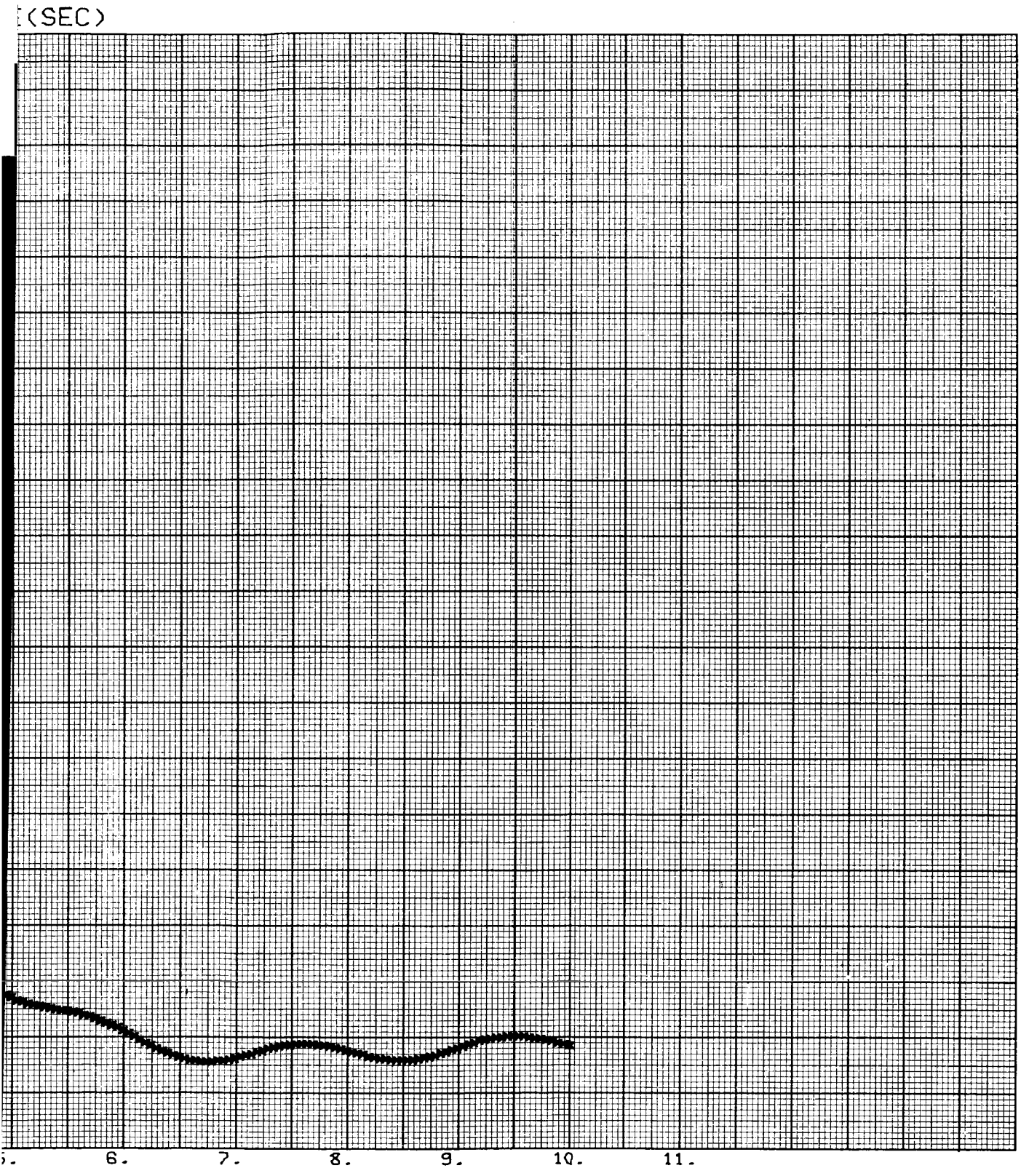

Figure 116. Nominal Actuation System, Vehicle Rate Versus Time, DM = 0.5 Deg

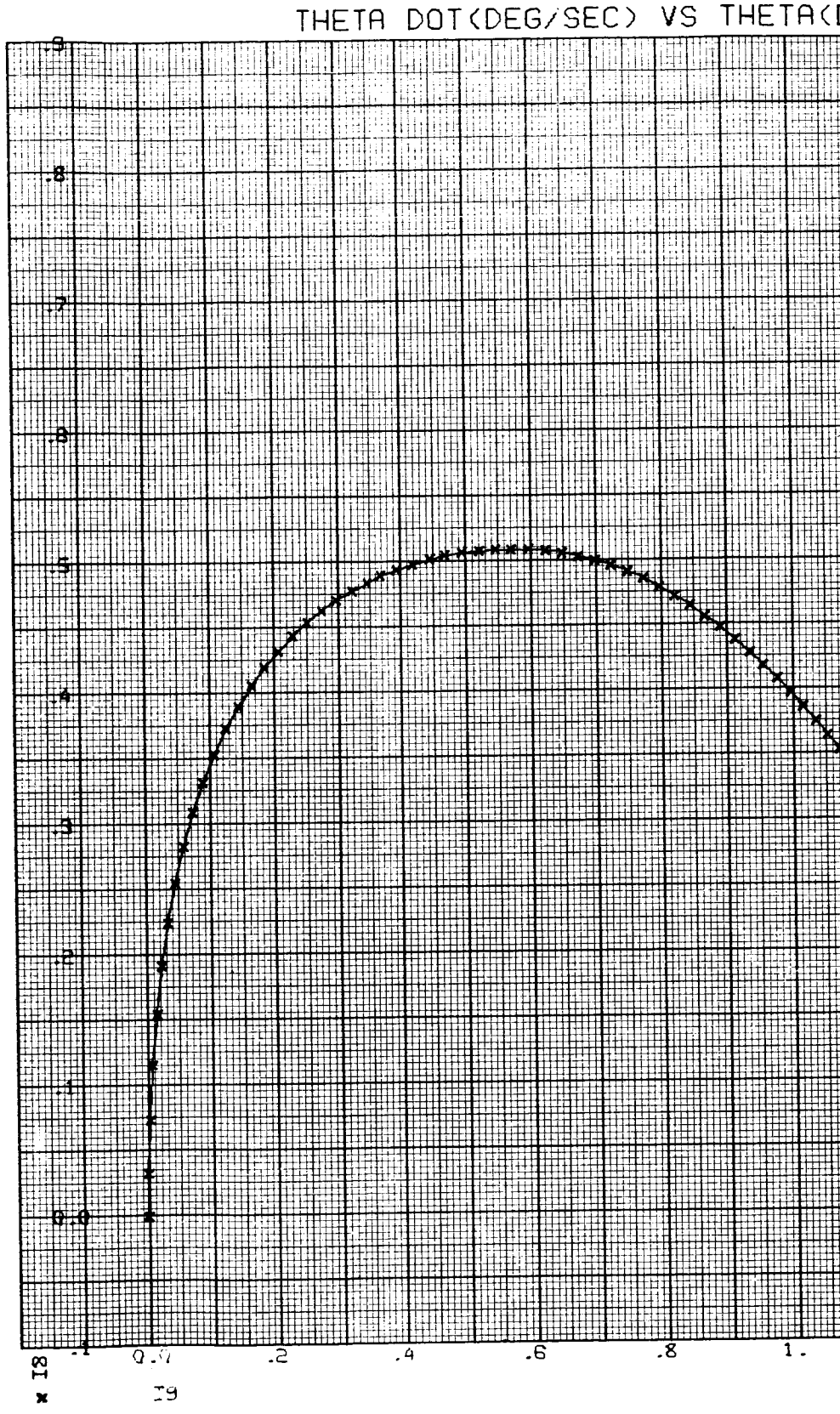
THETA DOT(DEG/SEC) VS THETA(
.9
.8
.7
.6
.5
.4
.3
.2
.1
0.0
-.1
0.0
.2
.4
.6
.8
1.
I8
I9

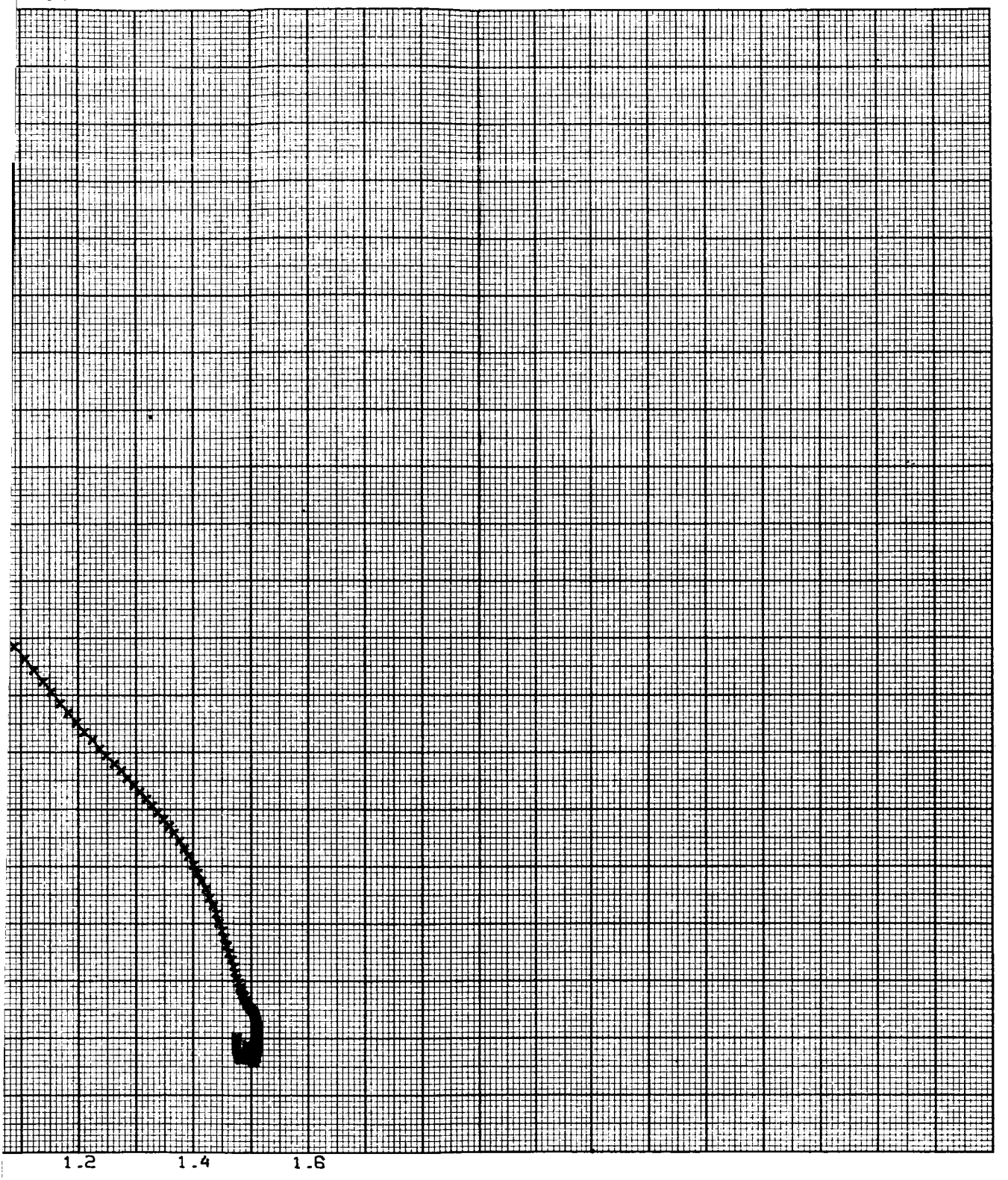

Figure 117. Nominal Actuation System, Attitude Rate Versus Vehicle Attitude, DM = 0.5 Deg

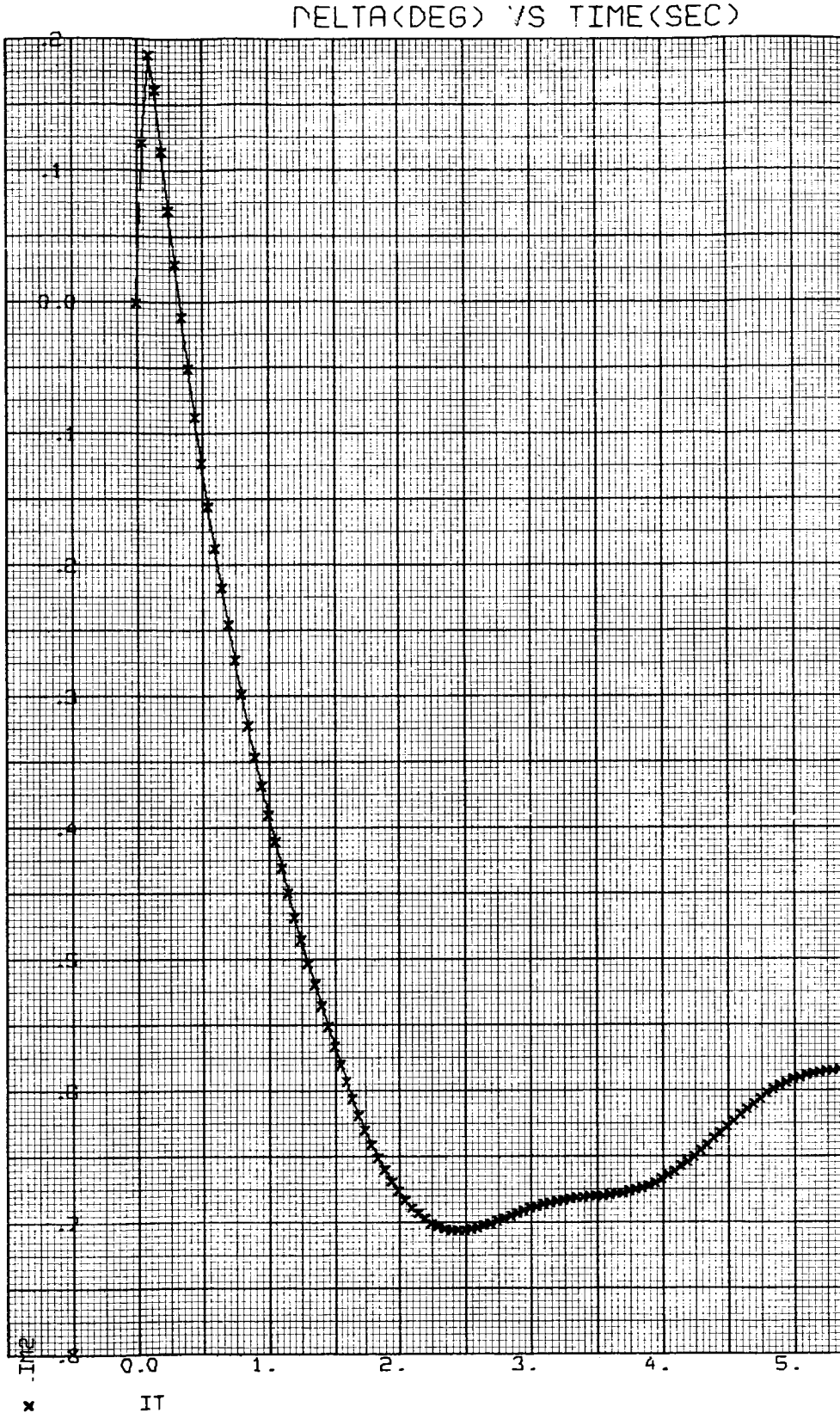
DELTA(DEG) VS TIME(SEC)
.2
.1
0.0
-.1
-.2
-.3
-.4
-.5
-.6
-.7
-.8
0.0
1.
2.
3.
4.
5.
IT

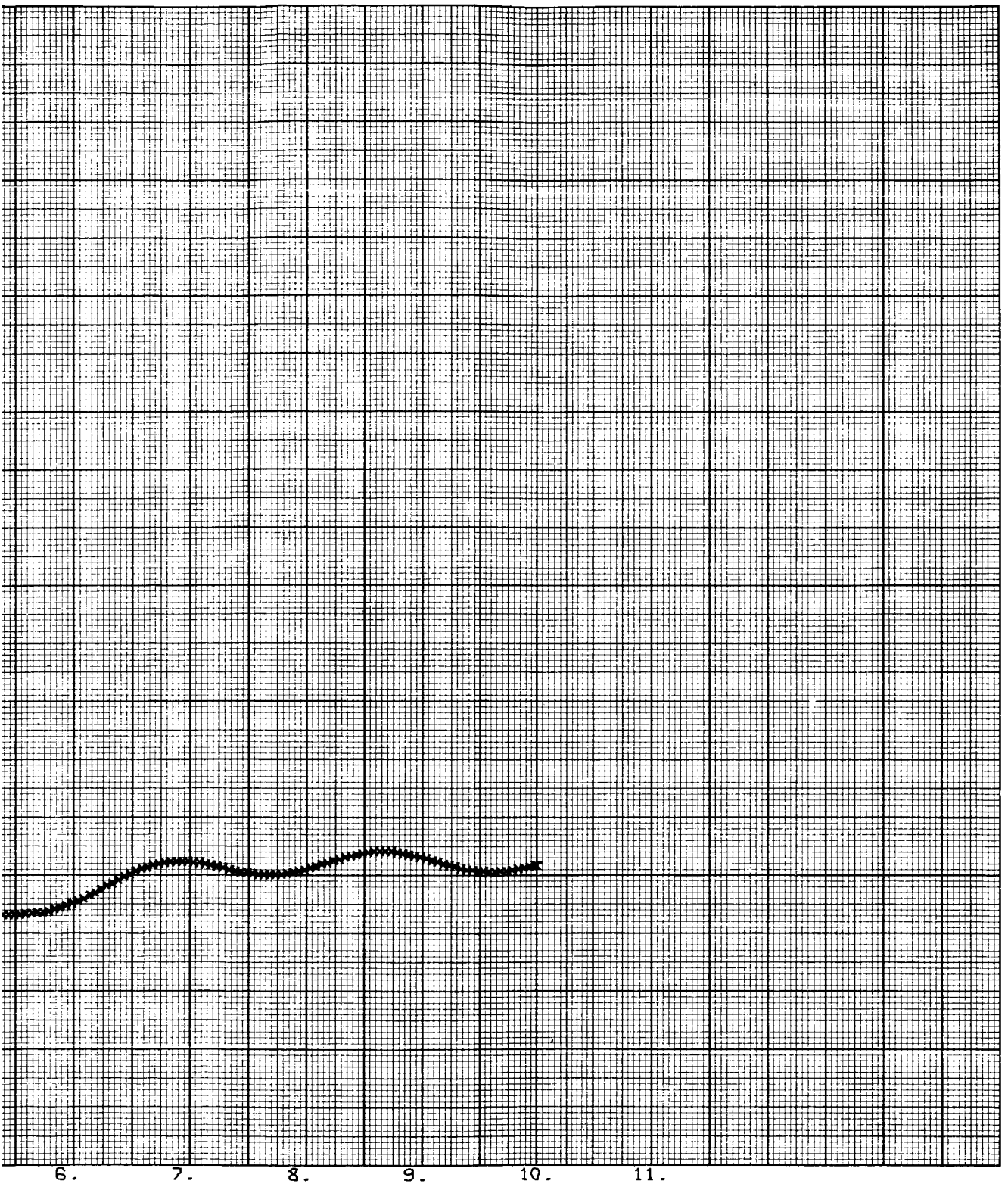

Figure 118. Nominal Actuation System, Engine Angle Versus Time, DM = 0.5 Deg

DELTA DOT(DEG/SEC) VS TIME(SEC)

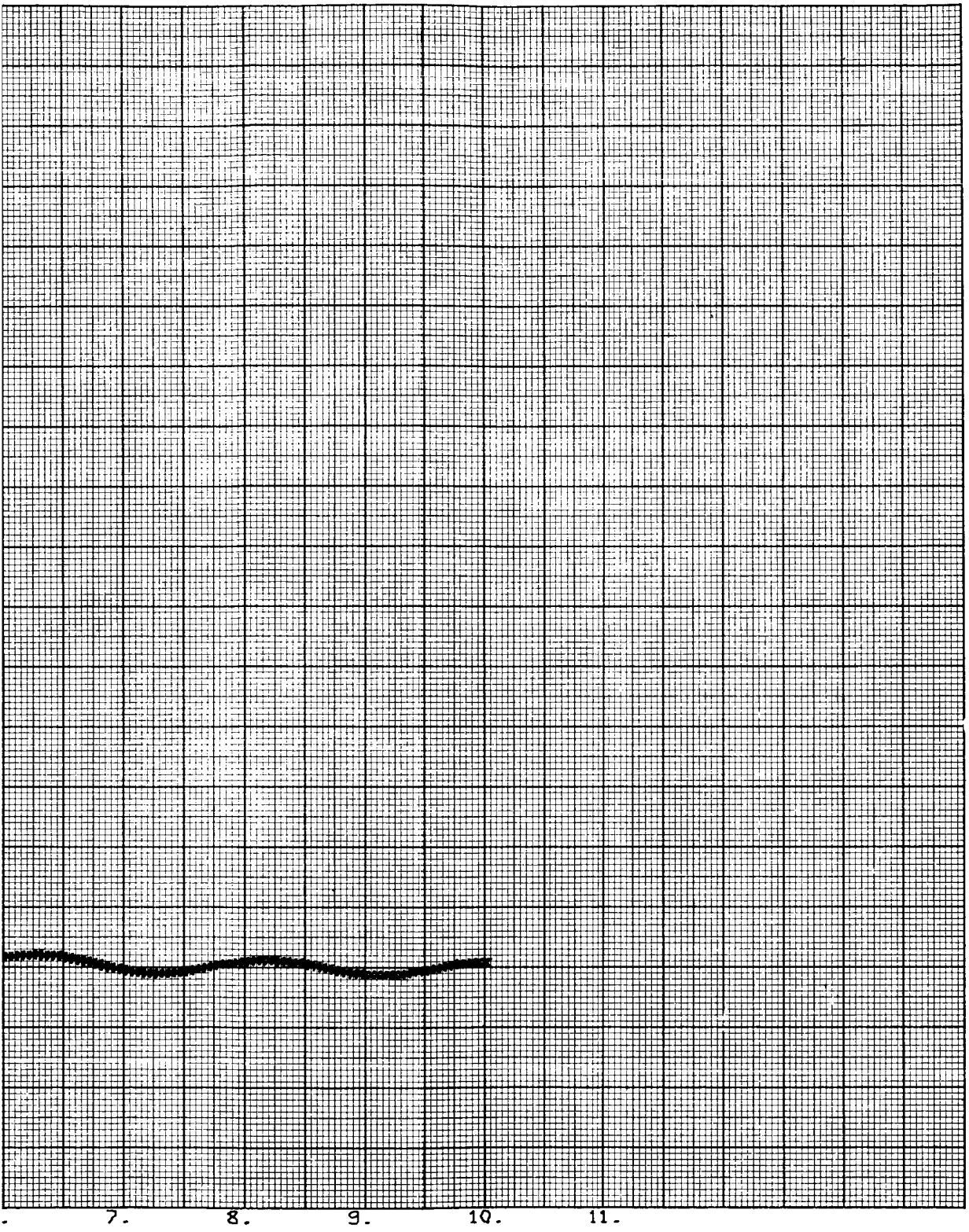

Figure 119. Nominal Actuation System, Actuator Rate Versus Time, DM = 0.5 Deg

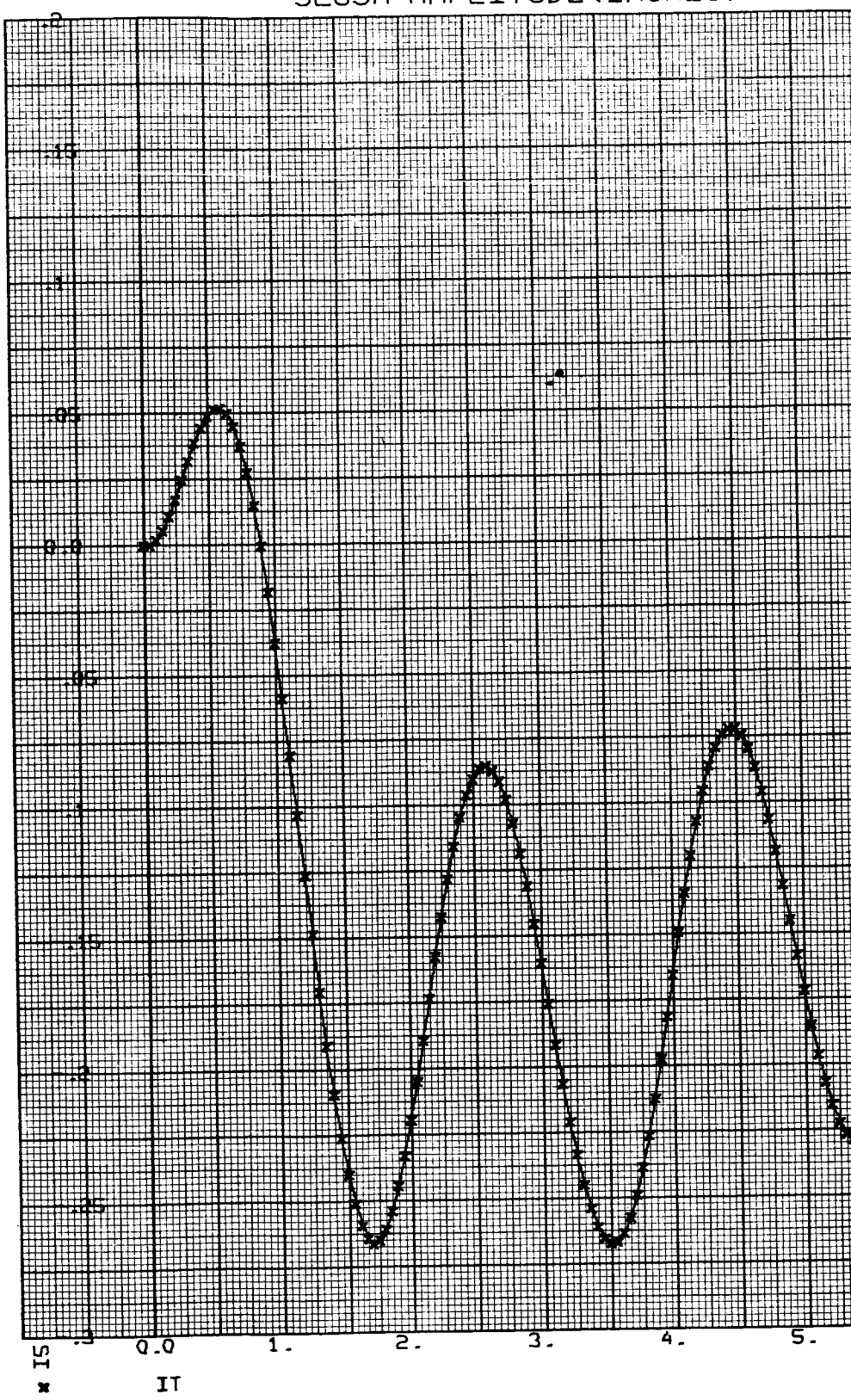
SLOSH AMPLITUDE(INCHES) VS TI
.2
.15
.1
.05
0.0
.05
.1
.15
.2
.25
-.3
0.0
1.
2.
3.
4.
5.
IS
IT

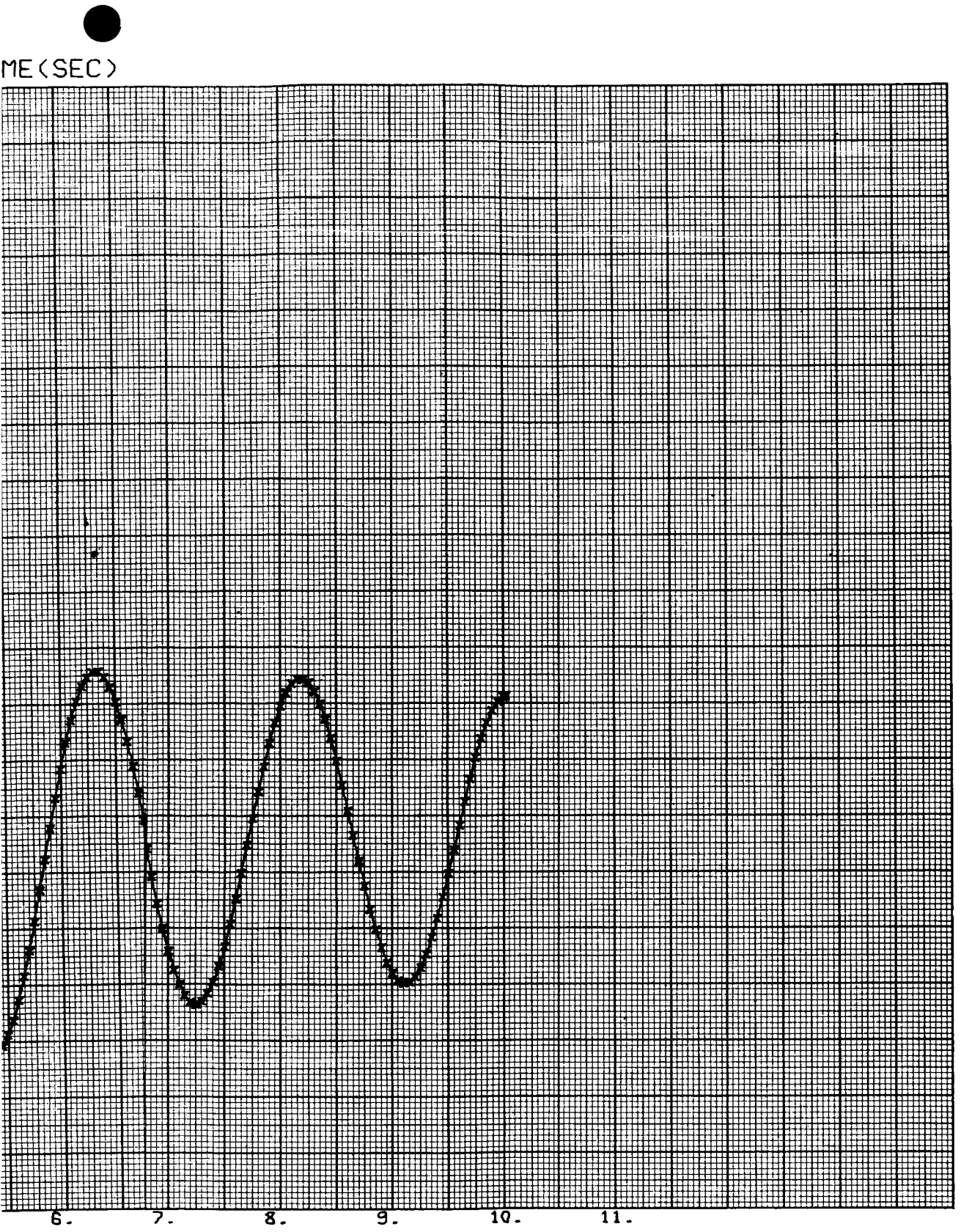

Figure 120. Nominal Actuation System, Slosh Amplitude Versus Time, DM = 0.5 Deg

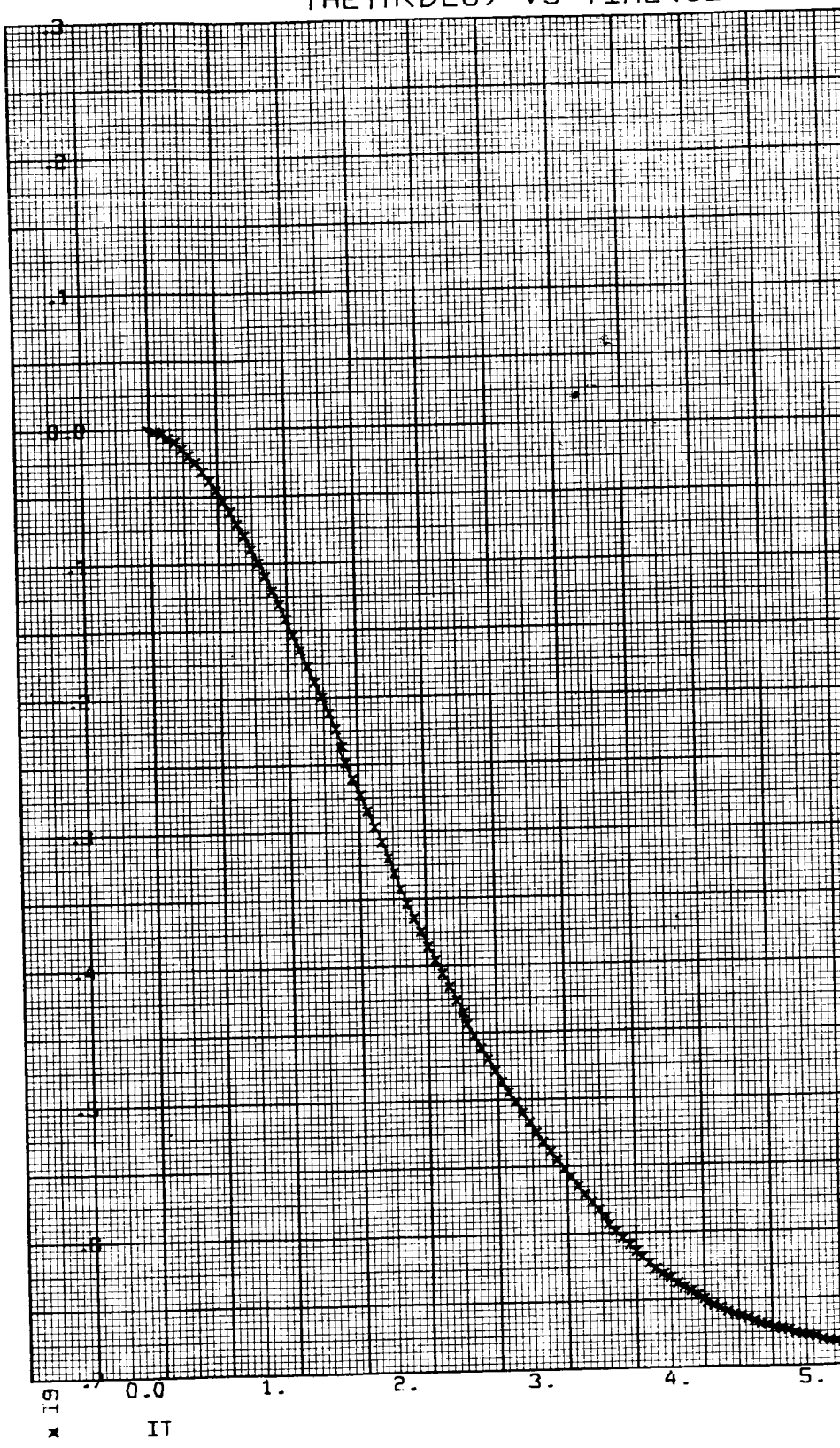
THETA(DEG) VS TIME(SEC) DM=
.2
0.0
-.2
-.4
-.6
-.8
0.0
1.
2.
3.
4.
5.
IT
x

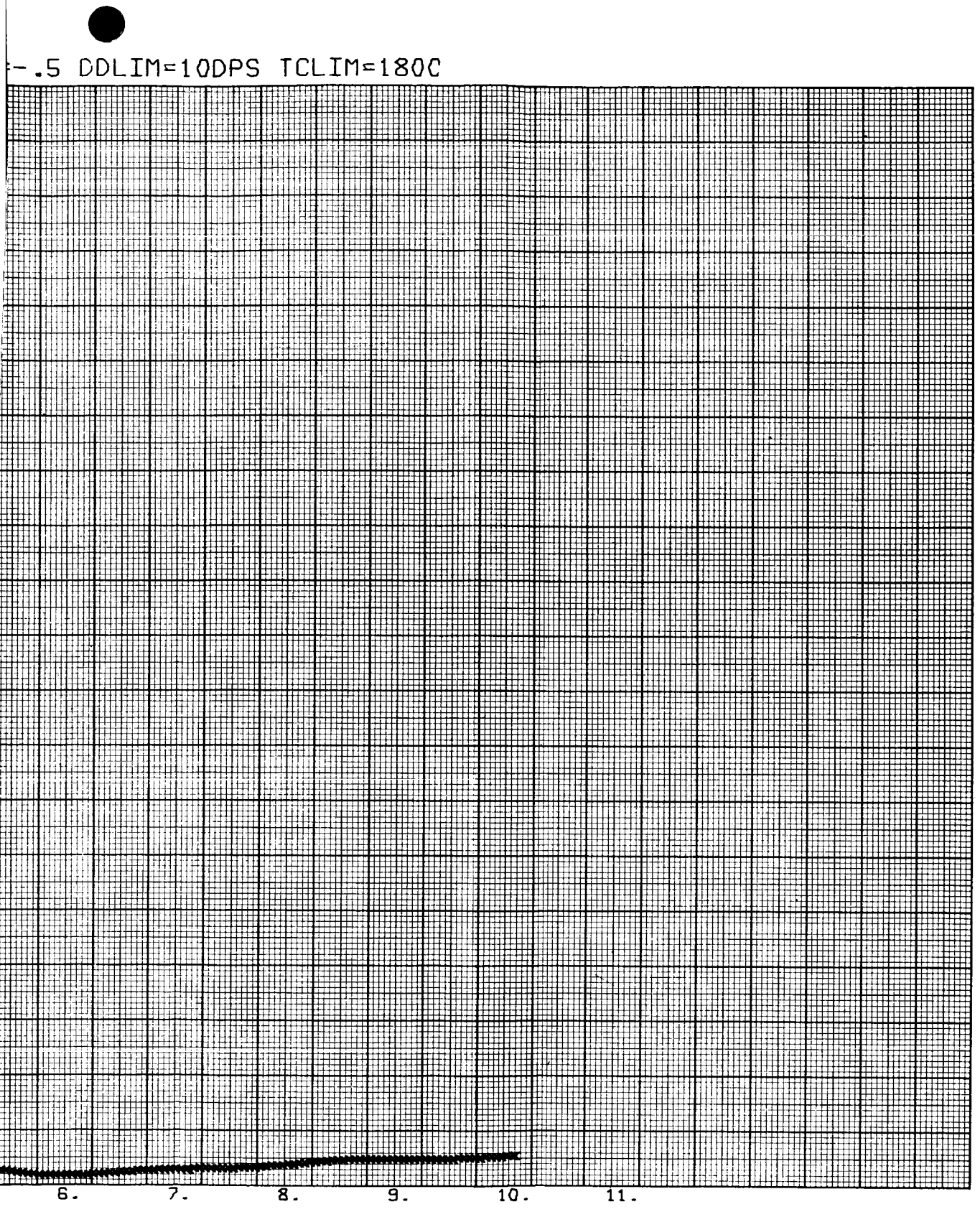

Figure 121. Nominal Actuation System, Vehicle Attitude Versus Time, DM = -0.5 Deg

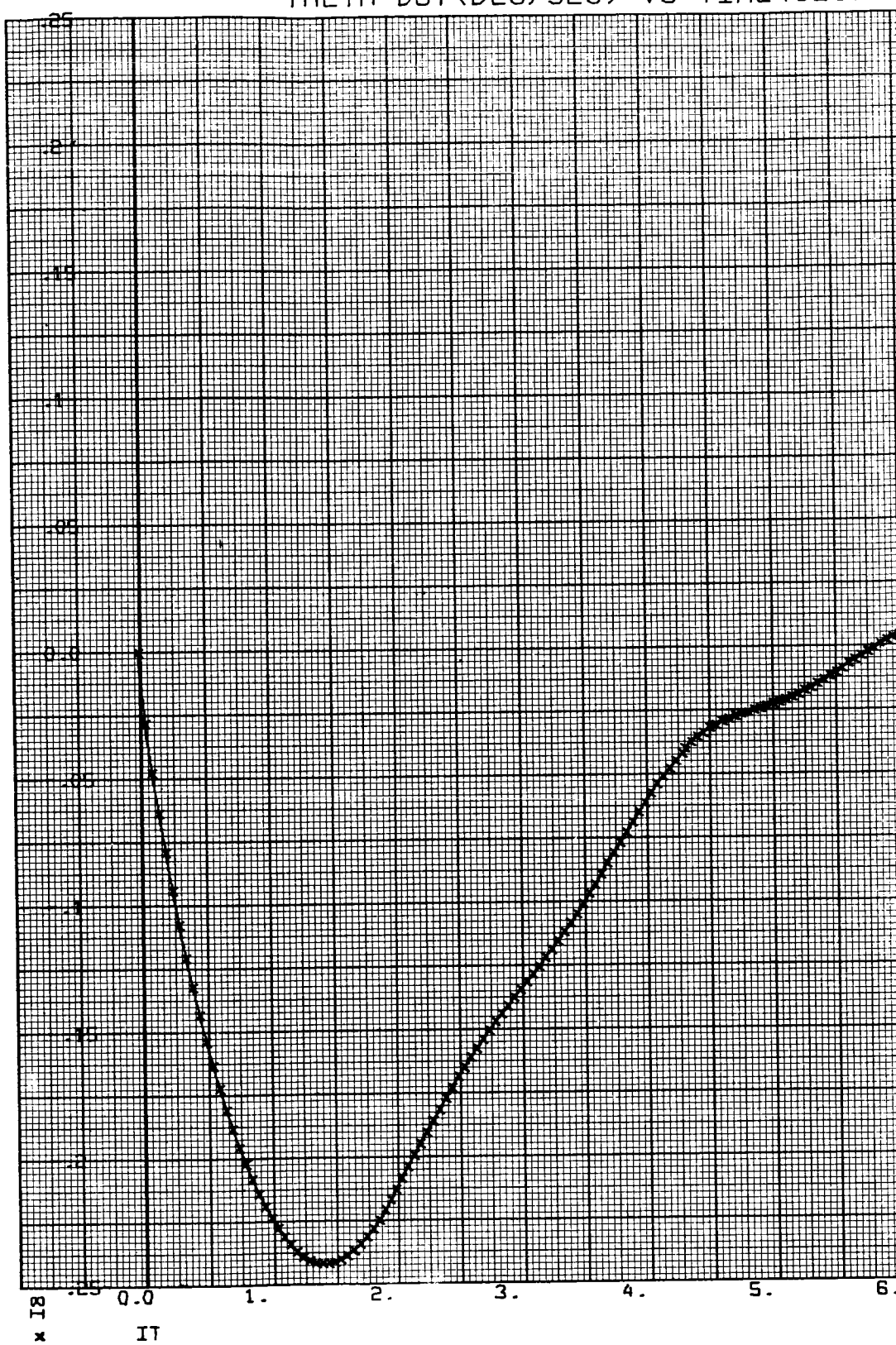
THETA DOT(DEG/SEC) VS TIME(SEC)
.25
.2
.15
.1
.05
0.0
.05
1.
2.
3.
4.
5.
6.
IT
IT

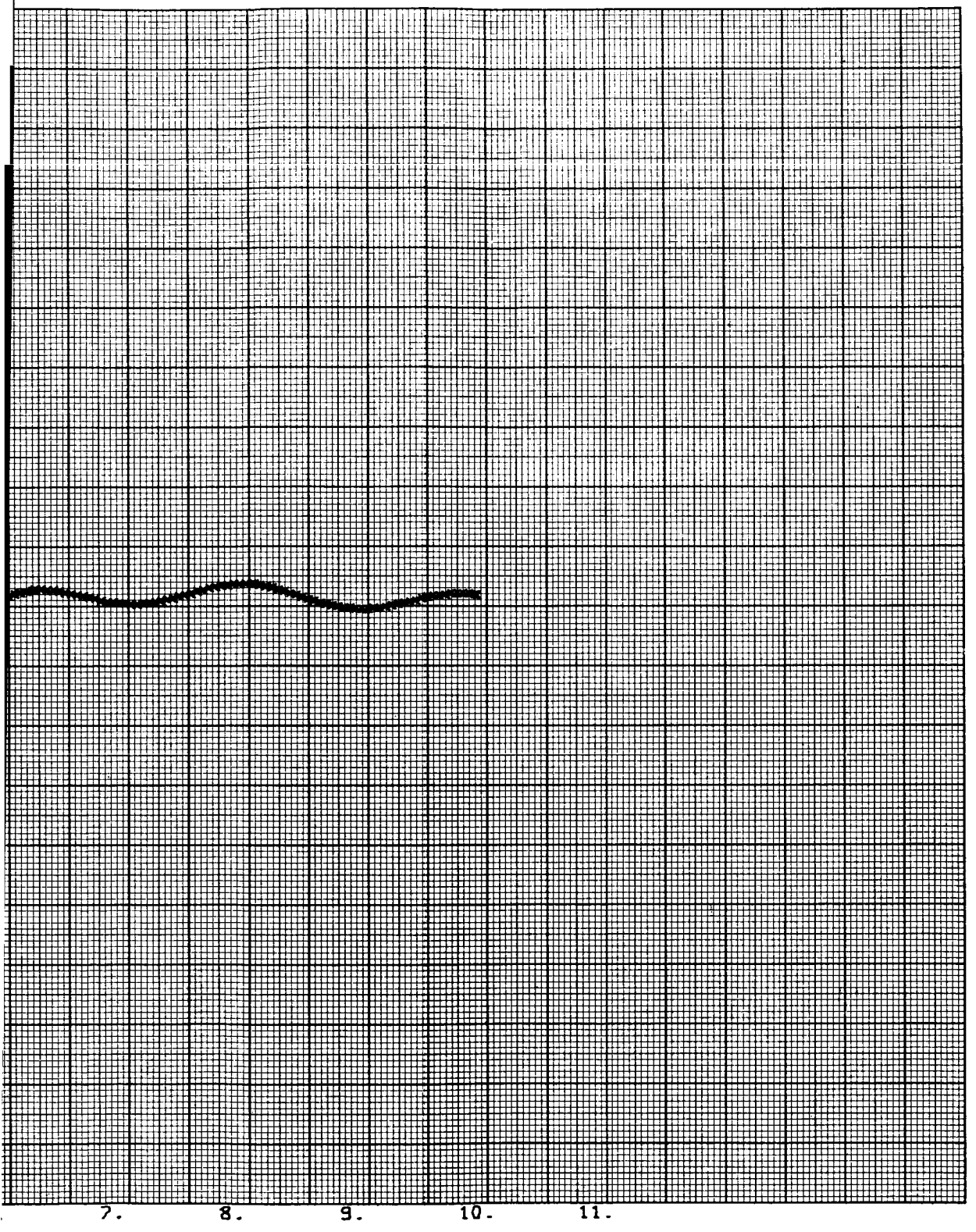

Figure 122. Nominal Actuation System, Attitude Rate Versus Time, DM = -0.5 Deg

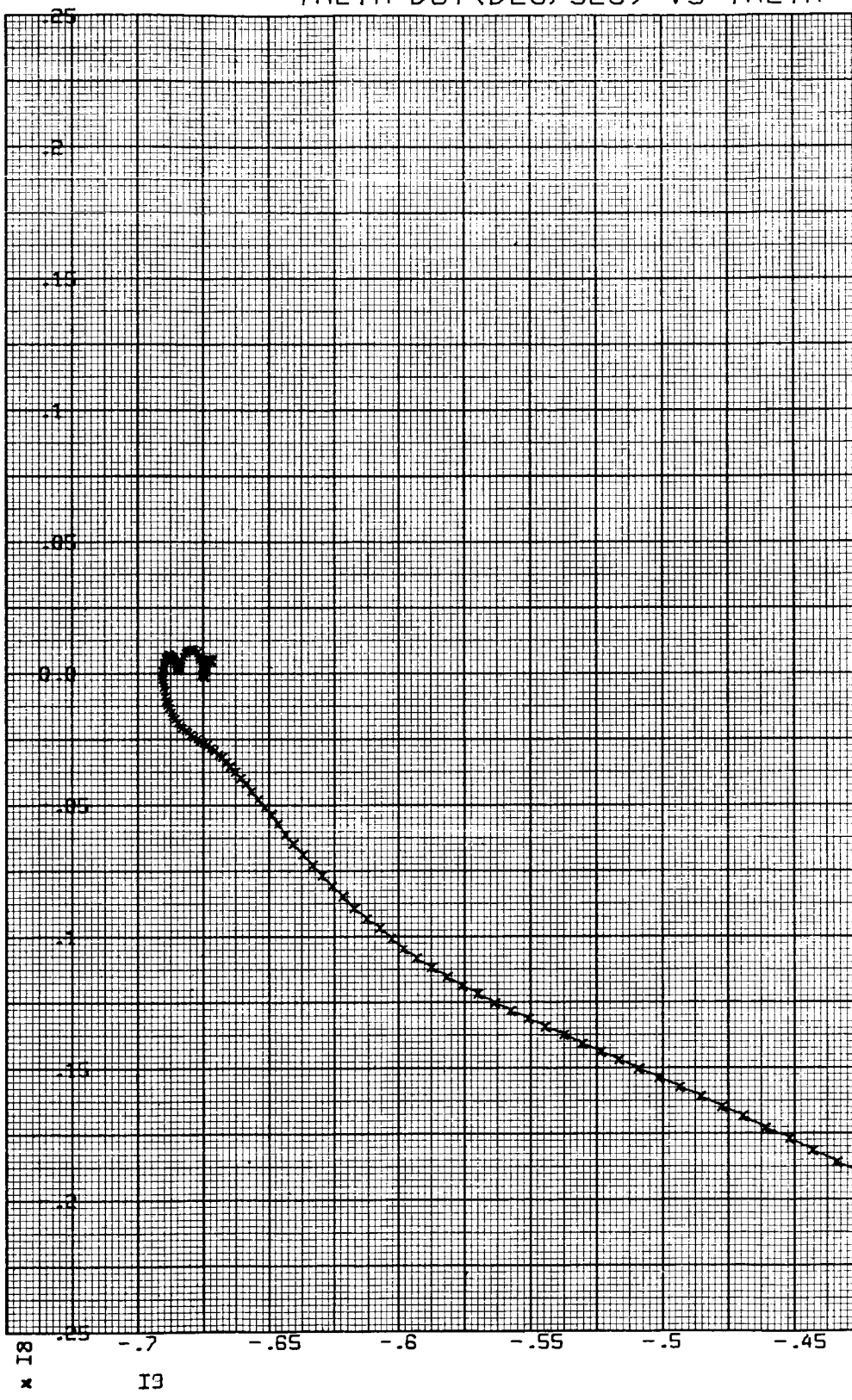
THETA DOT(DEG/SEC) VS THETA
.25
.2
.15
.1
.05
0.0
-.05
-.1
-.15
-.2
-.25
-.7
-.65
-.6
-.55
-.5
-.45
I8
I3

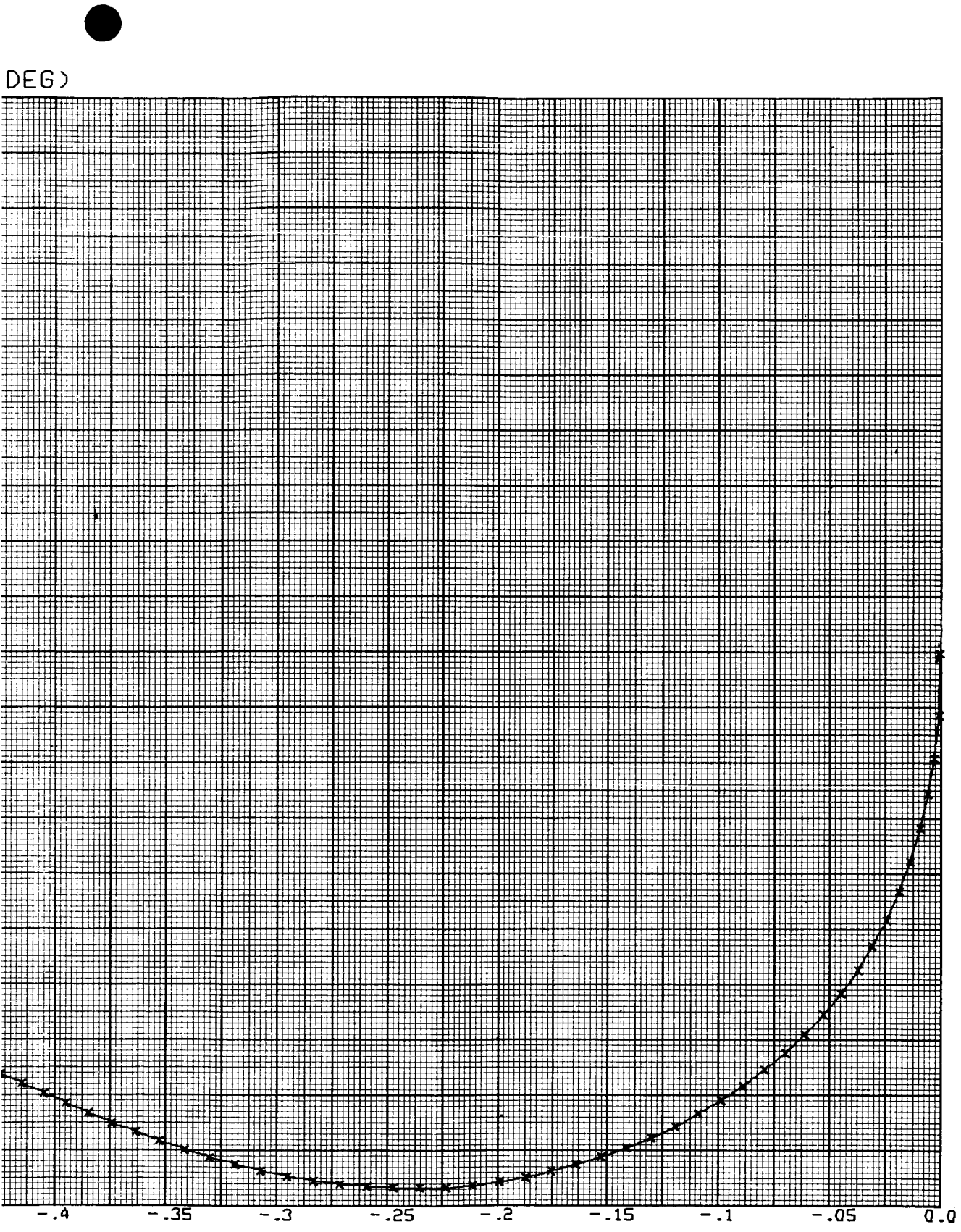

Figure 123. Nominal Actuation System, Attitude Rate Versus Vehicle Attitude, DM = -0.5 Deg

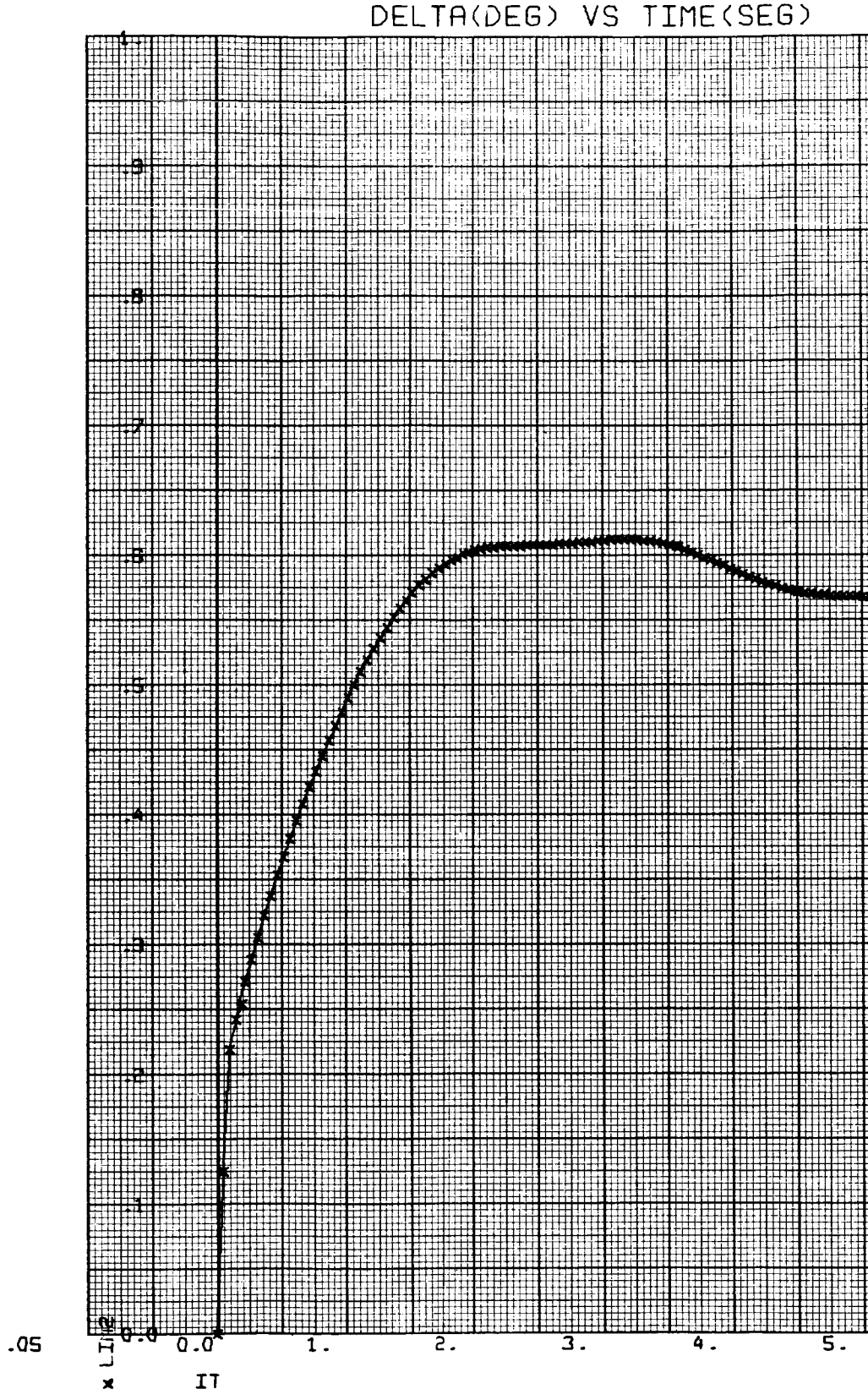
DELTA(DEG) VS TIME(SEG)
1.
.9
.8
.7
.6
.5
.4
.3
.2
.1
0.0
0.0
1.
2.
3.
4.
5.
.05
DELTA
x
IT

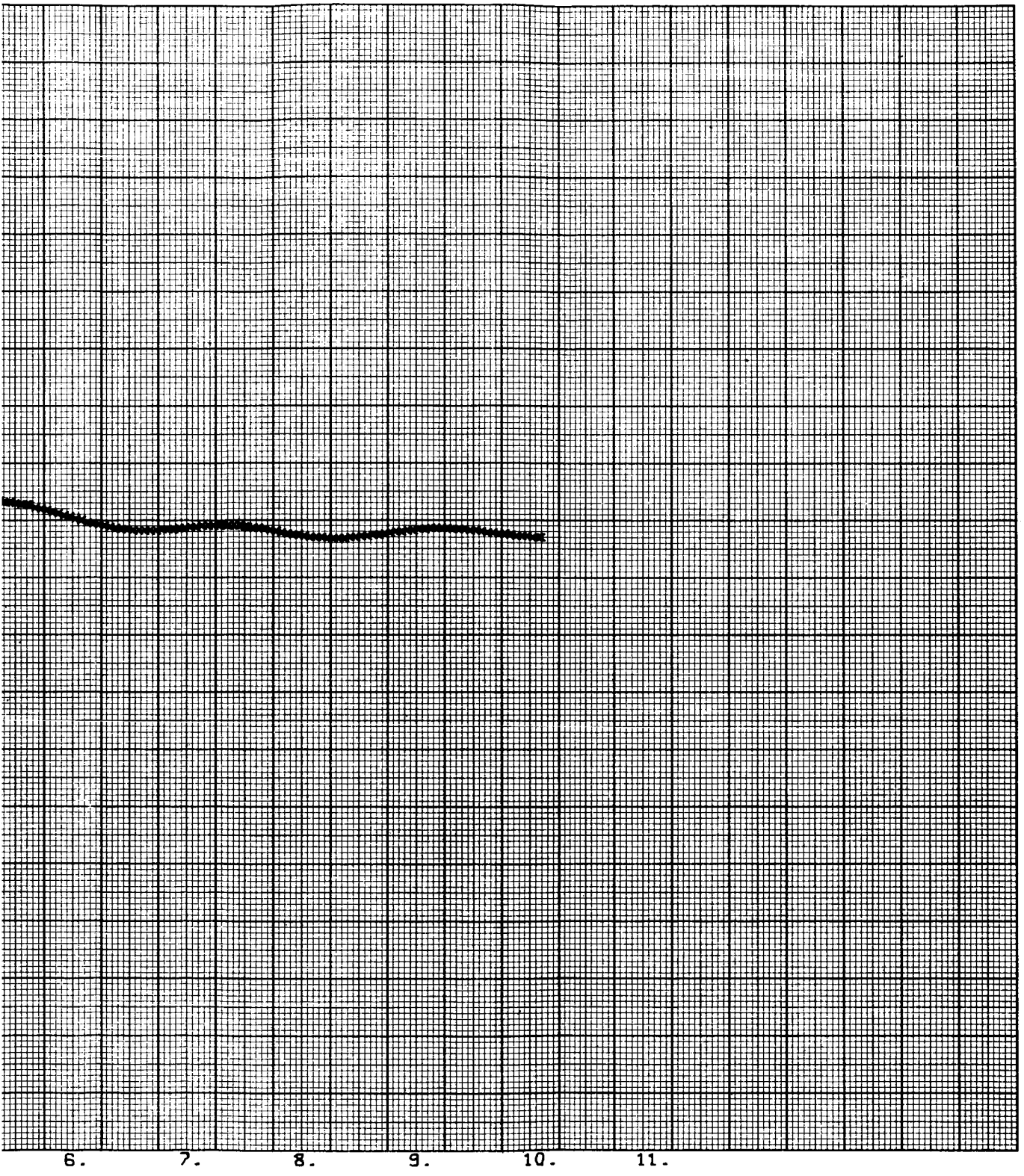

Figure 124. Nominal Actuation System, Engine Angle Versus Time, DM = -0.5 Deg

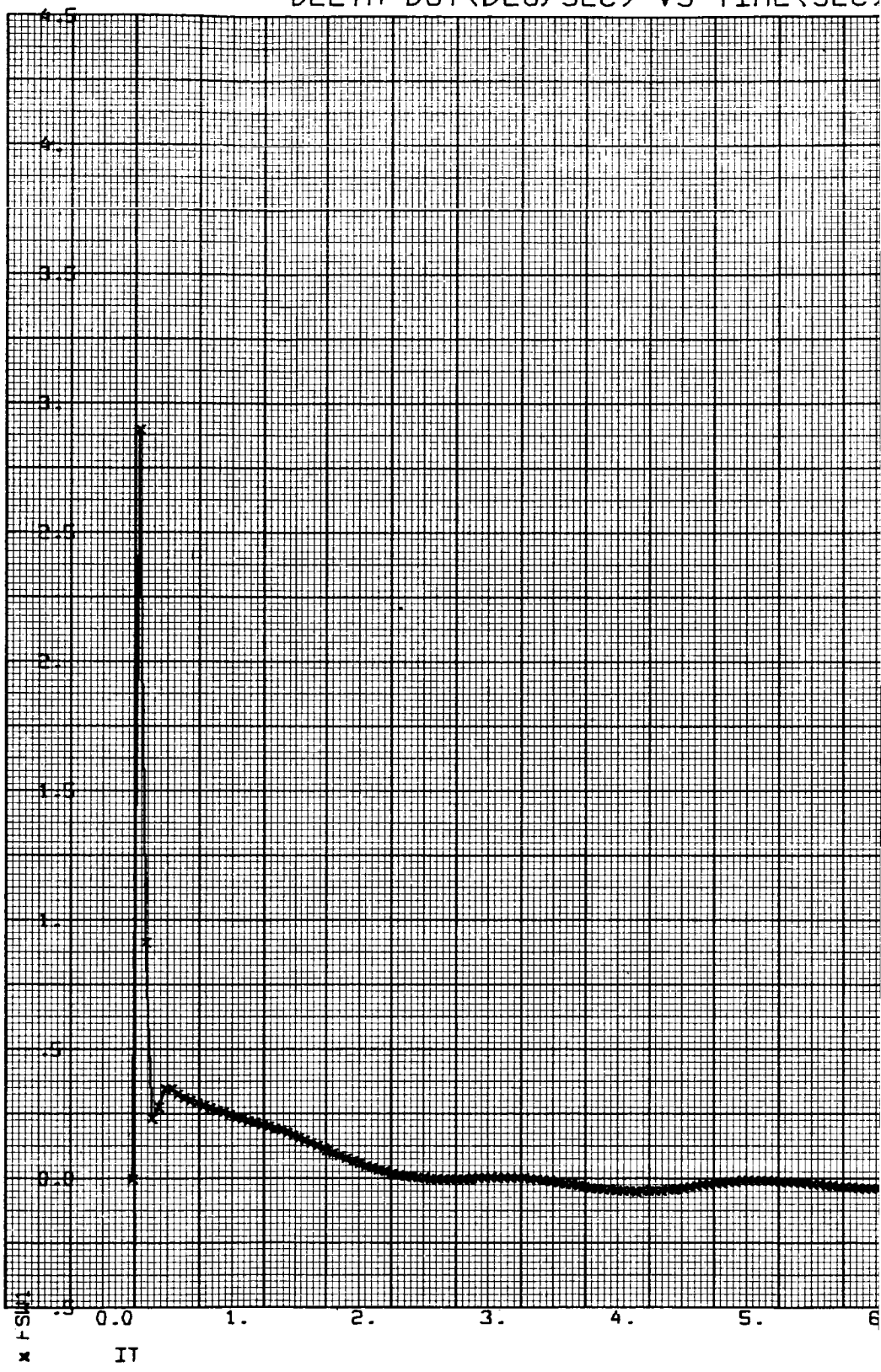
DELTA DOT(DEG/SEC) VS TIME(SEC)
4.5
4.
3.5
3.
2.5
2.
1.5
1.
.5
0.0
-.5
0.0
1.
2.
3.
4.
5.
6
IT

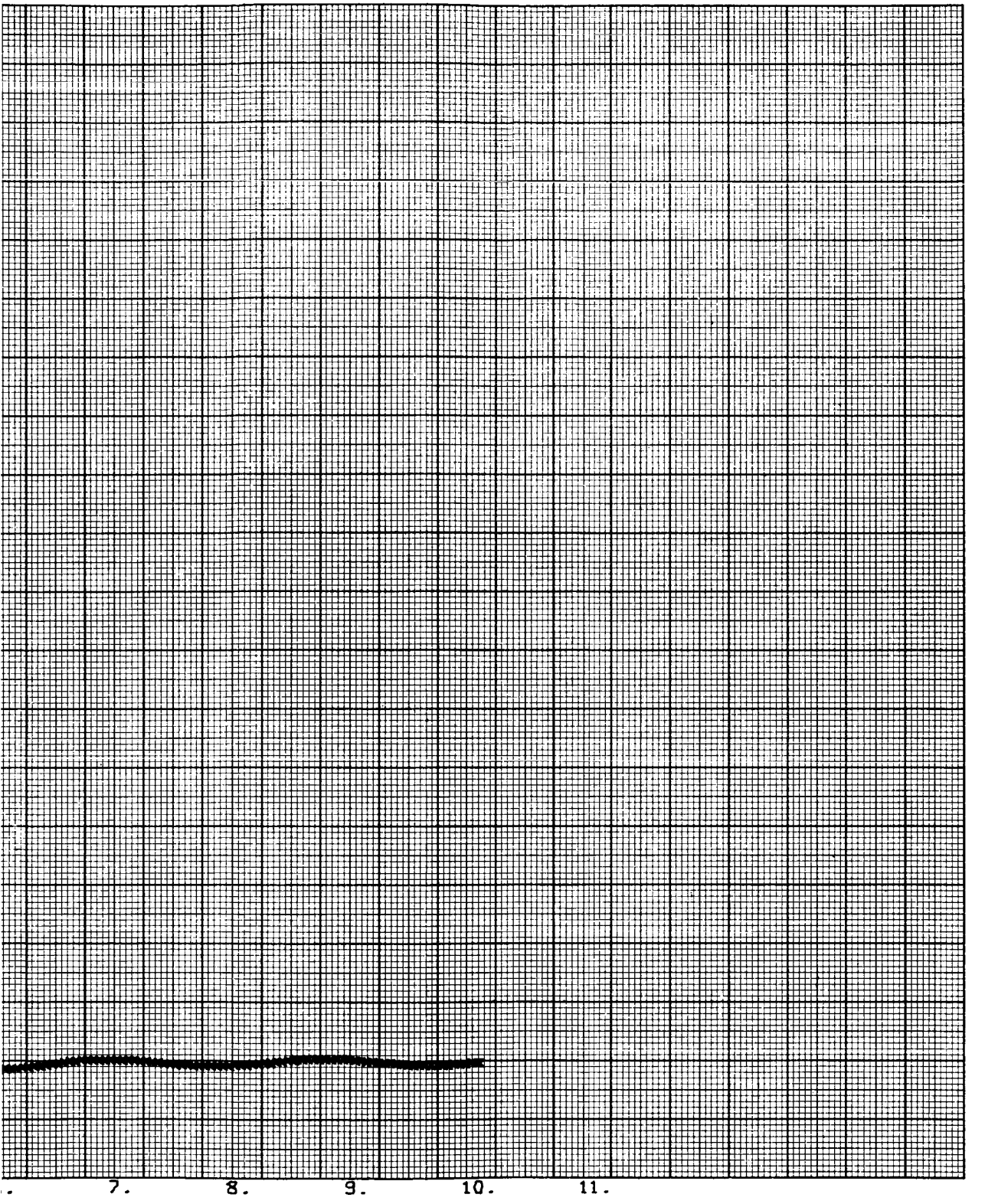

Figure 125. Nominal Actuation System, Actuator Rate Versus Time, DM = -0.5 Deg

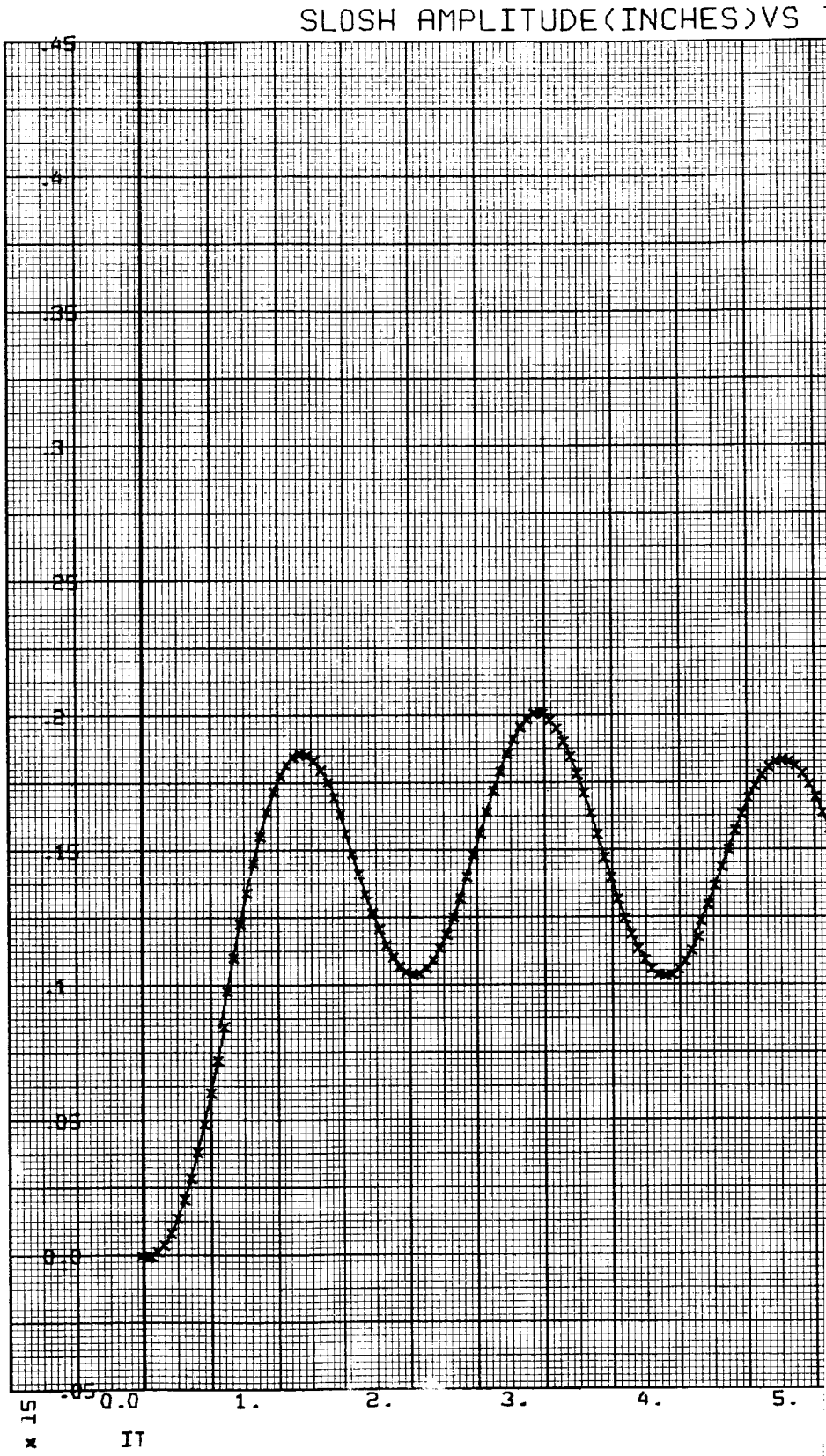
SLOSH AMPLITUDE(INCHES)VS
.45
.4
.35
.3
.25
.2
.15
.1
.05
0.0
-.05
0.0
1.
2.
3.
4.
5.
IT
ST

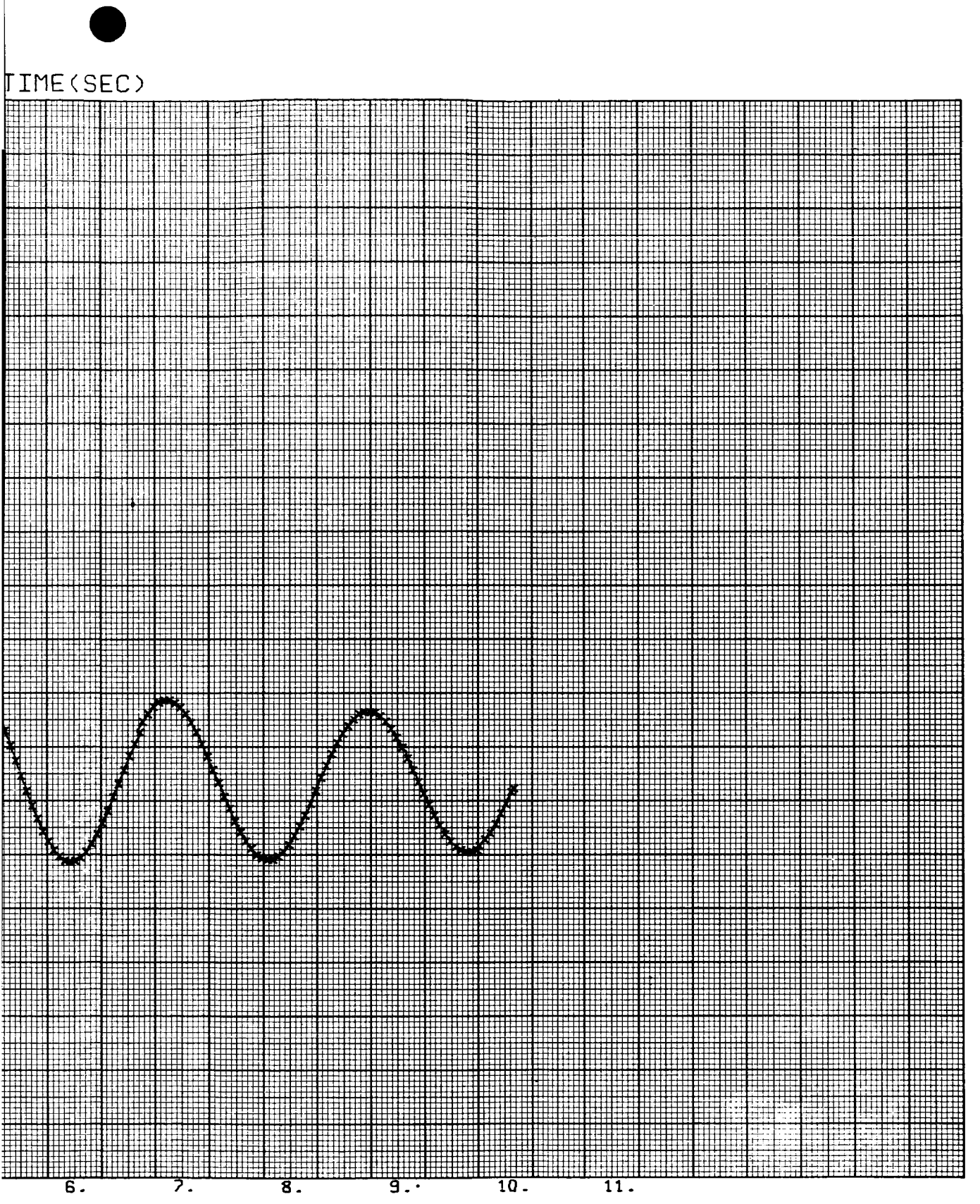

Figure 126. Nominal Actuation System, Slosh Amplitude Versus Time, DM = -0.5 Deg

where K_A is the clutch-amplifier gain = 1000 ft-lb/deg. Inserting values of TM = 200 ft-lb, K_G = 11 ft-lb/deg, the following steady-state values are obtained:

$$\theta_{ss} = 1.415 \text{ deg for DM} = 0.5 \text{ deg}$$

$$\theta_{ss} = -0.607 \text{ deg for DM} = -0.5 \text{ deg}$$

The maximum actuator rate for these cases was less than 3 deg/sec (much less than the 10 deg/sec limit) indicating that for these conditions a reduction in the actuator rate limit could be tolerated.

The response of the control system with the nominal actuation system is shown to be satisfactory. If the final design for this configuration includes a higher position gain (see Section 3), a more rapid response of the system could be obtained.

5.3.3 Without Initial Attitude Rates

In an attempt to produce an unsatisfactory system response with the perturbations employed previously, several cases were run in which the actuator torque limit and rate limits were reduced. The minimum actuator torque necessary to satisfy the design requirements given in Section 5.3.1 was 360 ft-lb. Figure 127 shows a phase plane plot in which the minimum torque limit and a rate limit of 1 deg/sec were used. The control system response was very similar to that for the nominal actuator design.

5.3.4 Stability Boundary with Initial Attitude Rates

Since the above perturbations did not impose significant constraints upon the actuation design, initial attitude rates were added in the simulation runs. For the nominal design, several initial rate cases were obtained. Phase plane plots for initial rates of 2, 3, and 3.5 deg/sec are shown, respectively, in Figures 128, 129, and 130. The control system is shown to pass through the initial rate stability boundary somewhere between 3 and 3.5 deg/sec. Similar runs are given in Figures 131 and 132 for an actuator rate limit of 7.5 deg/sec. The initial rate stability boundary is indicated to be between 2.5 and 3 deg/sec for this actuator

rate limit. Figures 133 through 135 show similar phase plane plots for an actuator rate limit of 5 deg/sec. The initial rate stability boundary is shown to lie between 1.5 and 2 deg/sec. An initial attitude rate stability boundary curve was constructed from all of the various cases obtained and is shown in Figure 136. A similar curve for negative initial rates would have been pursued if time had permitted. The polarity change relative to the thrust misalignment direction would produce a different boundary curve.

Figures 137 through 141 show the simulation time history plots for the nominal system with a 3-deg/sec initial rate. They are included for general interest since they pertain to the largest initial rate from which the nominal system could recover.

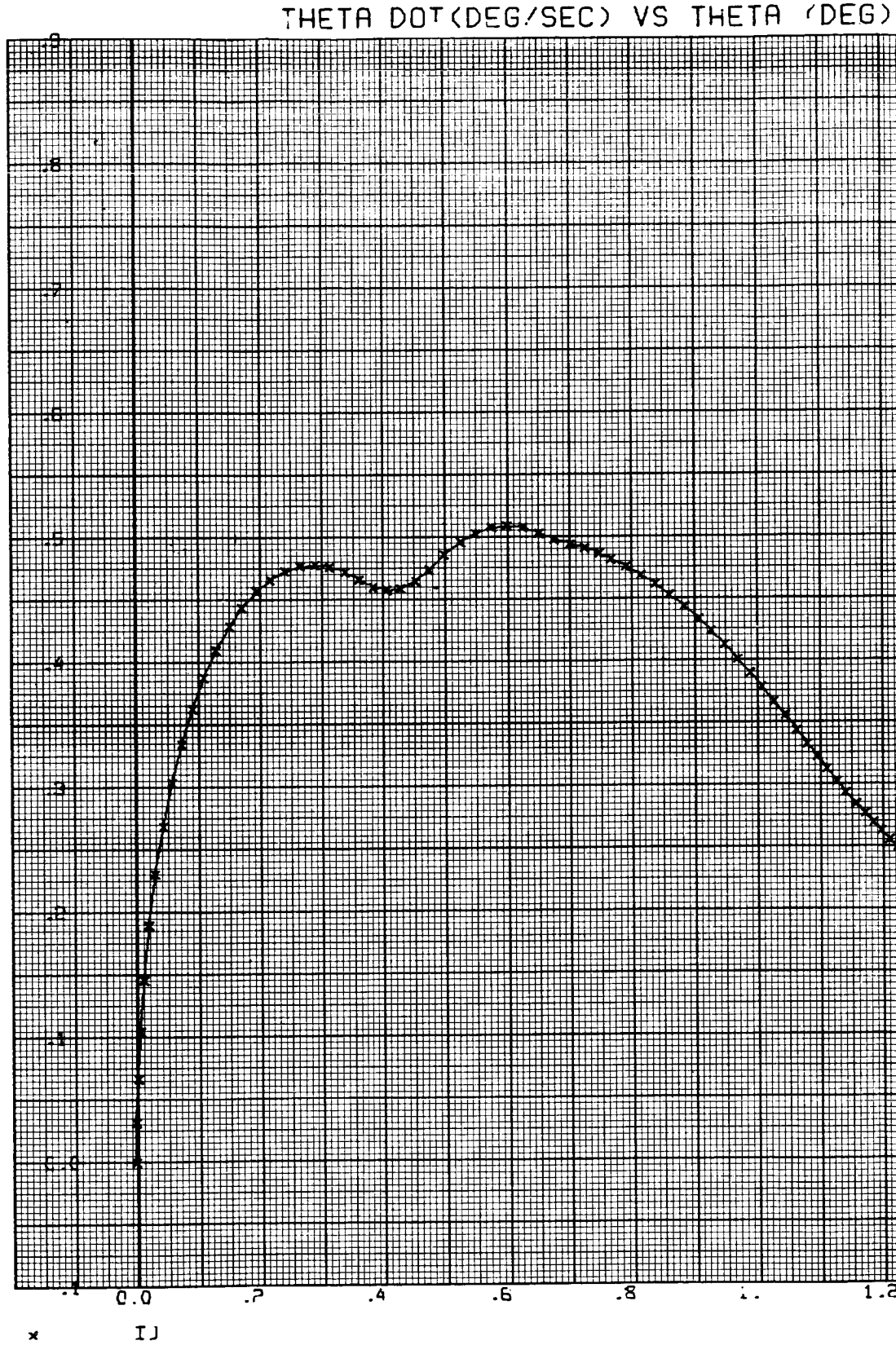
THETA DOT(DEG/SEC) VS THETA (DEG)
.8
.7
.6
.5
.4
.3
.2
.1
0.0
.2
.4
.6
.8
1.2
IJ

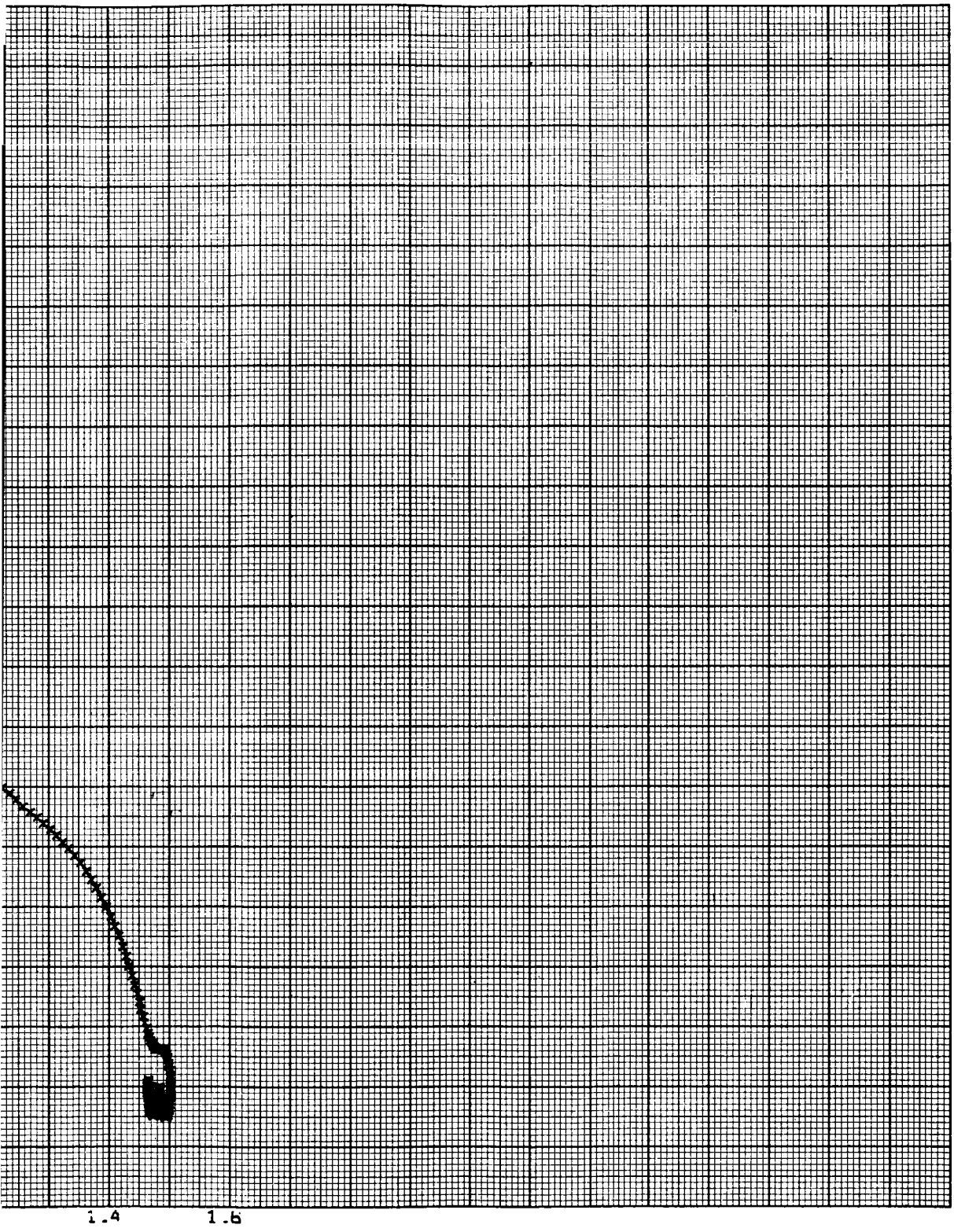

Figure 127. Attitude Rate Versus Vehicle Attitude, Actuator Rate Limit = 1 Deg/Sec, Torque Limit = 360 Ft-Lb, DM = 0.5 Deg

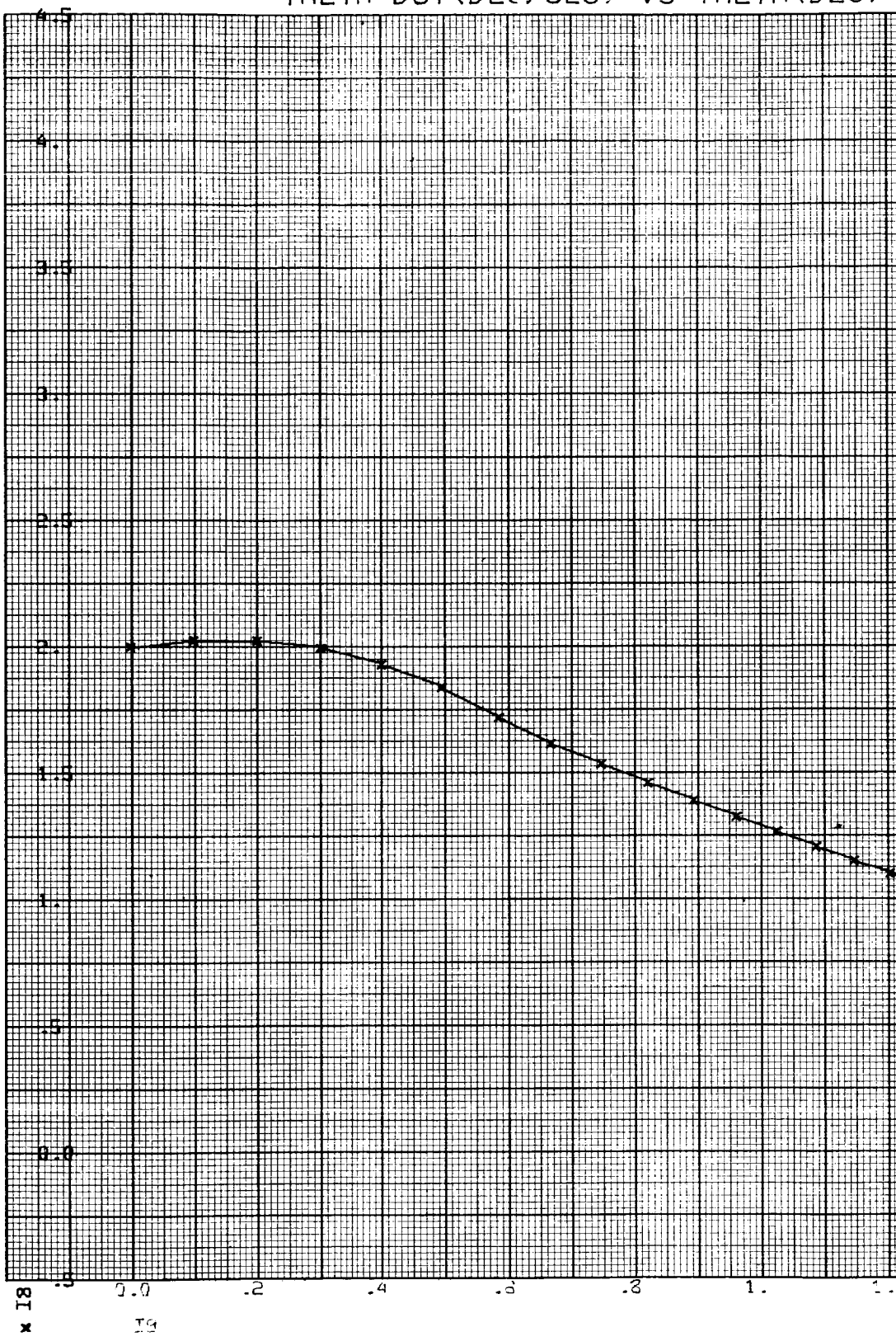
THETA DOT(DEG/SEC) VS THETA(DEG)
4.5
4.
3.5
3.
2.5
2.
1.5
1.
.5
0.0
-.5
0.0
.2
.4
.6
.8
1.
THETA

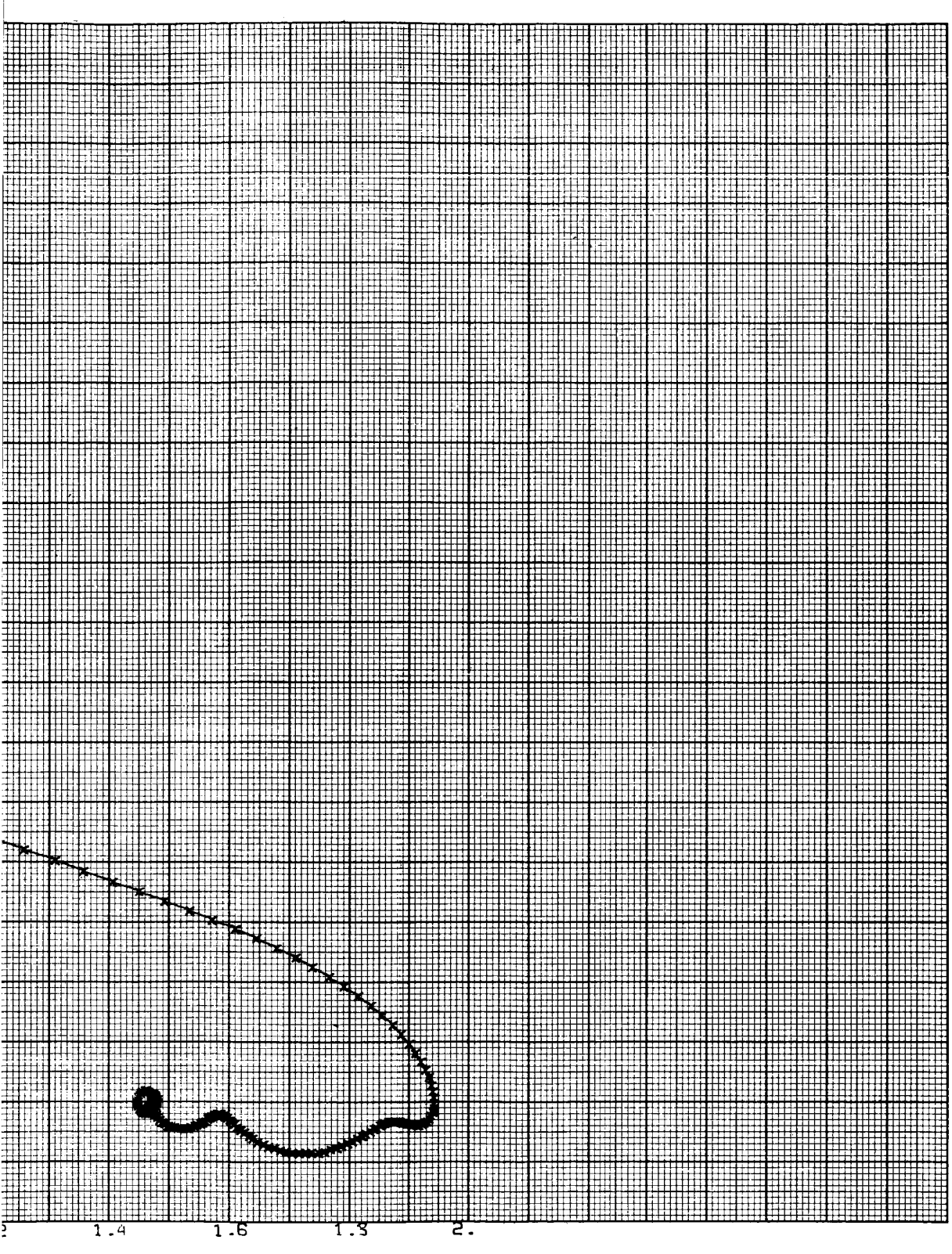

Figure 128. Attitude Rate Versus Vehicle Attitude, Actuator Rate Limit = 10 Deg/Sec, Initial Attitude Rate = 2 Deg/Sec

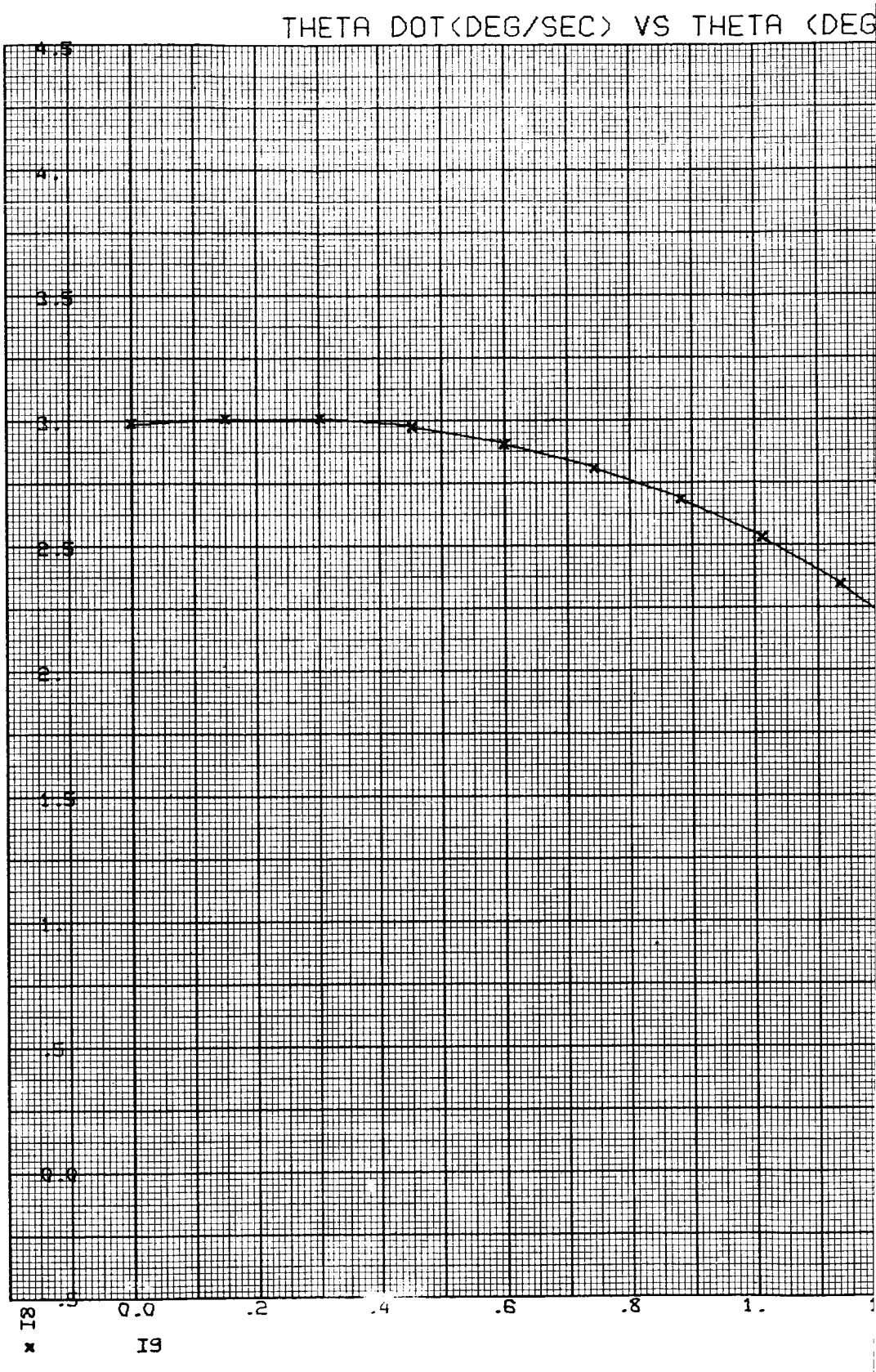
THETA DOT(DEG/SEC) VS THETA (DEG
4.5
4.
3.5
3.
2.5
2.
1.5
1.
.5
0.0
-.5
.2
.4
.6
.8
1.
I8
I9

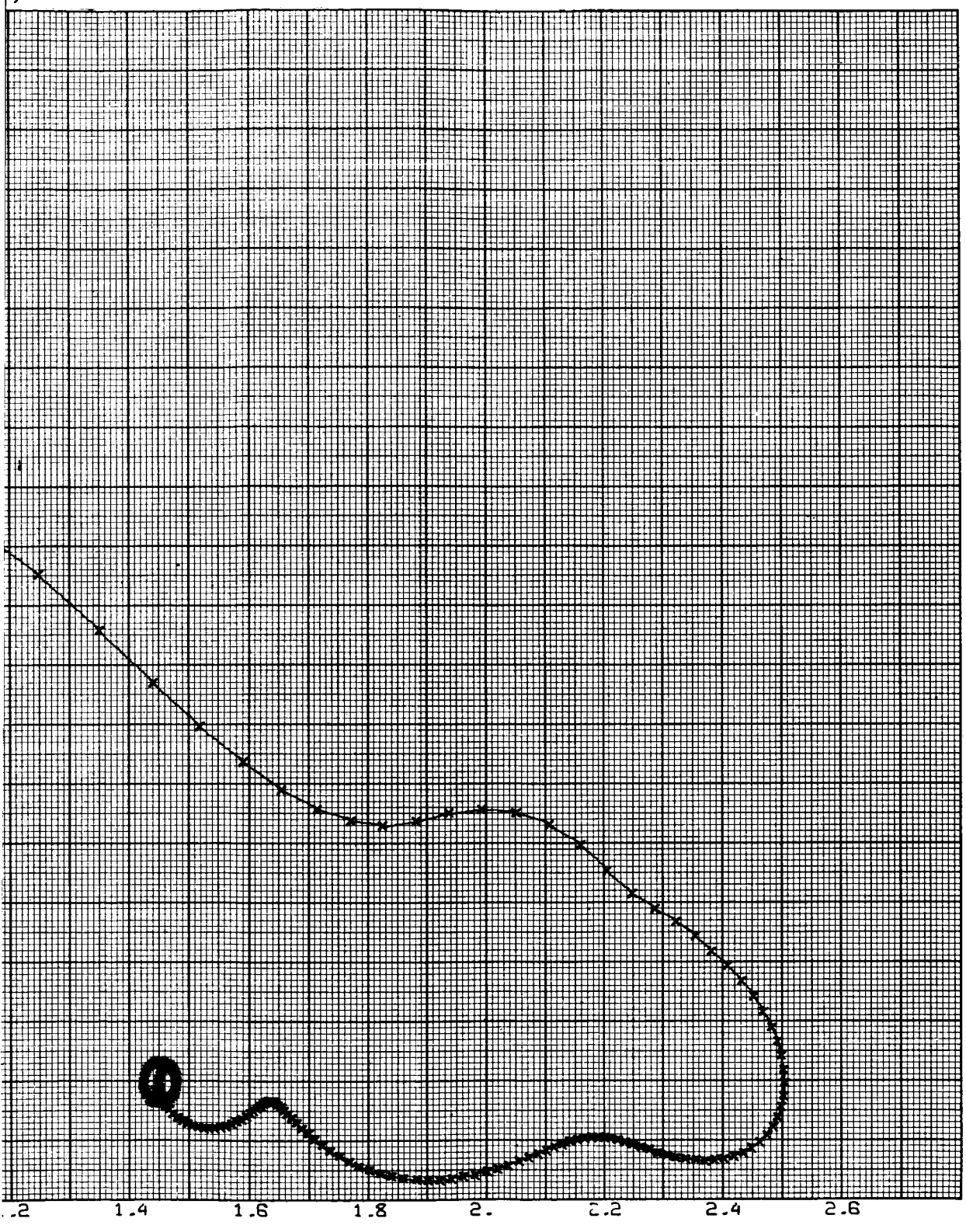

Figure 129. Attitude Rate Versus Vehicle Attitude, Actuator Rate Limit = 10 Deg/Sec, Initial Attitude Rate = 3 Deg/Sec

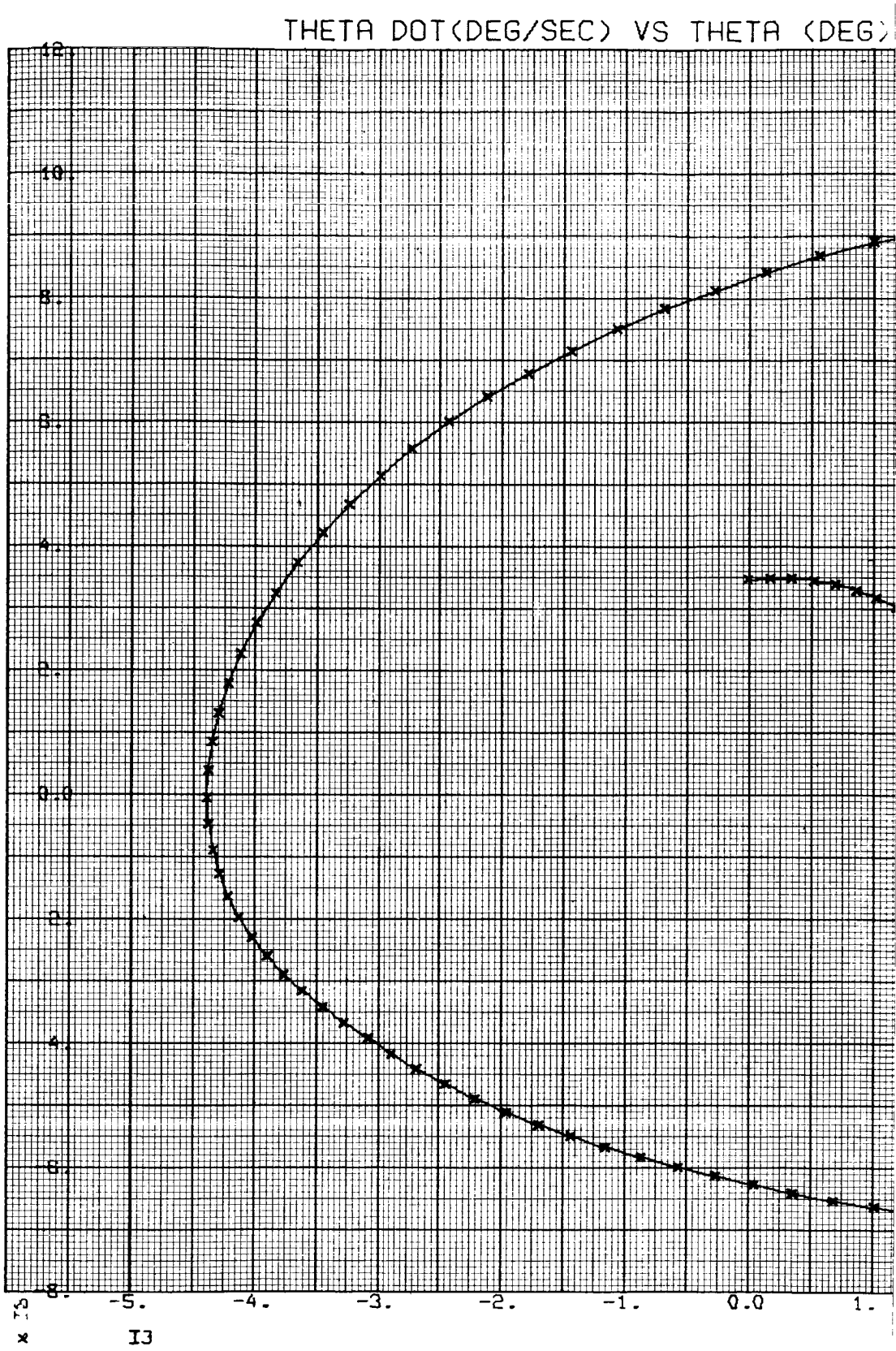
THETA DOT(DEG/SEC) VS THETA (DEG)
12.
10.
8.
6.
4.
2.
0.0
-2.
-4.
-6.
-8.
-5.
-4.
-3.
-2.
-1.
0.0
1.
I3

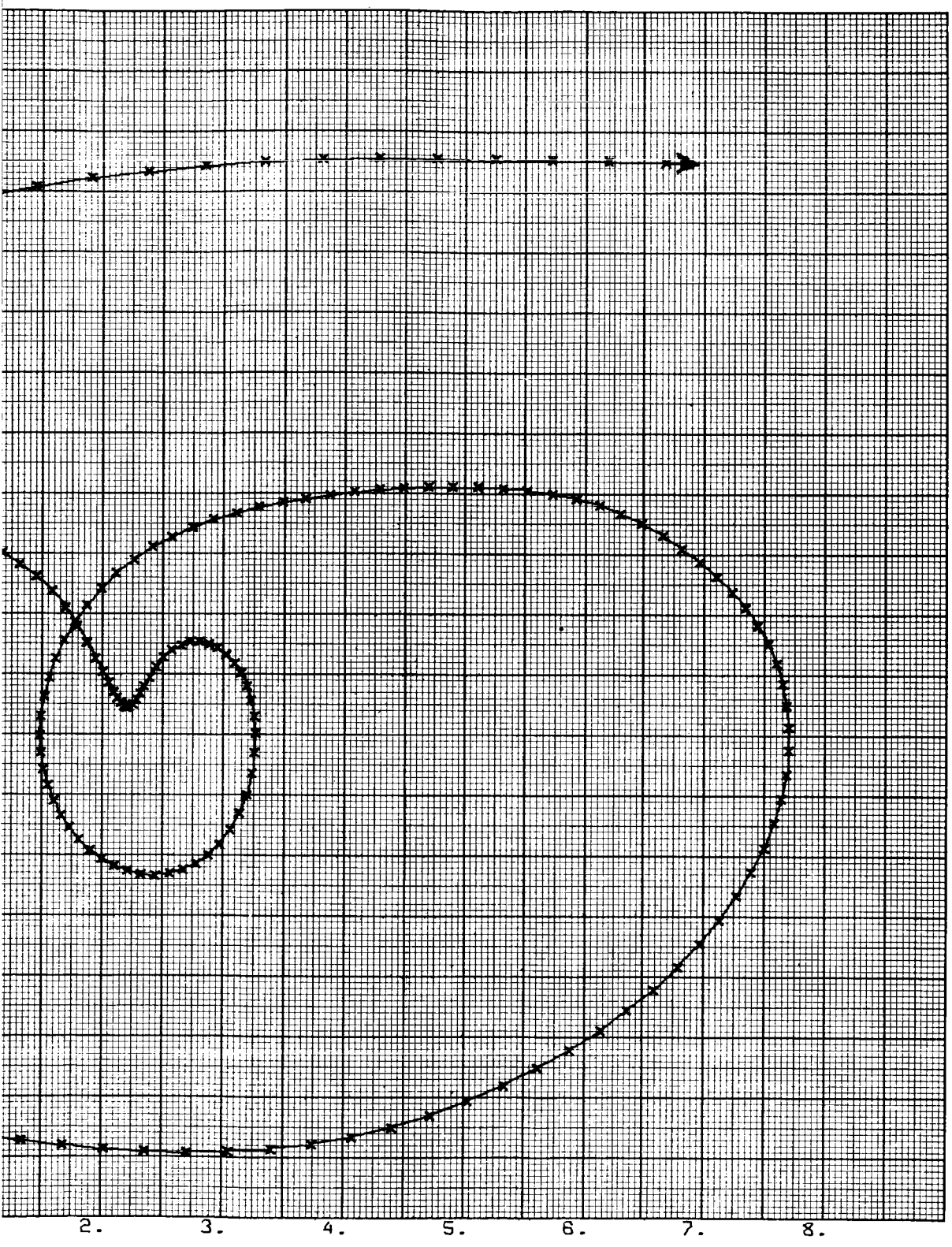

Figure 130. Attitude Rate Versus Vehicle Attitude, Actuator Rate Limit = 10 Deg/Sec, Initial Attitude Rate = 3 Deg/Sec

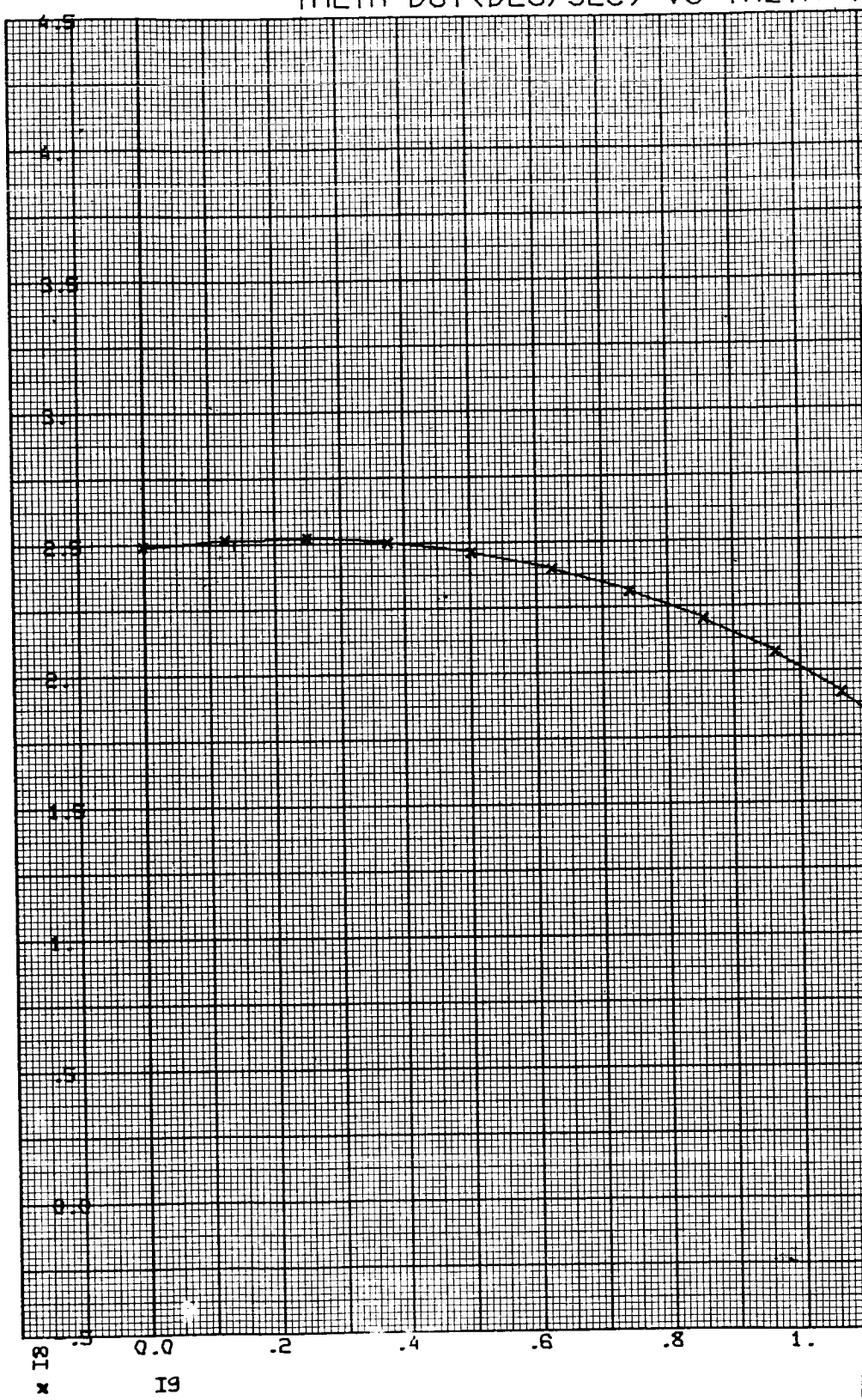
THETA DOT(DEG/SEC) VS THETA (
4.5
4.
3.5
3.
2.5
2.
1.5
1.
.5
0.0
-.5
0.0
.2
.4
.6
.8
1.
I9
I9

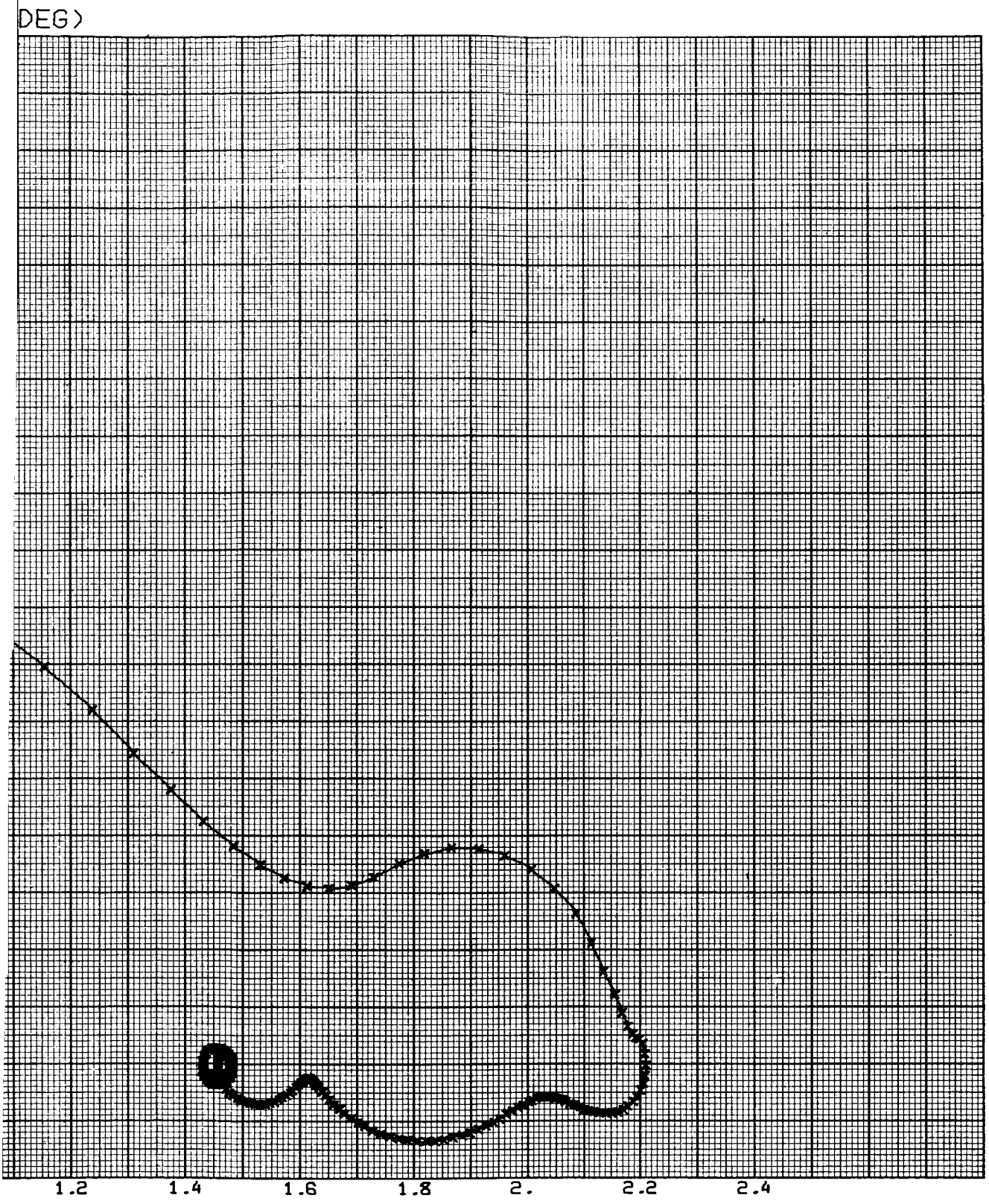

Figure 131. Attitude Rate Versus Vehicle Attitude, Actuator Rate Limit = 7.5 Deg/Sec, Initial Attitude Rate = 2.5 Deg/Sec

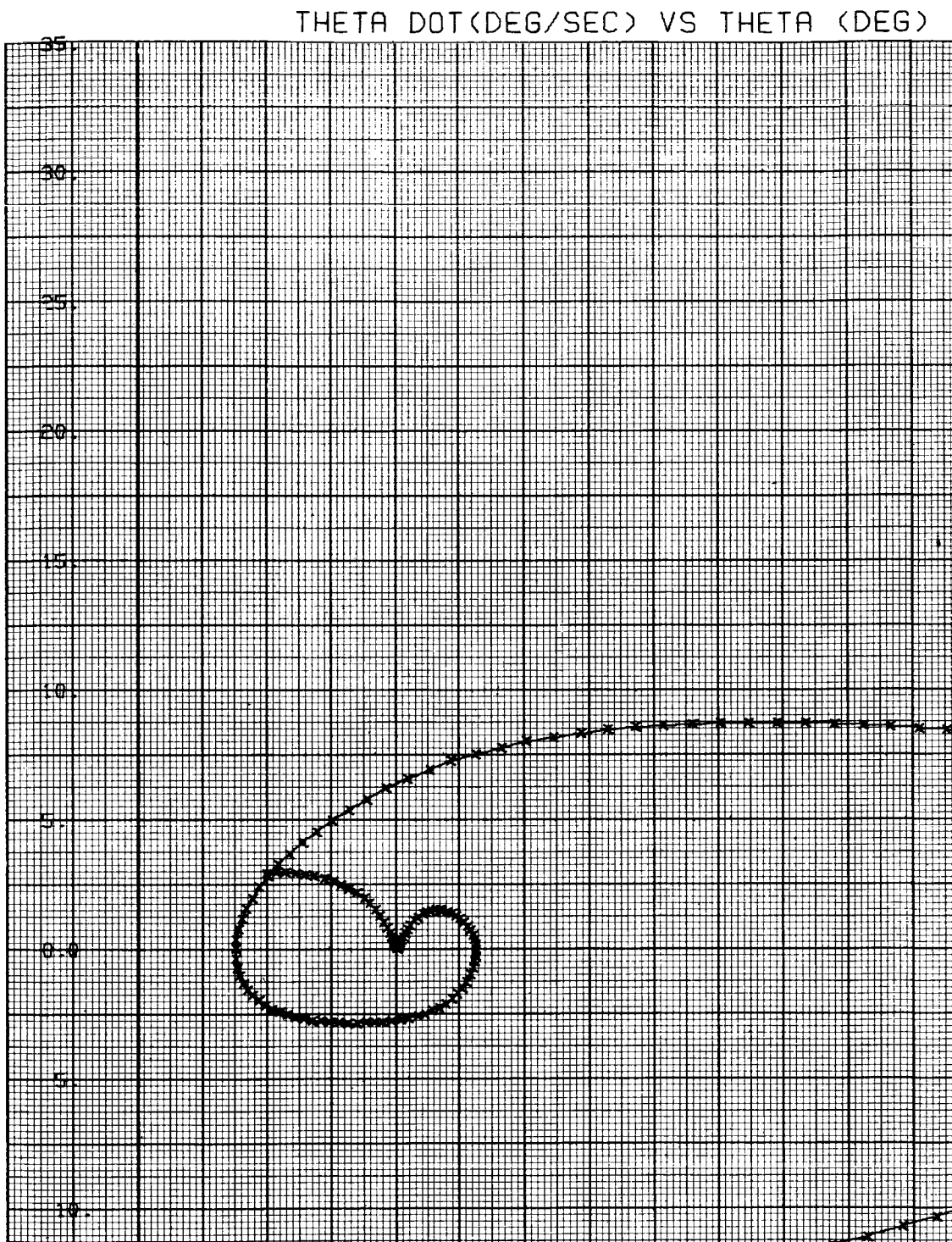
THETA DOT(DEG/SEC) VS THETA (DEG)
35.
30.
25.
20.
15.
10.
5.
0.0
-5.
-10.
-15.
-2.
0.0
2.
4.
6.
8.
10.
I8
I9

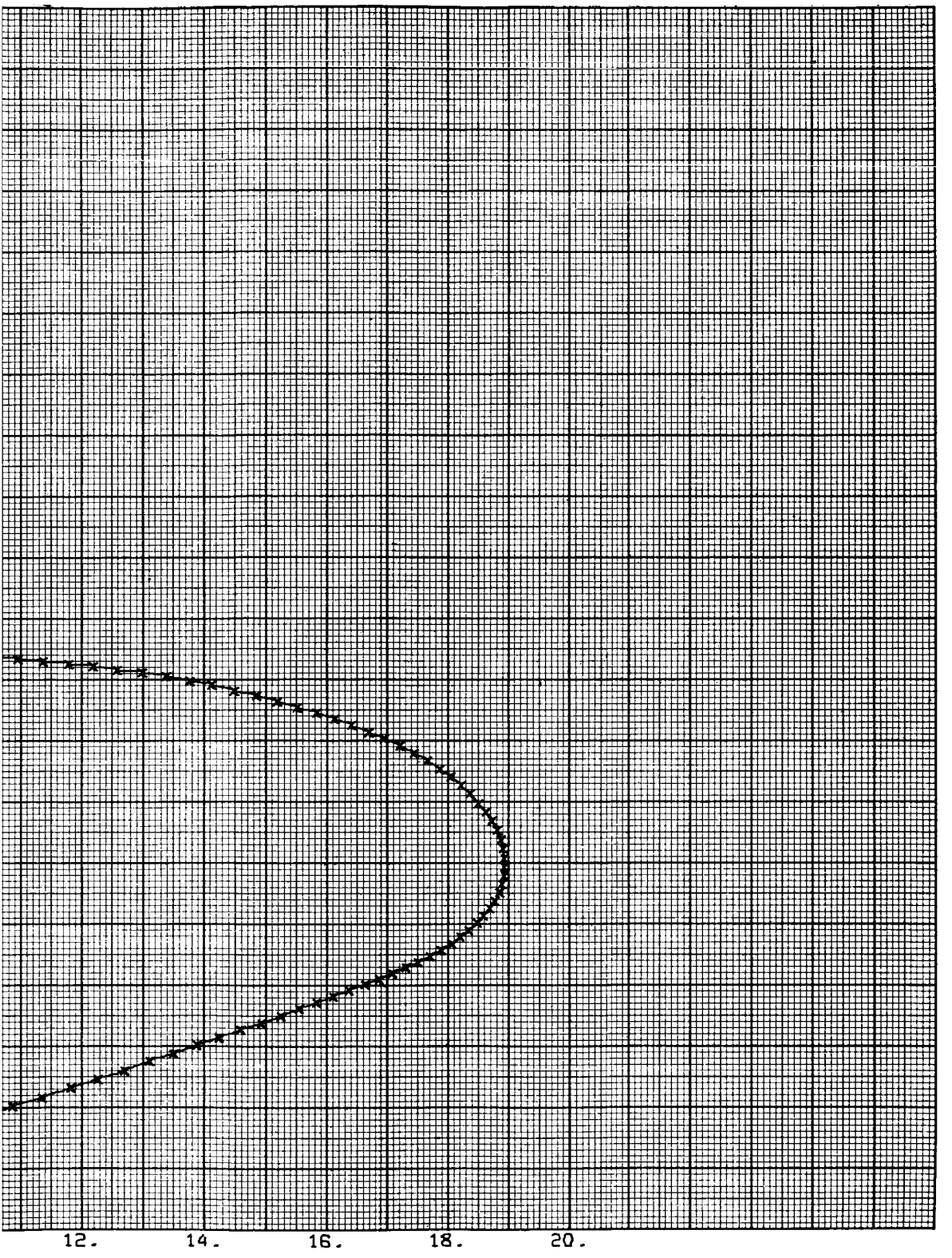

Figure 132. Attitude Rate Versus Vehicle Attitude, Actuator Rate Limit = 7.5 Deg/Sec, Initial Attitude Rate = 3 Deg/Sec

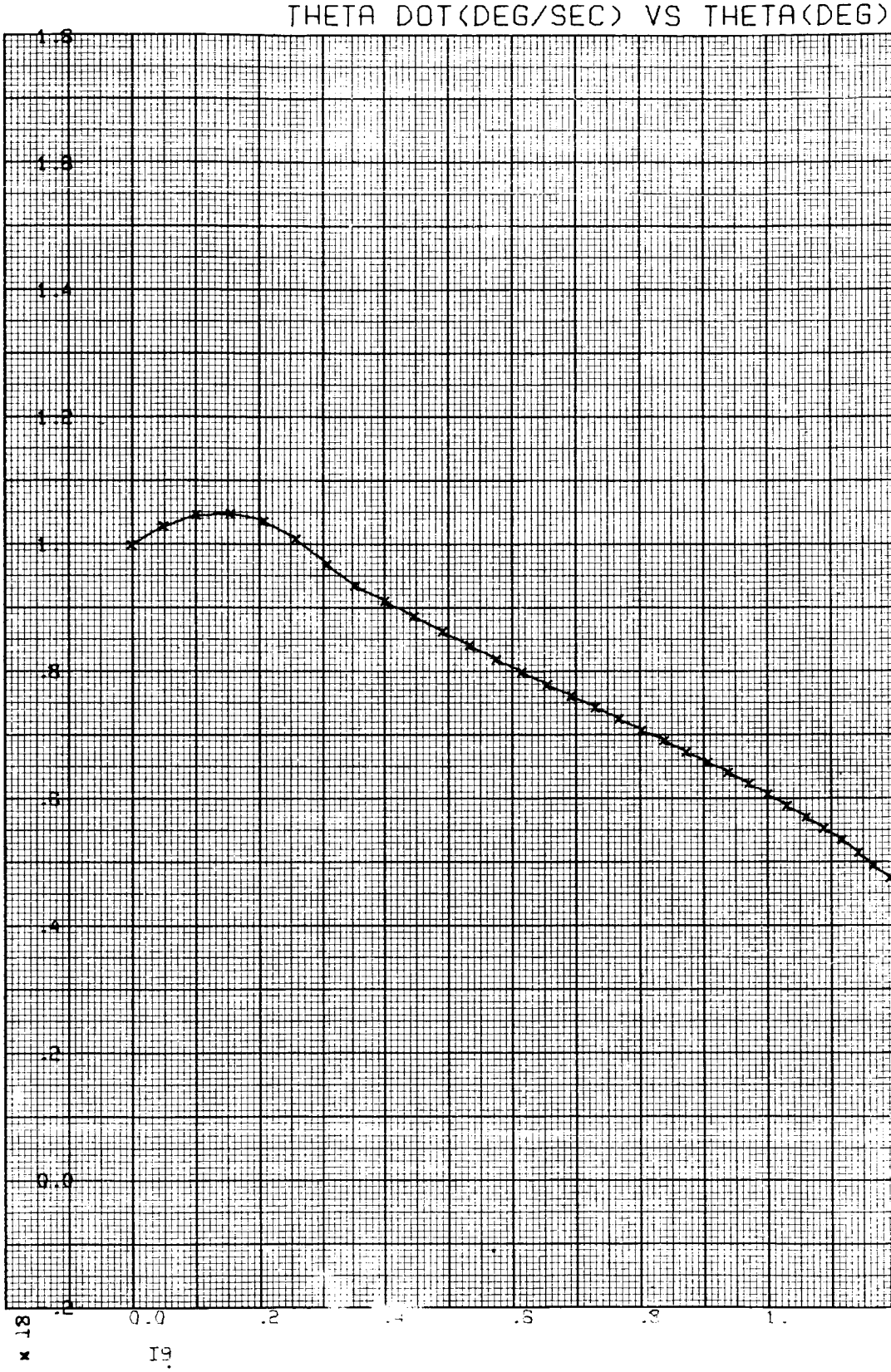
THETA DOT(DEG/SEC) VS THETA(DEG)
1.6
1.8
1.4
1.2
1
.8
.6
.4
.2
0.0
-.2
0.0
.2
.6
.8
1.

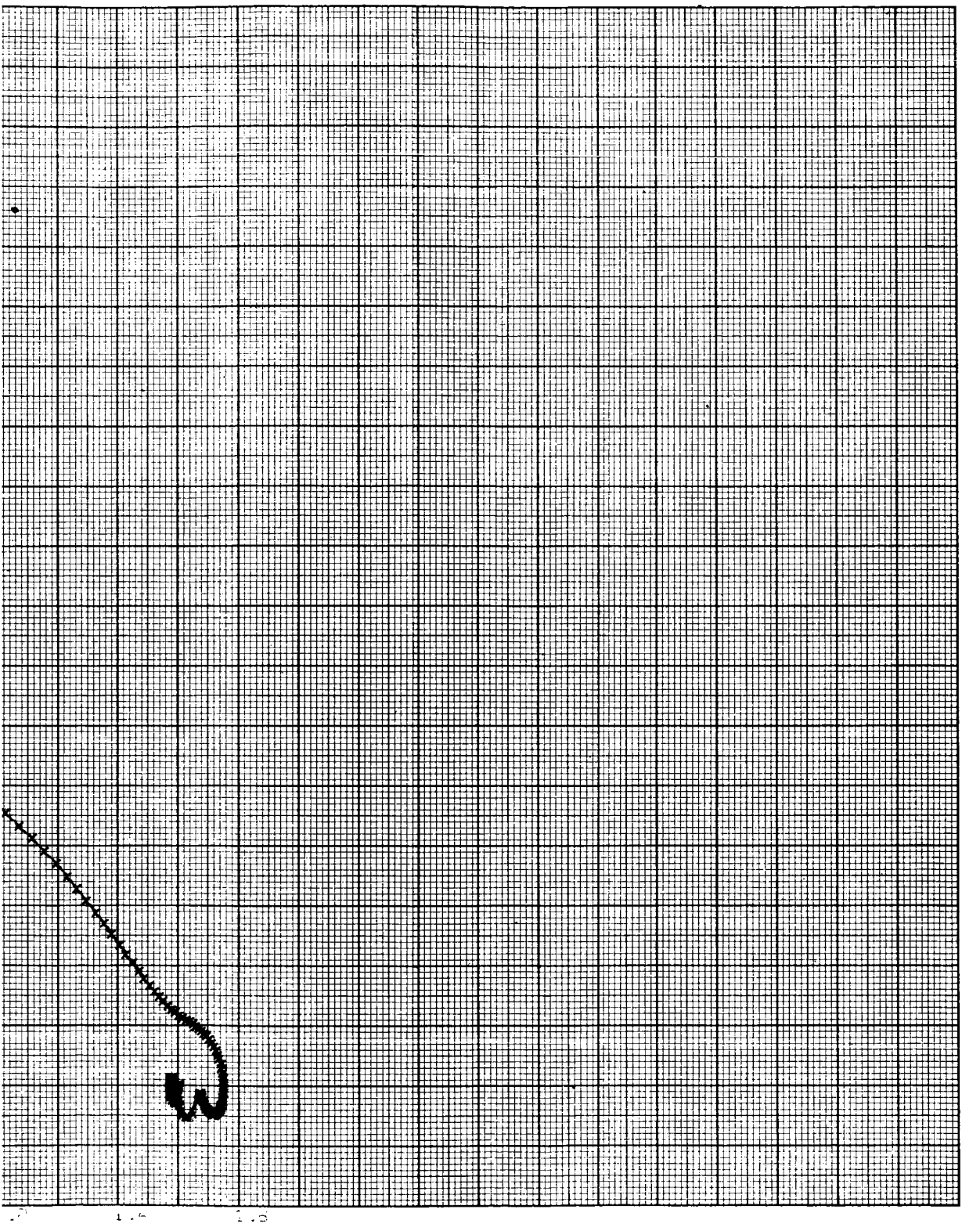

Figure 133. Attitude Rate Versus Vehicle Attitude, Actuator Rate Limit = 5 Deg/Sec, Initial Attitude Rate = 1 Deg/Sec

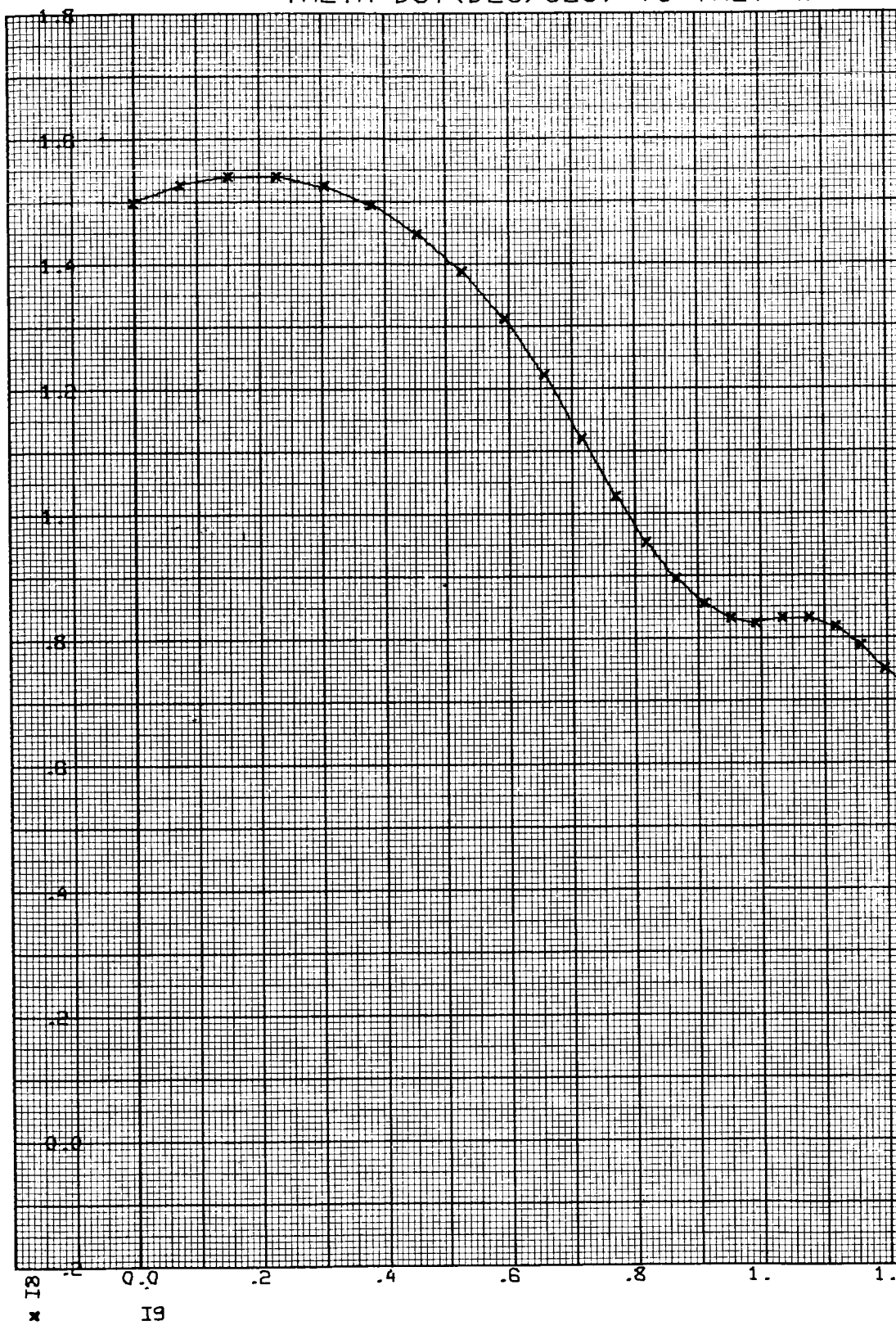
THETA DOT(DEG/SEC) VS THETA(DEG)
1.8
1.6
1.4
1.2
1.
.8
.6
.4
.2
0.0
-.2
0.0
.2
.4
.6
.8
1.
1.
I8
I9

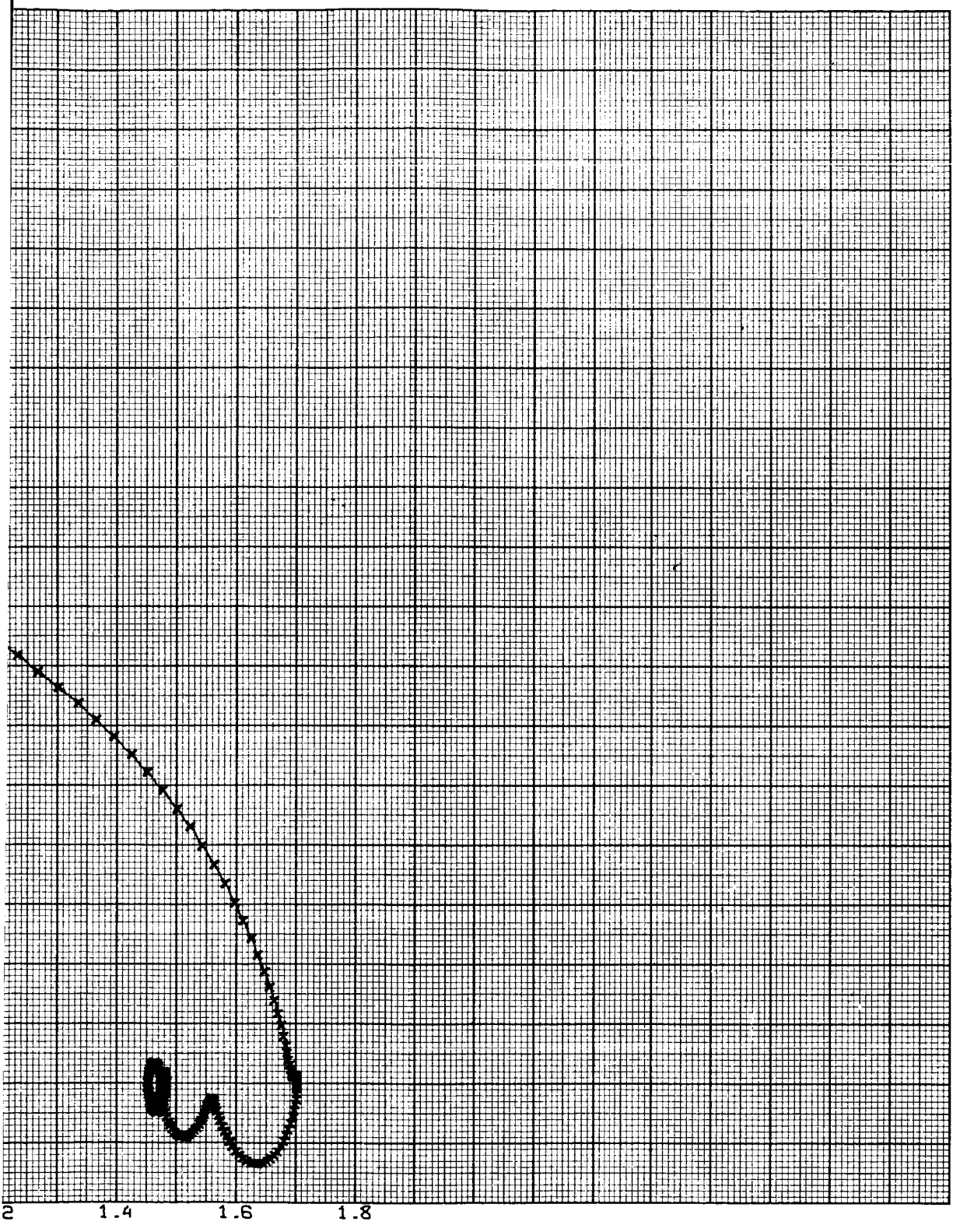

Figure 134. Attitude Rate Versus Vehicle Attitude, Actuator Rate Limit = 5 Deg/Sec, Initial Attitude Rate = 1.5 Deg/Sec

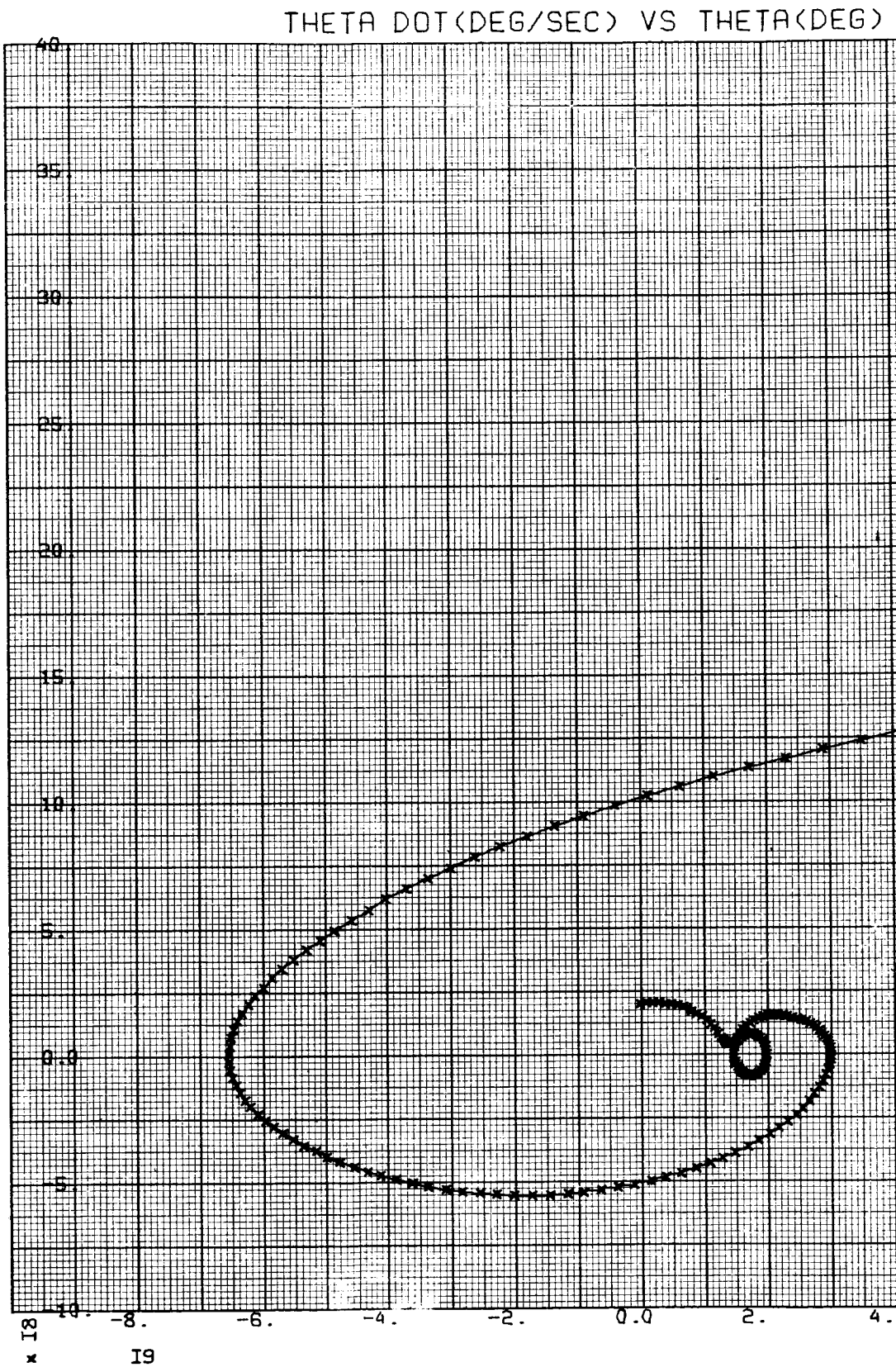
THETA DOT(DEG/SEC) VS THETA(DEG)
40.
35.
30.
25.
20.
15.
10.
5.
0.0
-5.
-10.
-8.
-6.
-4.
-2.
0.0
2.
4.
I8
I9

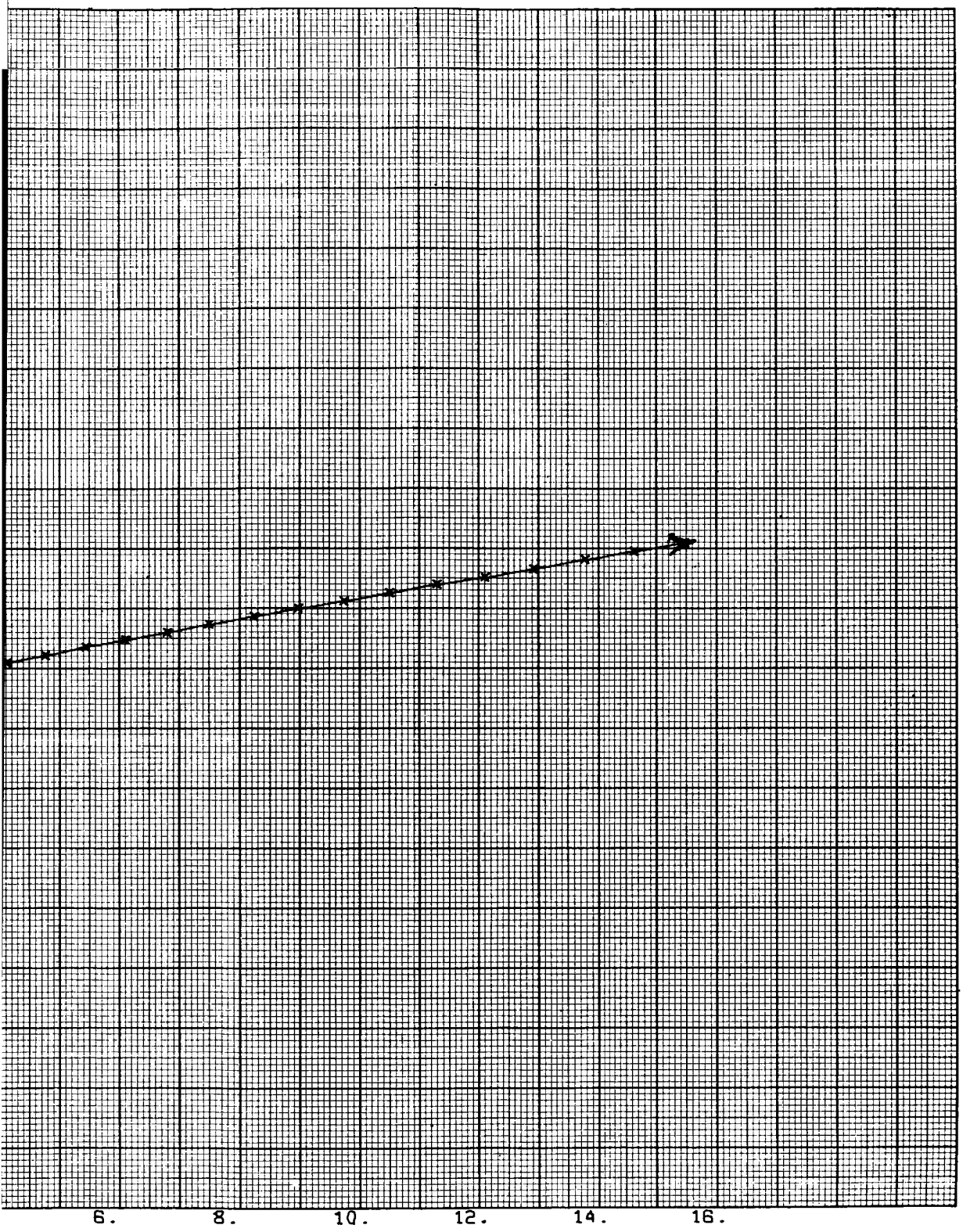

Figure 135. Attitude Rate Versus Vehicle Attitude, Actuator Rate Limit = 5 Deg/Sec, Initial Attitude Rate = 2 Deg/Sec

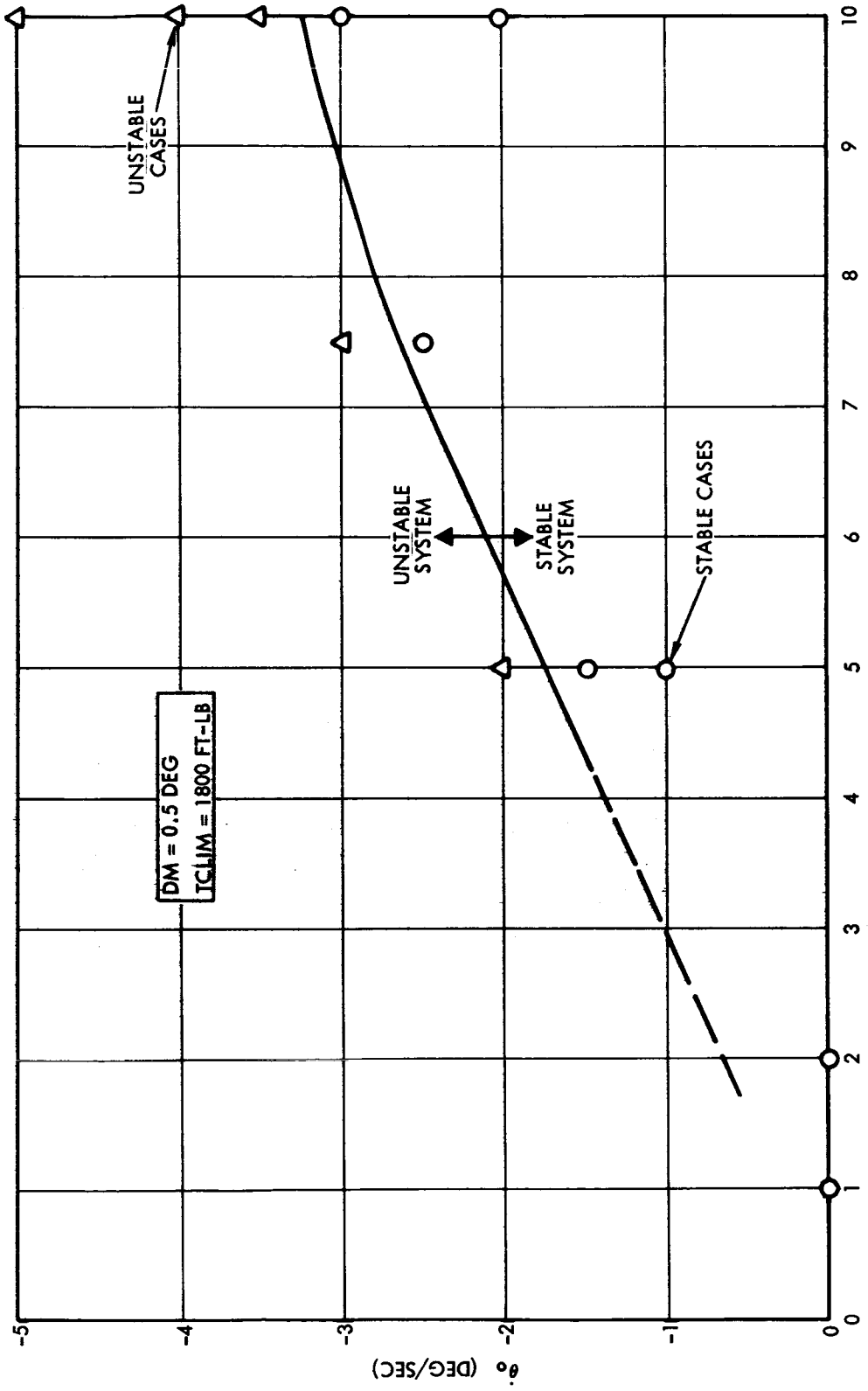

Figure 136. Initial Attitude Rate Stability Boundary Versus Actuator Rate Limit

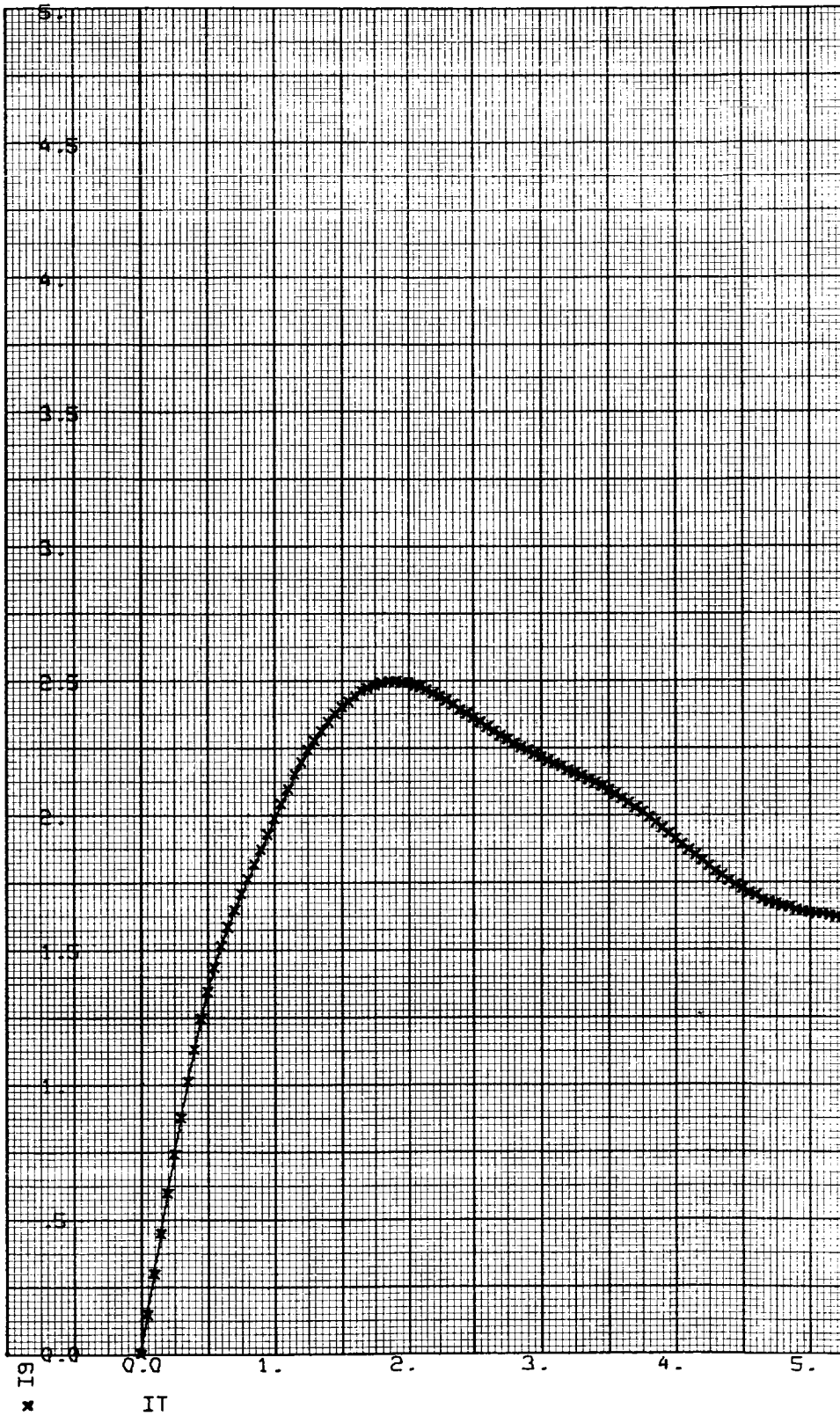
THETA(DEG) VS TIME(SEC) DM=
5.
4.5
4.
3.5
3.
2.5
2.
1.5
1
.5
0.0
0.0
1.
2.
3.
4.
5.
IG
IT

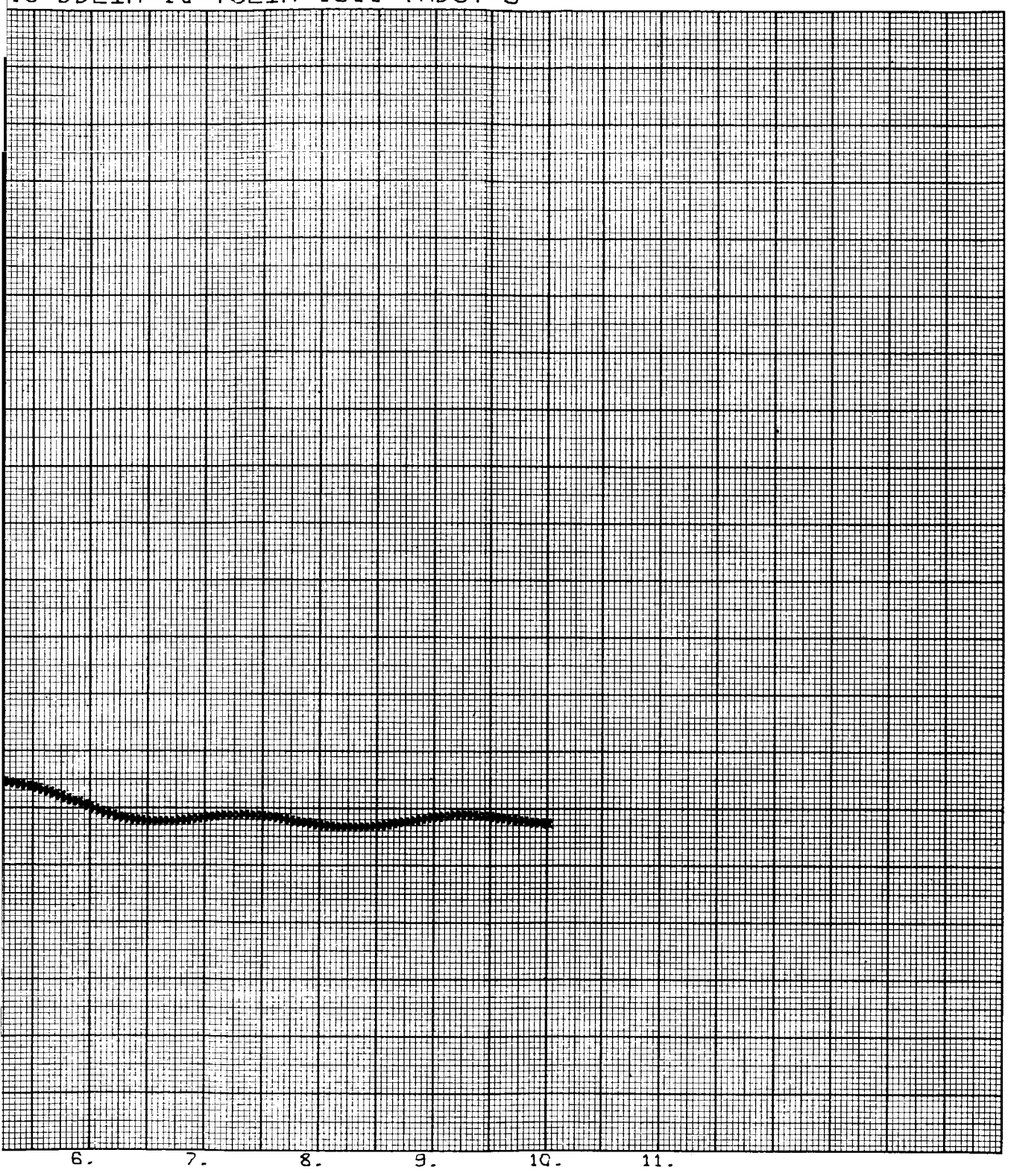

Figure 137. Vehicle Attitude Versus Time, Actuator Rate Limit = 10 Deg/Sec, Initial Attitute Rate = 3 Deg/Sec

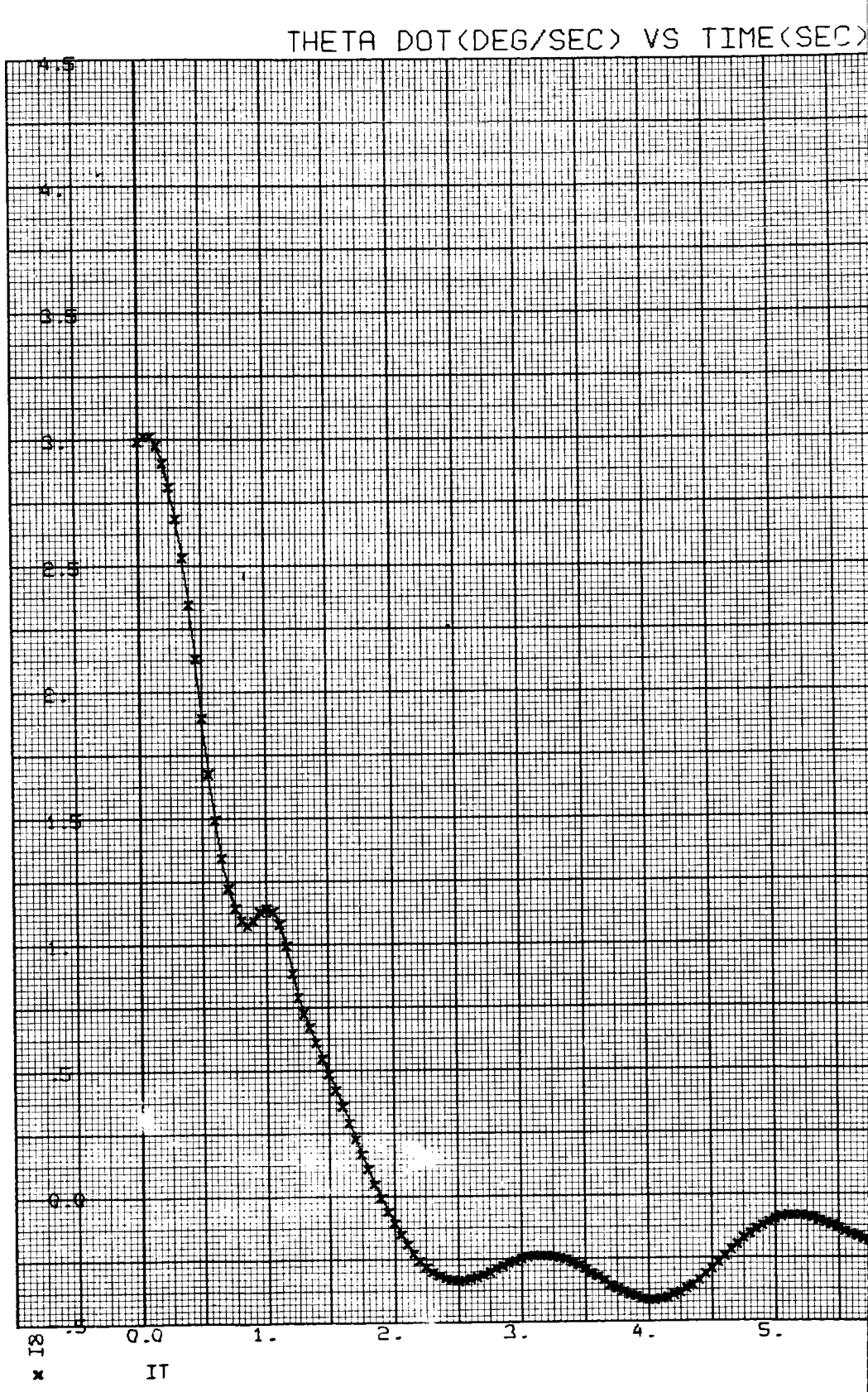
THETA DOT(DEG/SEC) VS TIME(SEC)
4.5
4.
3.5
3.
2.5
2.
1.5
1.
.5
0.0
-.5
0.0
1.
2.
3.
4.
5.
IT
IT

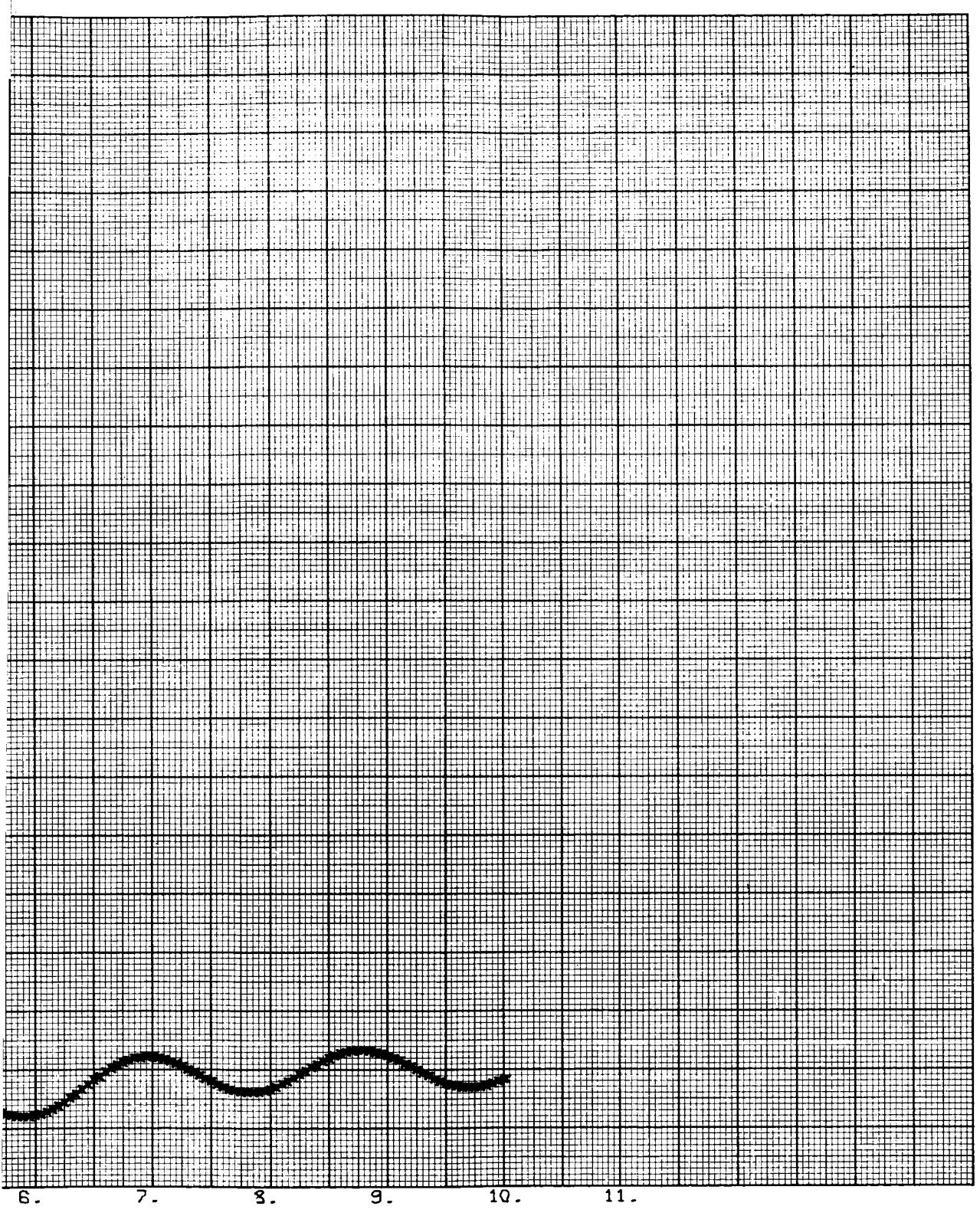

Figure 138. Attitude Rate Versus Time, Actuator Rate Limit = 10 Deg/Sec, Initial Attitude Rate = 3 Deg/Sec

DELTA(DEG) VS TIME(SEG)
5.
4.
3.
2.
1.
0.0
-1.
-2.
-3.
-4.
-5.
0.0
1.
2.
3.
4.
5.
LINE
IT

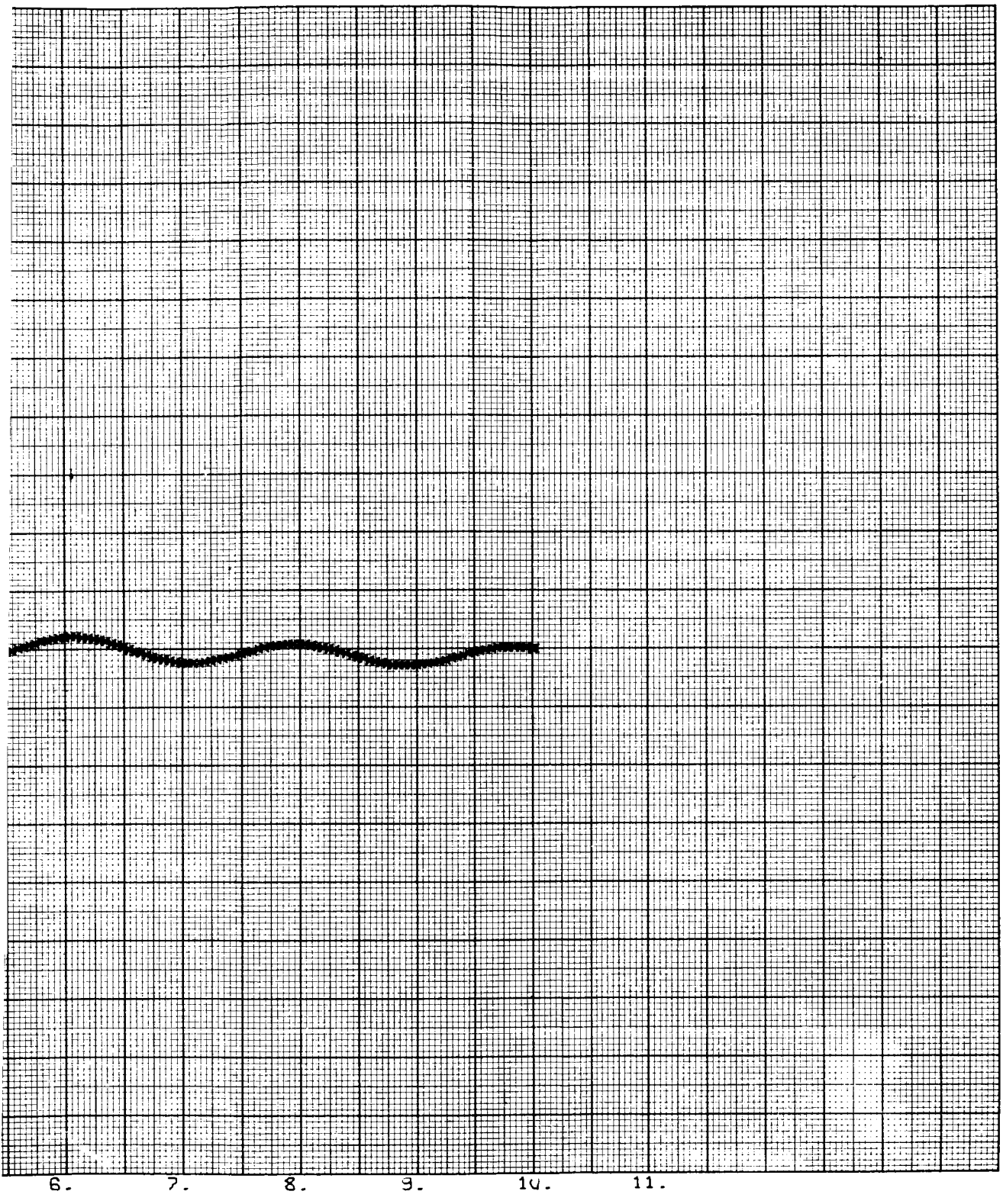

Figure 139. Engine Angle Versus Time, Actuator Rate Limit = 10 Deg/Sec, Initial Attitude Rate = 3 Deg/Sec

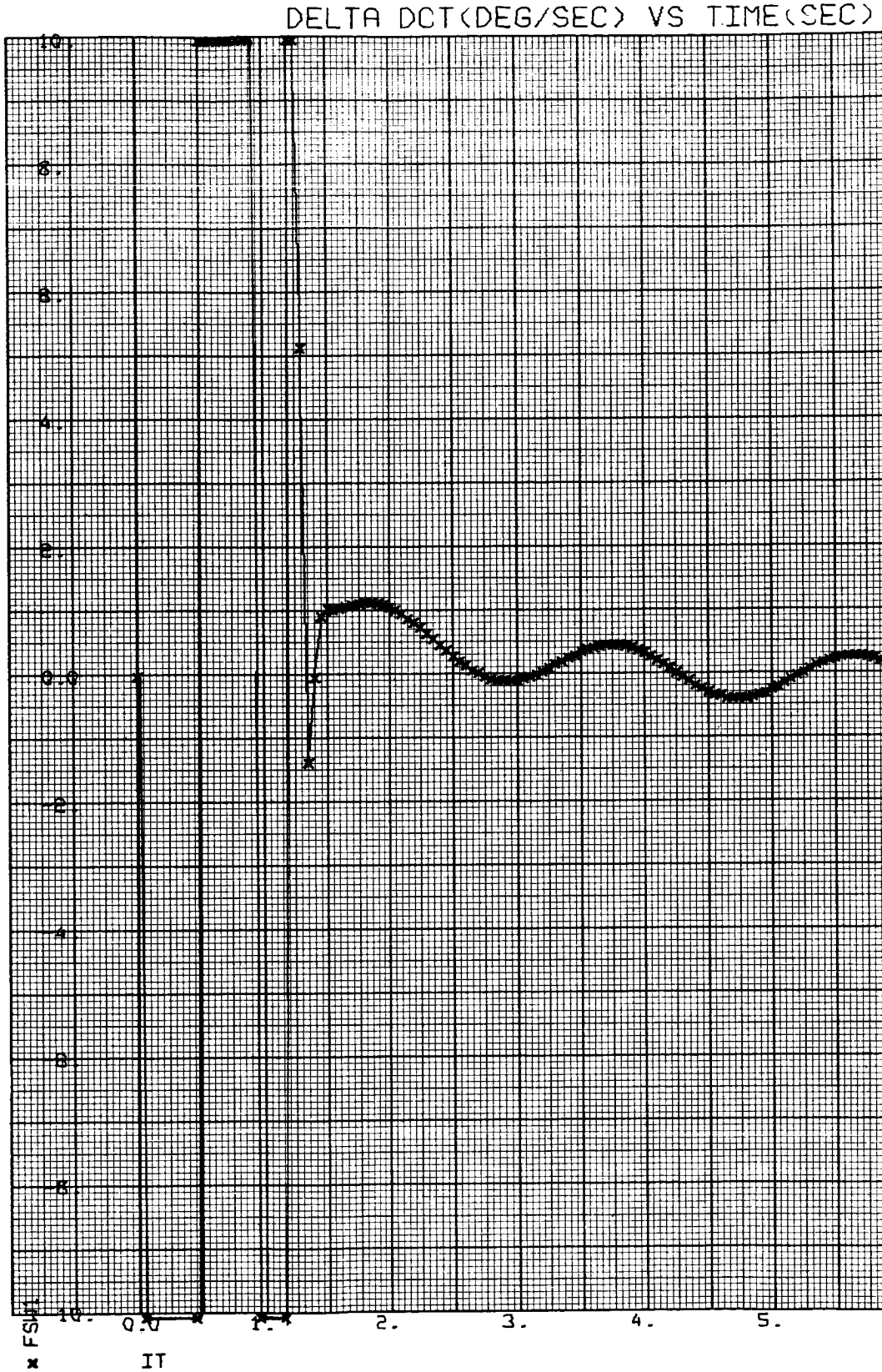
DELTA DCT(DEG/SEC) VS TIME(SEC)
10.
8.
6.
4.
2.
0.0
-2
-4
-6
-8
-10.
0.0
1.
2.
3.
4.
5.
FSH:
IT

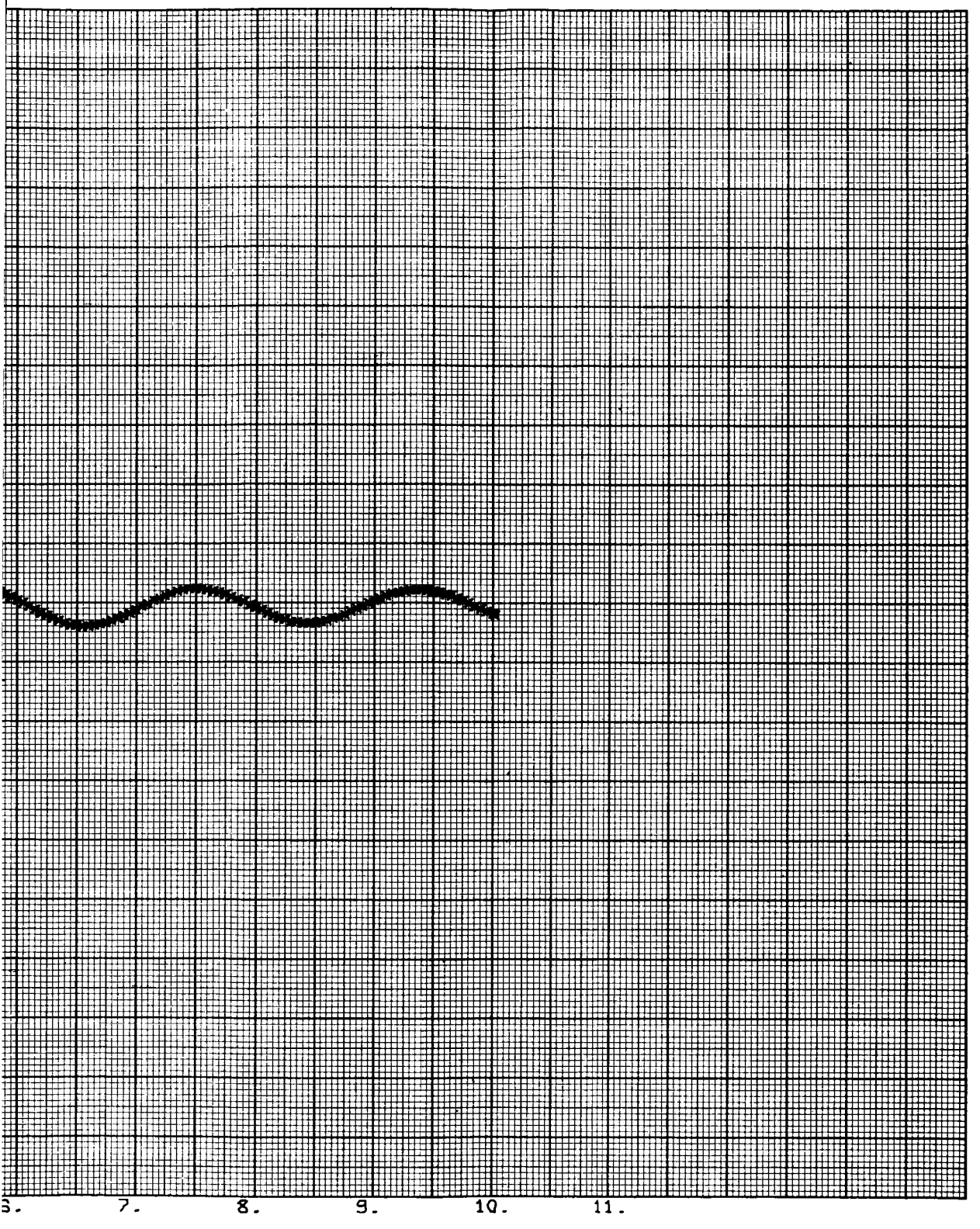

Figure 140. Actuator Rate Versus Time, Actuator Rate Limit = 10 Deg/Sec, Initial Attitude Rate = 3 Deg/Sec

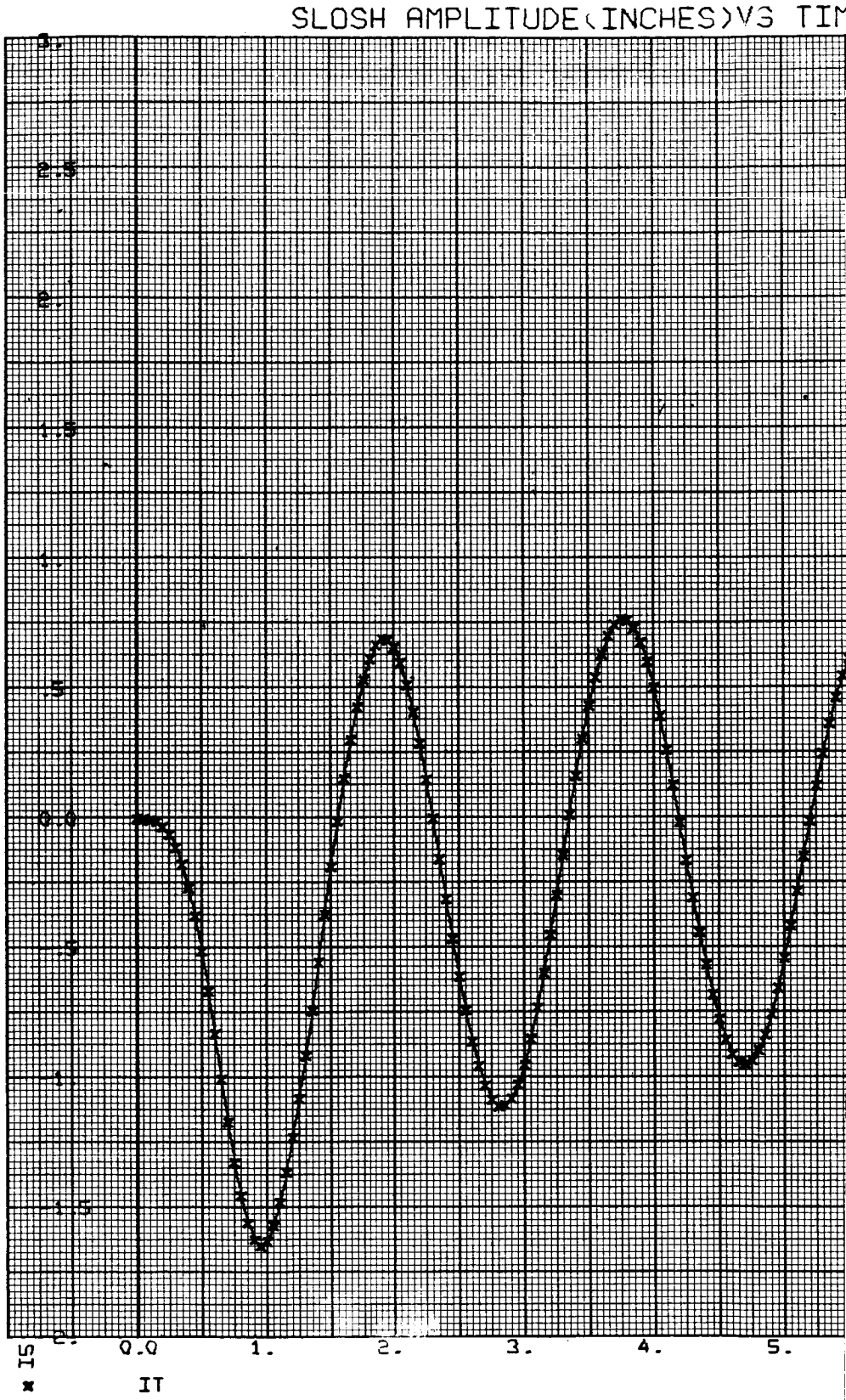
SLOSH AMPLITUDE(INCHES)VS TIM
2.5
2.
1.5
1.
.5
0.0
-.5
-1.
-1.5
-2.
0.0
1.
2.
3.
4.
5.
IS
IT

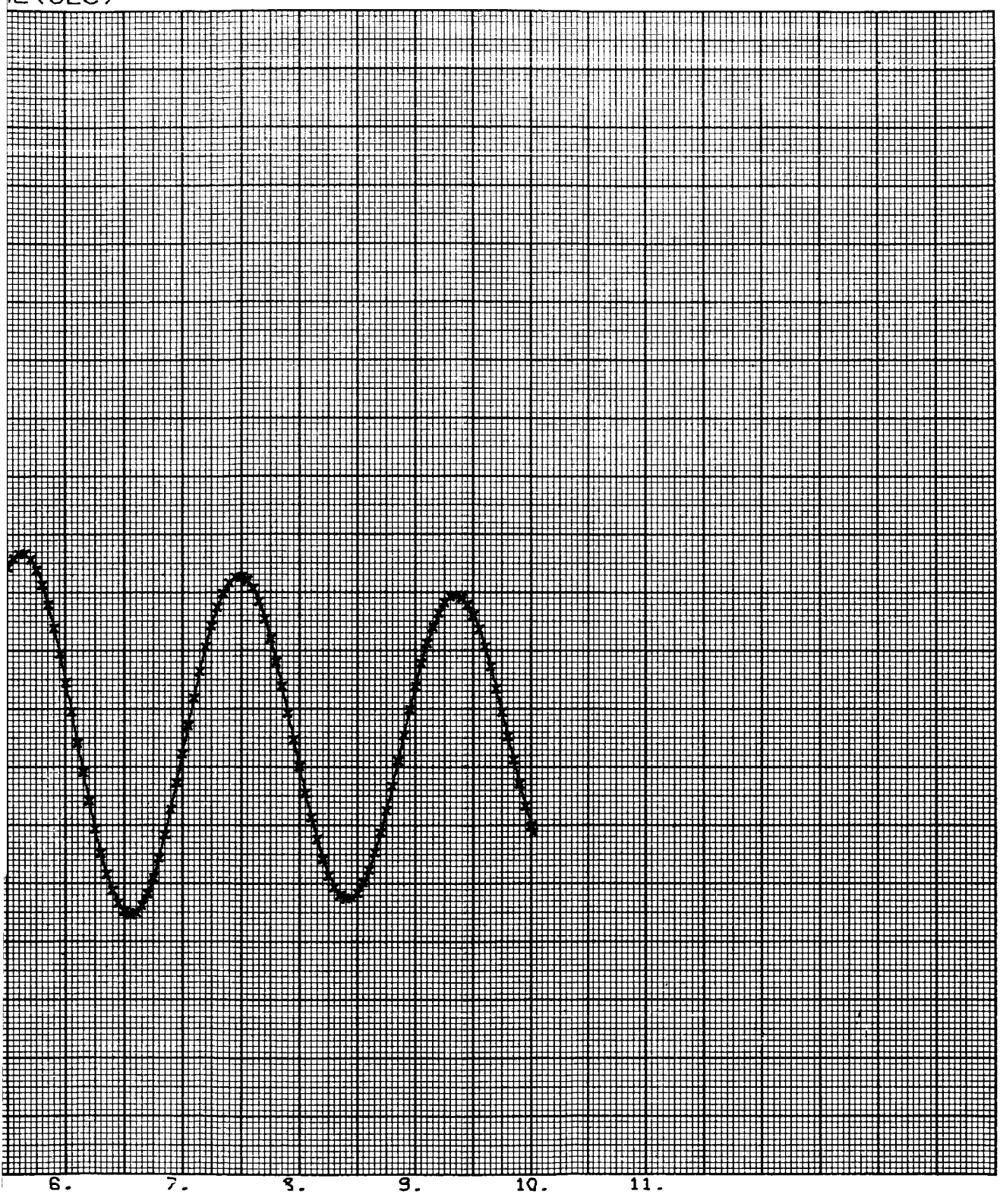

Figure 141. Slosh Amplitude Versus Time, Actuator Rate Limit = 10 Deg/Sec, Initial Attitude Rate = 3 Deg/Sec

PRECEDING PAGE BLANK NOT FILMED.

REFERENCES

1. TRW Systems, Report 04480-6006-R000, "Voyager Support Study, LM Descent Stage Applications, Final Report, Volume III, Propellant Hydrodynamics Studies," February 1967.

2. TRW Systems, Report 5710-6001-R0V02, "Phase IA, Task B, Final Technical Report, Voyager Spacecraft, Volume 2," 17 January 1967.

3. TRW Systems, Memorandum 66.7231.8-94, "Preliminary Evaluation of Torque and Gas Requirements Originated by Solar Radiation Pressure—Voyager Task C Reference Configuration," J.H. Decanini, 5 October 1966.

4. Southwest Research Institute, Technical Report No. 2, "Experimental and Theoretical Studies of Liquid Sloshing at Simulated Low Gravity," by F. T. Dodge and L.R. Garza, 20 October 1966, MSFC Contract NAS 8-20290.

5. TRW Systems, Memorandum 65-9713.6-79, "Low G Slosh Models," G.C. Yeh, 26 October 1965.

6. TRW Systems, Memorandum 66-3341.1-53, "High Energy Low G Sloshing—Preliminary Analysis," L.R. Koval, 2 August 1966.

7. TRW Systems, Memorandum 66-3341.1-81, "Equations for Low Energy Low G Slosh Models," L.R. Koval, 9 September 1966.

8. TRW Systems, Report 4388-6001-RU000, "Propellant Slosh Loads," R.E. Hutton and P.G. Bhuta, June 1965.

9. TRW Systems, Report STL/TR-59-0000-09960, "Final Report On An Experimental Investigation of Sloshing," 4 March 1960.

BLANK PAGE

PRECEDING PAGE BLANK NOT FILMED.

APPENDIX A

VOYAGER NATURAL MODES AND FREQUENCIES

This Appendix contains the results of the task defined in Reference A-1 and redefined informally in subsequent meetings and discussions. Contained here are the first four modes, for each of three time point configurations, of the LM-based Voyager used in the preliminary studies.

The existence in Voyager of a plane of near-symmetry was exploited in reducing the model to two dimensions. This reduction was judged to be consistent with the constraints of time and with the objectives of the preliminary control system study in which the modes are to be used*. The planar model was constructed of a system of uniform beam segments and the modes of the resulting system found by "UBEAM," a digital computer program described in Reference A-2. Results are presented in terms of displacements and slopes at stations. Input data listings are included and are based on information provided by Spacecraft Design Department of SVD. To aid in physical interpretation of results, there are plots of the modes for one of the time point configurations.

The single-degree-of-freedom model of the capsule was developed by JPL to reproduce dynamic interface loads for the first mode of what they envision as a reasonable design. The model was prepared by Ben Wada, their structural analyst.

The input data is listed in Figures A-7, A-8, and A-9 and may be compared with Figure A-2 where the segment and interconnector numbers are noted. It should be observed that mass is input in two ways— distributed along the segments and lumped between them as "eccentric" masses. The total weight shown below the segment data includes the eccentric masses.

---

* The plane used in this study was selected based on the anticipation of low-frequency modes associated with the appendages.

A few features of the UBEAM representation are worthy of special note.

- In shrinking the LEM structure to a beam, account was taken of shear deflection and rotary inertia, by Timoshenko beam theory. The interface with the connectors to the experiment module was reproduced by using near-rigid beams so that slope at the LM base would be reproduced across the whole span.

- Main and slosh propellant were lumped at the ends of segments 10 and 11 (see Figure A-2), respectively, with propellant rotary inertia being distributed in segment 11.

- The outboard links (interconnectors 1 and 5) are pinned at both ends and thus carry only tension; the inboard links (interconnectors 2 and 4) carry the shear load.

- The modes predicted by this analysis involve bending and stretching of the structure. The modes involving torsion were not sought because they would not be excited by the propulsion system.

- The LM descent engine was modeled as a rotary inertia and a lumped mass beamed rigidly from the base of the LM structure.

Table A-1 contains displacements for the four lowest frequency modes at each of three time points. The modes are all normalized to a generalized mass of 1.0. Modes shapes are plotted in Figures A-3, A-4, A-5 and A-6 for the four modes of the "start midcourse correction" configuration. They are representative of the first four modes for the other two time points as well except in the last where the capsule mode disappears and the fourth mode is of high frequency and involves stretching in the LM structure.

The motor is pinned in the LM structure at two points, stations 150.2 and 123.0. Deflection at the motor gimbal point, station 111.0, was, therefore, calculated from the equation

$$Y_m = Y_{123} + \left(\frac{Y_{123} - Y_{150}}{27.2}\right) 12.0$$

Displacement of the capsule slosh station (280.0) is simply the displacement at that point on the rigid beam.

Table A-1. Modal Data

Configuration	Mode	Frequency (rad/sec)	Displacement at Motor Station 111 Y_m (in.)	Slope at Motor Station 111 θ_m (in./in.)	Displacement at Slosh Y_s (in.)	Slope at Sensor Station 136 θ_s (in./in.)	Displacement at Capsule Slosh Station 280 Y_{cs} (in.)
Midcourse start-burn	1	10.07	-0.0608	-5.92×10^{-4}	-0.0424	-5.95×10^{-4}	0.0398
	2	24.97	-0.0259	-4.80×10^{-4}	-0.0011	-4.79×10^{-4}	0.0560
	3	37.50	0.0417	2.54×10^{-4}	0.0338	2.49×10^{-4}	-0.0003
	4	47.13	0.0314	5.43×10^{-4}	0.0146	5.38×10^{-4}	-0.0630
Midcourse burn-out (propellant depleted)	1	10.75	-0.1400	-10.89×10^{-4}	-0.1062	-10.89×10^{-4}	0.0440
	2	25.16	-0.0518	-6.99×10^{-4}	-0.0300	-6.99×10^{-4}	0.0673
	3	39.21	0.1150	6.87×10^{-4}	0.0938	6.78×10^{-4}	0.0016
	4	47.89	0.0849	9.49×10^{-4}	0.0553	9.42×10^{-4}	-0.0779
Orbit trim	1	10.96	-0.1681	-11.20×10^{-4}	-0.1336	-11.20×10^{-4}	
	2	25.76	0.0444	13.75×10^{-4}	0.0128	13.74×10^{-4}	
	3	49.27	0.0676	17.21×10^{-4}	0.0142	17.18×10^{-4}	
	4	399.3	0.0259	5.85×10^{-4}	0.0090	4.22×10^{-4}	

Generalized mass = 1.0 in.-lb-sec^2

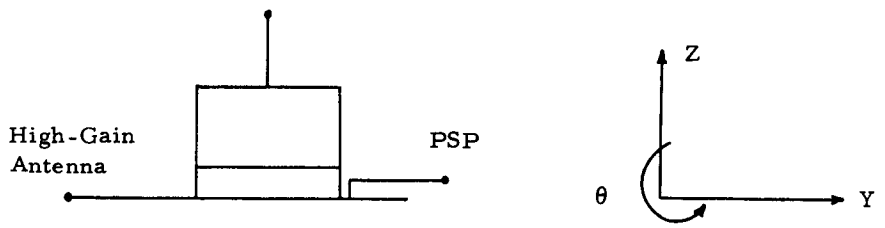

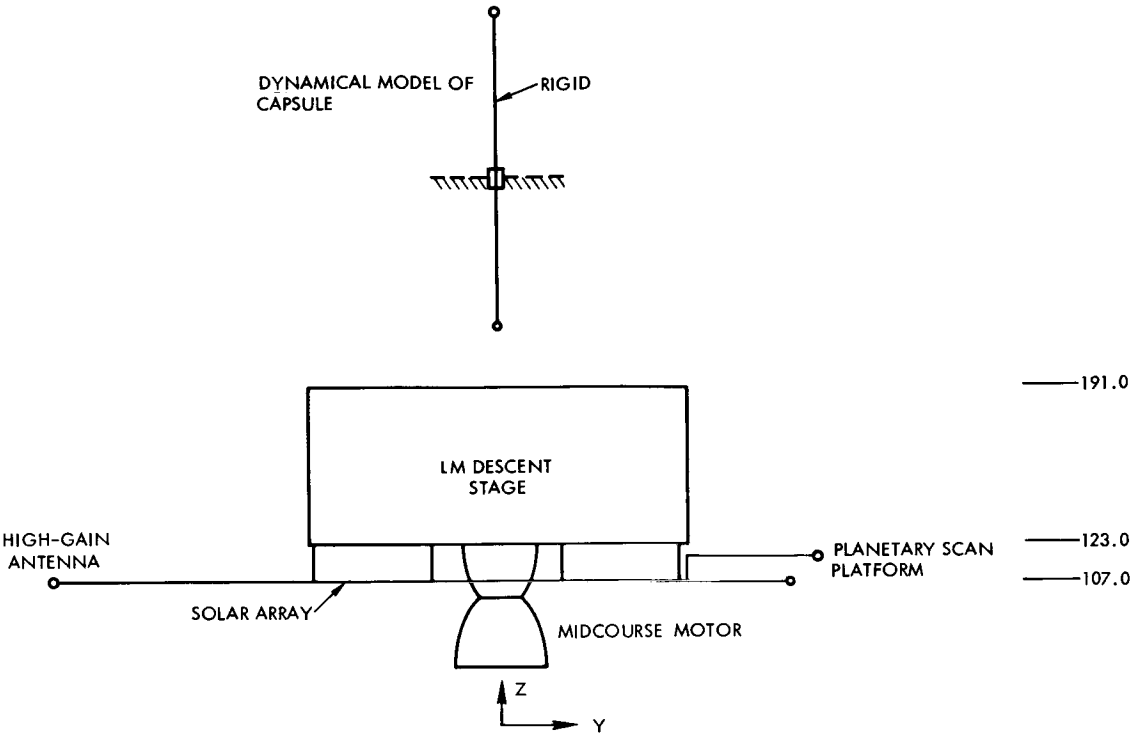

Figure A-1. Schematic of Voyager

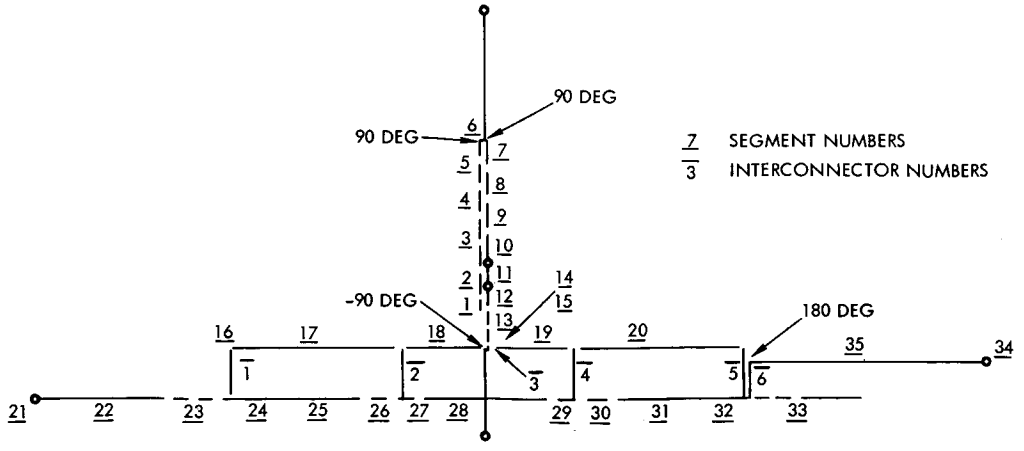

Figure A-2. U-Beam Model of Voyager

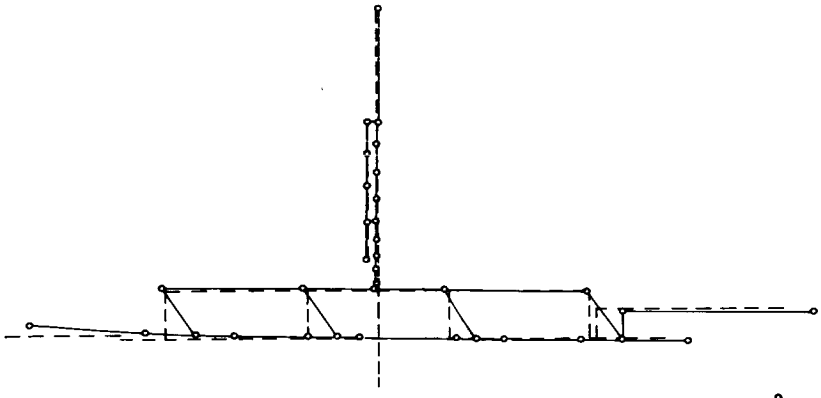

Figure A-3

Voyager Start Mid-course Correction First Mode, 10.07 Rad/Sec

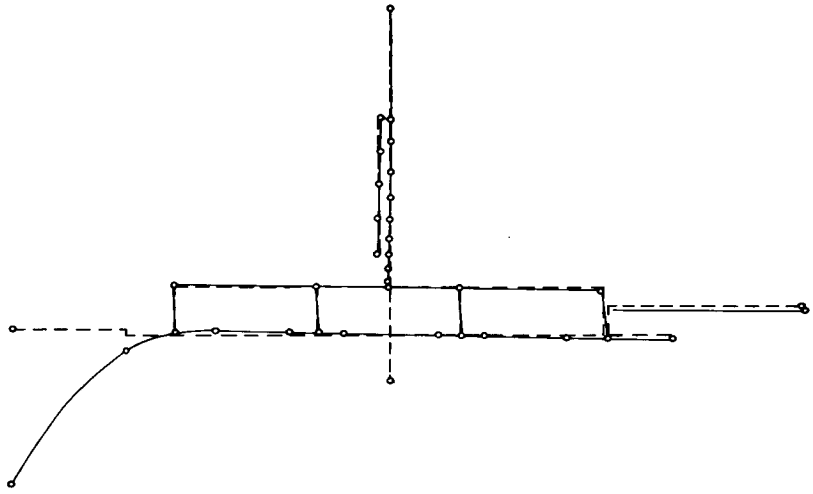

Figure A-4

Voyager Start Mid-course Correction Second Mode, 24.97 Rad/Sec

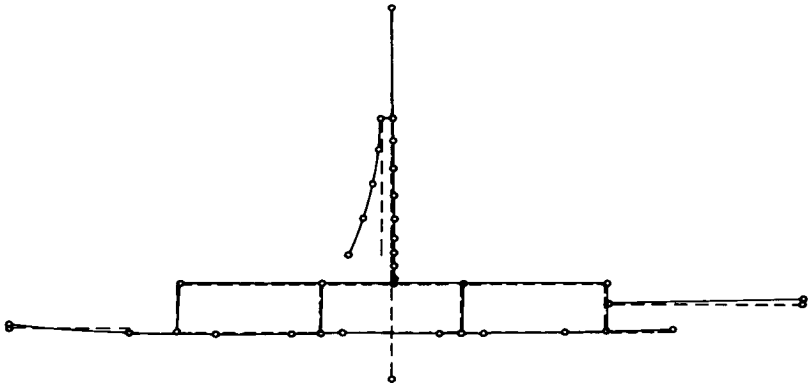

Figure A-5

Voyager Start Mid-course Correction Third Mode, 37.50 Rad/Sec

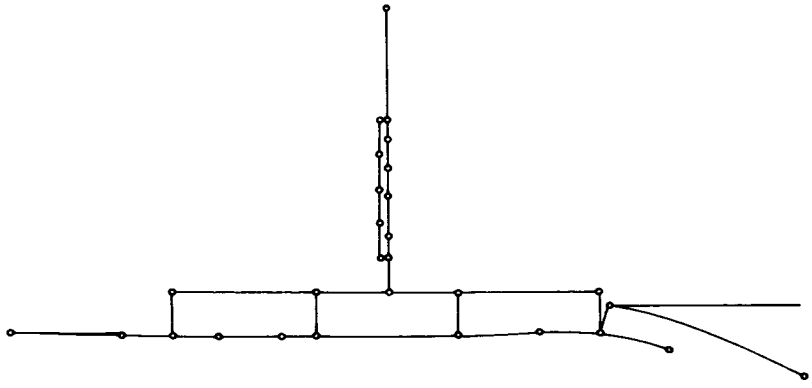

Figure A-6

Voyager Start Mid-course Correction Fourth Mode, 47.13 Rad/Sec

VOYAGER START MID-COURSE CORRECTION 4/24/67

BEAM PROPERTIES

BEAM NO.	DISTRIBUTED MASS MASS/LENGTH (LB-SEC-SQ/IN-SQ)	SHEAR STIFFNESS KAS (LB)	FLEXURAL RIGIDITY EI (LB-IN-SQ)	ROTARY INERTIA RHO-I (LB-SEC-SQ)	AXIAL INERTIA MASS/LENGTH (LB-SEC-SQ/IN-SQ)	AXIAL STIFFNESS EA (LB)	BEAM LENGTH L (IN)
END CONDITION OF FOLLOWING BEAM = FREE							
1	1.96000E 00	1.00000E 12	1.31400E 08	0.	1.96000E 00	1.00000E 12	1.00000E 00
2	1.00000E-08	1.00000E 12	1.31400E 08	0.	1.00000E-06	1.00000E 12	1.36000E 01
3	1.00000E-06	1.00000E 12	1.31400E 08	0.	1.00000E-06	1.00000E 12	1.30000E 01
4	1.00000E-06	1.00000E 12	1.31400E 08	0.	1.00000E-06	1.00000E 12	1.30000E 01
5	1.00000E-06	1.00000E 12	1.31400E 08	0.	1.00000E-06	1.00000E 12	1.30000E 01
6	1.00000E-06	1.00000E 12	1.00000E 12	3.41700E 03	1.00000E-06	1.00000E 12	1.00000E 00
7	1.33000E-01	5.62000E 07	2.07000E 11	2.94000E 02	1.33000E-01	7.61000E 07	8.00000E 00
8	1.06500E-01	5.62000E 07	2.07000E 11	2.68000E 02	1.06500E-01	7.61000E 07	1.40000E 01
9	1.19000E-01	5.62000E 07	2.07000E 11	3.13000E 02	1.19000E-01	7.61000E 07	1.00000E 01
10	1.26000E-01	5.62000E 07	2.07000E 11	3.37000E 02	1.26000E-01	7.61000E 07	1.48000E 01
11	1.25000E-01	5.62000E 07	2.07000E 11	3.76000E 03	1.53200E 01	7.61000E 07	8.20000E 00
12	1.25000E-01	5.62000E 07	2.07000E 11	3.39500E 02	1.25000E-01	7.61000E 07	6.00000E 00
13	1.49000E-01	5.62000E 07	2.07000E 11	3.90000E 02	1.49000E-01	7.61000E 07	6.00000E 00
14	1.75500E-01	5.62000E 07	2.07000E 11	3.86000E 02	1.75500E-01	7.61000E 07	6.00000E 00
15	1.00000E-06	5.62000E 07	2.07000E 11	1.19700E 03	1.00000E-06	7.61000E 07	1.00000E 00
LEFT END OF CONNECTOR NO. 3							
END CONDITION OF PREVIOUS BEAM = FREE							
END CONDITION OF FOLLOWING BEAM = FREE							
16	1.00000E-06	1.00000E 11	1.00000E 13	0.	1.00000E-06	1.00000E 11	0.
LEFT END OF CONNECTOR NO. 1							
17	1.00000E-06	1.00000E 11	1.00000E 13	0.	1.00000E-06	1.00000E 11	5.40000E 01
LEFT END OF CONNECTOR NO. 2							
18	1.00000E-06	1.00000E 11	1.00000E 13	0.	1.00000E-06	1.00000E 11	2.80000E 01
RIGHT END OF CONNECTOR NO. 3							
19	1.00000E-06	1.00000E 11	1.00000E 13	0.	1.00000E-06	1.00000E 11	2.80000E 01
LEFT END OF CONNECTOR NO. 4							
20	1.00000E-06	1.00000E 11	1.00000E 13	0.	1.00000E-06	1.00000E 11	5.40000E 01
LEFT END OF CONNECTOR NO. 5							
END CONDITION OF PREVIOUS BEAM = FREE							
END CONDITION OF FOLLOWING BEAM = FREE							
21	1.00000E-06	5.66000E 06	2.60000E 07	0.	1.00000E-06	3.03000E 07	0.
22	6.60000E-04	5.66000E 06	2.60000E 07	0.	6.60000E-04	3.03000E 07	8.10000E 01
23	1.05000E-02	7.00000E 05	4.15000E 07	0.	1.05000E-02	5.20000E 06	3.00000E 01
RIGHT END OF CONNECTOR NO. 1							
24	1.00400E-02	1.40000E 06	8.30000E 07	0.	1.00400E-02	1.04000E 07	2.20000E 01
25	9.67000E-03	1.40000E 06	8.30000E 07	0.	9.67000E-03	1.04000E 07	2.00000E 01
26	9.24000E-03	1.40000E 06	8.30000E 07	0.	9.24000E-03	1.04000E 07	1.20000E 01

Figure A-7. Input Data

```
RIGHT END OF CONNECTOR NO. 2
  27   1.32000E-02   2.80000E 06   1.66000E 08   0.          1.32000E-02   2.08000E 07   8.00000E 00
  28   7.44000E-03   2.80000E 06   1.66000E 08   0.          7.44000E-03   2.08000E 07   4.00000E 01
  29   1.33000E-02   2.80000E 06   1.66000E 08   0.          1.33000E-02   2.08000E 07   8.00000E 00
RIGHT END OF CONNECTOR NO. 4
  30   1.06000E-02   1.40000E 06   8.30000E 07   0.          1.06000E-02   1.04000E 07   1.20000E 01
  31   8.28000E-03   1.40000E 06   8.30000E 07   0.          8.28000E-03   1.04000E 07   2.00000E 01
  32   8.40000E-03   1.40000E 06   8.30000E 07   0.          8.40000E-03   1.04000E 07   2.20000E 01
RIGHT END OF CONNECTOR NO. 5
RIGHT END OF CONNECTOR NO. 6
  33   7.18000E-03   1.40000E 06   8.30000E 07   0.          7.18000E-03   1.04000E 07   3.80000E 01
END CONDITION OF PREVIOUS BEAM = FREE
END CONDITION OF FOLLOWING BEAM = FREE
  34   1.00000E-06   7.30000E 06   1.10000E 08   0.          1.00000E-06   3.90000E 07   0.
  35   6.90000E-04   7.30000E 06   1.10000E 08   0.          6.90000E-04   3.90000E 07   7.50000E 01
LEFT END OF CONNECTOR NO. 6
END CONDITION OF PREVIOUS BEAM = FREE
*TOTAL WEIGHT = 2.08454E 04 *OUNDS
```

CONNECTOR PROPERTIES

CON. NO..	FLEX1 (L*CU/6EI - L/KAG)	FLEX2 (L*SQ/2EI)	FLEX3 (L/EI)	FLEX4 (L/EA)	FLEX5 (L)
1	3.24000E 00	7.23000E-01	8.50000E-02	1.25000E-05	1.70000E 01
2	-8.95000E-03	1.10200E-07	1.29900E-08	2.40000E-05	1.70000E 01
3	0.	0.	0.	0.	0.
4	-8.95000E-03	1.10200E-07	1.29900E-08	2.40000E-05	1.70000E 01
5	3.24000E 00	7.23000E-01	8.50000E-02	1.25000E-05	1.70000E 01
6	-4.67000E-07	1.54000E-07	3.08000E-08	1.82000E-07	1.00000E 01

CORNERS

BEAM NO.	THETA (DEGREES)
5	9.00000E 01
8	9.00000E 01
15	-9.00000E 01
25	1.80000E 02

ECCENTRIC MASSES

BEAM NO.	MASS (LB-SEC*SQ/IN)	ECCENTRICITY (IN)
6	1.02600E 01	-4.17000E 01
10	1.92000E 01	0.
11	1.01400E 01	0.
18	1.00000E 00	2.85000E 01
21	8.30000E-02	0.
34	1.48900E-01	0.

Figure A-7. Input Data (Continued)

VOYAGER B. O. MID-COURSE CORRECTION (PROPELLANT DEPLETED) 4/24/67

BEAM PROPERTIES

BEAM NO.	DISTRIBUTED MASS MASS/LENGTH (LB-SEC*SQ/IN*SQ)	SHEAR STIFFNESS KAG (LB)	FLEXURAL RIGIDITY EI (LB-IN*SQ)	ROTARY INERTIA RHO-I (LB-SEC*SQ)	AXIAL INERTIA MASS/LENGTH (LB-SEC*SQ/IN*SQ)	AXIAL STIFFNESS EA (LB)	BEAM LENGTH L (IN)
11	1.2[illegible]E-01	5.62000E 07	2.07000E 11	5,10000E 02	1,53200E 01	7,61000E 07	8,20000E 00

TOTAL WEIGHT = 9,87937E 03 POUNDS

ECCENTRIC MASSES

BEAM NO,	MASS (LB-SEC*SQ/IN)	ECCENTRICITY (IN)
10	0.	0.
11	1,00000E 00	0,

Figure A-8. Input Data, Propellant Depleted (Changes from Start Midcourse Correction)

VOYAGER WITHOUT CAPSULE - ORBIT TRIM 4/25/57

BEAM PROPERTIES

BEAM NO.	DISTRIBUTED MASS MASS/LENGTH (LB-SEC**2/IN**2)	SHEAR STIFFNESS KAG (LB)	FLEXURAL RIGIDITY EI (LB-IN**2)	ROTARY INERTIA RHO-I (LB-SEC**2)	AXIAL INERTIA MASS/LENGTH (LB-SEC**2/IN**2)	AXIAL STIFFNESS EA (LB)	BEAM LENGTH L (IN)
END CONDITION OF FOLLOWING BEAM = FREE							
1	1.96000E 00	1.00000E 12	1.31400E 08	0.	1.96000E 00	1.00000E 12	0.
2	1.00000E-06	1.00000E 12	1.31400E 08	0.	1.00000E-06	1.00000E 12	0.
3	1.00000E-06	1.00000E 12	1.31400E 08	0.	1.00000E-06	1.00000E 12	0.
4	1.00000E-06	1.00000E 12	1.31400E 08	0.	1.00000E-06	1.00000E 12	0.
5	1.00000E-06	1.00000E 12	1.31400E 08	0.	1.00000E-06	1.00000E 12	0.
6	1.00000E-06	1.00000E 12	1.00000E 12	3.41700E 03	1.00000E-06	1.00000E 12	0.
11	1.20000E-01	5.62000E 07	2.07000E 11	5.10000E 02	1.53200E 01	7.61000E 07	8.20000E 00

*TOTAL WEIGHT = 5.15754E 03 POUNDS

ECCENTRIC MASSES

BEAM NO.	MASS (LB-SEC**2/IN)	ECCENTRICITY (IN)
6	0.	0.
10	0.	0.
11	1.00000E 00	0.

Figure A-9. Input Data, Orbit Trim (Changes from Start Midcourse Correction)

REFERENCES

A-1. IOC Memo No. 66-3343.3-196, "Cost Estimated for Determining Voyager Spacecraft Elastic Modes," D. H. Mitchell, 8 December 1966

A-2. IOC Memo No. 67-3343.4-76, "User's Manual for UBEAM (AS150A, B)," T. N. Gardner, 1 May 1967